NUMERICAL MODELLING OF THERMO-ACTIVE RETAINING WALLS

A thesis submitted to the Imperial College London in partial fulfilment of the requirements for the degree of Doctor of Philosophy

by

Eleonora Sailer

Department of Civil and Environmental Engineering

Imperial College London

London SW7 2AZ

June 2020

Declaration

The work presented in this thesis was carried out in the Department of Civil and Environmental Engineering at Imperial College London. This thesis is the result of my own work and any quotation from, or description of the work of others is acknowledged herein by reference to the sources, whether published or unpublished. This thesis is not the same as any that I have submitted for any degree, diploma or other qualification at any other university. No part of this thesis has been or is being concurrently submitted for any such degree, diploma or other qualification.

Eleonora Sailer

London, June 2020

Abstract

The exploitation of the energy stored in the ground through geotechnical structures poses new challenges to geotechnical engineers due to effects related to temperature changes that have to be considered in the design of these structures. Underground structures, such as piles, retaining walls or tunnel linings, can be equipped with heat exchanger pipes through which thermal energy is exchanged with the ground to provide low-carbon space heating and cooling. The exchange of energy imposes temperature changes to the structure and the ground, which can induce additional stresses and strains within the structures, as well as leading to thermo-hydro-mechanical (THM) interactions within the ground. The research presented in this thesis focuses on the analysis of these phenomena in relation to the utilisation of retaining walls as heat exchangers, also termed thermo-active retaining walls. The aim of this research is to assess the impact of temperature variations on the behaviour of thermo-active retaining walls and the surrounding soil and to provide efficient modelling approaches for their design.

In recent years, the Imperial College Finite Element Program (ICEFP) has been upgraded to include a fully coupled THM formulation for saturated soils as well as special types of elements for the simulation of the heat exchanger pipes, allowing the simulation of complex boundary value problems including thermo-active structures. Firstly, the phenomena taking place within the soil when temperature changes are applied are analysed in detail to provide the basis for the assessment and interpretation of the performance of thermo-active retaining walls. Subsequently, modelling approaches for the accurate simulation of the pipe-structure-soil interaction within three-dimensional analyses of thermo-active retaining walls are established and validated against field data. The findings are employed to develop simple and computationally efficient modelling approaches to simulate thermo-active walls in two-dimensional analyses, focussing both on their energy efficiency and structural behaviour.

Acknowledgements

Foremost, I would like to express my gratitude to my supervisors: Dr David Taborda, for his constant inspiration, enthusiasm and endless discussions which helped me develop many of the ideas in this thesis, and Prof. Lidija Zdravković, for her support, positive feedback and encouragement during these years.

This research was funded by the Department of Civil and Environmental Engineering of Imperial College London, and this financial support is greatly appreciated. I am also very thankful for the support received by the Faculty of Engineering Dean's Fund and for the indescribable kindness and generosity of the City and Guilds College Association. In particular, I would like to express my gratitude to Mr Chris Lumb and Prof. Robert Schroter, who made a very difficult period much easier. I also thank Prof. Catherine O'Sullivan, Ms Fionnuala Ni Dhonnabhain and Ms Sarah Willis for their advice and comfort during difficult times.

This research and the years spent in the ICFEP room wouldn't have been the same if it was not for Dr. Wenjie Cui and Dr Klementyna Gawecka, who shared with me their knowledge and (lots) of beers in the pub. Furthermore, I am also very grateful to Prof. David Potts, for many constructive comments, for sharing his invaluable experience and his passion for research. Lastly, I thank Ms Sara Bandera for the inspirations during uncountable coffee and lunch breaks and for being a special friend.

This work would not have been possible without the support of my family and friends. I would like to thank my brother Sebi, for his constant encouragement and interest towards my work throughout these years. I have to express my deepest gratitude to Memi and Sandro, who supported me like parents when I needed it the most. Lastly, I would have probably never undertaken this journey, let alone arrived to this point, if it wasn't for Dimitris. I cannot put into words how much his presence and love have helped me during these years.

Table of Contents

List of Figures

List of Tables

List of Symbols

Roman alphabet

A	Area
A_p	Cross-sectional area of heat exchanger pipe
A_p^{3D}	Cross-sectional area of heat exchanger pipe in 3D analysis
A_p^{2D}	Cross-sectional area of heat exchanger pipe in 2D analysis
$\overline{A_p^{3D}}$	Cross-sectional area of heat exchanger pipe per metre width in 3D analysis
$\overline{A_p^{2D}}$	Cross-sectional area of heat exchanger pipe per metre width in 2D analysis
A_T	Amplitude of temperature variation
A_{wall}	Area of wall in contact with ground
B	Width of wall panel
c'	Cohesion
C_p	Specific heat capacity
C_v	Volumetric heat capacity
c_v	Coefficient of consolidation
D	Diameter
d	Drainage path length; distance
d_e	Depth of excavation
D_r	Relative density
E	Young's modulus
E_d	Deviatoric strain invariant
E_{tot}	Total energy provided by geothermal system
E_Ω	Energy per unit volume
F	Force
$f(s)$	Function for calculation of Petrov-Galerkin weighting function
F_o	Fourier number
g	Specific gravity
$g(s)$	Function for calculation of Petrov-Galerkin weighting function
G_{max}	Maximum shear modulus

G_{min}	Minimum shear modulus
G_{ref}	Maximum shear modulus at a reference mean effective stress
Gr	Grashof number
G_{tan}	Tangent shear modulus
H	Thickness of wall
h	Convective heat transfer coefficient
h_e	Height of element
J	Deviatoric stress
$\|J\|$	Jacobian determinant
k	Permeability
k_0	Permeability model parameter
K_0	Coefficient of earth pressure at rest
k_{emb}	Permeability in embedded section of wall
K_f	Bulk modulus of fluid
K_{max}	Maximum bulk modulus of soil skeleton
K_{min}	Minimum bulk modulus of soil skeleton
K_{ref}	Maximum bulk modulus at a reference mean effective stress
K_s	Bulk modulus of soil skeleton
K_{tan}	Tangent bulk modulus
L	Length
L_c	Characteristic length
L_{exp}	Exposed length of wall
L_{emb}	Embedded length of wall
L_{wall}	Length of wall
M_i	Metric to quantify improvement of mesh refinement
m_G, m_k	Parameters defining the dependence of elastic stiffness on mean effective stress
n	Porosity
n_p	Number of vertical pipe segments
Nu	Nusselt number
P	Axial force

p_c	Pre-consolidation pressure
Pe	Péclet number
Pr	Prandtl number
p'	Mean effective stress
p'_{ref}	Reference mean effective stress
q	Heat flux
q_A	Heat flux per unit area
q_B	Heat flux per unit width
q_{cond}	Heat flux by conduction
q_{conv}	Heat flux by convection
q_e	Heat flux ratio
q_{emb}	Heat flux per unit area within embedded section of wall
q_{exp}	Heat flux per unit area within exposed section of wall
q_L	Heat flux per unit length
Q_T	Heat flux per unit volume
Q_w	Water flow rate
Q^f	Pore fluid source or sink
Q^T	Heat source or sink
Q_w^{3D}	Fluid flow rate in 3D analysis
Q_w^{2D}	Fluid flow rate in 2D analysis
R	Degree of heat transfer
r	Radius
Ra	Rayleigh number
Re	Reynolds number
$R_{G,min}$	Minimum normalised value of G_{tan}
$R_{K,min}$	Minimum normalised value of K_{tan}
s	Natural coordinate
s_{G1}, s_{G2}	Shear stiffness degradation parameter
s_{K1}, s_{K2}	Bulk stiffness degradation parameter
S_r	Degree of saturation

S_s	Specific storage
T	Temperature
t	Time; natural coordinate
$\bar{T}$	Average temperature
$\bar{T}_{emb}$	Average temperature of embedded section of wall
$\bar{T}_{exp}$	Average temperature of exposed section of wall
T_0	Initial temperature
T_∞	Ambient fluid temperature
T_b	Temperature at boundary
t_c	Duration of a full cycle of temeprature variation
T_{exp}	Temperature within heat exchanger pipes at interface between exposed and embedded section of wall
$T_{exp,in}$	Temperature within inlet branch of heat exchanger pipes at interface between exposed and embedded section of wall
$T_{exp,out}$	Temperature within outlet branch of heat exchanger pipes at interface between exposed and embedded section of wall
$T_{i,2D}$	Equivalent time-dependent temperature to be applied as a boundary condition in 2D
T_{in}	Inlet temperature at heat exchanger pipes
$T_{in,2D}$	Inlet temperature at heat exchanger pipes in 2D analysis
$T_{in,3D}$	Inlet temperature at heat exchanger pipes in 3D analysis
$T_{in,2D,CT,E}$	Inlet temperature at heat exchanger pipes in 2D analysis with constant temperature along exposed face computed with correction factor for transferred energy
$T_{in,2D,CT,HF}$	Inlet temperature at heat exchanger pipes in 2D analysis with constant temperature along exposed face computed with correction factor for long-term heat flux
$T_{in,2D,NF,E}$	Inlet temperature at heat exchanger pipes in 2D analysis with insulated boundary along exposed face computed with correction factor for transferred energy
T_{out}	Outlet temperature at heat exchanger pipes
t_p	Thickness of heat exchanger pipe in 2D analysis
T_r	Reference temperature
T_s	Body surface temperature
u	Pore water pressure; natural coordinate

u^*	Dimensionless parameter for evaluation of excess pore water pressures in thermo-hydro-mechanical analyses
u_e	Excess pore water pressure
V	Volume
v	Water flow velocity
$\{v_f\}$	Vector of seepage velocity
x	Geomertic coordinate
X	Correction factor for calculation of inlet temperature in 2D analysis with constant temperature along exposed face
y	Geomertic coordinate
Y	Correction factor for calculation of inlet temperature in 2D analysis for transferred energy
z	Geomertic coordinate

Greek alphabet

α	Coefficient of thermal expansion
α_H	Hydraulic diffusivity
α_{PG}	Petrov-Galerkin weighting factor
α_s	Coefficient of thermal expansion of soil
α_T	Thermal diffusivity
α_{TH}	Dimensionless parameter – ratio between thermal and hydraulic diffusivity
α_w	Coefficient of thermal expansion of water
β	Permeability model parameter
β_{PG1},β_{PG2}	Petrov-Galerkin weighting factors
γ	Bulk unit weight; shear strain
ΔL	Elongation
ΔL_{free}	Free elongation
ΔT	Change in temperature
Δt_{cr}	Critial time step
ΔT_e	Distribution of temperature change at a given time
ΔT_f	Final distribution of temperature change
ΔT_{in}	Temperature difference at pipe inlet

$\Delta T_{in,2D}$	Temperature difference at pipe inlet in 2D analysis
$\Delta T_{in,3D}$	Temperature difference at pipe inlet in 3D analysis
ΔT_p	Temperature differential between pipe inlet and outlet
Δu	Change in pore water pressure
Δu_{AN}	Excess pore water pressure calculated using analytical solution in undrained conditions
Δu_{FE}	Excess pore water pressure computed in FE analysis
Δu_{max}	Maximum excess pore water pressure calculated during an analysis
$\Delta u_{R,x(\Delta T=0°C)}$	Excess pore water pressure recorded at a given value of R at a distance x from the heat source where change in temperature is equal to 0°C
$\{\Delta\sigma_f\}$	Vector of incremental pore water pressure
ε	Normal strain
ε_{tot}	Total strain
ε_{mech}	Mechanical strain
ε_{th}	Thermal strain
ε_{vol}	Volumetric strain invariant
$\varepsilon_{vol,tot}$	Total volumetric strain
$\varepsilon_{vol,mech}$	Mechanical volumetric strain
$\varepsilon_{vol,th}$	Thermal volumetric strain
$\varepsilon_{th-restrained}$	Restrained thermal axial strain
$\varepsilon_{th-free}$	Free thermal axial strain
$\varepsilon_{th-free-pile}$	Free thermal axial strain for thermo-active piles
$\varepsilon_{free-wall}$	Free axial strain for thermo-active walls
ε_{obs}	Observed axial strain
$\eta_1, \eta_2, \eta_3, \eta_4, \eta_5, \eta_6$	Constants for calculation of correction factor Y
θ	Time-marching factor
λ	Thermal conductivity
$\bar{\lambda}$	Weighted average thermal conductivity
λ_{ref}	Reference thermal conductivity
μ	dynamic viscosity
ν	Poisson's ratio
$\xi_1, \xi_2, \xi_3, \xi_4$	Constants for calculation of correction factor X

ρ	Density
σ	Stress
σ_a	Axial stress
σ_{T_o}	Stress at ambient temperature
σ'	Effective stress
Φ_T	Heat content per unit volume
φ'	Angle of shearing resistance
ψ'	Angle of dilation
ω	Dimensionless parameter for estimation of excess pore water pressures ahead of changes in temperature

Subscripts

$2D$	Two-dimensional
$3D$	Three-dimensional
a	Air
a	Air
B	Quantity per unit width
c	Concrete
el	Element
emb	Embedded section of wall
exp	Exposed section of wall
f	Fluid
in	Inlet
L	quantity per unit length
$mech$	Mechanical
out	Outlet
TEM	Thermally enhanced material
$TEM - wall$	Thermally enhanced material including effect of plastic pipe wall
th	Thermal
tot	Total
s	Soil

$sect$	Section
vol	Volumetric
w	Water
$wall$	Wall
x	Component of quantity along x-axis
y	Component of quantity along y-axis
z	Component of quantity along z-axis

Abbreviations and acronyms

$1D$	One-dimensional
$2D$	Two-dimensional
$3D$	Three-dimensional
BC	Boundary condition
BHE	Borehole heat exchanger
COP	Coefficient of performance
CPT	Cone penetration test
CT	Constant temperaure
DOF	Degrees of freedom
EHE	Environmental heat exchange
FE	Finite element
HF	Heat flux
HM	Hydro-mechanical
$HDPE$	High density polyethylene
HEP	Heat exchanger pipe
$GSES$	Ground source energy system
$GSHP$	Ground source heat pump
HP	Heat Pump
$ICFEP$	Imperial College Finite Element Program
IOM	Intermittent operation mode
$MA1$, $MA2$	Modelling approach 1, modelling approach 2

NF	No heat flux
PG	Petrov-Galerkin
$T-CPT$	Thermal cone penetration test
TEM	Thermally enhanced material
TH	Thermo-hyraulic
THM	Thermo-hydro-mechanical
TM	Thermo-mechanical
TPT	Thermal performance test
TRT	Thermal response test

Chapter 1
Introduction

1.1 Background

The constant increase in energy demand, as well as stricter sustainability targets which aim at reducing the carbon-intensity of energy production, have led in the past decades to the development of new energy technologies. The heat stored in the ground is regarded as one possible source of sustainable, low-carbon energy, if adequately managed. It has the advantage of not requiring specific geological conditions (as the case of high-enthalpy geothermal resources) and is relatively unaffected by climatic conditions. In particular, shallow geothermal energy (i.e. using ground as a source or heat sink for depths <300m (Banks, 2012)), can be used for renewable and cost-effective space heating and cooling, thus contributing to the decarbonisation of the energy consumed by residential and commercial buildings, which are currently a major source of carbon emissions. Indeed, in the UK, about 25% of the final energy is consumed for space heating and domestic hot water, accounting for 15% of CO_2 emissions (Committee on Climate Change, 2019). The technology developed to explore these resources is generally designated as Ground Source Energy Systems (GSES) and can be classified in a simplified manner according to whether the energy is exchanged directly with the groundwater (open-loop) or through pipes in contact with the ground (closed-loop). In the latter, the operating principle consists of circulating a geothermal fluid through the heat exchanger pipes at a temperature lower than that of the ground in order to extract energy and provide heating to the building, with the opposite being the case for heat injection associated to the provision of cooling. The form in which the heat exchanger pipes are installed provides a further division in the classification of closed-loop GSES, as they can be installed horizontally in trenches ("horizontal closed-loop GSES" (Banks, 2012; Sailer, 2014)), vertically within boreholes ("borehole heat exchangers" (Banks, 2012; Sailer, 2014)) or embedded into

the concrete used in geotechnical structures ("thermo-active structures", Laloui & Di Donna, 2013). This thesis focuses only on the latter type, where the GSES involve underground structures, such as tunnel linings, foundation piles or retaining walls, which are equipped with heat exchanger pipes. Therefore, they serve a double purpose of providing both stability and energy to buildings and are often economically more advantageous than systems built for the single purpose of heat exchange, such as borehole heat exchangers (BHE). However, any exchange of heat will necessarily lead to changes in temperature of both the thermo-active structure and the surrounding soil. Clearly, this will induce additional loads within the structures as well as the transient development of ground movements arising from the complex and highly coupled thermo-hydro-mechanical (THM) behaviour of soil. Given the many uncertainties in the design of thermo-active structures and concerns regarding their safe use, numerous field and numerical studies have been carried out in the last decade, focusing mainly on thermo-active piles. For this type of structure, a simplified framework for understanding their behaviour when subjected to thermal loads has been developed based on theoretical considerations and subsequently validated using field observations (Bourne-Webb et al., 2009; Amatya et al., 2012; Bourne-Webb et al., 2013b).

Conversely, thermo-active retaining walls, which are the focus of this thesis, have been the subject of limited studies, especially regarding their thermo-mechanical behaviour, both in terms of field work (only one published work by Brandl (2006)) and numerical studies. Consequently, the design and operation of these structures remain uncertain, as they behave in a very different manner from piles given their more complex geometry and environmental interactions, since they are not fully surrounded by soil. Furthermore, the presence of the heat exchanger pipes, which represent discrete sources of heat, implies that these problems are inherently three-dimensional (3D), with temperatures varying both along its width and, more marginally, in the vertical direction. However, the assessment of these problems through numerical tools in 3D is computationally very expensive. Hence, modelling approaches to enable the simulation of thermo-active retaining walls in two-dimensional (2D) analyses that would replicate the observed behaviour in 3D are required. These may not be easily established, since, as observed for the simulation of fields of BHE (Sailer et al., 2018b), corrections are required to model accurately the temperature field developing in a 3D problem using 2D analyses.

The main aim of this research is to investigate in detail the thermal and thermo-mechanical behaviour of thermo-active retaining walls through numerical analyses, thus assessing both their energy performance and structural response (in terms of stability and serviceability) when subjected to changes in temperature. This is to be accomplished by providing sound modelling approaches that enable the full simulation of the pipe-structure-soil interaction as well as interpretative frameworks to improve the understanding of these complex problems. The analyses carried out throughout this research project are performed using the Imperial College Finite Element Program (ICFEP, Potts & Zdravković, 1999), which is capable of modelling fully coupled THM problems in geotechnical engineering (Cui et al.,

2018a), including also special types of structural elements which enable the explicit simulation of heat exchanger pipes (Gawecka et al., 2018; Gawecka et al., 2020).

1.2 Scope of research

The lack of field and laboratory data characterising the thermo-mechanical behaviour of thermo-active retaining walls as well as the incomplete set of numerical studies found in the literature highlights the need for further investigation into this topic. Given the numerical nature of this research project (i.e. field and laboratory tests are not included), the scope of this thesis includes the development and assessment of modelling procedures for thermo-active retaining walls using Finite Element (FE) analyses and the detailed characterisation of the mechanisms occurring in the structure and surrounding soil upon changes in temperature. This is to be accomplished by performing increasingly complex analyses, such that the effects of thermal loading on thermo-active retaining walls and the surrounding soil can be fully understood and considered in the safe and economic design of these structures.

The aims of this research include:

1) Development of an interpretative framework of the transient THM behaviour of thermo-active retaining walls by evaluating the origin and development of the THM interactions taking place within the soil. This is achieved by formulating simplified modelling approaches in order to assess the contributions of the different components of the THM formulation and by establishing analytical expressions and dimensionless parameters that aid in interpreting the observed phenomena;

2) Formulation of accurate modelling approaches for thermo-active retaining walls using 3D analyses that enable the reproduction of measured field data (e.g. Xia et al., 2012) and performing a detailed assessment of the observed behaviour. In particular, 3D effects in terms of temperature distributions and their implication on the heat transfer and distribution of forces are evaluated, with particular emphasis on the simulated interaction between the wall and the environment to which it is exposed;

3) Development of new modelling approaches to simulate these problems in 2D analyses, with the purpose of reducing the computational effort required when simulating thermo-active retaining walls. The modelling approaches proposed in this thesis aim at reproducing the thermal or thermo-mechanical behaviour observed in 3D and to provide simpler and more efficient design tools to engineering practitioners;

4) Assessment of the impact of varying problem parameters on the thermal performance and structural response of thermo-active retaining walls. In particular, the effect of different

parameters, such as the properties of soil and structure and the geometric configuration of the problem, on the development of heat transfer mechanisms, the thermo-mechanical behaviour and the development of THM interactions are analysed;

5) Evaluation of the long-term behaviour under various scenarios of cyclic thermal loading, both in terms of thermal performance and thermo-mechanical behaviour, thus aiming at identifying the effect of multiple periods of heating and cooling on the response of a thermo-active retaining wall in order to provide design considerations in terms of energy efficiency and structural safety.

1.3 Thesis outline

Chapter 2 provides background information to this research project. In the first part of the chapter, an overview of the context of thermo-active structures, the principles of heat transfer and thermo-mechanical material properties, the non-isothermal soil behaviour and thermal and thermo-mechanical design aspects of thermo-active structures are presented. Subsequently, the capabilities of ICFEP for simulating THM coupled problems and details of current modelling practices, resulting from previous research carried out with ICFEP, are outlined. The last part of the chapter includes an extensive review regarding design and modelling aspects of thermo-active retaining walls, summarising the research carried out to date in terms of field, laboratory and numerical studies.

Chapter 3 involves preliminary studies of a hypothetical thermo-active retaining wall installed in London where the heat exchange is simulated by a simple boundary condition applied for a long period of time, with the aim of providing insight into the fundamental mechanisms governing the transient soil-structure interaction problem resulting from the applied changes in temperature. For this purpose, simple one-dimensional (1D) problems are firstly analysed to characterise the different mechanisms taking place in the soil and the effect of ground parameters on the THM interactions. Subsequently, different modelling approaches are adopted to quantify the contribution of the identified THM interactions on the transient response of the thermo-active retaining wall and to provide the basis for an interpretative framework based on dimensionless parameters to ensure its applicability to ground conditions different from those used in this thesis. Lastly, the influence of varying ground properties on the thermo-mechanical response of the analysed retaining wall is assessed.

In *Chapter 4* the mechanisms governing the transfer of heat from the heat exchanger pipes to the structure and surrounding soil are analysed in detail by performing 3D analyses with inclusion of one-dimensional elements simulating the heat exchanger pipes and the transient advective-conductive heat transfer taking place within them. Two different modelling approaches to simulate the heat exchange – one which consists of prescribing the temperature of the geothermal fluid circulating within the heat exchanger pipes and one which mimics the operation patterns associated with the presence of heat

pumps – are assessed and validated against the monitoring data of a thermal performance test (Xia et al., 2012). Subsequently, the effect of the simulated boundary condition along the exposed face of the wall on the heat transfer and thermal performance is investigated.

Chapter 5 explores the long-term thermal performance of thermo-active retaining walls. Since modelling thermo-active retaining walls by means of 3D analyses is computationally expensive, in the first part of the chapter approximations to model this type of problems through 2D plane-strain analyses, which include one-dimensional heat exchanger pipe elements, are proposed. The aim is to enable the estimation of the long-term energy efficiency of thermo-active retaining walls and to reduce the computational effort. Thus, the approximations were determined by matching the computed thermal performance (in terms of heat flux or transferred energy) between that obtained in 3D and 2D analyses. Subsequently, an extensive study on the effect of geometric and thermal parameters on the thermal performance of thermo-active retaining walls is carried out. Lastly, the long-term energy efficiency for different scenarios including multiple cycles of heating and cooling is assessed.

Chapter 6 expands the concepts introduced in Chapter 4 and Chapter 5 to include the characterisation of the thermo-mechanical behaviour of thermo-active walls. In the first part of the chapter, 3D analyses employing the modelling approach validated in Chapter 4 are carried out and the results are assessed employing the interpretative framework established in Chapter 3. Furthermore, the effect on the response of the wall of the simulated condition along its exposed face, the geometric and thermal parameters and the modelling approach adopted in 3D are investigated. In addition, 3D effects on the distribution of forces within the wall panel are evaluated. Subsequently, a new method for simulating the transient thermo-mechanical response of thermo-active retaining walls in 2D analyses, which differs from that outlined in the previous chapter as it avoids the use of special elements for modelling in an explicit manner the presence of heat exchanger pipes, is proposed and validated against numerous 3D THM analyses. In addition, an analytical procedure to estimate the variation in axial forces in the out-of-plane direction is developed and successfully validated. In the last part of the chapter, the long-term thermo-mechanical response of a thermo-active retaining wall subjected to various scenarios of cyclic thermal loading is investigated.

In *Chapter 7* the main conclusions and results of this research are summarised and recommendations for further research are provided.

Chapter 2
Thermo-active structures

2.1 Introduction

This chapter presents fundamental concepts and information required to comprehend the background to this research project. In Section 2.2, an overview on the use of thermo-active structures is provided. Furthermore, the basic principles of heat transfer, the non-isothermal soil response, the criteria for the thermal design and the observed thermo-mechanical behaviour of thermo-active structures, mainly in the context of thermo-active piles, are explained. Section 2.3 outlines the existing modelling capabilities of the Imperial College Finite Element Program (ICFEP, Potts & Zdravković, 1999), which is used throughout this research project. In particular, the details of the thermo-hydro-mechanical (THM) formulation, the thermal boundary conditions, structural elements employed in THM analyses and examples of numerical challenges encountered when simulating fully coupled THM problems are provided. Lastly, in Section 2.4, an extensive review of the available literature regarding thermo-active walls, which are the focus of this research, is presented. This part includes information on current installation practice and characterisation of the thermal environment to which a wall is exposed. Furthermore, the relevant field, laboratory and numerical studies, focussing either on the thermal performance or on the thermo-mechanical behaviour of thermo-active walls, are discussed.

2.2 Preliminaries

In this section, the uses and roles of thermo-active structures are explained and the development of their application in the UK is assessed. Subsequently, details about the heat transfer phenomena occurring within the components of a thermo-active structure and the thermal and thermo-mechanical properties required to characterise THM phenomena are outlined. Insights into the non-isothermal soil behaviour

relevant to this research are then provided. Lastly, the evaluation of the thermal performance and a simplified framework used to understand the behaviour of thermo-active structures are discussed.

2.2.1 Thermo-active structures

Thermo-active structures, also called geothermal structures or energy geostructures, are underground structures, such as piles, retaining walls and tunnel linings, employed to produce or dissipate thermal energy by exchanging heat with the ground. As such, they are categorised as ground source energy systems (GSES), which are low enthalpy systems that deal with temperatures of less than 40°C and usually reach shallow depths (up to 300 m) (Banks, 2012), which distinguishes them from high enthalpy systems, where energy is produced with higher temperatures and typically at greater depths.

Thermo-active structures are classified as closed loop systems, which exchange heat directly with the ground. This is opposed to open loop systems, where energy is exchanged with ground water through extraction and injection wells. GSESs take advantage of the temperature of the ground, which, at their installation depths (in general for thermo-active structures, these may vary between 25.0 m and 50.0 m), can generally be assumed to be constant and equal to the average annual air temperature (Busby et al., 2009), i.e. around 10-15°C in temperate climates like those in Europe (it should be noted, however, that the temperature within the ground at shallow depths, i.e.10-15 m, is influenced by daily or seasonal fluctuations). Thus, as depicted in Figure 2-1, the ground is used as a heat source in the winter (heating mode) and a heat sink in the summer (cooling mode), where the air temperatures are respectively lower and higher than those of the ground.

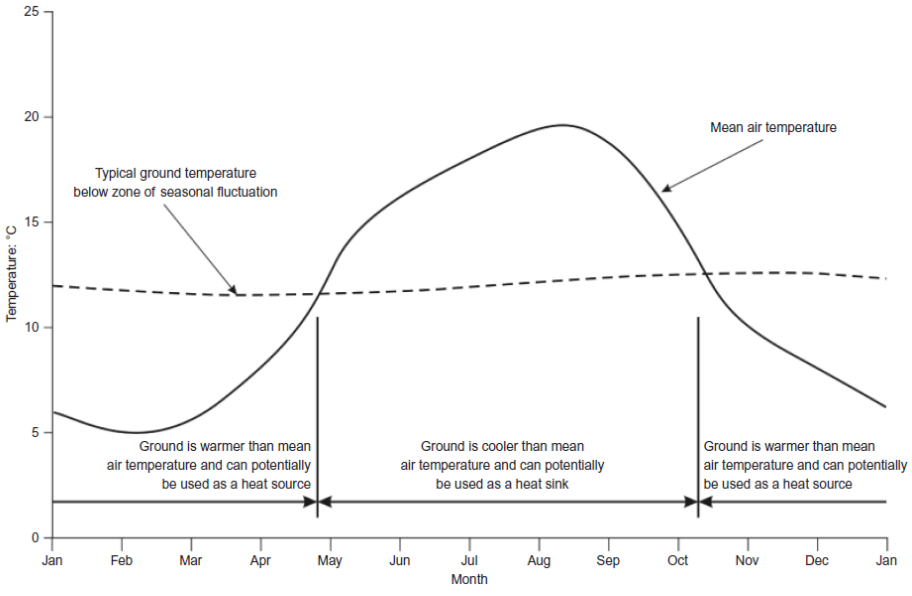

Figure 2-1: Relationship between surface air and ground temperature (Preene & Powrie, 2009)

Figure 2-2 displays a schematic representation of a GSES system. This is composed of a ground heat exchanger, a heat pump (HP) and the heat distribution system. The ground heat exchanger, in the particular application to thermo-active structures, is formed by a concrete structure (e.g. a pile, wall or

tunnel lining), within which heat exchanger pipes are embedded. A fluid (either water or an antifreeze solution) is circulated within the pipes at a certain flow rate and temperature. The fluid temperature is either higher or lower than that of the ground, to enable the injection or extraction of energy, respectively. Since the fluid temperatures are usually too low to be used directly to heat or cool a building, the heat exchanger pipes are connected to a heat pump. The function of the heat pump is to alter the fluid temperature to usable levels for space heating and cooling through an input of electrical energy. The system's efficiency is evaluated by the Coefficient of Performance (COP) of the heat pump, which is described by the following relationship:

$$COP = \frac{Energy\ output\ (kW)}{Energy\ input\ for\ operation\ (kW)} \tag{2-1}$$

Equation (2-1) implies that, for example, to achieve a COP of 4.0, 4.0 kW of thermal energy are produced with 1.0 kW of electrical input. Therefore, GSESs are considered to be a sustainable energy source, since, for a given amount of energy input, they provide more heating or cooling output.

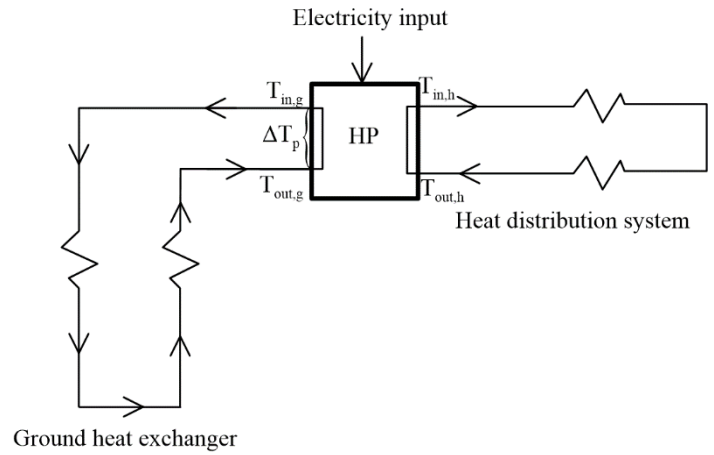

Figure 2-2: Schematic representation of the components of a Ground Source Energy System

The main purpose of thermo-active structures remains that of guaranteeing stability and thus they would be required even without the role of delivering energy. As such, their use is often more economical than that of systems built for the sole purpose of heat exchange (e.g. borehole heat exchanger, BHE), given that the main cost of these systems is related to drilling operations (Kavanaugh & Rafferty, 2014). Since thermo-active structures have a double purpose of providing both structural safety and energy to buildings, these two aspects are of concern during the design stage, thus requiring the collaboration between engineers from different disciplines, as summarised in Bourne-Webb et al. (2013a). Furthermore, as the heat exchange involves changes in ground temperature, the long-term sustainability of these systems needs to be ensured, by avoiding permanent temperature changes, guaranteeing an efficient long-term operation and preserving the ground water ecology (Haehnlein et al., 2010). Consequently, in some countries, the implementation of GSESs implies the involvement of various environmental agencies during project approval stage (ASHRAE, 2015).

While closed loop systems, in the form of either vertical systems or horizontal systems, have been in use since the 1950s, the introduction of absorber pipes within geotechnical structures begun only during the 1980s, where they were first embedded within foundation slabs, then in driven precast piles and later within bored piles and diaphragm walls (Adam & Markiewicz, 2009). According to Brandl (2006), thermo-active diaphragm walls were first utilised as heat exchangers in 1996 in Austria. In the UK, the first application to walls is reported by Suckling & Smith (2002), who describe the installation of a piled wall constructed in 2001, while the first known thermo-active diaphragm wall was installed in 2010 (Amis et al., 2010).

The use of ground source energy systems (i.e. all types of shallow geothermal systems) within the UK has increased noticeably in the last years, with an increase of 10.4% from 2017 to 2018 (Sanner, 2019). This is due to stricter sustainability targets imposed both by the EU (e.g. the European Union RES Directive (European Commission, 2009)) and the UK (e.g. the 2008 UK climate change act (UK Parliament, 2008)) to reduce CO_2 emissions by delivering renewable and sustainable heat (Curtis et al., 2019). According to Sani et al. (2019b), the use of thermo-active piles in the UK started in 2000 and, as shown in Figure 2-3, in 2010 more than 4000 energy piles have been installed, which increased to about 6000 in 2016. Sani et al. (2019b) also report that, as of 2016, a total accumulated saving of about 7545 t of CO_2 was achieved from the use of energy piles, indicating a clear benefit from the deployment of this technology.

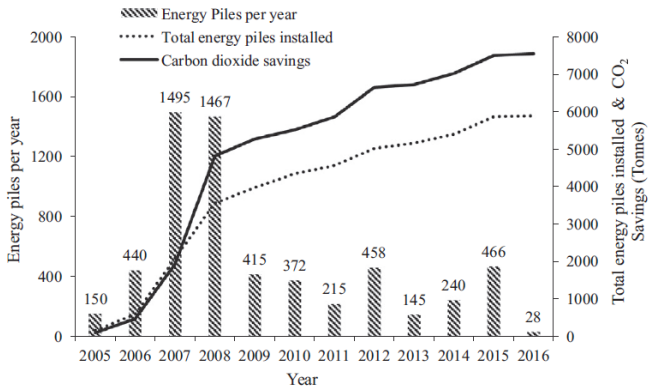

Figure 2-3: Number of thermo-active piles installed in the UK and the resultant savings in CO_2 (Sani et al., 2019b)

It should be noted that the number of energy piles installed in the UK is smaller than in other central European countries, e.g. in Austria, where Brandl (2013) reports that more than 6000 piles are installed each year. According to Sani et al. (2019b), the main issues related with the implementation of geothermal piles (which can be generalised to all types of thermo-active structures) in the UK are: (1) concerns regarding installation of pipes and their integrity, (2) shortage of skilled experts and (3) understanding the roles between different parties involved in the design and installation. As noted by numerous researchers, e.g. Amis & Loveridge (2014), Abuel-Naga et al. (2015), Bourne-Webb & Bodas Freitas (2020), the reduced number of installations of thermo-active structures in the UK when

compared to other countries (such as Austria, Switzerland and Germany) is due to concerns related to the impact of temperature changes on the structural and geotechnical performance of the structure, with clients requiring a sound assurance of its successful operation under both thermal and mechanical perspectives. Sani et al. (2019b) state that the current design practice relies on a conservative approach by increasing the safety factors, which however may unnecessarily increase the costs of the structure, thus reducing its attractiveness. Indeed, currently there are no standards for the design of thermo-active structures. For thermo-active piles, guidelines on best practice for installation and planning are available, such as those published by GSHP Association (2012) in the UK or by SIA (2005) in Switzerland, however the design recommendations are often limited or the specifications are site specific and thus not generally applicable. Furthermore, as will be detailed in Section 2.4, the use of thermo-active walls remains to date limited and there is a lack of field monitoring data that would allow their thermo-mechanical response to be understood. Hence, it is clear that, in general, further research is required in order to enable a safe and economical design of thermo-active structures and, more specifically, that the behaviour of thermo-active walls has to be more extensively investigated.

2.2.2 Heat transfer and thermal and thermo-mechanical properties

2.2.2.1 Heat transfer mechanisms

Conduction

The predominant heat transfer mechanism within fully saturated soils is heat conduction (Farouki, 1981; Mitchell, 1993). Similarly, conduction governs the heat transfer through the concrete structure. The process of conduction, often also referred to as diffusion, takes place due to a temperature difference and it occurs in all the phases of a material, i.e. within solids, liquids or gasses. The heat flow is generated on a molecular scale, moving from regions of higher temperature to those of lower temperature. The heat flux generated by conduction (q_{cond}) is directly proportional to the temperature gradient and is described by Fourier's law through the following equation:

$$q_{cond} = -\lambda \nabla T \tag{2-2}$$

where λ is the thermal conductivity of the material (W/mK) and ∇T is the temperature gradient. The negative sign indicates that heat flow occurs towards regions at lower temperatures.

The transient heat conduction equation can be obtained by considering the conservation of energy and Equation (2-2). This is expressed as:

$$\rho C_p \frac{\partial T}{\partial t} - \nabla \cdot (\lambda \nabla T) = Q^T \tag{2-3}$$

where ρ is the density of the material (kg/m^3), C_p is the specific heat capacity (J/kgK), t is time (s) and Q^T is a heat source or sink (W/m^3).

Convection

Convection is the major heat transfer process occurring in fluids. It is generated by two different processes at microscopic and macroscopic scales, where the first is due to conduction and the second due to advection, the latter being defined as the heat transfer occurring due to the bulk motion of the fluid which carries energy with it (Al-Khoury, 2012). The expression for convection for one-dimensional flow is given in Equation (2-4), where the first term is related to conduction (see Equation (2-2)) and the second to advection:

$$q_{conv,x} = -\lambda_x \frac{dT}{dx} + \rho_f C_{p,f} v_x (T - T_r) \tag{2-4}$$

where ρ_w, $C_{p,w}$ and v_x are respectively the density (kg/m^3), the specific heat capacity (J/kgK) and the flow velocity (m/s) of the fluid and T_r is a reference temperature (K). In soils with high degree of saturation, convection is caused by transport of water (Brandl, 2006), and this phenomenon is important mainly within granular materials, where the water flow may be significant (Farouki, 1981). Moreover, ground water flow, and therefore the convective heat transfer process in soils, is often neglected when designing GSES, as this process becomes important only with high water flow velocities and because it has generally a beneficial effect, reducing permanent temperature changes. Conversely, convection governs the heat transfer within heat exchanger pipes (Gawecka et al., 2020) and in open loop systems (Cui et al., 2016a). In the case where the convective heat flux is dominated by advection (i.e. the second term on the right hand side of Equation (2-4)), the heat transfer is termed 'highly advective'. This can be measured by the dimensionless Péclet number, Pe, defined as:

$$Pe = \frac{C_{p,f} \rho_f v L_c}{\lambda} \tag{2-5}$$

where L_c is a characteristic length (m). If the Péclet number is greater than one, then the heat transfer is dominated by advection.

Convection also describes the heat loss of a body in contact with a moving fluid, as in the case of a face of a structural element (e.g. retaining wall) exposed to an environment. Since in such case the contribution of conduction and advection cannot be distinguished easily, the heat flux is expressed as being proportional to the temperature difference between the body and the fluid. The proportionality constant is the convective heat transfer coefficient, h (W/m^{2}K), and this process is described by Newton's law of cooling:

$$q_{conv} = h(T_s - T_\infty) \tag{2-6}$$

where T_s is the surface temperature of the body in contact with the fluid and T_∞ is the temperature of the fluid (or environment). The heat transfer coefficient, h, depends on many factors, such as the fluid properties, the type of fluid flow (e.g. laminar or turbulent), the origin of the flow (e.g. natural or forced) and the geometry of the body. A more detailed discussion on this parameter is reported in Section 2.4.2.

2.2.2.2 Thermal and thermo-mechanical properties

Heat capacity

The specific heat capacity (C_p), expressed in J/kgK, of a material describes its potential for energy storage and is defined as the amount of energy required to change the temperature of a unit mass by one degree:

$$C_p = \frac{Q}{m\Delta T} \tag{2-7}$$

where Q is the amount of energy exchanged (J), m is the mass (kg) and ΔT is the change in temperature (K).

The volumetric heat capacity (expressed in J/m^{3}K) of a material is defined as the product between its density (ρ) and the specific heat capacity and indicates the ability to store heat per unit volume:

$$C_v = \rho C_p \tag{2-8}$$

Since soils are multi-phase materials, composed by fractions of air, water and solid particles, the volumetric heat capacity can be determined by summing the contribution of the individual components according to their volume proportion (Rees et al., 2000). In soils, this is related to the porosity of the material (n) and the degree of saturation (S_r). The weighted volumetric heat capacity is given by:

$$\rho C_p = (1-n)\rho_s\, C_{p,s} + (nS_r)\rho_w\, C_{p,w} + n(1-S_r)\rho_a\, C_{p,a} \tag{2-9}$$

where the subscripts s, w and a indicate properties related to the soil, water and air particles respectively. For fully saturated soils, for which S_r=1.0, the volumetric heat capacity merely depends on the properties of soil and water.

The specific heat capacity can be determined through laboratory tests (as described in Brandl (2006)). It is intuitive that soils with larger heat capacities are thermally more efficient due to their high capability of storing heat, which is of advantage in geothermal systems. Typically, the volumetric heat capacity of soils varies between 1.3 and 3.8 MJ/m^{3}K (VDI, 2010). For concrete, this parameter is less variable and usually around 2.0 MJ/m^{3}K (Tatro, 2006).

Thermal conductivity

The thermal conductivity (λ) indicates the ability of a material to conduct heat and is defined as the rate of heat transfer through a unit thickness per unit area under a unit temperature gradient. As stated by Brandl (2006), the ground thermal conductivity can be evaluated either through empirical correlations or field and laboratory tests, where the latter are recommended for large projects. The most commonly performed field test is the thermal response test (TRT), which requires the construction of a borehole or a pile. A fluid heated using a known power is circulated within pipes placed in the borehole and its inlet and outlet temperatures are measured. The change in fluid temperature is then related to the thermal conductivity by approximating the borehole to an infinite line source (Carslaw & Jaeger, 1959). To allow an estimation of the variation in thermal conductivity with depth, TRTs can be carried out including fibre optic temperature sensing (Fujii et al., 2009). Alternatively, TRTs using heating cables installed in the pipes, which allow to reduce the power required to conduct the test as well as measuring the thermal conductivity at different depths, can be performed (Raymond & Lamarche, 2014; Raymond et al., 2015; Vélez Márquez et al., 2018). Recently, the thermal cone penetration test (T-CPT) has been proposed for measuring the thermal conductivity (Akrouch et al., 2016; Vardon et al., 2019). A thermocouple is attached to a standard cone penetration test (CPT) device, which enables the heat diffusion to be measured at given depths during the test, alongside with measuring the usual properties obtained using a standard CPT test. This procedure is generally much quicker than other tests. For shallow depths, needle probe field tests can be performed, as described in King et al. (2012). Alternatively, the thermal conductivity can also be determined by laboratory tests (e.g single needle test or dual probe heat test (Martinez Calonge, 2017)).

The thermal conductivity of the ground is influenced by its porosity, water content and the minerals composing the solid mass (see Gawecka et al. (2017) for a review on conductivity models for two-phase materials). Typically, the thermal conductivity of soils and rocks ranges between 1.0 and 3.0 W/mK, where the presence of quartz, which has a high thermal conductivity, substantially affects the thermal conductivity of soils. In the context of thermo-active structures, a high thermal conductivity is favourable in cases where the system operates in a single mode (i.e. only for heating or cooling) such that the changes in ground temperature do not build up close to the structure, lowering its thermal potential. When a system is employed for heating and cooling, an intermediate value of thermal conductivity could be beneficial since it allows taking advantage of the heat stored during one year of operation.

The thermal efficiency of thermo-active structures is also affected by the value of the thermal conductivity of the structure, which is usually made of concrete. High values of thermal conductivity are preferable to avoid high temperatures within the structure, which are detrimental for the thermal performance and may also affect their mechanical behaviour. The conductivity of concrete is affected by the minerology of its aggregates, where high contents of quartz or siliceous sands increase the

thermal conductivity, and by its moisture content (CIRIA, 2007). An extensive review on the thermal conductivity of concrete (e.g. Khan, 2002; Kim et al., 2003; Tatro, 2006; Neville, 2011) showed that this parameter is reported to vary between 1.0 and 3.6 W/mK, with lower values obtained for lightweight concretes (which are not employed for geotechnical structures). The value recommended by design guidelines is generally around 1.5-1.6 W/mK (VDI, 2010; GSHP Association, 2012).

Thermal diffusivity

The thermal diffusivity (α_T) is calculated as the ratio between the thermal conductivity (λ) and volumetric heat capacity (C_v) and has units of m^2/s:

$$\alpha_T = \frac{\lambda}{C_v} \tag{2-10}$$

This quantity describes the rate at which a heat pulse is transmitted through a medium and, therefore, controls the transient heat transfer, as can be seen from the analytical expressions reported in Appendix A. This parameter is incorporated in a dimensionless measure of time, i.e. the Fourier number, employed in heat transfer calculations.

Coefficient of thermal expansion

The coefficient of thermal expansion indicates changes in size provoked by a unit change in temperature. The linear coefficient of thermal expansion (α) denotes a change in length (L) due to temperature:

$$\alpha = \frac{1}{L}\frac{dL}{dT} \tag{2-11}$$

where T is temperature. Equally, it can be expressed in terms of changes in area (A) and volume (V). The latter, termed the "volumetric thermal expansion coefficient", α_{vol}, can be obtained for isotropic materials as 3α.

Since this is a thermo-mechanical property, it is particularly important when analysing the thermo-mechanical behaviour of thermo-active structures or the THM interactions within the soil. Indeed, it controls the thermal deformation of the thermo-active structure and the development of thermally-induced stresses (see Section 2.2.4 for more details). A typical value of α for concrete is 1.0×10^{-5} m/mK (Tatro, 2006), while similar values of the coefficient of thermal expansion is reported for soil minerals (Fei, 1995; Delage, 2013). However, the overall expansion of soils is more complex and further discussed in Section 2.2.3. In addition, as depicted in Figure 2-4, the coefficient of thermal expansion of water, α_w, is generally larger than that of solid particles (e.g. it is equal to 6.5×10^{-5} m/mK at 20°C (Çengel & Ghajar, 2011)), which leads to the development of thermally-induced excess pore water pressures (see next section). It should also be noted that the coefficient of thermal expansion of water largely varies with temperature (see Figure 2-4), while it can be considered approximately independent

of pressure. An expression that can be used to estimate the linear coefficient of thermal expansion of water with temperature is provided in Cui et al. (2020), which was obtained from the data reported in Çengel & Ghajar (2011):

$$\alpha_w = 1.48 \times 10^{-10} T^3 - 3.64 \times 10^{-8} T^2 + 4.88 \times 10^{-6} T - 2.02 \times 10^{-5} \quad (2\text{-}12)$$

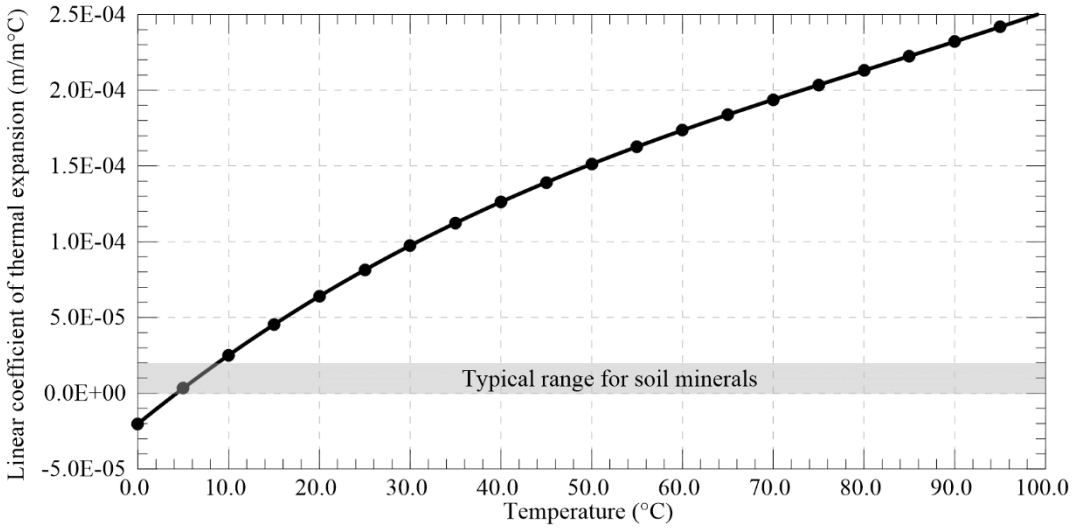

Figure 2-4: Variation of linear coefficient of thermal expansion of water with temperature (according to Equation (2-12)) and typical range of linear expansion coefficient for soil minerals (according to Fei (1995))

2.2.3 Non-isothermal soil behaviour

In the past decades, considerable effort was put into understanding the effects of temperature on soil behaviour through experimental studies. The focus of these studies was mainly on clays (due to their application in nuclear waste disposal), for which several aspects of the soil response under non-isothermal conditions, such as the volumetric behaviour, changes in strength and stiffness, preconsolidation pressure, excess pore water pressure, compressibility and permeability, were investigated. The findings of these studies led to the development of thermo-plastic constitutive models to take into account the observed behaviour under non-isothermal conditions. An extensive literature review on the effects of temperature on the above mentioned characteristics of fine grained soils and the available constitutive models is reported in Gawecka (2017). In this research project the main features of THM soil response considered are related to the effect of temperature on the volume changes and excess pore water pressure generation and further details on these aspects are provided herein.

2.2.3.1 Clays

Volumetric behaviour

The volumetric behaviour of clays upon changes in temperature was investigated by laboratory tests under drained conditions undertaken by numerous researchers, such as those conducted by: Campanella & Mitchell (1968) on remoulded illitic clay; Baldi et al. (1988) and Hueckel & Baldi (1990) on Boom, Kaolin and Pontida clays; Delage et al. (2000) and Sultan et al. (2002) on Boom clay; Cekerevac &

Laloui (2004) on MC clay; Abuel-Naga et al. (2006), Abuel-Naga et al. (2007a), Abuel-Naga et al. (2007b) on soft Bangkok clay; Martinez Calonge (2017) on London Clay.

Most of these studies show consistent findings and have generally observed a comparable behaviour amongst all different types of clay. As an example, the results presented by Baldi et al. (1988) for Pontida Clay, by Cekerevac & Laloui (2004) for MC clay, by Abuel-Naga et al. (2007a) for soft Bangkok clay and by Sultan et al. (2002) for Boom clay are collected in Figure 2-5. The experimental results have shown that the volumetric behaviour of clays depends on the stress history and the applied temperature change. Contrary to what would be expected for an engineering material (i.e. expansion upon heating and contraction upon cooling), normally consolidated (NC) samples displayed contraction upon heating, which was shown to be irreversible, suggesting that the increase in temperature may have induced plasticity. Conversely, highly overconsolidated (OC) soils showed expansion during heating which was reversible (elastic). For intermediate levels of OCR, the volumetric behaviour depends on the temperature increase during heating, with expansion being observed first, followed by contraction. The temperature at which this phenomenon occurs increases with OCR (see e.g. Figure 2-5 (d)). During cooling, all studies observed soil contraction, which was independent of the level of OCR and temperature. The irreversible strains observed for NC and lightly OC soils may be due to changes in soil structure as a consequence of rearrangement of the soil particles (Campanella & Mitchell, 1968). This behaviour was interpreted within an elasto-plastic framework by Abuel-Naga et al. (2007a) to be related to the reduction in pre-consolidation pressure (p_c) upon heating. Since for normally consolidated clays the pre-consolidation pressure is equal to the current stress at ambient temperature (σ_{T_0}), any increase in temperature will lead to stress states that induce irreversible deformations. Conversely, for overconsolidated soils reversible strains can take place since the initial stress state lies within an elastic domain (i.e. the effective stress at ambient temperature is less than the pre-consolidation pressure, $\sigma_{T_0} \ll (p_c)_{T_0}$).

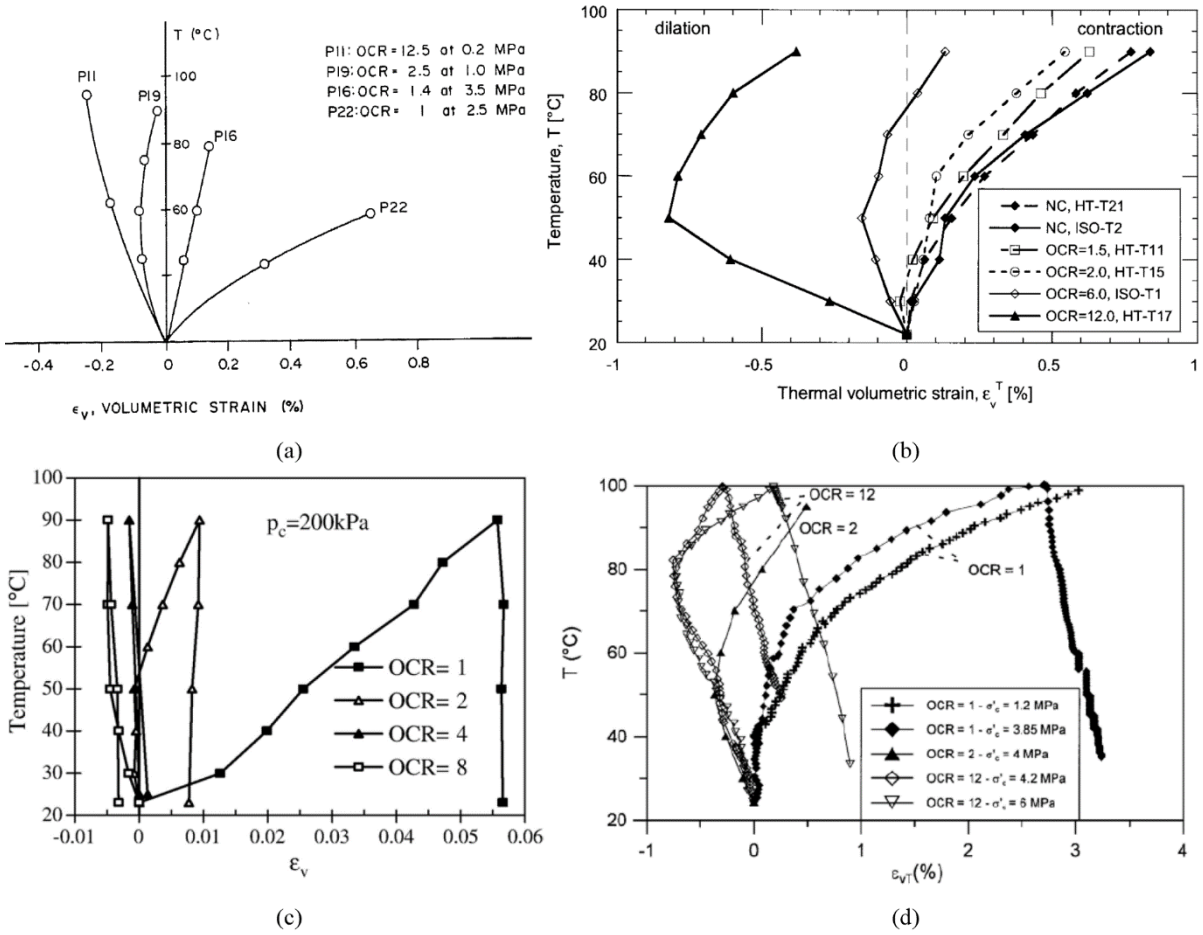

Figure 2-5: Changes in volumetric strain with temperature and OCR (a) for Pontida clay (Baldi et al., 1988), (b) for MC clay (Cekerevac & Laloui, 2004), (c) for Bangkok clay (Abuel-Naga et al., 2007a) and (d) for Boom Clay (Sultan et al., 2002) – positive strain indicates contraction

It should be noted that the direct measurement of volume changes is challenging. Thus, Campanella & Mitchell (1968) and Baldi et al. (1988) proposed expressions for an indirect measurement according to the volumetric thermal expansion of water and solids and the measured volume of drained water. The two expressions differ in some assumptions regarding the behaviour of drained water, however Delage et al. (2000) compared the two methods and found negligible differences. Furthermore, the thermal coefficient of expansion of water, α_w, varies largely with temperature (see e.g. Equation (2-12)) and slightly with pressure, and hence this characteristic has to be taken into account when performing the calculations. Martinez Calonge (2017) showed that the employed coefficient of thermal expansion of water has a large effect on the results obtained. It was shown that the expression used in Baldi et al. (1988) to calculate α_w presents an inconsistency in the units used for its calculation, which has been later corrected by Cekerevac et al. (2005). Martinez Calonge (2017) determined a new expression of the variation of the coefficient of thermal expansion of water with temperature and pressure according to the data published by the International Association for the Properties of Water and Steam, showing that the ones suggested by Baldi et al. (1988) and Cekerevac et al. (2005) were not consistent with that data. Martinez Calonge (2017) used the new expression to interpret the drained heating tests performed

on London Clay adopting the free water approach proposed by Campanella & Mitchell (1968). The results obtained differ from the others published in literature, showing that all the samples, regardless of the stress history, contract upon heating and expand upon cooling, as shown in Figure 2-6 (a). Furthermore, it was found that for the NC samples, part of the strain developed during the first heating cycle is irreversible, while subsequent heating and cooling cycles at the same temperature did not lead to an accumulation of strain. For OC samples, the thermal volumetric strain resulted to be reversible.

Martinez Calonge (2017) re-interpreted these results calculating α_w according to Cekerevac et al. (2005) (Figure 2-6 (b)) and Baldi et al. (1988) (however, with consistent units – see Figure 2-6 (c)), demonstrating a large effect of the calculation of the variation of this parameter with temperature and pressure, where the results depicted in Figure 2-6 (b) show a similar trend to those published in literature (see above).

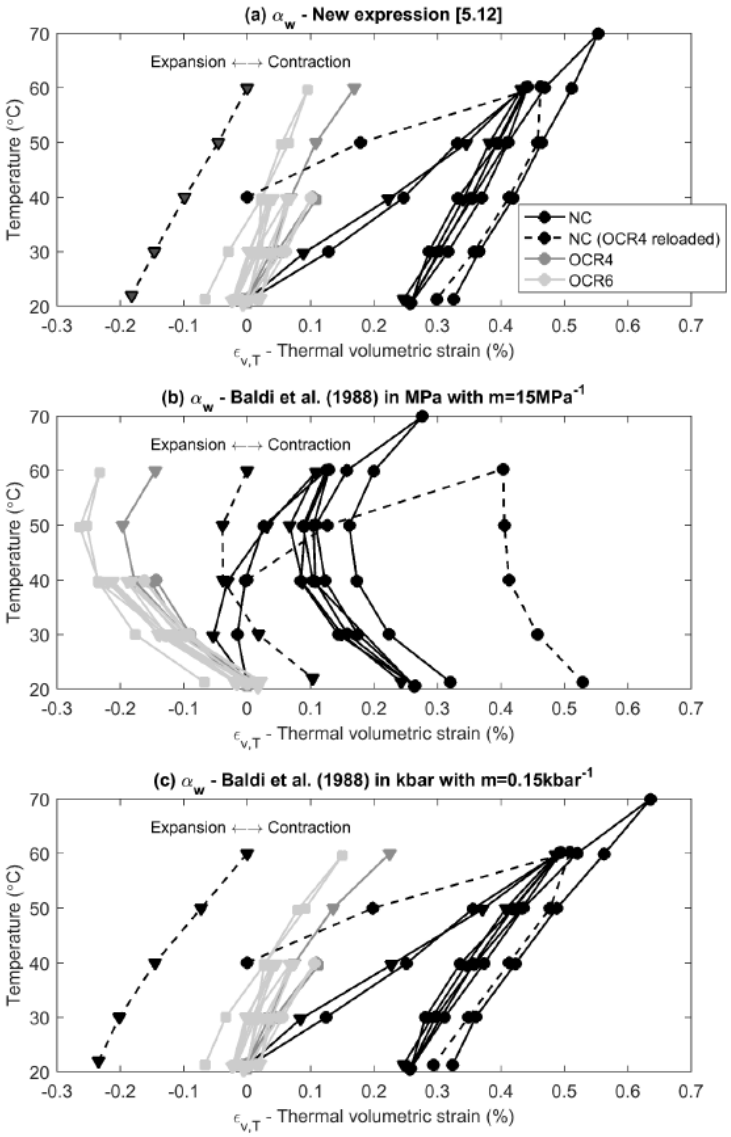

Figure 2-6: Thermal volumetric strains for London Clay at different OCR levels and using different expressions for α_w (Martinez Calonge, 2017)

Pore water pressure generation

Different studies, such as those presented in Campanella & Mitchell (1968) on illitic clay and San Francisco Bay mud, Savvidou & Britto (1995) on Kaolin Clay, Abuel-Naga et al. (2007a) on Bangkok Clay and Chen et al. (2019) on London Clay, have investigated the changes in pore water pressures due to temperature changes during undrained heating tests. Figure 2-7 shows the results of an undrained heating test performed on a reconstituted, normally consolidated sample of London Clay, which was heated from 21°C to approximately 37°C and subsequently allowed to naturally cool back to 21°C. An increase in compressive excess pore water pressures is observed during heating and a decrease during cooling, which agrees with the findings from the other studies. The variations in pore water pressures are mainly due to the difference between the coefficient of thermal expansion of solids and water, where, for the employed range of temperatures, the one of water is considerably higher than that of solids (see Figure 2-4). Hence, when a sample is heated, the water undergoes a larger thermal expansion than the soil particles.

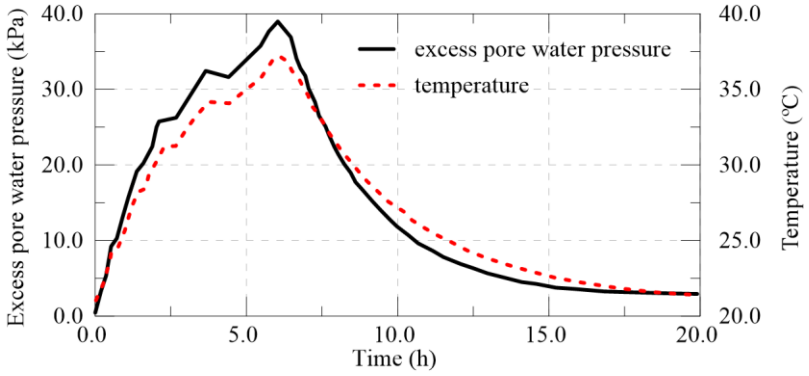

Figure 2-7: Development of excess pore water pressures and temperature with time during undrained triaxial test on reconstituted London Clay (data from Chen et al. (2019))

2.2.3.2 Sands

A more limited number of studies investigated the volumetric behaviour of sands. The most notable were carried out by Ng et al. (2016) who tested Toyura sand for three different relative densities (21%, 70% and 90%), Martinez Calonge (2017) assessed the response of 16/30 sand with a relative density of 55% and Liu et al. (2018) investigated the behaviour of Fujian sand at a relative density of 90%. The drained heating tests were interpreted following the procedure proposed by Campanella & Mitchell (1968).

Martinez Calonge (2017) observed that the medium-dense sand sample expanded upon heating and contracted upon cooling, with the volumetric strains being reversible. Liu et al. (2018) also reported thermal expansion during heating tests on Fujian sand. The tests conducted by Ng et al. (2016) found that the volumetric behaviour of Toyura sand depends on its relative density (D_r), as shown in Figure 2-8. The loose (D_r=21%) and medium-dense (D_r=70%) samples initially displayed contraction followed by expansion at higher temperatures. Conversely, the dense sand (D_r=90%) exhibited only

expansion, of a similar magnitude of the expansion of the sand particles (as indicated by the dashed line in Figure 2-8). The different behaviour with varying D_r was interpreted as a consequence of particle rearrangement occurring in the loose and medium-dense samples, which does not take place in the denser samples as they have a more stable structure.

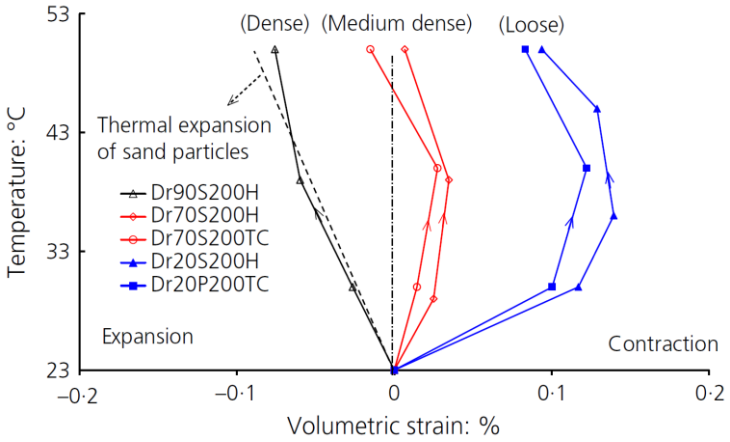

Figure 2-8: Volumetric strain of Toyura sand with different relative densities (Ng et al., 2016)

2.2.4 Thermal performance and thermo-mechanical behaviour of thermo-active structures

As previously outlined, thermo-active structures have the double purpose of providing both energy and stability to buildings. Figure 2-9 displays a flow chart of the design process adopted when dealing with thermo-active structures, which requires the interaction between the thermal and geotechnical design. In general, the dimensions of the underground structures are provided by the geotechnical design, whereas the thermal design evaluates the energy potential of the installed system and optimises the system's performance through various design choices.

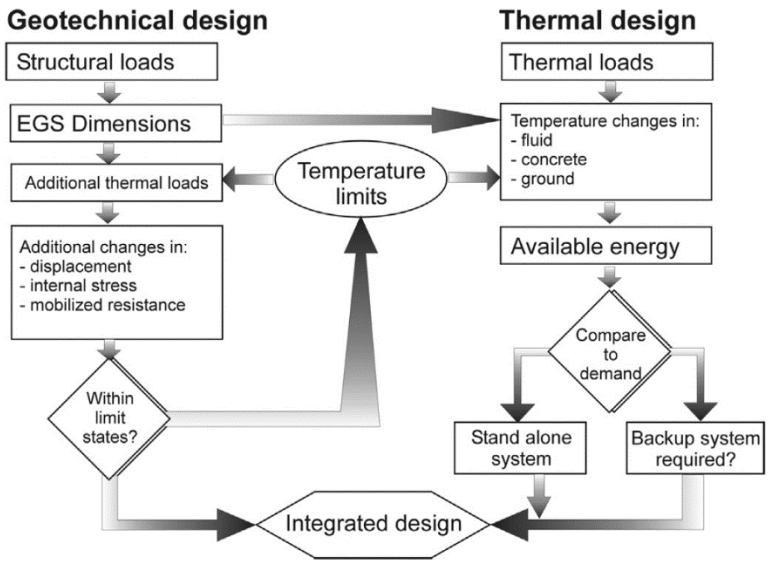

Figure 2-9: Design process for thermo-active structures (Bourne-Webb et al., 2016a)

Thermal performance

As explained in Section 2.2.1, ground source energy systems are composed of a ground heat exchanger, which, in this context, is the thermo-active structure, connected to a heat pump. The exchange of heat occurs when circulating a fluid through the heat exchanger pipes embedded within the structure, whose temperature depends on the operation mode (i.e. whether the system is providing heating or cooling) and on the energy demand the system is required to satisfy. However, the fluid temperatures are usually controlled such that they do not reach excessively low or high values, to avoid ground freezing or large changes in temperature within and around the structure (see Figure 2-9). Since the temperatures are generally limited to the range between 0°C to 40°C (Brandl, 2006), it may occur that the system is not able to provide the entire energy required by the end users. Hence, back-up systems in the form of conventional heating/cooling systems are often installed in conjunction with ground source energy systems to guarantee the system's function during periods of peak thermal loads. Furthermore, since a geothermal system is subjected to peak demands for a fraction of its operation time, the use of supplementary systems to satisfy periods of peak load may reduce the initial installation costs (Preene & Powrie, 2009). In the absence of a back-up system, Bourne-Webb et al. (2016a) recommend that a system should be designed to provide 10% more energy than the estimated demand.

A ground source energy system may operate in a single or dual operation mode, meaning that it may be employed solely for heating or cooling, or for both. In either case, the system may be balanced, i.e. the net energy exchanged with the ground during a year of operation is equal to zero, or it may be unbalanced, i.e. more energy is extracted than injected or vice versa. If the system operation is unbalanced, it is important to avoid the build-up of long-term temperature changes, which may be detrimental for the thermal performance, as well as harm the biological life in the ground and groundwater (de Moel et al., 2010). In such case, it should be ensured that the natural recovery process of the ground, which can occur by solar energy at shallow depths or through ground water flow (Rawlings & Sykulski, 1999), allows permanent temperature changes to be kept to a minimum. Furthermore, it should be noted that for systems installed in urban environments, the temperature changes may affect adjacent structures and hence this may have to be accounted for during the design. However, currently there is no regulation or guideline regarding this issue (Bourne-Webb et al., 2016a).

The thermal performance of ground source energy systems is usually evaluated by computing the rate at which energy is extracted from or in injected into the ground, q (kW), and the total energy provided by the geothermal system during the operation period, E_{tot} (kWh). These two quantities are calculated through Equations (2-13) and (2-14), respectively:

$$q = C_{v,w} A_p v (T_{in} - T_{out}) \tag{2-13}$$

where $C_{v,w}$ is the volumetric heat capacity of water (kJ/m^{3}K), A_p is the cross-sectional area of the heat exchanger pipe (m^2), v is the water flow velocity within the heat exchanger pipes (m/s) and T_{in} and T_{out} are the heat exchanger pipe inlet and outlet temperatures (K), respectively;

$$E_{tot} = \sum_{i=1}^{n} q_i \Delta t_i \tag{2-14}$$

where q_i is the extracted/injected power (calculated with Equation (2-13)) during time interval Δt_i. Given the large dimensions of retaining walls, both in terms of length and width, these quantities are often normalised by the length of the wall (L), the width of the wall (B) or by the area of wall in contact with the ground (A_{wall}) (see Figure 2-10). It should be noted that GSES usually work intermittently, i.e. the heat pump is switched on and off multiple times during the day, with continuous operation being required only during peak energy demand periods.

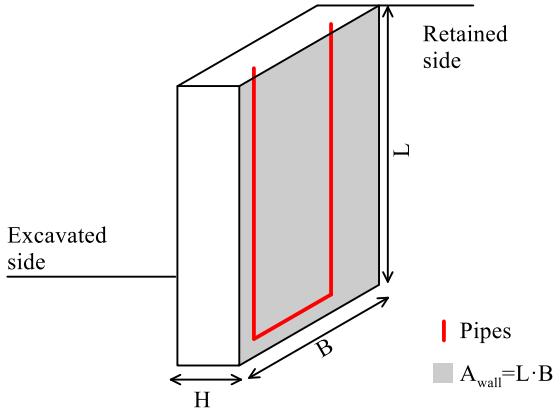

Figure 2-10: Schematic representation of thermo-active wall panel geometry

The thermal performance of thermo-active structures can be evaluated by performing Thermal Performance Tests (TPT), where the heat carrier fluid is injected with a constant temperature and the outlet temperature and water flow rate is measured in order to calculate the heat flux, q, through Equation (2-13) (You et al., 2014). Such a test was performed on thermo-active walls by Xia et al. (2012) and is described in Section 2.4. However, it should be noted that the heat flux varies with time, hence long-term field tests would be required to provide realistic long-term energy potential estimates for thermo-active structures (Loveridge et al., 2020). For pre-design of thermo-active structures, Brandl (2006) suggests the following values of heat exchange for different types of structures:

- pile with diameter = 0.3–0.5 m: 40–60 W/m (metre length)
- pile with diameter ≥ 0.6 m: 35 W/m^2 (area of contact with ground)
- diaphragm walls, pile walls (fully embedding the soil): 30 W/m^2 (area of contact with ground)
- base slabs: 10–30 W/m^2 (area of contact with ground)

Since the dimensions of thermo-active structures are usually not dictated by the thermal design but by the geotechnical design, the aspects that are included within the thermal design, and which can be optimised, are the following (Faizal et al., 2016):

- type, position and configuration of pipe loops (i.e. enhanced pipe material, concrete cover, geometrical arrangement of pipes, etc.);
- thermal parameters of concrete (where a high thermal conductivity is favourable);
- type of heat carrier fluid (recently, the employment of nano-fluids to enhance heat transfer is considered) and fluid flow rate;
- thermal losses from system components.

Some of these aspects were assessed for retaining walls by different researchers and are further discussed in Section 2.4, while Chapter 4 and Chapter 5 comprise detailed investigations on the heat transfer mechanisms and the factors affecting the thermal performance for thermo-active walls. It should be noted that, while there are numerous analytical and semi-analytical approaches to evaluate the thermal performance of borehole heat exchangers (e.g. the finite line source (Eskilson, 1987)) and, to some extent, for thermo-active piles (see Bourne-Webb et al. (2016a) and Fadejev et al. (2017) for a review), a limited number of approaches have been proposed for thermo-active walls (e.g. Sun et al. (2013) developed a conductive heat transfer model). Due to the more complex geometry when compared to borehole heat exchanger, the thermal performance of thermo-active structures is often assessed by employing numerical methods (such as Finite Element or Finite Difference), which allow different levels of complexity to be simulated, i.e. ranging from heat conduction problems where the heat exchange is simulated with simple boundary conditions (e.g. Sani et al., 2019a) to modelling the whole pipe-structure-soil interaction (e.g. Batini et al., 2015) (Bourne-Webb et al., 2016a).

Thermo-mechanical behaviour

The thermo-mechanical behaviour of thermo-active structures has been investigated mainly for piles. Numerous field tests have been carried out either on a single pile (e.g. Bourne-Webb et al., 2009; Laloui et al., 2006; Bouazza, 2011) or pile groups (e.g. Mimouni & Laloui, 2015; Murphy et al., 2015). These studies, the details of which are not reported for brevity, provided valuable insights into the mechanical response of thermo-active piles. Detailed reviews of these tests can be found in Gawecka (2017), Bourne-Webb & Bodas Freitas (2020), Bourne-Webb et al. (2019) and Sani et al. (2019b).

A simplified framework for understanding the behaviour of thermo-active piles under thermal loads has been proposed by Bourne-Webb et al. (2009), Amatya et al. (2012) and Bourne-Webb et al. (2013b). According to this approach, the main factor influencing the mechanical response of thermo-active piles when subjected only to changes in temperature is the magnitude of the so called "restrained strain", $\varepsilon_{th-restrained}$, which is defined as the part of the free thermal strain, $\varepsilon_{th-free}$, that is impeded from

developing due to the restriction imposed to the pile either by the soil or by end restraints and which causes loads to develop:

$$\varepsilon_{th-restrained} = \varepsilon_{th-free} - \varepsilon_{obs} \tag{2-15}$$

where ε_{obs} is the actual observed strain (i.e. that measured in field). Note that, as expected in the case of a thermo-active pile, all the strains in Equation (2-15) are considered to be in the axial direction. The free thermal strain (i.e. if no restraint to the pile would exist) of a thermo-active pile is:

$$\varepsilon_{th-free-pile} = \alpha_c \Delta T \tag{2-16}$$

where α_c is the linear coefficient of thermal expansion of the concrete and ΔT is the temperature change. Consequently, any restrained strain calculated for a pile subjected only to a thermal load must be directly associated to changes in axial stresses and forces:

$$\sigma_a = E\varepsilon_{th-restrained} \tag{2-17}$$

$$P = AE\varepsilon_{th-restrained} \tag{2-18}$$

where σ_a is the axial stress (kN/m^2), P is the axial force (kN), A is the cross-sectional area of the pile (m^2) and E is the Young's modulus of concrete (kN/m^2).

In the ideal scenario of an unrestrained pile, as schematically represented in Figure 2-11, when heated, the structure is able to develop the full thermal strain, i.e. the restrained strain and consequently the axial load is equal to zero. Conversely, for a fully restrained pile, the thermal strain is equal to zero and hence $\varepsilon_{th-restrained} = -\varepsilon_{th-free}$, with the consequent development of a compressive axial force calculated through Equation (2-18), while the opposite occurs in cooling.

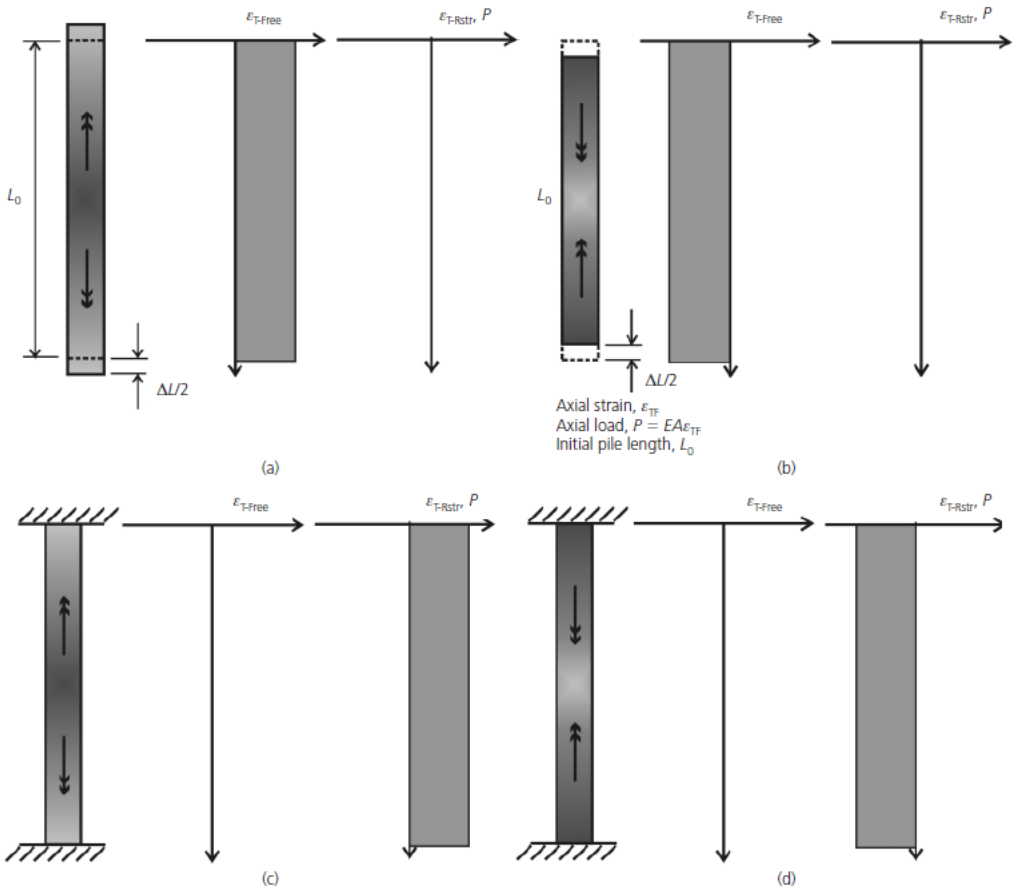

Figure 2-11: Thermal response of free and restrained bodies: (a) heating, free body; (b) cooling, free body; (c) heating, restrained body; (d) cooling, restrained body (Bourne-Webb et al., 2013b)

In reality, a pile will be partially restrained by the soil along its shaft and any restraints at its ends. Depending on the stiffness of the ground, the type and position of the restraints, the mechanical load and the magnitude and type (i.e. heating or cooling) of the thermal load, the profiles of the axial strain, axial force and mobilised shaft friction will vary. Figure 2-12 represents schematically a number of scenarios, with and without mechanical loading, of a pile subjected to heating or cooling with no end restraints. In the absence of a mechanical load, when cooled or heated (Figure 2-12 (b) and (d), respectively), the pile develops the maximum restrained strain at mid-length, since it is free to expand both at the top and bottom, however it is restrained by the soil along the shaft. With the addition of a mechanical load, the two effects, i.e. mechanical and thermal, are superimposed.

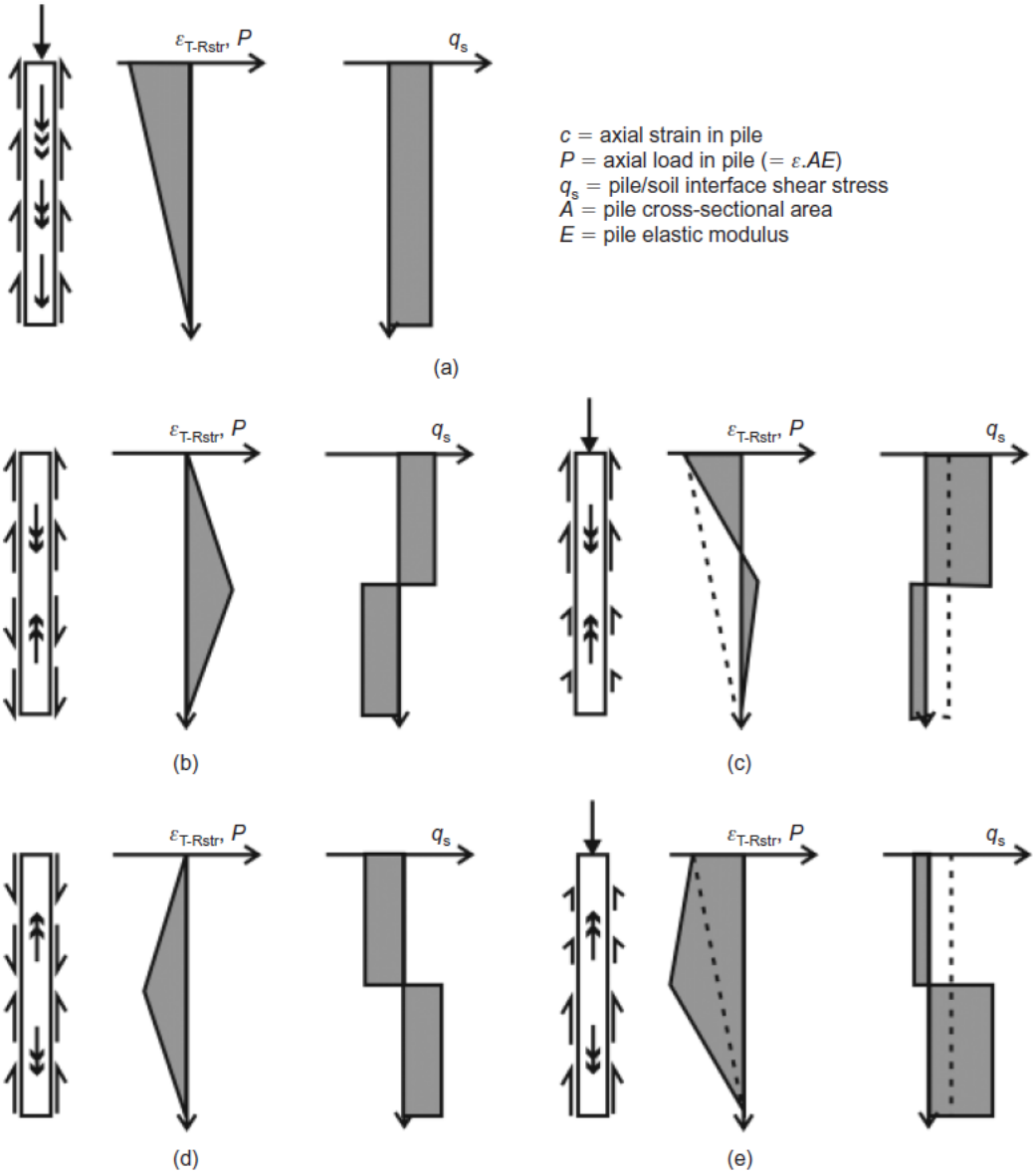

Figure 2-12: Response mechanism for pile undergoing thermo-mechanical loading; heating and cooling with no end restraint: (a) load only; (b) cooling only; (c) combined load and cooling; (d) heating only; (e) combined load and heating (Amatya et al., 2012)

Bourne-Webb et al. (2019) analysed the data obtained from numerous field tests and showed that, generally, the movement of the pile occurs within the limit of a free body, where the average value of the pile head movement normalised by its movement when in an unrestrained condition was found to be around 0.6, i.e. 60% of the free thermal strain occurs (and hence 40% is restricted from occurring). Consistent with the simplified framework, they found that the restraint of the thermal deformation is directly related to the changes in stresses within the pile, where larger movements are associated with lower changes in stress. The recorded stresses due to changes in temperature were in many cases significant and comparable to those induced by mechanical loads.

The tests performed on groups of thermo-active piles involved both scenarios where only some or all piles were used as heat exchangers (Mimouni & Laloui, 2015). In the first case, differential settlement

amongst the piles was recorded, with the heated pile moving more than the adjacent piles, which affected also the recorded load as a consequence of load redistribution within the foundation system. In the second case, all the piles displaced by a larger amount, reducing the differential settlements and the axial loads. It can therefore be concluded that the configuration of the heating scheme influences the overall response of the foundation and the superstructure and should therefore be possibly accounted for during the design stage. It is clear that this would implicate the performance of three-dimensional (3D) analyses which are computationally expensive. For this reason, Rotta Loria & Laloui (2016) proposed an interaction factor method to take into account group effects within thermo-active piles.

While the behaviour of thermo-active piles provides insights into the thermo-mechanical response of thermo-active structures, its applicability to thermo-active walls is naturally very limited. Indeed, these latter structures are much more complex from a geometrical point of view (e.g. they are not fully embedded in soil; the geometry of the excavation may vary with different levels of lateral support; a variety of pipe configurations can be installed, etc.) and hence the simplified framework would only be applicable to fully embedded walls, which are, however, not realistic. Nonetheless, the results obtained from field tests on piles help identify and interpret the main mechanisms involving thermo-active structures, both in field and within numerical analyses. This is especially important considering the lack of field data for thermo-active walls.

2.3 Existing modelling capabilities for thermo-hydro-mechanical problems in ICFEP

The Imperial College Finite Element Program (ICFEP, Potts & Zdravković, 1999), which is used throughout this research to perform numerical simulations, has been in development for 40 years for the analysis of geotechnical problems, including coupled hydro-mechanical, dynamic and partially-saturated problems. Furthermore, it features various structural elements (such as beams, bar, shells, etc.) and numerous advanced constitutive models. Through the work of Cui (2015), who implemented a fully coupled THM formulation and new boundary conditions, and Gawecka (2017), who implemented the THM formulation for 3D bars and beams, the Petrov-Galerkin FE method for the simulation of highly advective flows and a thermo-plastic constitutive model, ICFEP is capable of simulating complex fully coupled THM analyses.

This section provides an overview of the existing modelling capabilities of ICFEP relevant to the research presented in this thesis. Full details on the finite element method, the hydro-mechanical coupling, boundary conditions and structural elements for isothermal problems can be found in Potts & Zdravković (1999) and Potts & Zdravković (2001). The full THM formulation, its implementation and validation are described in detail in Cui (2015) and Cui et al. (2018a).

2.3.1 Coupled THM formulation

THM coupling is illustrated in Figure 2-13, which indicates the interaction between the three physical systems that exist in fully saturated soils, i.e. the mechanical system (governed by force equilibrium), the hydraulic system (described by the continuity equation) and the thermal system (considering energy conservation). The hydro-mechanical coupling accounts for stresses and strains in the soil generated by changes in pore fluid pressures and fluid flow occurring due to mechanical volumetric changes. The thermo-mechanical coupling addresses thermally-induced stress and strain changes. The thermo-hydraulic coupling describes the changes in pore fluid pressure due to temperature variations and the heat transfer by fluid flow (i.e. convection). This results in a stiffness matrix for the governing finite element system of equations which can be divided into 3×3 submatrices and where the nodal degrees of freedom are displacements, pore water pressures and temperatures. It should be noted that ICFEP was developed such that any of these three systems can be disabled if not needed during an analysis, therefore allowing only HM, TM or TH analyses to be performed.

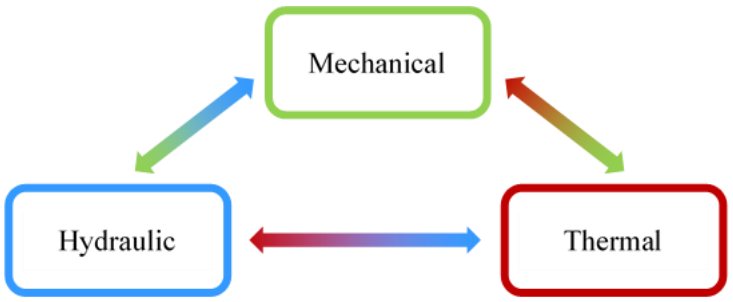

Figure 2-13: Thermo-hydro-mechanical coupling

According to Cui (2015) and Cui et al. (2018a), the main assumptions of the THM formulation adopted in ICFEP are:

(1) the temperature of the soil particle is equal to that of the pore fluid, implying an instantaneous thermal equilibrium between the two phases;
(2) the thermal expansion of soil particles is equal to that of the solid skeleton, meaning that, for an unrestrained and free draining soil, changes in temperature produce volumetric thermal strains that do not affect the void ratio. Consequently, only the volumetric strains induced by changes in effective stresses (also termed 'mechanical') can alter the void ratio;
(3) the effect of radiation is considered negligible and is therefore ignored.

Mechanical formulation

Under non-isothermal conditions, the total incremental strain $\{\Delta\varepsilon_{tot}\}$ is given by the sum of the mechanical strain $\{\Delta\varepsilon_{mech}\}$ (due to stress changes) and the thermal strain $\{\Delta\varepsilon_{th}\}$ (due to temperature changes), resulting in the following (Cui, 2015; Cui et al., 2018a):

$$\{\Delta\varepsilon_{tot}\} = \{\Delta\varepsilon_{mech}\} + \{\Delta\varepsilon_{th}\} \tag{2-19}$$

where the thermal strain is given as $\{\Delta\varepsilon_{th}\}^T = \{\alpha\Delta T \quad \alpha\Delta T \quad \alpha\Delta T \quad 0 \quad 0 \quad 0\}$.

Therefore, referring to the simplified framework for thermo-active piles presented in Section 2.2.4, it is clear that the free thermal strain ($\varepsilon_{th-free}$) is simply the axial component of the thermal strain in a THM analysis (ε_{th}). Similarly, the restrained strain in Equation (2-15), which encapsulates the effects of any restraint on a pile, is identical to the mechanical strain (ε_{mech}), though with opposite signs ($\varepsilon_{mech} = -\varepsilon_{th-restrained}$), given their distinct nature (the former represents a thermal strain that did not develop, while the latter refers to the action responsible for suppressing the deformation). Lastly, given these definitions, it can be concluded that $\varepsilon_{obs} = \varepsilon_{tot}$, i.e. both denote the combined effect of the mechanical and thermal strains.

With the definition of strains given in Equation (2-19) and applying the principle of effective stress, the total stress is expressed as (Cui, 2015; Cui et al., 2018a):

$$\{\Delta\sigma\} = [D']\left(\{\Delta\varepsilon_{tot}\} - \{\Delta\varepsilon_{th}\}\right) + \{\Delta\sigma_f\} \tag{2-20}$$

where $\{\Delta\sigma_f\}^T = \{\Delta u \quad \Delta u \quad \Delta u \quad 0 \quad 0 \quad 0\}$, Δu is the change in pore fluid pressure and $[D']$ is the effective constitutive matrix which depends on the adopted constitutive relations.

Hydraulic formulation

The formulation of the hydraulic equation under non-isothermal conditions is expressed in ICFEP through the following equation (Cui, 2015; Cui et al., 2018a):

$$\nabla \cdot \{v_f\} - \frac{n}{K_f}\frac{\partial u}{\partial t} - 3n(\alpha_w - \alpha_s)\frac{\partial T}{\partial t} - Q^f = -\frac{\partial\left(\varepsilon_{vol,tot} - \varepsilon_{vol,th}\right)}{\partial t} \tag{2-21}$$

where $\{v_f\}$ is the vector of seepage velocity, n is the porosity, u is the pore fluid pressure, K_f is the bulk modulus of the pore fluid, α_w and α_s are respectively the linear coefficients of thermal expansion of the pore water and the soil skeleton, T is temperature, Q^f is any source or sink of pore fluid, $\varepsilon_{vol,tot}$ and $\varepsilon_{vol,th}$ are respectively the total and thermal volumetric strains and t is time. In this equation, if the source/sink term is disregarded, there are two terms which are responsible for the generation of excess pore water pressures in a coupled THM analysis. The first arises from the difference between the linear coefficients of thermal expansion of soil (α_s) and water (α_w), with the latter being larger than the former, leading to increases in pore water pressures during heating and the opposite during cooling. The second mechanism establishes the generation of excess pore water pressures due to the variation of pore space arising from mechanical volumetric strains, expressed in this case by the difference between total and thermal volumetric strains (as previously explained, $\varepsilon_{vol,tot} - \varepsilon_{vol,th} = \varepsilon_{vol,mech}$). Note that this

term describes the hydro-mechanical coupled behaviour and is independent of whether heat transfer is being considered (i.e. it is present even in isothermal analyses). A detailed study at a fundamental level on simulating excess pore water pressures measured during various experimental studies (triaxial tests by Savvidou & Britto (1995) and centrifuge tests by Britto et al. (1989)) was carried out by Cui et al. (2020). Additional details on the development of excess pore water pressures in non-isothermal analyses and the THM interactions taking place in coupled problems are presented in Chapter 3.

Thermal formulation

The heat transfer problem is described by the law of energy conservation (Cui, 2015; Cui et al., 2018a):

$$\frac{\partial(\Phi_T dV)}{\partial t} + \nabla \cdot Q_T dV - Q^T dV = 0 \tag{2-22}$$

where Φ_T is the heat content of the soil per unit volume, Q_T is the heat flux per unit volume (which is given by the sum of the heat flux through conduction and advection) and Q^T is a heat source or sink. The heat content can vary due to three phenomena, namely (1) temperature changes, (2) thermal volumetric changes and (3) mechanical volumetric changes. This latter expresses the interaction between the thermal and mechanical system. The advective heat transfer is evaluated as the sum of the heat transfer induced by (1) pore fluid flow due to a temperature gradient and (2) hydraulic gradient. This latter term is equal to zero in the case of uniform flow.

2.3.2 Thermal boundary conditions

Prescribed temperature

A prescribed temperature boundary condition is a Dirichlet-type boundary condition, which can be specified along a line or a surface, in the case of a 3D analysis.

Prescribed heat flux and heat sources and sinks

This is a Neumann-type boundary condition through which a heat flux can be specified, where heat is injected or abstracted from a boundary (line, area or volume). A special case of this boundary condition is the heat sources and sinks boundary condition, whereby the heat flux is specified at a node.

Convection

The convection boundary condition, which in ICFEP is named 'natural heat loss', applies a heat flux, Q_T, according to Newton's law of cooling:

$$Q_T = \int_{\Omega} -h(T_s - T_\infty) d\Omega \tag{2-23}$$

where T_s is the temperature of the body (K), T_∞ is the temperature of the surrounding environment (K) and h is the convective heat transfer coefficient (W/m^{2}K). In a problem involving thermo-active structures, this boundary condition is typically employed to simulate the interaction between the

structure and the environment (such as the ground surface or the inside of an excavation). It should be noted that this boundary condition is non-linear, since the temperature of a body varies over an increment.

Coupled thermo-hydraulic

The coupled thermo-hydraulic boundary condition (named 'convection' in ICFEP) is used in coupled thermo-hydraulic problems (e.g. Cui et al. (2016a)) and is applied along the boundaries where water enters or leaves the finite element mesh. It prescribes a heat flux along this boundary to balance the energy carried by the water:

$$Q_T = \int_{\Omega} C_{v,w}\{v_f\}T_b d\Omega \tag{2-24}$$

where $C_{v,w}$ is the volumetric heat capacity of water (kJ/m^{3}K), $\{v_f\}$ is the water velocity in the direction perpendicular to the boundary (m/s) and T_b is the temperature at the boundary (K). Since both $\{v_f\}$ and T_b vary during an increment, this boundary condition is non-linear. The use of this boundary condition applied to boundary value problems is detailed in Section 2.3.5.

2.3.3 Thermo-plastic constitutive model

Thermo-plasticity, as subsequently outlined, is not considered in this research project. Nonetheless, an overview of the temperature-dependent constitutive model implemented into ICFEP by Gawecka (2017) (the so-called "IC Thermal model") is presented. The aim of the model is to enable the simulation of two main features of non-isothermal behaviour of clays observed during laboratory tests, i.e. the decrease in preconsolidation pressure with increasing temperature and the volumetric behaviour described in Section 2.2.3.

The formulation of model is based on the critical state framework, with its isothermal formulation being adopted from the Georgiadis (2003) and the Tsiampousi (2011) models, which, however, were used to simulate unsaturated soils. Figure 2-14 (a) shows the shape of the primary yield surface in the $p' - J - T$ space. In the $p' - J$ plane, on the wet side, the Lagioia et al. (1996) yield surface and plastic potential is adopted, while, on the dry side, a non-linear Hvorslev surface, adapted from Tsiampousi (2011) and Tsiampousi et al. (2013), describes the behaviour of overconsolidated soils (note that Figure 2-14 (a) represents a case where the Hvorslev surface is taken as linear). To simulate the influence of increasing temperature on the reduction of the size of the yield surface, an isotropic yield limit (termed "primary" in Gawecka (2017)) exists in the $p' - T$ space. A second plastic mechanism is introduced to simulate the volumetric behaviour observed for intermediate to highly overconslidated soils (which were shown in Section 2.2.3 to contract upon reaching a certain temperature). This "secondary" yield limit is depicted in Figure 2-14 (b). The initial position of the secondary yield limit is identified through the "thermal overconsolidation ratio", defined as the ratio between the temperature associated with the

secondary yield limit, T_0, and the current temperature of the soil. The volumetric strains are considered elastic and expansive inside the yield surfaces (calculated as $\alpha\Delta T$), whereas contractive volumetric strains are generated once one or both yield surfaces are activated.

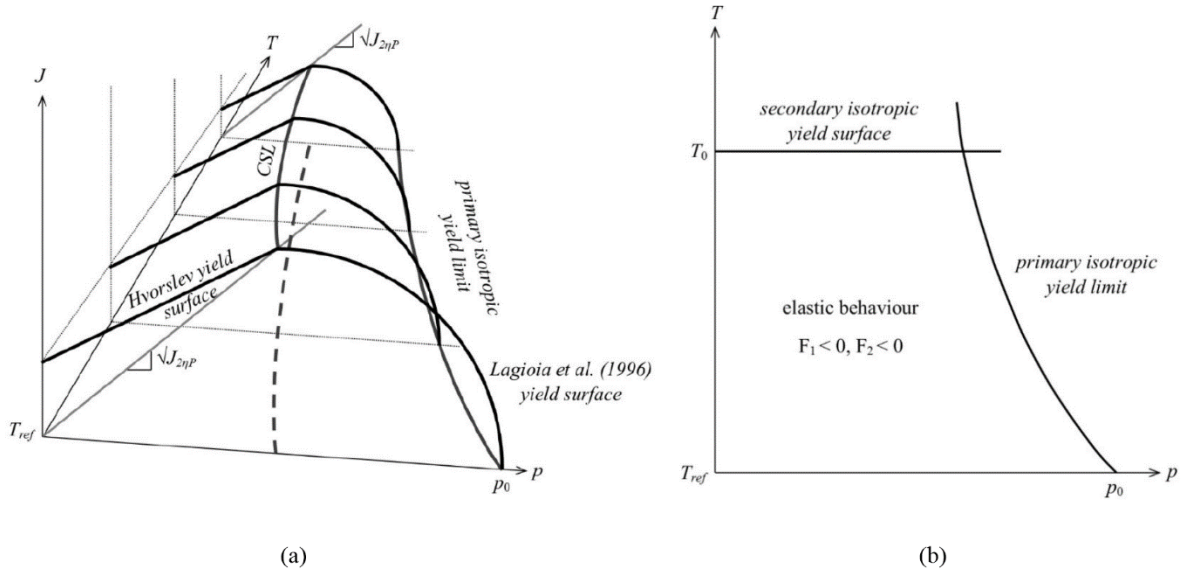

Figure 2-14: IC Thermal model (a) Primary yield surface in $p - J - T$ space and (b) Primary and secondary yield functions in the $p - T$ plane

Gawecka (2017) calibrated the model for three different soil types (Boom Clay, Soft Bangkok Clay and MC Clay), obtaining a good match with the laboratory data. Subsequently, hypothetical thermo-active piles embedded in Boom Clay and Soft Bangkok Clay were simulated and the effect of the adoption of a thermo-plastic constitutive model was assessed for both serviceability and ultimate limit state. The results showed that, for the first case, a negligible influence of the non-isothermal constitutive model was evaluated, since the soil response was predominantly elastic for normally consolidated and overconsolidated soils. Conversely, the ultimate pile capacity varied between ±10% with respect to that computed when temperature effects on the strength of the soil were not accounted for. Given the limited effect of the temperature-dependent constitutive model and the uncertainties regarding the actual soil response (refer to Section 2.2.3), the analyses presented in subsequent chapters assume a thermo-elastic soil response.

2.3.4 Structural elements

As previously mentioned, ICFEP includes a variety of finite elements that can be employed to simulate structural components in a simplified manner when compared to the use of solid elements. These comprise beam, bar, shell and membrane elements, and may result in computationally more efficient analyses since their use typically leads to a reduction in the required number of elements in comparison to solid elements (Potts & Zdravković, 1999).

The THM formulation of 2D beam and bar and 3D shell and membrane elements is described in Cui (2015) and Cui et al. (2018b), while that of 3D beam and bar elements can be found in Gawecka (2017) and Gawecka et al. (2018), which are based on the curved Mindlin's beam element developed by Day (1990) and Day & Potts (1990). The difference between beam and bar elements (and between shells and membranes) resides in their mechanical formulation, where the latter have only displacement degrees of freedom and therefore deform only axially. Conversely, beam and shell elements also present rotation degrees of freedom, allowing the computation of bending moments and shear forces. Hence, for the simulation of structural elements, bars are often employed to model props supporting an excavation, while beams are used to model walls or base slabs, where a significant deflection is expected. It should be noted that beam and bar elements employed in a 2D analysis are, respectively, the equivalent of shells and membranes employed in a 3D analysis.

A variety of problems can be simulated using these structural elements in non-isothermal analyses, such as:

- a 2D beam or a 3D shell element with a thermo-mechanical coupling can be employed, respectively in a 2D or 3D analysis, to simulate a structural element used as heat exchanger, such as a wall. Clearly, the simplification adopted in simulating a wall with such elements can be significant (see Zdravković et al. (2005) for a comparison of simulating conventional walls with solid or beam elements);
- 2D or 3D beam or bar elements, for application in a 2D or 3D analysis respectively, with a fully coupled THM formulation can be employed in the simulation of thermal drains used to accelerate consolidation beneath embankments (e.g. Pothiraksanon et al., 2010);
- 2D or 3D beam or bar elements with temperature and fluid pressure degrees of freedom (and displacement degrees of freedom in a fully coupled THM analysis) can be employed to model heat exchanger pipes, i.e. an element through which water flows and heat transfer takes place through advection and conduction. This is the type of application most used throughout this research project.

2.3.5 Numerical challenges and current modelling practice

The simulation of fully coupled THM problems is complex and comprises a series of numerical challenges the user should be aware of. In this section, the outcome of recent research carried out within the numerical group in the Geotechnics section at Imperial College is outlined, which defines the current modelling practice for THM simulations carried out with ICFEP and adopted within this thesis.

Time-step constraints

Cui et al. (2016b) and Cui et al. (2019) have shown that, when simulating thermal or coupled thermo-hydraulic problems, hydraulic and thermal shock problems can be encountered. These occur if the size of the time step is not adequate and lead to oscillations of pore water pressures or temperatures, respectively. It was found that there is a critical time step below which these phenomena take place.

The critical time step, Δt_{cr}, depends on the type of element employed, i.e. whether the adopted shape functions are linear or quadratic, and was shown to be generally graver for heat transfer problems when compared to those focusing on modelling consolidation. Hence, only the minimum time step for the former type of problem is outlined in this section.

To avoid the thermal shock problem for one-dimensional heat conduction or coupled heat conduction-advection analyses, Cui et al. (2016b) proposed time step constraints, which were determined adopting two non-oscillatory criteria: (1) non-negative temperatures at any node within the mesh and (2) monotonically decreasing temperature with distance from the heat source.

The minimum time step that satisfies both non-oscillatory criteria for linear and quadratic elements is given, respectively, in Equations (2-25) and (2-26) (Cui et al., 2016b):

$$\Delta t \geq \frac{C_v h_e^2}{3\theta\lambda(2+Pe)} \tag{2-25}$$

$$\Delta t \geq \frac{3C_v h_e^2}{20\theta\lambda(3+Pe)} \tag{2-26}$$

where C_v is the volumetric heat capacity (J/m^{3}K), h_e is the size of the element in the direction of heat transfer (m), θ is the time-marching factor (the time-marching scheme adopted in ICFEP is the θ-method (Wood, 1990; Potts & Zdravković, 1999)), λ is the thermal conductivity (W/mK) and Pe is the Péclet Number (see Equation (2-5)). It should be noted that the minimum time-step for the special case when only heat conduction takes place is obtained by setting Pe = 0.0 in the expressions above.

The critical time step for two-dimensional heat conduction is more complex to establish. Indeed, Cui et al. (2019) found that for quadratic two-dimensional elements not only it is not possible to satisfy the criterion (2) listed above but also the order of integration has a considerable effect on the size of the minimum time step required to satisfy criterion (1). This led to conclude that for 2D transient problems, the use of quadratic elements may not always be beneficial, noting that, in this context, this refers solely to the order of the shape functions adopted to describe temperature fields. For linear elements, Cui et al. (2019) showed that the minimum time step depends on the aspect ratio when rectangular elements are employed. Furthermore, in such case, criterion (2) could only be satisfied for aspect ratios lower than 1.2.

In some cases, the calculated critical time-step may be too large, leading to inaccurate solutions. In order to overcome this problem, while at the same time avoiding spatial oscillations, Cui et al. (2016b) provide the following recommendations:

(1) reducing the element size close to the location where the boundary condition is applied;

(2) applying the boundary condition gradually over multiple steps, ensuring that the total time is equal to the critical time step.

Thermo-hydraulic coupled problems

Coupled thermo-hydraulic problems involve heat transfer and water flow occurring simultaneously within a medium. These are particularly significant in the context of geothermal systems when modelling, for example, open loop systems or the heat transfer occurring within heat exchanger pipes. In Section 2.3.2 it was stated that, in such cases, the application of the thermo-hydraulic boundary condition is necessary along the boundaries where the water enters or leaves the mesh. This is due to the fact that the water carries energy with it, which, if not balanced along these boundaries, induces an unrealistic build-up of temperatures. This phenomenon is shown in Figure 2-15 (Cui et al., 2016a), which depicts the temperature distribution along a bar at an initial temperature of 10°C, through which water flows from left to right. At one end of the bar, a prescribed temperature of 20°C was applied, while the other end was considered adiabatic. As can be noted, at the end of the bar where the water leaves the mesh, an unrealistic temperature rise is observed, with temperatures exceeding those prescribed at the other end. This problem is solved by applying the thermo-hydraulic boundary condition. This boundary condition is therefore necessary, for example, at the outlet of heat exchanger pipes, while it can usually be avoided at the inlet, since the temperature is often prescribed in that position (see Chapter 4). It should be noted that, due to the non-linear nature of this boundary condition, small time-steps may be required to ensure convergence.

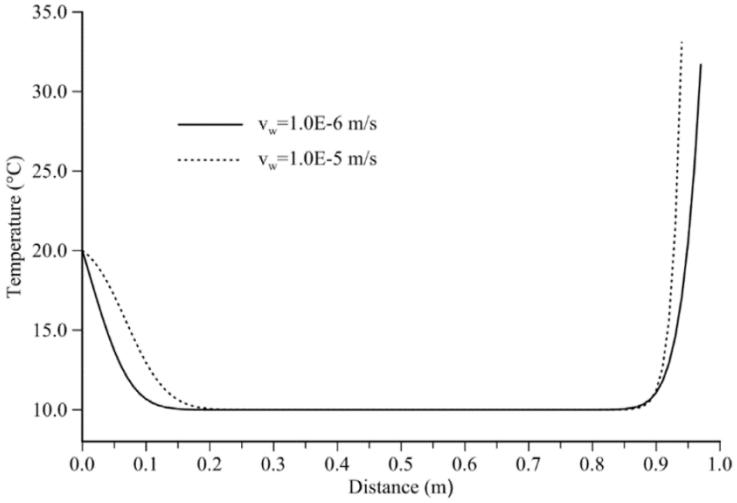

Figure 2-15: Temperature distribution along a bar with different water flow velocities without the application of the thermo-hydraulic boundary condition (Cui et al., 2016a)

Highly advective flows

In advection dominated problems, i.e. in cases where the Péclet number (see Equation (2-5)) is larger than 1.0, instabilities of the numerical solution, in the form of spatial oscillations, are encountered when using the Galerkin FE method (Cui et al., 2016a). The occurrence of these oscillations also depends on

the employed boundary conditions. For example, a bar with prescribed temperatures on both ends displays oscillations at steady state (Figure 2-16 (a)), whereas with prescribed temperature on one end and the thermo-hydraulic boundary condition on the other end, oscillations occur after thermal breakthrough, while stable solutions are obtained at steady state (Figure 2-16 (b)).

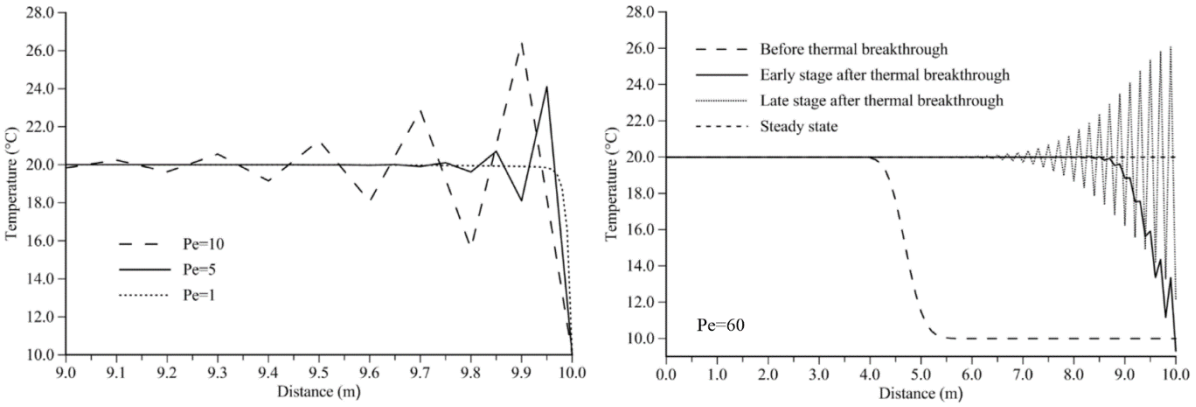

Figure 2-16: Spatial oscillations in highly advective flows along a bar (a) effect of Péclet number on steady state solution with prescribed temperature on both ends and (b) with prescribed temperature on one end and thermo-hydraulic boundary condition on the other end at different time instants (Cui et al., 2016a)

In order to avoid these issues, the Péclet number has to be reduced, which can only be obtained by decreasing the element size (see Equation (2-5)). However, to ensure a $Pe \leq 1.0$, elements need to be very small, such that it would lead to an extremely large number of elements within the mesh, with the associated increase in computational cost. An alternative way to overcome this problem is to adopt the Petrov-Galerkin (PG) FE method, which is one type of upwind finite element methods. As such, the principle behind the PG formulation is the introduction of modified nodal weighting functions according to which the contribution of the upstream node is larger than that of the downstream node. The choice of the Petrov-Galerkin FE method over other types of upwind formulations was justified by Gawecka (2017) and Cui et al. (2018c) since their research showed it being able to provide accurate and stable solutions, for both transient and steady-state advection-conduction problems. For this to be the case, contrary to some of the approaches proposed in the literature, they found that the modified weighting functions should be applied to all the terms of the time-dependent advection-conduction equation (Cui et al., 2018c).

The details of the PG formulation, implementation and application for one-dimensional and two-dimensional linear and quadratic elements are outlined in Gawecka (2017) and Cui et al. (2018c), where novel weighting functions for 8-noded quadratic 2D elements have been proposed. Furthermore, the formulation implemented in ICFEP is also able to produce stable results in cases of multi-dimensional flows and with meshes containing distorted elements.

Simulating heat exchanger pipes

As previously outlined, 2D and 3D beam and bar elements can be employed to simulate heat exchanger pipes within ground source energy systems, given their coupled thermo-hydraulic formulation. Clearly, due to the highly advective flows taking place within the pipes, the Petrov-Galerkin FE method has to be adopted when simulating such problems. However, 2D and 3D beam and bar elements, as described in Section 2.3.4, are one-dimensional, zero-thickness elements. As depicted in Figure 2-17, which compares the evolution with time of the outlet temperature obtained when simulating a single pipe using either a beam element or solid elements with an actual cross-sectional area with prescribed inlet temperature and water flow, Gawecka et al. (2020) showed that the sole use of beam elements leads to a potential underestimation of the heat transfer between the pipes and the surrounding medium, particularly in the short term. This is attributed to the fact that one-dimensional elements have a zero-lateral area of contact with the surrounding medium, thus reducing radial heat transfer rates.

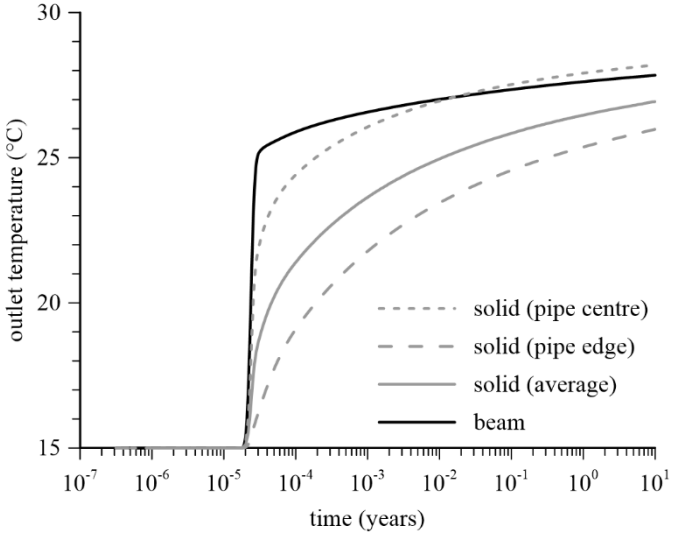

Figure 2-17: Outlet temperatures in the pipe modelled with solid elements and beam elements (Gawecka et al., 2020)

Through an extensive study, Gawecka et al. (2020) proposed a new modelling approach which is able to eliminate the impact of the aforementioned phenomenon. This approach consists of surrounding the one-dimensional elements by solid elements having properties of a new material, termed "Thermally Enhanced Material" (TEM), through which only conduction is simulated. These solid elements have the same cross-sectional area as the water inside the pipe (i.e. $\pi D^2/4$, with D being the inner diameter of the pipe) and an increased thermal conductivity than that of water or concrete, enhancing the heat transfer. In fact, Gawecka et al. (2020) demonstrated that a suitable thermal conductivity for the TEM, λ_{TEM}, is 10 W/mK, and that this value is independent of any other problem parameter, such as the thermal conductivity of the material in which the pipe is placed, the water flow rate, and the pipe diameter. Furthermore, an additional study was carried out to identify the effect of the plastic pipe wall (i.e. the presence of a low conductivity material between the water and concrete). Accounting for this

leads to a reduced thermal conductivity of the TEM, which depends directly on the pipe diameter, according to the following equation:

$$\lambda_{TEM-wall} = 3.62 \ln(D) - 7.33 \quad (2\text{-}27)$$

where D is the pipe inner diameter (mm), limited to 10 mm $\leq D \leq$ 40 mm.

This approach was validated in Gawecka et al. (2020) by using 3D thermo-hydraulic analyses to reproduce two thermal response tests, one involving a borehole heat exchanger within a laboratory environment (Beier et al., 2011) and one conducted on a pile installed in London (Loveridge et al., 2014). The results showed an excellent agreement with the measured data (pipe temperatures and temperatures within and in the vicinity of the heat exchanger) when the TEM was included in the simulation. A further verification of this modelling approach applied to thermo-active walls is presented in Chapter 4.

Coupled THM analyses with heating and cooling cycles

Laboratory tests have shown that the soil presents a stiffer response when a change in loading direction takes place, i.e. when a sample is unloaded after a loading stage or vice versa (Atkinson et al., 1990; Jardine, 1992). When a non-linear stiffness model is adopted (such as that described in Chapter 3), this can be simulated by re-setting the model's hardening parameters such that the stiffness reverts to its maximum value. Schroeder et al. (2004) provided insights into the importance of this when simulating boundary value problems under mechanical loading. Gawecka et al. (2017) have demonstrated that this phenomenon should also be taken into account when simulating thermal analyses, since heating/cooling may imply a change in the loading direction when compared to a previous stage (where heating can be generally, but not strictly, associated to a loading stage and cooling to unloading). Gawecka et al. (2017) reproduced numerically the Lambeth College Pile Test (see Bourne-Webb et al. (2009) for details), performing different analyses where the reset of the stiffness to its maximum value was performed at different stages, as depicted in Figure 2-18 together with the results in terms of pile head displacement with time. In particular, in analysis LC1, the resetting was performed at every mechanical unloading and reloading stage and at the start of the cooling and heating stages; analysis LC2 is similar to LC1, with the exception that no resetting was performed at the start of the initial cooling stage, while LC3 did not include any resetting of the stiffness. The results shown in Figure 2-18, together with a better match for analyses LC1 to other measured quantities during the field test (see Gawecka et al. (2017) for details), led to conclude that resetting the stiffness upon heating and cooling produces more accurate results. However, its effect is less crucial than during mechanical loading.

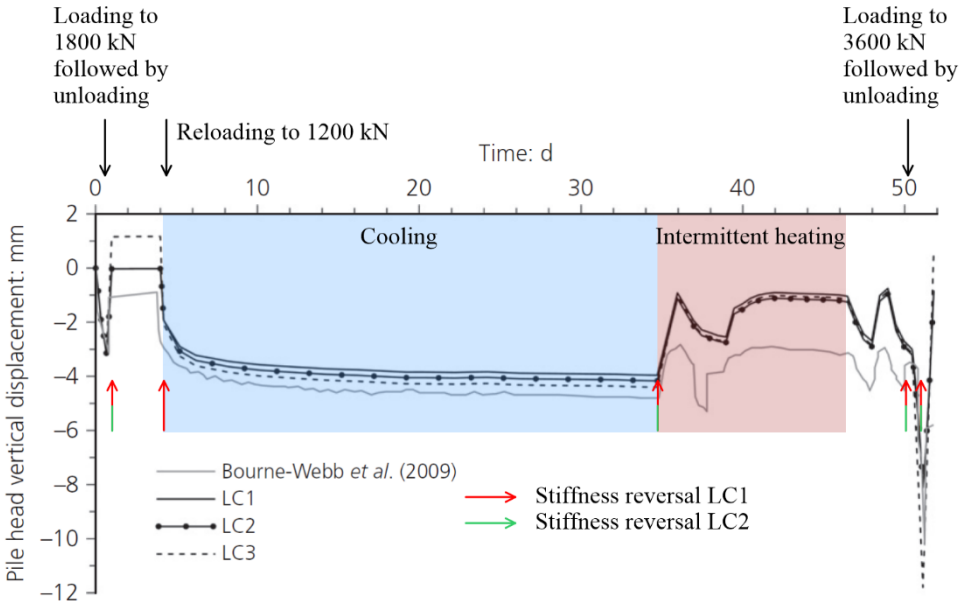

Figure 2-18: Measured and predicted pile head vertical displacement during Lambeth College Test (adapted from Gawecka et al. (2017))

2.4 Thermo-active retaining walls

Thermo-active walls can be constructed as piled walls or diaphragm walls, where the choice of the type of structure depends on many factors which are related to their geotechnical design, such as cost, ground conditions, limits on movements, etc. (CIRIA, 2017; Institution of Civil Engineers, 2007). When used as heat exchangers, piled walls are made of a series of piles, where usually only some include heat exchanger pipes, depending on their construction method (Suckling & Smith, 2002; Brandl, 2006); diaphragm walls consist of rectangular wall panels and generally all panels are equipped with heat exchanger pipes. This type of wall has been the focus of recent investigations and is analysed within this research project. As outlined at the beginning of this chapter, the use of thermo-active walls is more recent when compared to that of piles. This is probably due to the limited field investigations performed on thermo-active walls (e.g. Brandl, 2006; Xia et al., 2012; Sterpi et al., 2018) and their complex nature, both in terms of geometry and installation on site. Figure 2-19 shows a schematic representation of a thermo-active wall panel forming part of a diaphragm wall used to support an excavation. Its components are the concrete structure and the heat exchanger pipes, through which energy is exchanged with the ground. Contrary to thermo-active piles, which are fully embedded in soil, thermo-active walls are partly exposed to an environment. Thus, heat exchange takes place both with the soil through conduction (or convection if water flow is significant) across the soil-wall interface and with the environment through convection (according to Equation (2-6)) along the exposed part of the wall. The thermal interaction with the environment is affected by different factors (as subsequently discussed). Furthermore, the underground space may be composed of different levels such that the wall is connected to permanent internal structures, with their properties and type of connection affecting the structural

behaviour of the wall. It should be noted that in some cases the base slabs are also used as heat exchangers (Brandl et al., 2010; Sterpi et al., 2018; Makasis et al., 2019).

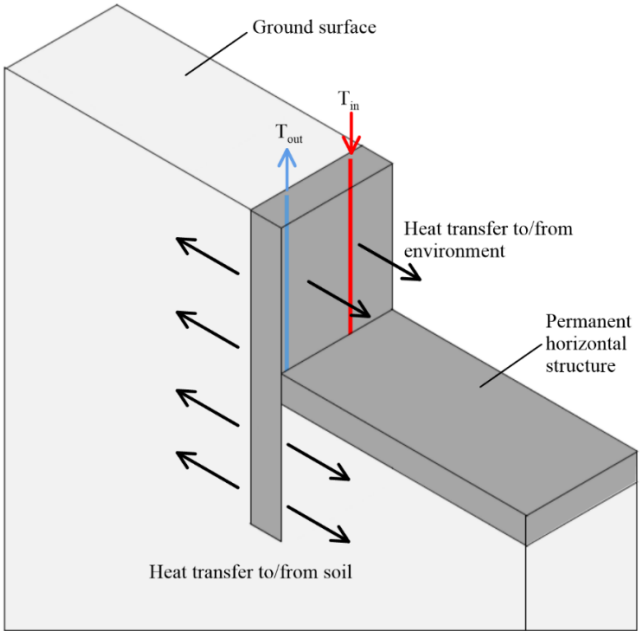

Figure 2-19: Schematic representation of thermo-active retaining wall problem

2.4.1 Current practice

Very little information is currently available on the design practice for thermo-active walls. Indeed, information on the installation procedure is mainly available from case studies.

Figure 2-20 depicts a typical reinforcement cage equipped with heat exchanger pipes. The latter are usually made of high-density polyethylene with an internal diameter in the order of 25.0 mm. The pipes can either be fixed to the cage before or while it is being lowered into the trench (see Figure 2-20 and Figure 2-21, respectively).

Figure 2-20: Reinforcement cage with heat exchanger pipes for thermo-active diaphragm wall (Hofinger & Kohlböck, 2005)

The position and configuration of the pipe loops, as described in Section 2.2.4, is one of the aspects that are designed to satisfy the energy requirement of the building. However, the pipe layout may be affected by the practicability of installation on site (Amis et al., 2010). The adopted configuration of the pipes differs amongst projects, but, generally, vertical pipes are installed (e.g. Amis et al., 2010; Brandl et al., 2010; Soga et al., 2014), as those depicted in Figure 2-21 (Bulgari Hotel in Knightsbridge (London), Amis et al. (2010)). Brandl (1998) describes the loops installed within the retaining walls constructed for an Arts Centre in Austria, which were horizontal, as shown in Figure 2-22. A similar configuration was initially also considered for the Bulgari Hotel in Knightsbridge (London). However, due to the complexities related to the transportation of the cages and installation of the pipe loops on site, vertically placed pipes were preferred (Amis et al., 2010). Most of the projects described in literature present pipe loops installed on the retained side, as it is considered to be more efficient than placing pipes on the excavated side of the wall, due to possible heat losses towards the excavation. According to Hofinger & Kohlböck (2005), the position of the pipes within the panel depends on the combination between the expected use of the system (whether it is used predominantly for heating or cooling) and the conditions inside the excavation: if low temperatures are expected inside the excavation and the system is employed for heating, then the pipes should be placed on the retained side to take advantage of the soil temperatures; conversely, if it is used for cooling and relatively low temperatures are encountered in the summer months inside the excavation, pipes on this side would enhance heat injection.

(a) (b)

Figure 2-21: Installation of thermo-active diaphragm wall at Bulgari Hotel, London (Amis et al., 2010)

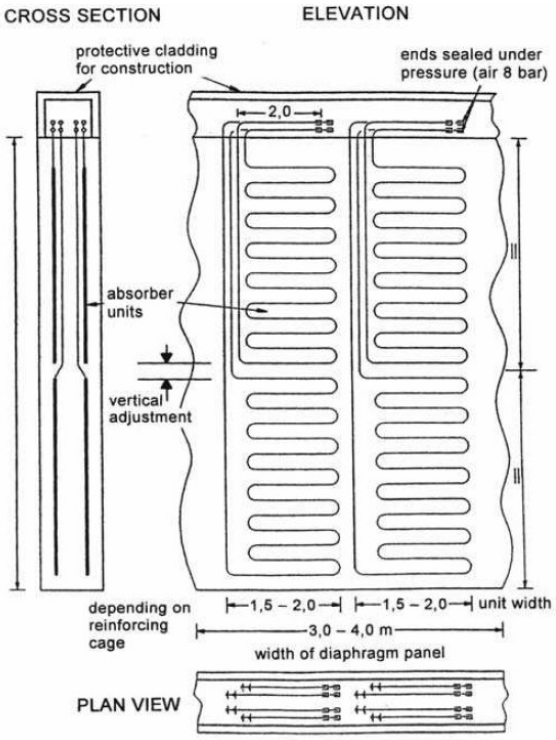

Figure 2-22: Pipe layout at the Arts Centre in Bregenz, Austria (Brandl, 1998)

Brandl et al. (2010) describe the planning and construction process of the geothermal systems installed in four stations of the U2 Vienna Metro Line in Austria. Heat exchanger pipes were included in several types of structural elements, including piles, walls, slabs and tunnel linings. During the planning phase, Brandl et al. (2010) report that, initially, there were concerns from the water agency regarding changes in temperature within the ground. These were overcome by assuring the agency, through numerical computations, that the effect of changes in ground temperature is restricted to 5-10 m around the structures, which would be even less if ground water flow would have been considered in the simulation. The project was able to obtain all the permissions constituting a precedent for future ground source installations in Austria. During the tender process, a particular problem was the regulation surrounding the integrity of pipe loops, which tend to fail frequently even in the case of a careful installation. However, it is also stated that the failure of some of the loops may not compromise excessively the system, since it will merely lead to somewhat higher/lower temperatures within the remaining heat exchanger pipes. In this specific case, within the tender, a failure of 3% of the total loop length was considered acceptable. During installation, the loops were tested multiple times (after installation within the cages and during some stages of concreting) through pressure tests and it resulted that only 1% of the loops had failed. During the detailed design stage, Brandl et al. (2010) report that investigations were carried out to evaluate the effects of heat exchange on the mechanical response of the structures and whether ground freezing could occur. However, no details are provided about the outcome of these studies, nor if and how the design of the structures was affected to take into account temperature effects. To evaluate the performance of the system, from a thermal and mechanical perspective, numerous

temperature sensors and strain gauges have been installed within one of the diaphragm walls at the Taborstraße station. To date, only preliminary temperature data are available in Brandl et al. (2010), which are discussed in Section 2.4.3.

Amis et al. (2010) and Bourne-Webb et al. (2013a) provide details on the construction process of the thermo-active diaphragm walls installed at the Bulgari Hotel in Knightsbridge, which is the first project of its kind in the UK. The diaphragm walls are 36.0 m long and 0.8 m thick, with two U-shaped pipe loops within each panel (Figure 2-23). The main concerns prior to the construction of the walls were related to the installation of the pipe loops, which should not increase the congestion of the reinforcement cage, nor delay the construction process. To accommodate the pipes, which were attached on the outside of the reinforcement cage on the retained side (see Figure 2-23), the concrete cover was increased to keep the same concrete cover of 75.0 mm and the arrangement of the bars on that side of the wall was altered to avoid congestion. Even in this case, no details were provided regarding the design process and if temperature effects were considered in the structural design.

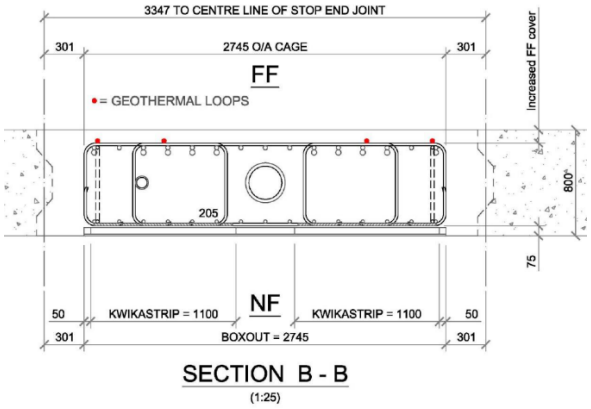

Figure 2-23: Plan view of a thermo-active diaphragm wall panel at Bulgari Hotel, London (Amis et al., 2010)

2.4.2 Characterisation of the thermal environment

One of the peculiarities of thermo-active walls when compared to other closed loop systems, such as borehole heat exchangers or thermo-active piles, is that they are not fully surrounded by soil, but partly exposed to an environment. This implies that, when designing these structures, the interaction between the wall face above excavation level and the environment of the underground space has to be characterised. Indeed, this affects the heat transfer from the wall to the surrounding environment, which thus influences the temperatures within the wall and, consequently, its thermal performance and mechanical behaviour.

The characterisation of the thermal environment of the underground space is not simple, as its conditions depend on many factors, such as the function of the space, its geometry, the climatic conditions, etc. Herein, it is assumed that most of the thermo-active retaining walls are built to support an underground space and are hence in contact with air (there is a possibility they would also be

supporting water filled chambers, e.g. shafts, or be part of a river wall). The interaction between the wall and the surrounding environment is governed by convection (Newton's law of cooling), expressed through Equation (2-6). The uncertainty in evaluating the heat flux from the structure to the surrounding fluid resides in the estimation of the convective heat transfer coefficient h. This depends mainly on the air flow velocity within the space, which in turn categorises the convective heat transfer into either forced convection or natural convection. In forced convection, the flow of fluid is generated by external means (e.g. a pump or fan), while in natural convection it occurs due to natural means, such as the buoyancy effect, where flow is driven by differences in density resulting from changes in temperature (Çengel & Ghajar, 2011). Hence, the former is characterised by high flow velocities, whereas these are very low (less than 1.0 m/s) in the latter. According to Awbi & Hatton (1999), the convective heat transfer coefficient for surfaces of buildings is affected by the shape of the space, the surface temperature, the presence of forced air (caused by breezes or devices, such as fans and radiators) and the surface roughness.

In general, the convective heat transfer coefficient, h (W/m^{2}K), for plane surfaces (such as walls) is expressed by the following equation:

$$h = Nu\frac{\lambda}{L} \tag{2-28}$$

where Nu is the Nusselt Number (-), λ is the thermal conductivity of the fluid (W/mK) and L is the length of the surface (m). The Nusselt number depends on the type of convection, i.e. whether it is forced or natural, and on the geometry of the surface, and is usually determined experimentally (herein only expressions for plane surfaces are reported).

Within the context of thermo-active structures exposed to an underground space (i.e. either retaining walls or tunnels), focus has been given to characterising environments where high flow velocities may occur, such as railway stations and tunnels, thus characterised by forced convection.

Çengel & Ghajar (2011) report the expressions for the average Nusselt Number for forced convection along a plate, for either laminar (Equation (2-29)) or turbulent (Equation (2-30)) flow:

$$Nu = 0.664Re^{0.5}Pr^{\frac{1}{3}} \qquad Re < 5 \times 10^5 \tag{2-29}$$

$$Nu = 0.037Re^{0.8}Pr^{\frac{1}{3}} \qquad 10^5 \leq Re \leq 10^7, 0.6 \leq Pr \leq 10^7 \tag{2-30}$$

where Re and Pr are, respectively, the dimensionless Reynolds and Prandtl Number, defined as:

$$Re = \frac{\rho v L}{\mu} \tag{2-31}$$

$$Pr = \frac{\mu C_p}{\lambda} \tag{2-32}$$

where ρ is the density (kg/m^3), v is the velocity of the fluid (m/s), μ is the dynamic viscosity (kg/sm), C_p is the specific heat capacity (J/kgK) and λ is the thermal conductivity (W/mK). The Reynolds Number expresses the ratio between inertia and viscous forces and determines the flow regime (laminar or turbulent), while the Prandtl number is defined as the ratio between the momentum diffusivity (also kinematic viscosity) and thermal diffusivity (see Equation (2-10)) and therefore indicates the rate at which heat diffuses relative to momentum (Çengel & Ghajar, 2011). For gasses, the Prandtl number is ~1.0.

It should be noted that numerous expressions exist for the calculation of the convective heat transfer coefficient (h) for flat surfaces, which may be a function of either the wind speed and the surface length, or of the thermal boundary layer type (as the ones above) (see Palyvos (2008) for a summary of different available expressions). Bourne-Webb et al. (2016b) provide a comprehensive review of information on the thermal environment within tunnels, where studies on forced convection were taken into account. The relationship between the convective heat transfer coefficient and the air flow velocity is depicted in Figure 2-24 for a variety of correlations. It can be seen that the value of h at a given velocity v varies over a large range and, overall, it is found to vary between approximately 4.0 W/m^{2}K to 30 W/m^{2}K.

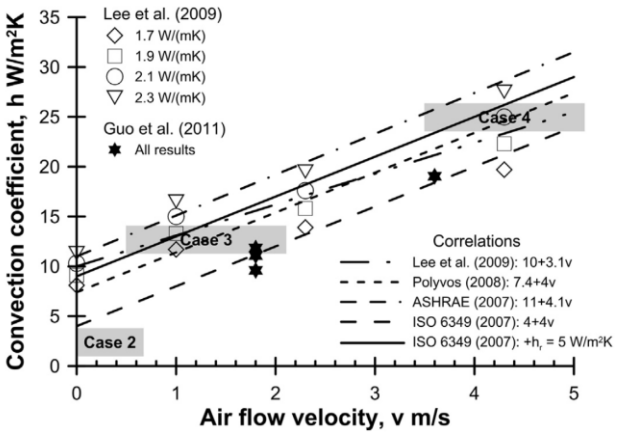

Figure 2-24: Correlations for convective heat transfer coefficient for forced convection from different sources (Bourne-Webb et al., 2016b)

Clearly, the underground space to which thermo-active retaining walls are exposed is not necessarily an open environment or subjected to forced convection. Indeed, it may be a storage room, basement or a museum for example, where low flow velocities are expected. In such case, it is considered that the heat transfer between the structure and the environment is characterised by natural convection, for which the heat transfer coefficient is much lower than in the case of forced convection. For natural convection, the Nusselt Number is a function of the Prandtl Number and the Grashof Number, Gr. The

latter has a similar meaning to the Reynolds number for forced convection, and is expressed as the ratio of the buoyancy force to the viscous force (Çengel & Ghajar, 2011):

$$Gr = \frac{g\alpha_{vol}(T_s - T_\infty)L_c^3}{(\mu/\rho)^2} \tag{2-33}$$

where g is the gravitational acceleration (m/s^2), α_{vol} is the volumetric coefficient of thermal expansion (1/°C), T_s is the surface temperature (°C), T_∞ is the ambient temperature (°C) and L_c is the characteristic length of the geometry (m).

The product of the Grashof Number and the Prandtl Number is defined as the Rayleigh Number, Ra:

$$Ra = Gr\ Pr \tag{2-34}$$

Similar to the convective coefficient for forced convection, which was a function of the fluid flow velocity incorporated in the Reynolds number, in the case of natural convection, h depends on the temperature difference between the surface and the ambient temperature (i.e. $\Delta T_s = T_s - T_\infty$) employed to calculate the Grashof number.

There are numerous expressions for the convective heat transfer coefficient for natural convection which were determined experimentally (see Peeters et al. (2011) and Khalifa (2001) for extensive reviews on correlations for different geometries). Churchill & Chu (1975) proposed the following expression for the Nusselt Number for natural convection over a vertical plate, which is valid for any value of Ra:

$$Nu = \left\{0.825 + \frac{0.387Ra_L^{1/6}}{[1 + (0.492/Pr)^{9/16}]^{8/27}}\right\}^2 \tag{2-35}$$

The variation with the temperature difference ΔT_s of the convective heat transfer coefficient reported by Wallentén (2001) and Awbi & Hatton (1999) from different correlations for a plane surface is depicted in Figure 2-25 and Figure 2-26, respectively, which show that h varies between 0.0 W/m^{2}K and 5.0 W/m^{2}K, within a range of ΔT_s of 0°C to 25°C. Thus, it is clear that the convective heat transfer coefficient in the case of natural convection varies within a more limited range when compared to that of forced convection. Furthermore, since it is dependent on ΔT_s, for thermo-active structures, it is expected to vary both due to the operation of the GSES (which affects the surface temperature) and the temperature within the underground space, which may be affected by the seasonal temperature variations of the external temperature. Lastly, it should be noted that the value of h suggested by ISO (2017) for horizontal heat from vertical surfaces within an environment with flow velocity of zero (still air) is 2.5 W/m^{2}K, which is in between the extremes found in literature.

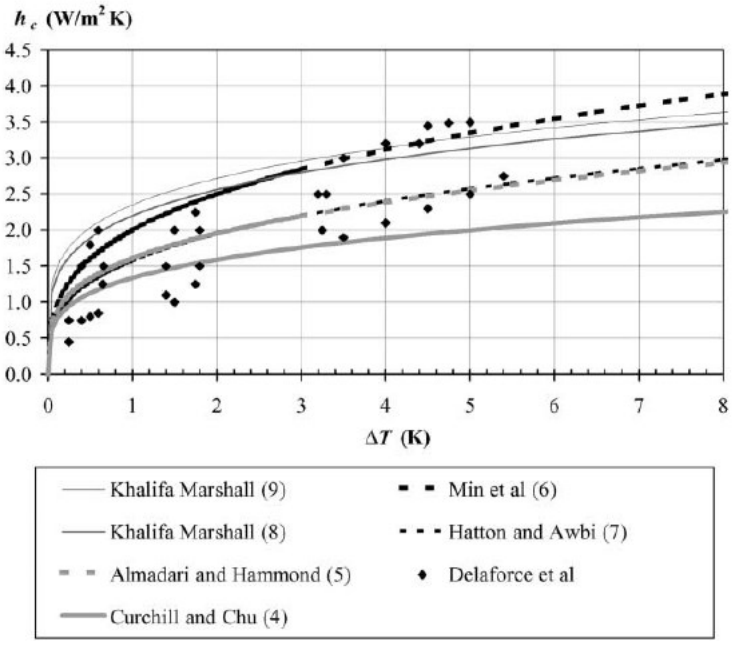

Figure 2-25: Correlations for convective heat transfer coefficient for natural convection for wall surfaces from different sources (Wallentén, 2001)

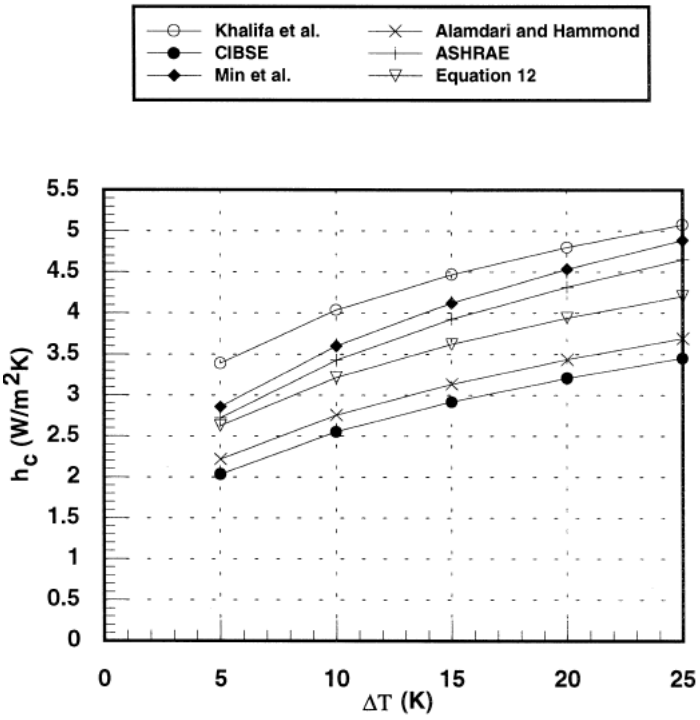

Figure 2-26: Correlations for convective heat transfer coefficient for natural convection for wall surfaces from different sources (Awbi & Hatton, 1999)

The impact of different boundary conditions along the exposed face of a thermo-active retaining wall is investigated throughout this thesis, with its effect on the heat transfer mechanisms and the thermal performance being evaluated in Chapter 4 and Chapter 5, whereas Chapter 6 assesses its impact on the thermo-mechanical behaviour.

2.4.3 Observed behaviour in field and laboratory tests

Table 2-1 presents a summary of the research conducted on thermo-active walls by either field monitoring or laboratory tests, which is rather limited compared to that carried out on thermo-active piles. Most of the monitoring schemes comprise only temperature data, while a comprehensive set of data including strain measurements is not available. While the majority of the studies are applied to concrete diaphragm walls, there are two laboratory studies that assess the use of new types of application, namely heat exchanger pipes installed within seal panels instead of the concrete structure (Kürten et al., 2015) and sheet pile walls (Ziegler et al., 2019).

Table 2-1: Summary of field monitoring and laboratory tests on thermo-active retaining walls

Reference	Type of study	Wall details	Monitored data
Markiewicz (2004); Brandl (2006) (Lainzer Tunnel)	Field monitoring	Contiguous pile wall L = 17.0 m D = 1.2 m d_e = 10.0m	○ strain measurements/horizontal movements ○ temperatures within concrete structures
Markiewicz (2004); Brandl et al. (2010) (Taborstraße)	Field monitoring	Diaphragm wall H = 0.8 m	○ pipe temperatures ○ strain measurements/horizontal movements (not published) ○ temperatures within concrete structures (not published)
Amis et al. (2010); Amis (2010); Bourne-Webb et al. (2013a)	Field test	Diaphragm wall L = 36.0 m H = 0.8 m B = 3.3 m d_e = 24.0m	○ short-term inlet and outlet temperatures
Xia et al. (2012)	Field test	Diaphragm wall L = 38.0 m H = 1.0 m B = 1.5 m d_e = 18.5 m	○ measured heat flux
Qi (2015); Soga et al. (2014)	Field test	Diaphragm wall L = 40.0 m H = 1.0 m d_e = 25.0 m	○ short-term inlet and outlet temperatures
Sterpi et al. (2018); Sterpi et al. (2020); Angelotti & Sterpi (2018)	Field monitoring	Diaphragm wall L = 15.5 m H = 0.5 m B = 2.4 m d_e= 9.5 m	○ inlet and outlet temperature ○ flow rate ○ ground temperature at different locations ○ wall temperature
Dong et al. (2019)	Large-scale laboratory test	Concrete wall	○ inlet and outlet temperatures ○ ground temperature ○ vertical strain
You et al. (2019)	Centrifuge test	Copper wall	○ inlet and outlet temperatures ○ ground temperature ○ vertical strain
Kürten et al. (2015)	Large-scale laboratory test	Wall seal panel	○ measured heat flux ○ inlet and outlet temperatures
Ziegler et al. (2019)	Large-scale laboratory test	Sheet pile wall	○ measured heat flux

Key: L = length; H = thickness, B = width, D = diameter, d_e=excavation depth

Field monitoring

The only case study presenting strain measurements within a thermo-active wall is the one included in Markiewicz (2004) and Brandl (2006). The thermo-active wall, forming part of a cut-and-cover tunnel section of the Lainzer Tunnel in Austria, consists of a bored piled wall, where every third pile is used as a heat exchanger (59 in total). The diameter of the piles is 1.2 m and their average length is 17.0 m, with an excavation depth of 10.0 m. The heat exchanger pipes are made of high density polyethylene (HDPE), with an internal diameter of 20.0 mm and a wall thickness of 5.0 mm. According to the drawings included in Markiewicz (2004) and Brandl (2006), 4 to 5 U-loops are installed within each pile, with a total pipe length of 9709 m. Six piles were instrumented, with temperature sensors located towards the retained side at different depths (approximately 8.0 m intervals). One of these piles includes combined temperature and strain sensors, on both the excavated and retained side of the pile, which were installed every 4.0 m along the length of the pile. The heat pump operation started in February 2004 and monitoring data is reported until December 2004. During the first six weeks of operation, the system was able to deliver 40 MWh of energy (assuming continuous operation, this corresponds roughly to 40W per metre length of thermo-active pile). Bouazza & Adam (2012) report that in autumn 2004 the system was connected to a school building and provided 186.2 MWh and 193.9 MWh, respectively during the 2004/2005 and 2005/2006 winter seasons. The recorded temperatures show that during intense operation periods, uniform temperature distributions develop within the concrete structure, both with depth and across the thickness of the piles. During periods of low energy demand or when the system is switched off (spring/summer), substantial differences in temperature are recorded along the depth of the pile, with higher temperatures within the top part (above the base slab). In this region, a temperature gradient was recorded across the thickness of the pile. Conversely, below the base slab, uniform temperatures were recorded along this dimension. This indicates the effect of the wall-environment interaction, where a temperature gradient develops within the wall due to the natural temperature changes within the tunnel environment, which are not experienced below the base slab, where the wall is fully surrounded by soil. Figure 2-27 displays the changes in wall axial strains before and during heat pump operation as re-examined by Bourne-Webb et al. (2016b) for different time intervals. According to Brandl (2006), the temperature-induced strains are much smaller than those due to mechanical stresses. Furthermore, as can be seen when comparing Figure 2-27 (a) and (b), i.e. before the start of the operation of the geothermal system, to Figure 2-27 (c), i.e. after the operation has begun, larger changes in axial strain developed due to the natural temperature fluctuation within the tunnel when compared to the temperature changes generated by the heat pump operation. Indeed, as previously mentioned, this latter leads to a more uniform temperature within the wall profile, thus reducing the differential strains between the head and toe of the wall, as well as across its thickness.

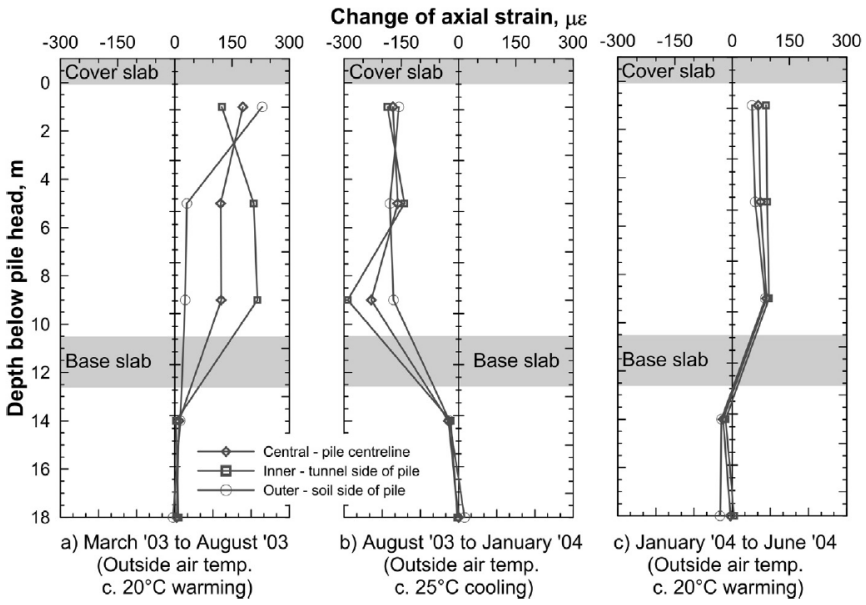

Figure 2-27: Variations in wall axial strain prior and during heat pump operation of thermo-active wall within Lainzer Tunnel (Bourne-Webb et al. (2016b) adapted from Brandl (2006))

Brandl et al. (2010) provide the temperature values measured within one panel of the thermo-active diaphragm wall installed at the Vienna metro station of Taborstraße, which was only used for cooling, with pipe loops installed on both sides of the wall. The temperatures were recorded at the excavation and retained sides of the wall and show that the retained side is cooler than the excavated side in the summer and warmer in the winter. This justifies the installation of the pipes on both sides of the wall in order to take advantage of the favourable conditions on different sides of the wall during different seasons. Furthermore, the temperatures on the excavation side vary considerably along the depth of the wall during winter, which is attributed to the different temperatures of adjacent rooms, thus demonstrating the effect the use of the underground space can have on wall temperatures and, potentially, on the thermal performance of the system. The measured inlet and outlet temperatures showed a temperature difference of 1.0°C in the summer, where the energy demand was higher, and of 0.5°C in winter. It is not reported, however, if the energy demand was met entirely through the geothermal operation. Unfortunately, the lack of installed sensors outside structural elements means that this case study cannot be used to draw conclusions on the potential of long-term changes in ground temperatures (and their impact on the thermal performance of the system) arising from the use of unbalanced (in this case, cooling only) geothermal systems.

Amis et al. (2010) describe the construction and installation of geothermal loops within the diaphragm walls of the Bulgari Hotel in Knightsbridge, London. Two thermal response tests (TRT) were carried out, one before excavation and one as the 24.0 m deep basement was fully excavated, to verify the assumed thermal design parameters. Limited data (e.g. Amis, 2010) has been reported so far. Bourne-Webb et al. (2013a) state that the effective thermal conductivity value obtained during the second test was only 10% lower than that calculated during the first test, providing confidence in the employed

value. However, no indication on the test interpretation was provided, i.e. whether the traditional method employed to interpret TRTs, that is applicable to line/cylindrical heat sources, was adopted. Soga et al. (2014) and Qi (2015) analysed the monitored inlet and outlet temperatures recorded during a TRT conducted within a diaphragm wall panel of the Crossrail Tottenham Court Road station (London), before the excavation took place. According to the authors, the conventional methods employed to interpret TRT data for GSESs, such as the infinite line source commonly employed when analysing borehole heat exchangers, do not provide accurate results due to the different heat transfer taking place within walls as a consequence of the different geometry. Indeed, Soga et al. (2014) and Qi (2015) have shown through numerical simulations that the heat exchange during the duration of a conventional TRT test (1-2 days) occurs mainly within the concrete and thus the short-term response of thermo-active walls is mainly affected by the thermal parameters of this material.

Xia et al. (2012) report the results of a field trial carried out on diaphragm wall panels installed within the Natural History Museum of Shanghai to evaluate the energy potential of thermo-active walls. Within the 38.0 m long, 1.0 m thick and 1.5 m wide panels, different pipe layouts were installed (Figure 2-28): "type (a)" consists of two U-loops, with a pipe-to-pipe spacing of 0.15 m, installed on the retained (termed soilward in Figure 2-28) and excavated sides of the wall, with the pipes connected at the top of the panel; "type (b)" is similar to "type (a)", however the U-loop on the retained side has a pipe-to-pipe spacing of 0.75 m; "type (c)" has only one U-loop on the retained side with a pipe-to-pipe spacing of 0.75 m. In addition to the pipe layout, within the field test, the effects of the water flow velocity, v (ranging from 0.25 m/s to 1.5 m/s), the inlet temperature (32°C, 35°C and 38°C) and the operation mode (continuous vs intermittent) were assessed for a period of 48h.

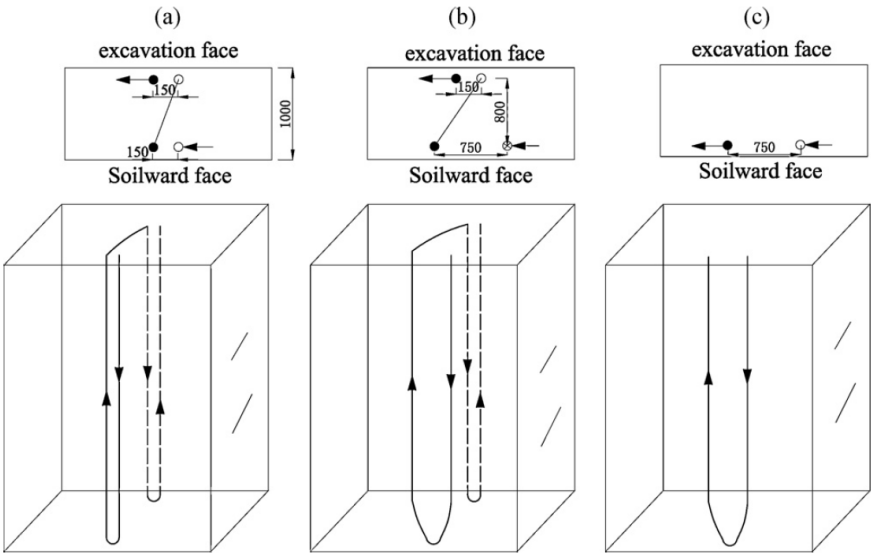

Figure 2-28: Pipe configurations analysed in field trial at the Shanghai Natural History museum (Xia et al., 2012)

The results show that pipe configuration "type (b)" provides the largest heat flux, followed by "type (a)" and "type (c)", as can be seen in Figure 2-29 (a). A larger heat exchange is obtained with a longer

pipe loop and with a larger spacing between the pipes, which decreases the thermal interaction amongst adjacent portions of pipes. Furthermore, as the inlet temperature increases, the heat exchange rate increases, due to the larger temperature differential between the fluid temperature and the surrounding concrete. Although the lines in Figure 2-29 (a) are not completely parallel, Xia et al. (2012) estimated an average increase of performance of 15% for every degree of increase in inlet temperature. The effect of the water flow velocity on the computed heat flux after 48h of operation for pipe configuration "type (b)" and an inlet temperature of 7°C (thus the system is extracting energy and the heat flux is plotted as negative) is reported in Figure 2-29 (b). According to these results, a substantial increase in thermal performance is obtained when water flow velocities increase from 0.25 m/s to 0.9m/s, after which the thermal performance is only marginally affected by this parameter. It should be noted that the water flow velocity, on one hand, affects the time required for the temperature change to reach the pipe outlet (i.e. for thermal breakthrough to occur) and, on the other hand, it is included within the calculation of the heat flux (see Equation (2-13)). Thus, the presented results may not be conclusive for long-term operations, where the first aspect is negligible. Regarding the effect of the operation mode, as expected, an intermittent operation mode results in a higher heat flux when compared to a continuous operation mode. This is due to the fact that the temperatures within the wall are able to dissipate during the period the system is switched off, and hence, on average, a higher temperature difference between the pipes and the concrete is obtained when compared to a continuous operation mode, where the temperatures in the wall increase more steadily with time. However, the two scenarios clearly deliver different total quantities of energy since they operate for different amounts of time. While this case study provided some insights into different aspects of the thermal performance of thermo-active walls, the obtained conclusions are limited to very short-term operational conditions.

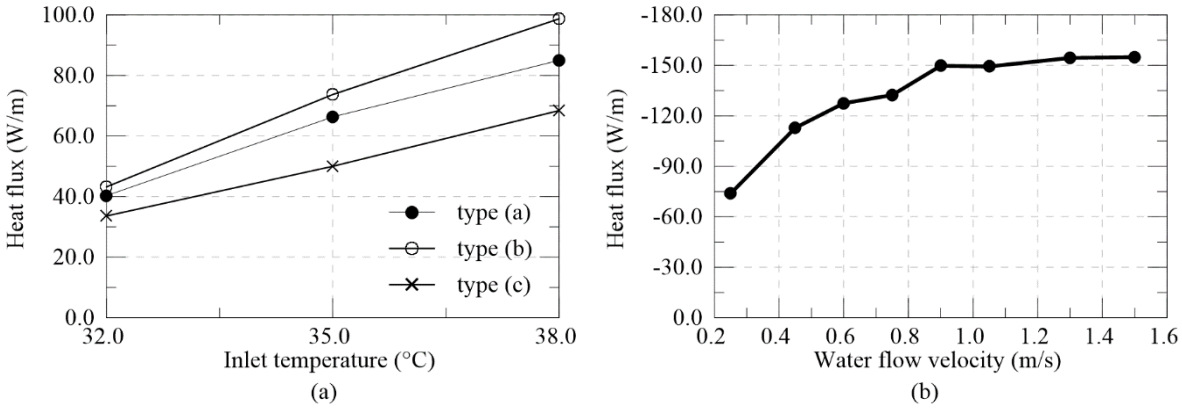

Figure 2-29: Results of field tests on thermo-active walls at the Natural History museum of Shanghai (a) effect of pipe layout and inlet temperature (v=0.6 m/s) and (b) effect of water flow velocity (v) for pipe layout "type (b)" and inlet temperature of 7°C (data from Xia et al. (2012))

The best documented field monitoring of a thermo-active wall is provided by Sterpi et al. (2018), Sterpi et al. (2020) and Angelotti & Sterpi (2018). The thermo-active wall forms part of the basement of a low energy building in Italy, which comprises also thermo-active slabs and a ground water well as energy

sources. The basement wall consists of 66 wall panels, each 15.0 m long, 0.5 m thick and 2.4 m wide. In every panel, two pipe loops are installed facing the retained side of the wall, as shown in Figure 2-30. Each pipe loop has a total width of 0.8 m and forms a coil loop consisting of six vertical branches, with a spacing of 0.16 m. The pipes are in high density polyethylene (HDPE) with an inner diameter of 16.0 mm and a wall thickness of 4.0 mm. The basement is 10.0 m deep, supported by two ground anchors and embedded within coarse to fine gravel, with the water table at a depth of 9.7 m. The geothermal system is monitored by various temperature sensors installed within the wall at different depths, along the excavated and retained sides of the wall, and the ground temperatures are monitored through temperature sensors fixed to the upper anchor (see Figure 2-30). In addition, the monitoring system comprises also sensors for measuring the thermal power, the flow rate within the heat exchanger pipes and the inlet and outlet temperatures at the pipes. Unfortunately, the possibility of measuring strains was not included, thus the mechanical behaviour is not investigated.

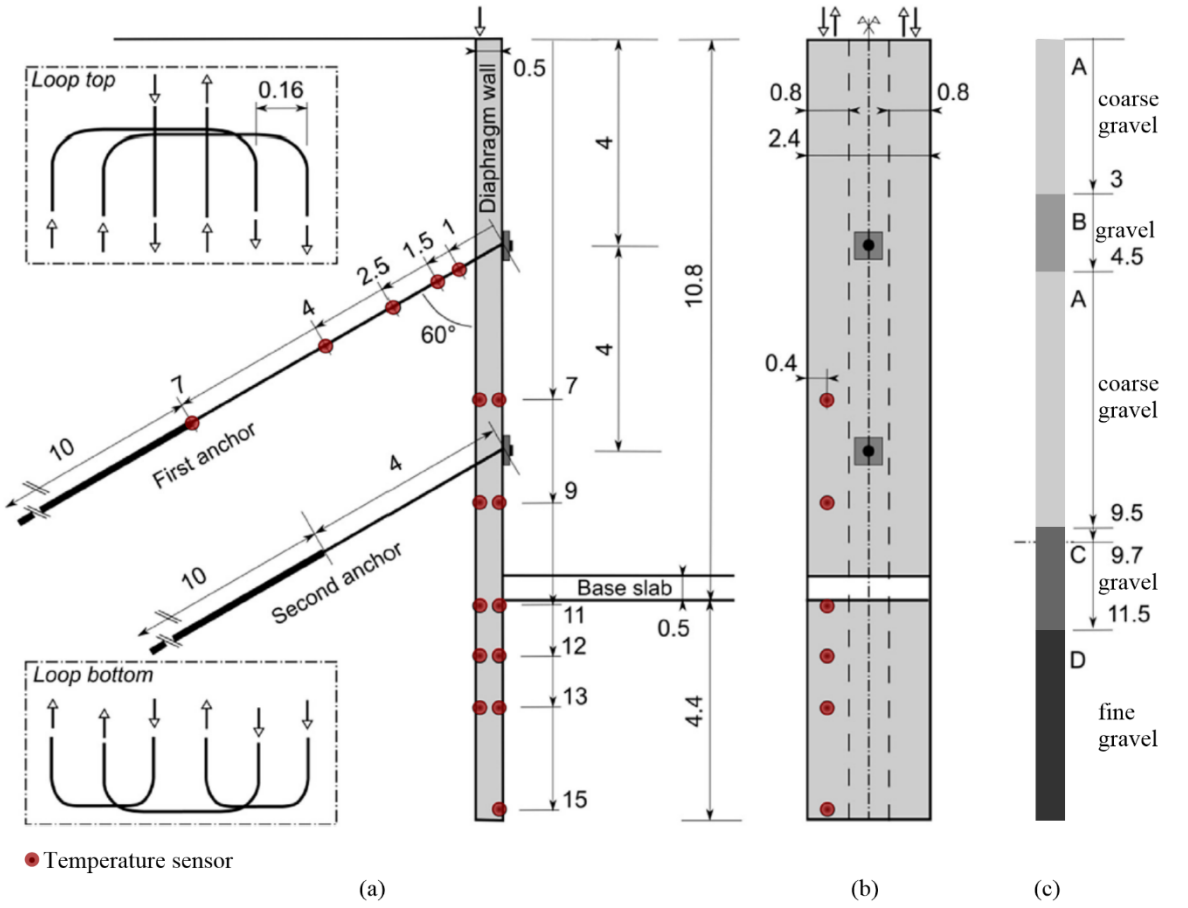

Figure 2-30: Geometry of thermo-active wall in Italy (a) cross-section, (b) front view and (c) soil stratigraphy (adapted from Sterpi et al. (2018))

Detailed development of temperatures recorded by the different sensors during a two year period are reported in Sterpi et al. (2018). By comparing the temperatures recorded within the wall above and below the base slab, the effect of the interaction with the environment within the basement was assessed. The temperatures measured within the wall on the excavation (ES) and soil side (SS) above the base

slab (ES7 and SS7) and below the base slab (ES13 and SS13) are depicted respectively in Figure 2-31 (a) and (b). The temperatures fluctuate with time as a consequence of the natural temperature fluctuation within the basement and the heat exchange. A different temperature distribution across the thickness of the wall is recorded above and below the base slab, as schematically represented in Figure 2-31 by the red lines. Indeed, above the excavation level, the temperatures recorded along the excavated side of the wall are lower than those on the soil side in winter (during heat extraction) and higher in summer (during heat injection). Thus, the interaction with the environment affects negatively the heat exchange, acting as a heat sink during the winter and a heat source during the summer (Sterpi et al., 2018). Below the excavation, the opposite is observed, meaning that, within the embedded section, the soil provides a positive contribution to the heat exchange. The negative influence of the thermal conditions of the basement could be alleviated by modifying the boundary condition with the introduction, for example, of thermal insulation or by increasing or decreasing the fluid temperature. However, the inlet temperatures reported in Sterpi et al. (2020) already reached values close to 0°C during the winter operation, meaning that decreasing further the temperature may not be possible.

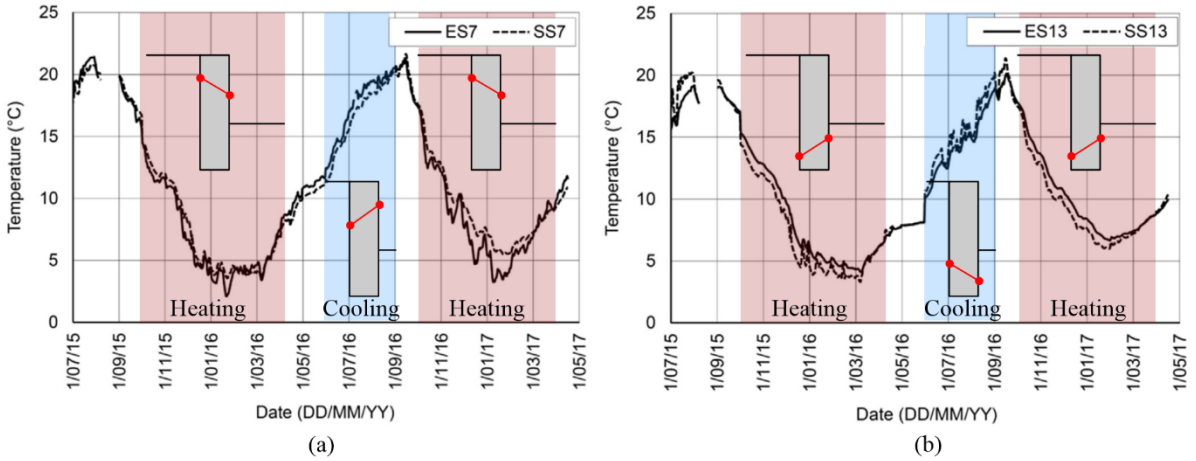

Figure 2-31: Temperature variations with time from monitoring data (a) above base slab and (b) below base slab (adapted from Sterpi et al. (2018))

From the monitored inlet and outlet temperatures, Sterpi et al. (2020) and Angelotti & Sterpi (2018) have provided energy performance data for the first winter season (Figure 2-32). The seasonal average heat extraction rate was evaluated to be 13.9 W/m^2, which is significantly higher than that computed for the base slab, which was equal to 5.2 W/m^2. The heat extraction rate of the wall is lower than that measured by Xia et al. (2012), which could be due to the shorter wall length (smaller contact area with the ground), different pipe configuration and the longer period of operation. The reduction in performance between December and January is probably due to the intense operation during these cold months, while the lower extraction rate observed in March is attributed to a lower energy demand (Angelotti & Sterpi, 2018). The average daily extracted energy from the three components installed (i.e. thermo-active walls, slabs and groundwater wells) also show that the thermo-active walls contribute to a large proportion of the energy extracted by the whole system, varying between 60% and 80%.

Assuming the system works for 1800h a year in heating mode and considering the seasonal average extraction rate, with a total surface area of the walls of 2376 m^2, the system is able to provide a total energy of around 60.0 MWh in one season. No data is provided on the energy design of the building and whether this figure meets the actual energy demand of the residents. Nonetheless, the calculated COP (see Equation (2-1)) varies between 5.0 and 4.2, a range which is generally considered efficient for a geothermal system.

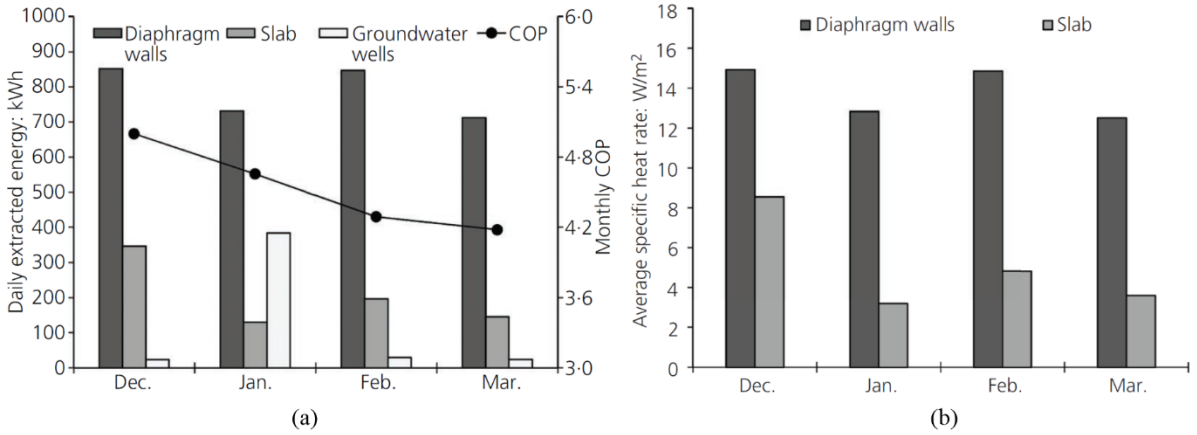

Figure 2-32: Energy performance of thermo-active wall (a) average daily extracted energy and COP and (b) heat extraction rate per unit area (Angelotti & Sterpi, 2018)

Laboratory studies

Dong et al. (2019) conducted a large-scale laboratory test of a concrete wall equipped with heat exchanger pipes and fully embedded in dry sand within a steel box of 2.0 × 2.0 × 2.0m. The wall was 2.0 m long, 0.2 m thick and 1.8 m wide and the heat exchanger pipes, of 8.0 mm internal diameter, were located 0.05 m from the concrete edge on the left-hand side of the wall. These formed a single pipe loop with multiple branches running vertically across the wall width, each with a pipe-to-pipe spacing of 0.17 m. Water was circulated within the pipes at a flow rate of 0.03 m^3/h (i.e. velocity of 0.17 m/s) and at a temperature of 50°C for 75h. The system was monitored by temperature sensors at different distances and depths within the wall and the soil, by strain measurements within the wall at different depths and by earth pressure cells at the soil-wall interface. The temperatures within the soil show differences along the width of the wall, with the soil temperatures close to the pipe inlet being 3°C to 4°C higher than those recorded close to the outlet for the shallowest sensors (0.33 m depth), while this effect is less pronounced for the deeper sensors (2°C difference at 1.67 m depth). This may indicate the influence of the soil being in contact with the ambient temperature. The changes in temperature in the transversal direction (i.e. within the vertical plane that is perpendicular to the wall and contains the pipe), depicted in Figure 2-33 (a), were shown to increase rapidly with time, reaching changes in temperature of approximately 3°C at the end of the operation at a distance of 0.6 m from the left-hand side, which is closest to the heat exchanger pipes. At the same distance on the right-hand side, the changes in temperatures were much higher (10°C), which is probably due to the presence of concrete

for a thickness of 0.15 m which has a higher conductivity than soil (1.2 W/mK and 0.32 W/mK, respectively). The strain measurements within the wall indicate that the wall thermally expands upon heating and that the vertical strain is larger in the upper part of the wall (see Figure 2-33 (b)). This can be explained by the fact that the wall is less restrained in this region. The development with time at most of the measurement locations displays a peak in expansive strain, after which either a plateau or a reduction is observed. This is surprising, since the wall's and soil's temperatures are still increasing, however the wall stopped expanding after approximately 20h of operation. Furthermore, the magnitude of the strain at the end of the test is between 55 and 80 με. Considering that the coefficient of expansion of concrete is 10 με/°C (Dong et al., 2019) and that the change in temperature within the wall is, on average, 35°C, this would indicate that the free thermal strain of the wall is equal to 350 με (assuming it to be free to expand in all directions or having a Poisson's ratio of zero, see Chapter 3). According to Equation (2-15), the restrained strain would range between 270 and 300 με. Consequently, given the wall's stiffness of 12 GPa (Dong et al., 2019), a compressive stress of 3420 kN/m^2 and an axial force of 1900 kN/m would develop within the wall. These values are much larger than those generally computed for thermo-active walls. Dong et al. (2019) also reproduced the problem by finite element analyses and computed axial stresses of approximately 200 kN/m^2 while matching the measured axial strains (see Figure 2-33). No explanation on the development or magnitude of the strain was found, thus it is considered that the results should be carefully assessed.

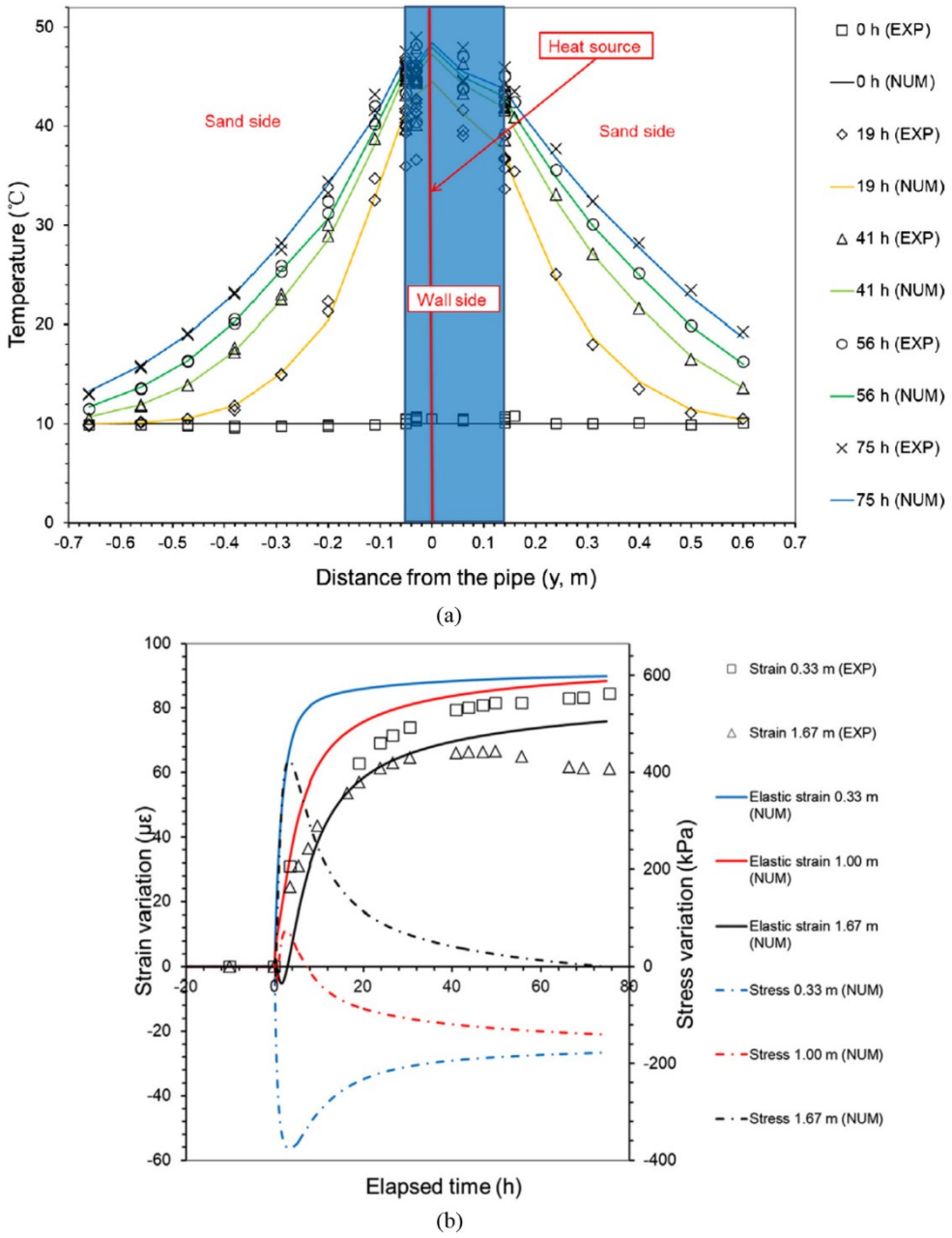

Figure 2-33: Results from large scale laboratory test (a) Temperature versus distance from the pipe at different times in the middle of the panel and (b) vertical strain and stress versus elapsed time on the left-hand side at x=0.28 m (Dong et al., 2019)

You et al. (2019) simulated a cantilevered thermo-active wall within a centrifuge under 50g. The wall was made of copper and was 0.3 m high, 0.2 m wide and 0.014 m thick (this corresponds to 15.0 m, 10.0 m and 0.7 m, respectively, in prototype scale). The depth of excavation was 0.1 m (5.0 m in prototype scale) and a semiconductor chilling plate was employed to heat the wall from ambient temperature of 28°C to 50°C. Three tests were conducted: (1) no excavation, heating to 50°C; (2) excavation at ambient temperature; (3) heating of wall after completed excavation. The testing scheme included strain, temperature and soil pressure measurements; only the results for the recovery stage (i.e. once temperature application has been discontinued) are presented. The temperature distribution with

time in test (1) and (3) are comparable in magnitude and show a rapid decrease in temperature close to the wall, whereas an increase at larger distances is observed. This is due to the transient heat transfer, whereby the heat front moves with time. During heating, the strains were expansive, decreasing with time as the wall and soil cool down. Before excavation, a rather uniform strain along the depth of the wall is observed (with one sensor predicting very low values in comparison to other ones, which may indicate it was damaged). After excavation, the strains are less uniform and highest in the upper part of the wall, for both the excavated and retained side. This may be due to the smaller restriction against the thermal expansion applied by the soil in this region. The axial stresses are compressive at the end of heating and reduce with time as the system cooled down and any restriction applied by the soil is released. According to the authors, the large strains (350 με) and stresses (35 MPa) recorded are due to the high expansion coefficient of copper in comparison to that of concrete (almost twice).

Special applications

Kürten et al. (2015) propose to install heat exchanger pipes within seal panels employed to protect concrete walls from ground water. The thermal performance of these panels was tested through large-scale laboratory tests, where a concrete wall and the attached seal panel were embedded within granular soil in a box of 3.0 × 3.0m in plan and 2.0 m in depth. It should be noted that the wall panel was fully embedded and in contact with the ground on one side, while on the other side an insulation layer was present, hence removing any possible interaction with the environment in front of the wall. Within the seal panels, two different pipe configurations, namely U-loop or W-loop, were installed. The test set-up was such that, within the soil, the velocity of the ground water and temperature could be controlled, while within the heat exchanger pipes, the water flow rate and inlet temperature could be varied. The system was tested in heating mode (i.e. heat extraction) and, similar to the results obtained by Xia et al. (2012), it was observed that increasing the water flow rate and the difference between inlet and ground temperature increases the potential for heat exchange, while no effect of the ground water flow was recorded. Regarding the pipe layout, a larger heat extraction per unit length of pipe was computed for the U-shaped loop, however the total exchanged power was higher for the W-shaped loops. The calculated heat extraction rates vary between 36 W/m^2 and 150 W/m^2, which are large compared to other published values for thermo-active walls. Indeed, these values represent the very short-term condition, with the soil being minimally affected by temperature changes. Furthermore, the more controlled laboratory environment and the fact that the wall is fully embedded within the ground may contribute to an increased energy performance.

A similar laboratory study is outlined by Ziegler et al. (2019), who investigate the performance of steel sheet pile walls used as river walls equipped with heat exchanger pipes. Two possible solutions are proposed, where either the heat exchanger pipes are welded onto the sheet pile facing the soil side or add-on elements are added to existing sheet pile walls and installed on the water side. The sheet pile walls are installed in a box of 3.0 × 3.0 m in plan and 2.5 m in depth, which is half occupied by sand

and half by water. During the test, the water flow within the heat exchanger pipes, the inlet temperature and the water flow of the open water section were varied and their effect on the thermal performance was monitored by a total of 105 temperature sensors placed at the pipe loops, within the soil and water. The variation of heat extraction rate with water flow within the pipes is consistent with what was observed by Kürten et al. (2015). The performance of the heat exchanger elements placed in open water (i.e. the add-on elements) is notably larger than the one where the pipe elements are placed in contact with the ground due to the considerably larger heat capacity of water when compared to that of the soil, and it increases as the stream velocity increases, due to the replenishment in temperature as the water flows. The values of heat extraction per metre of thermally-activated length (which is equal to 2.0 m and 1.5 m for the welded pipes and the add-on elements, respectively) reported for this type of thermo-active walls are very high and range between 250 and 1750 W/m of activated sheet pile length. According to the width of the wall (2.7 m), this translates into a heat flux of 93 to 650 W/m^2.

2.4.4 Numerical studies

In recent years, numerous researchers have investigated the behaviour of thermo-active walls through numerical simulations, by either performing finite element or finite difference analyses. It should be noted that, due to the lack of field data regarding the behaviour of thermo-active walls, most of the numerical approaches could not be validated and hence, generally, parametric studies are carried out to evaluate the effect of conditions or material parameters where most uncertainty exists. The majority of the studies on thermo-active walls focus on the assessment of their thermal performance, while fewer analysed their thermo-mechanical behaviour. Numerical simulations allow the effect of numerous design parameters to be efficiently analysed and long-term simulations to be performed, thus enabling the assessment of aspects of behaviour of these structures which are difficult to capture in field. Before providing details of the published literature, it is worth noting that different authors employ different types of software and have different modelling approaches. Hence, an overview of some modelling aspects to simulate thermo-active walls is provided first.

Numerical modelling of thermo-active retaining walls

There are different aspects that characterise the modelling approach of thermo-active walls, the most important being the type of analysis, the way the heat exchange is modelled and the boundary condition employed to simulate the interactions with the environment (both at ground surface and along the exposed face of the wall).

(1) Type of analysis

The type of analysis can be categorised as thermal (T), thermo-mechanical (TM), thermo-hydraulic (TH) and thermo-hydro-mechanical (THM). A further distinction is made when the heat transfer is modelled as a transient phenomenon or at steady state (thermal equilibrium). Furthermore, while in ICFEP any combination of two or more coexisting systems (thermal, hydraulic and mechanical) is

evaluated in a coupled manner (as outlined in Section 2.3.1), this is not always the case for other software. For example, the finite element software ABAQUS (Dassault Systèmes, 2019) allows different types of thermal analyses to be performed, e.g. uncoupled heat transfer analyses (i.e. the mechanical behaviour is not assessed), sequentially coupled thermal-stress analyses (i.e. the temperature field is established first which is then used to evaluate associated stress changes) and fully coupled thermal-stress analyses (i.e. changes in temperature and stress are solved simultaneously). Analyses of thermo-active walls employing ABAQUS include those presented by Bourne-Webb et al. (2016b) and by Sterpi et al. (2017), who performed, respectively, steady-state sequentially coupled thermal-stress analyses and transient sequentially coupled thermal-stress analyses. The effect of different types of analyses on the transient thermo-mechanical response of a thermo-active wall is assessed in Chapter 3.

(2) Modelling heat exchange

In order to fully capture the heat transfer mechanisms within thermo-active walls, when characterising their thermal performance, 3D analyses are often performed. In such cases, the heat exchanger pipes are modelled either employing one-dimensional elements (similar to those described in Section 2.3.4) or using solid elements, where both heat transfer and water flow are modelled. The heat exchange is then simulated by applying a prescribed temperature at the pipe inlet and the outlet temperature is evaluated to calculate the heat flux (see Chapter 4 for a detailed description). One-dimensional elements with a coupled thermo-hydraulic formulation are included in the software FEFLOW (Diersch, 2014). It should be noted that Diersch et al. (2011) and Di Donna & Barla (2016) mention that the pipe was surrounded by a "surplus material" of increased thermal conductivity equal to 1000 W/mK. This seems similar to the approach proposed by Gawecka et al. (2020), however no justification for the adopted parameter has been provided.

Since 3D analyses are computationally expensive, often simpler, two-dimensional (2D) plane-strain analyses are carried out, especially when the coupled TM or THM behaviour is evaluated, where a larger number of degrees of freedom exist within the analysis. In such cases, the heat exchange is modelled in a more simplistic manner by applying boundary conditions, such as prescribed temperature or prescribed heat flux, over the whole surface of the wall or along a line where the pipes are located. It should be noted that none of the 2D modelling approaches adopted in the literature has been checked against an equivalent analysis in 3D and hence the implications of reducing a 3D problem into a 2D one have not yet been investigated. The aspects of modelling thermo-active walls in 2D plane-strain analyses are extensively analysed in Chapter 5 and Chapter 6.

(3) Boundary conditions to simulate soil-air and wall-air interface

The interface between the soil and the environment, i.e. the ground surface, is usually modelled by applying a prescribed temperature or, in some cases, a convective heat transfer boundary condition.

These can be applied by assigning a constant value of temperature throughout the analysis, usually equal to the average annual temperature or the average temperature during the considered season. The temperatures can, however, also vary with time according to a seasonal temperature fluctuation if transient analyses are performed. The wall-air interface is simulated by applying a prescribed temperature, a convective heat flux or imposing no heat flux across the wall surface (i.e. simulating a fully insulated wall). The values of temperature applied are either constant with time, with season, or varying over specific time frames.

Thermal performance

The studies conducted to evaluate the thermal performance of thermo-active walls are listed in Table 2-2. It should be noted that, of the listed analyses, the modelling approach was validated only by Di Donna et al. (2017), who showed a good agreement with the heat flux calculated by Xia et al. (2012) for the "type (c)" pipe layout, and by Sterpi et al. (2020) and Angelotti & Sterpi (2018), who compared their numerical results to the field monitoring data from the residential building in Italy (see previous section for details).

Table 2-2: Summary of numerical studies on the thermal performance of thermo-active walls

Reference	Software/ type of analyis	Modelling of heat exchange	Duration and operation mode	Wall details	Wall-air interaction	Parametric study
Bourne-Webb et al. (2016b)	ABAQUS 2D) (top view)	Prescribed temperature along pipe circumference	steady state cooling	H = 0.8 m B = 2.0	Convective heat transfer/ Prescribed constant temperature	○ Position of pipes (only soil or soil and excavated side) ○ Convective heat transfer wall-air interface
Bourne-Webb et al. (2016b)	ABAQUS 2D (side view)	Prescribed temperature along line	steady state cooling	L = 20.0 m H = 1.0 m d_e = 10.0m	Convective heat transfer/ Prescribed constant temperature	○ Convective heat transfer wall-air interface ○ Thermal conductivity of concrete
Di Donna (2016)	FEFLOW 3D	1D HEP, constant T_{in}	3 years – cooling and heating	L = 15.5 m H = 0.8 m B = 2.5 m d_e= 9.5 m	Prescribed constant temp-erature or adiabatic	○ Wall-air interaction ○ Ground water flow
Sterpi et al. (2014) Sterpi et al. (2017)	ABAQUS 3D	Solid HEP, constant T_{in}	steady state	L = 15.0 m H = 0.5 m	Prescribed constant temperature	○ Pipe layout ○ Water flow velocity in pipes
Sterpi et al. (2017)	ABAQUS 3D	Solid HEP, T_{in} constant during each operation mode	6 years – 6 months heating and 3 months cooling	L = 15.0 m H = 1.0 m B = 1.2 m d_e = 10.0 m	Prescribed constant temperature	

Table 2-2 cont.: Summary of numerical studies on the thermal performance of thermo-active walls

Reference	Software/ type of analyis	Modelling of heat exchange	Duration and operation mode	Wall details	Wall-air interaction	Parametric study
Di Donna et al. (2017)	FEFLOW 3D	1D HEP, constant T_{in}	2 months – cooling	L = 20.0 m H = 0.8-1.2 m B = 1.5 m d_e= 10.0-16.0 m	Prescribed constant temperature	○ Pipe spacing ○ Thermal conductivity of concrete ○ Temperature difference between soil and excavation ○ Thickness of wall panel ○ Concrete cover of pipes ○ Water flow velocity in pipes ○ Depth/excavation ratio
Rammal et al. (2018)	FLAC3D 3D	Prescribed uniform temperature	3 years – cooling and heating	L = 32.5 m H = 1.2 m B = 1.0 m d_e= 22.0 m	Adiabatic	○ Ground water flow velocity
Barla et al. (2020)	FEFLOW 3D	1D HEP, constant T_{in}	1 month – heating 3 years – 3 months heating and 3 months cooling	L = 15.5 m H = 0.8 m B = 2.5 m d_e= 9.5 m	Adiabatic	○ Pipe layout ○ Water flow velocity ○ Ground water flow velocity

Table 2-2 cont.: Summary of numerical studies on the thermal performance of thermo-active walls

Reference	Software/ type of analyis	Modelling of heat exchange	Duration and operation mode	Wall details	Wall-air interaction	Parametric study
Sterpi et al. (2020)	ABAQUS 3D	Solid HPE, T_{in} varying with time	6 months cooling and heating	L = 15.5 m H = 0.5 m B = 1.2 m d_e= 10.0 m	Prescribed temperature varying with time	○ Soil thermal conductivity ○ Concrete thermal conductivity ○ Pipe layout
Angelotti & Sterpi (2018)	ABAQUS 3D	Solid HPE, T_{in} varying with time	1 year – cooling and heating	L = 15.5 m H = 0.5 m B = 1.2 m d_e= 10.0 m	Prescribed temperature varying with time	

Key: HEP = heat exchanger pipe; T_{in}= Pipe inlet temperature, L = length; H = thickness; B = width; d_e = excavation depth

Bourne-Webb et al. (2016b) presented two studies on thermo-active walls using 2D plane-strain finite element analysis performed with the finite element code ABAQUS. The domain was discretised using 8-noded elements with temperature degrees of freedom at each node. One analysis consists of a wall panel in top view, 0.8 m in thickness and 2.0 m in width, with soil only on one side. The heat exchange was simulated by applying a constant temperature around the circumference of the pipes, which have been modelled as a void in the mesh with a pipe-to-pipe spacing of 0.5 m. The second case simulated a 20.0 m long and 1.0 m thick retaining wall in side view with a 10.0 m deep excavation. In this case, the pipes were modelled by prescribing the temperature along a line. For both analyses, the heat exchanger pipes were located at 0.075 m from the concrete edges and the effect of having pipes only on the retained side (termed soil side) or on both sides of the wall was investigated, where 27°C were applied to simulate heat injection (i.e. 15°C above the initial soil temperature). Furthermore, along the exposed part of the structure, the effect of the wall-air interaction was assessed by varying the thermal boundary condition, applying either a constant temperature of 15°C (i.e. h=∞ W/m^{2}K) or simulating a convective heat transfer with coefficient, h, of 2.5 W/m^{2}K, 12.5 W/m^{2}K or 25.0 W/m^{2}K and air temperature of 15°C. An additional analysis simulated convection with h of 2.5 W/m^{2}K and radiation with an emissivity of 0.9. For the analysis in side view, the effect of varying the concrete and soil thermal conductivity was also assessed. The initial temperature was 12°C and the ground surface was simulated with a convection boundary condition with heat transfer coefficient, h, of 10 W/m^{2}K and an air temperature of 25°C. It is stated that only steady-state conditions are considered, thus the transient behaviour is not assessed. The results, depicted in Figure 2-34 (b) for the problem simulated in side view, show that a large impact on the heat exchange is observed when different boundary conditions are applied along the exposed part of the wall, with the case of constant temperature leading to the highest heat flow, while the lowest is computed when a convective heat transfer with h of 2.5 W/m^{2}K is simulated, which is consistent with Equation (2-6). Furthermore, the heat flow towards the excavation was significantly larger than that towards the soil side, for both pipe configurations. This could be explained by the ground surface temperature being hotter than the air inside the excavation, thus favouring heat transfer towards the excavation. As a consequence, a large difference in heat flux is observed between the two different pipe configurations, where the one with pipes on both sides predicts twice the heat flux when compared to a configuration where only pipes on the soil side are modelled, which is due to the larger heat transfer towards the excavation. The heat flux towards the excavated side is also highly affected by the concrete thermal conductivity (see Figure 2-34 (a)), since the heat transfer occurs entirely through the concrete structure. Consequently, no effect is observed when varying the soil thermal conductivity, which only affects the heat flux towards the soil, which was shown to be low.

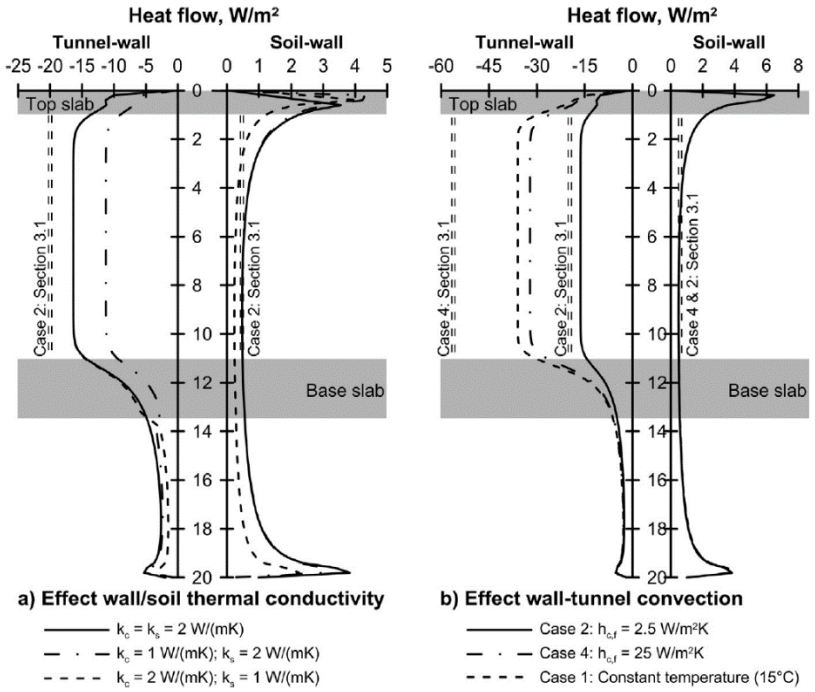

Figure 2-34: Heat flux computed towards excavation and soil (a) effect of soil and concrete thermal conductivity and (b) effect of wall-air interaction (Bourne-Webb et al., 2016b)

Di Donna et al. (2017) present an extensive parametric study for the thermal performance of a 20.0 m long and 1.5 m wide thermo-active wall panel simulated in 3D finite element analyses using the software FEFLOW. The heat exchange was modelled by including one-dimensional elements to simulate heat exchanger pipes, within which water flows at a constant velocity. Heat was injected by prescribing a constant inlet temperature with the heat flux being calculated according to Equation (2-13) using the computed outlet temperatures. A constant temperature was applied at the excavation boundaries and the ground surface (assigning a higher value than the initial soil temperature of 12.0°C – see Table 2-3) and the analyses lasted 2 months. The modelling approach was validated by reproducing the field test described in Xia et al. (2012) for "type (c)" pipe configuration. It should be noted that the validation exercise was modelled with initial conditions which were not in thermal equilibrium, thus generating heat fluxes from regions at different temperature even without the operation of the geothermal system. The parameters investigated in the parametric study together with the results are reported in Table 2-3. To assess the effect of the different parameters, a statistical method (Taguchi analysis) was adopted, whereby more than one variable is changed at the same time and the results are then analysed based on a statistical analysis providing a ranking of the influence of each of the parameters (as summarised in Table 2-3). This approach leads to time savings due to the smaller number of analyses required (8 in this case), however it does not allow to fully capture the effects of the individual parameters. According to the results, the impact of the parameters differs with time: in the short term, the spacing between the pipes and the difference between the soil and air temperature have the most significant effects on the thermal performance; in the medium term, the effect of the concrete thermal conductivity is higher than that of pipe spacing. These factors affect the interaction at the wall-air interface which was shown to

largely contribute to the heat exchange. Given this, it is therefore surprising that the depth/excavation ratio showed little effect on the computed results.

Table 2-3: Parametric study and results presented in Di Donna et al. (2017)

Parameter	Value		Effect short term (5 days)	Effect medium term (60 days)
	low	high		
Panel width (m)	0.8	1.2	++	++
Depth/excavation ratio L/d_e (-)	1.25	2.0	+	+
Spacing between pipes (m)	0.25	0.75	---	--
Pipe concrete cover (m)	0.05	0.1	+	+
Fluid velocity (m/s)	0.2	1.2	+	+
Difference in soil and excavation temperature (°C)	2.0	6.0	+++	+++
Concrete thermal conductivity (W/mK)	1.5	3.0	++	+++

Key: effect on thermal performance: + increases with increasing parameter; - increases with decreasing parameter
+/- limited effect (ranking 5-7); ++/-- medium effect (ranking 3-4); +++/--- substantial effect (raking 1-2)

Sterpi et al. (2014) and Sterpi et al. (2017) conducted 3D steady state analyses of an idealised, fully embedded wall panel to investigate the effect of the pipe layout and the water flow velocity. It is shown that the increase in energy efficiency is not necessarily related to the total length of the pipes, but rather to their configuration, where portions of pipes presenting large temperature differences should be kept distant from each other to avoid thermal interaction. Regarding the water flow velocity, which was varied between 0.005 m/s and 0.1 m/s, a large impact of this value was found, with an optimal velocity being 0.01 m/s. However, these values are considerably lower than those adopted in practice for GSES (e.g. Xia et al., 2012; Loveridge et al., 2013).

Sterpi et al. (2017) simulated using ABAQUS a similar wall geometry as the one installed in the residential building in Italy presented in Sterpi et al. (2018), but with the adoption of a simpler pipe geometry, consisting of two single U-loops placed in the middle of the panel (see Figure 2-35(a)). Due to symmetry, only half of the panel was modelled. The heat exchanger pipes, although not explicitly stated, were modelled through solid elements with simulation of water flow and conductive-advective heat transfer. A prescribed fluid velocity of 0.05 m/s and an inlet temperature of either 2°C or 30°C, respectively during winter and summer operation, were prescribed. The initial temperature was 15°C, which was kept constant at the bottom boundary. Inside the excavation, a constant temperature of 18°C was prescribed, while at the ground surface a yearly cyclic temperature was imposed. Before the start of the simulation, the model was run to thermal equilibrium with the imposed boundary conditions. The simulation period of the geothermal operation was six years by simulating 3 months of heat injection

during the summer and 6 months of heat extraction during winter, with two periods of 1.5 months each in between. The exchanged energy varies during each operation, with the transferred energy decreasing between the first and last month of operation, due to the smaller temperature differences at the pipe outlet. Furthermore, between the first year and the 6th year of operation, the thermal performance has increased by 6.2% in the summer months and decreased by 1.2% in the winter months. The changes in ground temperature close to the wall were shown to be mainly affected by the operation of the geothermal system, with considerable yearly fluctuations. Further away from the wall (the distance is not indicated), the soil close to the ground surface was affected by the yearly fluctuation in temperature imposed at that boundary, while at larger depths the effect of the heat exchange led to permanent reductions in temperature by about 1.0°C at the end of six years. Sterpi et al. (2017) report that the soil underwent significant changes in temperature (no value reported) up to a distance of 10.0 m from the wall at the end of the six years period. Similar to the results reported by Bourne-Webb et al. (2016b), it was found that a higher heat flux occurs towards the excavation when compared with that taking place through the soil side. Lastly, it is pointed out that considerable temperature differences are computed across the width of the wall for the exposed section of the wall, ranging between 6°C/m and 8°C/m, while lower values (<2.0°C/m) were recorded for the embedded section (see Figure 2-35 (b)). This is related to the different heat transfer mechanisms above and below the excavation (see Chapter 4). This temperature variation in the x-direction is experienced in the soil up to a distance of 3.0 m from the wall, after which negligible differences are recorded.

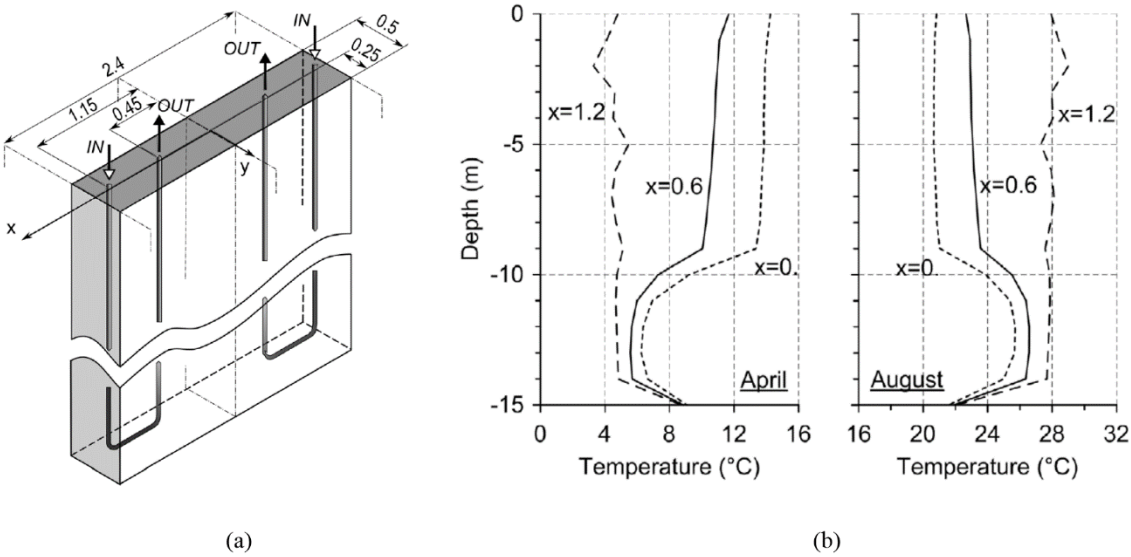

(a) (b)

Figure 2-35: Simulation of retaining wall (a) geometry and (b) wall temperatures at different times and positions along the width of the panel (after Sterpi et al., 2017)

Sterpi et al. (2020) and Angelotti & Sterpi (2018) have modelled numerically the thermo-active wall constructed in Italy which was previously described in Section 2.4.3 and compared their results to the monitored data. Furthermore, Sterpi et al. (2020) also performed a parametric study on the optimisation of the loop layout. The analyses were conducted with ABAQUS and are similar to those described in

Sterpi et al. (2017). The heat exchanger pipes were modelled with square solid elements with an equivalent cross-sectional area equal to the area of the pipe (inner diameter of 16 mm) where water flow and heat transfer were simulated. At the ground surface, a yearly variation in temperature, with a mean value of 13.4°C, was applied. Along the excavation boundary, a similar yearly variation was simulated, however with an amplitude reduced by applying a coefficient of 0.66, which was established according to the monitored temperatures at the wall face. The flow rate within the pipes and temperature at the pipe inlet were taken from the monitoring data. The simulated results agree relatively well with the monitoring data, although, while the wall is being cooled, higher ground and outlet temperature are predicted numerically, thus overestimating the heat flux. In order to overcome this issue, Sterpi et al. (2020) conducted a sensitivity analysis, where the thermal conductivity of soil and concrete as well as the imposed boundary condition along the excavation were varied. The thermal parameters seemed to either have little effect or lead to worse reproductions of the monitored data, while the best approximation was found by changing the characteristics of the modelled wall-air interaction. The analysis that matched the monitoring data best was shown to be that employing a damping coefficient of 0.66 during summer months and of 1.0 during winter months for the temperature applied at the wall. This was justified by the fact that the natural ventilation within the basement allows the mitigation of the temperature oscillations during the summer months but not in the winter. Regarding the study on different pipe layouts, these are depicted in Figure 2-36. Figure 2-36 (a) illustrates the pipe layout employed in the case study, while those shown in Figure 2-36 (b) and (c) are the two optimised solutions. The rationale behind the proposed layouts was to increase the spacing between the pipes, to avoid thermal interaction, and to increase the pipe length within the embedded section to take advantage of the conditions below the excavation which were shown to be beneficial for the heat exchange. The pipe layout (b) and (c) present overall less pipe length than the original pipe layout, respectively 45% and 67% of that depicted in Figure 2-36 (a). Nonetheless, given the optimised configuration of the pipe loops, both layouts perform better, with an increase in performance of 10% and 15%, respectively for layout (b) and (c), computed during the December month. The increase in efficiency for pipe layout (c) is somewhat limited compared to that computed by Xia et al. (2012) for the configuration with pipes on both sides. However, in the latter study, the wall was much longer and the pipes installed on the excavation side had a beneficial effect given the positive interaction with the environment within the excavation.

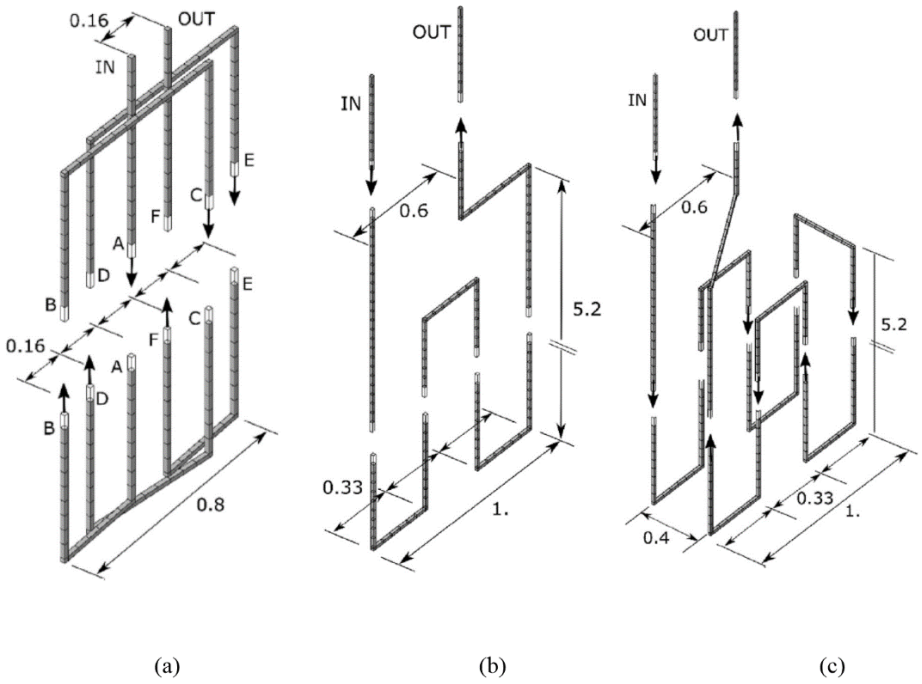

Figure 2-36: Pipe layouts for thermo-active wall case in Italy (a) original layout, (b) optimised solution 1 and (c) optimised solution 2 (after Sterpi et al. (2020))

Barla et al. (2020) analysed the energy efficiency of a 15.5 m long, 0.8 m thick and 2.5 m wide wall panel supporting a 9.5 m deep excavation and investigated the effect of the ground water flow velocity on the exchanged heat performing 3D analyses. The analyses were conducted using FEFLOW and the simulation procedure is similar to that described in Di Donna et al. (2017), i.e. 1D elements were employed to simulate the heat exchanger pipes. A preliminary analysis where the domain consisted of only the wall panel with soil on one side and adiabatic conditions along the face of the wall was carried out to analyse the effect of the pipe layout, which was varied according to Figure 2-37, and of the water flow velocity (between 0.1 and 1.0 m/s) within the pipes. The study, which simulated 1 month of heat extraction, showed that configuration (c) in Figure 2-37 resulted in a higher efficiency per metre length of pipe, while the water flow velocity has shown little effect on the thermal performance, with 0.2 m/s being chosen as the value for subsequent analyses.

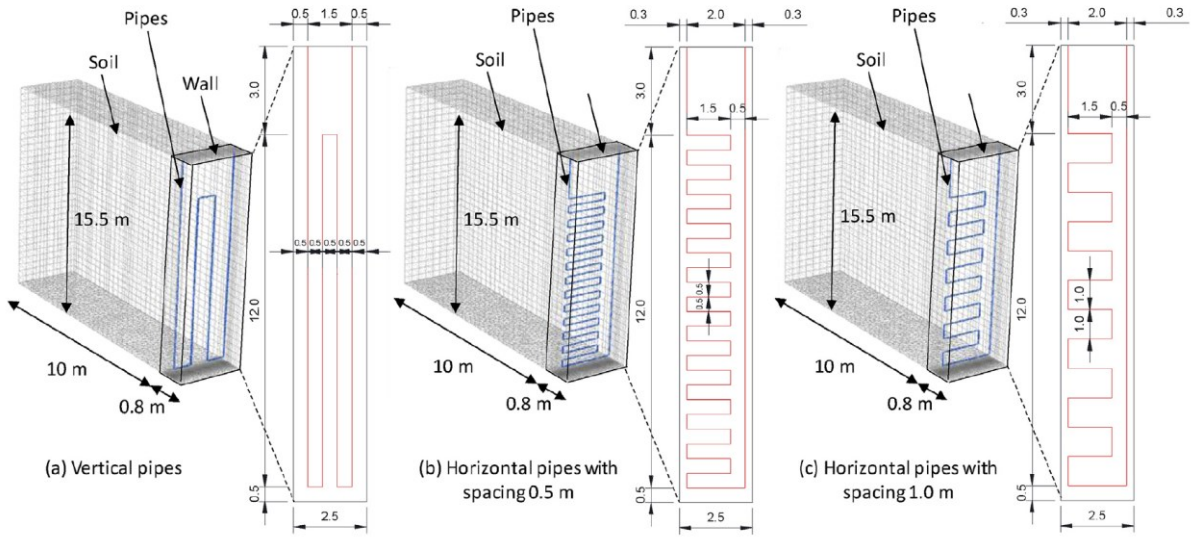

Figure 2-37: Wall panels with different pipe layouts (Barla et al., 2020)

Subsequently, Barla et al. (2020) performed analyses on the full wall geometry with layout (c) and excavation width of 25.0 m (a similar case was also presented in Di Donna (2016)). The inside of the excavation was "*modelled through finite elements having air thermal properties* (not reported)*, neglecting the heat exchange between wall and air*" (Barla et al., 2020). The ground surface temperature varied cyclically with time and a 3-year operation was simulated by varying the pipe inlet temperature to simulate both heat injection and extraction each over a period of three months. Simulations with either no water flow or a water flow of 1.5 m/day (1.7×10^{-5} m/s) with flow direction perpendicular to the wall were carried out. The results showed that, in the presence of ground water flow, a higher heat flux (4 times the one without ground water flow) is obtained, since there is less accumulation of heat around the structure. However, it has almost no influence on the changes in ground temperature at a distance of 5.0 m. At this location, the heat exchange induces changes in temperature of about ±1.5°C relatively to undisturbed conditions. In the analyses presented by Di Donna (2016), the impact of the wall-air interface maintained at constant temperature (either at 18°C or 14°C, where the latter is equal to initial temperature) as opposed to an insulated boundary was assessed. In both winter and summer operation, the adoption of an insulated boundary leads to a lower heat flux, while between the two scenarios of constant temperature, the wall maintained at a higher temperature is more efficient during the winter season and less performant during the summer season, due to, respectively, higher and smaller differences to the inlet temperature.

Another study assessing the impact of ground water flow (in a direction perpendicular to the wall) on the thermal performance of a thermo-active wall is the one presented in Rammal et al. (2018). A 3D simulation of a 32.5m long, 1.2 m thick and 1.0 m wide wall panel, supporting a 22.0 m deep excavation, was carried out with the finite difference program FLAC. The initial ground temperature was 14°C and, at the bottom boundary, a geothermal flux of 0.0544 W/m^2 was applied. In order to reach thermal

equilibrium before the start of the analysis, 2.5 years were simulated. The heat exchange was simulated by changing uniformly the temperature of the whole wall during the various seasons, i.e. applying 25°C in summer, 9°C in autumn, 5°C in winter and 21°C in spring (since the wall is 1.0 m thick and pipes are not modelled, a 2D analysis would have sufficed in this case). First, one winter season is modelled to assess the effect of ground water flow and then three consecutive cycles are simulated to investigate the effect of heating and cooling cycles. The heat exchange is assessed by analysing the distribution of the conductive and advective divergences (i.e. using the divergence theorem), giving thus an indication of the direction of the heat flux. Indeed, positive divergence indicates zones acting as a heat source (flux is outward), while the contrary is true for negative divergence. The results show, for all the ground water flow velocities, that the exchanged power through conduction is one order of magnitude larger than that through advection (which comprises only 2.5% of the total power), dominating the heat transfer. Only a slight increase in efficiency is obtained with varying ground water flow, considered a consequence of the low ground water flow velocities simulated (these ranged from 8.34×10^{-8} to 3.34×10^{-6} m/s, which are 1 to 3 orders of magnitude smaller than those simulated by Barla et al. (2020)). A last study on the active length of the wall led to the conclusion that equipping the whole wall with heat exchanger pipes, as opposed to only a part of it, enhances the capability of exchanging power and is more influential than ground water flow.

Thermo-mechanical behaviour

As detailed in Section 2.2.4, field tests on thermo-active piles have shown that additional forces and strains develop due to heating and cooling, which have to be taken into account during the design of these structures. Therefore, it is particularly important to be able to predict the thermo-mechanical behaviour of thermo-active walls, to provide a reliable and cost-effective design. For this purpose, researchers have carried out numerical simulations to evaluate the effect of changes in temperature on the mechanical behaviour of thermo-active walls. The most relevant studies are summarised in Table 2-4, where some of the case studies previously described in terms of their thermal performance were employed to evaluate also their thermo-mechanical behaviour.

Table 2-4: Summary of numerical studies of the thermal-mechanical behaviour of thermo-active walls

Reference	Software/type of analyis	Modelling of heat exchange	Duration and operation mode	Wall details	Wall-air interaction
Bourne-Webb et al. (2016b)	ABAQUS 2D TM	Prescribed temperature along line	Steady state cooling	L = 20.0 m H = 1.0 m d_e = 10.0m	Convective heat transfer/ Prescribed constant temperature
Sterpi et al. (2017)	ABAQUS 3D TM	Solid HEP, prescribed inlet temperature varying with time	6 years – 6 months heating and 3 months cooling	L = 15.0 m H = 0.5 m B = 2.4 m d_e = 10.0 m	Prescribed constant temperature
Barla et al. (2020)	FLAC 2D TM	Prescribed temperature along pipe circumference	2 years and 9 months – 3 months heating and 3 months cooling	L = 15.5 m H = 0.8 m B = 2.5 m d_e= 9.5 m	Prescribed constant temperature
Rui & Yin (2018); Yin & Rui (2019)	Cambridge THM (*) 2D THM	Prescribed temperature along line	20 years – cyclic cooling and heating	L = 41.0 m H = 1.0 m d_e= 28.9 m	Prescribed temperature varying with time
Dai & Li (2019)	PLAXIS 2D THM	Prescribed temperature along line	30 years – cyclic cooling and heating	L = 41.0 m H = 1.0 m d_e= 28.9 m	Prescribed temperature varying with season

Key: HEP = heat exchanger pipe; L = length; H = thickness; B = width; d_e = excavation depth; (*) no further details on the software are given

Bourne-Webb et al. (2016b) evaluated the thermo-mechanical response of the thermo-active wall modelled in 2D plane-strain analysis in side view, as previously described. It should be noted that steady state, sequentially coupled, thermo-mechanical analyses were performed, which therefore ignore the transient changes in temperature and the hydraulic behaviour within the soil. The soil was modelled as linear-elastic perfectly-plastic with a Tresca failure criterion. The assessed quantities were the changes in bending moment and horizontal displacement with respect to the end of construction, where also those due to the activation of the thermal boundary conditions, i.e. those due to natural conditions within the tunnel, were assessed. The presented results show the effect on these quantities of the simulated boundary condition along the excavated part of the wall, the heat injection mode (pipe only on soil side or on both sides of the wall) and the ratio between the thermal expansion coefficient of soil and concrete. Bourne-Webb et al. (2016b) computed that the majority of the observed effect is actually provided by the application of the thermal boundary conditions rather than the heat exchange, thus concluding that the natural environmental conditions have a more important role than the heat exchange (see Figure

2-38). This may be attributed to the simulated steady state conditions, where transient effects are ignored. Furthermore, it should be noted that the temperature applied at the ground surface is similar to that prescribed along the pipes. A rather significant influence is observed when changing the coefficient of expansion of the soil to be twice that of concrete, which leads to larger displacements and bending moments. This is expected due to the larger volumetric expansion of the soil upon heating, thus inducing a larger deflection and hence increasing the bending moment of the wall.

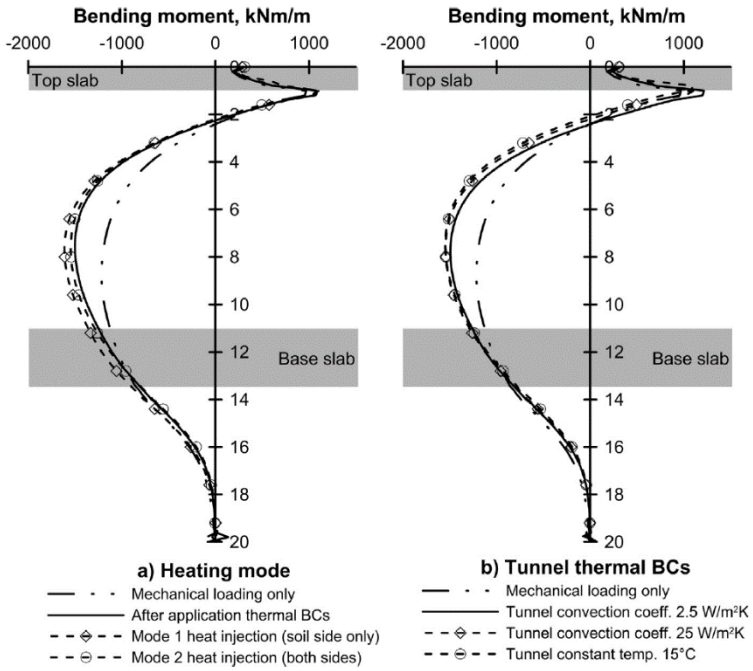

Figure 2-38: Computed bending moments (a) different heat injection modes and (b) different wall-air interactions (Bourne-Webb et al., 2016b)

The same 3D geometry previously described for the study on the thermal performance carried out by Sterpi et al. (2017) was also used to perform thermo-mechanical analyses. These were carried out by first simulating the excavation procedure and subsequently applying an initial temperature field computed for undisturbed conditions using the previously described thermal equilibration phase. Subsequently, the operation of the geothermal system was simulated for one year by conducting a transient thermo-mechanical analysis, with no hydraulic coupling since the soil was assumed to be fully drained. In this analysis, the heat exchanger pipes are not modelled, but the operation of the system is simulated by applying temperature variations established in previous thermal analyses. The soil and concrete were simulated as thermo-elastic materials, with the adopted constitutive model for the soil being non-associated perfectly-plastic, with a Mohr-Coulomb failure surface. The stiffness of the soil varies linearly with depth. The first finding was that, contrary to what reported by Bourne-Webb et al. (2016b), the natural variations in temperature do not greatly affect the mechanical behaviour of the analysed wall, justified by the rather uniform temperature field obtained. Once the geothermal operation commences, changes in vertical and horizontal wall displacements and in axial forces and bending

moments are observed. The wall displayed horizontal displacement towards the excavation during summer (heat injection) of 7.0 mm, which corresponds to an increase of 8% with respect to the displacement after construction. The movement during winter changes very marginally. The relative variation of the thermally-induced vertical displacements is higher than that of the horizontal displacements, though its absolute value is smaller. As shown in Figure 2-39, the cyclic heating and cooling leads to expansion and contraction of the structure, with seasonal fluctuations in the order of 2.0 mm. It is interesting to note that smaller vertical displacements are computed within the embedded section (below 10.0 m depth), which is attributed to a larger restriction in this area, where soil is present on both sides of the wall.

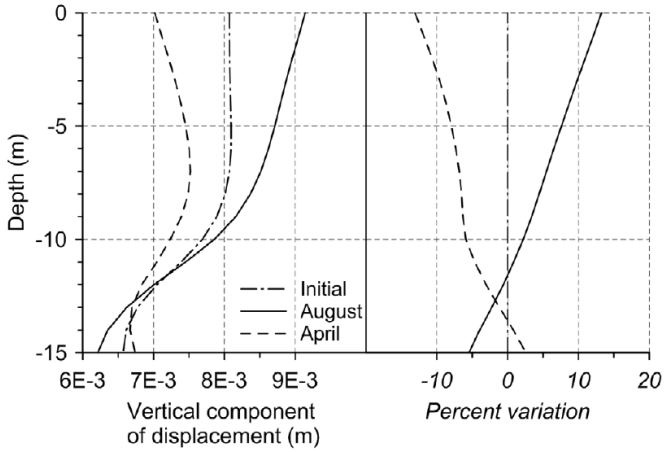

Figure 2-39: Vertical displacement and percentage variation during operation of geothermal system (Sterpi et al., 2017)

The axial forces and bending moments were computed for different sections along the width of the wall panel. This allows the evaluation of the effect of the non-uniform temperature distribution across this dimension (as was previously shown in Figure 2-35 (b)). Figure 2-40 shows the variation of the axial force with depth at two different locations, i.e. x=1.2 m (closest to pipe inlet) and x=0.0 m (mid-section of the wall panel) – refer to Figure 2-35 (a) for the wall panel geometry. It is found that the axial force presents different magnitudes at different locations across the width of the wall and, more notably, they are also of opposite sign. This is due to the distribution of stresses within the wall being affected by the differential expansion between wall sections at different temperatures, which leads to an interaction between adjacent sections (this aspect is exhaustively explained in Chapter 6). The changes in axial force due to the operation of the geothermal system leads to a maximum increase of about 600 kN/m when compared to the axial force computed after construction. Furthermore, it is worth mentioning that the interaction with sections at different temperature and the consequent development in stresses cannot be captured by a 2D analysis, which therefore could underestimate the axial forces. In terms of bending moments, a decrease in negative bending moment (i.e. the wall is subjected to a positive bending moment) during the summer operation and an increase in negative bending moment during the winter operation is computed. Sterpi et al. (2017) report that the variation in bending moment is related to the

shear stress acting at the soil-wall interface, which is of opposite directions during the two operation modes (as can be deduced by the wall vertical deformation). Regarding the change across the width of the wall, smaller bending moments are computed for the section furthest away from the inlet pipe, which presents a lower temperature (also this aspect is discussed in Chapter 6). Sterpi et al. (2017) highlight that the computed forces, even though significant, were not detrimental to the stability of the structure.

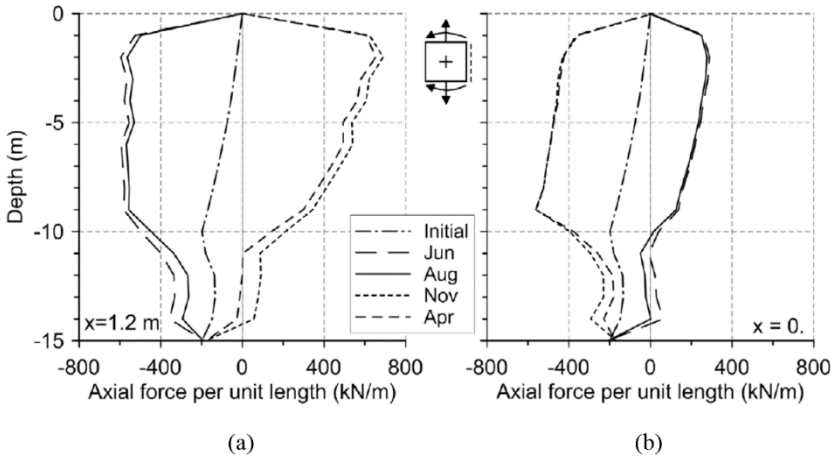

Figure 2-40: Variation of axial force with depth during operation of geothermal system at (a) x = 1.2 m (close to inlet) and (b) x = 0.0 m (between the two U-loops) (Sterpi et al., 2017)

Barla et al. (2020) investigated the behaviour of a wall (see previous section for description on geometry) by performing a 2D plane-strain finite difference analysis using the software FLAC. The pipes were assumed to be horizontally laid within the wall panel (see Figure 2-37 – configuration (c)) and were discretised within the mesh as a void. The heat exchange is simulated by applying, along the pipe contour, the average temperature over the width of the pipes computed in the previously reported 3D thermo-hydraulic analysis. Both soil and concrete were modelled as thermo-elastic materials. The concrete was simulated as linear-elastic, while the soil as elastic perfectly-plastic. The analyses were thermo-mechanical only, where the hydraulic behaviour was not simulated. After the simulation of the excavation, the same thermal boundary conditions as in the 3D thermo-hydraulic analyses were applied, with the exception of the internal boundary of the basement, where a fixed temperature of 14°C was applied (it is not stated whether an additional 3D analysis with this boundary condition was carried out to determine the temperatures applied at the pipes, which are affected by the boundary condition along the wall – see Chapter 4). Before the start of the operation of the geothermal system, 3 years were simulated with external air temperature only varying at the ground surface, after which 2 years and 9 months of operation were simulated, with periods of 3 months of heating and cooling being modelled, separated by periods of 3 months with no operation. The results at different time instants, i.e. at the end of construction, during thermal equilibration of the natural conditions and different heating and cooling cycles, in terms of horizontal displacements and bending moments, are depicted in Figure 2-41. The simulation of the external conditions with no heat exchange induces an additional wall movement of around 3.0 mm. The heating and cooling cycles lead to a cyclic horizontal displacement of the top of

the wall, which is unrestrained, with a maximum change in one season of 4.0 mm. The change in bending moment is largest in winter with a maximum of 460 kNm/m (increase of 17% with respect to that computed with natural temperature fluctuations), which is reported to be well within the strength limits of this wall. As can be observed, the development of the bending moment does not reflect that of the displaced shape, where the larger movements observed in the summer operation generate a lower bending moment. Although this aspect of thermo-active retaining wall behaviour is not commented on in Barla et al. (2020), it is believed that in these structures the link between deformed shape and bending moment is not as direct as in the case of non-thermo-active structures – this is explained in detail in Chapter 6.

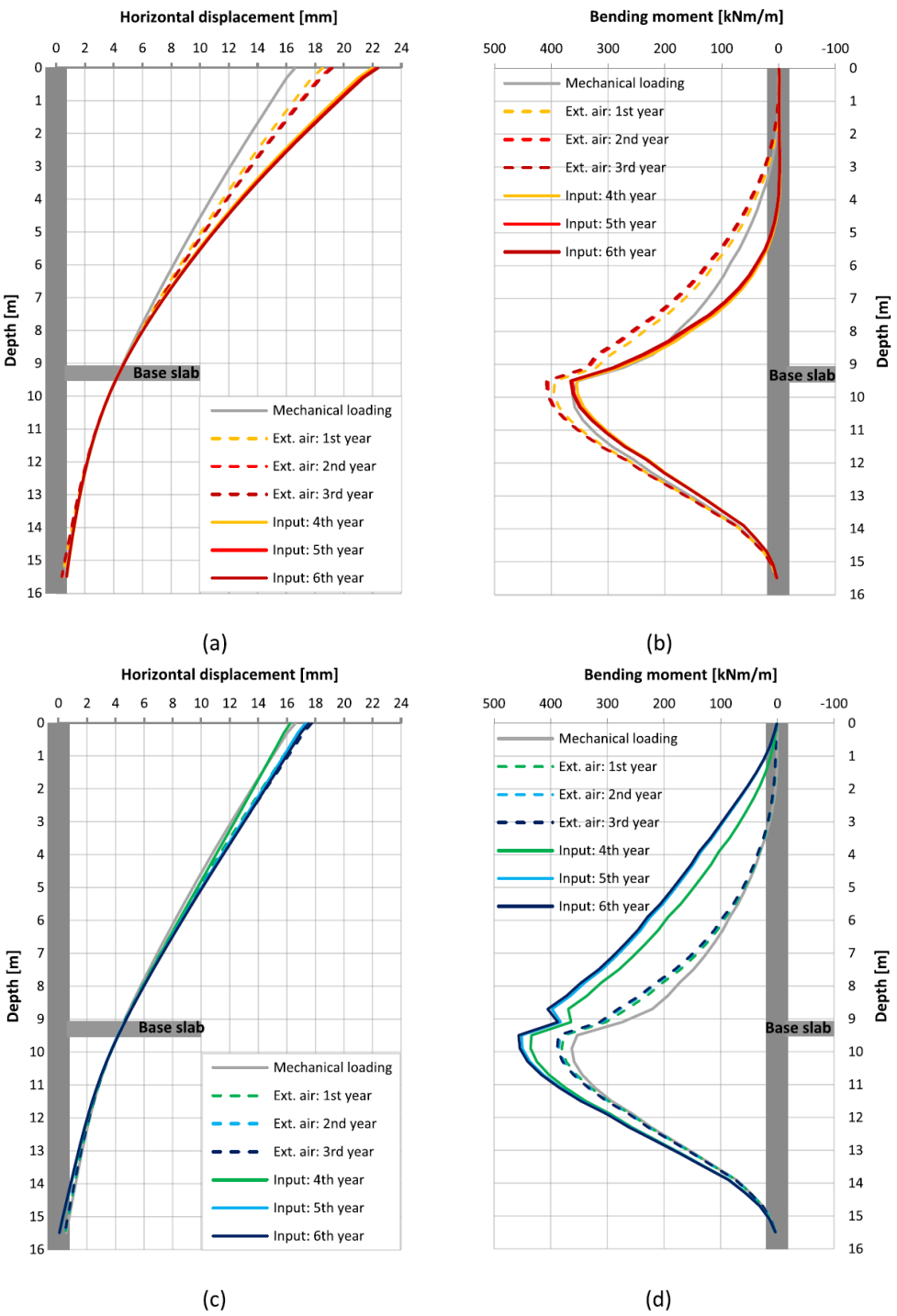

Figure 2-41: Results of thermo-active wall analysis (a) horizontal displacement in summer, (b) bending moment in summer, (c) horizontal displacement in winter and (d) bending moment in winter (Barla et al., 2020)

Rui & Yin (2018) and Yin & Rui (2019) performed 2D plane-strain fully coupled THM analyses of a thermo-active diaphragm wall installed at the Crossrail Tottenham Court Road Station in London employing an in-house finite element code developed at the University of Cambridge (Rui, 2014). The wall is 41.0 m long and 1.0 m thick, supporting a 28.9 m deep excavation, embedded in a typical London ground profile (see Rui & Yin (2018) for details), with the majority of the wall being embedded in London Clay. During construction, the wall was supported by 4 temporary props, which were removed

after the construction of the base slab and the 4 floor slabs. All materials are considered thermo-elastic and the soils were modelled as linear-elastic, perfectly-plastic with a Mohr-Coulomb failure surface. An additional case was analysed in Rui & Yin (2018), where non-linear elasticity was simulated for all soil layers. However, little effect of this aspect was observed during the operation of the thermo-active wall when compared to the linear-elastic model. The initial soil temperature was 12°C, which was maintained constant at the far field boundaries. The excavation was maintained at a constant temperature of 18°C and the ground surface was simulated as insulated. These thermal boundary conditions were applied immediately after construction. The heat exchange was modelled by applying a constant temperature along a line where the pipes are located (0.25 m from the concrete edge on the retained side) with a temperature of 2°C and 18°C, respectively in winter and summer, for a total of 20 years, with 6 months of cooling and 6 months of heating. The hydro-mechanical soil models and the construction sequence during excavation were validated by comparing the computed displacements to those monitored in the field, showing a good agreement. To evaluate the effect of the operation of the geothermal system, the results are compared to those obtained during a 20-year iso-thermal analysis, where thus only the equilibration of the excess pore water pressures due to construction takes place. The main findings are:

- the geothermal operation delays the dissipation of the excess pore water pressures due to additional excess pore water pressures generated during heating;
- the horizontal displacements of the wall vary seasonally with a maximum change of $\pm$1.2 mm and are due to volume changes within the soil (i.e. thermal deformation of the soil mass and volumetric changes due to excess pore water pressures) and of the wall itself. These are much smaller than those computed during construction, where a maximum of around 20.0 mm was evaluated;
- heating/cooling cycles lead to a variation in bending moment of about 400 kNm/m. These changes are well within the design capacity of the analysed wall.

Although the importance of the THM coupling, with consequent changes in pore water pressure due to the differential expansion of water and soil, is highlighted within the publications, no mention of the employed coefficient of thermal expansion of water could be found.

Dai & Li (2019) analyse the same wall geometry and perform 2D plane-strain fully coupled THM analyses using PLAXIS (PLAXIS, 2019). The clay layers were modelled using the Hardening Soil model with small strain stiffness and the sandy soils with a linear elasto-plastic Mohr-Coulomb model. Both soils and concrete were considered as thermo-elastic. Although it is stated that temperature effects on the development of pore water pressures are simulated, the value of the coefficient of thermal expansion of water was not provided and the exact THM formulation adopted by PLAXIS has not been described in detail in this paper (an outline on the THM formulation can be found in PLAXIS (2015)). Similar thermal boundary conditions to those employed by Rui & Yin (2018) and Yin & Rui (2019)

were applied to the far field boundaries and inside the excavation, where the permanent structures were also modelled and maintained at 18°C. On the ground surface a prescribed temperature, varying between 4°C in winter and 23°C in summer, was imposed, while the initial temperature was 12°C. The heat exchanger pipes, with same temperatures as prescribed on the ground surface, are modelled "*as plane elements with two thermal boundaries, which is able to generally consider the equivalent effect of 3D spaced heat exchange tubes by thermal function in the PLAXIS 2D model. The top thermal boundary and these two heat-exchanging boundaries are controlled by thermal functions inside PLAXIS*." (Dai & Li, 2019). Based on the results shown, it appears that the application of the thermal loading consisted of specifying temperatures along a line within the retaining wall, though some uncertainty on this issue remains. Moreover, no reference was found in the manual for PLAXIS 2D to the reproduction of 3D temperature fields using 2D analyses. The simulation involved 30 years with three different scenarios: (1) hydro-mechanical only (i.e. thermally inactive), (2) thermo-active with no geothermal operation to evaluate the effects of seasonally varying ground temperatures and (3) thermo-active with geothermal operation. All the thermal boundary conditions were applied at the end of construction. As depicted in Figure 2-42 (a), the horizontal displacements in scenario (2) are initially affected by the application of the thermal boundary condition, which lead to an expansion of the permanent horizontal structures and a movement towards the retained side. Little effect of the seasonal temperature variation at the ground surface with time is observed. Simulating the geothermal operation leads to some cyclic movements during the first year, while, in the long term, the upper part of the wall moves permanently inside the excavation, whereas little differences during heating and cooling cycles are observed (Figure 2-42 (b)). The long-term movement inside the excavation could be due to the larger heat injection when compared to extraction, leading to a permanent expansion of the soil mass. The simulation of the temperature boundary conditions in scenario (2) also lead to vertical displacements of the wall as a consequence of the thermal expansion. This is larger in scenario (3), where cyclic displacements are computed, which, after 30 years, are 8.0 mm larger than in scenario (2). Surprisingly, the magnitude of the vertical soil movements is less affected by the geothermal operation, with similar displacements computed in scenarios (2) and (3). The base slab heaves in all cases due to the equilibration of the excess pore water pressures, which were tensile after construction. A larger heave is experienced in scenario (2) than in scenario (1), which was isothermal. Although not mentioned, this may be due to the thermal expansion of the soil as the thermal boundary condition within the basement is activated, which heats up the soil beneath it. In scenario (3), a further increase in heave is observed, which is due to the increase in temperature during summer operation. An insignificant effect of both seasonal variation and geothermal operation on the internal forces both in the wall and the base slab were computed.

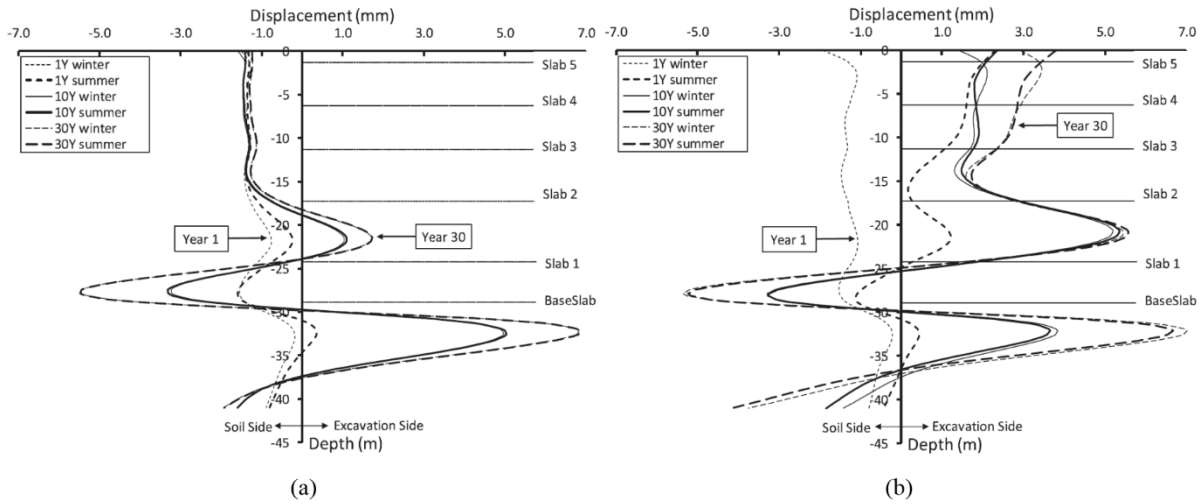

Figure 2-42: Change in horizontal displacement for (a) scenario (2) and (b) scenario (3) (Dai & Li, 2019)

2.5 Summary and conclusions

This chapter provides background information to this research project.

Section 2.2 first introduces the concept of thermo-active structures and their implementation in Europe and the UK. Thermo-active structures are underground structures employed to exchange heat with the surrounding ground in order to provide energy for space heating and cooling to buildings through the installation of heat exchanger pipes within the structure. Due to their double purpose of providing both stability and energy to buildings, they are often more economical than structures built for the sole use of heat exchange. Conversely, concerns regarding their mechanical performance arise due to the unknown effects of thermal loading. This aspect is considered to be the main factor delaying the deployment of these systems in the UK, with this research aiming to provide further insight into the behaviour of walls used as heat exchangers and the temperature effects on the structure and surrounding soil. As described subsequently in Section 2.2, the heat transfer from the pipes to the surrounding materials is dominated by conduction within the soil and concrete, while convection dominates the heat flux within the pipes. The temperature effects on soil behaviour, as determined from laboratory tests, are characterised by thermal expansion/contraction and the development of excess pore water pressures upon heating. Most of the studies agree that highly overconsolidated soils expand upon heating and contract elastically upon cooling. Different responses were observed for normally consolidated and lightly overconsolidated soils. However, it is considered that, at the operational temperatures of ground source energy systems and when dealing with overconsolidated soils such London Clay, simulating a thermo-elastic soil response appears to be adequate. Lastly, details on the thermal performance and the thermo-mechanical response of thermo-active structures are provided, where it is highlighted that an integrated design considering both thermal and mechanical aspects is required. The dimensions of thermo-active structures are usually derived from the geotechnical design, while the thermal design assesses the energy potential and aims at enhancing the thermal performance by providing optimised

solutions in terms of the configuration of the pipe loops, the thermal parameters of the system's components, etc. Regarding the geotechnical design, limited guidance in the form of design standards is available to date. Most of the research carried out so far has been focussed on energy piles, for which a simplified framework for understanding their behaviour when subjected to heating and cooling has been developed. While it provides valuable insights into thermal effects on the mechanical behaviour of piles, its application remains limited for thermo-active walls given the more complex geometry of the latter. Therefore, numerical analyses are a useful tool to assess their thermo-mechanical response.

In Section 2.3 the existing capabilities of the Imperial College Finite Element Program (ICFEP) relevant to the simulation of THM problems are outlined. The THM formulation, which can account for the coupled effects of temperature on variations of stresses, strains and water flow as well as the influence of water flow on heat transfer, was outlined. The thermal boundary conditions and structural elements, together with their use in coupled THM problems, were described. Regarding the latter type of elements, the use of beam and bar elements to simulate heat exchanger pipes was introduced. Lastly, a summary of recent research on coupled thermal analyses was presented and the associated numerical challenges were highlighted. These include time-step constraints to avoid oscillations in the computation of temperatures, which were shown to be dependent on the element type employed. Furthermore, the use of the coupled thermo-hydraulic boundary condition within boundary value problems, to avoid unrealistic build-up of temperatures along the boundaries where the water enters or leaves the mesh, was explained. The concept of the Petrov-Galerkin FE method employed to avoid spatial oscillations in temperature in the presence of highly advective flows was introduced. It was shown that this is particularly important when modelling heat exchanger pipes, where high fluid flow velocities are simulated. In addition to the numerical stability within heat exchanger pipes, it was observed that the sole use of one-dimensional beam or bar elements, which have, by definition, a zero contact area, is not sufficient to properly simulate the heat transfer. For this reason, Gawecka et al. (2020) proposed the pipes to be surrounded by a thermally enhanced material (TEM), which has a higher thermal conductivity than concrete, to enhance the heat transfer. A further aspect to be aware of when modelling coupled THM problems is the change in stiffness upon heating and cooling, which can be considered analogous to mechanical loading or unloading stages. This is important when analysing the thermo-mechanical behaviour of thermo-active structures. Consequently, it is suggested that the stiffness is to be reversed to its maximum value whenever heating or cooling loads represent a potential change in the loading direction with respect to the previous stage of the analysis.

The last part of this chapter provided an extensive review of the available literature on thermo-active walls. Firstly, the current practice on the installation of this type of structures was described, with reference to some case studies. These highlighted the importance of adequate procedures during pipe installation to ensure the functionality of these systems, as well as describing the need to consider the practicability of installation on site when selecting the final pipe configuration. Subsequently, a

discussion on the characterisation of the interaction with the environment to which a wall is exposed is provided. Indeed, differently from piles, which are fully surrounded by soil, thermo-active walls are partly exposed to an environment and the thermal interaction, as subsequently discussed, may affect its thermal performance and mechanical behaviour. The heat transfer from the exposed face of the wall to the environment is characterised by convection and, depending on the use of the underground space, it may be governed by natural or forced convection. In the first case, the convective heat transfer coefficient is much lower (0-5 W/m^2K) and is mainly controlled by the temperature difference between the fluid and the surface. In the case of forced convection, the convective heat transfer coefficient depends on the flow velocity of the surrounding air and varies between 4-30 W/m^2K.

Regarding the thermo-mechanical behaviour of thermo-active walls, limited field studies are available, most of which comprise only temperature data. In terms of the mechanical behaviour, the only study including strain measurements is the one described in Brandl (2006), which consists of the monitoring of a piled wall. It was observed that the natural temperature fluctuations within the tunnel had a larger effect than the heat exchange, since the latter induced more uniform temperatures within the structure. However, the monitoring data are limited to a short period of seven months of operation and the long-term response is not known. Sterpi et al. (2018), Sterpi et al. (2020) and Angelotti & Sterpi (2018) described the monitoring data collected from a diaphragm wall installed in a residential building in Italy. The measured temperatures indicated that, above the excavation level, the interaction with the environment had a negative impact on the heat exchange, whereas a positive contribution was provided by the soil. Furthermore, it was highlighted that the pipe layout may have been inefficient, given the large number of closely spaced pipes installed. Nonetheless, a good energy performance was evaluated. The field test outlined in Xia et al. (2012) provided some insights into the aspects controlling the thermal performance of thermo-active walls, where the parameters analysed included the pipe configuration, the water flow velocity inside the pipes and the inlet temperature. All the parameters seem to have a large effect on the energy potential. However, it should be noted that the tests lasted for only 48h and therefore the conclusions may not be directly applicable to long-term operations.

Given the limited number of field and laboratory studies, the thermal and thermo-mechanical behaviour of thermo-active walls has been analysed by several authors performing numerical analyses (e.g. Bourne-Webb et al., 2016b; Sterpi et al., 2017; Di Donna et al., 2017; Rammal et al., 2018; Barla et al., 2020; Rui & Yin, 2018; Yin & Rui, 2019; Dai & Li, 2019). The analyses differ in complexity, where, in general, for the evaluation of the thermal performance 3D analyses are carried out with the simulation of the heat exchanger pipes. For thermo-mechanical analyses, mainly two-dimensional analyses were performed, given the increased number of degrees of freedom and consequent increase in computational cost. Regarding the thermal aspects, the studies showed a large effect of the simulated boundary condition along the excavated face of the wall on the thermal performance. While additional parametric studies were carried out, the impact of the single parameter on the energy efficiency of thermo-active

walls was not analysed in detail. The research carried out to evaluate the thermo-mechanical response comprises simple steady state analyses, transient thermo-mechanical analyses or fully coupled THM analyses. Within the latter group of studies, the effect of the generated excess pore water pressures due to changes in temperature was highlighted, however there is a clear lack of understanding in terms of the transient processes within these problems. 3D thermo-mechanical analyses carried out by Sterpi et al. (2017) provided information on 3D effects encountered in thermo-active walls due to the presence of the heat exchanger pipes. However, the mechanisms governing the development of thermally-induced forces in the structure require further investigation.

Chapter 3
Preliminary study of the behaviour of thermo-active retaining walls

3.1 Introduction

In this chapter, the behaviour of thermo-active retaining walls is investigated by performing a series of numerical Finite Element (FE) analyses using ICFEP. The analyses presented herein focus on providing first insights into soil-structure interaction phenomena associated with the non-isothermal long-term transient behaviour of thermo-active walls. It should be noted that, due to the lack of field tests characterising the thermo-mechanical behaviour of thermo-active walls (see Chapter 2 for an overview of the available literature), the analyses presented describe the hypothetical scenario where a real wall geometry of a deep basement in London (Wood & Perrin, 1984b) is used as a heat exchanger. Furthermore, thermo-elasticity is assumed, with the coefficient of thermal expansion of soils, α_s, taken as positive (i.e. soils expand upon heating). This assumption is regarded to be adequate according to the laboratory studies described in Chapter 2 (see Section 2.2.3) and the good agreement obtained by Gawecka et al. (2017), who adopted this approach when simulating a field test of a thermo-active pile installed in London. Lastly, the coefficient of thermal expansion of water, α_w, was adopted as a temperature-independent parameter.

In the first part of this chapter, the wall geometry and construction sequence is described and the results obtained through numerical simulations are compared to the monitoring data presented in Wood & Perrin (1984b) with the aim of validating the hydro-mechanical soil properties and the modelling procedure adopted for the isothermal stages of the analyses. Subsequently, the thermo-hydro-mechanical (THM) interactions occurring within the soil are studied by performing simple one-dimensional analyses. These represent idealised conditions for simulating the retained and excavated

sides of a thermo-active retaining wall problem and focus on identifying in detail the main mechanisms taking place in fully coupled THM analyses and how these are affected by ground properties. The last part of the chapter presents analyses based on the wall geometry described in Wood & Perrin (1984b). It includes a study on the effect of the modelling approach employed to simulate thermo-active walls, where particular emphasis is given to the time-dependent behaviour as a consequence of the THM interactions occurring in the soil, which were previously identified in the one-dimensional problems. In addition, the impact of varying ground properties on the response of thermo-active walls simulated in fully coupled THM analyses is investigated. The contents of this chapter were published in part or whole in Sailer et al. (2018a), Sailer et al. (2019b) and Sailer et al. (2020b).

Throughout this thesis, the sign convention is such that positive values refer to tensile axial forces in the wall, bending moments associated with tension on the excavated side of the wall, upwards vertical movements, horizontal movements towards the retained soil, tensile strains, and compressive pore water pressures.

3.2 Description of retaining wall problem

The wall geometry employed for the analyses within this chapter is based on a deep basement located in London, with details of its construction being presented in Wood & Perrin (1984b) and Wood & Perrin (1984a). This case study was chosen since detailed information regarding the construction sequence and extensive monitoring data are provided in the literature. Indeed, wall movements were recorded through inclinometers installed within the diaphragm wall. Thus, this case study allows the validation of the modelling procedure for the simulation of the excavation and construction of the basement and of the employed hydro-mechanical soil models, material properties and initial ground conditions. Clearly, a comparison with field data characterising the thermo-mechanical behaviour of a thermo-active wall would have provided a better illustration of the performance of the modelling approach presented in this chapter. However, as detailed in Section 2.4, a complete dataset including details of both the thermo-active structure and the behaviour of the surrounding soil is currently unavailable, rendering such an exercise impossible.

3.2.1 Geometry and construction sequence

The simulated structure is an 18.0 m deep, 0.8 m thick diaphragm wall which supports an 11.0 m deep excavation for an underground car park, 100.0 m × 60.0 m in plan, of a six-storey building located in central London. The plan view and cross section of the basement are depicted in Figure 3-1, which also indicates the positions of the inclinometers installed in the east and west walls. Indeed, in order to limit the impact of modelling simplifications (Zdravković et al., 2005), two-dimensional (2D) plane-strain analyses were carried out on a section perpendicular to these walls, which are of greatest length, as this type of analyses is typically employed to simulate structures of large dimension in the out-of-plane direction (Potts & Zdravković, 1999).

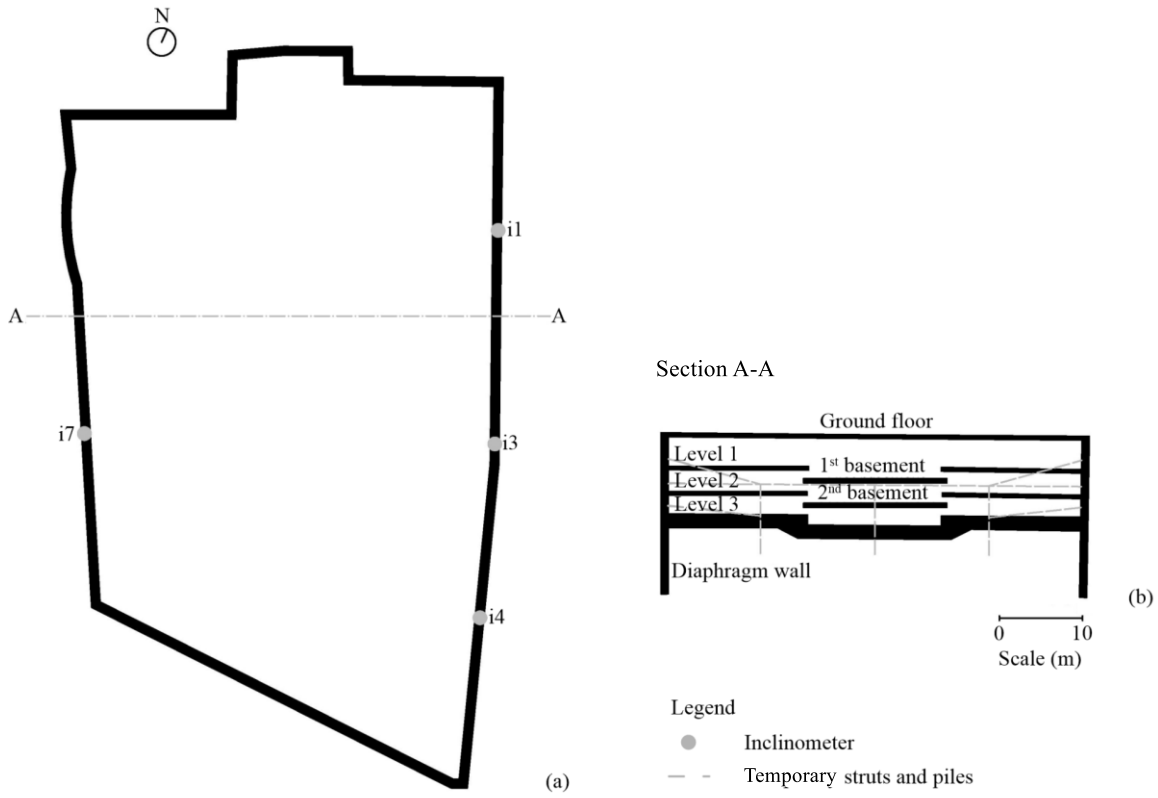

Figure 3-1: Geometry of analysed problem (a) plan view and (b) cross-section A-A (adapted from Wood & Perrin (1984b))

The excavation took place in four stages and the wall was supported by a temporary propping system consisting of a steel frame supported by concrete soldier piles. As shown in Figure 3-2, three temporary prop levels were installed and the struts were pre-stressed in the field, with design values of 50 kN/m, 80 kN/m and 120 kN/m for prop levels 1, 2 and 3, respectively (Wood & Perrin, 1984b). Each of the temporary props were removed after construction of the permanent structures, i.e. the concrete base slab (1.5 m thick) and the three slab levels (0.35 m thick).

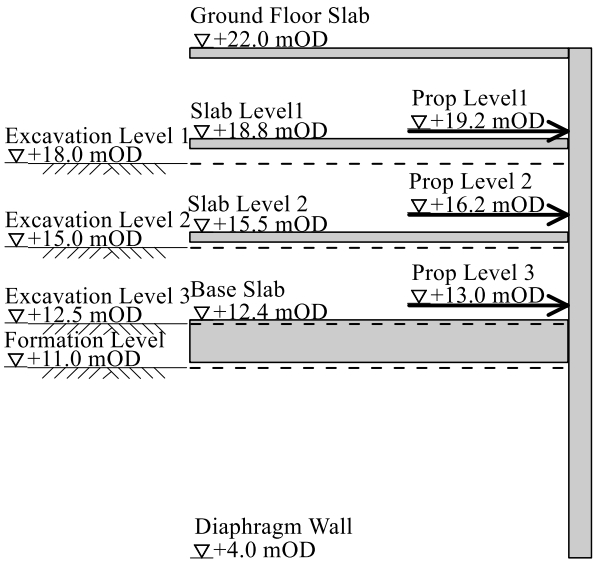

Figure 3-2: Cross-section of diaphragm wall and construction levels

3.2.2 Ground conditions

The ground profile was determined from the site investigation information reported in Wood & Perrin (1984b) and from available borehole data around the site. These indicated the level of ground surface to be at +22.0 mOD and a ground profile consisting of 4.8 m of Made Ground (MG), 2.0 m of Terrace Gravel Deposits (TGD), 40.0 m of London Clay (LC), 12.0 m of Lambeth Group Clay (LGC) and 7.0 m of Thanet Sand (TS) overlying Chalk (CH), as displayed in Figure 3-3. The groundwater table was located at 4.0 m below ground level, i.e. at +18.0 mOD, and the pore water pressure was assumed to be 0.0 kPa above that datum. For the initial conditions prior to excavation, the pore water pressure was assumed to vary hydrostatically within the Made Ground, the Terrace Gravel Deposits and the Thanet Sand. Moreover, according to the Environment Agency's records (Environment Agency, 2015), the water table for the lower aquifer at the time of construction (early 1980) was estimated to be located at the top of the Thanet Sand layer. As a result, within the London Clay and Lambeth Group Clay, the pore water pressure profile was assumed to be underdrained, in equilibrium with the hydraulic boundary conditions described above and consistent with the permeability profile (further details on the adopted hydraulic properties are given in Section 3.2.4), as shown in Figure 3-3 (a). The adopted K_0 profile is similar to that described in Gawecka et al. (2017) and is displayed in Figure 3-3 (b). This is based on the profile provided by Schroeder et al. (2004) which had been established according to the field data presented in Hight et al. (1993).

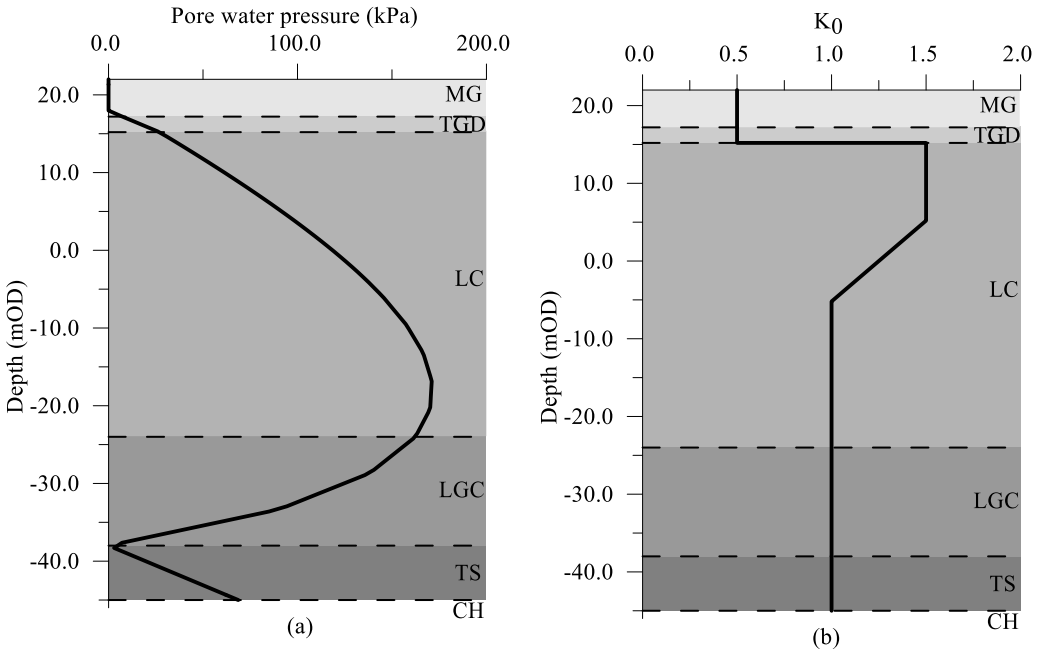

Figure 3-3: Initial ground conditions (a) pore water pressure and (b) K_0 profile

3.2.3 Finite element model

Figure 3-4 shows the FE mesh with an indication of its dimensions and the position of structural components. A symmetric excavation was assumed, hence only half (30.0 m) of the full excavation width (60.0 m) was modelled. Furthermore, no indication of the arrangement of internal columns was provided in the reference paper, which were therefore assumed to be 0.25 m wide and spaced 6.0 m apart. Eight-noded quadrilateral solid finite elements were used to model all soils, with displacement and temperature degrees of freedom at all the nodes and with pore water pressure degrees of freedom added to the corner nodes of the finite elements discretising consolidating materials (i.e. London Clay and Lambeth Group Clay). Details on the performance of these hybrid finite elements in THM analyses are described in Cui et al. (2016b). The structural components were simulated using eight-noded solid finite elements with displacement degrees of freedom at all the nodes. The connection between the diaphragm wall and the internal structures was simulated as a pin connection, i.e. only axial and shear forces can be transferred.

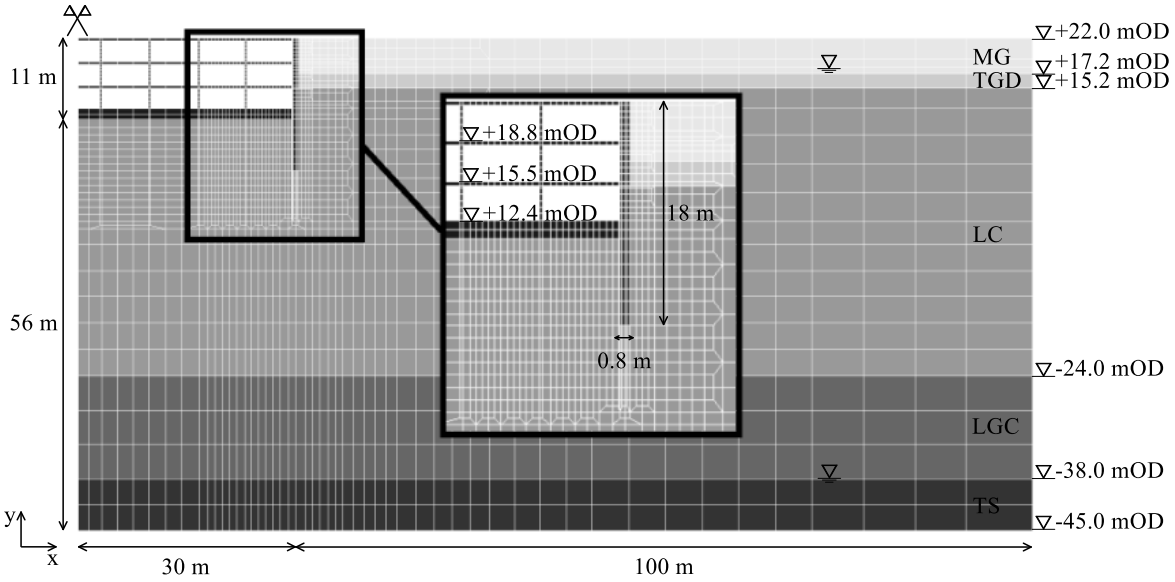

Figure 3-4: Finite element mesh for 2D plane-strain analysis of deep basement in London according to geomery presented in Wood & Perrin (1984b)

3.2.4 Material properties

Concrete was modelled as a linear-elastic material with a stiffness of 30.0 GPa, as indicated in Wood & Perrin (1984b). Excluding the Made Ground, which was modelled as a linear elasto-plastic material with a Mohr-Coulomb failure surface, all other soil layers were modelled as non-linear elasto-plastic materials, coupling a Mohr-Coulomb failure surface (see Potts & Zdravković (1999) for details) with the IC.G3S non-linear elastic stiffness model (Taborda et al., 2016). The latter allows the simulation of the non-linear decay of the soil's stiffness with strain level within the elastic region, improving the predictions of the pre-yield soil response. The full formulation of the IC.G3S model is described in Taborda et al. (2016), with only a summary of the model's equations being provided herein.

The tangent shear modulus, G_{tan}, is given by:

$$G_{tan} = G_{max} \cdot \left[R_{G,min} + \frac{1 - R_{G,min}}{1 + \left(\frac{E_d}{s_{G1}}\right)^{s_{G2}}} \right] \geq G_{min} \tag{3-1}$$

where E_d is the second invariant of the strain tensor (Equation (3-2)), G_{max} and G_{min} are the maximum and minimum shear stiffness, respectively, and s_{G1}, s_{G2} and $R_{G,min}$ are model parameters.

$$E_d = \left(\frac{4}{6} \cdot \left[\left(\varepsilon_x - \varepsilon_y\right)^2 + \left(\varepsilon_y - \varepsilon_z\right)^2 + \left(\varepsilon_z - \varepsilon_x\right)^2 \right] + {\gamma_{xy}}^2 + {\gamma_{yz}}^2 + {\gamma_{xz}}^2 \right)^{\frac{1}{2}} \tag{3-2}$$

In Equation (3-1), the maximum shear stiffness, G_{max}, is defined as:

$$G_{max} = G_{ref} \cdot \left(\frac{p'}{p'_{ref}} \right)^{m_G} \tag{3-3}$$

where p' is the mean effective stress, p'_{ref} is a reference pressure (assumed to be equal to the atmospheric pressure, i.e. 101.3 kPa), while G_{ref} and m_G are model parameters (within this thesis, the latter is assumed to be 1.0, i.e. the shear stiffness varies linearly with p').

Similarly, the tangent bulk modulus, K_{tan}, is given by:

$$K_{tan} = K_{max} \cdot \left[R_{K,min} + \frac{1 - R_{K,min}}{1 + \left(\frac{|\varepsilon_{vol}|}{s_{K1}} \right)^{s_{K2}}} \right] \geq K_{min} \tag{3-4}$$

where ε_{vol} is the volumetric strain (i.e. the first invariant of the strain tensor, see Equation (3-5)), K_{min} is the minimum bulk modulus and s_{K1}, s_{K2} and $R_{K,min}$ are model parameters.

$$\varepsilon_{vol} = \varepsilon_x + \varepsilon_y + \varepsilon_z \tag{3-5}$$

In Equation (3-4), the maximum bulk modulus, K_{max}, is calculated using:

$$K_{max} = K_{ref} \cdot \left(\frac{p'}{p'_{ref}} \right)^{m_K} \tag{3-6}$$

where K_{ref} and m_K are model parameters (as for the shear stiffness, the latter is assumed to be 1.0, i.e. the bulk modulus varies linearly with p').

Regarding the hydraulic properties, the consolidating materials, i.e. London Clay and Lambeth Group Clay, were modelled with a non-linear permeability model, where the permeability decreases with increasing mean effective stress, p', according to the following relationship:

$$k = k_0 e^{-\beta p'} \tag{3-7}$$

where the parameters k_0 and β are model parameters and were taken respectively to be equal to 1.0×10^{-10} m/s and 0.0023 1/kPa according to Schroeder et al. (2004).

For the thermal analyses, the soil layers were considered thermo-elastic with temperature independent parameters.

All soil properties were adopted from Gawecka et al. (2017), who accurately reproduced the thermo-mechanical response of a thermo-active pile installed in London (see Section 2.3.5 for more details). The mechanical properties are listed in Table 3-1, Table 3-2, Table 3-3 and Table 3-4, while the thermal and thermo-mechanical properties are given in Table 3-5.

Table 3-1: Linear-elastic material properties

Material	E (kPa)	ν (--)
Concrete	30×10^6	0.3
Made Ground	10×10^3	0.2

Table 3-2: Mohr-Coulomb strength properties (adopted from Gawecka et al., 2017)

Material	c' (kPa)	φ' (°)	ψ' (°)
Made Ground	0.0	30.0	0.0
Terrace Gravel	0.0	35.0	17.5
London Clay	5.0	25.0	12.5
Lambeth Group Clay	25.0	27.0	13.5
Thanet Sand	0.0	40.0	20.0

Table 3-3: Small strain stiffness properties – shear modulus (adopted from Gawecka et al., 2017)

Material	G_{ref} (kPa)	s_{G1} (--)	s_{G2} (--)	$R_{G,min}$(--)	G_{min} (kPa)
Terrace Gravel	41939.61	0.000145	1.0	0.03511	3000.0
London Clay	51743.55	0.000056	0.9	0.06450	2667.0
Lambeth Group Clay	51924.52	0.000110	0.95	0.04662	2667.0
Thanet Sand	65275.23	0.000046	0.85	0.02631	2000.0

Table 3-4: Small strain stiffness properties – bulk modulus (adopted from Gawecka et al., 2017)

Material	K_{ref} (kPa)	s_{K1} (--)	s_{K2} (--)	$R_{K,min}$ (--)	K_{min} (kPa)
Terrace Gravel	49843.08	0.000247	1.25	0.15440	3000.0
London Clay	26692.73	0.000127	1.80	0.13275	5000.0
Lambeth Group Clay	61331.71	0.000065	1.40	0.07589	5000.0
Thanet Sand	29813.53	0.000155	1.10	0.27947	5000.0

Table 3-5: Thermal and thermo-mechanical properties (adopted from Gawecka et al., 2017)

Material	γ (kN/m^3)	α_s (m/mK)	α_w (m/mK)	K_f (GPa)	C_v (kJ/m^{3}K)	λ (W/mK)
Concrete	24.0	8.5×10^{-6}	--	--	--	--
Made Ground	18.0	1.7×10^{-5}	--	--	1900	1.40
Terrace Gravel	20.0	1.7×10^{-5}	--	--	1900	1.40
London Clay	20.0	1.7×10^{-5}	6.9×10^{-5}	2.2	1820	1.79
Lambeth Group Clay	20.0	1.7×10^{-5}	6.9×10^{-5}	2.2	1760	2.20
Thanet Sand	20.0	1.7×10^{-5}	--	--	1760	2.40

Note: γ= saturated bulk unit weight; α_s = linear coefficient of thermal expansion of solid skeleton; α_w = linear coefficient of thermal expansion of pore fluid; K_f = bulk stiffness of pore fluid; C_v = volumetric heat capacity; λ = thermal conductivity

3.3 Validation of the hydro-mechanical soil models

In this section, the modelling sequence of the excavation and construction stages of the previously described diaphragm wall problem is illustrated and the numerical results in terms of horizontal wall displacement at different stages of the analysis are compared to the monitoring data reported in Wood & Perrin (1984b). The aim is to validate the modelling procedure and the employed hydro-mechanical soil models and properties for this case study, in order to provide greater confidence in the accuracy of the simulation of the soil-structure interaction for subsequent non-isothermal analyses.

3.3.1 Modelling procedure

A plane-strain fully coupled hydro-mechanical (HM) analysis was carried out to simulate the excavation and construction of the permanent structures according to the construction sequence outlined in Table 3-6.

The domain was restrained in the vertical direction along the bottom boundary and in the horizontal direction along the lateral and bottom boundaries. In terms of hydraulic boundary conditions, no water flow was allowed across the lateral boundaries, while the Made Ground, the Terrace Gravels and Thanet Sand were considered to be free-draining materials (imposing therefore no change in pore water pressures at the top of the London Clay layer and the bottom of the Lambeth Group Clay layer). Each of the temporary struts were simulated as a spring acting at a node with an assumed stiffness of 50 MN/m^2. The pre-stress of the struts was simulated by applying a nodal force equal to the design pre-stress value indicated in Wood & Perrin (1984b), i.e. 50 kN/m, 80 kN/m and 120 kN/m for prop levels 1, 2 and 3, respectively.

The wall was “wished in place” (i.e. the wall construction is not simulated and installation effects are neglected) and full friction was assumed at the soil-wall interface. Given the consolidating nature of the clayey materials, the excavation and construction events have been simulated by reproducing the actual

periods of time according to the construction sequence outlined in Wood & Perrin (1984b) (see Table 3-6), whereas the installation of the temporary struts was simulated as an instantaneous event. Moreover, at the start of the construction of the internal structures, the soils' stiffness was reset as a consequence of the associated reversal in loading direction (Gawecka et al., 2017; Schroeder et al., 2004). This was achieved by setting to zero the values of the hardening parameters corresponding to the deviatoric and volumetric deformation levels employed, respectively, in the calculation of the tangent shear (Equation (3-1)) and bulk (Equation (3-4)) stiffness.

Table 3-6: Analysis sequence

Excavation of the basement	
Excavation stage 1	Excavate to 18.0 mOD (4.0 m bgl) – 45 days
Installation Prop 1	Construct prop level 1 and apply pre-stress (50 kN/m) at 19.15mOD (2.85m bgl)
Drainage stage	Drain Terrace Gravel Deposits inside excavation
Excavation stage 2	Excavate to 15.0 mOD (7.0 m bgl) – 30 days
Installation Prop 2	Construct prop level 2 and apply pre-stress (80 kN/m) at 16.2mOD (5.80m bgl)
Excavation stage 3	Excavate to 12.5 mOD (9.5 m bgl) – 90 days
Installation Prop 3	Construct prop level 3 and apply pre-stress (120 kN/m) at 13.0mOD (9.0m bgl)
Excavation stage 4	Excavate to 10.6 mOD (11.4 m bgl) – 60 days
Construction of internal structure	
Construction stage 1	Construct base slab – 30 days
Removal Prop 3	Remove prop level 3
Construction stage 2	Construct columns 3rd floor and slab 2nd floor – 30 days
Removal Prop 2	Remove prop level 2
Construction stage 3	Construct columns 2nd floor and slab 1st floor– 30 days
Removal Prop 1	Remove prop level 1
Construction stage 4	Construct columns 1st floor and slab ground floor– 30 days

3.3.2 Comparison between measured and computed results

The results of the numerical analysis in terms of horizontal wall movements are compared to the monitoring data from inclinometers labelled as "i1", "i3", "i4" and "i7" in Wood & Perrin (1984b), positioned along the east and west walls, as depicted in Figure 3-1. The horizontal displaced shapes at different construction stages are displayed in Figure 3-5.

In general, the predictions of the FE analysis agree well with the measured data. The wall response is especially well simulated during the first two excavation stages and during construction of the permanent floors and columns, whereas a larger wall deflection is predicted by the numerical analysis at about 10.0 m depth during the last two excavation stages. These discrepancies, while important, are

deemed to be acceptable, particularly when considering that, apart from the stratigraphy, limited site-specific data were available regarding the behaviour of the materials or the initial K_0 profile. Furthermore, the temporary support system consisted of a complex steel frame (see Wood & Perrin (1984b) and Wood & Perrin (1984a)), the modelling of which under plane-strain assumptions is inherently approximate. In addition, no characterisation of its stiffness had been provided in the literature, meaning that a nominal value had to be assumed (50 MN/m^2).

Clearly, the good agreement between the numerical and measured responses provides confidence in the ability of the numerical model (including initial conditions, finite element discretisation, hydraulic and mechanical parameters and boundary conditions) to simulate accurately the complex soil-structure interaction phenomena associated with the construction of this retaining structure. As a result, it is expected that this validation exercise contributes to the reduction in the uncertainty associated with the modelling of this wall under hypothetical thermal loads.

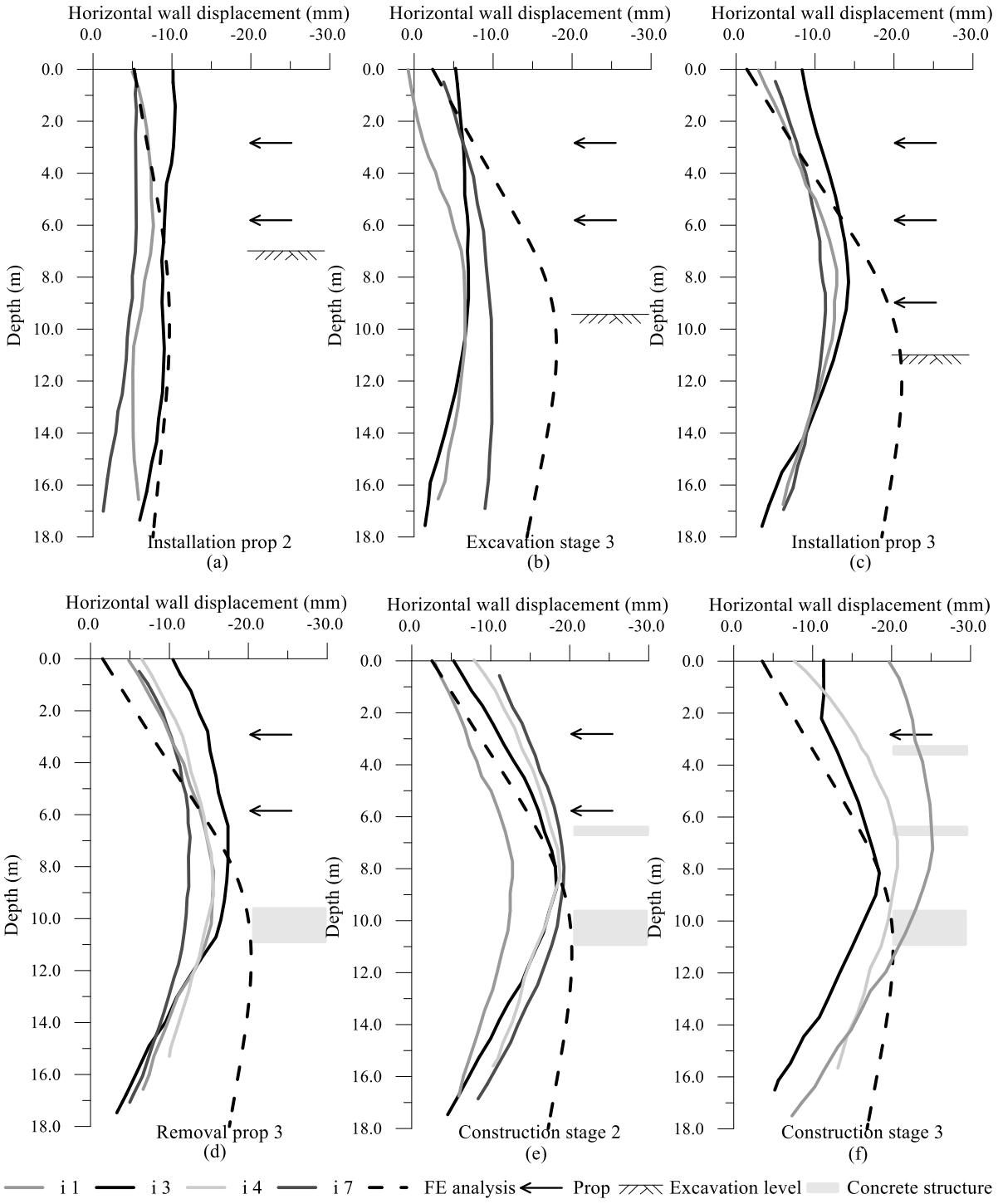

Figure 3-5: Comparison between measured and simulated horizontal wall displacement at different simulation stages

3.4 Characterisation of thermo-hydro-mechanical interactions in thermo-active retaining wall problems

Before detailing the analyses performed on the previously described wall problem hypothesising its use as heat exchanger, insights into the THM interactions occurring within the soil when subjected to temperature changes are provided. For this purpose, simple, one-dimensional problems are analysed in this section to explain the origin and manifestations of the main mechanisms taking place in complex fully coupled THM analyses. To assist in the interpretation of the results, analytical expressions for calculating excess pore water pressures resulting from changes in temperature in undrained conditions are developed. Furthermore, to evaluate the impact of varying ground properties on the observed THM interactions, various dimensionless parameters are established.

The two one-dimensional problems considered in this section are characterised by different mechanical and hydraulic boundary conditions, with the aim of representing the conditions within the retained (Problem A – one-dimensional expansion) and excavated (Problem B – fully restricted) sides of a thermo-active wall simulated in a 2D plane-strain analysis, as schematically represented in Figure 3-6.

It should be noted that the idealisation of the retained side assumes the soil mass is free to expand in the horizontal direction. This may not reproduce accurately the deformation mode of the soil mass in this region, where an important displacement in the vertical direction takes place. However, the adopted approximation of the problem offers the advantage of a simple one-dimensional model where the displacements occur in the same direction as heat transfer and water flow. Furthermore, it allows a useful comparison to be established with the analytical solutions for excess pore water pressure generation in one-dimensional elements subsequently proposed. Hence, the adopted simplification was deemed appropriate for the characterisation of the THM interactions occurring within the retained side.

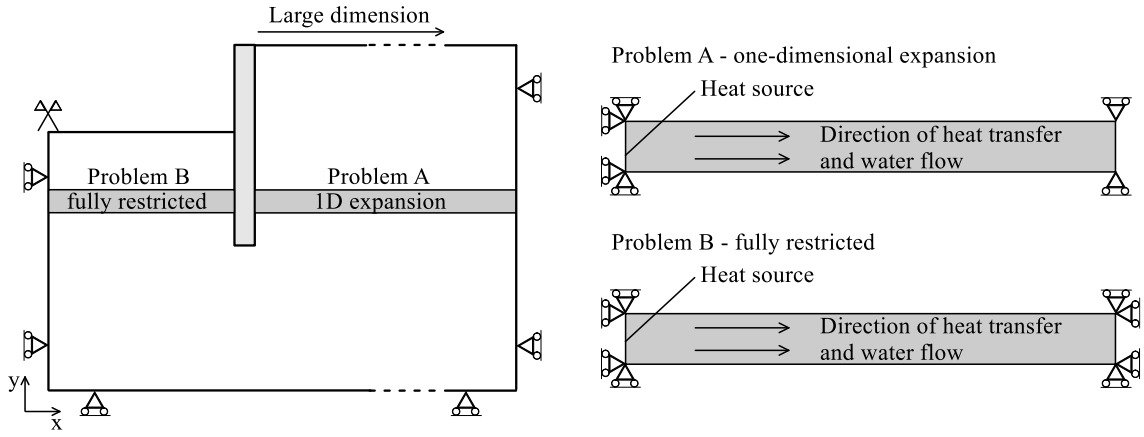

Figure 3-6: Schematic representation of idealisation of one-dimensional problems in a retaining wall analysis

3.4.1 Generation of excess pore water pressures

As described in Section 2.2.3, experimental results showed that soils subjected to changes in temperature under undrained conditions generate excess pore water pressures (e.g. Campanella & Mitchell, 1968, Abuel-Naga et al., 2007a). This is a fundamental aspect that leads to various THM interactions within the soil.

The general hydraulic equation for fully coupled THM analysis implemented in ICFEP is described in Cui et al. (2018a) and was previously outlined in Section 2.3.1. Equation (2-21) is here rewritten adopting a compression-positive sign convention:

$$\underbrace{-\nabla \cdot \{v_f\}}_{(i)} + \frac{n}{K_f}\frac{\partial u}{\partial t} - \underbrace{3n(\alpha_w - \alpha_s)\frac{\partial T}{\partial t}}_{(ii)} + Q^f = \underbrace{\frac{\partial\left(\varepsilon_{vol,tot} - \varepsilon_{vol,th}\right)}{\partial t}}_{(iii)} \tag{3-8}$$

where the terms (i), (ii) and (iii) define different mechanisms that contribute to the variation of pore water pressures in a coupled THM analysis, which will be used throughout this study to describe changes in pore water pressures occurring due to different phenomena:

- the term labelled as (i) represents pore water pressures changes due to water flow into and out of the soil element due to a hydraulic head gradient and is controlled by the permeability (or hydraulic conductivity) of the soil (Darcy's law). The change in pore water pressures computed as a consequence of this phenomenon will be called "hydraulically-induced";
- the term labelled as (ii) calculates changes in pore water pressures as a result of the difference between the linear coefficients of thermal expansion of soil (α_s) and water (α_w). Since the latter is typically larger than the former, an increase in pore water pressures is observed during heating, with the opposite registered during cooling. The excess pore water pressures arising due to this mechanism will be designated as "thermally-induced";
- the term labelled as (iii) relates to the mechanism where changes in pore water pressures take place due to the variation of pore space arising from mechanical volumetric strains $\varepsilon_{vol,mech}$ (i.e. $\varepsilon_{vol,tot} - \varepsilon_{vol,th}$) and these will be termed "mechanically-induced" (i.e. coupled-consolidation).

To assess the impact of these different mechanisms on the THM interactions within the soil, analytical expressions for the calculation of excess pore water pressures in undrained conditions are developed. Specifically, these were computed for single elements subjected to temperature changes and presenting different boundary conditions that aim to simulate the previously described Problems A and B.

Under undrained conditions, it is assumed that no flow of water occurs, hence v_f and Q^f in Equation (3-8) are equal to zero. Furthermore, approximating $\partial\varepsilon_{vol,tot}/\partial t$ as $\Delta\varepsilon_{vol,tot}/\Delta t$, $\partial\varepsilon_{vol,th}/\partial t$ as $\Delta\varepsilon_{vol,th}/\Delta t$, $\partial u/\partial t$ as $\Delta u/\Delta t$ and $\partial T/\partial t$ as $\Delta T/\Delta t$, and noting that $\Delta\varepsilon_{vol,mech} = \Delta p'/K_s$, Equation (3-8) can be re-written as:

$$\frac{\Delta u}{K_f} n - \underbrace{3n(\alpha_w - \alpha_s)\Delta T}_{(ii)} = \underbrace{\frac{\Delta p'}{K_s}}_{(iii)} \tag{3-9}$$

where $\Delta p'$, Δu and ΔT are the changes in mean effective stress, pore water pressure and temperature, respectively, and K_f and K_s are the bulk moduli of pore water and soil skeleton, respectively, and n is the porosity. In Equation (3-9) – and in those in the following paragraphs – the labels (ii) and (iii) refer to the mechanisms previously outlined.

The change in mean effective stress, $\Delta p'$, is defined as:

$$\Delta p' = \left(\Delta \sigma'_x + \Delta \sigma'_y + \Delta \sigma'_z\right)/3 \tag{3-10}$$

where $\Delta \sigma'_x$, $\Delta \sigma'_y$ and $\Delta \sigma'_z$ are the changes in effective stress in the x, y, and z-directions, respectively.

Note that $\Delta p'/K_s$ is equivalent to the change in mechanical volumetric strain, $\Delta \varepsilon_{vol,mech}$:

$$\Delta \varepsilon_{vol,mech} = \Delta \varepsilon_{x,mech} + \Delta \varepsilon_{y,mech} + \Delta \varepsilon_{z,mech} \tag{3-11}$$

where $\Delta \varepsilon_{x,mech}$, $\Delta \varepsilon_{y,mech}$, $\Delta \varepsilon_{z,mech}$ are the changes in the mechanical strains in the x, y, and z-directions. According to Hooke's law for linear-elastic materials, these are defined as:

$$\Delta \varepsilon_{x,mech} = \frac{\Delta \sigma'_x}{E} - \frac{\nu}{E}\left(\Delta \sigma'_y + \Delta \sigma'_z\right) \tag{3-12}$$

$$\Delta \varepsilon_{y,mech} = \frac{\Delta \sigma'_y}{E} - \frac{\nu}{E}\left(\Delta \sigma'_x + \Delta \sigma'_z\right) \tag{3-13}$$

$$\Delta \varepsilon_{z,mech} = \frac{\Delta \sigma'_z}{E} - \frac{\nu}{E}\left(\Delta \sigma'_x + \Delta \sigma'_y\right) \tag{3-14}$$

where E is the Young's modulus and ν the Poisson's ratio.

Single element representation of Problem A

Problem A is represented by an element subjected to plane-strain conditions being free to expand in the x-direction only, as shown in Figure 3-7 (a). Thus, the total strains ($\varepsilon_{tot} = \varepsilon_{mech} + \varepsilon_{th}$) in the y and z-directions are equal to zero, meaning that the mechanical strains are equal to the thermal strain but of opposite sign, i.e $\varepsilon_{mech} = -\varepsilon_{th} = \alpha_s \cdot \Delta T$. Furthermore, the total stress in the x-direction is equal to zero and hence the change in effective stress is given by $\Delta \sigma'_x = -\Delta u$. As a consequence, Equations (3-13) and (3-14) can be written as:

$$\frac{\Delta \sigma'_y}{E} - \frac{\nu}{E}\left(\Delta \sigma'_z - \Delta u\right) = \alpha_s \cdot \Delta T \tag{3-15}$$

$$\frac{\Delta\sigma'_z}{E} - \frac{\nu}{E}\left(\Delta\sigma'_y - \Delta u\right) = \alpha_s \cdot \Delta T \tag{3-16}$$

Which leads to:

$$\Delta\sigma'_y + \Delta\sigma'_z = \frac{2(E \cdot \alpha_s \cdot \Delta T - \nu \cdot \Delta u)}{(1-\nu)} \tag{3-17}$$

Therefore, the change in mean effective stress $\Delta p'$ is equal to:

$$\Delta p' = \frac{\Delta\sigma'_x + \Delta\sigma'_y + \Delta\sigma'_z}{3} = \frac{2}{3}\frac{(E \cdot \alpha_s \cdot \Delta T - \nu \cdot \Delta u)}{(1-\nu)} - \frac{\Delta u}{3} \tag{3-18}$$

Substituting the expression above into Equation (3-9) (and noting that $3K_s = E/(1-2\nu)$) and rearranging, the excess pore water pressure calculated due to a change in temperature ΔT for the assumed boundary conditions is equal to:

$$\Delta u = \underbrace{\frac{3n(\alpha_w - \alpha_s) \cdot \Delta T}{\frac{n}{K_f} + \frac{1}{3K_s}\left(\frac{1+\nu}{1-\nu}\right)}}_{(ii)} + \underbrace{\frac{2\alpha_s\left(\frac{1-2\nu}{1-\nu}\right) \cdot \Delta T}{\frac{n}{K_f} + \frac{1}{3K_s}\left(\frac{1+\nu}{1-\nu}\right)}}_{(iii)} \tag{3-19}$$

Single element representation of Problem B

Problem B is subjected to a further restriction in the lateral direction (x-direction, see Figure 3-7 (b)) compared to Problem A. Therefore, there will be an additional stress component, since the mechanical strains in all directions are equal to $\alpha_s \cdot \Delta T$, which leads to:

$$\Delta\varepsilon_{vol,mech} = \Delta\varepsilon_{x,mech} + \Delta\varepsilon_{y,mech} + \Delta\varepsilon_{z,mech} = 3\alpha_s \cdot \Delta T \tag{3-20}$$

Hence

$$\Delta\sigma'_x + \Delta\sigma'_y + \Delta\sigma'_y - 2\nu\left(\Delta\sigma'_x + \Delta\sigma'_y + \Delta\sigma'_y\right) = 3E \cdot \alpha_s \cdot \Delta T \tag{3-21}$$

Which can be rewritten as

$$3\Delta p' = \frac{3E \cdot \alpha_s \cdot \Delta T}{(1-2\nu)} \tag{3-22}$$

Thus:

$$\Delta p' = \frac{E \cdot \alpha_s \cdot \Delta T}{(1-2\nu)} = 3K_s \cdot \alpha_s \cdot \Delta T \tag{3-23}$$

Substituting this expression into Equation (3-9) and rearranging, the excess pore water pressure due to temperature changes for a fully restricted soil element in undrained conditions is given by:

$$\Delta u = \underbrace{3(\alpha_w - \alpha_s) \cdot K_f \cdot \Delta T}_{(ii)} + \underbrace{3\alpha_s \cdot \frac{K_f}{n} \cdot \Delta T}_{(iii)} \tag{3-24}$$

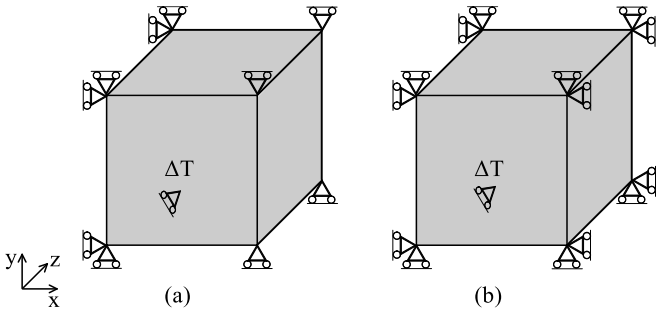

Figure 3-7: Single element representation of (a) one-dimensional expansion and (b) fully restricted

3.4.2 Analysis of one-dimensional problems

For this study, a 50.0 m long and 1.0 m high strip of soil is analysed in plane-strain conditions with boundary conditions representing either Problem A or Problem B. For both cases, the same geometry is adopted to allow more direct comparisons between the two sets of analyses. The finite element mesh consists of eight-noded quadrilateral solid elements, each with dimensions 0.5 m × 1.0 m, with displacement degrees of freedom associated to each node and temperature and pore pressure degrees of freedom at the corner nodes. An initial temperature, T_0, of 0.0°C and hydrostatic pore water pressures were assumed, while different mechanical and hydraulic boundary conditions were simulated for the two problems. The soil was considered linear-elastic and the material properties are outlined in Table 3-7. The total duration of the analysis was of 5 years and suitable time-steps were chosen according to Cui et al. (2016b) to avoid oscillations arising from thermal shock.

Table 3-7: Material properties of one-dimensional problems

Bulk modulus of soil skeleton (MPa)	K_s	83.3
Poisson's ratio (-)	ν	0.3
Permeability (m/s)	k	1.0×10^{-10}
Thermal conductivity (W/mK)	λ	2.0
Volumetric heat capacity (kJ/m^{3}K)	C_v	3000.0
Coefficient of thermal expansion of soil (m/mK)	α_s	1.0×10^{-5}
Coefficient of thermal expansion of water (m/mK)	α_w	6.9×10^{-5}
Bulk modulus of fluid (GPa)	K_f	2.2
Porosity (-)	n	0.5

3.4.2.1 Analysis of Problem A – One-dimensional expansion

Problem A approximates the conditions within the retained side of a thermo-active wall problem by considering a strip of soil analysed in plane-strain conditions which is free to expand in the horizontal direction. The geometry and boundary conditions of the problem are shown in Figure 3-8: a constant

temperature boundary condition of 15°C was applied at the nodes of the left-hand side boundary to model a source of heat, with no water flow allowed across this boundary; no changes in temperature and pore water pressure were imposed at the right-hand side boundary, simulating the conditions of a far field boundary. To retain its characteristics as a one-dimensional problem, the nodes along the top and bottom boundaries were free to displace laterally but not vertically and no heat flux or water flow was allowed across these boundaries.

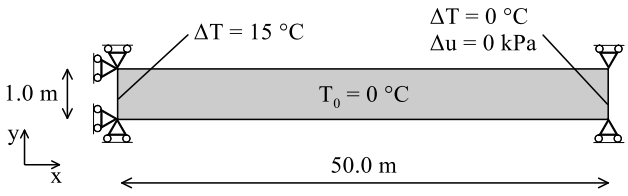

Figure 3-8: Schematic of Problem A - one-dimensional expansion

The changes in temperature and pore water pressures along the strip of soil at different time instants are displayed in Figure 3-9. For a single element subjected to a ΔT of 15 °C, the excess pore water pressures in undrained conditions calculated with Equation (3-19) are equal to 195.8 kPa. Conversely, the change in pore water pressures generated at the heat source (i.e. x = 0.0 m) in Problem A is equal to 80.4 kPa, i.e. less than half of the value computed with Equation (3-19). This indicates that the problem is not fully undrained and that water flow occurs due to the resulting pore water pressure gradient. Indeed, as highlighted in Figure 3-9, it can be noted that further away from the heat source, excess pore water pressures develop even in regions where changes in temperature have not yet taken place, which are due to term (i) of Equation (3-8) (i.e. hydraulically-induced). Clearly, this suggests that, in the analysed problem, water flow is occurring at a faster rate than heat transfer, which, in the present case, is dominated by conduction. With time, as the heat front propagates and thus additional pore water pressures are generated due to changes in temperature, the hydraulically-induced excess pore water pressures increase as a larger volume of water flows through the soil mass towards the right-hand side boundary, which acts as a drain.

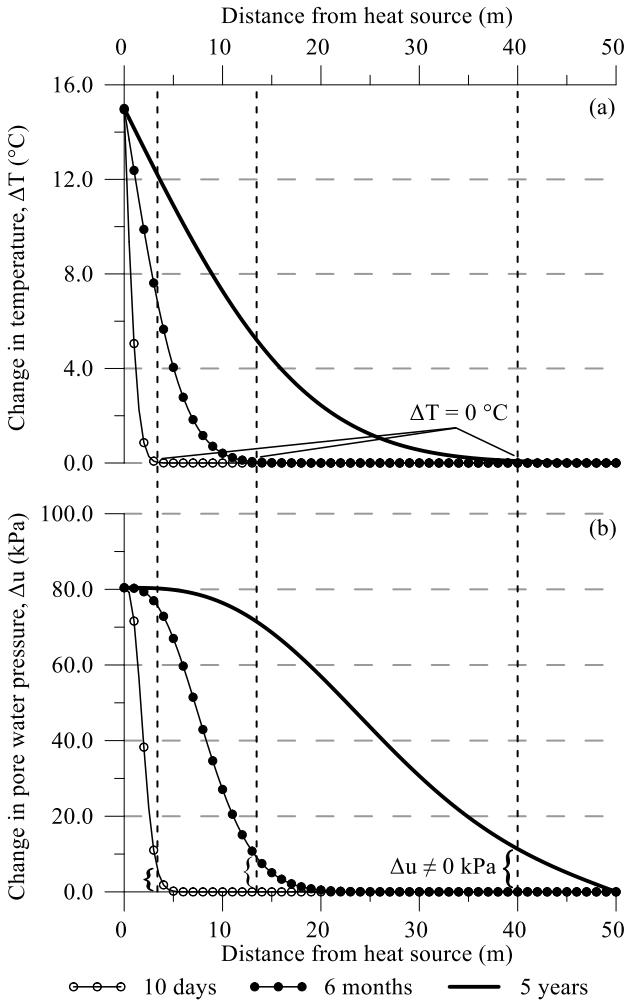

Figure 3-9: One dimensional expansion – distributions with distance from heat source of (a) change in temperature ΔT and (b) change in pore water pressure Δu at three different time instants

In order to analyse the mechanically-induced excess pore water pressures, a further analysis was performed where $\alpha_w = \alpha_s = 1.0 \times 10^{-5}$. Hence, only term (iii) in Equation (3-8) contributes to the generation of pore water pressure as a consequence of temperature changes. In fully undrained conditions, the analytical solution in Equation (3-19) would suggest a rise in pore water pressures at the heat source of 22.4 kPa, which is approximately 90% less than in the previous case, indicating that the largest part of generated excess pore water pressures is linked to the fact that $\alpha_w > \alpha_s$, i.e. are due to term (ii) in Equation (3-8) (thermally-induced).

Similar to the previous case, the value obtained in the FE analysis is equal to 9.2 kPa, i.e. less than 50% of what is determined using the analytical solution. Moreover, as can be observed from Figure 3-10, the evolution with time of the distribution of pore water pressures within the soil strip is similar in shape to that calculated previously (i.e. $\alpha_w \neq \alpha_s$), though reduced in magnitude by approximately 90%. Thus, it can be concluded that the differential thermal expansion between the two soil phases (soil skeleton and pore fluid) affects the magnitude of the thermally- and hydraulically-induced excess pore water

pressures, whereas their development with time is controlled by their rate of dissipation and hence by the permeability of the material.

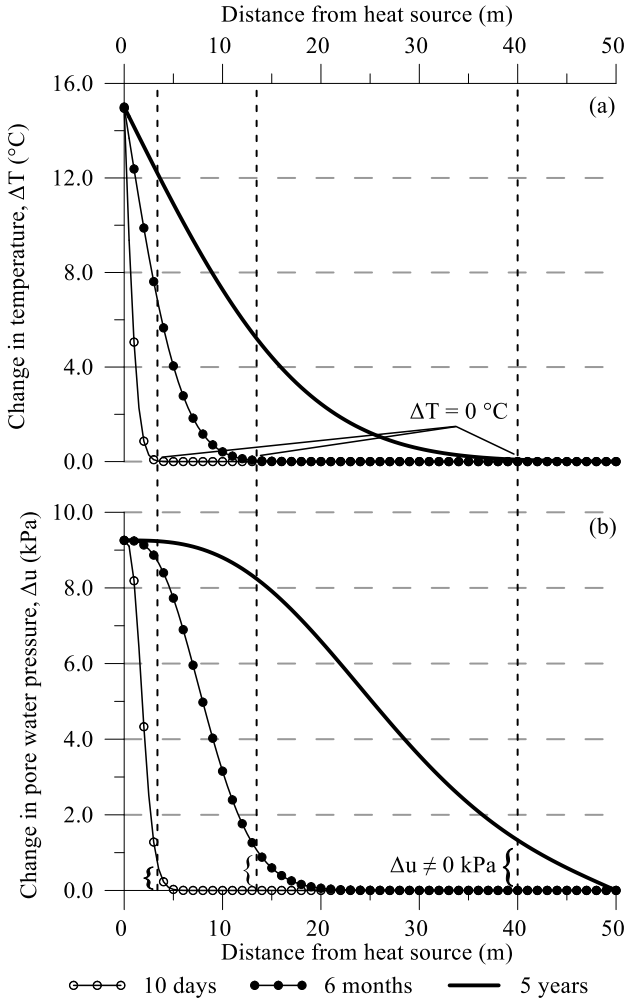

Figure 3-10: One dimensional expansion $\alpha_w = \alpha_s$ – distributions with distance from heat source of (a) change in temperature ΔT and (b) change in pore water pressure Δu at three different time instants

3.4.2.2 Analysis of Problem B - Fully restricted

To simulate the soil conditions beneath the excavation, the boundary conditions were varied with respect to problem A to simulate the presence of the axis of symmetry on the boundary away from the heat source (i.e. the right-hand boundary), as illustrated in Figure 3-11. This was modelled by introducing an additional mechanical restriction in the horizontal direction and by preventing water flow across the right-hand boundary. Moreover, while it is clear that symmetry considerations should have meant that no heat flux should be allowed across this boundary, such option was discarded as it would reduce the scope for comparisons with Problem A. Therefore, no change in temperature from the initial condition was imposed, meaning that, for excavations of reduced width, the temperature field beneath the excavation may not be reproduced accurately. However, it is considered appropriate for the purpose of identifying the fundamental mechanisms involved. All other boundary conditions are identical to those adopted in Problem A.

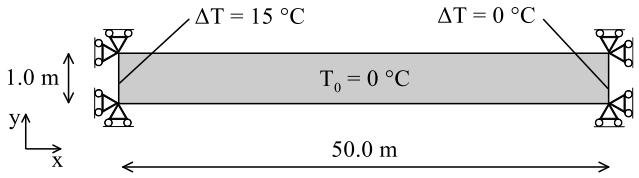

Figure 3-11: Schematic of the fully restricted case

The pore water pressure distributions calculated for this problem (see Figure 3-12) are substantially different from those computed for Problem A – both in terms of magnitude and variation with lateral extent. As expected, the excess pore water pressures are larger due to the larger mechanical volumetric strains resulting from the additional stress component in the horizontal direction (as shown by Equation (3-24)). Furthermore, since water is not allowed to leave the system, pore water pressures accumulate over the entire horizontal distance, increasing with time as additional excess pore fluid pressures develop with further changes in temperature. In terms of comparison with the analytical solution (Equation (3-24)), it should be noted that this was established assuming that the entire soil mass would change temperature simultaneously, which, as seen in Figure 3-12, does not correspond to the modelled thermal response in this one-dimensional problem. It is therefore unsurprising that substituting ΔT = 15°C in Equation (3-24) returns significantly higher values of excess pore water pressure. A more adequate comparison consists of using in Equation (3-24) the average temperature change at a given time instant obtained in the FE analysis (Figure 3-12 (a)). The predicted change in pore pressure is then in good agreement with the average pore water pressure computed in the FE analysis (Figure 3-12 (b)). Indeed, the average temperature change along the strip of soil, for example, after 6 months, is equal to 1.15°C. With this value, a change in pore water pressure of 600.0 kPa is calculated using Equation (3-24), while the average change computed in the FE analysis is equal to 575.0 kPa. This demonstrates the value of this analytical approach in the interpretation of the complex coupled phenomena taking place in the soil mass.

Lastly, it is interesting to point out that, when assuming $\alpha_w = \alpha_s$, the calculated pore water pressures close to the heat source are approximately 25% of those shown in Figure 3-12, a slightly larger proportion than that observed in Problem A, where this ratio was about 10%, indicating the effect of the additional mechanical boundary conditions.

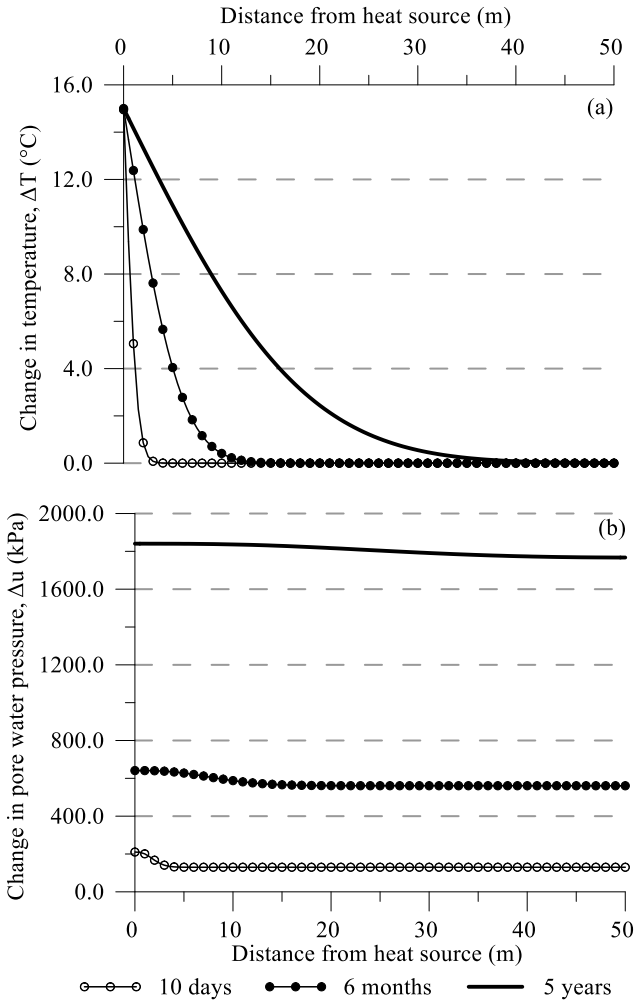

Figure 3-12: Fully restricted – distributions with distance from heat source of (a) change in temperature ΔT and (b) change in pore water pressure Δu at three different time instants

3.4.3 Influence of soil properties on THM interactions

The influence of ground properties on the observed THM interactions is analysed for Problem A. Dimensionless parameters are introduced first, which allow the response of problems with different ground properties to be compared and facilitate the assessment of the ongoing phenomena.

3.4.3.1 Dimensionless parameters

Relative thermo-hydraulic diffusivity

As demonstrated by the results of the simplified problems analysed in the previous section, the significance and nature of THM interactions are related to the rates of heat transfer and water flow, which are controlled, respectively, by the thermal and hydraulic diffusivity of the soil. The differential equation of one-dimensional heat transfer by conduction is expressed by Equation (3-25):

$$\frac{\partial T}{\partial t} = \alpha_T \frac{\partial^2 T}{\partial x^2} \tag{3-25}$$

where α_T is the thermal diffusivity (m^2/s), which is defined as the ratio between the thermal conductivity λ (W/mK) and volumetric heat capacity C_v (J/m^{3}K).

Similarly, the differential equation of one-dimensional consolidation is defined as:

$$\frac{\partial u_e}{\partial t} = \alpha_H \frac{\partial^2 u_e}{\partial x^2} \tag{3-26}$$

where u_e is the excess pore water pressure and α_H is the hydraulic diffusivity (m^2/s), which is often also referred to as the coefficient of consolidation, c_v. However, the former definition is employed herein to establish a direct link between heat transfer and water flow. The hydraulic diffusivity can be expressed as:

$$\alpha_H = \frac{k}{S_s} \tag{3-27}$$

with k (m/s) being the permeability and S_s (1/m) the specific storage, which is defined as (Jorgensen, 1980):

$$S_s = \rho_w g \left(\frac{n}{K_f} + \frac{1}{K_s} \right) \tag{3-28}$$

where ρ_w is the density of water (kg/m^3), g the acceleration due to gravity (m/s^2), n the porosity (adim), and K_f and K_s are the bulk moduli (kN/m^2) of the pore fluid and the soil skeleton, respectively.

To measure the relative rates between heat transfer and water flow, the dimensionless parameter α_{TH} is introduced:

$$\alpha_{TH} = \frac{\alpha_T}{\alpha_H} \tag{3-29}$$

Clearly, given its analytical definition, the variation of α_{TH} is mainly controlled by the value of the permeability, k, as all other material properties vary within a significantly more limited range.

Degree of heat transfer

As previously outlined, the thermal diffusivity controls the rate of heat transfer. Thus, analyses with different values of α_T but equal thermal boundary conditions, will reach thermal equilibrium at different time instances. For the purpose of comparing such problems, the dimensionless parameter R is introduced, establishing a parallel with the theory of one-dimensional consolidation. By using this parameter, the same temperature distributions are considered for analyses with different values of α_T, even if that corresponds to different time instances. Furthermore, it allows the determination of how far the problem is from steady state. Indeed, similar to the average degree of consolidation (Craig, 2004), the average degree of heat transfer R indicates the ratio, in terms of a percentage, between the amount of heat transferred up to a given time instant and the total heat transfer required to reach steady state, and is expressed as:

$$R = \frac{\int_0^L \Delta T_e \, dx}{\int_0^L \Delta T_f \, dx} \tag{3-30}$$

where ΔT_e is the distribution of temperature change at a given time, ΔT_f is the final distribution of temperature change (i.e. at steady state, when $t \to \infty$) and L is the length of the one-dimensional solid. A value of R = 0.0 means that heat transfer has not yet begun, whereas a value of R = 1.0 implies that thermal steady state has been reached.

The distributions of ΔT_e and ΔT_f, hence also the evolution of R with time, depend on the initial conditions and the boundary conditions of the analysed problem. Assuming a uniform initial temperature, with the temperature boundary conditions specified in the previous section, i.e. fixed temperatures at both boundaries (one being the heat source and the other the constant far field temperature), the distribution of change in temperature at steady state, ΔT_f, is triangular. Conversely, if no heat flux would be allowed through the boundary opposite the heat source (e.g. modelling an axis of symmetry, which would apply to Problem B), this would lead to a ΔT_f which is constant and equal to the induced temperature at the heat source. Curves of the degree of heat transfer R against the dimensionless time F_o for these two conditions are depicted in Figure 3-13, where the similarity to the consolidation curves can be clearly identified. It should be noted that the dimensionless time F_o (i.e. Fourier number, expressed as $\alpha_T t/L^2$, where t is time (Çengel & Ghajar, 2011)) is similar to the time factor, T_v, employed in one-dimensional consolidation calculations (with T_v being equal to $\alpha_H t/d^2$, with d being the drainage path length). As expected, the first scenario reaches thermal steady state earlier with respect to the second one, demonstrated by the curve in Figure 3-13 yielding R=1.0 at a lower value of F_o. Analytical solutions for the calculation of ΔT_e with the outlined boundary conditions are presented in Appendix A.

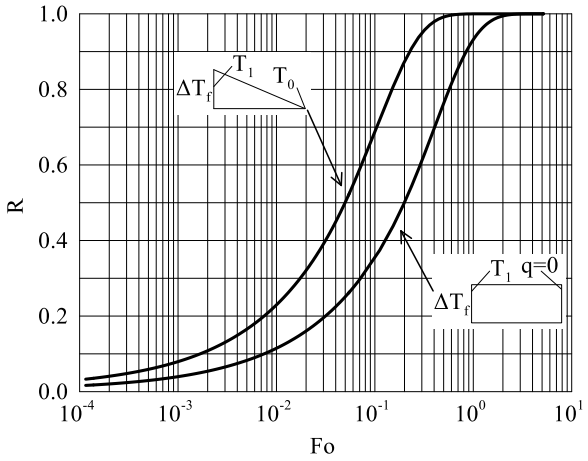

Figure 3-13: Relationship between degree of heat transfer R and Fourier number

Degree of excess pore water pressure generation

Thermally and mechanically induced excess pore water pressures

At very small distances from the heat source, the soil elements are subjected to an almost uniform temperature field and therefore the conditions of the single element represented in Figure 3-7 (a) are best reproduced. Thus, a comparison between the excess pore water pressures calculated through the analytical solution given by Equation (3-19) and the FE results can be performed. For this purpose, the following dimensionless parameter is introduced:

$$u^* = \frac{\Delta u_{FE}}{\Delta u_{AN}} \tag{3-31}$$

representing the ratio between the computed excess pore water pressure at the heat source in the FE analysis (Δu_{FE}) and the one obtained using the analytical solution (Δu_{AN}) expressed by Equation (3-19). Hence, the parameter u^* measures how undrained the problem is, with u^* = 1.0 indicating a fully undrained case (i.e. the FE analysis yields the same result as the perfectly undrained problem assumed in the analytical solution) and u^*= 0.0 meaning that any generated excess pore water pressures have dissipated.

Hydraulically-induced excess pore water pressures

In order to quantify the amount of excess pore water pressures generated ahead of changes in temperature due to water flow, a further dimensionless parameter, ω, is defined, with the parameters needed for its calculation being schematically represented in Figure 3-14. The parameter ω evaluates the percentage of excess pore water pressures computed at a given value of R and x-coordinate where changes in temperature have not yet occurred ($\Delta u_{R,x(\Delta T=0°C)}$) with respect to the maximum excess pore water pressure generated during the analysis (Δu_{max}, typically at the start of the analysis, i.e. R = 0.0, and at the heat source (x = 0.0)):

$$\omega = \frac{\Delta u_{R,x(\Delta T=0°C)}}{\Delta u_{max}} \tag{3-32}$$

This parameter is needed to consistently compare the amount of hydraulically-induced excess pore water pressures between analyses characterised by different values of α_{TH}.

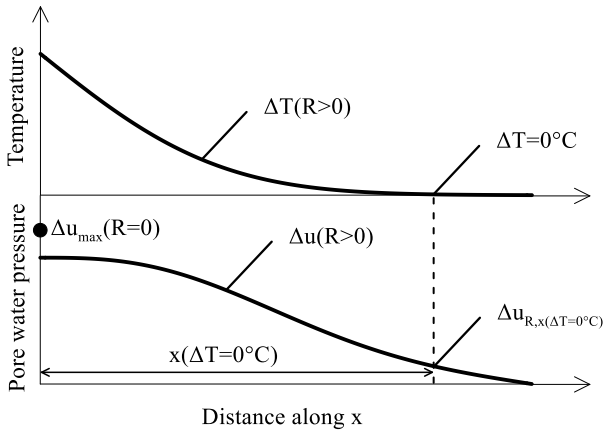

Figure 3-14: Schematic representation of calculation of ω

3.4.3.2 Parametric study on Problem A

A parametric study on the influence of α_{TH} on the different mechanisms involving excess pore pressure generation and dissipation, i.e. those due to changes in temperature and those due to water flow, was carried out based on Problem A. Different values of α_{TH} were analysed by varying the permeability, as shown in Table 3-8, with the values for all other parameters remaining as listed in Table 3-7. Moreover, additional analyses were carried out where other parameters were varied (e.g. thermal conductivity) in order to obtain the same value of α_{TH}. The results, presented in Appendix B, showed that, despite the different combination of parameters, the same response is obtained, confirming that α_{TH} controls the magnitude of the THM interactions. Clearly, changing the thermal parameters, i.e. varying α_T, affects the rate of heat transfer and hence the temperature distribution at a given time instant. Thus, for problems having the same α_{TH}, the same response is observed for equal values of the dimensionless time, F_o, or, similarly, of degree of heat transfer, R. Naturally, these correspond to different time instants if different values of α_T are used.

Table 3-8: Performed analyses for parametric study on the influence of α_{TH}

α_T (m^2/s)	k (m/s)	α_H (m^2/s)	α_{TH} (-)
6.67×10^{-7}	1.0×10^{-14}	8.34×10^{-11}	8.0×10^{3}
	1.0×10^{-12}	8.34×10^{-9}	8.0×10^{1}
	1.0×10^{-10}	8.34×10^{-7}	8.0×10^{-1}
	1.0×10^{-9}	8.34×10^{-6}	8.0×10^{-2}
	1.0×10^{-8}	8.34×10^{-5}	8.0×10^{-3}
	1.0×10^{-7}	8.34×10^{-4}	8.0×10^{-4}
	1.0×10^{-6}	8.34×10^{-3}	8.0×10^{-5}
	1.0×10^{-5}	8.34×10^{-2}	8.0×10^{-6}

Influence of α_{TH} on excess pore water pressures at the heat source

Figure 3-15 shows the variation of u^* with α_{TH} calculated at the first increment of the analysis (i.e. $R \cong 0$), where Δu_{AN} was obtained using Equation (3-19). The results show that, for large values of α_{TH}, the ratio u^* is unity, meaning that the FE analysis yields pore water pressures identical to those predicted by the analytical solution. This suggests, as expected, that soils characterised by large values of α_{TH} (i.e. heat transfer takes place more rapidly than dissipation of excess pore water pressures) display an undrained behaviour when subjected to temperature changes. As the value of α_{TH} reduces, u^* decreases, reaching a value of 0.0 at very low α_{TH}. Indeed, for such magnitudes of α_{TH}, no or very little excess pore water pressures are generated due to the rate of pore water pressure dissipation being significantly higher than that of heat transfer.

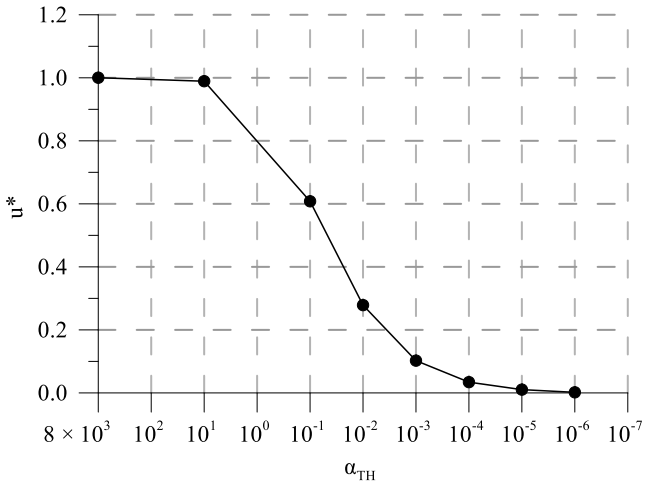

Figure 3-15: Variation of u^* at the heat source at beginning of the analysis with α_{TH}

Figure 3-16 shows the evolution of u^* at the heat source with R for selected values of α_{TH}. For very high values of α_{TH}, the curve remains approximately constant at a value of u^*= 1.0, starting to drop only as thermal steady state approaches (i.e. R = 1). This indicates that, with high α_{TH}, dissipation of pore water pressures occurs only when no further changes in temperature take place. As the value of α_{TH} decreases, the value of R at which u^* starts reducing also decreases, meaning that excess pore water pressure dissipation starts earlier and while temperature changes are still occurring. Indeed, a low value of α_{TH} indicates that water flow is faster when compared to heat transfer, with the time needed to reach hydraulic equilibrium being less than that required for achieving thermal steady state.

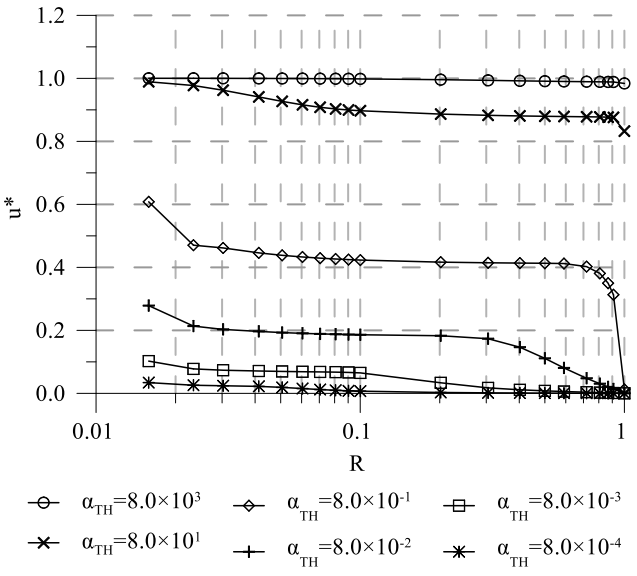

Figure 3-16: Variation of u at heat source with R for different α_{TH}*

Influence of α_{TH} on hydraulically-induced excess pore water pressures

To investigate the influence of α_{TH} on the amount of pore water pressures generated prior to changes in temperature (i.e. ahead of the propagating heat front), two time instants corresponding to two values of R were considered, namely R = 0.1 and R = 0.5. For these stages of the analysis, the variations of ω with α_{TH} are shown in Figure 3-17, demonstrating that hydraulically-induced excess pore water pressures are also largely influenced by the value of α_{TH}. It should be noted that the position of the heat front was arbitrarily established as the x-coordinate of the first node where the change in temperature, ΔT, is less than 0.002°C.

At time instant R = 0.1, for high values of α_{TH}, ω is equal to 0.0, since, as previously observed, such values of α_{TH} lead to an undrained soil response, hence low water flow. Similarly, for very low values of α_{TH}, ω is very small. In this case, excess pore water pressures are immediately dissipated given the higher rate of water flow when compared to heat transfer. It should be noted that, although the lowest value of α_{TH} still displays a ω of about 5%, this corresponds to negligible pore water pressures in absolute terms as the ones generated at the heat source (Δu_{max}) are very small (see Figure 3-15). For intermediate values of α_{TH}, ω reaches values of up to of 70%, indicating that the balance between the thermal and hydraulic systems is such that water flow occurs at a sufficiently fast pace that leads to excess pore water pressures in regions where no changes in temperature have yet taken place. Hence, it can be expected that for these combinations of parameters, excess pore water pressures may develop at considerable distances away from a heat source.

For R = 0.5, ω is very low for all the analyses, because, as time progresses and heat propagates, larger amounts of pore water pressures dissipate and leave the system through the right-hand side boundary. It is interesting to note that the peak of the curve of ω shifts to a different value of α_{TH} with increasing

R, thus a direct correlation between ω and α_{TH} cannot be established as this mechanism is time-dependent. In fact, ω for different values of α_{TH} varies differently with R: for a low value of α_{TH}, ω varies more rapidly with R when compared to soils with a high value of α_{TH} since, with those conditions, the pore water pressures dissipate at a faster rate, confirming the conclusions drawn from Figure 3-16.

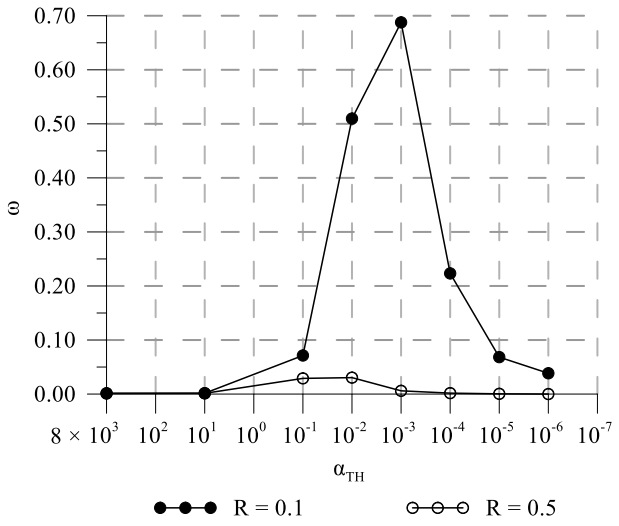

Figure 3-17: Variation of ω with α_{TH} for R = 0.1 and R = 0.5

3.5 Thermo-active retaining wall analysis

The same numerical model described in Sections 3.2 and 3.3 was used to perform further FE analyses hypothesising that the wall was subjected to thermal loads. Therefore, a fully coupled THM analysis was carried out, aiming at providing insight into the behaviour of this type of structure in the short and long term and at evaluating the influence of THM interactions on its transient behaviour, where parallels with the mechanisms observed in the one-dimensional problems are identified. Two main aspects are investigated in this study: firstly, the impact of the modelling approach is evaluated, where simplified analyses are performed by deactivating some components of the THM formulation; subsequently, the effect of varying ground properties is assessed. The first set of analyses highlights the relative contribution of the different mechanisms taking place in non-isothermal analyses and characterises the implications to the design of thermo-active walls of adopting different modelling approaches (a similar study on circular shafts employed as heat exchangers is presented in Sailer et al. (2019d)). The second set evaluates the impact of varying α_{TH}, hence of the rate at which the THM interactions occur, on the behaviour of thermo-active retaining walls modelled in fully coupled THM analyses.

3.5.1 Numerical analysis

The finite element mesh, the mechanical and hydraulic boundary conditions and material properties adopted in the THM analyses are the same as those outlined in Sections 3.2 and 3.3. These were deemed

appropriate given the good agreement between the simulated and measured response of the considered retaining wall during excavation and construction.

Once construction was completed, the diaphragm wall and internal structures were loaded assuming a surcharge corresponding to 10.0 kPa per storey of the building. This load was applied to the floor slab and the wall at ground level. In addition, a surcharge of 20.0 kPa was applied to each of the basement slabs. In order to simulate the presence of the drainage system reported by Wood & Perrin (1984b), a pore water pressure of 0.0 kPa was prescribed along the underside of the base slab. Before the application of any heat load, the excess pore water pressures generated during the previous stages (excavation, construction and loading) were allowed to dissipate fully. While realistically any GSES would be expected to start operating soon after the completion of the building, this dissipation stage was deemed necessary in order to facilitate the interpretation of the THM behaviour of the retaining wall by isolating it from the effects of previous construction stages. Furthermore, it should be noted that, since the application of the thermal load generally implies a reversal of the loading direction (see Gawecka et al. (2017) for additional details), the stiffness of all soils was reset to its maximum value prior to any changes in temperature being applied, according to the procedure previously described in Section 3.3.1.

The initial temperature of the ground was set to 13°C, as measured for a site in East London (Loveridge et al., 2013). The thermal boundary conditions consist of allowing no heat flux across the bottom and lateral boundaries of the domain, while the temperature at the ground surface was assumed to remain constant throughout the analysis (i.e. equal to 13°C). Moreover, no heat transfer through the internal structures was modelled, meaning that a perfect insulation barrier was simulated, preventing any heat losses from the soil to the basement and any heat transfer to the internal structures. To simulate the heat load applied to the retaining wall, a prescribed uniform temperature change of 15°C over 10 days (i.e. 1.5°C/day) was applied to all elements of the diaphragm wall, with the final temperature being kept constant for 10 years. Clearly, this does not reproduce a realistic operation mode for a GSES, where the heat load varies monthly or even daily. Additionally, representing the heat exchange by prescribing a uniform temperature over the whole wall neglects factors such as pipe arrangement, advection within the pipes, non-uniform temperature distribution along the pipe and within the cross-section of the wall and the heat conduction through the concrete. However, as stated at the beginning of this chapter, the purpose of this study is to provide the base knowledge of the fundamental soil-structure interaction mechanisms that take place due to thermal load application. It is therefore considered that both the long-term heating of the wall and the use of uniform temperature changes enable a clearer assessment of the phenomena occurring within a thermo-active wall problem, given the simplified modelling approach.

In addition to the concepts outlined in the previous section regarding pore water pressures, some aspects concerning the development of thermal strains within a THM analysis need to be considered. As

outlined in Section 2.3.1, the total strains (ε_{tot}) are given by the sum of the mechanical (ε_{mech}) and thermal strains (ε_{th}). While the latter are associated to the thermal expansion/contraction of the material when subjected to temperature changes, the former relate to changes in stress state, even when these arise from thermal loading. For example, when heating a confined material, the mechanical strain would have the same magnitude, but opposite sign, as the thermal strain, such that the total strain remains equal to zero to satisfy the boundary conditions. The mechanical strain would therefore be associated with a change in the stress state as determined by the constitutive model, which would be termed "thermally-induced", despite not being directly connected to the thermal strain. These concepts are used throughout this thesis to interpret the simulated coupled THM soil behaviour and its impact on the response of the wall.

Lastly, it should be noted that, for a retaining wall modelled in a 2D plane-strain analysis, the relationship used to calculate the free strain of a pile (see Equation (2-16)) cannot be directly applied due to the restriction to the deformation of the wall in the out-of-plane direction. In effect, in such a situation, there will be a contribution of the Poisson's ratio, ν, to the free axial strain of the wall, $\varepsilon_{free-wall}$, due to a temperature change:

$$\varepsilon_{free-wall} = \alpha_c \Delta T + \nu \alpha_c \Delta T \tag{3-33}$$

Note that, despite its thermal origin, this strain should not be designated as such, since the second term in Equation (3-33) is a mechanical strain which arises from the increase in stress in the out-of-plane direction. As a result, in the analysis of a thermo-active retaining wall, the potential strain developed due to temperature changes (i.e. the free strain) is larger than that of a thermo-active pile, with the difference depending on the Poisson's ratio of concrete.

3.5.2 Effect of modelling approach

To evaluate the influence of different modelling approaches on the behaviour of the thermo-active wall, different analyses were performed. These are summarised in Table 3-9 and are as follows:

- THM analysis: a fully coupled transient THM analysis where heat transfer, thermally-induced material expansion and pore water pressure build-up and dissipation are simulated, providing the most realistic representation of a thermo-active wall problem;
- HM analysis: a coupled hydro-mechanical analysis in which there is no heat transfer to the soil, meaning that temperature effects are restricted to the thermal expansion of the wall. This analysis disregards the thermal expansion of the soil and thermally-induced pore water pressures, thus enabling the assessment of their influence on the observed soil-structure interaction;
- dTM analysis: a drained coupled thermo-mechanical analysis where no changes in pore water pressures take place (i.e. neither due to temperature changes nor due to hydro-mechanical coupling),

but the soil is able to thermally expand. It allows the partial quantification of the effects of thermal soil expansion when compared to the results of the HM analysis. Similarly, when compared to the THM analysis, it provides insight into the impact of mechanically and thermally-induced pore water pressures;

- uTM analysis: an undrained coupled thermo-mechanical analysis in which only the behaviour of the soil-fluid mixture is considered (i.e. the two-phase nature of the soil is neglected, implying that $\alpha_w = \alpha_s$), hence excess pore water pressures are only generated as a consequence of changes in total stress and are not allowed to dissipate with time. This analysis provides an assessment of the impact of the generation of thermally-induced pore water pressures and their consequent dissipation on the transient behaviour of the retaining wall. It should be noted that there are two possible ways to model such a problem in ICFEP: one consists of disabling the hydraulic coupling, hence the hydraulic equation is not solved and pore fluid pressures are computed through the principle of effective stresses at the integration points; the second approach is to perform a coupled consolidation analysis by setting the permeability to a very low value and adopting α_w to be equal to α_s. The analyses carried out with these two approaches give very similar results and only the latter is used herein.

Table 3-9: Summary of the analyses performed

Analysis code	Transient seepage	Mechanically-induced pore water pressures (*)	Transient heat transfer	Thermal expansion of soil	Thermally-induced pore water pressures (**)
THM	Yes	Yes	Yes	Yes	Yes
HM	Yes	Yes	No	No	No
dTM	No	No	Yes	Yes	No
uTM	No	Yes	Yes	Yes	No

(*) term (iii) in Equation (3-8); (**) term (ii) in Equation (3-8)

3.5.2.1 Temperature

The temperature distributions for different time instants are depicted in Figure 3-18. These are equal for the analyses involving heat transfer through the soil, i.e. analysis THM, uTM and dTM, since the thermal parameters remain unchanged and seepage velocities are sufficiently low to mean that there is no measurable impact of advection. With time, the temperatures in the area immediately around the wall steadily increase and propagate further away from the heat source as a consequence of the constant temperature imposed within the wall.

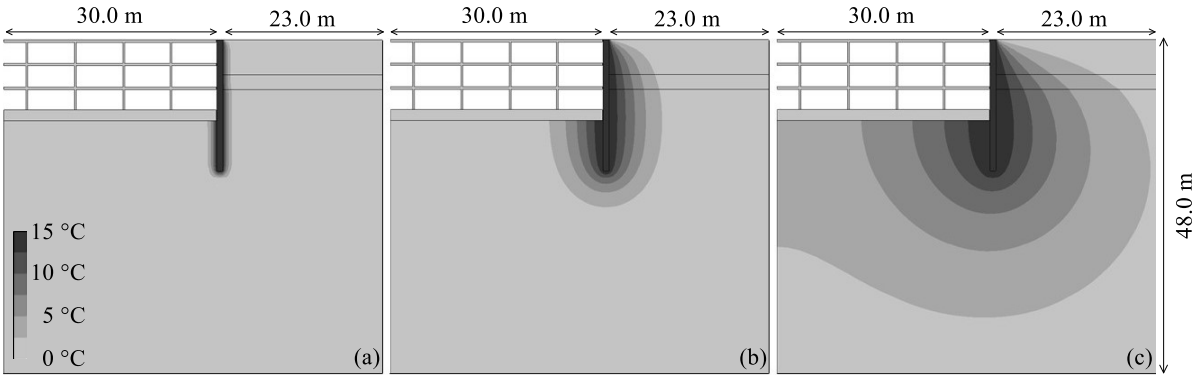

Figure 3-18: Temperature contours for thermal analyses (a) after 10 days, (b) after 6 months and (c) after 10 years

Figure 3-19 shows the evolution of temperature with time at mid-depth of the wall below the excavation and within the retained side at different distances from the wall. It can be observed that slightly higher temperatures develop on the excavated side since no heat flux was allowed into the building and through the left hand-side boundary, as it is an axis of symmetry. From the predicted temperature changes in the long term, it is clear that the latter boundary is sufficiently close to the heat source to induce a build-up of temperatures in that region. Indeed, the different thermal boundary conditions applied to the boundaries of the excavated and retained side of the wall lead to different temperature distributions at thermal steady state: within the retained side, steady state is reached earlier since heat can dissipate towards the ground surface; conversely, the adiabatic conditions simulated within the excavated side lead to a uniform temperature distribution at steady state, similar to that shown in Figure 3-13, meaning that larger temperatures are computed at greater distances from the wall and that thermal steady state occurs later in time, demonstrated by the temperature still increasing in this area at the end of the analysis.

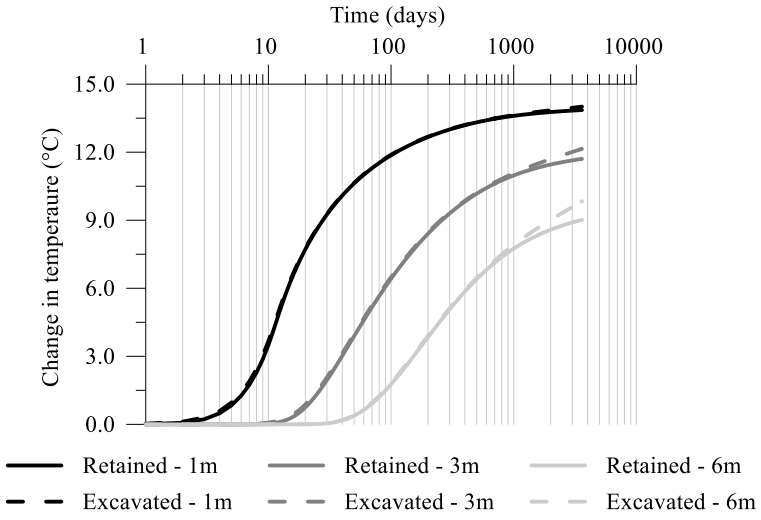

Figure 3-19: Change in temperature with time at mid-depth of embedded part of wall at different distances from wall within excavated and embedded sides of wall

3.5.2.2 Pore water pressure

The changes in pore water pressures are discussed for the THM, HM and uTM analyses, while no results are presented for the dTM analysis, since in this case no pore water pressures can be generated.

Figure 3-20 shows the contours of excess pore water pressures for the HM analysis at three different time instants, namely after 10 days, 6 months and 10 years from the start of heating. In the HM analysis, the soil does not undergo changes in temperature. Thus, term (ii) of Equation (3-8) is equal to zero and, hence, the only observed excess pore water pressures are those due to mechanical deformation of the soil as the wall thermally expands. After 10 days of heating (Figure 3-20 (a)), tensile pore water pressures develop along the shaft of the wall, whereas compressive pore water pressures are generated beneath the bottom of the structure. These are induced by the thermal expansion of the wall: the soil along most of the shaft is forced to expand in the vertical direction since full friction is simulated along the soil-structure interface, whereas the soil below the toe of the wall is compressed as the wall pushes against it. As there is no heat transfer within the soil mass and no associated thermally-induced pore water pressures, hydraulic equilibrium is reached rapidly: in fact, after 6 months from the beginning of heating almost full dissipation has taken place (Figure 3-20 (b)).

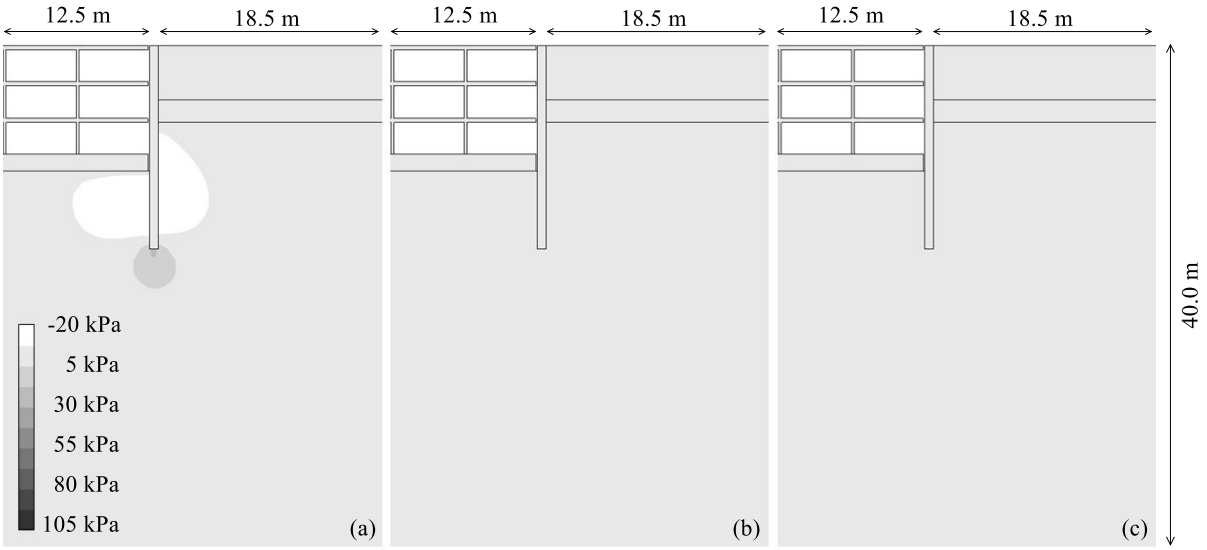

Figure 3-20: Contours of pore water pressures for HM analysis (a) after 10 days, (b) after 6 months and (c) after 10 years

This aspect can be clearly observed in Figure 3-21, which shows the development with time of the changes in pore water pressures at mid-depth of the embedded part of the wall at distances of 1.0 m and 3.0 m from the wall. Specifically, Figure 3-21 (a) and (b) report these changes within the retained and excavated sides, respectively. It can be noted that, once the final temperature of the wall has been reached (i.e. after 10 days) and hence no further thermal expansion of the wall occurs, the tensile excess pore water pressures steadily reduce as a consequence of the dissipation process until full equilibration is reached. Figure 3-21 also shows that slightly different magnitudes of excess pore water pressures are computed within the two sides of the wall, with these being larger within the excavated side. This is

attributed to the presence of the base slab, which moves upwards as the wall expands, inducing a larger expansion of the soil underneath it. Lastly, the dissipation takes place at a faster rate within the excavated side, which is due to the shorter drainage path in this region (i.e. drainage layer beneath the base slab).

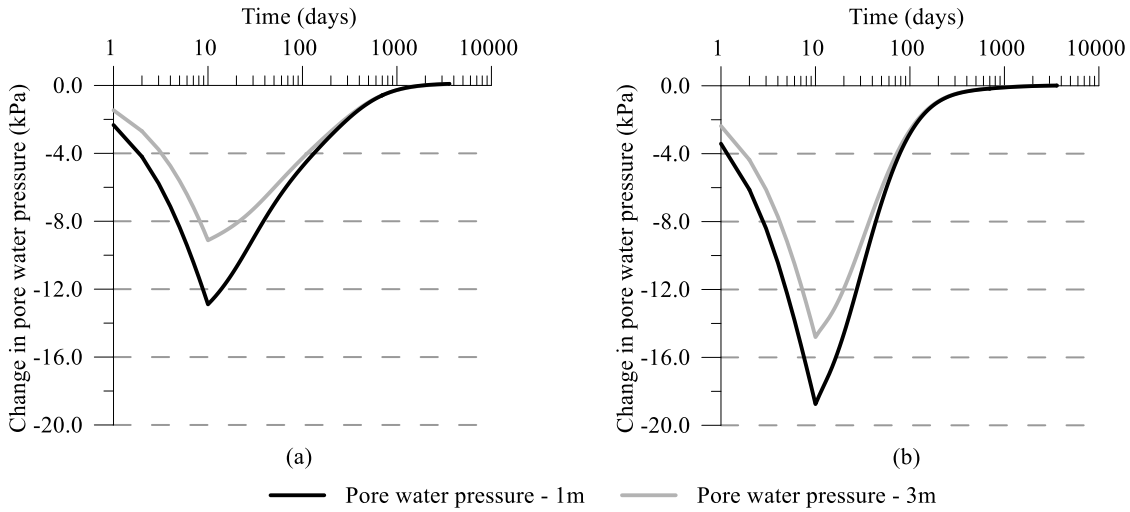

Figure 3-21: Changes in pore water pressure with time for HM analysis at 14.0m below ground level and at different distances from the wall (a) retained side and (b) excavated side

In the uTM analysis, the soil mass and the wall expand due to heating, however the clayey materials are treated as undrained, meaning that the pore water pressures are merely induced by a change in total stress and that there is no time-dependent dissipation of excess pore-water pressure. The contours of changes in pore water pressures for this analysis are depicted in Figure 3-22. Compressive excess pore water pressures develop due to the thermal expansion of the soil which is restricted in the out-of-plane direction, inducing an increase in total stress. With time, since the pore water pressures are not allowed to dissipate, they constantly increase as a result of the propagation of heat and consequent changes in stress. After 10 years, the maximum value registered at the back of the wall increases substantially, reaching a maximum of approximately 100.0 kPa.

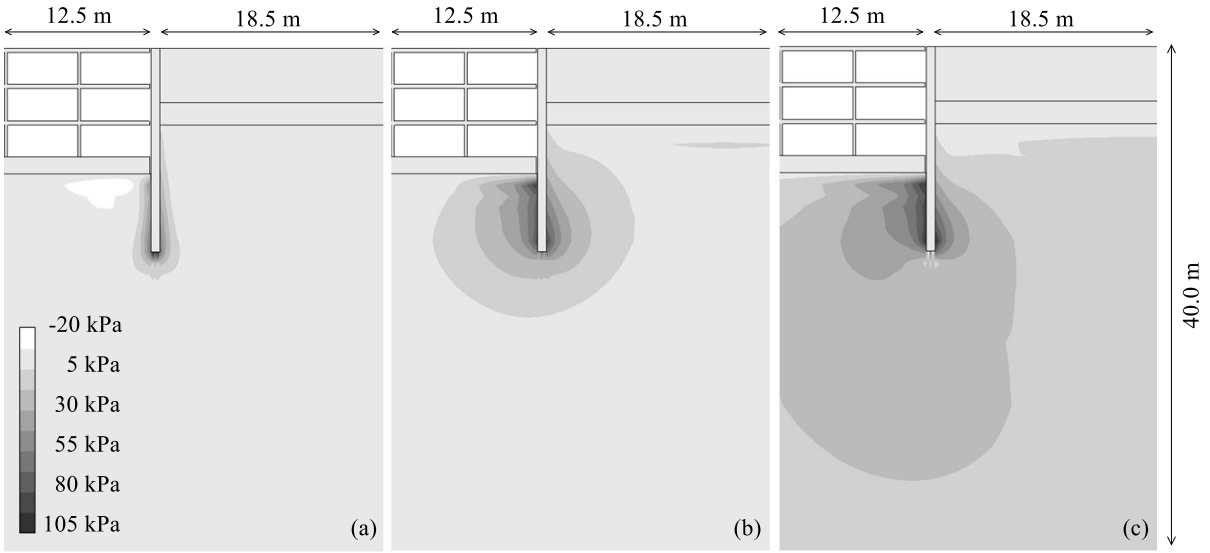

Figure 3-22: Contours of pore water pressures for uTM analysis (a) after 10 days, (b) after 6 months and (c) after 10 years

The time-dependent behaviour can be better observed in Figure 3-23, which depicts the evolution of changes in pore water pressure and temperature with time at specific locations. These are evaluated at mid-depth of the embedded part of the wall at a distance of 1.0 m and 3.0 m from the wall, on the retained and excavated sides (Figure 3-23 (a) and (b), respectively). Firstly, it can be seen that compressive changes in pore water pressures take place only once the heat front has reached the monitored location. This is because there is no time-dependent water flow, hence the hydraulically-induced excess pore water pressures are equal to zero. Furthermore, the pore water pressures steadily increase until no further change in temperature takes place. Indeed, it can be noted that, on the retained side (Figure 3-23 (a)), changes in pore water pressure stop occurring once the temperature has stabilised. On the other hand, within the excavated side, both temperatures and pore water pressures are still increasing at the end of the analysis (see previous section for comments on temperature distributions). The larger pore water pressures observed within the excavation side are due to the larger mechanical restriction applied to this side of the wall, both by the base slab and the lateral restriction provided by the axis of symmetry, which lead to an increase in total stress (similar to what was observed in the one-dimensional problems).

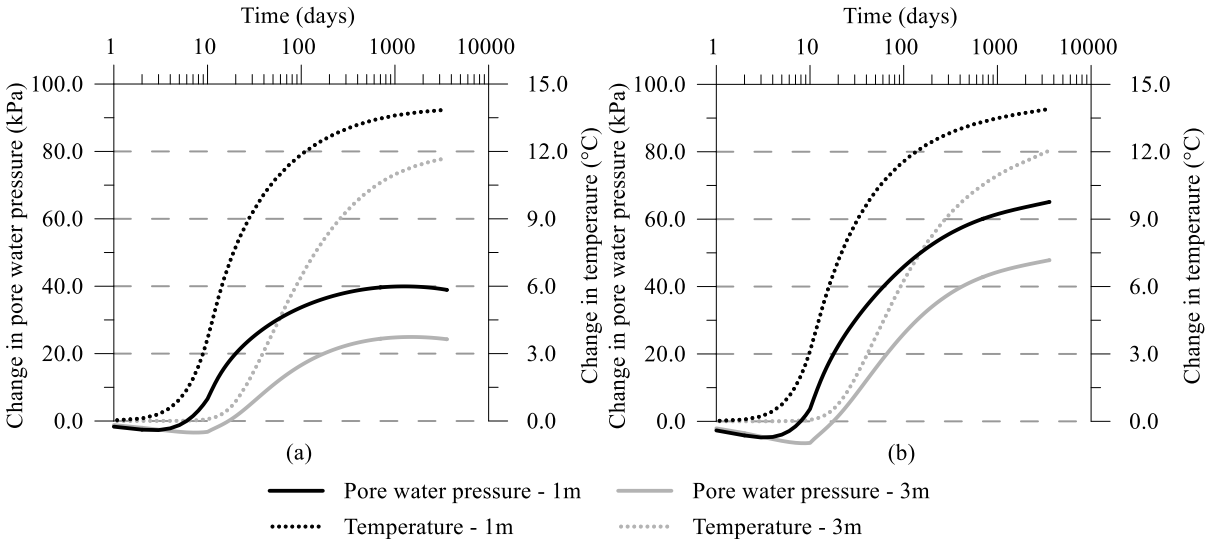

Figure 3-23: Change in pore water pressure and temperature with time for uTM analysis at 14.0m below ground level and different distances from the wall (a) within retained side and (b) within excavated side

In the THM analysis, all the components of the hydraulic equation are active, i.e. it simulates soil thermal expansion, differential expansion between water and soil upon heating and time-dependent water flow. At the end of the first heating phase, i.e. after 10 days (see Figure 3-24 (a)), compressive excess pore water pressures, with a maximum value of around 100.0 kPa, develop along the shaft and at the bottom of the wall. These are due to two main phenomena: (1) the thermal coefficient of expansion of water is greater than that of soil, with an increase in temperature inducing generation of compressive pore water pressure (term (ii) in Equation (3-8)); (2) additional mechanically-induced pore water pressures (term (iii) in Equation (3-8)) are generated due to the expansion of the wall compressing the soil beneath it. With time, as excess pore water pressures dissipate close to the wall, further compressive excess pore water pressures develop within the consolidating materials at greater distances from the heat source. As can be noted in Figure 3-24 (c), after 10 years, the pore water pressures still increase in regions further away from the structure where greatest changes in temperature take place (see Figure 3-18 for temperature contours). Concurrently, as a consequence of dissipation, the maximum value along the back of the wall has reduced to around 30.0 kPa after 10 years.

Comparing to the other two analyses, it can be noticed that:

- the magnitude of the generated pore water pressures in the HM analysis is considerably smaller than that observed in the THM analysis. In the former, maximum tensile pore water pressures of -20.0 kPa develop along the shaft and maximum compressive pore water pressures of around 20.0 kPa are registered beneath the toe of the wall (thus, approximately 80% less than in the THM analysis). Considering that the wall expansion is similar in the two analyses, this suggests that the thermally-induced pore water pressures – i.e. due to α_w being larger than α_s in term (ii) of Equation (3-8) – are approximately 80.0 kPa.

- in the short term, the changes in pore water pressure in the uTM analysis are smaller compared to the THM analysis, with a maximum along the shaft of around 60.0 kPa close to the toe of the wall (a reduction of 40%), because, as shown earlier (see Section 3.4), a large part of the excess pore water pressures results from the differential thermal expansion of fluid and soil particles, which is neglected in this analysis. Only in the long term the analysis reaches comparable maximum values to those experienced in the THM analysis, however the time-dependent behaviour is very different.

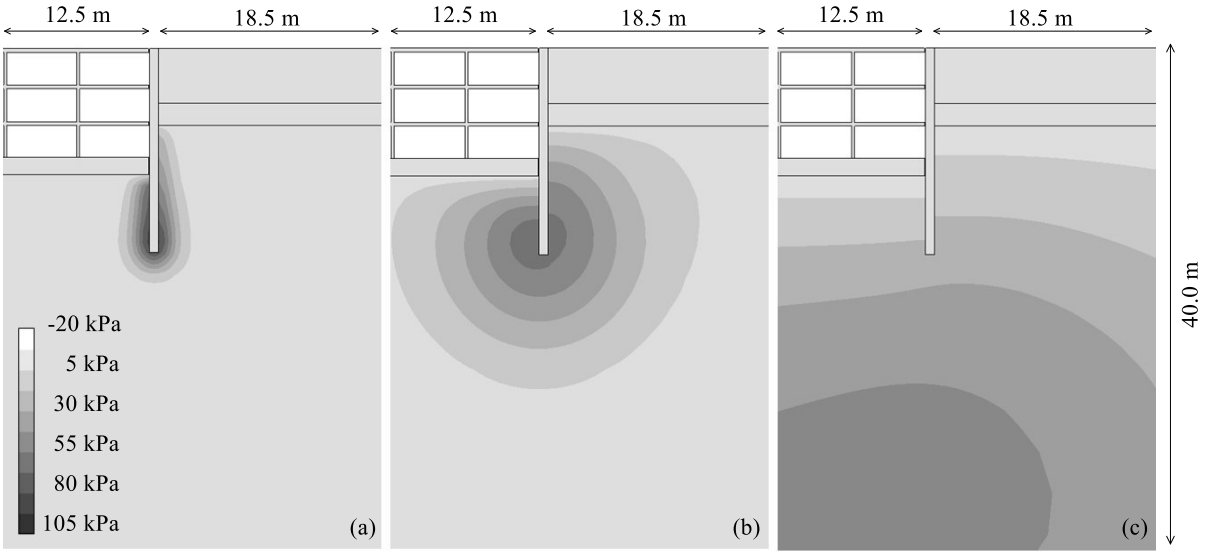

Figure 3-24: Contours of pore water pressures for THM analysis (a) after 10 days, (b) after 6 months and (c) after 10 years

To establish a comparison with the observed mechanisms of excess pore water pressure generation identified for the 1D problems analysed in Section 3.4, the distributions of both changes in temperatures (ΔT) and pore water pressures (Δu) for the THM analysis are shown for the retained and excavated sides of the wall in Figure 3-25 (a) and (b), respectively. These are evaluated along a horizontal line at mid-depth of the embedded part of the wall for different time instants, i.e. after 10 days, 6 months and 10 years from the start of heating. The three mechanisms of excess pore water pressure generation identified in Section 3.4 can be clearly observed in this complex boundary value problem and are marked in Figure 3-25 as: (i) due to water flow, (ii) induced by a temperature change and (iii) as a consequence of a mechanical restriction (the latter being more evident in the excavated side due to the closer proximity to the boundary). Naturally, closer to the heat source, pore water pressures are highest and driven mostly by temperature changes, as these are highest in this area of the problem. Moreover, the presence of additional drainage boundaries means that excess pore water pressures around the heat source dissipate faster in the wall problem than in the simplified one-dimensional problems considered in Section 3.4. At larger distances from the structure, Δu develop in areas where temperature changes have not yet taken place (i.e. ΔT = 0°C, marked in the figure as "i"), as was observed when analysing Problem A. It is also particularly interesting to note the similarity between the distributions of pore water pressures in the long term (10 years) beneath the excavated area and those computed in Problem

B (labelled as "iii" in Figure 3-25 (b)): the building up of a uniform profile of excess pore water pressures is due to the mechanical restriction imposed at the axis of symmetry. However, in the case of the retaining wall, when compared to the one-dimensional problem, the pore water pressures tend to accumulate later in time and to be of lower magnitude due to the availability of other drainage paths and the less effective mechanical restriction provided by the deforming soil mass above and below.

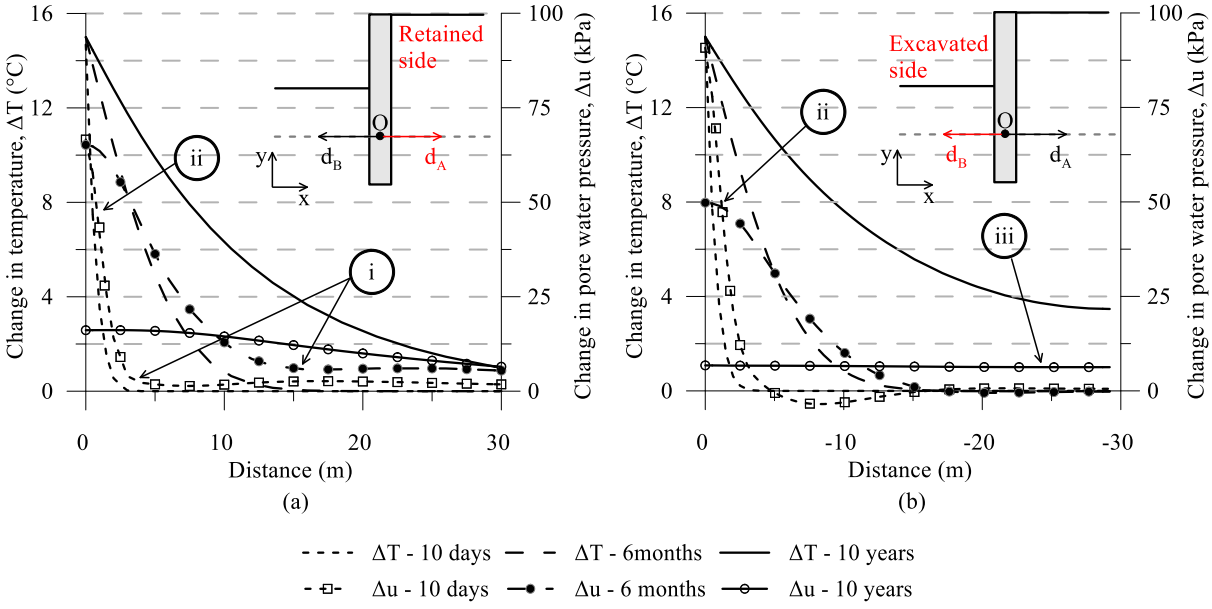

Figure 3-25: Distribution of change in temperature (ΔT) and change in pore water pressure (Δu) for THM analysis for different time instants on (a) the retained side and (b) the excavated side

These aspects can be further identified when observing Figure 3-26, which shows the development with time of changes in pore water pressures and temperatures at mid-depth of the embedded part at a distance of 1.0 m and 3.0 m from the wall, on the retained and excavated sides, depicted respectively in Figure 3-26 (a) and (b). It is shown that excess pore water pressures develop ahead of changes in temperature, with these being more pronounced for the point further away from the heat source, due to the larger amount of water flowing from the regions with higher pore water pressures due to higher temperatures. Furthermore, as previously observed for the uTM case, within the excavated side (Figure 3-26 (b)), larger excess pore water pressures develop in the short term due to the additional mechanical restriction in this area. Conversely, a lower magnitude is observed in the long term, which is attributed to the shorter drainage path in this area, where water can flow across the boundary beneath the base slab leading to a faster rate of dissipation of pore water pressures. Indeed, it can be noted that the reduction of excess pore water pressures starts at an earlier time instant when compared to the retained side.

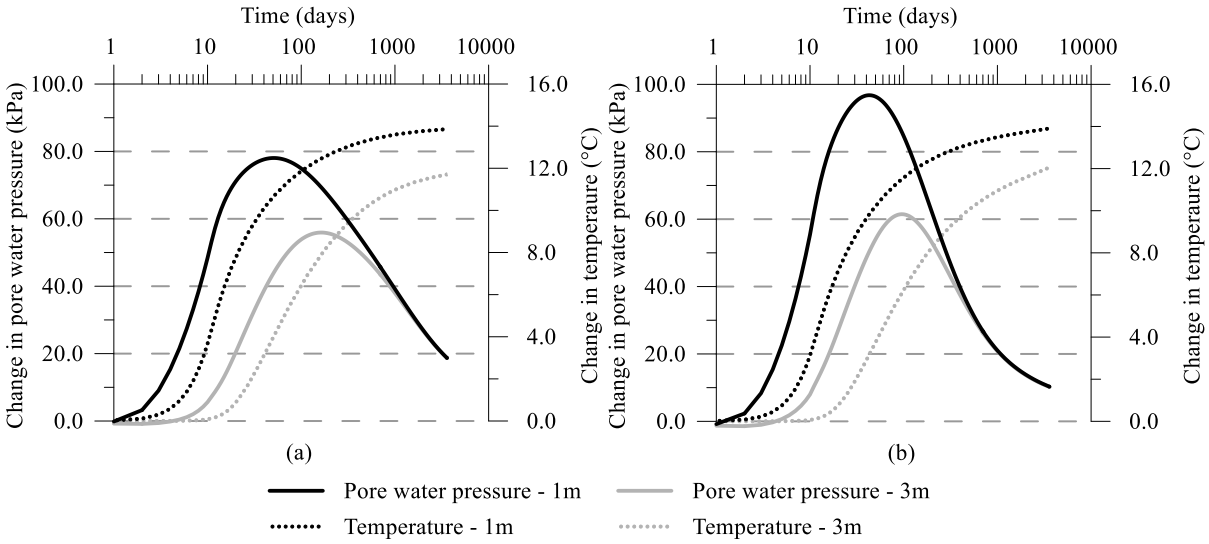

Figure 3-26: Change in pore water pressure and temperature with time for THM analysis at 14.0m below ground level and different distances from wall (a) within retained side and (b) within excavated side

3.5.2.3 Volumetric strains

Figure 3-27 and Figure 3-28 depict, respectively, the mechanical and total volumetric strains after 10 days, 6 months and 10 years from the start of heating for the HM analysis. Since no heat transfer is simulated through the soil, the mechanical volumetric strains and the total volumetric strains in the soil are the same (i.e. ε_{th} is equal to zero). The only difference between the mechanical and total volumetric strains is the one observed within the wall. Indeed, the total volumetric strain of the wall is tensile, indicating it is thermally expanding, whereas the mechanical strain is very small. Within the soil, the volumetric strains are compressive beneath the toe due to the thermal expansion of the wall compressing the soil. Along the shaft, the expansion of the wall induces tensile strains, as full friction is simulated along the soil-structure interface. Furthermore, within the consolidating materials, an increase in tensile volumetric strains is observed in the medium to long term, which indicates soil swelling as a consequence of the dissipation of the tensile excess pore water pressures, leading to a reduction in mean effective stress.

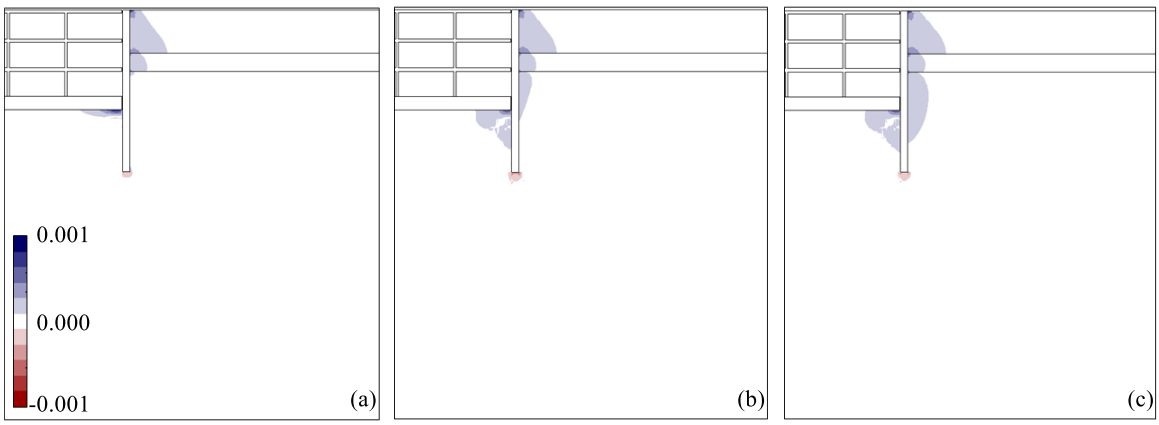

Figure 3-27: HM analysis – mechanical volumetric strains (a) after 10 days, (b) after 6 months and (c) after 10 years

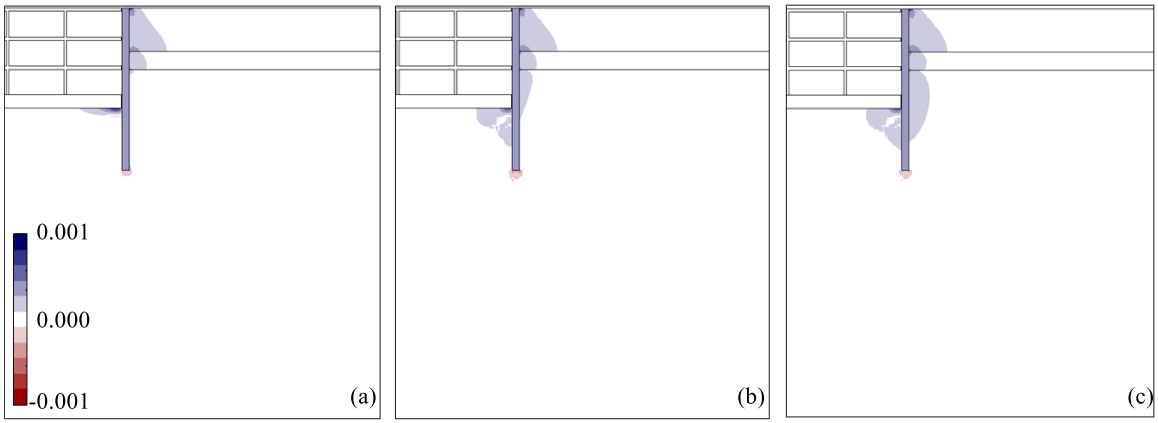

Figure 3-28: HM analysis – total volumetric strains (a) after 10 days, (b) after 6 months and (c) after 10 years

The mechanical and total volumetric strains after 10 days, 6 months and 10 years from the start of heating for the dTM analysis are shown in Figure 3-29 and Figure 3-30, respectively. In this analysis, no generation of excess pore water pressures is simulated, hence the change in mechanical volumetric strains are due to stress changes associated with the thermal expansion of both the wall and the soil. Since this is impeded in the out-of-plane direction, it leads to a mechanical compression of the soil, which increases with time as the temperature within the soil increases and propagates further away from the wall, as can be seen from Figure 3-29. Furthermore, a larger compression is observed within the excavated side. As noted earlier, this is attributed to the larger mechanical restriction provided by the base slab in the vertical direction and the restricted movement in the horizontal direction at the axis of symmetry. Conversely, the total volumetric strain is expansive due to the thermal expansion of the soil upon heating and considerably lower than the thermal volumetric strain (i.e. $3\alpha_s\Delta T$ – for 15°C, this would be equal to approximately 8.0×10^{-4}) due to the development of the compressive mechanical volumetric strains.

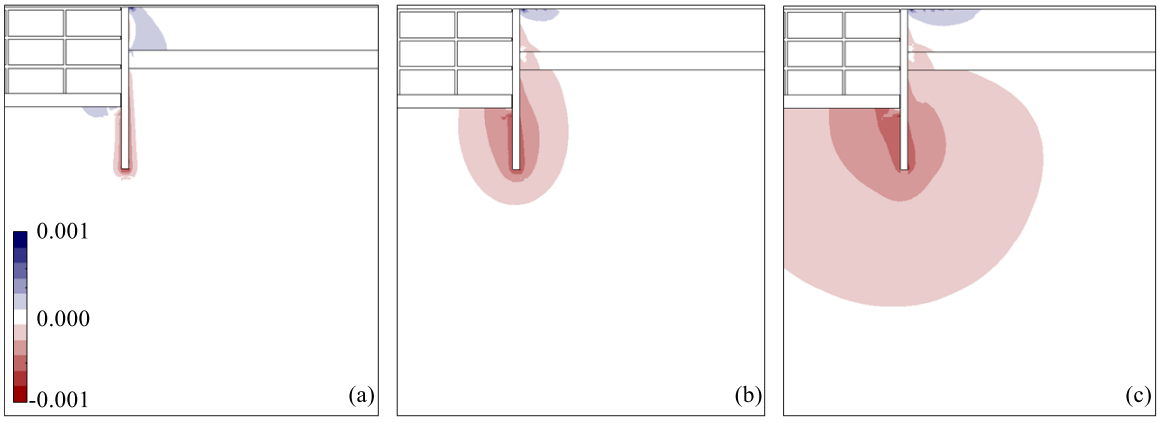

Figure 3-29: dTM analysis – mechanical volumetric strains (a) after 10 days, (b) after 6 months and (c) after 10 years

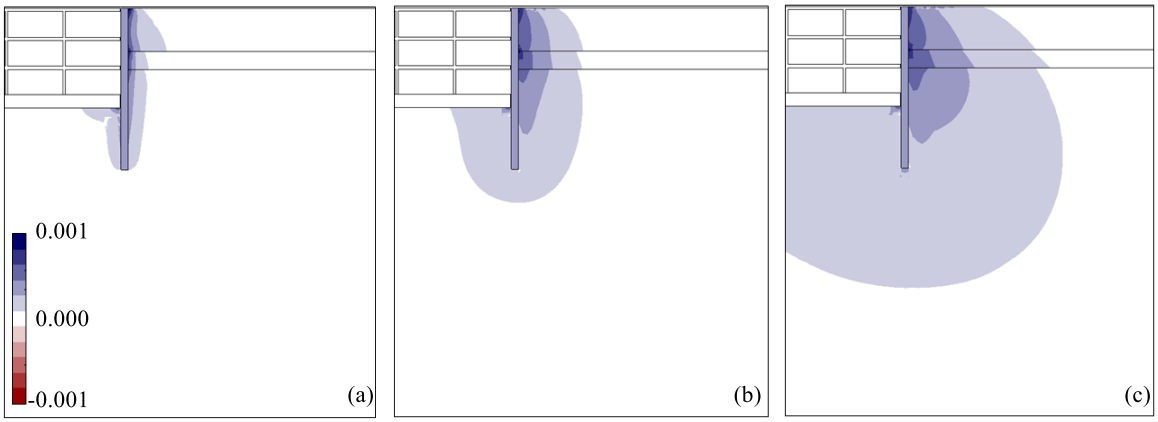

Figure 3-30: dTM analysis – total volumetric strains (a) after 10 days, (b) after 6 months and (c) after 10 years

The mechanical and total volumetric strains computed in the uTM analysis are displayed in Figure 3-31 and Figure 3-32, respectively. As can be noted from Figure 3-31, the mechanical volumetric strains within the clayey materials are very small and not visible at the represented scale, since these are treated as undrained and thus are characterised by a high bulk stiffness. As a consequence, the total volumetric strain is essentially equal to the thermal strain. Indeed, the absence of the compressive mechanical volumetric strains means that the total strain occurring in the uTM analysis is much larger compared to that observed in the dTM analysis, following the contours of temperature changes (see Figure 3-18), as this strain is merely induced by the temperature change in the soil (i.e. $3\alpha_s\Delta T$).

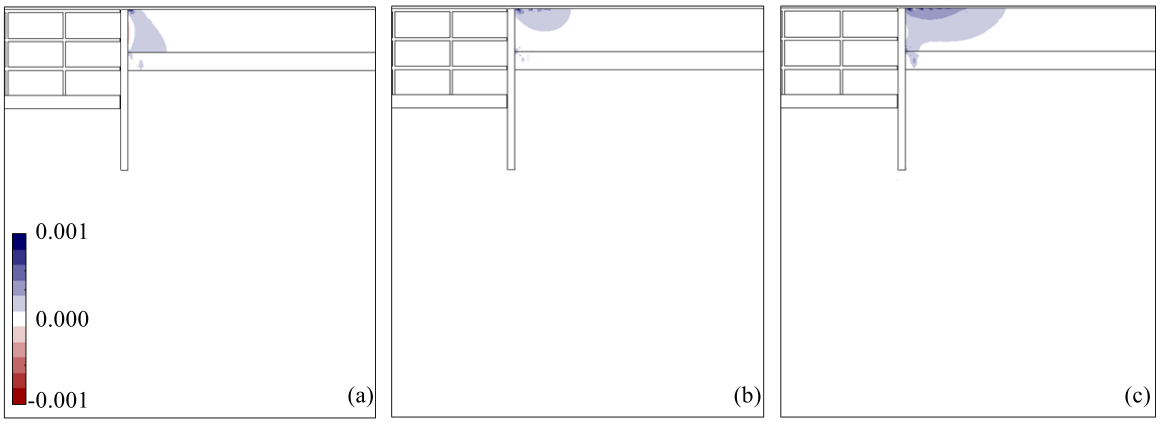

Figure 3-31: uTM analysis – mechanical volumetric strains (a) after 10 days, (b) after 6 months and (c) after 10 years

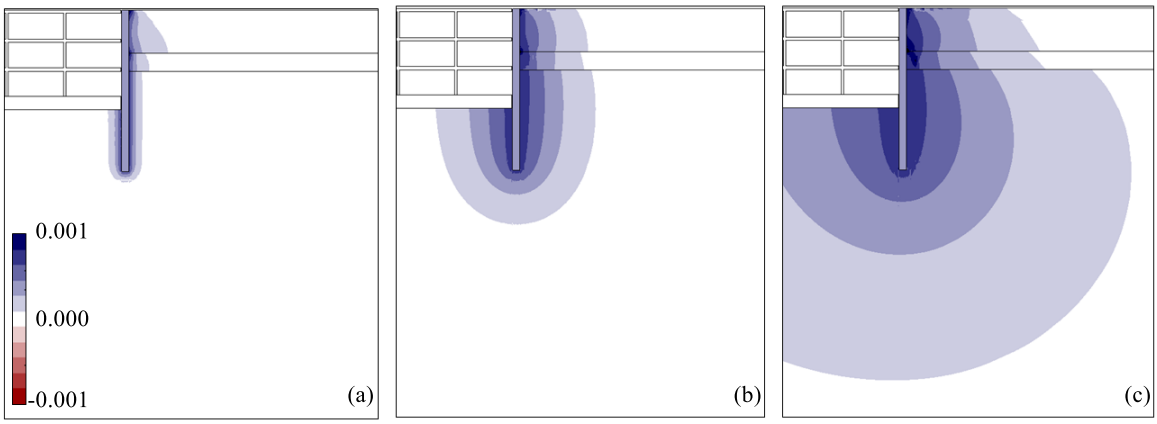

Figure 3-32: uTM analysis – total volumetric strains (a) after 10 days, (b) after 6 months and (c) after 10 years

From Figure 3-33 and Figure 3-34 it is clear that the THM analysis displays a more complex behaviour when compared to the other analyses. Indeed, mechanical volumetric strains are induced by the mechanical expansion of the wall and by changes in stress occurring as a consequence of the generation and dissipation of excess pore water pressures. At the beginning of the thermal phase, the mechanical volumetric strains around the wall are tensile, indicating the soil is swelling. This is due to the generation of compressive excess pore water pressures, which leads to a reduction in mean effective stress. As time progresses and the heat front propagates, soil swelling occurs at larger distances from the wall, where compressive changes in pore water pressures take place. Concurrently, close to the wall, the generated pore water pressures dissipate, which leads to the development of compressive mechanical volumetric strains as the soil starts contracting. The total volumetric strains in the short term, depicted in Figure 3-34 (a), are tensile and larger than those developing in the uTM analysis due to the aforementioned contribution of effective stress changes induced by the generation of compressive excess pore water pressures. Conversely, in the long term (see Figure 3-34 (c)), the total strains close to the wall are compressive, indicating that the mechanical strains arising from the dissipation of excess pore water pressures are larger than those generated by thermal expansion.

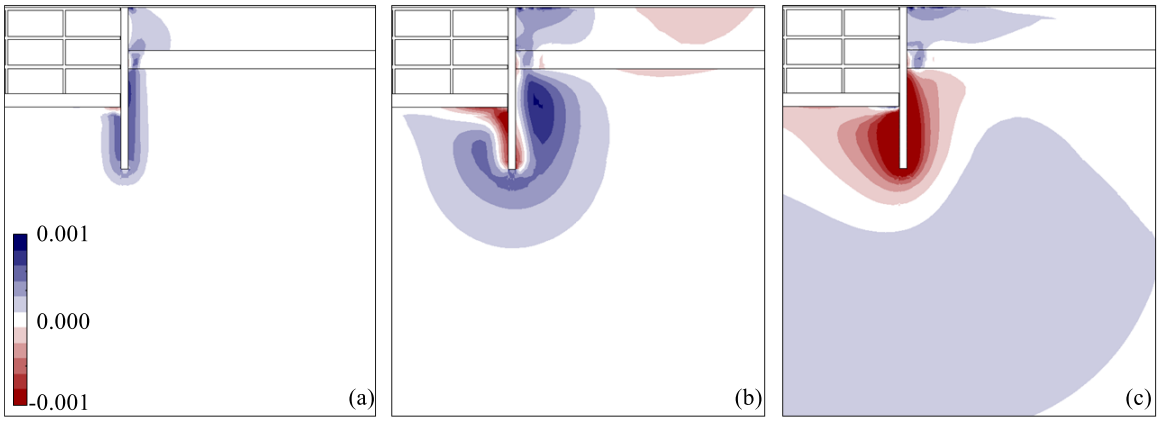

Figure 3-33: THM analysis – mechanical volumetric strains (a) after 10 days, (b) after 6 months and (c) after 10 years

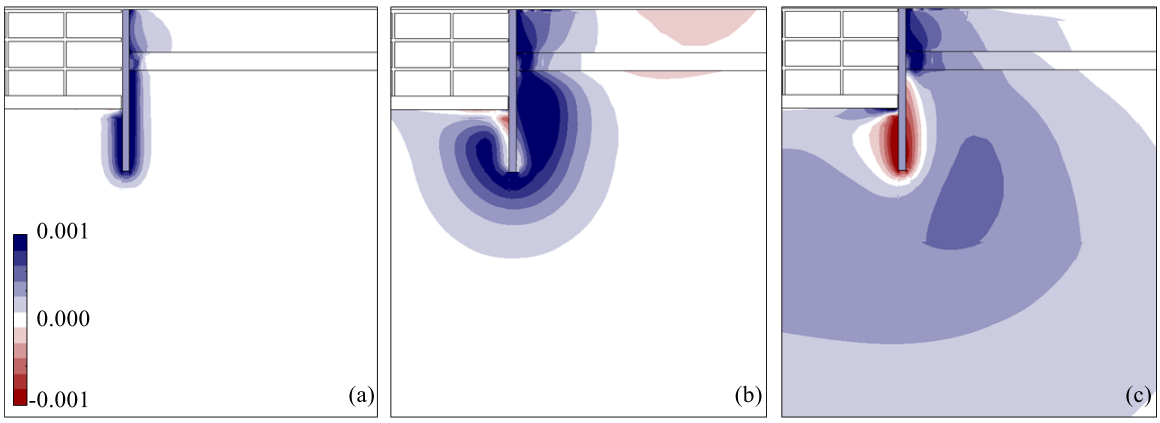

Figure 3-34: THM analysis – total volumetric strains (a) after 10 days, (b) after 6 months and (c) after 10 years

3.5.2.4 Structural forces and horizonal wall movements

Axial force

Figure 3-35 shows the changes in axial forces along the depth of the wall for different time instants for all the four analyses. It is evident that the largest changes in axial force take place within the embedded part of the wall, as this is where the structure is more restricted by the soil. In fact, the upper part of the wall experiences a minimal increase in axial force and it is very similar for all the analyses. Moreover, as can be noted in Figure 3-35 (a), the increase in temperature induces mechanical compression within the wall in the short term (i.e. after 10 days of heating): the structure expands due to heating, however the soil restricts part of this deformation, leading to the development of compressive axial forces. The largest change in axial force at the end of initial heating is recorded in the HM analysis, whereas much lower axial forces are registered during the THM analysis. This difference in the short-term predictions are due to a complex combination of effects:

- the smallest change in axial force (maximum of -37.0 kN/m) is calculated in the THM analysis because, as the soil heats up and expands, it reduces the restriction it applies to the wall (this does not occur in the HM analysis). Furthermore, the generation of compressive excess pore water pressures leads to soil swelling (see mechanical volumetric strains - Figure 3-33 (a)), hence inducing further tension within the wall (as outlined in Table 3-9, thermally-induced pore water pressures do not exist in the HM, uTM and dTM analyses);
- the higher axial forces predicted in the HM analysis (maximum of -206.0 kN/m) are due to the larger restriction the soil applies as it is not thermally active and hence does not expand with temperature;
- in the dTM analysis, no pore water pressures are generated but the soil thermally expands, releasing part of the restriction of the soil, explaining the lower axial force when compared to that of the HM analysis (maximum of -126.0 kN/m). It is interesting to note that the difference between this analysis and the THM is merely given by the absence of pore water pressure generation in the former. Therefore, the fact that the average force along the embedded part is 98.0 kN/m larger in

the dTM analysis provides an insight into the substantial contribution of soil swelling due to pore water pressure generation to the releasing of the restriction applied to the wall. On the other hand, the difference between the HM and dTM analysis indicates the effect of soil expansion on the axial force, since pore water pressure generation in the former, as stated above, is limited. Within the embedded section, the predicted axial force in the dTM analysis is, on average, 62.0 kN/m lower with respect to the one registered in the HM analysis, hence suggesting that thermal volumetric changes of the soil have a more limited effect on the development of axial forces when compared to that of pore water pressures.

- the calculated axial forces of the uTM analysis are similar to the dTM. Although the total strains are larger for this analysis (see Figure 3-32) – which would indicate a less effective restriction provided by the soil – given the undrained nature of the problem, a stiffer soil response is simulated in the short term.

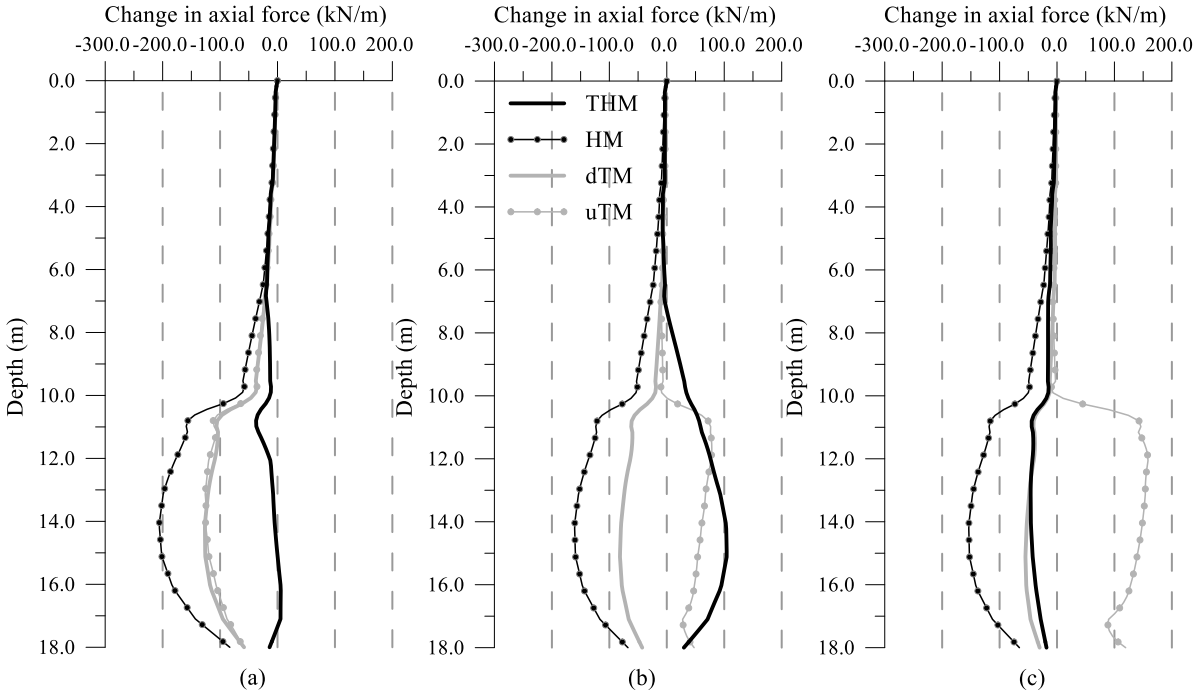

Figure 3-35: Change in axial force with depth for all analyses (a) after 10 days, (b) after 6months and (c) after 10 years

After the imposed temperature change of 15°C is reached, it can be noticed from Figure 3-35 (b) and (c), as well as from Figure 3-36 (which shows the development of the axial force with time at a depth 14.0 m below ground level where, on average, the greatest changes in axial force take place), that the analyses display a different behaviour in the medium to long term. In the THM analysis, a non-linear transient long-term behaviour can be observed. On the other hand, the remaining analyses display a significantly less non-linear behaviour with time. Indeed, for all analyses except the THM, the compressive axial force merely reduces with time as a consequence of volumetric deformation due to either changes in pore water pressures (HM) or soil thermal expansion (dTM) or a combination of the two (uTM). For the HM analysis, the dissipation of tensile excess pore water pressures results in soil

swelling (see Figure 3-27 and Figure 3-28), reducing the compression in the wall. Indeed, no further changes in axial force are recorded once the excess pore water pressures have dissipated. Conversely, the reduction of the compressive axial force with time in the dTM analysis is due to the soil's thermal expansion which reduces the imposed restriction. The undrained behaviour simulated in the uTM analysis leads to a larger overall expansion (see Figure 3-32), hence the wall is subjected to larger tensile forces, which, at the end of the analysis, are four times larger than those calculated in the THM analysis.

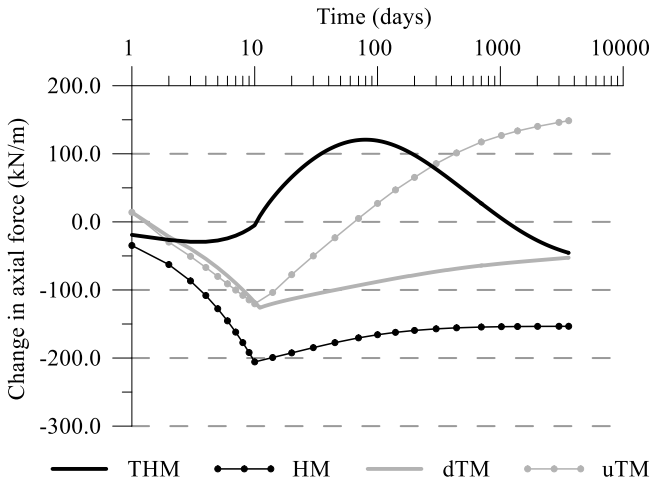

Figure 3-36: Change in axial force with time at depth of 14.0 m bgl for all analyses

The non-linear transient long-term behaviour observed in the THM analysis is induced by different THM interactions prevailing over different time instants, as shown in more detail in Figure 3-37. Initially, when the wall is heated and consequently expands, the axial forces are compressive and increase as further changes in temperature are applied (zone marked as "SR" – **S**oil **R**estriction – in Figure 3-37). With time, as more heat is transferred to the soil, it thermally expands, reducing its restriction to the expansion of the wall. Indeed, during this second period (zone "TE" – **T**hermal **E**xpansion), the structure is subjected to tensile loading, which reduces the compressive axial force generated initially and eventually leads to the development of tensile forces within the structure. Subsequently, a third period can be identified, where the soil exerts compressive forces on the structure, reducing the tensile axial force and producing a final value which is compressive and slightly larger than the one generated during the first phase (SR). This compression, highlighted in Figure 3-37 as zone "DC" (**D**issipation and subsequent **C**onsolidation), is caused by the dissipation of the compressive excess pore water pressures close to the structure, which induces soil settlement and thus compression of the wall, as can be clearly observed also in Figure 3-33 and Figure 3-34.

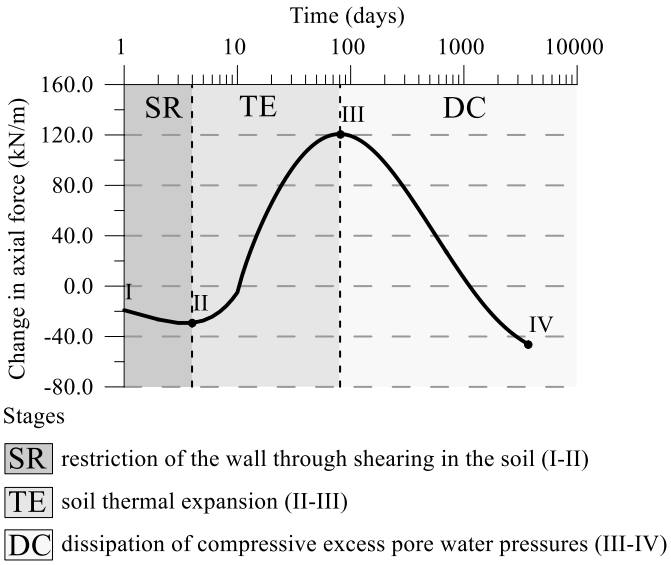

Figure 3-37: Change in axial force with time at depth of 14.0 m bgl for THM analysis

Bending moment and horizontal wall movements

Figure 3-38 depicts the thermally-induced bending moments with depth, which are directly related to the horizontal wall movements shown in Figure 3-39. These are due to volumetric changes in the soil induced by changes in temperature and pore water pressures. Therefore, the low bending moments and horizontal movements observed in the HM analysis are perhaps unsurprising since the soil does not thermally expand and the generated pore water pressures are low. It can be noted that in the short term (i.e. Figure 3-38 (a) and Figure 3-39 (a)), the bending moments and horizontal displacements are largest for the THM analysis, because the largest changes in pore water pressures and volumetric strains are generated in this simulation (refer to Section 3.5.2.2 and 3.5.2.3, respectively). The maximum change in bending moment, of 51.0 kNm/m, takes place at the position of the base slab.

For the analyses simulating heat transfer through the soil, the largest horizontal displacement takes place at the toe of the wall, which moves towards the retained side, indicating a larger volumetric expansion within the excavated side. This is due to larger temperatures developing in this region in the long term (see Figure 3-19). It should be noted that the changes in horizontal wall movements are generally small and of an order of magnitude less than those experienced during the excavation and construction of the basement (see Figure 3-5).

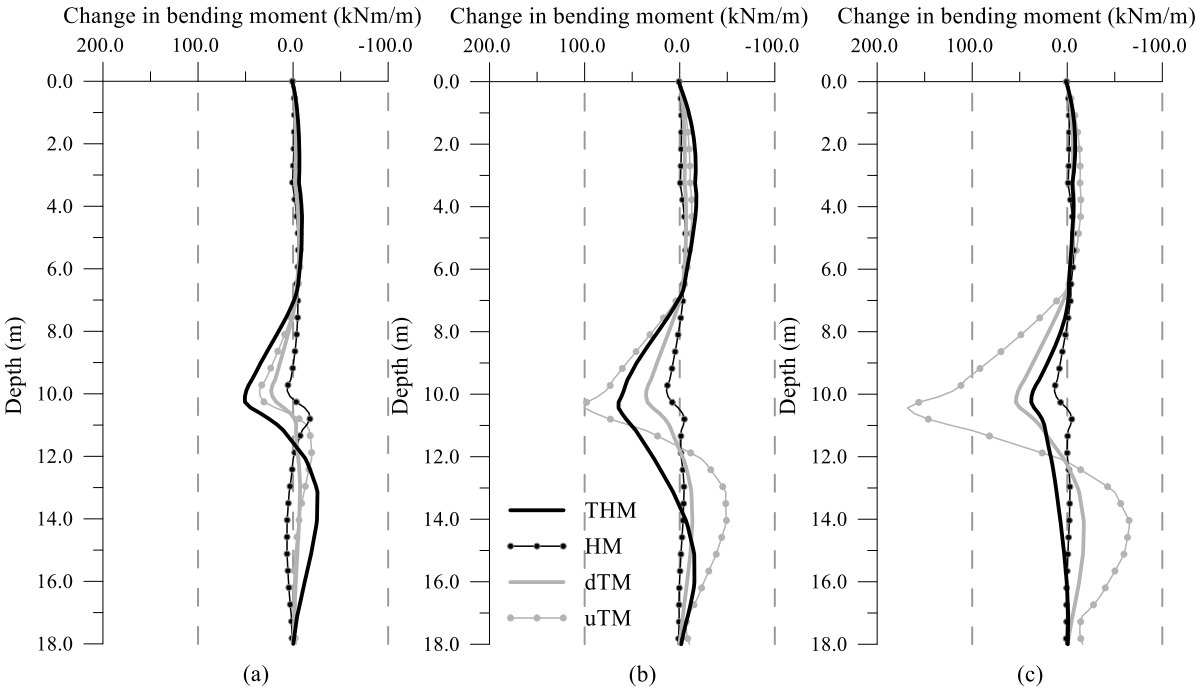

Figure 3-38: Change in bending moment with depth for all analyses (a) after 10 days, (b) after 6months and (c) after 10 years

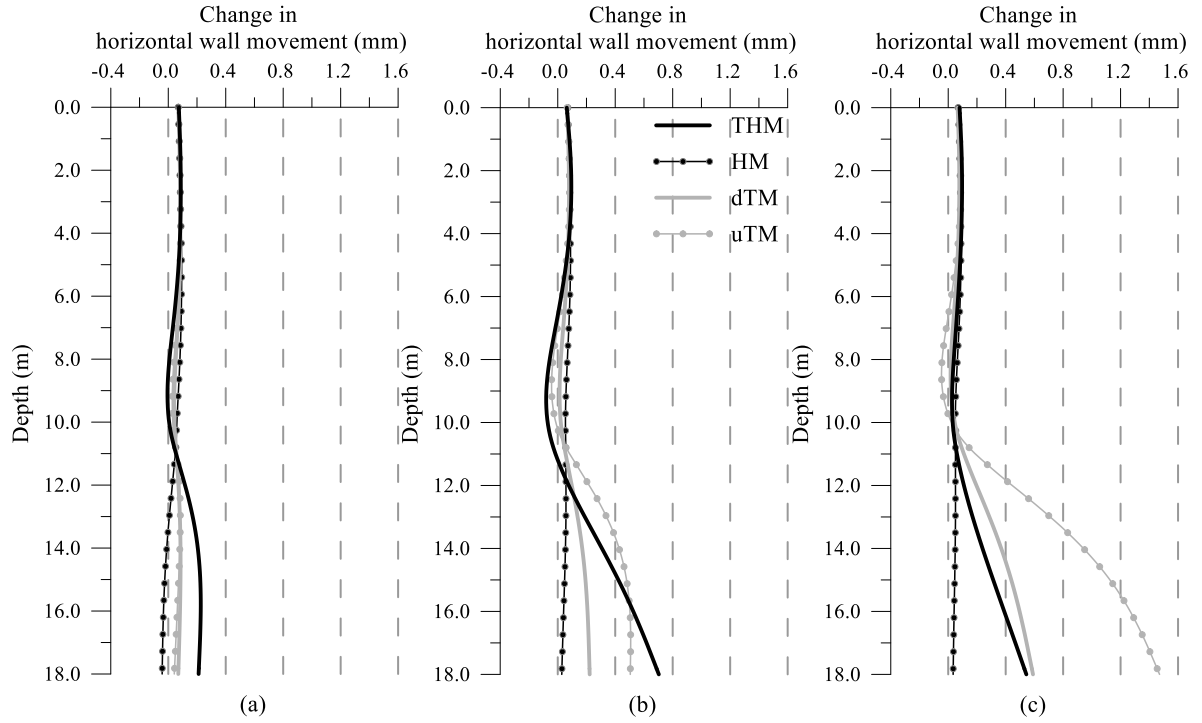

Figure 3-39: Change in horizontal wall movements with depth for all analyses (a) after 10 days, (b) after 6months and (c) after 10 years

The evolution with time of the bending moment at the level of the base slab (where the largest positive bending moment is calculated) for the different analyses is displayed in Figure 3-40. Similar to the development with time of axial forces, the THM analysis displays a non-linear behaviour, whereas, for all other analyses, the change in bending moment is rather linear. The results can generally be explained

by the mechanisms outlined previously regarding axial forces. Namely, the increase in bending moment for the dTM and uTM analyses is due to thermal soil expansion. As can be observed from the horizontal displaced shape in Figure 3-39, the wall movements increase with time and are larger in the uTM analysis, due to smaller mechanical volumetric strains (Figure 3-31), which imply that larger overall movements take place. Indeed, in the long term, the largest bending moments are calculated for the uTM analysis: after 10 years, a maximum positive bending moment of 168.0 kNm/m is computed, which is in excess of four times the one predicted in the THM analysis. Conversely, in the HM analysis, the bending moment initially reduces as a consequence of the dissipation of the tensile pore water pressure which leads to a wall movement towards the retained side; in the long term, no changes are observed due to hydraulic equilibrium being reached at an early stage during the analysis.

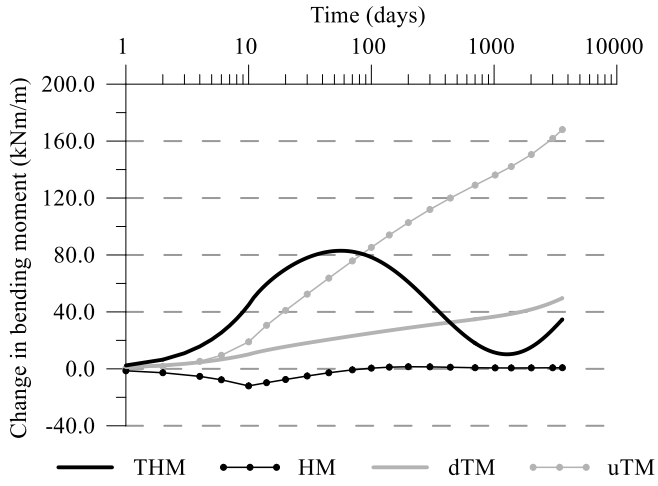

Figure 3-40: Change in bending moment with time at depth of 10.5 m bgl for all analyses

Regarding the THM analysis, the evolution of the bending moment with time can be divided into three different periods, within which different mechanisms can be identified as the predominant cause for changes in the bending moment (Figure 3-41). The propagation of heat within the soil mass leads to soil expansion, which will occur both in the vertical and horizontal directions. As previously seen, the soil mass expands more within the excavated side, and, as a consequence, the bottom of the wall moves towards the retained soil. Therefore, in the time interval where soil thermal expansion dominates the problem (zone "TE" in Figure 3-41), the bending moment increases. As the compressive excess pore water pressures dissipate and the soil consequently contracts, the wall moves back towards its initial position (this can be more clearly observed in Figure 3-42) and the bending moment decreases, which is marked as zone "DC". There is a subsequent increase in bending moment which is due to further horizontal soil movements towards the retained soil. This movement, taking place in zone "BC" (effect of mechanical **B**oundary **C**ondition), is caused by the interaction of the thermal expansion of the soil with the lateral boundary, i.e. the axis of symmetry, where the imposed boundary conditions restrict horizontal movements, hence impeding further expansion in that direction. As seen previously for the pore water pressure mechanism "iii" (i.e. mechanically induced pore water pressures), the effects of

this mechanical restriction are experienced only once the heat front has reached the boundary. This is confirmed when observing Figure 3-42, which shows the change in temperature occurring at the axis of symmetry and the horizontal wall movements with time at mid-depth of the embedded part of the wall. Indeed, soon after the temperature front reaches the axis of symmetry, the toe of the wall is pushed towards the retained side: as the temperatures are still increasing in the excavated side (refer to Figure 3-19), the soil mass thermally expands towards the retained side, because further soil movement towards the axis of symmetry is impeded by the restriction it applies. Since the presence of this boundary condition affects only the horizontal response of the embedded part of the retaining wall, it is perhaps unsurprising to see it influencing only the bending moment and not the axial force. Consequently, it can be concluded that, for a thermo-active retaining wall, the magnitude of bending moments, as well as horizontal wall movements and pore water pressures within the excavated side, will be highly influenced by the width of the excavation.

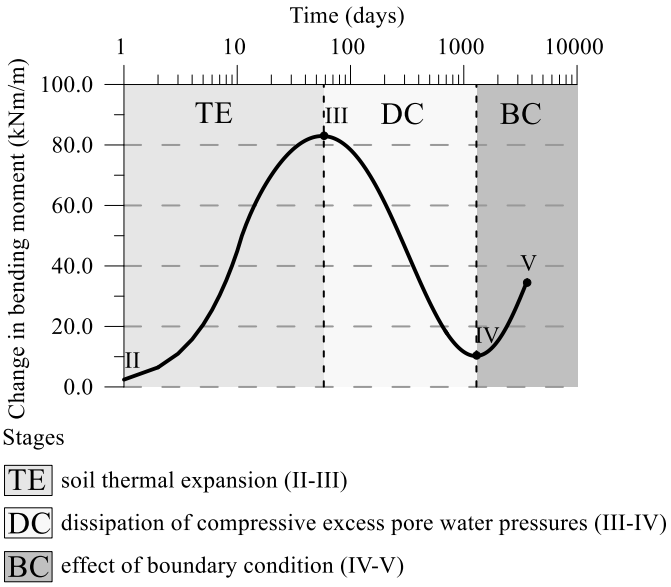

Figure 3-41: Change in bending moment with time at depth of 10.5 m bgl for THM analysis

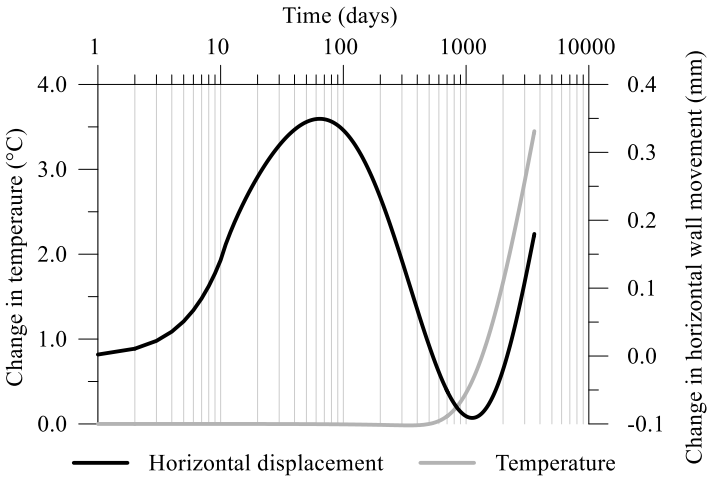

Figure 3-42: Change in temperature at axis of symmetry with time and change in horizontal wall movement at 14.0 m bgl with time

Total axial force and bending moment

The effect of thermally-induced forces on the overall performance of the wall was analysed by comparing the total axial force and total bending moment computed during the THM analysis at different time instants after the beginning of heating to the ones registered before changes of temperature are applied (i.e. after excavation, building loading and pore water pressure dissipation), labelled in Figure 3-43 as "initial". Figure 3-43 also displays the envelope of maximum forces computed during the analysis. On average, along the embedded part of the wall, variations in axial force range from a reduction of about 25% to an increase of about 10% with respect to the axial forces computed at the start of the thermal analysis, depending on the considered time instant. These changes fall generally within the envelope of maximum forces, where only the axial force in the long term exceeds the ones registered during construction. Similarly, increases in bending moments are limited to a maximum of 7% computed after 6 months of heating with respect to the bending moment registered at the beginning of the thermal analysis. This is lower than the maximum bending moment calculated during the construction stages. Although these changes do not appear to be very significant, it should be noted that the magnitude of the thermally-induced structural forces will be highly dependent on the connection to the internal structures and the restraint imposed at the top of the wall. Furthermore, different modelling techniques for modelling heat exchange, as well as boundary conditions along the exposed face of the wall, will influence the development of the structural forces within the wall. Lastly, it should also be noted that the use of thermo-active base slabs, which may be installed in conjunction with a thermo-active retaining wall, will induce further forces into the wall. Some of these aspects are further investigated in subsequent chapters of this thesis.

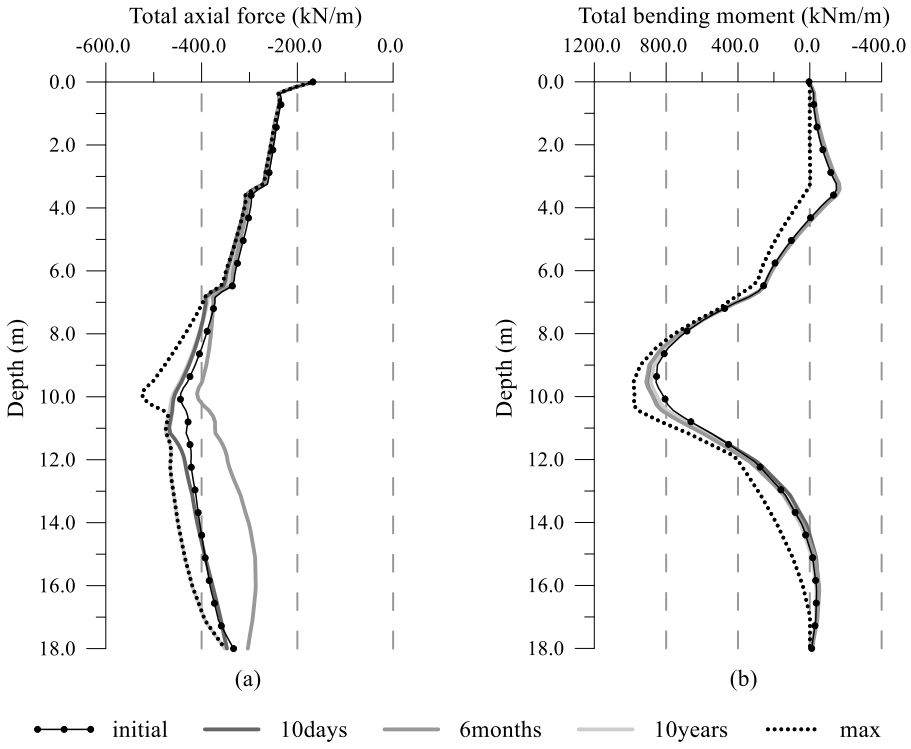

Figure 3-43: Effect of temperature changes on total forces for THM analysis (a) axial force with depth and (b) bending moment with depth

3.5.2.5 Vertical wall displacement

Vertical displaced shapes of the wall for all analyses and different time instants are shown in Figure 3-44, while Figure 3-45 depicts the vertical movements of the top of the wall with time.

The initial temperature change of 15°C induces an elongation ΔL of the wall in all the analyses. The free expansion of the wall, ΔL_{free}, can be determined using:

$$\Delta L_{free} = \varepsilon_{free-wall} \cdot L_{wall} \tag{3-34}$$

where $\varepsilon_{free-wall}$ is the free axial strain of the wall (which is obtained from Equation (3-33)) and L_{wall} is the total length of the wall (18.0 m).

The free elongation of the analysed wall (i.e. when the effect of the restriction applied by the soil is not considered) calculated through Equation (3-34) is equal to 2.984 mm. Although the lines in Figure 3-44 (a) appear to be parallel, there is a slight difference in their gradient, meaning that the value ΔL is different for the various analyses. In the THM analysis, this value is in fact highest and very close to ΔL_{free}, explaining the calculated small increase in axial force. As can be expected, since the axial forces are highest for the HM analysis, the corresponding value of ΔL is the smallest among the four considered analyses.

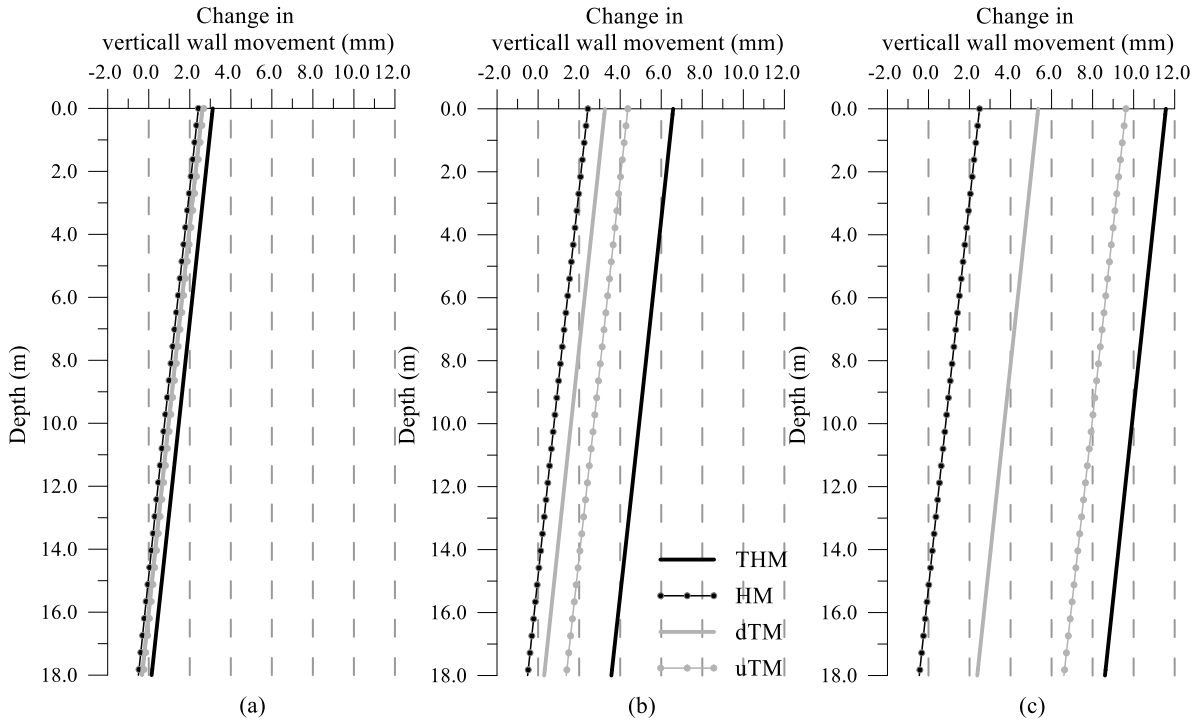

Figure 3-44: Change in vertical wall movement for all analyses (a) after 10 days, (b) after 6months and (c) after 10 years

At the end of initial heating, i.e. after 10 days, the displacement of the top of the wall is different for the analysed cases (see Figure 3-45), because the wall moves not only due to its thermal expansion but also as a consequence of soil deformation due to changes in temperature and pore water pressures. With time, in the analyses where heat transfer in the soil is simulated, the wall keeps moving upwards due to the ongoing thermal soil expansion. However, the wall itself is subjected to limited elongation, as can be concluded from the gradients of the displaced shapes not changing between Figure 3-44 (b) and (c). Moreover, it is interesting to note that larger movements are observed in the uTM analysis with respect to the dTM analysis, an effect attributed to larger volumetric stiffness in the former analysis which prevents the mechanical compression occurring in the dTM analysis and hence leads to larger total volumetric strains (see Figure 3-30 and Figure 3-32, respectively for dTM and uTM analyses). In the HM analysis, as clearly shown in Figure 3-45, no changes are observed after the initial heating phase due to the almost absence of time dependent phenomena (no thermal expansion and very limited pore water pressure dissipation, see Figure 3-20). The largest vertical movement of the top of the wall is observed for the THM analysis, reaching a value of 11.6 mm after 10 years.

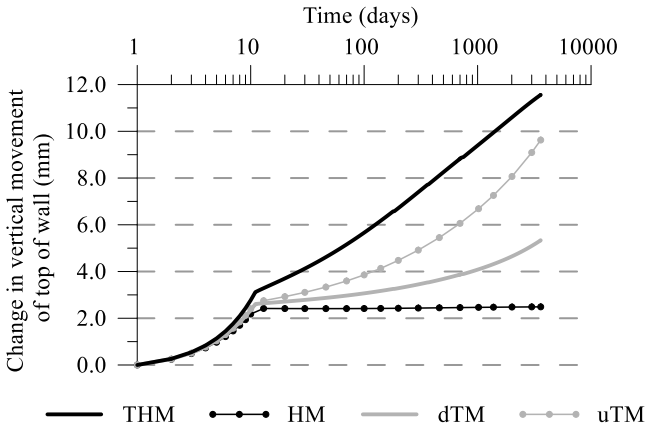

Figure 3-45: Change in vertical wall movement of top of wall with time for all analyses

3.5.2.6 Vertical and horizontal ground movements

The vertical movements of the ground surface behind the wall after 10 days and 10 years from beginning of heating are shown in Figure 3-46 (a) and (b), respectively. The conclusions are similar to those outlined for the vertical wall displacements, with a maximum value of 11.6 mm being calculated close to the wall for the THM analysis after 10 years. Furthermore, in this analysis, the ground surface displacements extend to a significant distance behind the wall (e.g. a value of 5.0 mm is obtained at a distance of approximately 25.0 m from the wall), suggesting a substantial area of influence of the analysed thermo-active structure.

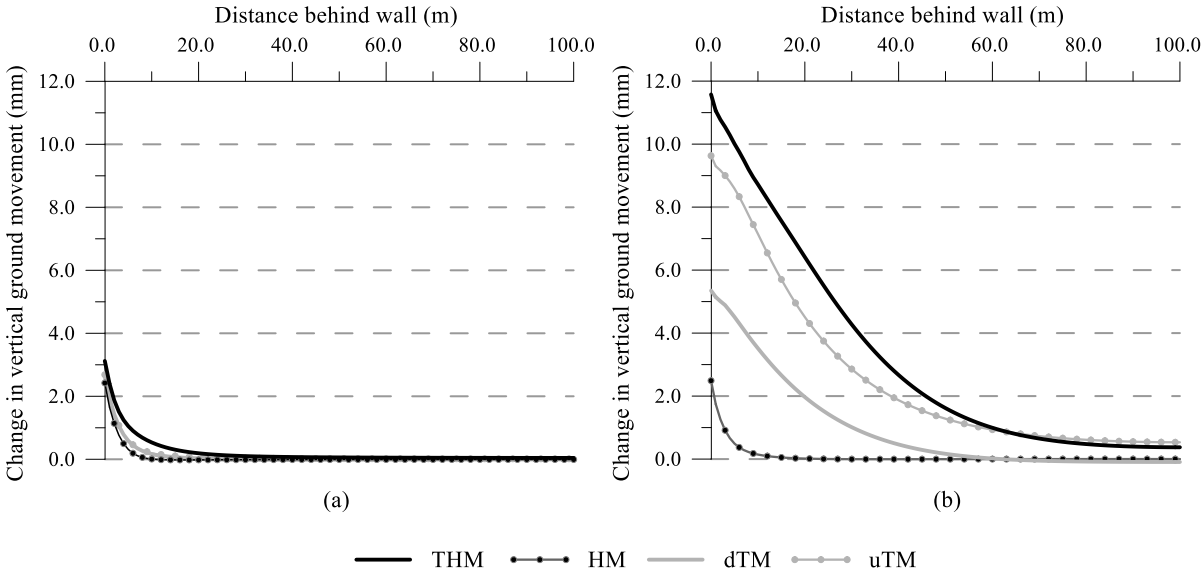

Figure 3-46: Change in vertical surface ground movements with distance behind wall for all analyses (a) after 10 days and (b) after 10 years

The horizontal movements of the ground within the retained side at mid-depth of the embedded part of the wall after 10 days and 10 years from beginning of heating are depicted in Figure 3-47 (a) and (b), respectively. The horizontal ground movements are largest for the THM analysis, both in the short and in the long term. As the soil thermally expands, it moves towards the retained side, as can be concluded

from the ground movements being positive in all the analyses simulating heat transfer within the soil after 10 days from heating. While for the dTM and uTM this trend is still valid after 10 years, the THM analysis displays horizontal ground movements towards the excavated side at short distances from the wall. This is attributed to the soil contraction due to the dissipation of excess pore water pressures close to the wall, while the larger movements further away from the wall are due to soil swelling as a combination of thermal expansion and generation of compressive pore water pressures due to changes in temperature. The maximum horizontal movement recorded in the THM analysis is 3.5 mm, approximately 25.0 m behind the wall, indicating that, as was shown for structural movements, vertical displacements are significantly larger than the horizontal ones.

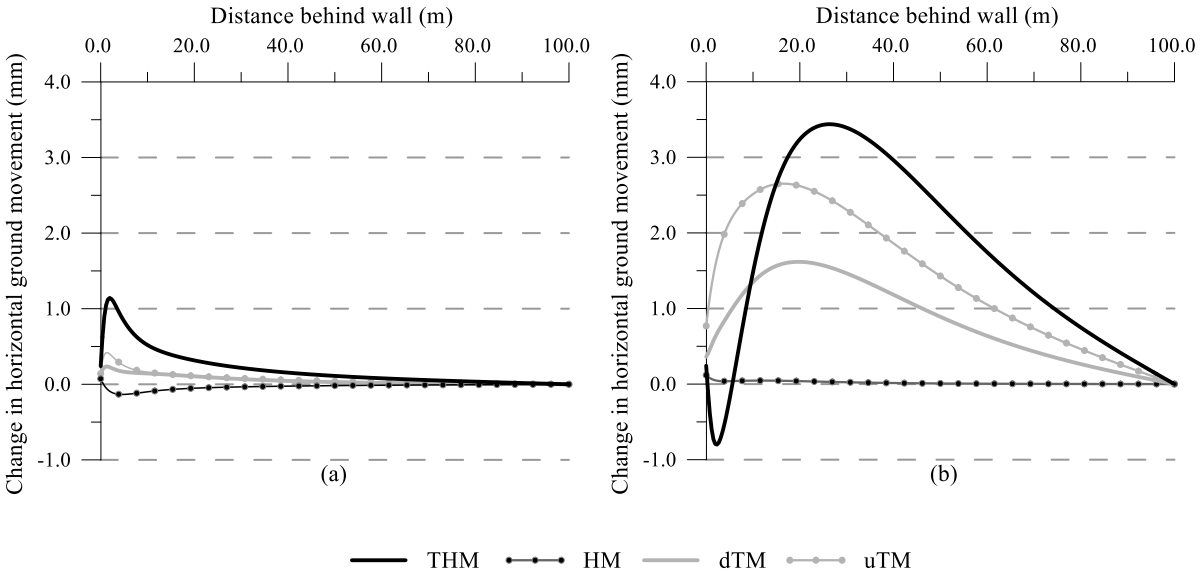

Figure 3-47: Change in horizontal ground movements within retained side at 14.0m bgl with distance behind wall for all analyses (a) after 10 days and (b) after 10 years

Important ground movements were recorded in the THM analysis both in the vertical and horizontal direction. While in a real application such a magnitude may not be measured, as it is a consequence of the application of a constant temperature for a long period of time, these results highlight that for structures involving heat exchange with the ground, wall and ground movements should be carefully assessed in order to verify their serviceability and possible interactions with any neighbouring structures that might be affected (see Sailer et al. (2019a) for a study on such aspect).

3.5.3 Influence of ground properties on thermo-active retaining wall behaviour

In Section 3.4.3.2 it was shown that, in a simplified one-dimensional problem, the parameter α_{TH} (i.e. the ratio between the thermal and hydraulic diffusivity – see Equation (3-29)) controls the development of the excess pore water pressures and hence the development with time of the THM interactions. Therefore, this section investigates the effect of varying this parameter on the response of the same thermo-active retaining wall problem described in the previous section by performing fully coupled THM analyses. To obtain comparable results to those outlined in Problem A included in Section 3.4.3.2

(i.e. the one-dimensional problem simulating the conditions within the retained side of a thermo-active wall problem), the boundary conditions at the right-hand side far field boundary have been changed to impose no change in temperature and in pore water pressure with respect to the initial conditions. This had no effect on changes in temperature and pore water pressures computed in the previously described problem. However, for problems presenting a different hydraulic diffusivity, the pore water pressures are affected by the hydraulic boundary conditions at the far field. Furthermore, since large water flow velocities can occur when employing a large hydraulic diffusivity, the coupled thermo-hydraulic boundary condition (described in Section 2.3.2, with its full details provided in Cui et al. (2016a)) was applied along the drainage boundaries to avoid a build-up of temperatures at the locations where the water leaves the system.

Since the wall is embedded within different materials with different properties and the permeability of the consolidating materials was modelled as being stress-dependent (see Equation (3-7)), a unique value of α_{TH} for the entire model cannot be established. Furthermore, the hydraulic diffusivity (Equation (3-27)) depends on a further non-constant parameter, i.e. the bulk modulus of the soil K_s, which, according to the employed small strain stiffness model, varies with both stress level and volumetric strain (see Equations (3-1) to (3-6) for a summary of the constitutive relations used). Therefore, as an approximation, values at the start of the thermal analysis of permeability and mean effective stress at mid-depth of the embedded section of the wall and 1.0 m away from the wall on the retained side were chosen to determine α_{TH} for this problem (i.e. at 14.5 m depth, within the London Clay). Furthermore, the current value of the elastic bulk modulus, K_s, was approximated by its maximum value, K_{max}, given by the small strain stiffness model employed in the analysis, i.e. Equation (3-6), calculated using a value of p' of 255.0 kPa, corresponding to the same position as described above. Similarly, the thermal parameters employed in the calculation of α_T are those associated to London Clay. Based on the material properties listed in Table 3-5 and the methodology outlined above, values of α_H and α_T of 3.8×10^{-7} m^2/s and 9.8×10^{-7} m^2/s, respectively, were determined for the analysis presented in the previous section (denoted as "Base case" in Table 3-10). This leads to a ratio of α_{TH} of 2.6×10^{0}. To illustrate the impact of this parameter on the behaviour of the thermo-active retaining wall, two additional analyses were performed: one with a value of α_{TH} increased by two orders of magnitude (i.e. "high" in Table 3-10, $\alpha_{TH} = 2.6\times10^{2}$) and one where it is reduced by two orders of magnitude (i.e. "low" in Table 3-10, $\alpha_{TH} = 2.6\times10^{-2}$). As shown in Table 3-10, this was achieved by adjusting the parameters for the adopted permeability model. It should be noted that, as previously mentioned for the 1D problems, identical results would have been obtained using any other parameter combination that would have resulted in the same value of α_{TH}. This is confirmed by the analyses included in Appendix B.

Table 3-10: Parameters of parametric study for THM interactions in thermo-active retaining wall problem

Analysis	k_0 (m/s)	k_{emb} (m/s)	α_H (m²/s)	α_T (m²/s)	α_{TH} (-)
High	1.0×10^{-12}	5.5×10^{-13}	3.8×10^{-9}		2.6×10^{2}
Base case	1.0×10^{-10}	5.5×10^{-11}	3.8×10^{-7}	9.8×10^{-7}	2.6×10^{0}
Low	1.0×10^{-8}	5.5×10^{-9}	3.8×10^{-5}		2.6×10^{-2}

3.5.3.1 Pore water pressures

Figure 3-48 depicts the temperature and pore water pressure distributions within the retained side at mid-depth of the retaining wall for the three analyses at three different time instants. It can be clearly noted that the magnitudes and evolution of excess pore water pressure are influenced by the value of α_{TH}, to an extent similar to that observed in the simplified one-dimensional problem (Problem A, Section 3.4.3). In general, the results show that higher thermally-induced pore water pressures are predicted for higher values of α_{TH}.

Regarding the pore water pressures generated in the vicinity of the heat source, these increase with increasing α_{TH}, as seen for Problem A, since larger values of α_{TH} correspond to problems where the response is closer to being characterised as undrained. Moreover, in such cases, the dissipation with time of these pore water pressures is significantly slower. Conversely, for a low value of α_{TH}, the excess pore water pressures close to the wall are very low, as was observed in Problem A. It should be noted that, in the retaining wall problem, additional mechanical effects contribute to the generation of pore water pressures, such as the thermal expansion of the wall. Furthermore, the presence of additional free draining boundaries influences the rate of dissipation.

Similar to what was observed for Problem A, excess pore water pressures develop ahead of changes in temperature, as marked on Figure 3-48. These are quantified through the parameter ω calculated using Equation (3-32). At the beginning of the analysis (i.e. 10 days), a high value of ω (51%) is obtained for a low value of α_{TH}=2.6×10^{-2}, which rapidly decreases with time due to the high rate of dissipation; conversely, considerably lower values are obtained for higher values of α_{TH}. It should be noted that, as mentioned earlier, in the retaining wall problem, due to the presence of additional hydraulic boundary conditions, the dissipation process is accelerated. Furthermore, the mechanical restriction in the horizontal direction along the right-hand side far field boundary leads to mechanically induced pore water pressures similar to those observed in Problem B, hence the slight increase of pore water pressures towards the far field with time observed for the high value of α_{TH}.

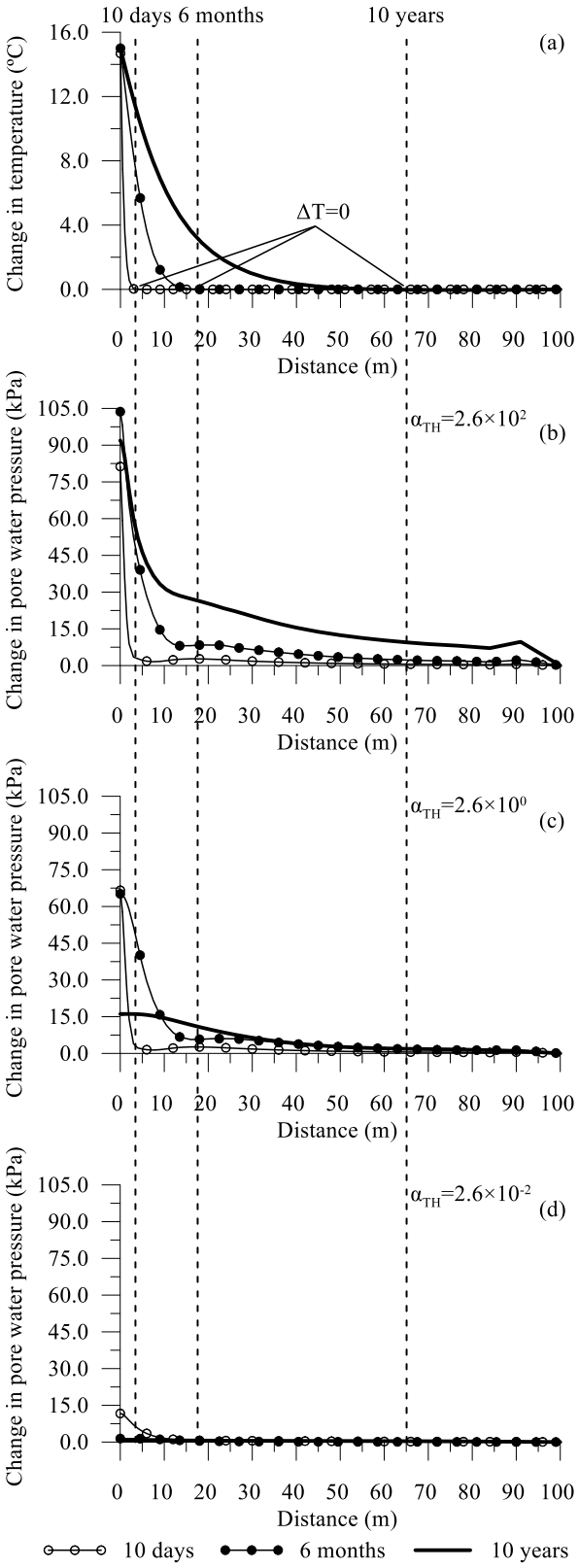

Figure 3-48: Distribution along a horizontal line at mid-depth of the wall for different time instants of (a) change in temperature, (b) change in pore water pressure for $\alpha_{TH} = 2.6\times10^{2}$, (c) change in pore water pressure for $\alpha_{TH} = 2.6\times10^{0}$and (d) change in pore water pressure for$\alpha_{TH} = 2.6\times10^{-2}$

3.5.3.2 Structural forces

Since varying the value of α_{TH} affects the time-dependent soil behaviour (as seen in the analysis of the one-dimensional problem), its effect on the response of the retaining wall is evaluated by analysing the changes in forces with time, shown in Figure 3-49. The development of axial forces and bending moments with depth at different time instants are depicted in Figure 3-50 and Figure 3-51.

Figure 3-49 (a) shows the influence of α_{TH} on the evolution with time of thermally-induced axial forces at a depth of 14.0 m and Figure 3-49 (b) depicts the variation of bending moments, evaluated at the level of the base slab (i.e. depth of 10.5m). It is confirmed that the transient behaviour of a thermo-active retaining wall is largely controlled by the generated excess pore water pressures during the heating stage and by the ability of the soil to dissipate them. In fact, both phenomena lead to mechanical volumetric changes within the soil mass, which affect the mechanical response of the structure.

In Figure 3-49 (a), the three previously identified stages characterising the development of axial force with time in a THM analysis are highlighted, i.e. the restriction through shearing ("SR" – I-II), thermal expansion ("TE" – II-III) and dissipation of compressive pore water pressures ("DC" – III-IV). The time periods over which each of these prevails depends directly on the value of α_{TH} – in some cases some of these stages may be even absent. The restriction through shearing along the soil-structure interface (I-II) is larger for a lower value of α_{TH} because a smaller compressive excess pore water pressures are generated. Consequently, the soil swells less, inducing a larger mechanical restriction to the structure, which leads to a larger initial compressive axial force. Interestingly, although larger excess pore water pressures are generated for a higher value of α_{TH} (which would suggest more swelling), the axial force during the first 10 days of heating is rather similar to the base case which is characterised by an intermediate value of α_{TH}. This suggests that the reduction of the restraint to the wall expansion resulting from soil swelling is compensated by its higher volumetric stiffness arising from behaving in a more undrained manner (i.e. its low permeability prevents additional changes in volume from taking place). In the long term, the axial force for the case of low α_{TH} is merely controlled by soil thermal expansion (II-III), hence a reduction in compressive axial force is observed. This is due to the fact that the low magnitudes of generated excess pore water pressures (see Figure 3-48 (d)), which also dissipate at a fast rate, do not contribute to further changes in volume of the soil with time. On the other hand, with a high value of α_{TH}, the period over which the change in axial force is governed by soil thermal expansion (II-III) is longer than in the base case because in the former excess pore water pressures dissipate at a slower pace and therefore the resulting changes in volume take place at a later time instant of the analysis.

The evolutions with time of the bending moment (see Figure 3-49 (b)) confirm some of the patterns identified based on the variations of axial force. In effect, for the low value of α_{TH}, the bending moment is seen to be mainly affected by soil thermal expansion (II-III), with the stage where the dissipation of

compressive pore water pressures dominates wall response (III-IV) being completely absent. The opposite is observed for the two other values of α_{TH}, where this stage appears to have a substantial impact (though it tends to be less important and to take place at a later time instant for larger values of α_{TH}). For all analysed cases, the final part of the evolutions with time of the bending moment of the wall seem to be fundamentally controlled by the effect of the mechanical restriction to thermal expansion imposed by the mechanical boundary condition at the axis of symmetry (IV-V), which had been previously identified in the context of the one dimensional problem idealising the conditions within the excavated side, i.e. Problem B, as well as described in detail in Section 3.5.2.4 when analysing the base case.

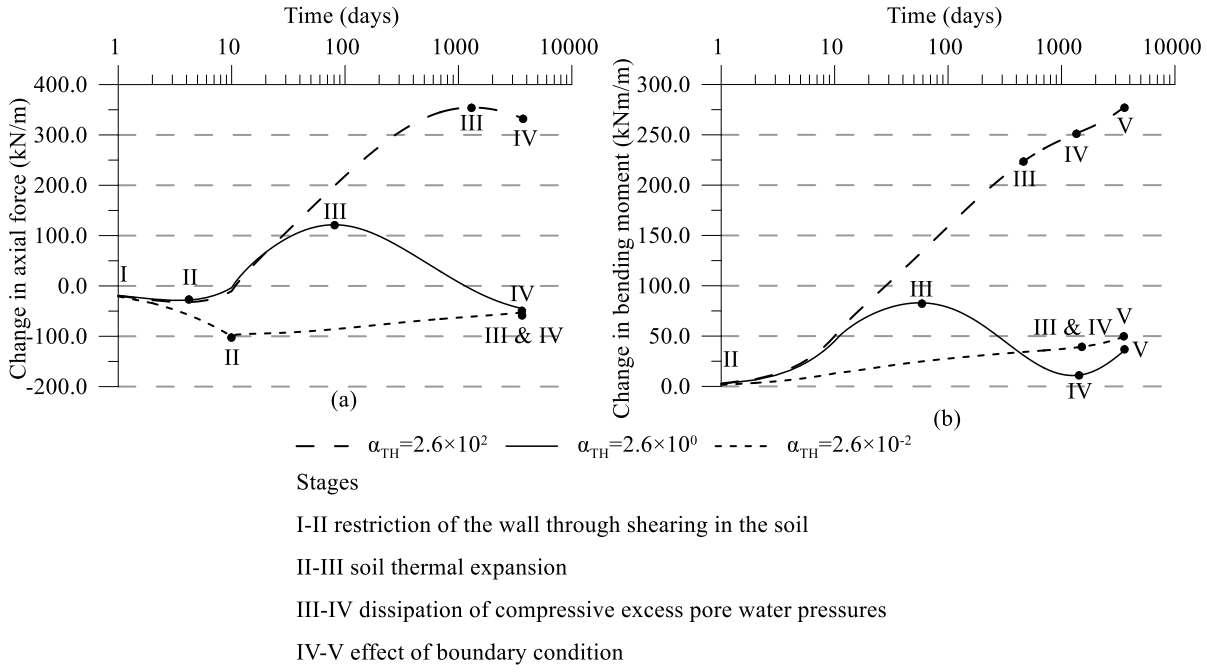

Figure 3-49: Influence of α_{TH} on change in (a) axial force at depth of 14.0 m bgl and (b) bending moment at depth of 10.5 m bgl

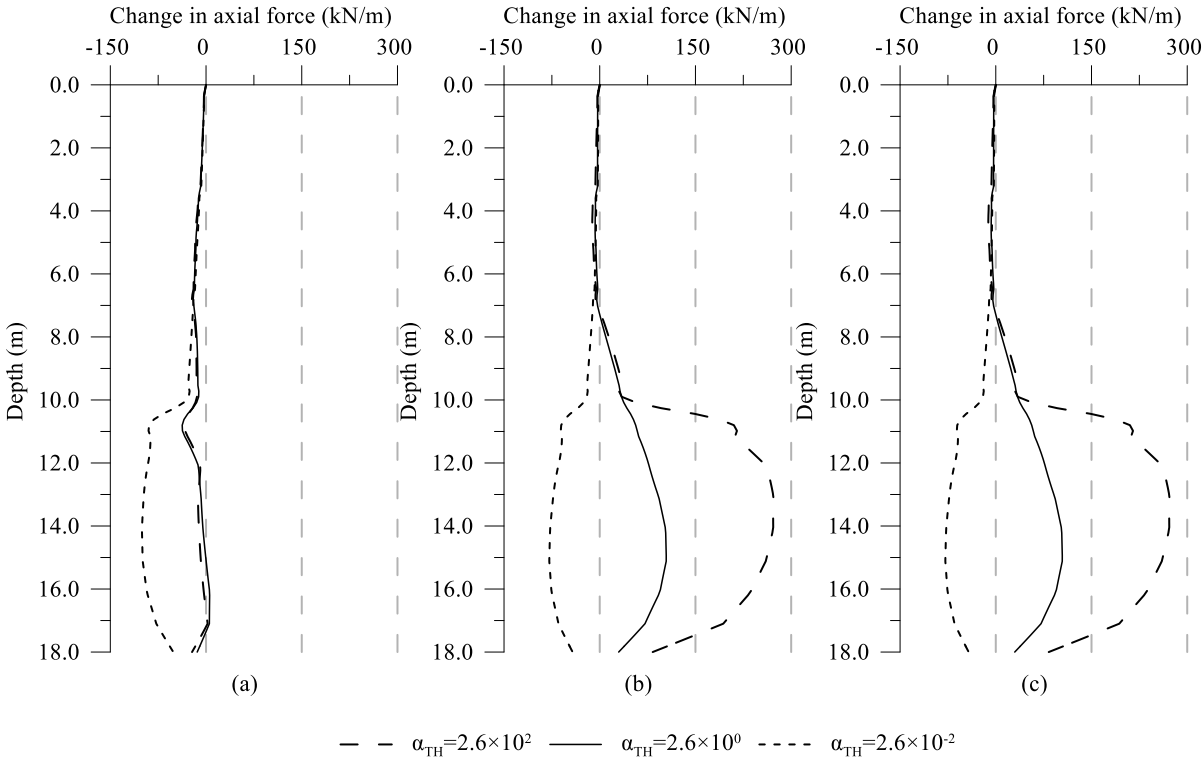

Figure 3-50: Influence of α_{TH} on change in axial force with depth (a) after 10 days, (b) after 6 months and (c) after 10 years

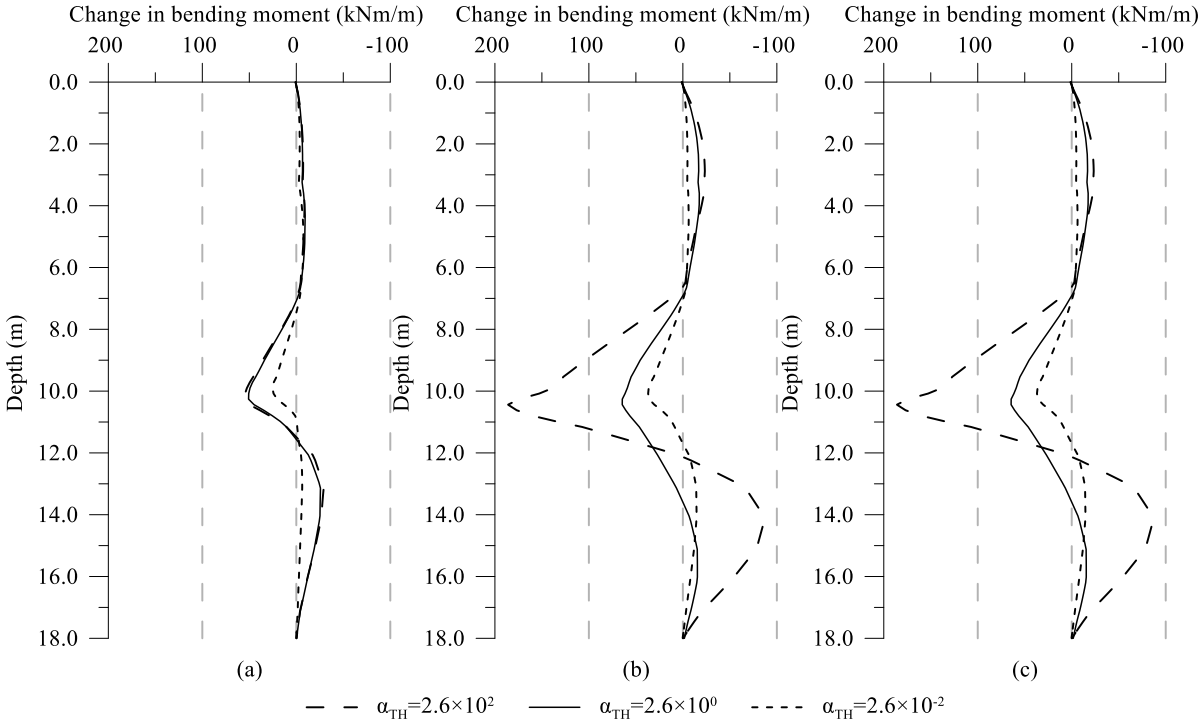

Figure 3-51: Influence of α_{TH} on change in bending moment with depth (a) after 10 days, (b) after 6 months and (c) after 10 years

3.5.3.3 Vertical wall displacement

The development of vertical displacements with time for different values of α_{TH} are displayed in Figure 3-52. As observed in Section 3.5.2.3, the generation and dissipation of excess pore water pressures considerably affects the volumetric behaviour of the soil mass. It is therefore unsurprising that, for the analysis with the higher value of α_{TH}, larger movements of the top of the wall are computed. Indeed, larger excess pore water pressures develop and a slower dissipation takes place for such ground conditions, leading to a maximum wall movement which is approximately twice the one registered in the base case. Conversely, smaller wall movements are computed for the low value of α_{TH}. A slightly different time-dependent behaviour is observed when this analysis is compared to the base case: for the low value of α_{TH}, after the change in temperature of 15°C is reached, the vertical displacement remains constant for a period of time and then it increases towards the end of the analysis. This is attributed to the fact that dissipation occurs at an early time instant, thus, in the short term, the thermal expansion is compensated by soil settlement due to the consolidation process and hence limited wall displacement occurs. With time, since excess pore water pressures have fully dissipated (see Figure 3-48 (d)), thermal expansion prevails and leads to an increase in the vertical movement.

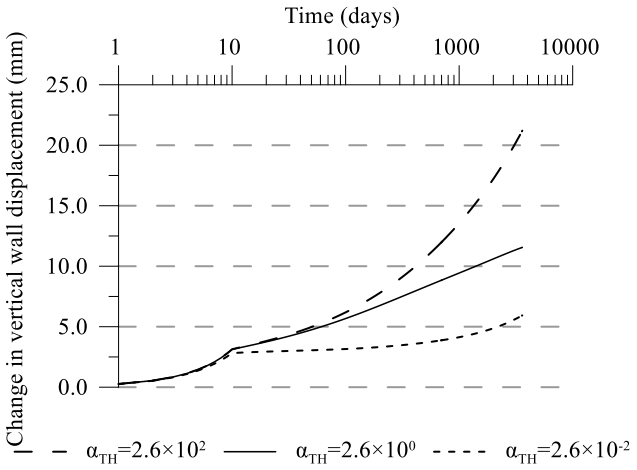

Figure 3-52: Influence of α_{TH} on change in vertical movement of top of wall with time

3.6 Summary and conclusions

The first part of this chapter presents the details of the numerical modelling of the excavation and construction stages of a deep basement in London described in Wood & Perrin (1984b) and Wood & Perrin (1984a). Given the lack of field data characterising the thermo-mechanical behaviour of thermo-active walls, this case study was employed to perform hypothetical thermal analyses to evaluate the response of the wall under non-isothermal conditions. The good agreement between the monitoring data presented in Wood & Perrin (1984b) and the computed results during excavation and construction provided confidence in the employed soil models, material properties and initial conditions.

The second part of this chapter includes a series of analyses to investigate the THM interactions occurring in the soil within fully coupled THM analyses. These were assessed by analysing simple, one-dimensional problems which aim to represent the conditions within the retained and excavated sides of a thermo-active wall problem, consisting therefore of different mechanical and hydraulic boundary conditions. Furthermore, to assist in the interpretation of the ongoing phenomena, analytical expressions for the calculation of excess pore water pressures in undrained conditions have been developed, while dimensionless parameters were defined to evaluate the influence of ground properties on the THM interactions. The main findings can be summarised as follows:

- there are three main processes that lead to the generation of excess pore water pressures in a fully coupled THM analysis, namely changes in temperature (thermally-induced), water flow (hydraulically-induced) and mechanical actions (mechanically-induced). These depend on the adopted boundary conditions as well as the soil properties: the differential expansion between water and soil was shown to have a large contribution to the development of excess pore water pressures due to changes in temperature, while mechanical restrictions lead to an increase in pore water pressures due to increase in mechanical volumetric strain as the thermal expansion is impeded;
- the THM interactions are controlled by the relative rate at which heat transfer and water flow progress. This was quantified through the dimensionless parameter α_{TH}, expressed as the ratio between the thermal diffusivity (α_T) and hydraulic diffusivity (α_H). It was observed that soils with equal value of α_{TH} obtained with different combinations of parameters display the same time-dependent behaviour. However, for problems displaying different values of α_T, the same response is obtained for equal temperature distributions, which necessarily occur at different time instants;
- a direct correlation between α_{TH} and the pore water pressures generated at the heat source (i.e. thermally-induced) exists, where Δu is highest for large values of α_{TH} (i.e. heat transfer is faster than water flow). Furthermore, the dissipation of the excess pore water pressures close to the heat source can also be related to this factor, where this happens earlier in time with lower α_{TH};
- excess pore water pressures occur even before changes in temperatures take place. These are due to water flow (i.e. hydraulically-induced) and are time-dependent. While no direct correlation with α_{TH} can be established, it was shown that there are intermediate values of this parameter for which this phenomenon is enhanced.

The last part of the chapter presents analyses based on the basement wall geometry modelled in the first part of the chapter, hypothesising it was used as a heat exchanger. Two main aspects were investigated, namely the effect of adopting different modelling approaches to model thermo-active walls (i.e. fully coupled THM analysis and simpler approaches where components of the THM formulation are disabled) and the influence of ground properties (in terms of varying α_{TH}) on the time dependent behaviour. The key conclusions can be summarised as follows:

- the behaviour of retaining walls subjected to temperature changes is highly transient in nature as a result of the high rates at which heat transfer and pore water pressure dissipation take place under plane-strain assumptions. The THM interactions within the soil have a significant effect on the structural response of the wall, with different phenomena prevailing over different time periods, namely thermal soil expansion, volumetric deformations due to excess pore water pressure generation and dissipation, and interactions with the mechanical boundary conditions (which depend on the geometry of the problem). All or some of these aspects are not captured by the simpler modelling approaches;
- even though simpler modelling approaches tend to be conservative in terms of structural forces (in the analysed cases all of the simpler analyses resulted in larger axial forces in the short term than the fully-coupled THM analysis), the same is not true for wall and ground movements in the long term, which are severely underestimated;
- while relatively low magnitudes of thermally-induced forces and horizontal wall displacements were predicted in the THM analysis, the calculated changes in vertical wall and ground movements were shown to be significant, indicating the need to carry out adequate assessments during design in order to guarantee serviceability of the structure and evaluate any possible interaction with nearby structures;
- the mechanisms of pore water pressure generation identified in the 1D problems have been observed also in the simulations of the retaining wall problem. The parametric study on the effect of varying α_{TH} within the thermo-active retaining wall analysis has shown that the main conclusions drawn from the simulations on simple geometries are also applicable to more complex boundary value problems. However, it should be noted that, in such a context, the results will be affected by the presence of more complex drainage patterns than those enforced in the one-dimensional problems.
- varying the ground properties, and thus altering the THM response of the soil, led to important changes in the behaviour of the structure, with larger forces and movements evaluated for higher values of α_{TH}. Hence, it is evident that adequate estimates of the hydraulic and thermal parameters of the soil are important to guarantee a safe and reliable design of thermo-active walls. Furthermore, in order to account for the various interactions that take place in such problems, fully coupled transient THM analyses are required.

Chapter 4
Heat transfer mechanisms in thermo-active retaining walls

4.1 Introduction

This chapter aims at identifying the heat transfer mechanisms occurring within thermo-active retaining walls and evaluating their thermal performance. For this purpose, three-dimensional (3D) analyses of a reference case are carried out, which include one-dimensional elements (refer to Section 2.3.4) to simulate the heat exchanger pipes, enabling the modelling of the advective-conductive heat transfer taking place within these components of the ground source energy system.

Two different modelling approaches are assessed, which differ in the boundary conditions applied at the pipe inlet and outlet employed to simulate the heat exchange. The first approach, termed herein "Modelling approach 1" (MA1), consists of imposing a prescribed temperature boundary condition at the pipe inlet, and is a common approach used in literature to simulate ground source heat exchangers (e.g. borehole heat exchangers (Rees & He, 2013; Ozudogru et al., 2014), thermo-active piles (Gashti et al., 2014; Batini et al., 2015) and walls (Sterpi et al., 2017; Di Donna et al., 2017; Barla et al., 2020)). The second approach, named "Modelling approach 2" (MA2), simulates the presence of a heat pump by introducing a nodal heat flux boundary condition, hence imposing the temperature differential between the pipe inlet and outlet ($\Delta T_p = T_{in} - T_{out}$). This approach is similar to that employed by Bidarmaghz et al. (2016) for the simulation of vertical ground heat exchangers (i.e. borehole heat exchanger and thermo-active piles), however it has not been extensively employed in literature. Both approaches are validated herein for thermo-active walls by reproducing some of the field tests reported in Xia et al. (2012), where details on the tests can be found in Section 2.4.3.

After the description and validation of the modelling approaches, a reference case is simulated using the two modelling approaches and the main mechanisms of heat transfer are analysed in detail where focus is given to the impact of the simulated boundary condition along the exposed part of the wall. Three cases were analysed: a fully insulated wall (i.e. no heat flux (NF) occurs along the wall-air interface), a wall maintained at constant temperature (CT) and a wall-air interface characterised by a convective heat transfer coefficient, h, of 2.5 W/m^{2}K (CH). Furthermore, the two modelling approaches are compared and conclusions are drawn. The contents of this chapter were published partially in Sailer et al. (2019c).

4.2 Evaluating the thermal performance

As outlined in Section 2.2.4, there are several quantities that can be calculated to evaluate the thermal performance of geothermal systems, such as the power extracted from or injected into the ground, q , expressed in W (see Equation (4-1)) and the energy provided by the geothermal system during an operation period, E_{tot}, which has units of kWh (see Equation (4-2)). These quantities are expressed as:

$$q = C_{v,w} A_p v (T_{in} - T_{out}) \tag{4-1}$$

$$E_{tot} = \sum_{i=1}^{n} q_i \Delta t_i \tag{4-2}$$

where $C_{v,w}$ is the volumetric heat capacity of water (kJ/m^{3}K), A_p is the cross-sectional area of the pipe (m^2), v is the water flow velocity within the heat exchange pipes (m/s) and T_{in} and T_{out} are the pipe inlet and outlet temperatures (K), respectively, and q_i is the extracted/injected power (calculated with Equation (4-1)) during time interval Δt_i.

Given the large dimensions of retaining walls, both in terms of length and width, the extracted or injected power, q, is often normalised by the length of the wall (q_L, W/m), the width of the wall (q_B, W/m) or by the area of wall in contact with the ground (q_A, W/m^2). These quantities provide an indication of the energy potential of a thermo-active wall and are calculated through the following equations:

$$q_L = \frac{C_{v,w} A_p v (T_{in} - T_{out})}{L} \tag{4-3}$$

$$q_B = \frac{C_{v,w} A_p v (T_{in} - T_{out})}{B} \tag{4-4}$$

$$q_A = \frac{C_{v,w} A_p v (T_{in} - T_{out})}{A} \tag{4-5}$$

where L is the total length of the wall panel (m), B is the width of the wall panel and A is the area of the wall (m^2) in contact with the ground, i.e. $L \cdot B$ (for a schematic of a wall panel see Figure 4-1).

Clearly, if in Equation (4-2) the quantities $q_{L,i}$ (W/m), $q_{B,i}$ (W/m) or $q_{A,i}$ (W/m^2), are employed instead of q_i, the energy output per metre length, $E_{tot,L}$ (kWh/m), per metre width, $E_{tot,B}$ (kWh/m), or per unit area, $E_{tot,A}$ (kWh/m^2), is computed.

The energy per unit volume exchanged between the heat exchanger pipes and the surrounding materials (i.e. concrete and soil) from the start of operation until a given time instant, $E_{i,\Omega}$ (kJ/m^3 or kWh/m^3), can be evaluated by using the following equation:

$$E_{i,\Omega} = C_v \cdot \left(\bar{T}_{i,\Omega} - T_0\right) \tag{4-6}$$

where C_v is the volumetric heat capacity of the considered material (kJ/m^{3}K), T_0 is the initial temperature and $\bar{T}_{i,\Omega}$ is the average temperature (°C) over a region Ω of volume V_Ω at a time instant $t = t_i$:

$$\bar{T}_{i,\Omega} = \frac{\iiint_\Omega T_i \, dV}{V_\Omega} \tag{4-7}$$

The average temperature, $\bar{T}_{i,\Omega}$, is determined by numerical integration according to the equations reported in Appendix C, for 3D elements as well as for 2D elements in plane-strain and axi-symmetric analyses.

The quantity $E_{i,\Omega}$ allows the quantification of the energy transferred to any material surrounding the pipes and to determine the contributions of different materials to the exchanged heat, as well as assisting in the interpretation of the heat transfer mechanisms taking place. Indeed, $\bar{T}_{i,\Omega}$ may be evaluated only for parts of a material (e.g. only for a part of the wall or a portion of soil, which will require the use of the corresponding V_Ω) and thus allow to determine the heat transfer occurring within different parts of the finite element mesh.

4.3 Description and validation of modelling approaches

The two modelling approaches adopted to simulate thermo-active walls within 3D analyses are validated by comparing the results obtained with ICFEP to those measured by Xia et al. (2012) in the field tests conducted on the thermo-active diaphragm walls installed at the Natural History Museum of Shanghai (see Section 2.4.3 for additional details). Before performing the validation exercise, the general aspects for modelling thermo-active structures in 3D analyses and details of the two modelling approaches are provided.

4.3.1 General

Generally, due to the presence of heat exchanger pipes at discrete locations within the structure, 3D analyses are required to account for the geometric configuration of GSESs, since out-of-plane effects, which cannot be captured in a two-dimensional analysis, are encountered (e.g. Sterpi et al., 2017).

The general approach to simulate thermo-active walls follows the same principles as those outlined in Gawecka et al. (2020) (see Section 2.3.5), where the heat exchanger pipes are modelled employing one-dimensional elements (see Section 2.3.4 for a summary and refer to Gawecka et al. (2018) and Gawecka (2017) for the full formulation, implementation and validation of such elements). These allow the simulation of the conductive-advective heat transfer using a coupled thermo-hydraulic formulation. Note that, while the mechanical aspect could be included, it is of little importance to the heat exchanger pipe problem. In order to guarantee numerical stability in advection-dominated problems, the Petrov-Galerkin FE method is required. Furthermore, to appropriately model the heat transfer occurring from the heat exchanger pipes to the adjacent material, the one-dimensional elements are surrounded by solid elements to which properties of a Thermally Enhanced Material (TEM) are assigned, i.e. a higher conductivity than that of concrete, through which only conduction is simulated and heat transfer is enhanced. This corrects the reduced heat transfer taking place from the pipes to the surrounding concrete due to the zero lateral contact area of the former when simulated using one-dimensional elements. Throughout this study, the heat transfer occurring within all other materials surrounding the pipes (i.e. concrete and soil) is simulated as purely conductive, hence assuming that negligible seepage velocities occur within the soil layers.

A further aspect to consider in the simulation of this type of problems is the spatial discretisation. It is known that the mesh discretisation affects the numerical solution (see e.g. the example of the mechanical response of footings with different mesh discretisations presented by Potts & Zdravković (2001)). Similar to the mechanical problems, where Potts & Zdravković (2001) highlight that smaller and thus more elements are required in zones where rapid changes in stresses and strains occur, in cases with rapid changes in temperature a similarly fine mesh is required to avoid significant errors in the calculated temperature distributions. This problem is assessed in Appendix D, where the effects on the evaluated changes in temperature are investigated for different types of boundary conditions (either a Dirichlet (i.e. prescribed temperature) or a Neumann (i.e. heat flux) boundary condition), element types (linear or quadratic), orders of integration (2×2 or 3×3) and element sizes. This detailed study concluded that when a heat flux boundary condition is applied, limited effects arise from all the considered factors, since the energy transferred to the system is specified. Conversely, when a prescribed temperature boundary condition is imposed, substantial differences are observed for different mesh discretisations. Furthermore, for coarser meshes, the element type was shown to substantially affect the results, whereas its impact was less pronounced for finer meshes. For all cases, the integration order had a negligible impact on the temperature distributions. It is also shown that a noticeable

improvement is obtained by refining only a small zone around the point of application of the boundary condition, thus enabling a reduction in the number of elements used. Hence, an efficient refinement is suggested, where two to four small elements close to the application of the boundary condition are sufficient to reduce mesh effects, leading to substantial savings in terms of computational costs compared to a uniformly refined mesh. Lastly, it should be noted that, although in the present study heat exchanger pipes are employed for the application of thermal loading, and therefore a prescribed temperature boundary condition is not directly applied to solid elements (as is the case in the analyses conducted in Appendix D), further studies demonstrated that the effects of spatial discretisation when employing heat exchanger pipes are similar to those observed when applying a prescribed temperature boundary condition. This means that for these cases similar refinement procedures are suggested.

4.3.2 Modelling approach 1

Modelling approach 1 (MA1) is schematically represented in Figure 4-1 for a thermo-active retaining wall equipped with a U-loop. Within the heat exchanger pipes, water flow is simulated by applying a fluid pressure differential across the inlet and outlet nodes. At the inlet node, a prescribed temperature boundary condition is applied to simulate the thermal load. The values of temperature applied are either higher or lower than the initial temperature, T_0, to simulate heat injection or extraction, respectively, and are in the typical range of operating temperatures for GSES, i.e. between 0°C and 45°C (Brandl, 2006). Note that temperatures may fall below 0°C if antifreeze solutions are employed for the heat carrier fluid. The temperatures at the inlet can be either constant or varying with time. However, generally, constant values with time are employed in the simulation of the long-term response of these systems. While this does not reflect the real operation mode of GSHP systems, where temperatures vary according to the energy demand, it is a simpler approach that allows the evaluation of the heat transfer potential in the long term, i.e. at quasi-steady state conditions. At the outlet node, the thermo-hydraulic boundary condition (Cui et al., 2016a) is applied to prevent accumulation of heat once the water leaves the system.

With a prescribed inlet temperature, the heat injected to or extracted from the system is calculated with the computed outlet temperature (employing Equation (4-1) or (4-3), (4-4) and (4-5), depending on the applied normalisation). This modelling approach (including the general aspects previously described) was validated by Gawecka et al. (2020) who demonstrated an excellent agreement between the measurements reported for two experimental thermal response tests on vertical heat exchangers and the corresponding numerical predictions, highlighting the need to introduce the TEM for a correct simulation of the heat transfer in the short term. Herein, the capabilities of this modelling approach are demonstrated by simulating the field tests performed on a thermo-active wall presented in Xia et al. (2012).

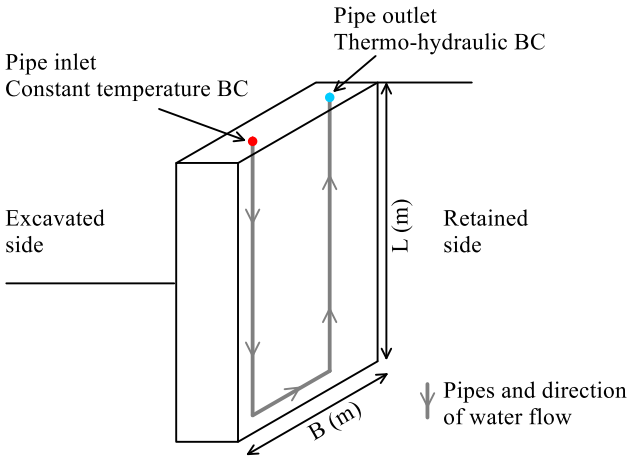

Figure 4-1: Schematic representation of modelling approach 1

4.3.3 Modelling approach 2

As described in Chapter 2, the heat exchanger pipes are connected to a heat pump, as schematically represented in Figure 4-2 and designated as "above ground circuit", which alters the temperature of the geothermal fluid through an input of electrical power, while a circulation pump ensures the recirculation of the geothermal fluid. Thus, rather than specifying the temperatures within the pipes, a heat pump generates a temperature differential across the pipe inlet and outlet, while the operating temperatures are controlled such that certain limits are not exceeded (Kavanaugh & Rafferty, 2014; Banks, 2012). The aim of modelling approach 2 (MA2) is to introduce the above ground circuit within a finite element simulation through the application of boundary conditions. Clearly, Figure 4-2 represents a simplified illustration of the problem, since, in reality, several wall panels are connected to a heat pump.

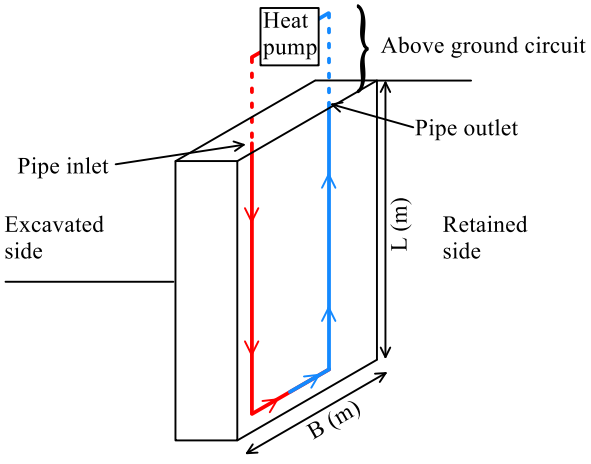

Figure 4-2: Schematic representation of thermo-active wall problem and above ground circuit

To introduce the above described features, the simulation procedure schematically represented in Figure 4-3 (a) is adopted, where the pipe elements are extended beyond the top of the structure (A-B for the inlet section and C-D for the outlet section in Figure 4-3 (a)) to allow for the application of the boundary conditions. A nodal heat flux boundary condition (see Section 2.3.2) is applied at the mid-length of the

extended section of the inlet pipe (position Q in Figure 4-3 (a)) to simulate the presence of a heat pump, while fluid pressure boundary conditions are imposed at the top nodes of the inlet (position A in Figure 4-3 (a)) and outlet (position C in Figure 4-3 (a)) branches to generate the water flow. In order to simulate the recirculation of geothermal fluid, the temperature at the top of the extended pipe element at the outlet branch at any time instant must be the same as the temperature at the top of the inlet (i.e. T_A=T_C). To achieve this, the temperature degrees of freedom (DOF) between these two nodes are tied, meaning the thermo-hydraulic boundary condition is not required in this modelling approach.

Since the protruding pipe elements are not in contact with other materials, they do not dissipate any heat and hence the temperatures along them do not vary, apart from the difference in temperature occurring due to the application of the heat source boundary condition, as shown in Figure 4-3 (b). Therefore, the value of the specified nodal heat flux encapsulates both the energy transferred by the heat pump to the panel being simulated and the heat losses in the above-ground circuit. Moreover, modelling the presence of a heat pump by applying a nodal heat flux boundary condition implies that the temperatures at the inlet and outlet are not controlled, even though the temperature differential across them (ΔT_p), and hence the heat flux, is. Thus, both the temperatures at the inlet and outlet vary with time, with the ΔT_p depending on the magnitude of the heat flux boundary condition. Clearly, this value does not correspond to the actual power of a single heat pump, but the portion of power that a heat pump transfers to a single wall panel.

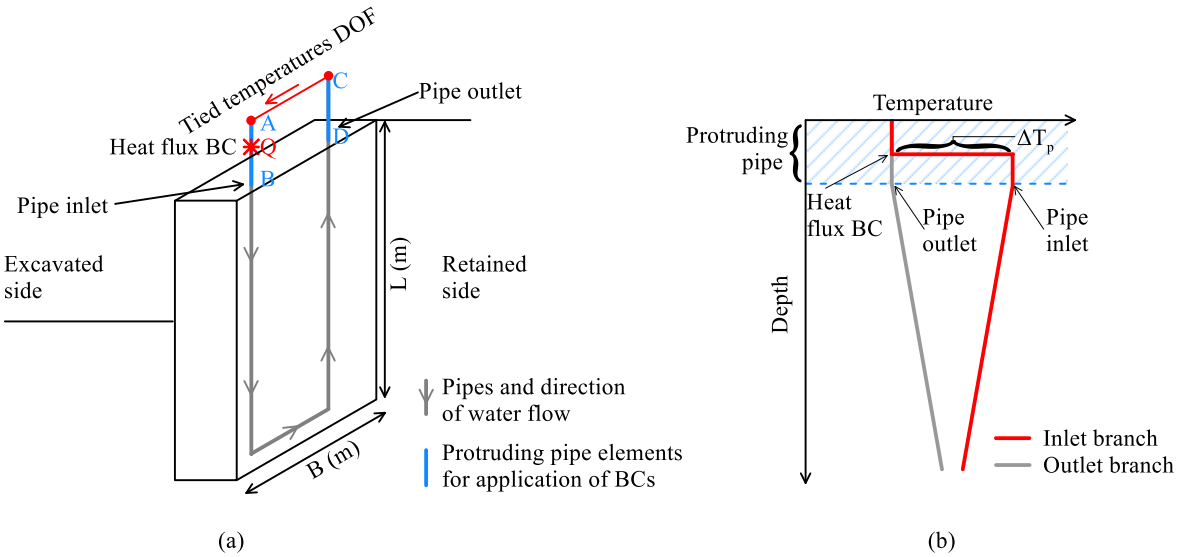

Figure 4-3: Schematic representation of modelling approach 2 (a) geometry and boundary conditions and (b) temperature distribution within heat exchanger pipes (heat injection)

In order to determine the magnitude of the heat flux boundary condition, a threshold criterion has to be defined, such that the temperature changes within the heat exchanger pipes, concrete or soil, remain within an acceptable range (in fact, the application of a heat flux boundary condition can potentially lead to unbounded changes in temperature with time). In the proposed approach, the inlet temperature

was limited to a desired temperature change, ΔT_{in} (°C), with respect to the initial temperature T_0 (i.e. $\Delta T_{in} = T_{in} - T_0$). Thus, the design process to determine the magnitude of the heat flux boundary condition that is required to reach such a temperature change is iterative and its value will depend on different factors, such as the boundary condition along the exposed face, the thermal parameters of concrete and soil, etc. It should be noted that ΔT_{in} is directly proportional to the value of the heat flux boundary condition, and, therefore, a maximum of two iterations are required to establish the magnitude of the heat flux boundary condition once a target ΔT_{in} is set.

Unfortunately, there are no field test data available in literature to directly validate this method for thermo-active retaining walls, since none of the reported field studies (e.g. Xia et al. (2012) and Sterpi et al. (2018)) provides values of the heat pump power employed in the tests. Thus, this method was verified by converting the monitoring data from Xia et al. (2012) into input parameters for the simulation of the field tests using this modelling approach.

It should be noted that the Petrov-Galerkin formulation implemented in ICFEP (Cui et al., 2018c) for one-dimensional elements (i.e. those employed for the simulation of heat exchanger pipes), was adopted from Huyakorn (1977) for linear elements and from Heinrich & Zienkiewicz (1977) for quadratic elements. The application of the former results in a balanced response from an energy perspective, with the sum of the proposed weighting functions being 1.0 at any point within the isoparametric element. However, further research showed that this was not the case for the weighting functions for quadratic elements, for which an excess in energy is simulated when a heat flux boundary condition is applied to the extremity nodes, while the opposite is obtained when it is applied to the middle nodes. Thus, alternative weighting functions, outlined in Appendix E, are proposed for one-dimensional quadratic elements, which were established according to the weighting functions developed by Cui et al. (2018c) for two-dimensional quadratic elements.

4.3.4 Validation of modelling approaches - Reproduction of a field test

Xia et al. (2012) and Sun et al. (2013) describe the tests conducted on thermo-active diaphragm wall panels forming part of the underground space of the Natural History Museum of Shanghai, which are described in detail in Section 2.4.3. For this validation exercise, the field tests performed on two pipe layouts (see Figure 4-4), which are termed “Type (b)” and “Type (c)” in Xia et al. (2012), while herein they are termed simply as W-loop and U-loop, respectively, are reproduced with ICFEP. Both modelling approaches previously outlined are adopted and 3D analyses are carried out.

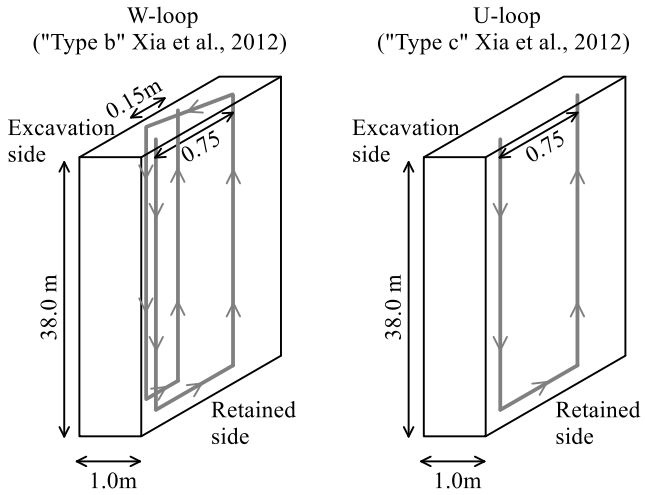

Figure 4-4: Schematic representation of wall panels included in the field tests carried out at the Natural History Museum of Shanghai reported in Xia et al. (2012)

4.3.4.1 Problem description

The wall panels are 38.0 m long, 1.0 m thick and 1.5 m wide (see Sun et al. (2013)). The excavation level is located at 18.5 m below the ground surface. The pipes, in polyethylene 100, have an outer diameter of 25 mm and a wall thickness of 2.3 mm (hence an inner diameter of 20.4 mm). They reach a depth of 37.5 m and are located at 0.1 m from the concrete faces. The employed heat carrier fluid was water, which was circulated at a velocity of 0.6 m/s and injected with a constant inlet temperature of 35°C for a duration of 48 h. Xia et al. (2012) report that the average initial wall and soil temperatures were 23°C and 16.3°C, respectively, suggesting the existence of a temperature gradient between the wall and retained soil. Unfortunately, the available data are not sufficient to assess whether these correspond to a possible steady-state or if they reflect the existence of other transient phenomena, e.g. seasonal variations in air temperature, heat resulting from concrete hydration, etc. Clearly, if these temperatures would be prescribed as initial temperatures to all the nodes of the wall and soil, a substantial transfer of heat would take place even without stimulating the circulation of the geothermal fluid.

4.3.4.2 Numerical analysis

Figure 4-5 shows the FE mesh in cross-section and plan view with an indication of its dimensions, where the soil extends by 2.0 m either side of the wall (i.e. front and back). Detailed studies were carried out to ensure that the dimensions of the FE mesh were sufficiently large so that the simulated temperature fields were not affected by the proximity of the boundaries. Figure 4-5 also depicts the position of the one-dimensional pipe elements and the solid elements assigned with the properties of TEM, where the outer perimeter of the region is equal to the inner circumference of the pipe. Eight-noded hexahedral solid elements, with temperature degrees of freedom at each node, were employed for concrete, soil and TEM. The heat exchanger pipes were modelled with 2-noded bar elements which combine the three displacement degrees of freedom at each node with additional temperature and fluid

pressure degrees of freedom. Since only thermo-hydraulic analyses of the chosen thermo-active wall problem have been carried out (i.e. its mechanical behaviour is not evaluated), lower order elements with linear fluid pressure and temperature shape functions could be employed without affecting the accuracy of the analysis, while reducing greatly the number of degrees of freedom and hence the required computational effort. However, it should be noted that displacement degrees of freedom exist in the analysis as these cannot be deactivated in ICFEP. As previously discussed, the calculated temperature distributions are only marginally affected by the type of elements (linear or quadratic), provided the region close to the application of the prescribed temperature boundary condition, or, in this case, the one-dimensional pipe elements, is sufficiently refined. For this reason, as detailed in Figure 4-5, the region associated with properties of TEM (approximately 20 mm × 20 mm in size), was discretised by 12 elements in plan, including 2 divisions either side of the pipe element, to minimise mesh effects.

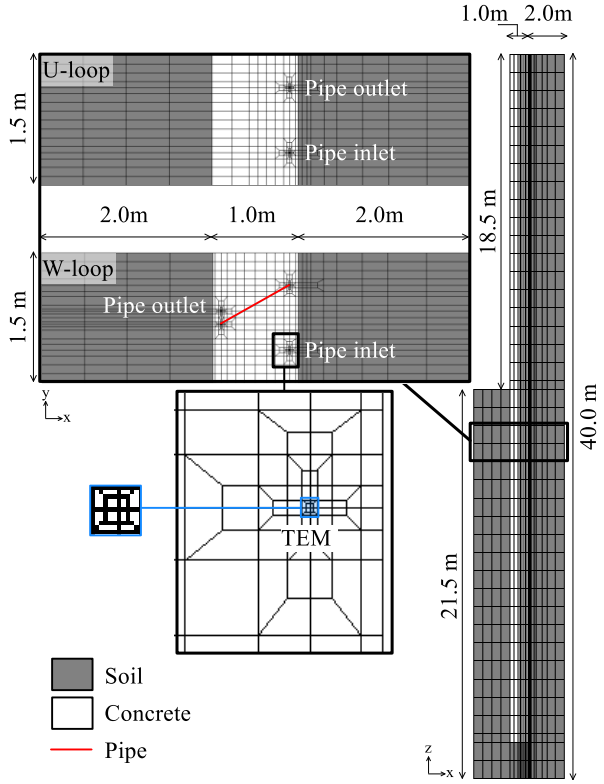

Figure 4-5: Finite element mesh for simulation of field tests reported in Xia et al. (2012)

A uniform initial temperature of 23°C was assigned to all the elements of the FE mesh. As previously reported, field measurements had shown the existence of a thermal gradient between the soil and the wall. However, no further details are provided (e.g. the location of the measuring point of the soil temperature with respect to the wall), meaning that such a complex initial state could not be modelled with sufficient confidence. Furthermore, since the field tests lasted for a short time period, the heat exchange takes place mainly within the concrete (Soga et al., 2014). Thus, for the purpose of reproducing these field tests, a uniform initial temperature equal to that measured in the wall was

assumed. This also ensures that the analyses are in thermal equilibrium before the application of any other thermal boundary condition.

The boundaries in the x-z plane (see Figure 4-5) were considered as planes of symmetry, hence no heat flux was allowed through these boundaries. Equally, all other surfaces were modelled as thermally insulated, with the exception of the surface corresponding to the exposed part of the wall for the analysis simulating the W-shaped loop. Indeed, due to the proximity of the pipes to this boundary, this analysis is substantially affected by the type of boundary condition applied to this surface, whereas no effect of the boundary condition had been encountered for the U-loop case due to the relatively short duration of the test (less than 50 hours). Thus, when considering the W-shaped pipe layout, two simulations are carried out varying the thermal boundary condition prescribed to the exposed part of the wall: one simulates a fully insulated wall (i.e. no heat flux (NF) is allowed across the wall-air interface), while the other models a wall maintained at a constant temperature (CT) of 23°C (i.e. imposing no change from the initial temperature). These two cases correspond to two extreme scenarios with respect to the thermal interaction between the wall and the environment, corresponding to a convective heat transfer coefficient, h (W/m^{2}K), either of zero (NF) or infinity (CT) W/m^{2}K. In reality, the interaction between the wall and the thermal environment to which it is exposed is characterised by values of h included within these two extremes. However, the estimation of this coefficient is challenging as it depends on numerous factors, such as the function and the geometry of the underground space, the climatic conditions, airflow velocities, etc. (see Section 2.4.2). Thus, the real response of the simulated system should lie somewhere in between the results obtained when applying these two boundary conditions.

The water flow within the pipes was simulated by applying a fluid pressure differential between the inlet and outlet nodes of the heat exchanger pipes to achieve a constant water flow velocity of 0.6 m/s, as measured in the field. In addition, since the heat flux within the pipes is advection-dominated, the Petrov-Galerkin FE method was adopted to guarantee numerical stability.

The thermal boundary conditions simulating the application of the thermal load for the two modelling approaches were the following:

- MA1: a constant prescribed temperature boundary condition of 35°C was applied at the inlet node of the pipe loop (as described in the test), whereas the coupled thermo-hydraulic boundary condition was applied at the outlet node. The temperature at the outlet is measured to calculate the heat flux, which is compared to the one given in Xia et al. (2012);
- MA2: the heat flux per unit length, q_L, reported in Xia et al. (2012) and shown in Figure 4-6 was converted to a total heat flux (i.e. $q_L \cdot L$) and this was applied as a heat flux boundary condition on a node at mid-length of the protruding portion of pipe at the inlet branch. The temperature degrees of freedom were tied between the top nodes of the inlet and the outlet branches to simulate the recirculation of the geothermal fluid. The computed temperatures at the pipe inlet and outlet are

then compared to those measured in the field test, where the outlet temperature was back-calculated from the heat flux using the reported inlet temperature of 35°C.

The thermal properties of all materials are listed in Table 4-1. Sun et al. (2013) have provided indicative values for the thermal properties for soil, water and concrete. The reported thermal conductivity of concrete (2.34 W/mK) is closer to the upper limit of the range expected for this material, which is usually adopted for concretes with quartz aggregates or with addition of siliceous sands (CIRIA, 2007). Given that the description in Xia et al. (2012) does not provide specifications on the aggregate type minerology of the employed concrete, a concrete conductivity more in line with the values reported in the literature (e.g. VDI, 2010; Tatro, 2006) was chosen (1.6 W/mK). The other material properties were adopted directly from Sun et al. (2013). The employed thermal conductivity of the TEM (3.5 W/mK) was that suggested by Gawecka et al. (2020) for an inner pipe diameter of 20.0 mm and a pipe wall thickness of 3.0 mm. For comparison, analyses using the same finite element discretisation but without the inclusion of TEM are also presented.

Table 4-1: Thermal material properties for simulation of field test

Material	C_v (kJ/m^{3}K)	λ (W/mK)
Soil	3042	1.74
Concrete	2615	1.60
Water	4200	0.60
TEM	1	3.50

4.3.4.3 Comparison of measured and simulated results

Modelling approach 1

MA1 is validated by comparing the heat flux per unit length, q_L (W/m), provided in Xia et al. (2012) with the one obtained by the numerical analyses calculated through Equation (4-3), where the length of the wall, L (m), is 38.0 m. The results are shown in Figure 4-6 (a) and (b) for the U-shaped and W-shaped pipe configurations, respectively. The computed heat flux for the analyses including the TEM is in good agreement with the field data. Indeed, for the U-shaped loop, a difference in heat flux of 7.0 W/m (14%) is registered after 48h. This value corresponds to a difference in the predicted outlet temperature of only 0.3°C. Without the inclusion of the TEM, the outlet temperature is 0.75°C higher than the one measured during the field test, leading to a heat flux which is 16.0 W/m (32 %) lower than that reported in Xia et al. (2012). For the W-shaped loop, the results obtained from the two analyses (NF and CT) with the presence of the TEM plot just above and below the monitoring data, as expected. Indeed, at the end of the simulated period, the analysis with an insulated boundary (i.e. NF) underestimates the heat flux by 6.0 W/m (8%), while modelling a wall maintained at a constant

temperature (i.e. CT) overestimates the heat flux by 3.0 W/m (4%). Such a narrow band provides a reassuring confirmation that, for the small durations typically associated to thermal response tests, the uncertainty surrounding the thermal boundary condition on the exposed face has only a limited effect on the obtained results. Moreover, the analyses without the TEM underestimate the heat flux after 48h by 12.0 W/m (16%) and 17.0 W/m (23%) for CT and NF conditions, respectively.

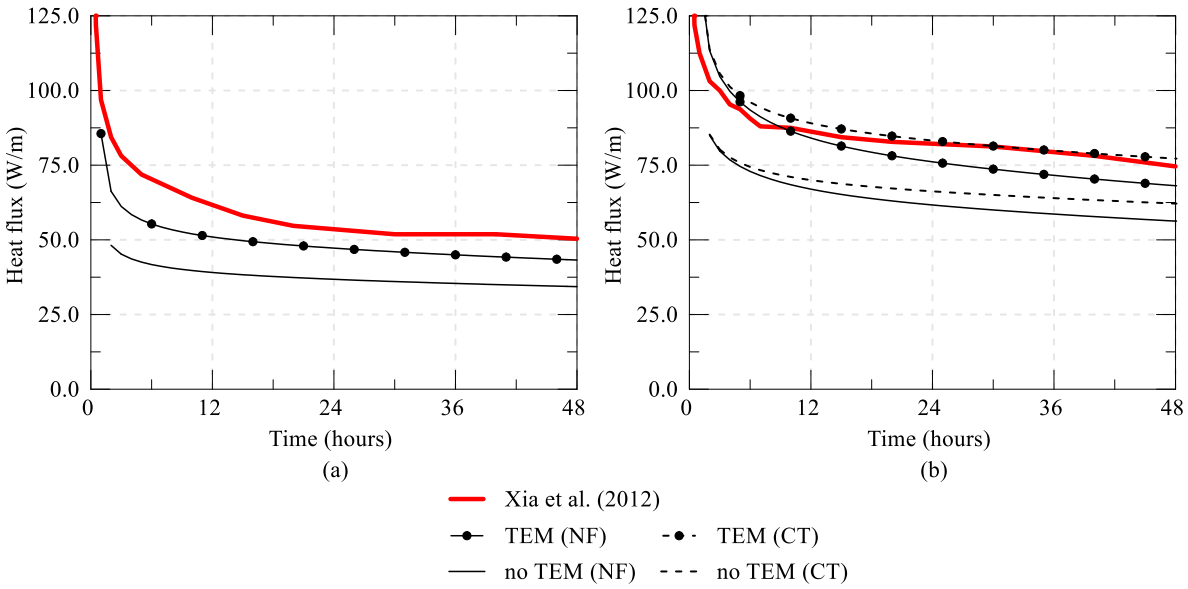

Figure 4-6: Comparison between measured and computed heat flux per unit length (a) U-shaped pipe loop and (b) W-shaped pipe loop

Modelling approach 2

As previously mentioned, MA2 cannot be directly validated since the values of the actual applied power are not reported in Xia et al. (2012). Therefore, the approach is verified by comparing the temperatures at the pipe inlet and outlet from the field data to those obtained by ICFEP, where the heat flux boundary condition was calculated from the reported heat flux (see Figure 4-6), thus the same ΔT_p as in the field test is simulated. Furthermore, since the inlet temperature was constant during the field test, the outlet temperature of the field test was back-calculated from the reported heat flux rearranging Equation (4-3). Thus, this study allows to check whether, upon application of the power calculated from the test (i.e. the same ΔT_p), similar operating temperatures are evaluated by ICFEP.

The evolution of the inlet and outlet temperatures with time for the U-loop and W-loop geometry are displayed in Figure 4-7. For the U-loop case, an initial increase in temperature is observed, which may be due to the instantaneous application of the heat flux boundary condition. However, after 7 hours a slight decrease occurs and the temperatures eventually stabilise. After 48h, the difference between the computed and measured temperatures is 1.45 °C (12%) when using the TEM. As expected, larger differences are obtained for the analyses without TEM, with computed temperatures being 5.0°C (42%) higher than those reported in Xia et al. (2012), confirming that not adopting this modelling technique

underestimates considerably the heat transfer between the heat exchanger pipes and the surrounding concrete. For the W-loop, similar to what was observed for MA1, the field test data plot just in between the results obtained from the analyses simulating a NF or CT boundary condition along the exposed face of the wall including the TEM, with differences of -0.8°C (7%) and 0.6°C (5%) for the NF and CT analyses, respectively. Similar to the U-loop simulation, larger temperatures are computed for the analyses without TEM, with differences ranging between 2.2°C (18%) and 3.6°C (30%).

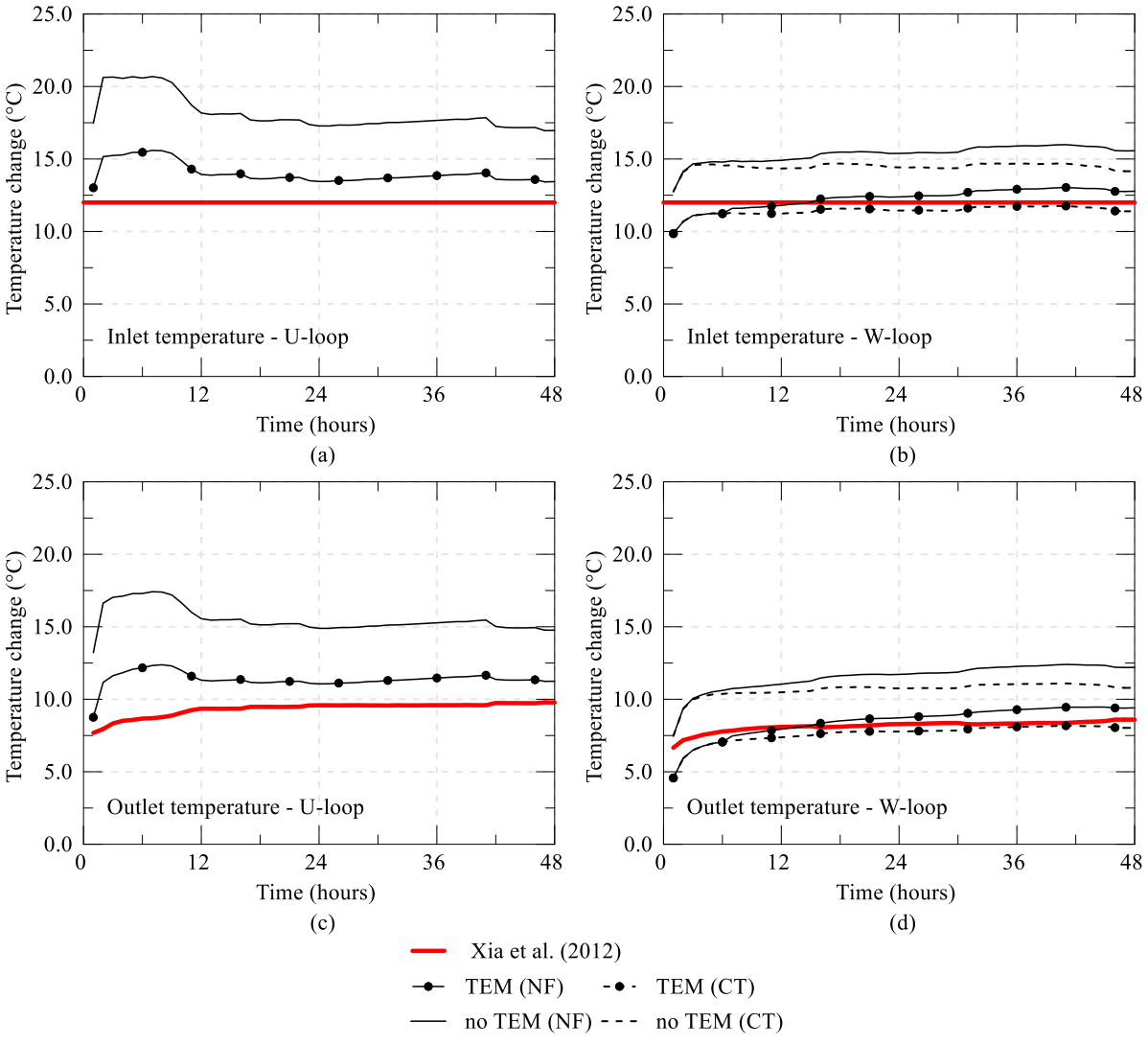

Figure 4-7: Comparison between measured and computed temperatures changes (a) inlet U-shaped pipe loop, (b) inlet W-shaped pipe loop, (c) outlet U-shaped pipe loop and (d) outlet W-shaped pipe loop

4.4 Simulation of a reference case

The very good agreement between the measured data and the computed results for both modelling approaches obtained in the previous section provides confidence in the suitability of the methodology proposed by Gawecka et al. (2020) to model thermo-active retaining wall problems in 3D analyses, especially considering the substantial uncertainties regarding the simulated field test (in particular in terms of initial conditions and material properties). In this section, a reference case is simulated employing the two different modelling approaches. The aim is to provide insights into the fundamental aspects that control the heat transfer and thermal performance of thermo-active walls. For this purpose, for each modelling approach, the calculated heat flux, the temperature changes within the wall and in the surrounding materials and the transferred energy are evaluated, where particular focus is given to the impact of the simulated boundary condition along the exposed face of the wall. Furthermore, the results obtained by the two modelling approaches are compared and the main differences are outlined.

4.4.1 Problem description

The geometry of the analysed wall problem is similar to the one described in Chapter 3, with the thermal loading being applied using heat exchanger pipes. Therefore, a 3D analysis is required. A single wall panel with a U-loop is modelled, assuming that in the out-of-plane direction (y-direction in Figure 4-8), symmetry conditions apply – hence the simulation of a single panel allows the representation of a continuous wall. Note that, due to the asymmetry of the temperature field resulting from the presence of the heat exchanger pipes, the modelling of a single panel means that the loops are installed with alternating orientation between inlet and outlet, i.e. similar to the configuration reported in Sterpi et al. (2018). However, this may not always be the case, since the disposition of pipe loops may be repeated in each panel, i.e. constant orientation between inlet and outlet. In such a case, more than one panel should be modelled to take into account the asymmetric conditions between adjacent wall panels, which would lead to a large increase in the required computational effort. Given the limited temperature changes across each pipe loop, it is uncertain whether such an increase in the size of the model would result in significant gains in accuracy.

The wall panel is 18.0 m long, 0.8 m thick and 1.5 m wide supporting an 11.0 m deep excavation, with a 1.5 m thick concrete base slab constructed above the base of excavation. The ground profile consists of 4.8 m of Made Ground and 2.0 m of Terrace Gravel Deposit overlying London Clay, with an initial temperature of 13°C. A single U-shaped pipe loop is placed within each wall panel, consisting of two vertical pipe segments, with a pipe-to-pipe spacing of 0.75 m and placed 0.1 m from the edge of the concrete on the retained side. The pipes reach a depth of 17.5 m, where they are connected by a horizontal pipe segment. The pipes have an inner diameter of 20.4 mm (A_p= 3.27×10^{-4} m^2) and water is circulated at a velocity of 0.5 m/s, resulting in a water flow rate, Q_w, of 1.64×10^{-4} m^3/s.

4.4.2 Finite element model

The finite element mesh is depicted in Figure 4-8, where the boundaries are located 15.0 m either side of the wall. The mesh discretisation close to the one-dimensional elements was sufficiently fine to avoid mesh effects on the temperature distributions. Soil and concrete structures were modelled with eight-noded hexahedral solid elements, where each node only has temperature degrees of freedom. In effect, displacement degrees of freedom cannot be deactivated in ICFEP and therefore these exist in this analysis as well. Thus, in order to perform a thermo-hydraulic analysis, the coefficients of thermal expansion must all be set to zero. Lastly, the fact that no pore water pressure degrees of freedom are specified for the soil means that water flow within the soil mass was assumed to be negligible and therefore only conduction was simulated. The heat exchanger pipes were modelled with two-noded one-dimensional elements (Gawecka et al., 2018), where each node presents both temperature and fluid pressure degrees of freedom. Note that lower order elements are adopted since the mechanical behaviour is not evaluated and the effects on temperature distributions are minimised by a fine mesh discretisation around the one-dimensional elements. To guarantee numerical stability within the pipes, the Petrov-Galerkin finite element method (Cui et al., 2018c) was adopted. Note that, as demonstrated in Appendix F, the effect of the TEM in the analysed problem is significantly less relevant in the long term than observed in the validation example shown in the previous section. Furthermore, the absence of the TEM leads to conservative results in terms of the computed thermal performance. For these reasons, it has not been included in the analyses reported in this section. The thermal material properties are reported in Table 4-2, where those employed for the soil layers were adopted from Gawecka et al. (2017).

The simulation period of the analyses was six months and appropriate time-steps were used to avoid the thermal shock and hydraulic shock problems (Cui et al., 2016b). It was assumed that the system works in a continuous operation mode, with the water flow within the pipes being achieved by imposing a fluid pressure differential between the inlet and outlet nodes of the pipes to reach a constant water flow velocity of 0.5 m/s. Although in real applications ground source heat pump systems generally operate intermittently, i.e. the heat pump is switched off for a period of time during the day, it is expected that the assumption of a continuous operation does not affect the conclusions of this study (see Chapter 5 for an analysis which focuses on evaluating this aspect).

Throughout the analysis, the temperature along the ground surface was not allowed to change from its initial temperature of T_0 =13°C. All other boundaries of the domain, with the exception of the exposed part of the wall, were considered to be adiabatic. It was checked that the boundaries were sufficiently far away to not affect the temperature distributions. Along the exposed face, three different boundary conditions were applied. Two analyses represent extreme scenarios, with either a no flux (NF) or a constant temperature (CT) boundary condition equal to T_0, which simulate, respectively, walls characterised by a convective heat transfer coefficient, h, of 0.0 W/m^{2}K or ∞ W/m^{2}K. The third case represents an intermediate scenario, where a convective (CH) boundary condition was applied (see

Section 2.3.2 for details), characterised by a convective heat transfer coefficient, h, of 2.5 W/m^{2}K and an ambient temperature equal to the initial temperature T_0. The employed value of h is the average value for natural heat convection along planar surfaces (see Section 2.4.2). It is also suggested by ISO (ISO, 2017) for horizontal heat from internal, well ventilated planar building components.

It was assumed that the system operates in cooling mode, i.e. heat is injected into the ground. This was simulated differently for the two modelling approaches:

- MA1: a constant prescribed temperature of 28°C (i.e. ΔT_{in}=15°C) is imposed at the inlet node of the pipe loop for the whole simulation period, while at the outlet node, the coupled thermo-hydraulic boundary condition was employed;
- MA2: the value of the heat flux boundary condition was determined such that the same temperature change ΔT_{in} as the one applied for the simulations with MA1 (i.e. T_{in}=28°C) was achieved at the inlet of the pipe after six months of operation. Furthermore, the temperature degrees of freedom were tied between top nodes of the inlet and outlet branches of the pipe loop in order to model the recirculation of the fluid.

While the two modelling approaches are conceptually different, since one imposes the operating temperature while the second prescribes a given heat injection rate, adopting the same design criterion (ΔT_{in}=15°C) allows a comparison between the two methods.

Table 4-2: Material properties for reference analyses

Material	Thermal conductivity $\boldsymbol{\lambda}$ (W/mK)	Volumetric heat capacity $\boldsymbol{C_v}$ (kJ/m^{3}K)
Concrete	1.60	2160
Made Ground[1]	1.40	1800
Terrace Gravel[1]	1.40	1800
London Clay[1]	1.79	1800
Water	0.60	4180

[1]Gawecka et al. (2017)

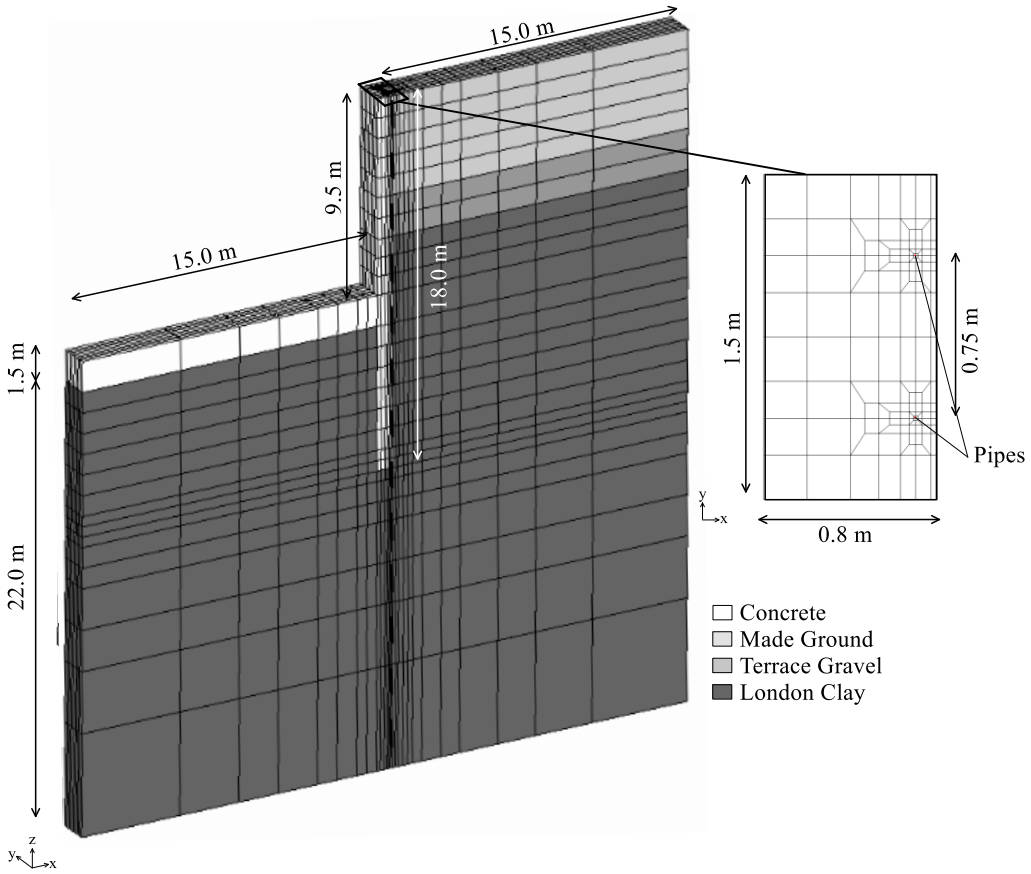

Figure 4-8: Finite element mesh for analysis of heat transfer mechanisms in 3D

4.4.3 Results

In this section, the results in terms of temperature changes, computed heat flux and energy obtained for the analyses corresponding to the three different boundary conditions are outlined. Firstly, the results obtained with MA1 are presented, with details on the heat transfer mechanisms being outlined. Subsequently, those obtained employing MA2 are shown and a comparison between the two modelling approaches is performed.

4.4.3.1 Identification of heat transfer mechanisms using modelling approach 1

Temperature changes

The changes in temperature of the wall panel recorded at different time instants within the exposed and embedded sections of the wall are displayed in Figure 4-9, Figure 4-10 and Figure 4-11 for the NF, CT and CH analyses, respectively.

In the short term (<10 days), the temperature distributions within the wall remain practically unaffected by the boundary condition along the exposed part of the wall because the heat transfer takes place primarily within the concrete. For the same reason, negligible differences are observed between the temperature distributions corresponding to the exposed and embedded sections of the wall. With time, differences between sections above and below the excavation level, as well as between the various analyses become more accentuated. Indeed, for an insulated wall (NF), i.e. no heat transfer is allowed

through the wall-air interface, heat can dissipate only towards the soil on the retained side for sections located above excavation level. Thus, this portion of the wall saturates with heat in the long term (see Figure 4-9), reaching an almost uniform temperature field T=T_{in} after 6 months. Conversely, within the embedded portion of the wall, the heat transfer occurs through both soil-wall interfaces, leading to overall lower temperatures: after 6 months, the average temperature of the embedded section is 1.6°C lower than that of the exposed section. For the wall exposed to an environment at constant temperature (CT), the contrary is observed: the temperatures within the exposed section of the wall are lower when compared to the embedded part since considerable quantities of heat dissipate through the wall-air interface. At the end of the simulation, the average temperature of the exposed portion of the wall is 5.6°C lower than that of the embedded portion. Moreover, when comparing for the same part of the wall but for different boundary conditions, the difference rises to 8.5°C, with the CT analysis registering, as expected, the lowest average temperatures. An intermediate behaviour is evaluated for the CH analysis: similar to the CT case, heat is dissipated through the wall-air interface, though at a different rate. Thus, the exposed section of the wall warms up more, where the average temperature change recorded within the exposed section after 6 months is 3.1°C larger than for the CT case.

It should be noted that, in general, the temperatures within the embedded sections are similar for all the analyses, with an average change in temperature ranging between 10°C and 11°C. Furthermore, as can be observed from the temperature contours in Figure 4-9, Figure 4-10 to Figure 4-11, the presence of the pipes, i.e. heat sources at discrete locations within the width of the wall panel (B), leads to non-uniform temperature distributions along this dimension, which are particularly accentuated in the short term, regardless of the boundary condition.

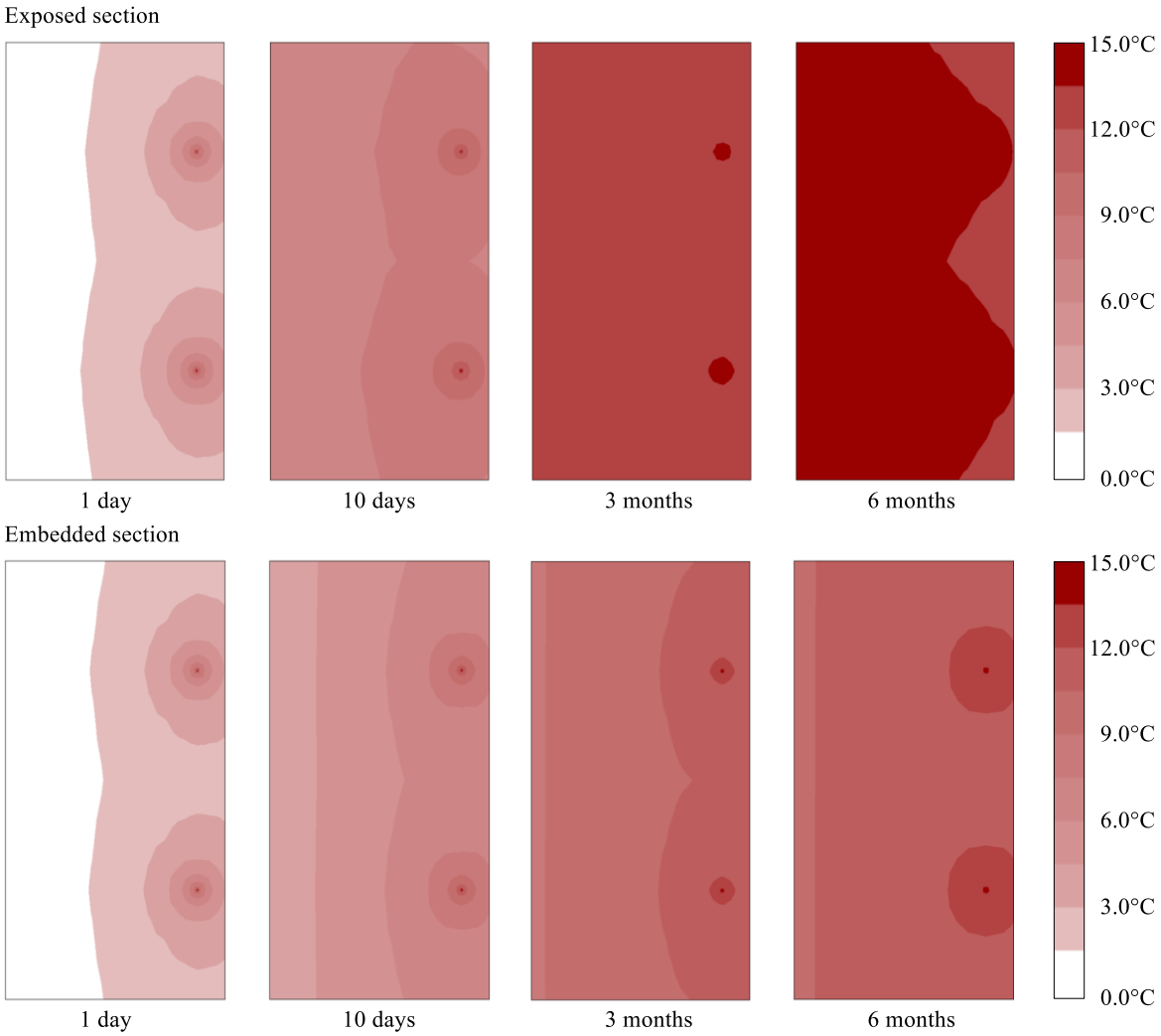

Figure 4-9: Changes in wall temperatures at mid-depth of exposed and embedded sections for NF analysis at different time instants – MA1

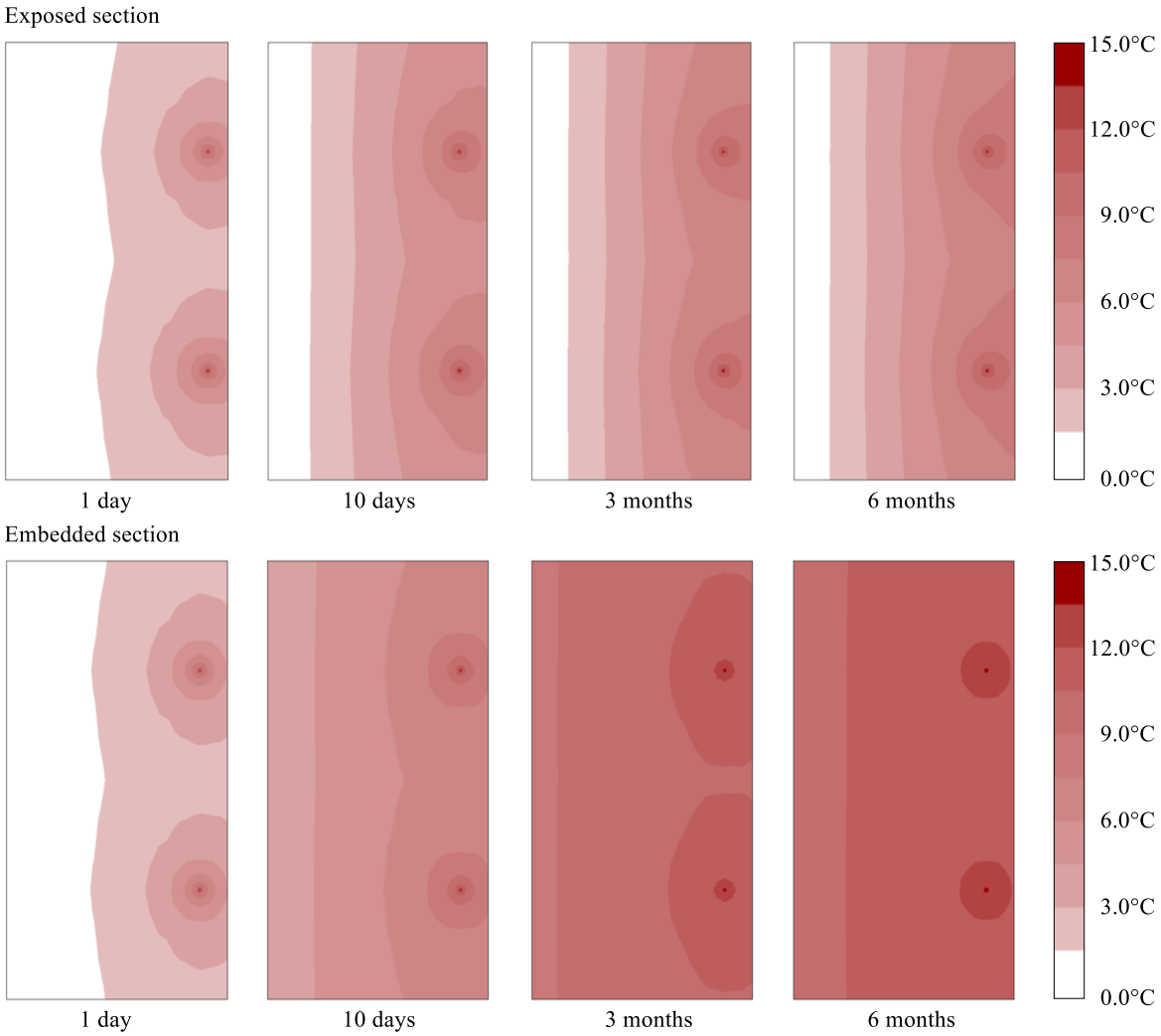

Figure 4-10: Changes in wall temperatures at mid-depth of exposed and embedded sections for CT analysis at different time instants – MA1

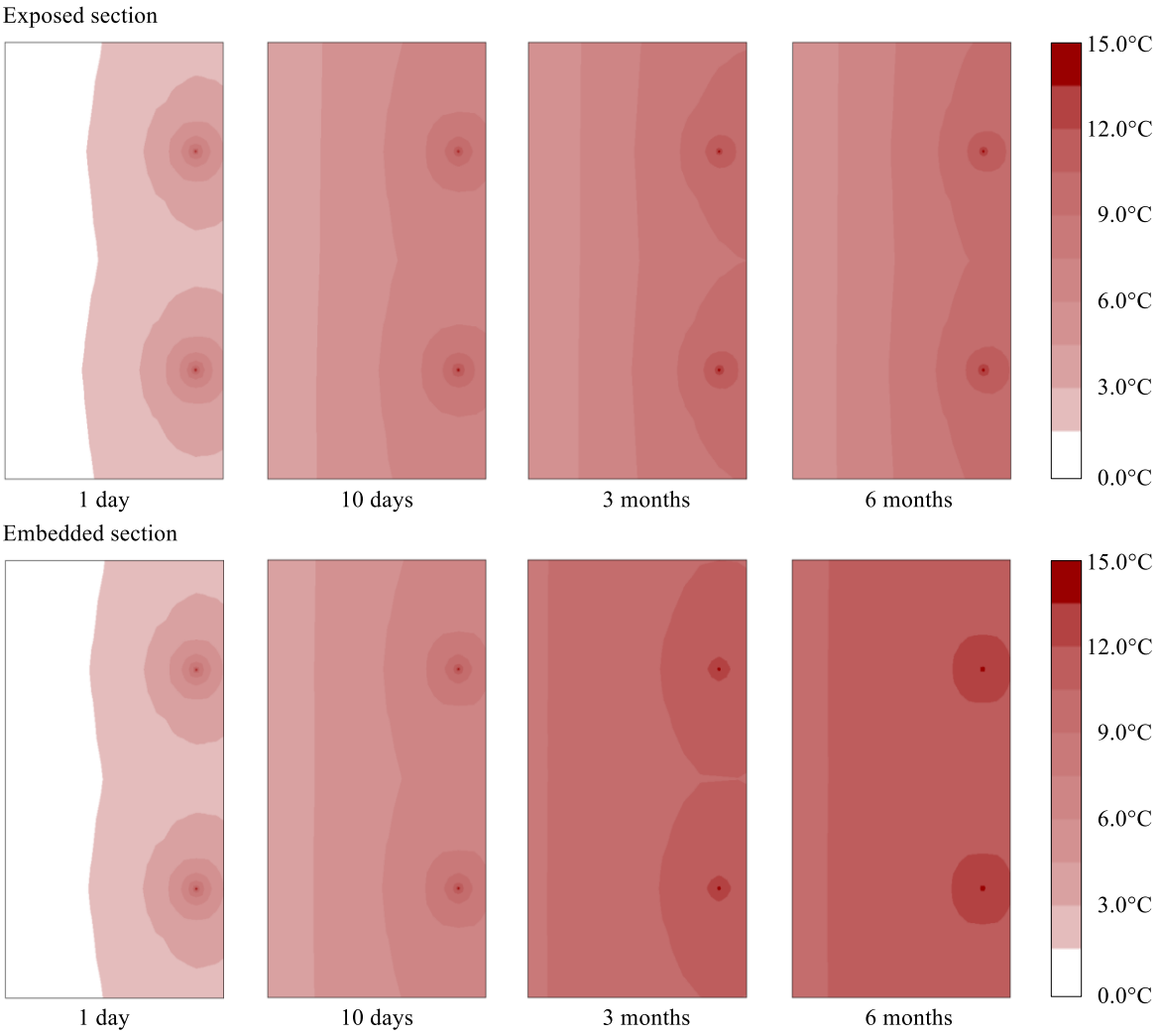

Figure 4-11: Changes in wall temperatures at mid-depth of exposed and embedded sections for CH analysis at different time instants – MA1

The changes in temperature at the depth of the base of excavation (11.0 m depth) with time at different distances behind the wall within the retained side are shown in Figure 4-12 for the three cases. Due to the non-uniform temperatures across the width of the wall, the changes in temperatures are reported as average temperatures along this dimension. Similar to what was observed for the wall temperatures, in the short term, limited differences in the computed temperature changes within the soil are obtained for the three analyses. At the soil-wall interface, after 30 days, the difference between the NF and CT cases is approximately 0.4°C. As time progresses, higher temperatures are recorded for the NF case: at the soil-wall interface, after 6 months, a maximum average temperature change of 12.2°C is evaluated, while this reduces to 11.7°C and 10.8°C for the CH and CT cases, respectively. At greater distances from the wall, the differences between the three analyses are generally smaller and require larger periods of time to appear. At the end of the simulation period, the changes in temperature at 2.5 m behind the wall range from 7.8°C to 9.3°C, for the CT and NF cases, respectively. At a distance of 5.0 m, the difference between the three analyses further reduces with similar temperature changes being recorded for the three different analyses, namely 3.2°C, 2.9°C and 2.7°C, for the NF, CH and CT cases,

respectively. At the soil-wall interface the temperatures in the long term seem to have stabilised, especially for the CT case, indicating that this region is close to steady state, while at larger distances they are clearly still increasing.

It should also be noted that, even though the temperatures within the wall were shown to be non-uniform across the width of the panel, within the soil only marginal changes in the out-of-plane direction (i.e. the y-direction in Figure 4-8) are computed. Indeed, for distances from the wall greater than 1.0 m, negligible differences between the maximum temperature and the average temperature along the y-direction are computed, indicating that the presence of the pipes affects the temperature distributions only for a short distance behind the wall.

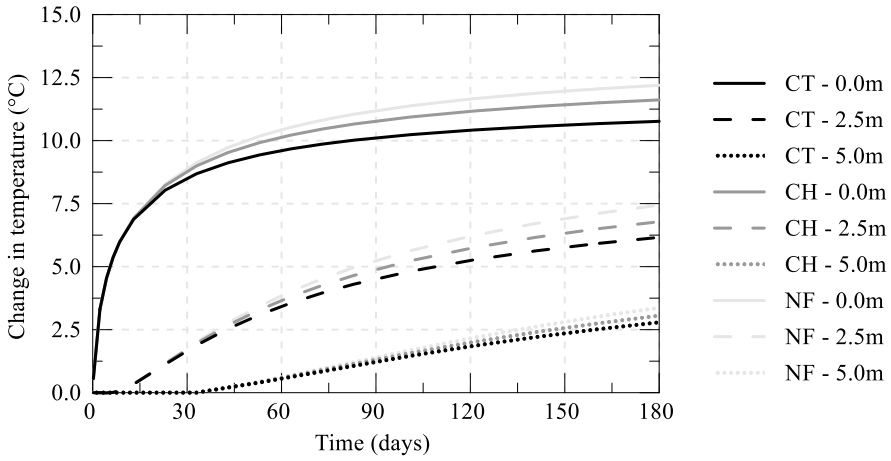

Figure 4-12: Average change in soil temperature with time at 11.0 m depth different distances within retained side – MA1

From the contours displayed in Figure 4-13 the area of influence of temperature changes around the wall can be estimated. While it was shown that generally larger temperatures are computed for the NF case, the overall temperature changes at greater distances from the wall are similar for all the cases. Indeed, these are slightly larger for the NF case only within the upper part of the retained side, while the temperature changes below the toe of the wall and below the excavation are approximately the same for all the analyses. Temperature changes larger than 1.5°C extend up to 8.0 m beyond the wall after 6 months of operation.

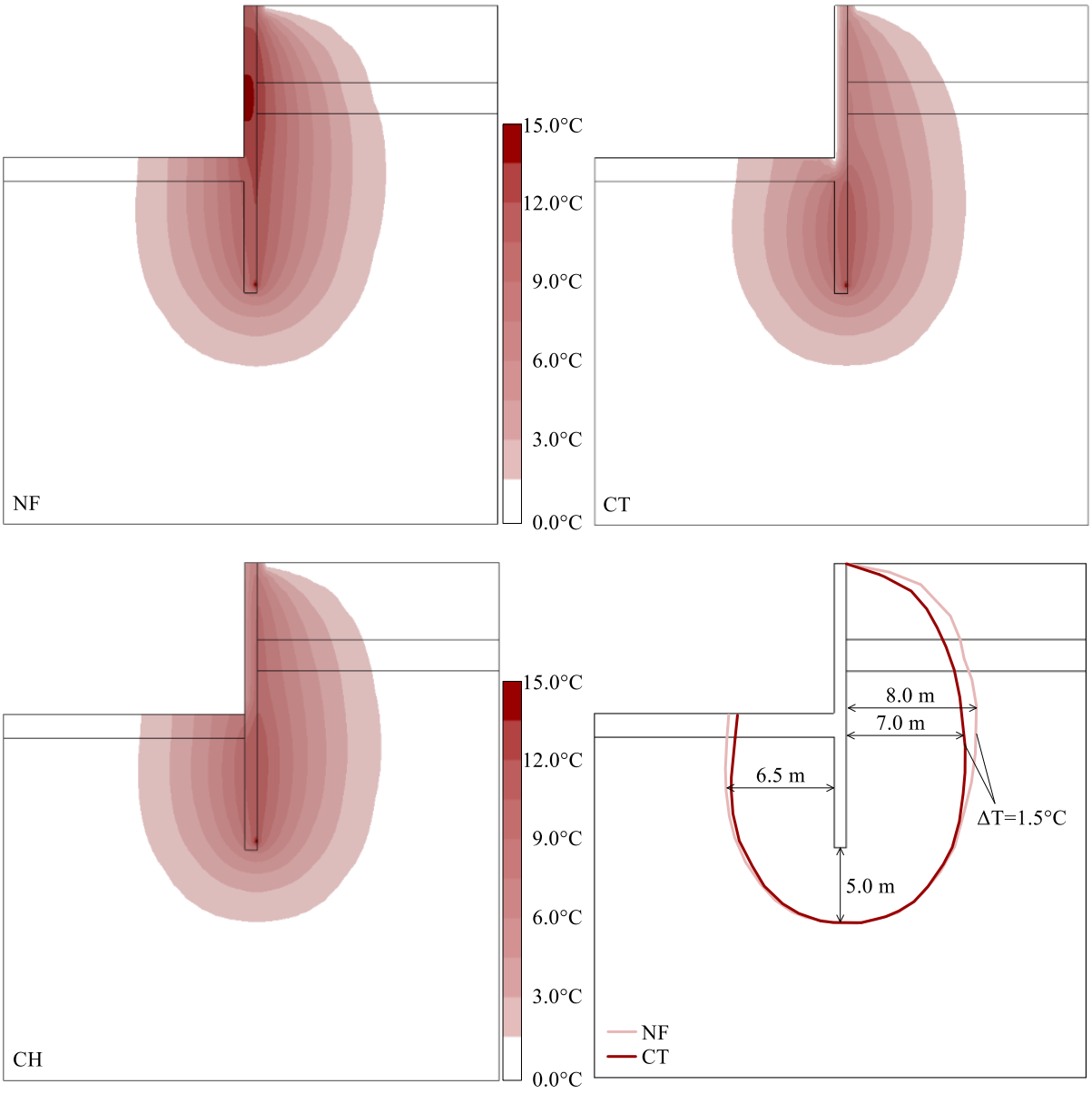

Figure 4-13: Contours of temperature changes after six months for all analyses – MA1

For comparison, the ground temperatures measured by Sterpi et al. (2018) over a two year period are analysed. Details of the case study are outlined in Section 2.4.3, where it should be noted that the system operated in both heating and cooling mode, with a larger demand for heating than cooling. Furthermore, Sterpi et al. (2018) reported that the ground surface was subjected to a natural temperature fluctuation characterised by an average temperature ($\bar{T}$) of 13.4°C and an amplitude (A_T) of 21.5°C. Figure 4-14 plots the temperatures monitored in the ground by sensors AS1 (depth (z) 4.5 m and at a distance (d) of ~0.35 m from the wall) and AS7 (7.5 m depth and 6.0 m from the wall) – refer to Figure 2-30 for details on the monitoring installation. Since the temperatures at superficial depths are influenced by temperature fluctuations at the ground surface, in order to evaluate the effect of the heat exchange on the recorded temperatures, the latter are compared to those obtained using the expression proposed by

Williams & Gold (1976) to estimate the variations in temperature with time (t) and depth (z) in "undisturbed" conditions:

$$T(z,t) = \bar{T} + A_T \cdot exp\left(-z\sqrt{\frac{\pi}{\alpha_T t_c}}\right) cos\left(\frac{2\pi t}{t_c} - z\sqrt{\frac{\pi}{\alpha_T t_c}}\right) \quad (4\text{-}8)$$

where t_c is the duration of a full cycle of temperature, which was equal to 1 year, and α_T is the thermal diffusivity (λ/C_v), calculated from the values reported in Sterpi et al. (2018), i.e. λ=2.2 W/mK and C_v=3170 kJ/m^{3}K. While approximate, the comparison with the temperatures obtained using Equation (4-8) allows the assessment of the impact of the heat exchange on the temperatures within the ground. As expected, the temperature fluctuations at depth calculated with Equation (4-8) within the ground are damped and delayed in comparison to the temperature fluctuations at ground surface. Comparing the monitoring data from the sensor furthest away from the wall (AS7), it can be noticed that small changes in ground temperatures were recorded as a consequence of cooling (i.e. heat injection). As mentioned, the cooling demand was less than the one for heating, and, as shown in Figure 4-14, cooling took place over a shorter operating period when compared to heating. Conversely, heating induced changes in temperature which diverge from the analytical solution by a maximum 1.5°C, with this occurring after the system was already turned off (April), presumably because of the transient heat conduction, which means that changes in temperatures require time to affect the soil at large distances from the wall. The changes in ground temperature closest to the wall (AS1) show a large difference with respect to those associated to undisturbed conditions (i.e. calculated through Equation (4-8)). The operation of the system clearly shifts the time instant of the peak (which is less delayed when compared to the ground surface fluctuation, indicating that it is influenced by the heat extraction in the cold season and by heat injection in the warm season) and leads to a temperature decrease of approximately 8.0°C during the first heating phase (January 2015). Slightly smaller differences are computed during the second heating phase, possibly due to either a more intense cooling operation, which has replenished the ground, or due to a smaller heating demand during the 2016/2017 winter. It should be noted that the inlet temperature in the first heating phase reached values of approximately 2.5°C (i.e. the temperature of the fluid was lower than that of the ground by about $\Delta T_{in} \cong$ 11.0°C) and the calculated average extraction rate was 13.9 W/m^2. This latter value is similar to the heat flux calculated for the CH analysis (see next section). Therefore, while the analyses presented in this section did not aim at reproducing directly the case study presented by Sterpi et al. (2018a), it is worth noting that the computed temperature changes in the ground are very similar to those measured in the field for both distances behind the wall. Hence, the presented results, although obtained by simulating a simple and relatively extreme operation pattern, predict similar thermal response to that observed in a real application.

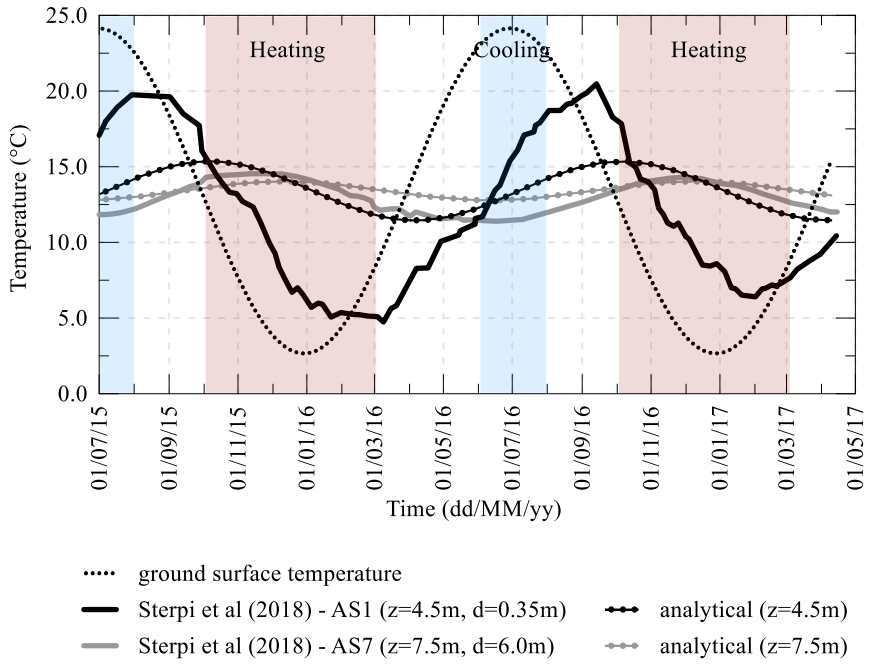

Figure 4-14: Comparison between measured temperatures reported in Sterpi et al. (2018) and those associated to undisturbed conditions calculated with Equation (4-8) from Williams & Gold (1976)

Heat flux

The evolution with time of the heat flux per unit area calculated with Equation (4-5) for the three different boundary conditions is shown in Figure 4-15 (a). In the short term (<10days), a limited effect of the boundary condition is registered because the heat transfer occurs mainly between the heat exchanger pipes and the surrounding concrete, hence no interaction takes place along the exposed boundary. This is confirmed when observing the temperature contours of the wall panel after one day depicted in Figure 4-9 to Figure 4-11, which were shown to be identical for all the cases and did not vary between exposed and embedded sections of the wall. Within this time frame, a high heat flux is calculated for all cases, due to the large temperature difference between the injected heat carrier fluid and the material surrounding the pipe, leading to a large temperature drop across the pipe inlet and outlet (ΔT_p). However, the heat flux rapidly drops as the wall warms up, leading to a reduction in ΔT_p. After approximately 30 days, it starts stabilising, indicating that thermal equilibrium is being reached. This occurs sooner for the CT analysis, due to the close proximity of a boundary that allows heat dissipation (see Figure 3-13 and Equation (A-1) in Appendix A). In the medium to long term, the effect of the adopted boundary condition is clearly noticeable. At the end of the simulation period, i.e. after 6 months, the calculated heat fluxes for the NF, CH and CT conditions are 7.4 W/m^2, 12.7 W/m^2 and 16.2 W/m^2, respectively. Thus, the CT case generates more than twice the heat flux obtained in the NF case. These values are lower than those suggested by Brandl (2006) for preliminary design of thermo-active walls, however they are in line with the ones measured by Sterpi et al. (2020) and Angelotti & Sterpi (2018), and those computed by Di Donna et al. (2017) and Barla et al. (2020). It should also be noted that the values recommended by Brandl (2006) are for fully embedded walls, which may lead to

an overestimation of the energy potential. The difference between the three analyses is a consequence of the increased heat exchange taking place through the wall-air interface with increasing convective heat transfer, h. Indeed, as previously observed, for a wall maintained at a constant temperature ($h = \infty$ W/m^{2}K), the temperature of the exposed part of the wall is lower than the inlet temperature and hence enhances heat transfer. Conversely, for the fully insulated wall (NF), no heat transfer takes place through this boundary and thus the concrete above the excavation level quickly saturates with heat, leading to a decrease in the heat injection rate (see Figure 4-10 for changes in temperature of the wall panel). For the analysis simulating a convective heat transfer coefficient of h = 2.5 W/m^{2}K, the heat flux plots almost exactly in between the two extreme cases. While Bourne-Webb et al. (2016b) indicated that a convective heat transfer, h, of 2.5 W/m^{2}K indicates near-zero air flow and, in their study, it is used as a lower bound for the characterisation of the wall-air interaction, it is highlighted that in the present study, large differences are computed between the CH and NF analyses and that assuming a convective heat transfer, h, of 2.5 W/m^{2}K may not be conservative for walls which present an insulation layer. Additional analyses using a geometry similar to that reported in this section, which are not reported for brevity, have shown that decreasing or increasing h by a factor of 10 (i.e. to 0.25 W/m^{2}K or 25.0 W/m^{2}K) leads to very large changes in the computed heat flux, with the lower value leading to a response similar to that of the NF case, while the higher value resulted in a heat flux very close to the one computed by the CT analysis.

To analyse further the effect of the boundary condition on the exchanged heat, the contributions of the excavated and embedded sections of the wall to the total heat flux are displayed in Figure 4-15 (b). The quantity q_e is calculated as the ratio q_{exp}/q_A or q_{emb}/q_A for the exposed and embedded sections, respectively, where q_A is the total heat flux calculated through Equation (4-5). The heat fluxes generated within the different wall sections are computed with the following equations:

$$q_{exp} = \frac{C_{v,w} v A_p \left(T_{in} - T_{exp,in}\right) + C_{v,w} v A_p (T_{exp,out} - T_{out})}{A_{wall}} \tag{4-9}$$

$$q_{emb} = \frac{C_{v,w} v A_p (T_{exp,in} - T_{exp,out})}{A_{wall}} \tag{4-10}$$

where $T_{exp,in}$ and $T_{exp,out}$ are the temperatures recorded within the pipe at the node corresponding to the level of the top of the base slab, respectively at the inlet and outlet branch of the pipe loop.

It can be observed that, in the short term (i.e. <5 days), the proportion of heat exchange taking place within the exposed and embedded sections of the wall is identical to the ratios of exposed and embedded lengths over the total length (i.e. $q_{exp}/q_A = L_{exp}/L = 0.53$ and $q_{emb}/q_A = L_{emb}/L = 0.47$) for all analyses. This is due to the heat transfer mechanism being characterised during the early stages of operation by the heat transfer between the heat exchanger pipes and the surrounding concrete. Naturally,

in such a situation, the heat transfer will be simply proportional to the area of contact between the pipes and the wall, which are defined, in a normalised manner, by L_{exp}/L and L_{emb}/L. However, as time progresses, the effect of the boundary condition on the heat transfer occurring within the two sections of the wall becomes evident. For the NF case, a larger heat exchange (57% of the total value) takes place within the embedded section, where the heat transfer can take place either side of the structure through the soil. Conversely, for the CT case, the largest proportion of heat transfer takes place within the excavated part of the structure. Indeed, after six months of operation, approximately 68% of the total heat flux in this case occurs within this section of the wall. Similar to the CT case, for the CH case the exposed section contributes substantially to the heat transfer, i.e. to 64% of the total heat flux, which is a just slightly lower proportion than the one computed in the CT case.

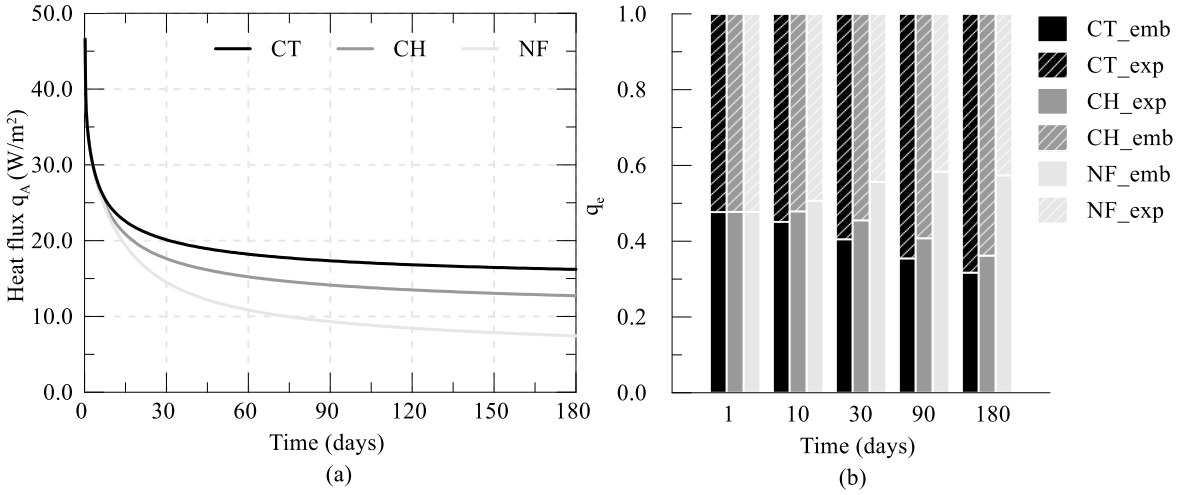

Figure 4-15: Variation with time of (a) heat flux and (b) heat flux ratio q_e – MA1

This aspect is further analysed by plotting the temperatures along the two pipe branches (i.e. inlet and outlet) for two different time instants in Figure 4-16. After 10 days (Figure 4-16 (a)), as expected since a similar heat flux is calculated for all cases, only small differences in the temperatures along the pipe loop are computed for the different analyses. Furthermore, in accordance with Figure 4-15 (b), very limited impact of the boundary condition along the exposed face is observed. Indeed, the rate of change in temperature with distance occurring above and below the top of the base slab (9.5 m depth) is very similar, as can be concluded by the gradient of the line being approximately the same. Conversely, after 6 months (Figure 4-16 (b)), a noticeable difference in the temperature drop along the pipe within the two wall sections is observed, which is especially evident for the CT analysis. For this case, a larger temperature drop is computed within the excavated section, which leads to a larger contribution to the total heat flux, while the opposite is observed for the NF case. From Figure 4-16 it can also be noted that generally the temperature differential between the pipe inlet and outlet (ΔT_p) is less than 1.0°C (a larger difference is recorded only at time instants of <10 days), which is in line with other values found in literature (e.g. Brandl et al., 2010). It should be noted that this temperature difference does not

necessarily represent the temperature difference at the heat pump, since more than one U-loop is typically connected to a heat pump.

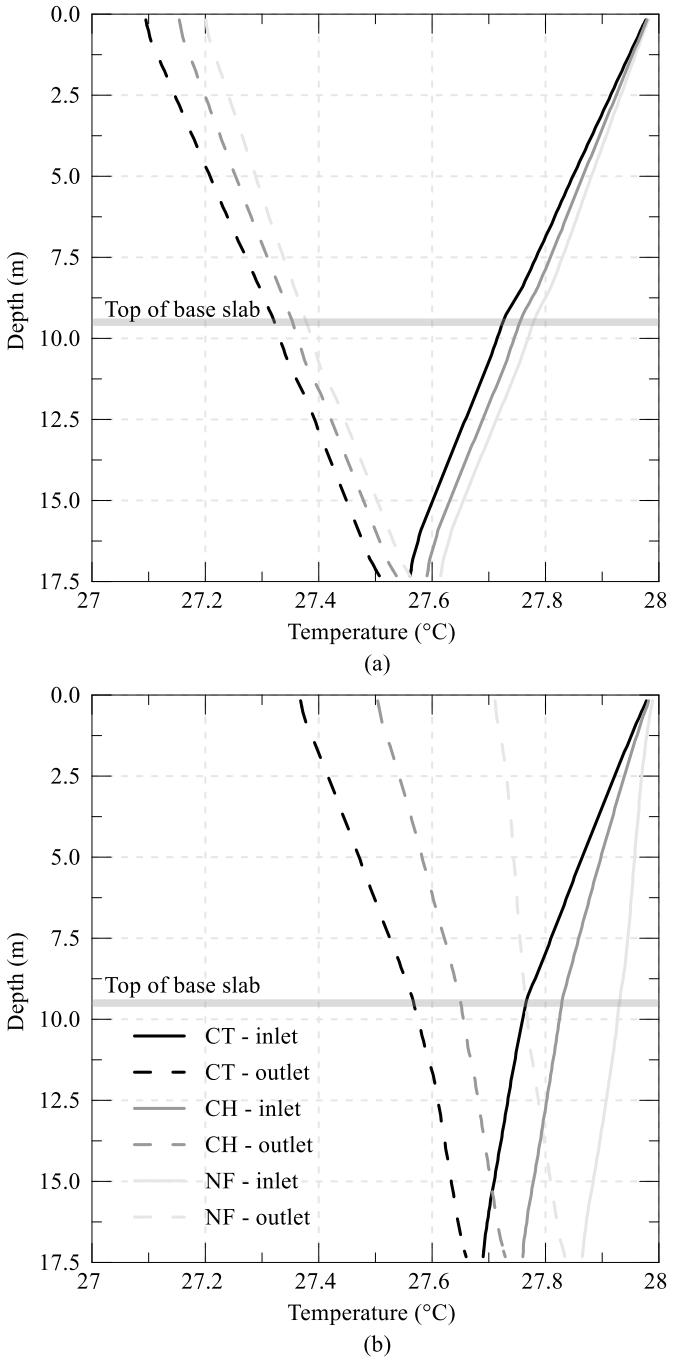

Figure 4-16: Temperature along pipe with depth (a) after 10 days and (b) after 6 months – MA1

Transferred energy

The total energy, E_{tot}, injected by the system calculated through Equation (4-2) and the energy transferred to the materials surrounding the pipes evaluated by summing E_{Ω} computed through Equation (4-6) for all different materials, are plotted in Figure 4-17 (a). The difference between these two quantities can be interpreted as the heat exchange taking place through the boundaries in contact with

the environment and is termed herein "environmental heat exchange" (EHE), which is plotted separately in Figure 4-17 (b). For the NF case, the EHE takes place only at the ground surface where a constant temperature boundary condition is applied since all other boundaries are adiabatic, while for the CT and CH analyses this occurs also along the exposed face of the wall. It should be noted that the values reported in Figure 4-17 are normalised by the width in the out-of-plane direction (B).

As expected, given the calculated heat flux, the lowest amount of injected energy is calculated for the NF analysis and the largest for the CT analysis. The total amount of energy injected after 6 months of operation is equal to 890 kWh/m, 1220 kWh/m and 1450 kWh/m, for the NF, CH and CT cases, respectively. It can also be noted that, while the energy is increasing at almost the same rate throughout the operation period for the latter two analyses, the NF case displays a clear reduction in the rate of injected energy with time. This is because of the constant increase in temperature within the wall due to the insulated boundary, which prevents any heat transfer at the wall-air interface, thus reducing the potential for transferring energy. As a consequence, the difference between the energy injected and the one exchanged with the environment (Figure 4-17 (b)) is very limited, indicating that little interaction takes place through the ground surface. Furthermore, the EHE starts occurring at later stage in comparison to the other two analyses, meaning that heat transfer towards the ground surface commences only once a considerable amount of energy has been transferred to the soil.

Conversely, the steady increase in energy observed in the CT case and similarly, but with a slightly lower rate, for the CH case, is due to the interaction with the boundary condition at the wall-air interface, which increases the heat transfer. Indeed, from the difference between the injected and transferred energies (see Figure 4-17 (b)), it can be concluded that a large part of the injected energy is converted into EHE, i.e. the heat transfer taking place through the wall-air interface, confirming the previous observations.

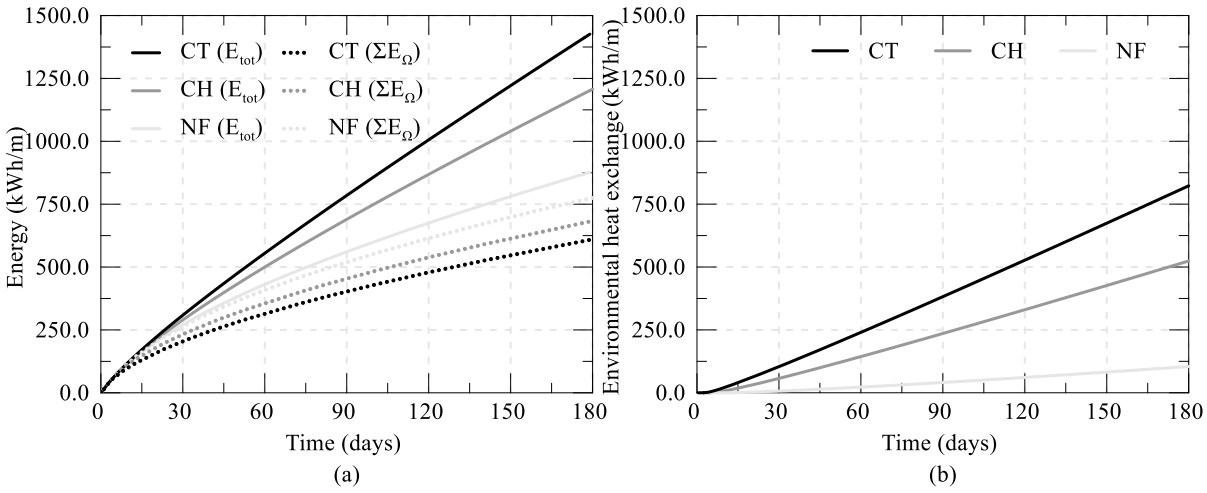

Figure 4-17: Variation of energy with time (a) total exchanged (E_{tot}/B) and transferred energy ($\Sigma E_{\Omega}/B$) with time and (b) environmental heat exchange – MA1

This aspect can be observed in more detail in Figure 4-18, which shows the percentage of energy transferred to the concrete wall and base slab, soils and the boundaries in contact with the environment (i.e. EHE). In the short term, similar results are computed for all the analyses and most of the heat transfer occurs within the wall, i.e. the concrete is subjected to the largest temperature changes. As time progresses, more heat is transferred to the soil, where, in relative terms, a larger amount is transferred to the London Clay, since most of the structure is in contact with this material. In the first month, almost no interaction with the boundaries in contact with the environment is computed for the NF analysis, while its effect is clear for the CT and CH analyses already after 10 days of operation, where it contributes to 21% and 9% of the total energy, respectively. At the end of the analysis, for the CT case, most of the energy (58%) is transferred through the boundaries at constant temperature, while 41% is transferred to the soil (where 30% to London Clay) and only 7% to the concrete structures. Conversely, for the NF analysis, 69% of the total energy is transferred to the soil, 21% to the concrete structures and 12% through the ground surface. The CH case behaves similar to the CT case, with slightly less heat transfer through the boundaries at constant temperature (44%), which is compensated by a larger temperature increase of the soil and concrete structures, to which respectively 46% and 11% of the energy is transferred.

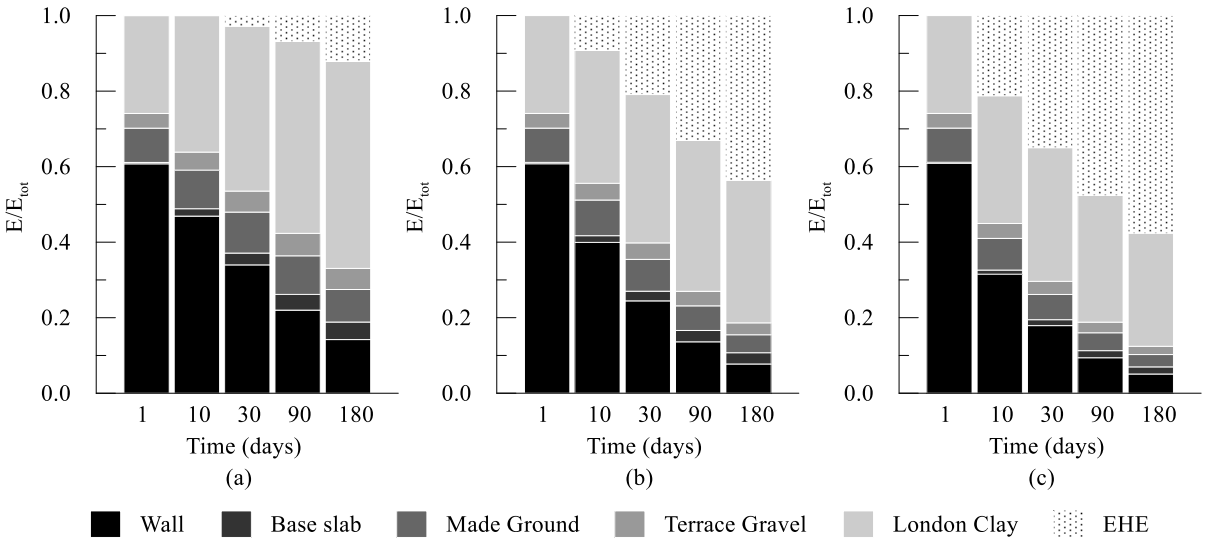

Figure 4-18: Percentage of energy transferred to different materials at different time instants (a) NF, (b) CH and (c) CT – MA1

4.4.3.2 Comparison with Modelling approach 2

Heat flux

When adopting MA2, firstly the value of the heat flux boundary condition has to be determined. As described in Section 4.3.3, this is evaluated iteratively until the target change in temperature at the pipe inlet, ΔT_{in}, is obtained. In this case, a ΔT_{in} of 15°C at the inlet pipe was set as target to enable a direct comparison with MA1. This resulted in the following values of the heat flux boundary condition for the three analysed cases: 0.244 kW (insulated wall, NF), 0.447 kW (constant temperature, CT) and 0.361 kW (convective heat transfer, CH).

As previously seen for MA1, the CT case is the most thermally efficient. It is therefore unsurprising that the largest heat flux boundary condition was determined for this case. Indeed, the power required to reach a ΔT_{in} of 15°C at the inlet pipe for the CT case is 1.8 and 1.2 times larger than the ones required to achieve the same ΔT_{in} for the NF and CH cases, respectively, due to the larger potential of exchanging energy through the wall-air interface.

Since the applied power is constant, the calculated heat flux, q_A, is also constant with time and yields values of 8.8 W/m^2, 13.2 W/m^2 and 16.2 W/m^2 for the NF, CH and CT analyses, respectively, as depicted in Figure 4-19 (a). As expected, these values are very similar to the long-term heat flux evaluated with MA1, as detailed in Table 4-3. Figure 4-19 (b) shows the percentage of heat flux deriving from the exposed and embedded sections of the wall (q_e), as calculated through Equations (4-9) and (4-10), which are very similar to those evaluated using MA1. Indeed, in the long term, the proportion of heat transfer occurring through the exposed section of the wall reaches values of 42%, 61% and 67% for the NF, CH and CT cases, respectively. Thus, it is evident that the adopted modelling approach does

not affect the simulated heat transfer mechanism from the wall to the surrounding materials, nor the interaction along the exposed face.

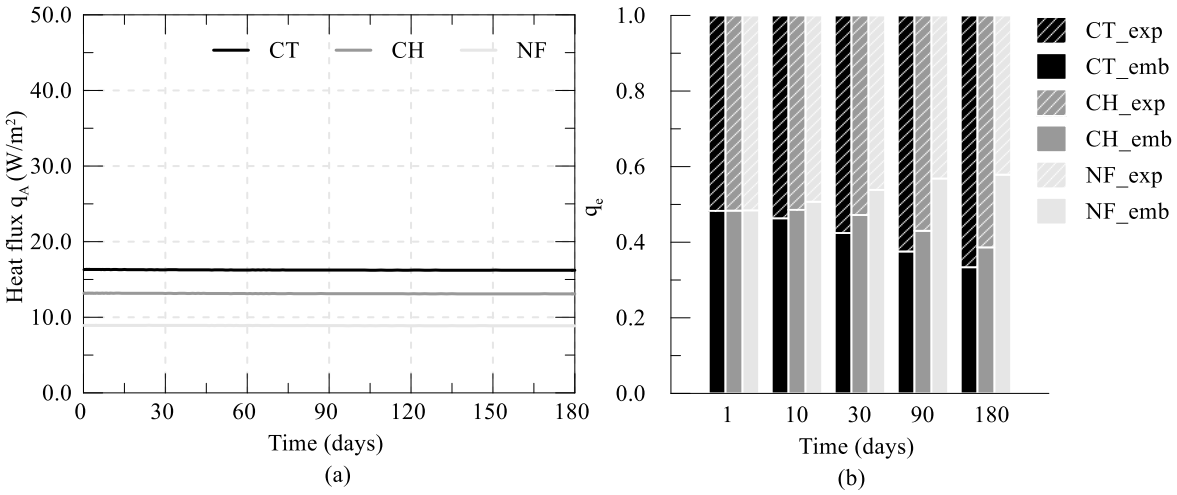

Figure 4-19: Variation with time of (a) heat flux and (b) heat flux ratio q_e – MA2

Table 4-3: Comparison between heat flux obtained with different modelling approaches

Analysis	Heat flux q_A after 6 months – MA1 (W/m²)	Heat flux q_A after 6 months – MA2 (W/m²)
NF	7.4	8.8
CH	12.7	13.2
CT	16.2	16.2

Figure 4-20 depicts the computed temperatures at the pipe inlet and outlet with time. Given the different magnitudes of the heat flux boundary conditions, different initial temperatures are computed for the three cases, with the lowest being evaluated for the NF case. It can be seen that the transient behaviour of the three cases is very different, with the rate of increase in temperature reducing much faster for the CT and CH cases than for the NF case. This is due to the insulated boundary along the wall-air interface preventing any heat loss. Clearly, given the values of applied power, which controls the temperature jump between the inlet and the outlet (ΔT_p), the smallest is obtained for the NF case (0.35°C), while larger values were determined for the CH and CT analyses (0.52°C and 0.64°C, respectively).

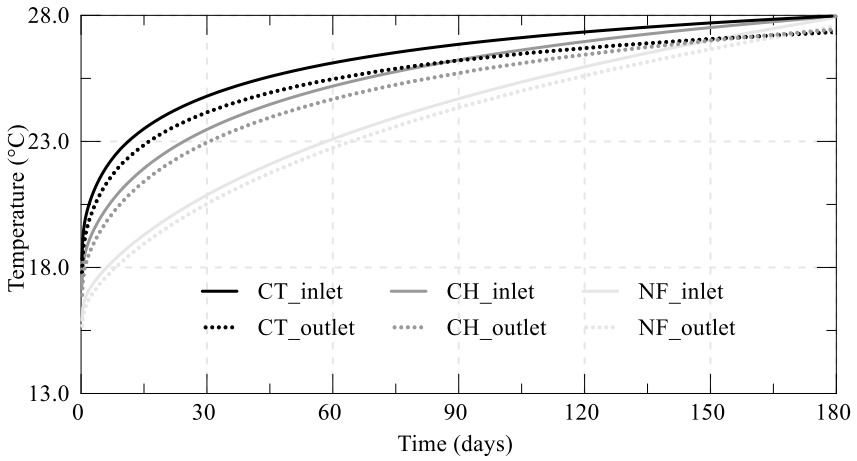

Figure 4-20: Temperatures at pipe inlet and outlet with time – MA2

Temperature changes

The temperature variations within the pipes with time and boundary condition obviously also affect the distributions of temperatures within the wall. Indeed, observing Figure 4-21, Figure 4-22 and Figure 4-23, the impact of the boundary condition is evident. Within the wall panel, in the short term, no difference is recorded between the exposed and embedded sections for any of the analyses, but clearly larger temperature changes are evaluated for the CT case. For this analysis, the average change in temperature of the wall after 1 day of operation is equal to 1.0°C, while smaller changes are recorded for the NF and CH cases, which are, respectively, 55% and 80% of that evaluated for the CT case. At the end of the simulation period, the average temperature change of the wall panel in the NF analysis increases to 11.4°C, and results to be 5.5°C and 3.0°C higher than that computed for the CT and CH analyses. Clearly, the evolution of temperature changes with time is very different when the two modelling approaches are compared (i.e. Figure 4-9, Figure 4-10 and Figure 4-11 for MA1 compared respectively to Figure 4-21, Figure 4-22 and Figure 4-23 for MA2). However, the temperatures within the wall in the long term obtained by the two approaches are very similar (less than 0.5°C difference, with those evaluated with MA1 being higher), as expected, given that the value of the heat flux boundary condition in MA2 was determined to achieve an inlet temperature value in the long term identical to that used in MA1.

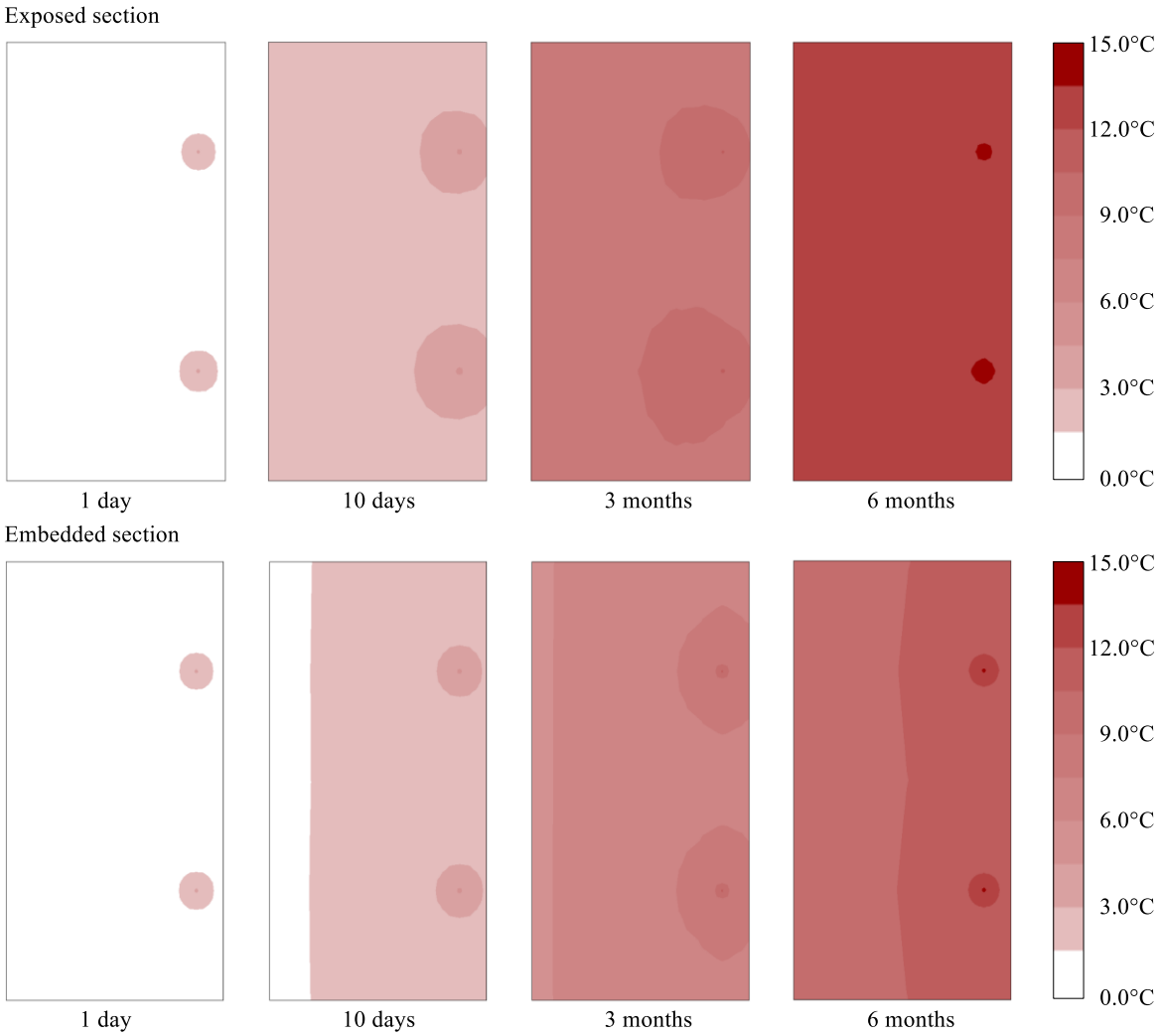

Figure 4-21: Changes in wall temperatures at mid-depth of exposed and embedded sections for NF analysis at different time instants – MA2

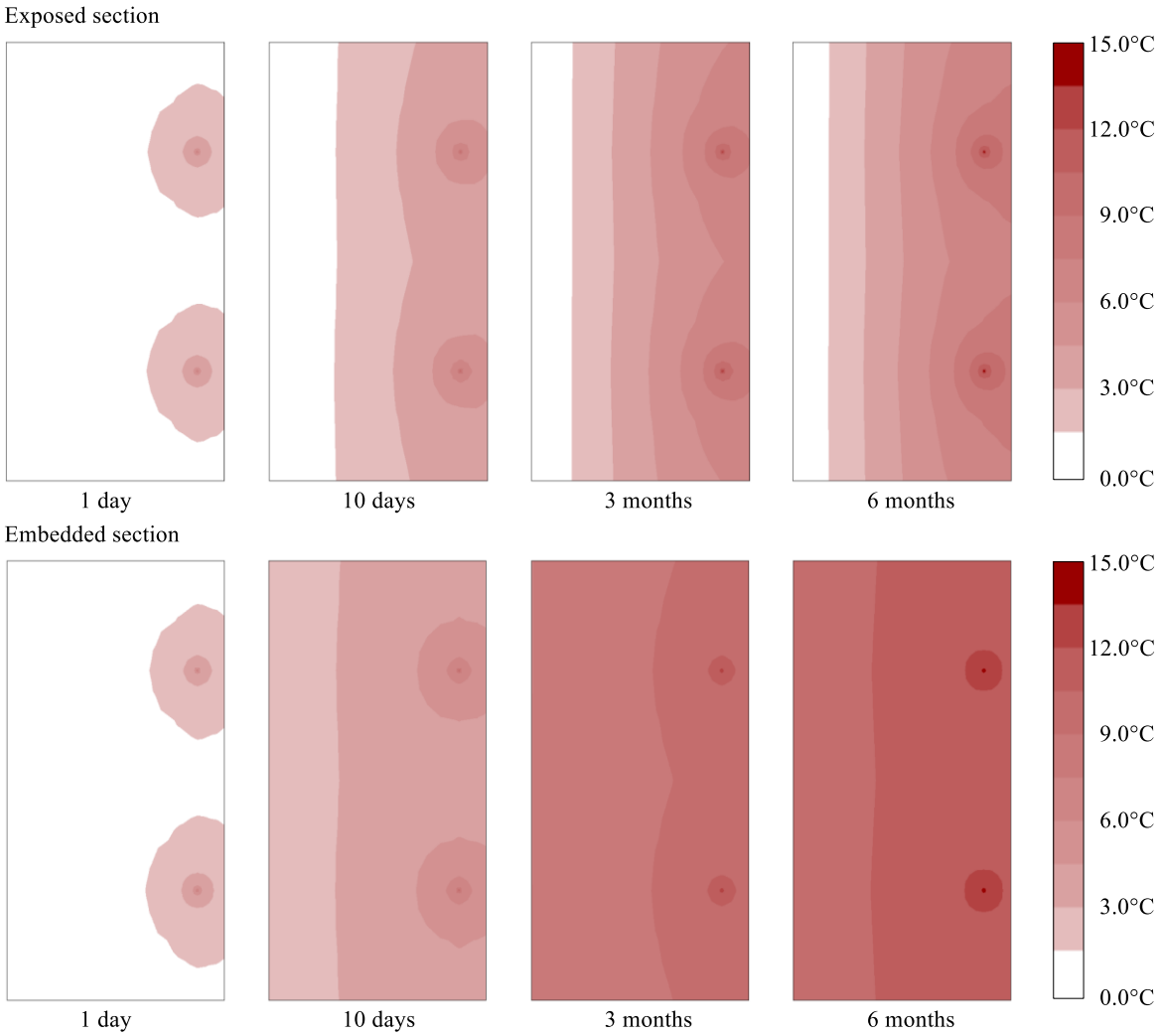

Figure 4-22: Changes in wall temperatures at mid-depth of exposed and embedded sections for CT analysis at different time instants – MA2

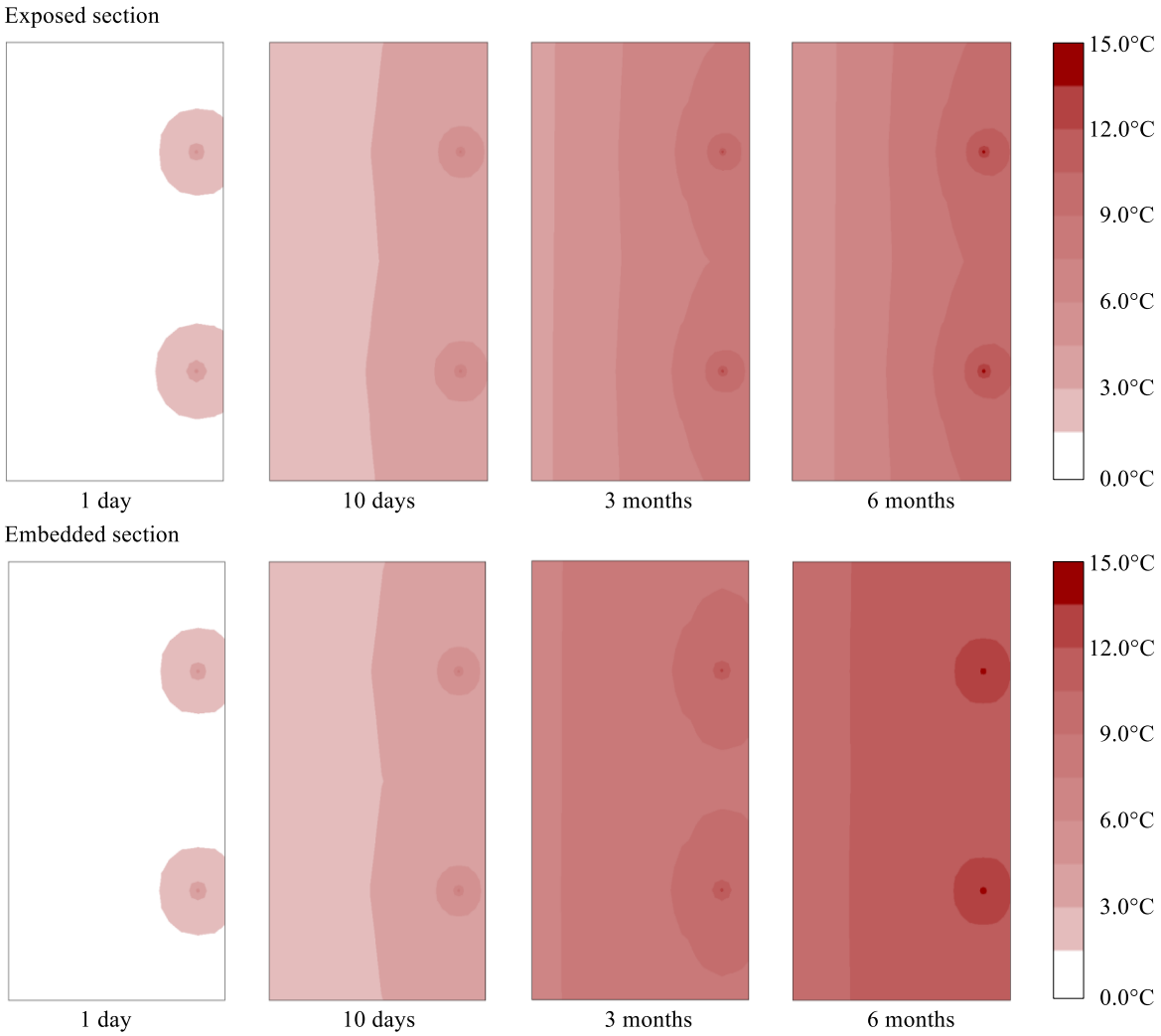

Figure 4-23: Changes in wall temperatures at mid-depth of exposed and embedded sections for CH analysis at different time instants – MA2

Figure 4-24 shows the average temperature change with time at a depth of 11.0 m within the soil at different distances from the wall within the retained side.

Larger temperature changes are recorded for the CT analysis for the majority of the simulation period. The temperature differences between the three analyses tend to increase with time until approximately 1 month of operation, after which they decrease and eventually the NF analysis displays larger temperatures when compared to the other two cases. Indeed, it can be noted from Figure 4-24 that, similar to the temperatures within the pipes, the rate of temperature increase with time for the NF analysis does not reduce as much with time as for the CT and CH cases. At the end of the simulation period, the temperature at the soil-wall interface for the NF case is 0.2°C and 0.65°C larger than for the CH and CT analyses, respectively.

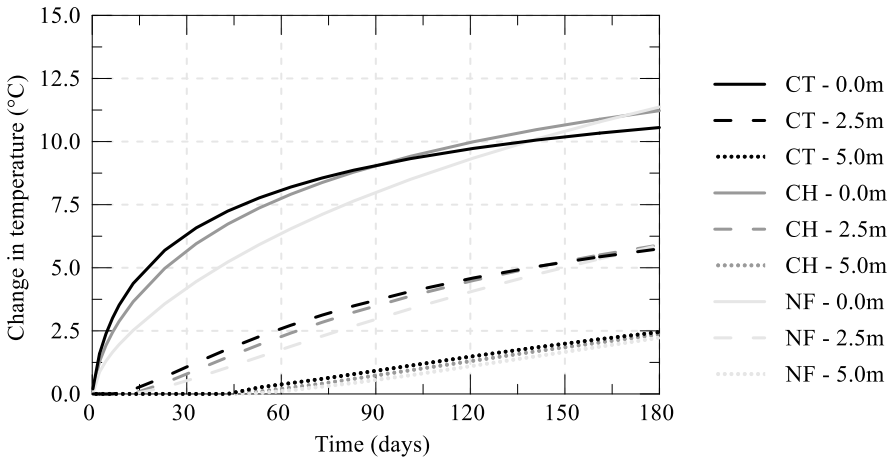

Figure 4-24: Average change in soil temperature with time at depth of 11.0m for different distances within retained side – MA2

Figure 4-25 (a) and (b) provide a comparison between the temperatures evaluated with the two modelling approaches, respectively at the soil-wall interface and at a distance of 2.5 m. It is evident that the transient temperature changes are very different for the two approaches, with those computed with MA1 displaying initially a more rapid increase with time. However, the long-term temperature changes are quite similar, with differences increasing with distance from the wall, due to the slower heat transfer rate in MA2. The largest differences are computed for the NF case and are equal to 1.5°C. This is similar to what was observed by Gawecka et al. (2017) in the simulation of thermo-active piles with constant temperature and heat flux boundary condition.

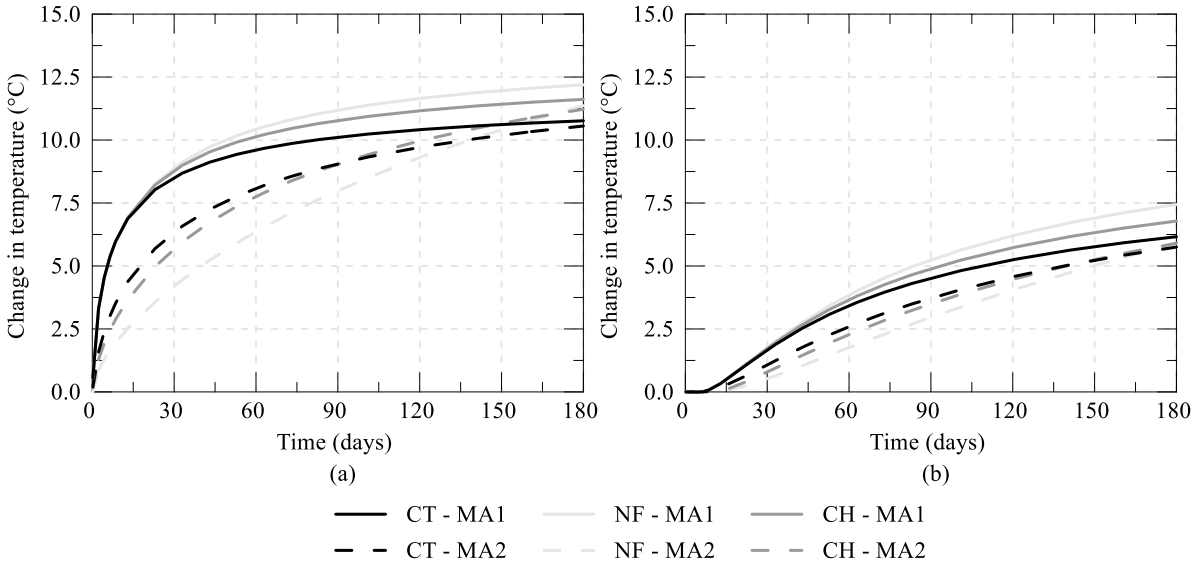

Figure 4-25: Comparison of changes in ground temperature for different modelling approaches at a depth of 11.0 m (a) soil-wall interface and (b) 2.5 m behind wall

Energy

The total energy injected into the system and the one transferred to the materials surrounding the pipes is depicted in Figure 4-26 (a), while Figure 4-26 (b) shows the environmental heat exchange, all

normalised by the width of the wall. As can be seen, the injected energy, for all cases, varies linearly with time. Indeed, its slope represents the magnitude of the applied heat flux boundary condition.

Similar temperature changes clearly indicate that approximately the same energy is being injected into the system using both modelling approaches. When comparing this quantity – displayed in Figure 4-17 and Figure 4-26 for MA1 and MA2, respectively – similar values are computed. The maximum difference is approximately 200 kWh/m (see Table 4-4), which is attributed to the larger amount of energy transferred in the short term in MA1 (this is clearly observed when comparing the heat fluxes in Figure 4-15 and Figure 4-19). However, as was also noted previously when analysing the heat flux, the modelling approach does not affect the heat transfer mechanisms, with the effects of the boundary condition along the exposed face of the wall and thus the environmental heat exchange (EHE) being similar for both sets of analyses. Equally, the heat transfer rates above and below the excavation, as well as the amount of energy stored in the various materials in contact with the heat exchanger pipes are not affected by the modelling approach. This is confirmed when observing Figure 4-27, which shows the percentages of energy transferred to the various materials at different time instants, where the values are almost identical to those computed with MA1.

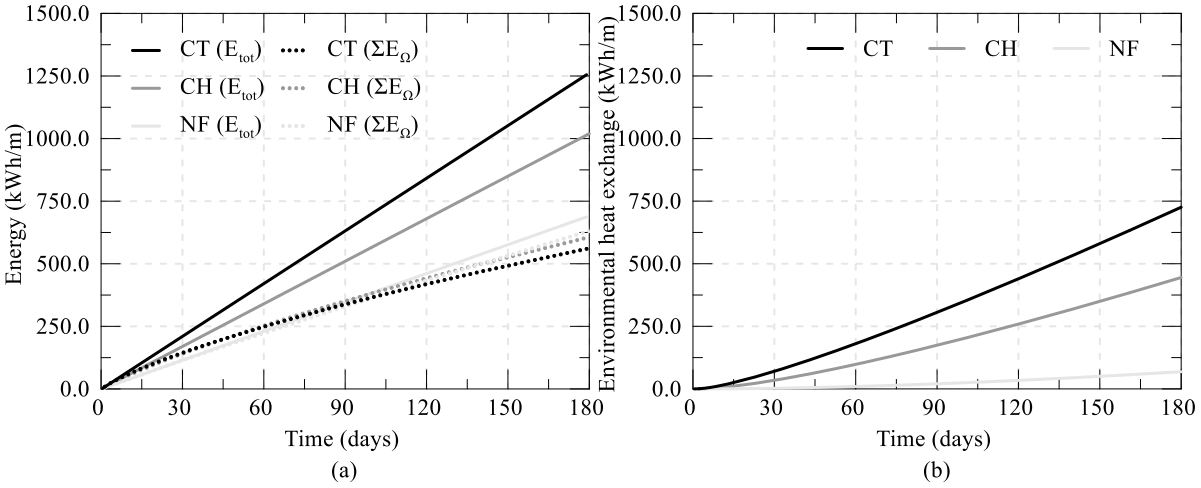

Figure 4-26: Variation of energy with time (a) total exchanged (E_{tot}/B) and transferred energy ($\Sigma E_{\Omega}/B$) with time and (b) environmental heat exchange

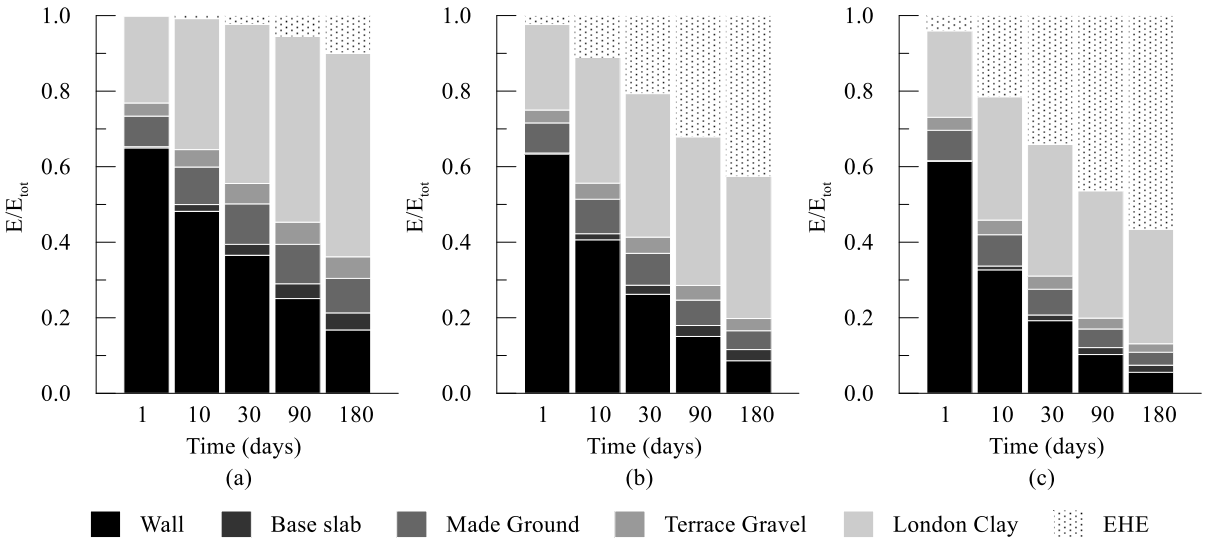

Figure 4-27: Percentage of energy transferred to different materials at different time instants (a) NF, (b) CH and (c) CT – MA2

Table 4-4: Comparison of total transferred energy per unit width for different modelling approaches

Analysis	Energy E_{tot}/B – MA1 (kWh/m)	Energy E_{tot}/B – MA2 (kWh/m)
NF	890	700
CH	1220	1050
CT	1450	1300

4.5 Summary and conclusions

The heat transfer occurring within thermo-active walls for different boundary conditions along the exposed face and their effect on the thermal performance was analysed by simulating a reference case. This was modelled adopting two different modelling approaches: the first modelling approach (MA1) consists of specifying the inlet temperature, with the heat flux being calculated based on the computed outlet temperature; the second modelling approach (MA2) introduces the presence of a heat pump, which is modelled with a nodal heat flux boundary condition, the magnitude of which is determined by setting a target change in temperature at the pipe inlet.

In the first part of this chapter, the two modelling approaches are outlined and validated by reproducing two field tests reported in Xia et al. (2012). While the data provided by Xia et al. (2012) were sufficient to simulate the problem adopting MA1, the input for MA2, namely the value of the heat flux boundary condition, had to be back-calculated. A very good agreement between the measured data and the computed results for both modelling approaches was obtained, with slightly larger discrepancies being observed for MA2. This is particularly noteworthy when considering the substantial uncertainties regarding the simulated field test, namely in terms of initial conditions and material properties. Thus,

this validation exercise demonstrates the suitability for thermo-active retaining wall problems of the modelling approach proposed by Gawecka et al. (2020). Indeed, it was shown that the inclusion of the thermally enhanced material (TEM) surrounding the heat exchanger pipes noticeably improves the results by increasing the accuracy with which the heat transfer from one-dimensional elements, which are not capable of reproducing the correct contact area between heat exchanger pipes and concrete, is simulated. Without the inclusion of the TEM, larger discrepancies between the field data are observed, with higher temperatures within the heat exchanger pipes being calculated, leading to a lower heat flux and hence underestimating considerably the heat transfer between the heat exchanger pipes and the surrounding concrete. Lastly, it is also highlighted that mesh effects on temperature distributions can be quite significant and may affect greatly the results.

Subsequently, a reference case was simulated, consisting of an 18.0 m long, 0.8m thick and 1.5 m wide wall panel embedded in a ground profile typical of the conditions found in the London basin. A U-shaped pipe loop is assumed to be installed within the wall panel, where water flows at a constant velocity. The heat transfer mechanisms for thermo-active walls are analysed for three cases, which differ in the boundary conditions applied along the exposed face of the wall, simulating different interactions at the wall-air interface: (1) an insulated wall (NF), (2) a wall maintained at constant temperature (CT) and (3) a wall surface having a convective heat transfer (CH), h, of 2.5 W/m^{2}K. It should be noted that the first two cases present extreme scenarios, representing surfaces with a convective heat transfer, h, of 0.0 and ∞ W/m^{2}K, respectively. The problem was simulated employing both modelling approaches, where the temperature change at the pipe inlet applied in MA1 (ΔT_{in}=15°C), was adopted as the target temperature change at the pipe inlet in MA2. For all the cases, the temperature changes within the wall panel and the soil, the calculated heat flux and energy were analysed. For these analyses, the TEM was not included, since it was shown by Gawecka et al. (2020) that, for a single pipe, the effect of the TEM reduces in the long term; this was confirmed herein by the results reported in Appendix F, where it was concluded that the TEM negligibly affects the heat transfer within thermo-active walls in the long term.

The boundary condition along the exposed part of the wall affects the temperature distributions within the wall and the soil and the heat transfer mechanism. The results obtained employing MA1 showed that the calculated heat flux ranges between 7.8 W/m^2 and 16.2 W/m^2, for the NF and CT cases, respectively. These values are in line with those found in literature (e.g. Sterpi et al., 2018). Comparing the analyses with different boundary conditions along the exposed part, the following conclusions can be drawn:

- for an insulated wall (NF), where no heat transfer is allowed through the wall-air interface, higher temperatures develop within the exposed section of the wall with respect to the other two cases, which consequently leads to a lower heat transfer rate and, hence, injected energy. A large

contribution to the total heat flux (57%) is provided by the embedded section of the wall, where the heat can dissipate towards the soil from both sides of the wall. Moreover, the ground temperatures are higher and consequently, a large part of the energy is transferred to the materials surrounding the wall (69% to soil and 21% to concrete structures), with very little energy being dissipated to the environment;

- for walls in contact with an environment at constant temperature (CT), smaller wall and ground temperatures are recorded. This is due to the imposed boundary condition along the exposed face, which allows heat to be dissipated. This also leads to a larger heat flux, which is 50% larger than that computed for an NF condition, with the majority (68%) being generated within the exposed section of the wall. Consequently, a larger transferred energy is evaluated for this case, with a large proportion being lost through the boundaries at constant temperature;
- the wall simulated with a wall-air interaction characterised by a convective heat transfer coefficient of 2.5 W/m^{2}K (CH) displays an intermediate behaviour with respect to the two extreme cases, both in terms of changes in temperature and computed heat flux. For this case, even though the heat transfer from the wall to the environment occurs with some resistance, a large proportion of the total heat flux (64%) occurs within the exposed section of the wall.

Similar conclusions can be drawn when analysing thermo-active walls simulated using MA2. Indeed, the calculated long-term heat flux and energy, the heat transfer mechanisms above and below the excavation as well as the long-term changes in ground temperature were similar for the two approaches. However, some differences between the two modelling approaches are observed:

- the variations in time of the pipe temperatures for MA1 are characterised by a constant inlet temperature, which is imposed, with the outlet temperature changing with time. Conversely, for MA2 the inlet and outlet temperatures both increase with time, while the temperature differential across them (ΔT_p), and hence the heat flux, remains constant. These depend on the value of the applied heat flux boundary condition, which varies considerably based on the boundary condition adopted along the exposed face of the wall;
- the wall temperatures for MA1 are equal for all cases in the short term, with the effect of the boundary condition being noticeable after 10 days of operation. However, for MA2, the temperatures within the wall are affected by the boundary condition from the beginning of the analysis since they are directly related to the heat flux boundary condition, and are thus initially highest for a wall exposed to a constant temperature boundary condition;
- the ground temperatures for MA1 are larger for the NF case and generally, close to the wall, the temperatures increase very quickly and eventually stabilise. A similar trend is observed for the changes in ground temperature further away from the wall, though with a time delay. For MA2, similar to the temperature within the pipes, the increase in ground temperature is more gradual with

time and initially higher temperatures are computed for the CT case, while at the end of the operation period higher temperature changes are recorded for the NF case;

- for MA1 the variation with time of the energy injected with time is considerably more non-linear, due to the heat flux changing with time. For MA2, the injected energy increases linearly with time, with its gradient representing the value of the heat flux boundary condition. The energy transferred during 6 months, as well as the energy exchanged through the boundaries maintained at constant temperature, is similar for the two approaches.

In summary, this study has shown that two different modelling approaches, but with similar assumptions, lead to comparable results. Furthermore, it highlights the importance of characterising the interaction mechanism between the wall and the environment to which it is exposed, since the thermal performance is largely affected by this aspect.

Chapter 5
Estimating the thermal performance in two-dimensional analyses

5.1 Introduction

As was shown in the previous chapter, the presence of heat exchanger pipes at discrete positions within a wall panel implies that these problems are inherently three-dimensional, leading to non-uniform temperature distributions across the width of the panel. However, performing long-term simulations of thermo-active walls by means of three-dimensional (3D) analyses is computationally very expensive. Indeed, the dimensions of the FE model (and hence the number of degrees of freedom) are generally large due to the problem's geometry (size of structure and width of excavation) and minimum distances from the mesh boundaries required to avoid any influence on the results when long-term simulations are performed. Thus, in this chapter, approximations designed to enable the modelling of thermo-active retaining wall problems in two-dimensional (2D) plane-strain analyses are proposed, which allow the computational effort to be reduced substantially, whilst providing an excellent estimation of the energy performance.

The 3D to 2D approximation procedures have been developed considering U-shaped pipe loops placed towards the retained side (which is a common configuration employed in practice, e.g. Amis et al. (2010)) and were established for both no flux (NF) and constant temperature (CT) boundary conditions along the exposed face of the wall, since it was shown in the previous chapter that these are the two extreme scenarios characterising the wall-air interaction. Chapter 4 detailed two different modelling approaches to simulate thermo-active walls, which were named modelling approach 1 (MA1) and modelling approach 2 (MA2). These two approaches differ in the boundary conditions applied to simulate the heat exchange. However, it was shown that the heat transfer mechanisms and energy

potential were marginally affected by the employed approach. Within this chapter, focus is given to the 2D approximations adopting MA1, while a briefer assessment of 2D analyses performed with MA2 being carried out. After detailing and validating the approximation procedures for modelling thermo-active walls in 2D plane-strain analyses, an extensive parametric study is carried out to outline the influence of different factors on the thermal performance. Lastly, long-term analyses are performed to assess the energy efficiency and changes in ground temperature after multiple cycles of operation. Parts of the contents described in this chapter were published in Sailer et al. (2019c).

5.2 Approximations for modelling the thermal performance in two-dimensional analyses

Within this section, approximations to model the thermal performance of thermo-active walls in 2D plane-strain analyses are proposed and their effectiveness is evaluated by comparing the results to those obtained in equivalent 3D analyses. Firstly, the reduction of a 3D thermo-active wall problem to a 2D plane-strain problem is conceptually explained. Subsequently, the necessary approximations for a correct evaluation of the thermal performance are outlined when MA1 is adopted, where different design criteria are assessed. Lastly, analyses are carried out in 2D using MA2 and the comparison to 3D analyses is assessed. In Chapter 4 it was highlighted that the boundary condition along the exposed face of the wall noticeably affects the heat transfer. Consequently, the proposed approximations have been developed considering both insulated walls (NF) and walls exposed to an environment at constant temperature (CT).

5.2.1 Simulating heat exchange in two-dimensional plane-strain analyses

Figure 5-1 and Figure 5-2 schematically represent a thermo-active wall problem simulated in 3D and respective 2D plane-strain analysis for MA1 and 2, respectively. In a 2D analysis, the heat exchanger pipes are simulated using one-dimensional elements to replicate water flow and the advection-dominated heat transfer taking place within the pipes (Cui et al., 2018b), where these correspond to a 1.0 m-wide region of a plane. Due to the adopted geometric simplification, the inlet is now positioned at the top of the wall, whereas the outlet is located at the bottom of the wall, where the water is removed from the mesh. For MA1, a prescribed temperature is applied at the pipe inlet, while the thermo-hydraulic boundary condition is applied at the pipe outlet (see Figure 5-1). For MA2, as depicted in Figure 5-2, two protruding pipe elements are added at the top and bottom of the wall for the application of the boundary conditions. The heat flux boundary condition is applied at the middle of the protruding pipe element at the top of the wall (position Q in Figure 5-2 (b)), while the temperature degrees of freedom are tied between the top and bottom nodes of the one-dimensional pipe element (i.e. between points A and D in Figure 5-2 (b)). Care should be taken not to connect the bottom protruding pipe

element to any thermally active node within the finite element mesh to avoid thermal interactions that will alter the results.

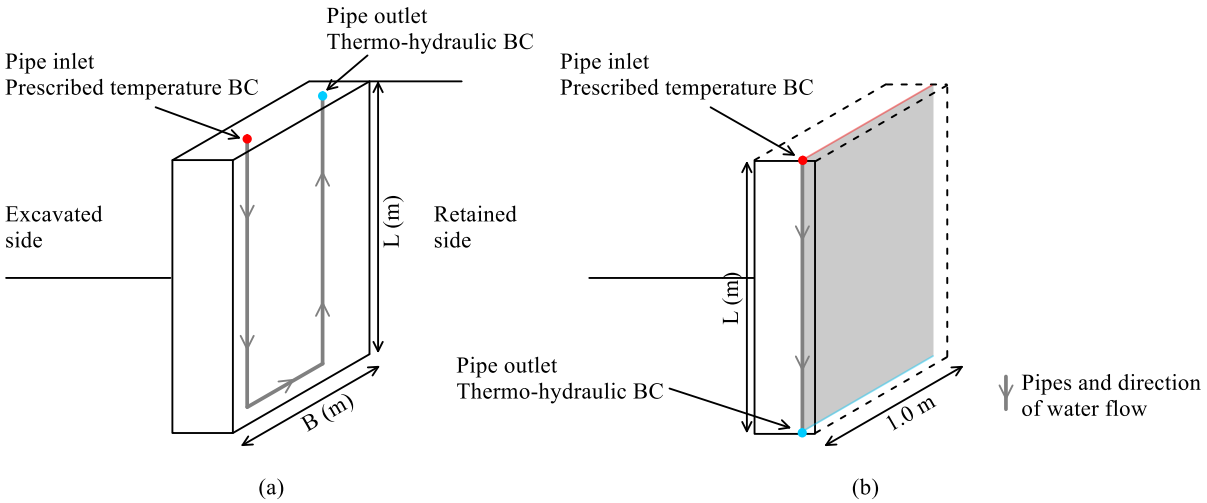

Figure 5-1: Schematic representation of thermo-active wall problem for modelling approach 1 (a) 3D analysis and (b) 2D plane-strain analysis

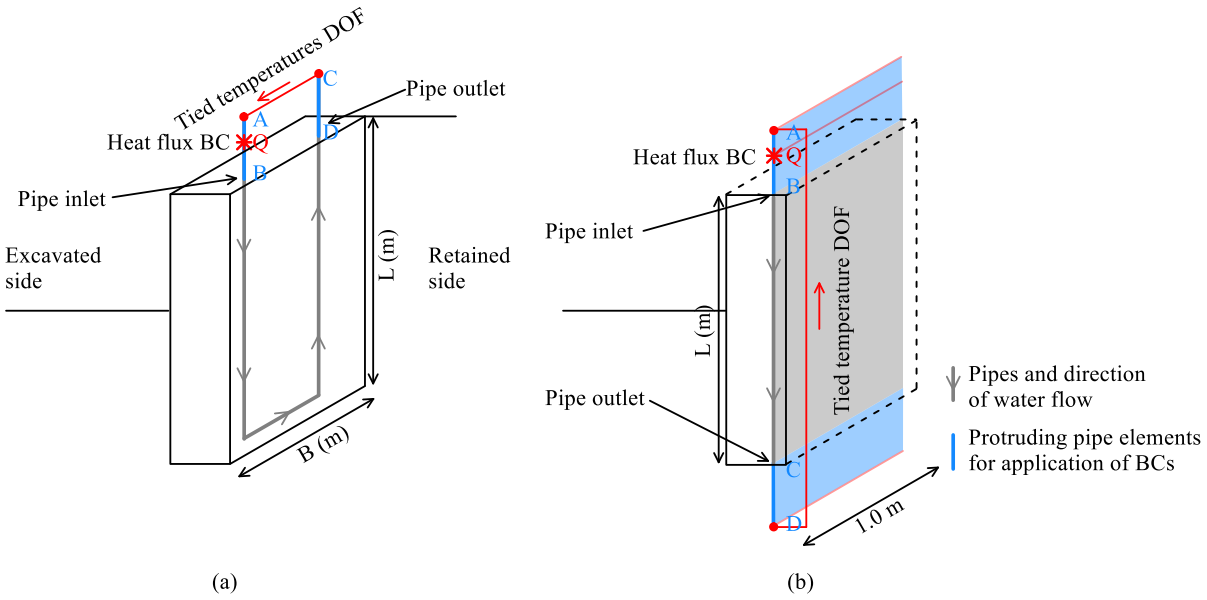

Figure 5-2: Schematic representation of thermo-active wall problem for modelling approach 2 (a) 3D analysis and (b) 2D plane-strain analysis

Clearly, a 3D analysis is able to simulate accurately the geometric configuration of the pipes within a panel. Conversely, as schematically represented in plan view in Figure 5-3, in a 2D plane-strain analysis the pipes are modelled as a continuous "wall" of water flowing within a unit width in the out-of-plane direction. The following aspects should be considered when modelling thermo-active walls in a 2D plane-strain analysis:

(1) The simulation of a continuous pipe element in the out-of-plane direction means that in a 2D plane-strain analysis there is a larger contact area between the pipe and the surrounding medium, which thus accelerates the heat transfer;
(2) The heat transfer between the heat exchanger pipe and surrounding medium is predominantly radial in a 3D analysis, leading to non-uniform temperatures within the wall panel in the out-of-plane direction (see Chapter 4); this aspect cannot be reproduced in 2D, where the heat transfer is merely planar (see Figure 5-3);
(3) The 3D effects will be less significant when a larger number of pipes is simulated within a panel (i.e. when the spacing between the pipes is smaller), since the conditions become closer to those simulated in a 2D plane-strain analysis.

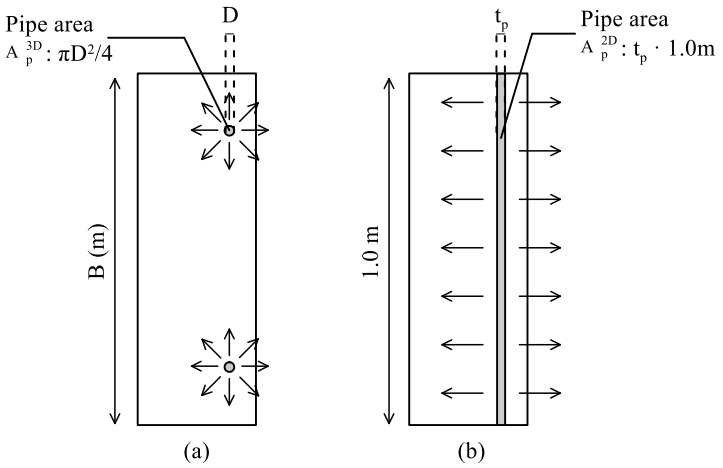

Figure 5-3: Schematic representation of simulations of a thermo-active retaining wall in plan view (a) in a 3D analysis and (b) in a 2D plane-strain analysis

To take into account the simplifications implied by the plane-strain assumptions, corrections are needed for an adequate modelling of the heat transfer in 2D. The corrections depend on the adopted modelling approach in 3D (i.e. MA1 or MA2, as described in Chapter 4) and on the design criterion the 2D approximation is required to meet. Indeed, when defining the 2D approximations in this study, the ability to reproduce several aspects of a thermo-active retaining wall problem are considered:

(1) estimation of long-term heat flux, thus providing an indication of the long-term energy potential where the 2D analysis is able to replicate the 3D behaviour at, or close to, thermal steady state;
(2) quantification of the energy transferred during a period of operation, thus taking into account also the transient development of the heat exchanged between the wall and the ground;
(3) assessment of the temperature changes within the ground.

For this purpose, the 2D approximations are validated by comparing the heat flux per unit area of wall, q_A (W/m^2, Equation (4-5)), or the energy per unit width $E_{tot,B}$ (kWh/m, Equation (4-2) normalised by the width of the panel, B), to those computed using 3D analyses. It should be noted that two geometric quantities used to calculate these quantities have different meanings in 3D and 2D:

(1) A_p, the cross-sectional area of the pipe (m^2) – as outlined in Figure 5-3, in 3D this is equal to the actual cross-sectional area of the heat exchanger pipe (i.e. $A_p = \pi D^2/4$), whereas in 2D it is calculated as the thickness of the pipe element (t_p) multiplied by the width of the region in the out-of-plane direction (1.0 m);

(2) B, the width of the wall panel (m) – in 3D, this is the actual width of the panel, while for a plane-strain analysis, the width in the out-of-plane direction is 1.0 m. This parameter is also used in the calculation of the area of the wall panel, A_{wall}=$L \cdot B$ (m^2), where L is the length of the wall, implying that this quantity also has differing meanings in 2D and 3D analyses.

5.2.2 Performed analyses

The wall geometry described in Chapter 4 is considered as the reference case to evaluate the performance of the proposed 2D approximations. Thus, an 18.0 m long, 0.8 m thick and 1.5 m wide wall panel and an excavation depth of 9.5 m is considered, with material properties for soil and concrete equal to those outlined in Chapter 4, Table 4-2. As outlined in Table 5-1, further analyses are performed varying the geometric configuration of the wall and heat exchanger pipes, in terms of the width of the wall (B) and the number of vertical pipe segments forming the pipe loop (n_p), thus changing the spacing between pipes (B/n_p). Furthermore, the depth of excavation (or, equally, the exposed length of the wall (i.e. L_{exp})) and thermal parameters (i.e. thermal conductivity of concrete (λ_c) and soil (λ_s)), were varied. It should be noted that $\overline{\lambda_s}$ in Table 5-1 denotes the weighted average of the soil thermal conductivity of the material in contact with the wall on the retained side, where for analyses IX to XII, the thermal conductivities of all the soil layers were halved or doubled with respect to those employed in the reference analysis (see Table 4-2). For all analyses listed in Table 5-1, it was assumed that the pipes have an inner diameter of 20.4 mm, form a U-shaped loop and are placed 0.1 m from the concrete edge on the soil side. For the analyses with n_p = 4, it was assumed that two U-loop exists within the panel, with the vertical pipe segments connected with horizontal ones, thus only one inlet and one outlet exist (see Figure 5-4; this configuration is also similar to that studied in Sterpi et al. (2017) and Barla et al. (2020) since in thermo-active retaining walls it is common to install one pipe loop per panel). The water flow velocity within the pipes was equal to 0.5 m/s.

Table 5-1: List of analyses for validation of 2D approximations

Analysis	L_{exp} (m)	B (m)	n_p (-)	λ_c (W/mK)	$\overline{\lambda_s}$ (W/mK)	$\Delta T_{in,3D}$ (*) (°C)
Ref	9.5	1.5	2	1.6	1.62	15°C
I	9.5	1.5	2	1.6	1.62	20°C
II	4.8	1.5	2	1.6	1.62	15°C
III	15.0	1.5	2	1.6	1.62	15°C
IV	9.5	1.5	4	1.6	1.62	15°C
V	15.0	1.5	4	1.6	1.62	15°C
VI	9.5	0.75	4	1.6	1.62	15°C
VII	9.5	1.5	2	2.4	1.62	15°C
VIII	9.5	1.5	2	1.2	1.62	15°C
IX	9.5	1.5	2	1.6	3.23	15°C
X	9.5	1.5	2	1.6	0.81	15°C
XI	9.5	1.5	4	1.6	3.23	15°C
XII	9.5	1.5	4	1.6	0.81	15°C

(*) temperature difference applied in MA1 – target temperature difference for MA2

The finite element mesh for the 3D and 2D analyses is depicted in Figure 5-4 (a) and (b), respectively. In order to obtain comparable results, both meshes present the same dimensions (boundaries located 15.0 m either side of the wall) and refinement, where the 2D mesh is identical to the one used in the 3D mesh on the plane containing the pipe. For the 2D analyses, soil and concrete structures were modelled with four-noded quadrilateral solid elements with temperature degrees of freedom at each node. The heat exchanger pipes were modelled with two-noded one-dimensional elements (Cui et al., 2018b), where each node presents both temperature and fluid pressure degrees of freedom. To guarantee numerical stability within the pipes, the Petrov-Galerkin finite element method (Cui et al., 2018c) was adopted.

Similar to the analyses described in Chapter 4, the simulation period was six months and a continuous operation mode was assumed. Equally, the same initial and boundary conditions were simulated, i.e. initial temperature, T_0, of 13°C, ground surface maintained at constant temperature equal to the initial temperature and no heat flux across all the other boundaries. Along the exposed face, either a no flux (NF) or a constant temperature (CT) boundary condition equal to T_0 was applied. For the 3D analyses, as outlined in Table 5-1, the temperature applied at the pipe inlet for MA1 was 28°C (i.e. $\Delta T_{in,3D}$ = 15°C) for all cases except analysis I where an inlet temperature of 33°C (i.e. $\Delta T_{in,3D}$ = 20°C) was specified. Regarding the 2D analyses, the values of the boundary conditions employed in the simulation

of the heat transfer are detailed in separate sections as they differ according to the proposed approximation.

It should be noted that, as discussed in Chapter 4 and demonstrated in Appendix F, the effect of the TEM for 3D analyses is significantly less relevant in the long term than observed in the validation example shown in Section 4.3.4. Moreover, and perhaps unsurprisingly given the larger area of contact, it does not appear to affect the results in 2D. Furthermore, not including the TEM leads to conservative results in terms of thermal performance, while the long-term temperature changes at greater distances from the wall are only very marginally affected. For these reasons, it has not been included in the 3D analyses employed to derive the approximations for modelling these problems in 2D plane-strain analyses.

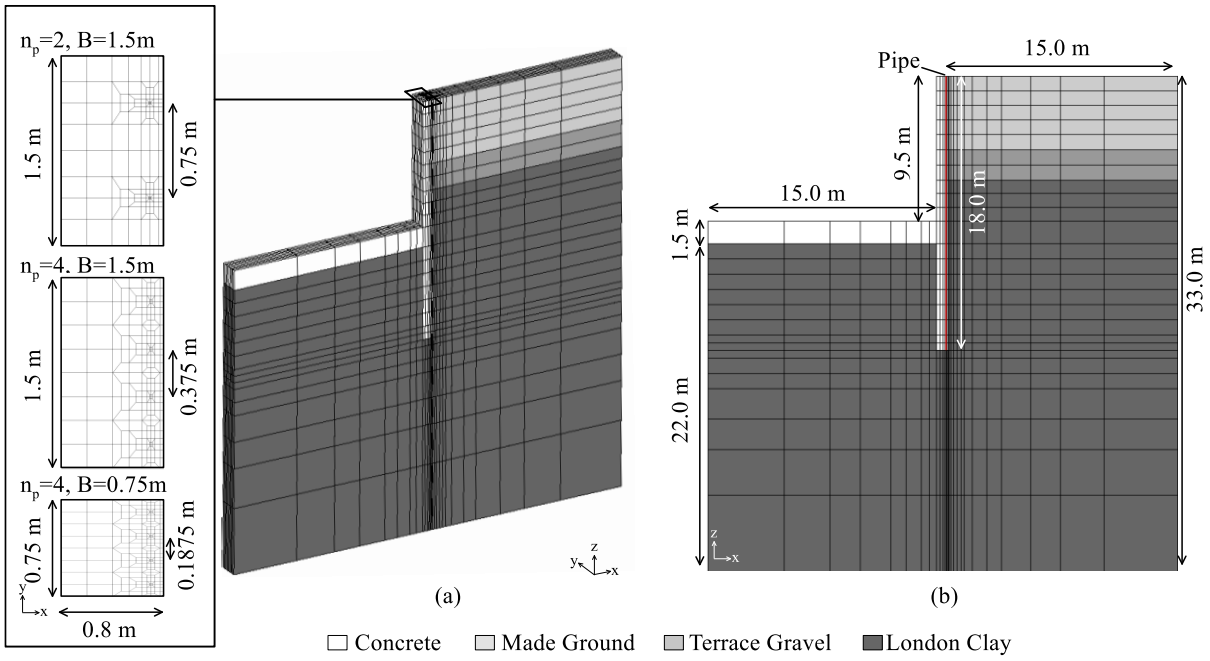

Figure 5-4: Finite element mesh with L_{exp} = 9.5 m (a) 3D analysis and (b) 2D analysis

5.2.3 Approximations for modelling approach 1

In the following, the approximations to model thermo-active walls using MA1, i.e. applying a prescribed temperature boundary condition at the pipe inlet (see Figure 5-1), are outlined. The design criteria considered when developing the approximations are the long-term heat flux per unit area (q_A) and the amount of transferred energy per unit width ($E_{tot,B}$) during an operation period. Lastly, the temperature changes in the ground are evaluated.

5.2.3.1 Approximation for equivalent energy input

As previously outlined, in a 2D analysis it is not possible to simulate the existence of a finite number of pipes within each wall panel. Hence, in order to model the same energy being introduced in 3D and equivalent 2D analyses, it must be ensured that the fluid flow rate (Q_w) per unit width of wall is the

same in both simulations. This applies to any 2D analysis including heat exchanger pipes and, thus, this conversion procedure is required for both MA1 and MA2.

The following equations can be used to calculate the fluid flow rate (Q_w) per unit width of wall in 3D and 2D:

$$\frac{Q_w^{3D}}{B} = \overline{A_p^{3D}} v \tag{5-1}$$

$$\frac{Q_w^{2D}}{1.0m} = \overline{A_p^{2D}} v \tag{5-2}$$

where Q_w^{3D} and Q_w^{2D} are the fluid flow rates (m^3/s) in 3D and 2D, respectively, B is the width of the panel in 3D (m), v is the water flow velocity (m/s), and $\overline{A_p^{3D}}$ and $\overline{A_p^{2D}}$ are the cross-sectional area of pipes per unit width (m^2/m) in 3D and 2D, respectively. Considering that the 3D problem presents U-shaped loops, $\overline{A_p^{3D}}$ is calculated as:

$$\overline{A_p^{3D}} = \frac{A_p^{3D} n_p}{B} = \frac{(\pi D^2/4)\, n_p}{B} \tag{5-3}$$

where A_p^{3D} is the cross-sectional area of a pipe in 3D (m^2) and n_p is the number of vertical pipe segments in 3D (-).

In 2D, as depicted in Figure 5-3, the pipe is represented as a continuous "wall" in the out-of-plane direction of thickness t_p (m) and width of 1.0 m, and thus $\overline{A_p^{2D}}$ is equal to:

$$\overline{A_p^{2D}} = \frac{A_p^{2D}}{1.0m} = \frac{t_p 1.0m}{1.0m} \tag{5-4}$$

Based on the expressions for $\overline{A_p^{3D}}$ and $\overline{A_p^{2D}}$, to ensure the same water flow rate per unit width of wall is simulated in 3D and 2D, Equations (5-1) and Equation (5-2) are rearranged, leading to:

$$\frac{Q_w^{3D}}{B} = \frac{Q_w^{2D}}{1.0m} \Rightarrow \left(\frac{A_p^{3D} n_p}{B}\right) v = \left(\frac{A_p^{2D}}{1.0m}\right) v \tag{5-5}$$

Adopting the same water flow velocity (v) in 3D and 2D, Equation (5-5) can be rearranged into an expression for the calculation of the cross-sectional area of the pipe in the 2D analysis, A_p^{2D}, which ensures that the same fluid flow rate per unit width is simulated:

$$A_p^{2D} = \frac{A_p^{3D} n_p}{B} \cdot 1.0m \tag{5-6}$$

It should be noted that this procedure neglects any horizontal pipe segments that connect the vertical portions of the pipes. This is considered to have a negligible effect on the results, since the heat transfer

occurring along these short pipe sections is very small compared to the heat exchange taking place along the vertical sections of the loop (see, for example, Figure 4-16).

Analyses

With a pipe area in 3D, A_p^{3D}, of 3.27×10^{-4} m^2, the water flow rate per unit width, Q_w^{3D}/B, for a wall panel of width of 1.5 m is equal to 2.18×10^{-4} m^3/s/m and to 4.36×10^{-4} m^3/s/m, respectively for n_p = 2 and n_p = 4. For a wall panel of 0.75 m in width and with 4 pipes (analysis VI), it is equal to 8.72×10^{-4} m^3/s/m.

According to Equation (5-6), to achieve the same water flow rate per unit width in the 2D analyses, the cross-sectional area assigned to the pipe elements within the 2D analyses, A_p^{2D}, has to be modified depending on the number of pipes (n_p) and the width of the panel (B) simulated in the 3D analysis. For the analyses listed in Table 5-1, the areas of the pipes employed in the 2D analyses are reported in Table 5-2.

Firstly, for all the analyses, the same inlet temperature employed in the 3D analyses (i.e. 28°C or 33°C for analysis I) is applied. Based on the long-term heat fluxes obtained in 3D and 2D, the capabilities of this approximation are assessed for the two boundary conditions applied along the exposed face, i.e. simulating an insulated wall (NF) or a wall maintained at a constant temperature (CT) equal to the initial temperature T_0.

Table 5-2: Area of pipe in 2D analysis for equivalent energy input

Analysis	B (m)	n_p (-)	A_p^{2D} (m^2)
Ref	1.5	2	4.36×10^{-4}
I	1.5	2	4.36×10^{-4}
II	1.5	2	4.36×10^{-4}
III	1.5	2	4.36×10^{-4}
IV	1.5	4	8.72×10^{-4}
V	1.5	4	8.72×10^{-4}
VI	0.75	4	1.74×10^{-3}
VII	1.5	2	4.36×10^{-4}
VIII	1.5	2	4.36×10^{-4}
IX	1.5	2	4.36×10^{-4}
X	1.5	2	4.36×10^{-4}
XI	1.5	4	8.72×10^{-4}
XII	1.5	4	8.72×10^{-4}

Results

The heat fluxes computed for the reference case in 3D and respective 2D analyses, for both boundary condition on the exposed face of the wall (NF and CT), are compared in Figure 5-5 (a), while in Figure 5-5 (b) the development of the relative and absolute errors with time are shown. For both scenarios, the 2D analysis simulates a larger heat exchange in the short term (<10 days), due to the effects of the plane-strain assumptions, i.e. the larger contact area between pipe and concrete enhances the heat transfer at the beginning of the analysis. This leads to large errors during the initial stage of the analysis, which exceed 100 W/m^2 at the very beginning of the simulation. However, for the NF case, these reduce rapidly with time and, after 10 days, the heat flux obtained in 2D is larger than the one calculated in 3D by 5.9 W/m^2, which corresponds to a relative error of 26%. After 30 days of operation, the difference between 3D and 2D has further reduced to 0.9 W/m^2 (6.2%), while after 6 months of operation it is limited to only 0.4 W/m^2 (5%), with the 2D analysis predicting a larger heat flux.

A different scenario is observed for the CT case, where the 2D analysis significantly overestimates the heat transfer in 3D throughout the whole simulation period. Indeed, after an initial reduction in the short term, after 6 months, the 2D analysis still overestimates the heat flux in 3D by approximately 10 W/m^2, i.e. 60%. This large error is considered to be due to the geometric simplification implied by the plane-strain assumption. Indeed, as was shown in the previous chapter, for insulated walls the heat transfer takes place mainly through the wall-soil interface, since no heat exchange can occur through the wall-air boundary. This latter aspect leads to high and uniform temperatures within the wall panel in the long term (refer to Section 4.4.3), and therefore conditions similar to those simulated in 2D develop. Conversely, for structures exposed to an environment maintained at constant temperature (CT), the heat transfer takes place mainly through the wall-air interface. This implies that: (1) larger 3D effects arise from greater non-uniform temperature changes across the width of the wall in 3D (see Figure 4-10) and (2) a 2D plane-strain analysis enhances the wall-air interaction due to a larger contact area between the pipe and the structure, leading to an increase in the exchanged heat.

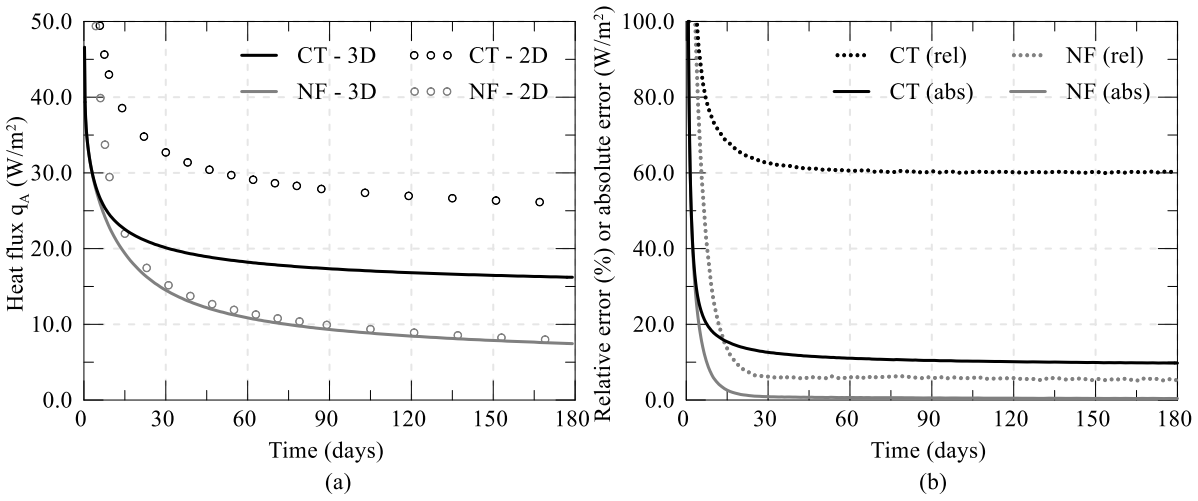

Figure 5-5: Comparison between 3D and 2D analyses for reference case with NF and CT boundary condition on the exposed face of the wall with approximation for equivalent energy input (a) heat flux with time and (b) relative and absolute error with time

Figure 5-6 compares the long-term heat flux obtained in 3D and respective 2D simulations for all the analyses listed in Table 5-1. It is shown that the current approximation is able to simulate the correct long-term heat flux for the NF analyses, where a maximum difference of 1.7 W/m^2 is computed, which translates in a relative error of 16%. Conversely, for walls exposed to a constant temperature, all the analyses overestimate the heat transfer by a substantially larger amount, with a maximum difference of 15 W/m^2, which corresponds to 80% of the value in 3D. It can be noted that the difference between the results obtained in 3D and 2D increases with increasing L_{exp} (e.g. reference case vs analysis III), confirming that the differences between 3D and 2D for the CT cases are affected by the interaction at the wall-air interface.

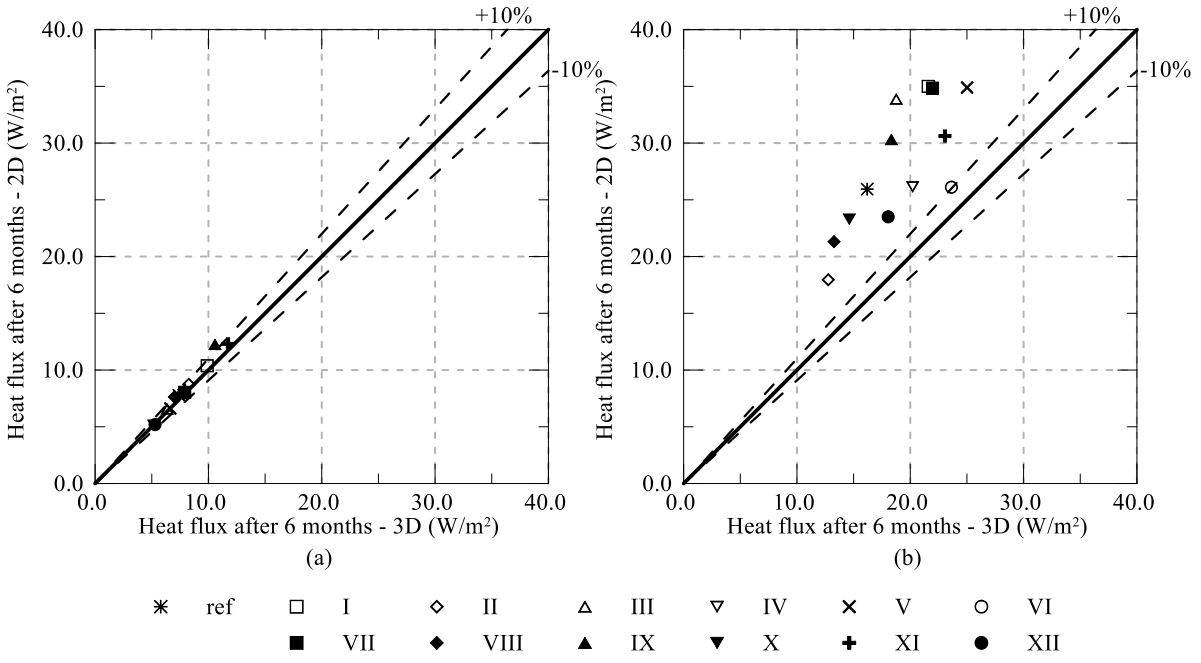

Figure 5-6: Comparison of long-term heat flux for all analyses with approximation for equivalent energy input (a) NF and (b) CT

5.2.3.2 Approximation for equivalent long-term heat flux for walls exposed to a constant temperature

The approximation procedure for the equivalent water flow rate between 3D and 2D analyses is required to consistently model the same energy input in both analyses and was shown to be sufficient to replicate the long-term heat flux for the NF cases. Conversely, a large divergence was observed for walls maintained at a constant temperature (CT). Therefore, for such cases, an additional correction is required to appropriately simulate the long-term heat flux in order to take into account the increased heat exchange through the wall-air interface occurring in the 2D analysis under such conditions. The proposed correction reduces the inlet temperature in the 2D analysis with respect to the one applied in 3D ($T_{in,3D}$). The inlet temperature in 2D to approximate the long-term heat flux for walls exposed to a constant temperature (CT), $T_{in,2D,CT,HF}$, is calculated using the following equation:

$$\Delta T_{in,2D} = T_{in,2D,CT,HF} - T_0 = X \cdot \left(T_{in,3D} - T_0\right) = X \cdot \Delta T_{in,3D} \tag{5-7}$$

where T_0 is the initial temperature, $T_{in,3D}$ is the inlet temperature in the 3D analysis, $\Delta T_{in,2D}$ and $\Delta T_{in,3D}$ are the temperature changes applied in the 2D and 3D analyses, respectively, and X is a reduction factor. Unfortunately, the expression for X cannot be determined easily from theoretical considerations and an empirical procedure is required. To establish an estimate for X, 2D analyses were carried out changing iteratively the inlet temperature until a good agreement with the 3D analyses in terms of the long-term heat flux was obtained. The 3D analyses employed to evaluate X are listed in Table 5-3, where analyses A1-A6 are performed using an idealised wall geometry and uniform soil profile, which is described in

detail in Chapter 6 (Section 6.2.2). This procedure showed that the correction factor is mostly a function of two characteristics of the analysed wall: (1) the proportion of wall in contact with the wall-air interface (denoted herein as L_{exp}/L, where L_{exp} is the exposed length of the wall), since the increased heat transfer taking place in the 2D analysis with respect to the 3D analysis occurs along this boundary, and (2) the spacing between the pipes in the out-of-plane direction in 3D, B/n_p, as a larger spacing (i.e. a smaller number of pipes within a panel) increases the differences between the 2D and 3D analyses. This was expected, since the results shown in the previous section showed larger differences for such cases. Based on the obtained results, the following form is proposed for the correction factor X:

$$X = \xi_1 \left(\frac{B}{n_p \cdot 1.0m} \right)^{\xi_2} \cdot \left(1 + \xi_3 \left(\frac{L_{exp}}{L} \right)^{\xi_4} \right) + 1.0 \quad (5\text{-}8)$$

ξ_1, ξ_2, ξ_3 and ξ_4 are constants equal to -0.38, 0.78, 0.83 and 2.64, respectively, which were obtained through a regression analysis. The adopted form suggests that, for the extreme case of a wall equipped with an infinite number of pipes (i.e. B/n_p = 0.0), the correcting factor is 1.0, meaning that, in such an ideal situation, the 2D representation of the 3D problem would be, as expected, exact. Moreover, the fact that ξ_1 is negative indicates that, in general, X<1, meaning that the applied correction reduces the inlet temperature in 2D. Furthermore, the proposed form for X suggests that, as the spacing between pipes (B/n_p) and the exposed proportion of the wall increase, the value of X reduces.

Table 5-3: 3D analyses performed to establish correction factor X

Analysis	L	L_{exp} (m)	B (m)	n_p (-)	H (m)	Long-term heat flux (W/m^2)
Ref	18.0	9.5	1.5	2	0.8	16.2
II	18.0	4.5	1.5	2	0.8	12.8
III	18.0	15.0	1.5	2	0.8	18.8
IV	18.0	9.5	1.5	4	0.8	21.0
V	18.0	15.0	1.5	4	0.8	26.6
VI	18.0	9.5	0.75	4	0.8	23.8
A1	20.0	4.0	2.0	2	1.0	10.9
A2	20.0	10.0	2.0	2	1.0	12.9
A3	20.0	16.0	2.0	2	1.0	13.6
A4	20.0	4.0	1.0	2	1.0	13.9
A5	20.0	10.0	1.0	4	1.0	16.6
A6	20.0	16.0	1.0	4	1.0	19.0

Note: H = thickness of wall

Analyses

The validity of the proposed approximation was checked by simulating the analyses listed in Table 5-1 specifying a CT boundary condition along the wall-air interface in 2D and applying the reduced inlet temperature according to Equations (5-7) and (5-8). As shown in Table 5-4, most of the analyses used to assess the performance of the proposed correction were not employed to establish X and, therefore, provide a form of independent verification. Since the correction factor depends only on geometric parameters (i.e. L_{exp}/L and B/n_p), the corrected inlet temperature does not vary with different thermal parameters (i.e. analyses IX and X have the same value of X listed in Table 5-4). All the analyses were performed applying the conversion for equivalent water flow rate per unit metre (see Section 5.2.3.1 and Table 5-2 for input parameters). Furthermore, while no correction beyond that of the flow rate was applied to the NF cases, the results for this case are reported and discussed for comparison.

Table 5-4: Correction factor and inlet temperature in 2D for CT boundary condition along exposed face

Analysis	L_{exp} (m)	B (m)	n_p (-)	X (-)	$T_{in,2D,CT,HF}$ (°C)
Ref (*)	9.5	1.5	2	0.65	22.7°C
I	9.5	1.5	2	0.65	26.0°C
II (*)	4.5	1.5	2	0.69	23.3°C
III (*)	15.0	1.5	2	0.54	21.1°C
IV (*)	9.5	1.5	4	0.80	24.9°C
V (*)	15.0	1.5	4	0.73	24.0°C
VI (*)	9.5	0.75	4	0.88	26.2°C
VII	9.5	1.5	2	0.64	22.7°C
VIII	9.5	1.5	2	0.64	22.7°C
IX	9.5	1.5	2	0.64	22.7°C
X	9.5	1.5	2	0.64	22.7°C
XI	9.5	1.5	4	0.80	24.9°C
XII	9.5	1.5	4	0.80	24.9°C

(*) Analyses used to establish correction factor X

Results

Figure 5-7 (a) compares the evolution with time of the heat flux computed for the reference case in 3D and 2D, while Figure 5-7 (b) shows the development of the relative and absolute errors with time.

The results indicate that the CT case now produces similar results to the ones observed for the NF case. In the short term, the 2D analysis simulates a larger heat flux due to the faster heat exchange under plane-strain conditions. This difference reduces rapidly with time and, after 10 days, the heat flux

obtained by the 2D analyses diverges from the one calculated in 3D by 3.0 W/m^2 (12%). After 30 days of operation it has further reduced to 1.0 W/m^2 (5%), while after 6 months of operation it is limited to 0.6 W/m^2 (4%), i.e. a slightly lower relative error than that of the NF case.

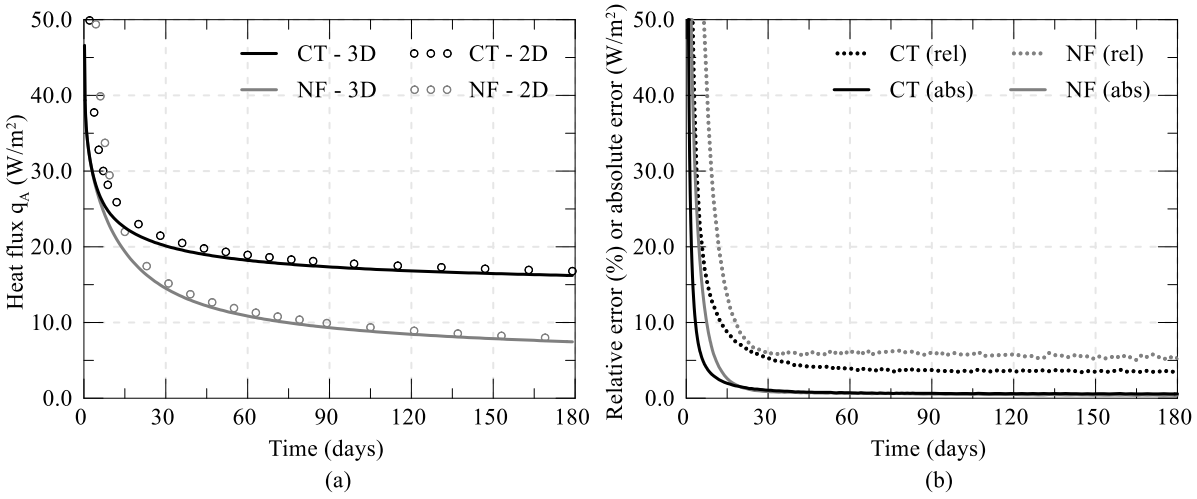

Figure 5-7: Comparison between 3D and 2D analyses for reference case with NF and CT boundary condition on the exposed face of the wall simulated with correction for long-term heat flux (a) heat flux with time and (b) relative and absolute error with time

The other analyses listed in Table 5-1 are characterised by the same level of accuracy as the reference case. The comparison between the heat flux after 6 months of operation obtained in 3D and respective 2D analyses for all the cases is shown in Figure 5-8 (a) and (b), for the NF and CT condition, respectively, while the detailed development of the heat flux with time and the relative and absolute errors are reported in Appendix F for all the analyses.

Figure 5-8 demonstrates that adopting the procedure to simulate an equivalent water flow rate per metre width in 3D and 2D and employing the correction factor X to reduce the inlet temperature for walls exposed to an environment at constant temperature (CT), enables the prediction of the long-term heat flux computed in 3D with excellent accuracy. Indeed, the maximum difference in heat flux is 1.7 W/m^2 and 1.25 W/m^2, for the NF and CT cases, respectively. These values correspond to an overestimation of the heat flux by 16% and 7%. While the relative errors may not seem negligible, it should be noted that the absolute errors are small and that the calculation of the heat flux is very sensitive to the values of the computed temperature differential across the pipe (ΔT_p), where a small discrepancy can lead to a significant difference in the heat flux. Indeed, the abovementioned differences in heat flux correspond respectively to differences in ΔT_p of only 0.18°C and 0.34°C. Furthermore, it should be noted that the 2D results, especially for the NF analyses, tend to generally overestimate the long-term heat flux obtained in 3D, meaning that the proposed approximation generates unconservative results. However, in the present case, such inaccuracy is offset by the fact that the 2D results are compared to 3D analyses without the inclusion of the TEM, meaning that the 3D analyses are potentially underestimating the real thermal performance.

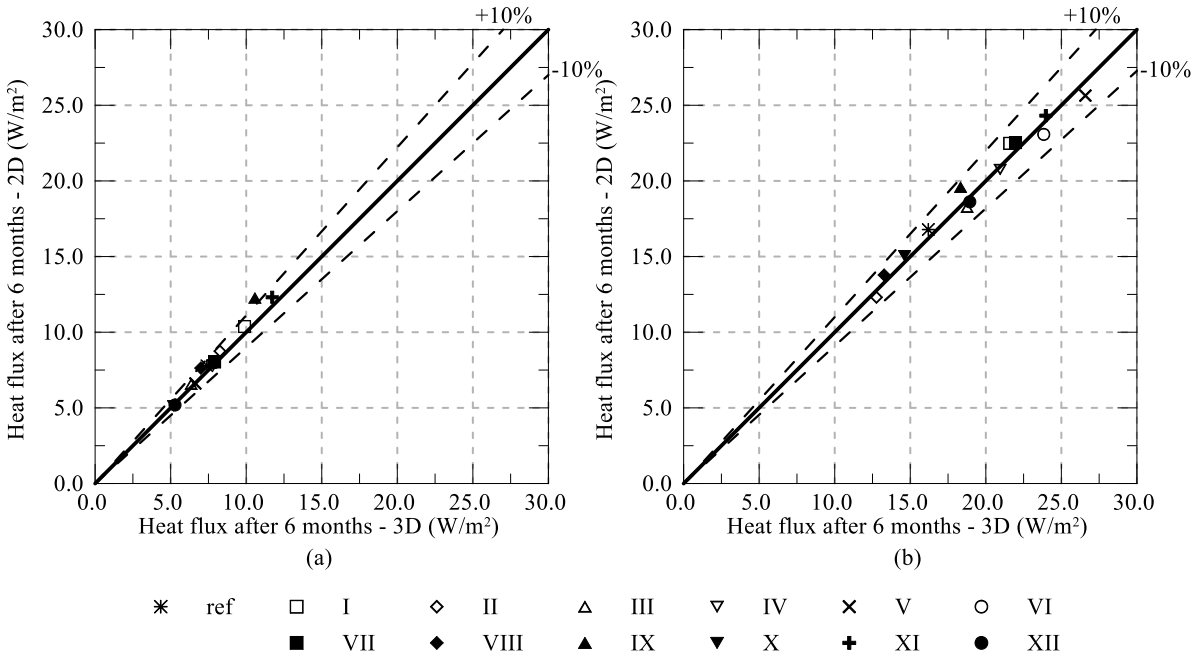

Figure 5-8: Comparison of long-term heat flux for all analyses simulated with correction for long-term heat flux (a) NF and (b) CT

The evolution of the injected energy with time during 6 months of operation normalised by the width of the wall (B) computed in 3D and 2D for the reference case is displayed in Figure 5-9 (a), while the relative and absolute errors are shown in Figure 5-9 (b). From these graphs it is evident that the 2D analyses overestimate the energy computed in 3D, particularly for the case of the insulated wall (NF). The discrepancies are mainly due to the overestimation of the heat transfer in the short term, as was noted earlier when comparing the heat flux, where the error is accumulated with time. For the NF case, the energy after 6 months in 2D is 175 kWh/m (20%) larger than in 3D, while for the CT case a smaller difference of 102 kWh/m (7%) is computed.

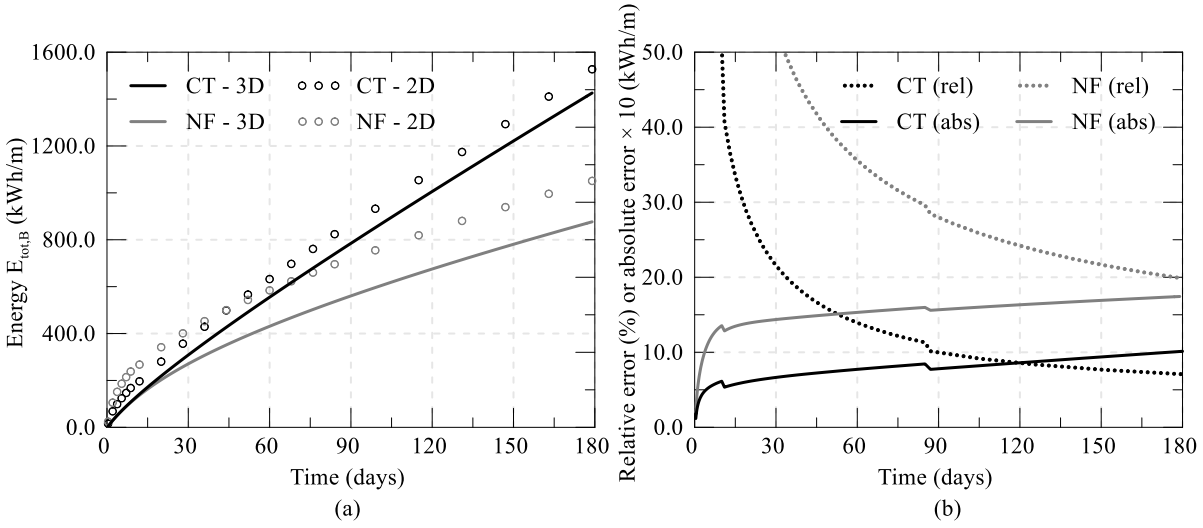

Figure 5-9: Comparison between 3D and 2D analyses for reference case with NF and CT boundary condition on the exposed face of the wall simulated with correction for long-term heat flux (a) energy with time and (b) relative and absolute error with time

The comparison between the 3D and 2D analyses in terms of injected energy after 6 months of operation for all the analyses listed in Table 5-1 are plotted in Figure 5-10 (a) and (b) for the NF and CT boundary conditions along the exposed face, respectively. As can be seen, for both boundary conditions, the energy transferred during 6 months is overestimated in 2D, with maximum differences of 370 kWh/m, corresponding to an error of 33%, for the NF case, and of 217 kWh/m (13%) for the CT case. Furthermore, as can be concluded from Figure 5-9 and as shown clearly in Figure 5-11 and Figure 5-12, which compare the energy transferred after 3 months and 1 month in 3D and 2D, the difference in the transferred energy increases as shorter operation periods are evaluated. Indeed, while the difference in heat flux between 3D and 2D stabilises rapidly (see Figure 5-7), a large divergence in the transferred energy is computed in the short to medium term. The differences are largest for the NF cases, for which the maximum errors in the transferred energy after 3 months and 1 month of operation are equal to 44% and 75%, respectively. For the CT cases, these are equal to 19% and 34%, respectively for 3 months and 1 month of operation. It should also be noted that, similar to what was previously observed for the long-term heat flux for the CT cases, the difference between 3D and 2D increases with increasing spacing between the pipes. In addition, it increases with L_{exp} for walls maintained at a constant temperature, while a larger difference is obtained with smaller L_{exp} for insulated walls. For both boundary conditions, a higher energy is predicted in 2D with increasing $\overline{\lambda_s}$ and decreasing λ_c, since these parameters affect the short-term response. According to these results, it was deemed necessary to establish a new correction to enable a better estimation of the energy transferred in a 2D analysis. This process is described in the following Section 5.2.3.3.

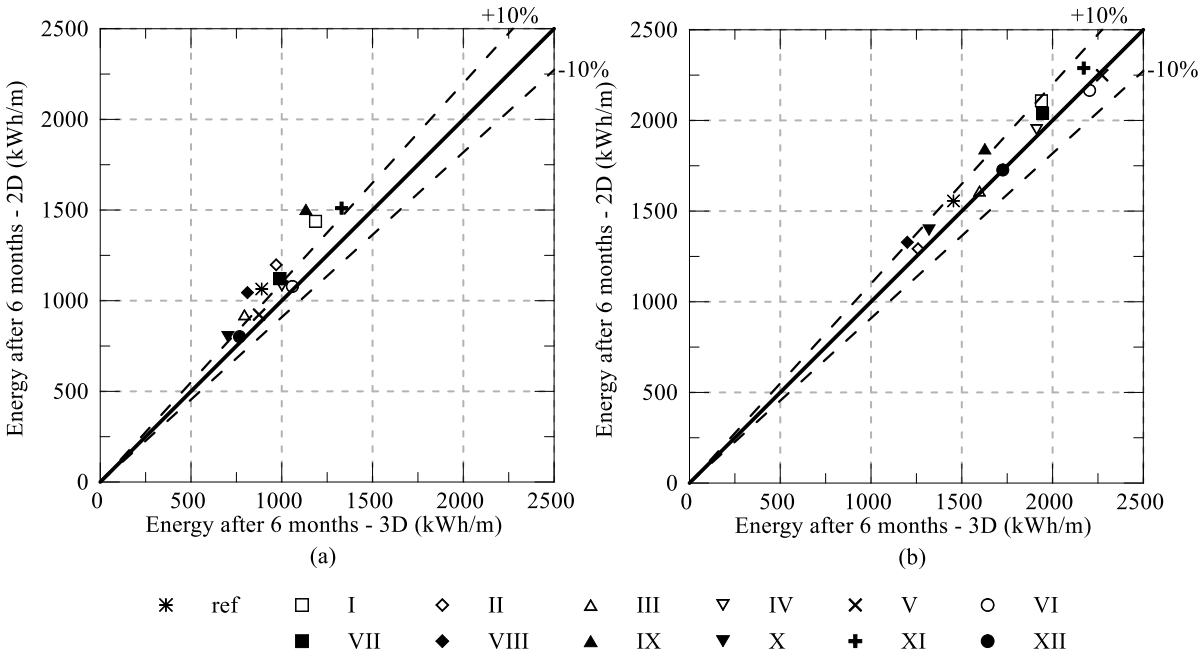

Figure 5-10: Comparison of energy transferred after 6 months for all analyses simulated with correction for long-term heat flux (a) NF and (b) CT

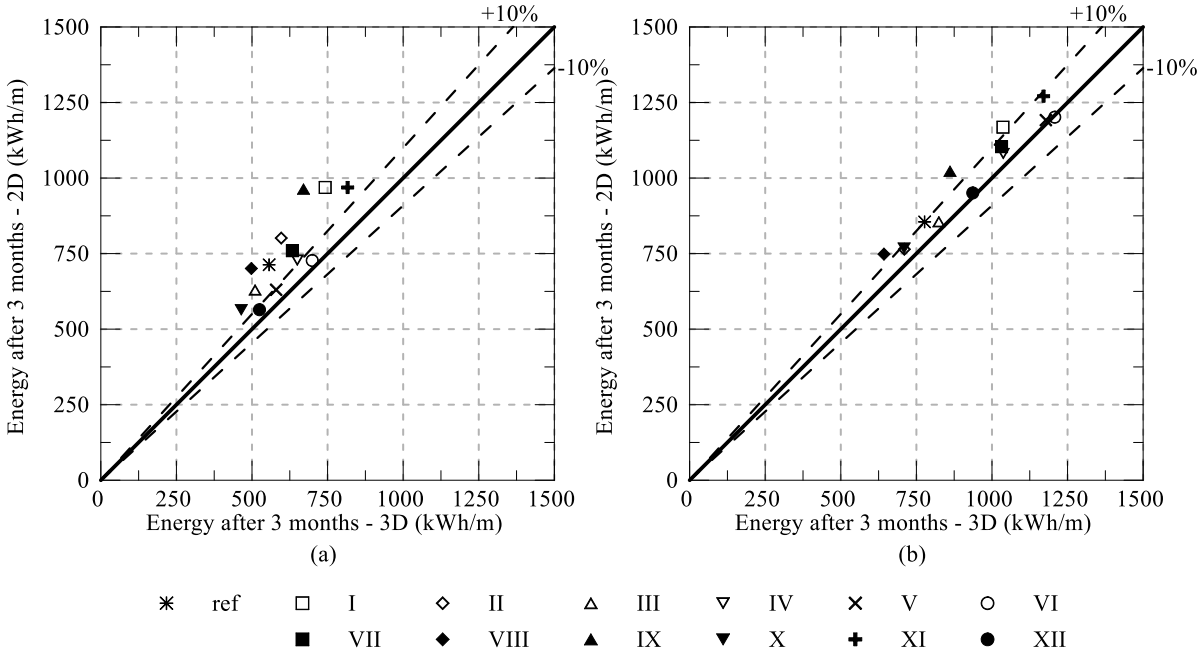

Figure 5-11: Comparison of energy transferred after 3 months for all analyses simulated with correction for long-term heat flux (a) NF and (b) CT

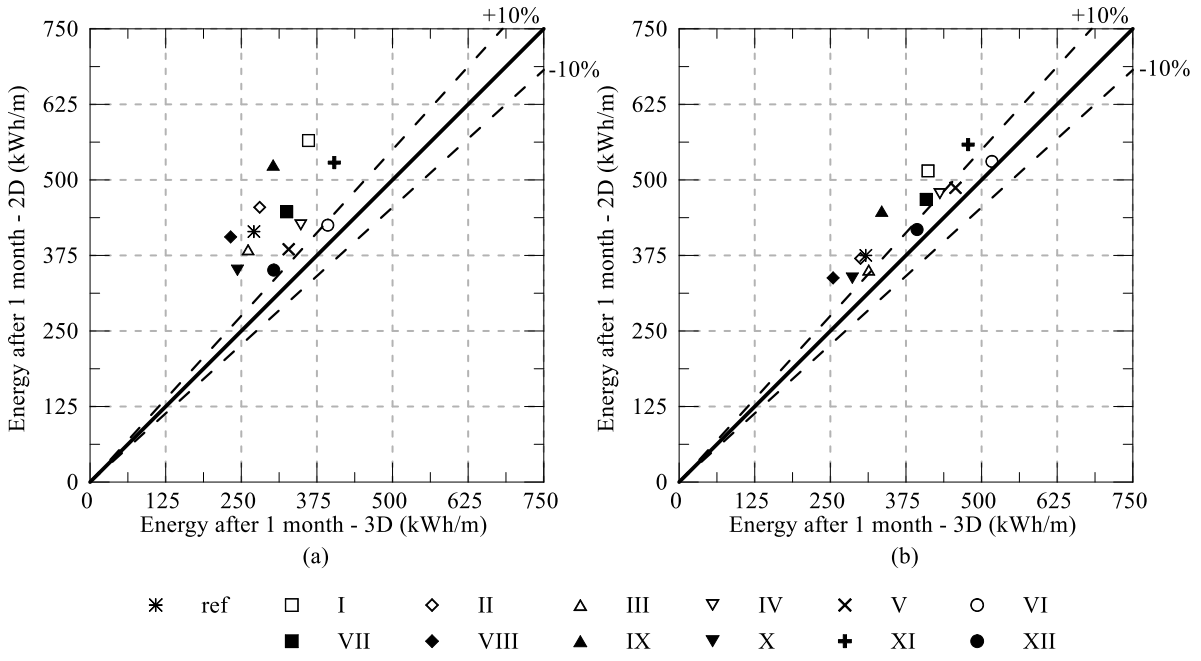

Figure 5-12: Comparison of energy transferred after 1 month for all analyses simulated with correction for long-term heat flux (a) NF and (b) CT

In Figure 5-13 the changes in temperature within the retained side at a depth of 11.0 m for the reference case modelled in 3D and 2D are compared. Note that, for the 3D analyses, the average temperatures along the width of the wall are reported (due to the non-uniform temperatures in 3D – see Chapter 4). For the NF case, the 2D analysis predicts larger changes in ground temperature with respect to the 3D analysis, with differences that are particularly evident at the soil-wall interface. At this location, temperature changes exceed the ones computed in 3D by 2.5°C in the long term. However, the difference reduces with increasing distance from the wall, with values of 1.0°C being computed at 5.0 m from the wall. Conversely, the CT case underestimates the long-term temperature changes close to the wall by 1.5°C, which is due to the lower inlet temperature (indeed, the temperature change at the wall-soil interface is equal to 9.3°C, thus it has almost reached the applied temperature change at the pipe inlet of 9.7°C). A very good match is obtained at larger distances. It should also be noted that, especially at the soil-wall interface, the change in temperature with time is more rapid for the 2D analysis, where it tends to a constant value after shorter periods of time, indicating the larger heat transfer occurring in 2D and hence the smaller amount of time required to reach thermal equilibrium.

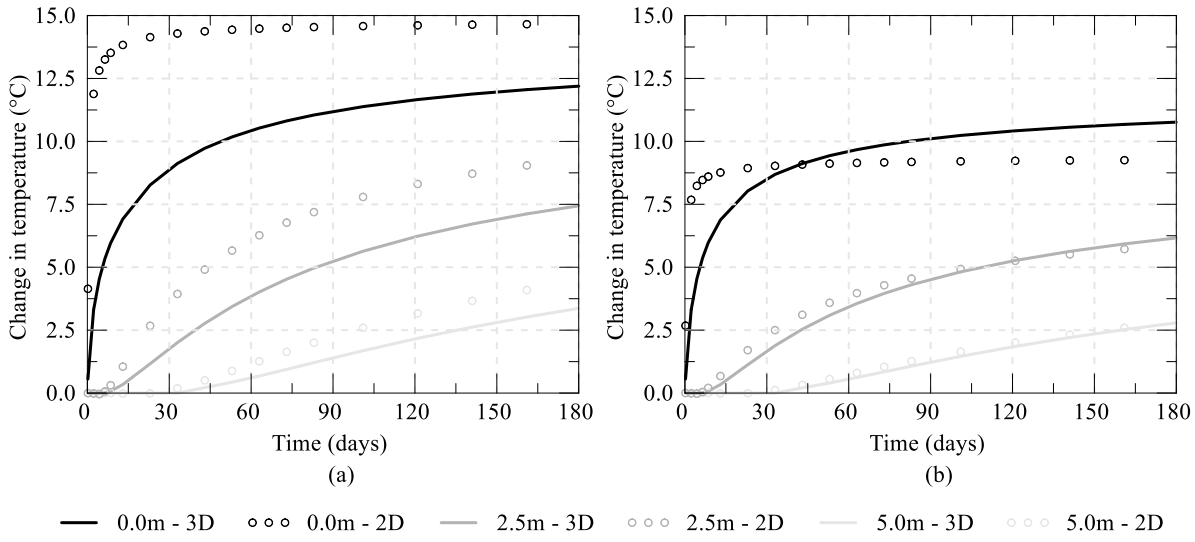

Figure 5-13: Comparison between 3D and 2D of temperature change with time at different distances from the wall within the retained side for reference case (a) NF analysis and (b) CT analysis

5.2.3.3 Approximation for equivalent transferred energy

As was shown above, 2D analyses overestimate the transferred energy. Thus, further corrections are required for both NF and CT conditions to enable a correct estimation of the transferred energy for thermo-active walls simulated in a 2D analysis. Due to the transient nature of the problem, where it was shown that a larger divergence exists between 3D and 2D in the short term, it is evident that different corrections are required for different periods during which the transferred energy is to be estimated.

Similar to the correction developed to ensure an equivalent long-term heat flux for a CT boundary condition outlined in the previous section, the correction proposed to achieve an equivalent transferred energy reduces the inlet temperature in 2D, for both a NF and CT boundary condition, according to the following equation:

$$\Delta T_{in,2D} = T_{in,2D,E} - T_0 = Y \cdot \left(T_{in,3D} - T_0\right) = Y \cdot \Delta T_{in,3D} \tag{5-9}$$

where Y is a dimensionless reduction factor.

All the analyses listed in Table 5-1 (together with those presented in Chapter 6) were used to determine the expression for Y. The adopted procedure follows the same principles as the one previously outlined, i.e. 2D analyses were carried out changing iteratively the inlet temperature until a good agreement with the 3D analyses in terms of total transferred energy per unit width, $E_{tot,B}$, is obtained. This procedure was repeated to achieve the same energy either after 6 months, 3 months or 1 month of operation in 3D and 2D. According to the results, the following form for the correction factor Y in Equation (5-9) was determined:

$$Y = \left[\eta_1 \left(\frac{B}{n_p \cdot 1.0m}\right)^{\eta_2} \cdot \left(1 + \eta_3 \left(\frac{L_{exp}}{L}\right)^{\eta_4}\right)\right] \times \left(\frac{\lambda_c}{\lambda_{ref}}\right)^{\eta_5} \times \left(\frac{\bar{\lambda_s}}{\lambda_{ref}}\right)^{\eta_6} + 1.0 \qquad (5\text{-}10)$$

where L_{exp} is the exposed length of the wall (m), L is the total length of the wall, B is the width of the wall, n_p is the number of pipes, λ_c is the concrete thermal conductivity, $\bar{\lambda_s}$ is the weighted average soil thermal conductivity over the length of the wall on the retained side, λ_{ref} is a reference thermal conductivity of 1.0 W/mK, and η_1, η_2, η_3, η_4, η_5 and η_6 are constants obtained through a regression analysis, the values of which are reported in Table 5-5.

While the correction factor X for the approximation of the long-term heat flux with a CT boundary condition along the exposed face depends only on geometric parameters (i.e. L_{exp}/L and B/n_p), the correction factor for approximating the transferred energy, Y, takes into account also the soil and concrete thermal conductivity, since these affect the heat transfer rate in the short to medium term (see Appendix F with detailed results on analyses with different thermal conductivities). Furthermore, the constants required to calculate Y (see Table 5-5) vary with the boundary condition along the excavated face of the wall and the time frame over which the 2D analysis aims to match the transferred energy in a 3D problem. From the results in Section 5.2.3.1, it is evident that the correction should yield higher inlet temperatures for the NF case. Furthermore, to take into account the increased heat transfer in 2D in the short term, lower temperatures are required for shorter operation periods. It should also be noted that the effect of the exposed ratio (L_{exp}/L), expressed mainly by the constant η_3, is opposite for walls with a NF or CT boundary condition along the exposed face, with this constant having different signs for the two cases. Indeed, for the CT case, a larger exposed length increases the differences between 3D and 2D due to the increased heat transfer through the wall-air interface in 2D; for the NF case, where no heat transfer takes place along this boundary, increasing its length reduces the impact of the 2D assumption due to the more uniform temperature within the wall.

Table 5-5: Constants for calculation of correction factor Y

Constant	6 months		3 months		1 month	
	CT	NF	CT	NF	CT	NF
η_1	-0.44	-0.60	-0.49	-1.78	-0.55	-1.95
η_2	0.65	1.15	0.66	1.04	0.60	0.87
η_3	0.38	-0.60	0.31	-0.82	0.26	-0.77
η_4	2.08	0.26	3.00	0.07	3.39	0.06
η_5	-0.15	-0.76	-0.12	-0.78	-0.17	-0.54
η_6	0.13	0.60	0.14	0.47	0.19	0.37

Results reference case

Only the results obtained simulating the reference case in 2D adopting the correction factor Y are assessed, since similar observations are valid for all other cases (all results are reported in Appendix F). Table 5-6 reports the calculated correction factors and inlet temperatures for both boundary conditions and different operation periods. As expected, these are higher for the NF case and decrease for shorter operation periods. Furthermore, it should be noted that the correction factor Y for the CT case is lower than the correction factor X, since the 2D cases overestimated the transferred energy when using the latter.

Table 5-6: Correction factors Y and inlet temperature for reference analysis

Operation period	Y_{NF} (-)	$T_{in,2D,E,NF}$ (°C)	Y_{CT} (-)	$T_{in,2D,E,CT}$ (°C)
6 months	0.80	25.0	0.60	22.0
3 months	0.75	24.3	0.57	21.6
1 month	0.64	22.5	0.52	20.8

The evolutions with time of transferred energy and the associated relative and absolute errors for the reference case with NF and CT boundary conditions obtained employing the correction factors Y corresponding to 6 months of operation are shown in Figure 5-14 (a) and (b), respectively. Compared to Figure 5-9, a noticeable improvement in the predicted energy is observed, with the difference after 6 months being an excess of 0.5 kWh/m (0%) for the NF case and an underestimation of -10.5 kWh/m (-1%) for the CT case. Clearly, given the lower inlet temperatures when compared to those employed in the previous section, an underestimation of the long-term heat flux is now expected.

Similar results are obtained for the energy transferred after 3 months and 1 month of operation when the respective correction factors are adopted, as depicted in Figure 5-15 and Figure 5-16, respectively. The difference in the transferred energy after 3 months has reduced to -18 kWh/m (-3%) for the NF case and -19 kWh/m (-2%) for the CT case. For one month of operation, the 2D analyses underestimate the transferred energy after one month in the respective 3D analyses by 8.0 kWh/m (-3%) and 7.0 kWh/m (-2%), for the NF and CT cases, respectively. It is interesting to note that, even when considering the shortest period of 1 month, large differences are still computed in the very short term, which decrease rapidly with time due to the smaller heat transfer simulated as the inlet temperature is reduced.

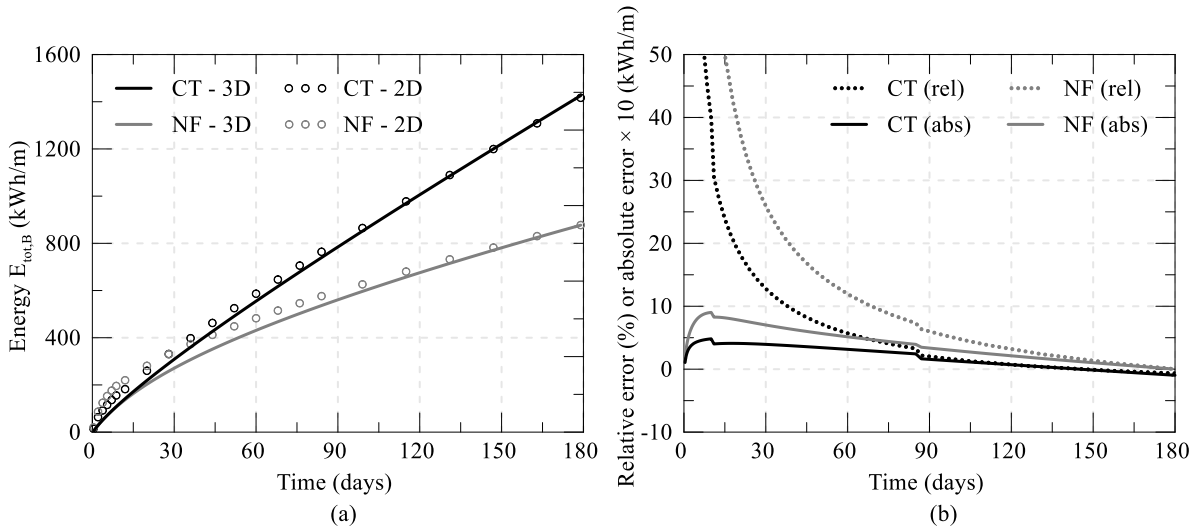

Figure 5-14: Comparison between 3D and 2D analyses for reference case with NF and CT boundary condition on the exposed face of the wall – correction Y 6months (a) energy with time and (b) relative and absolute error with time

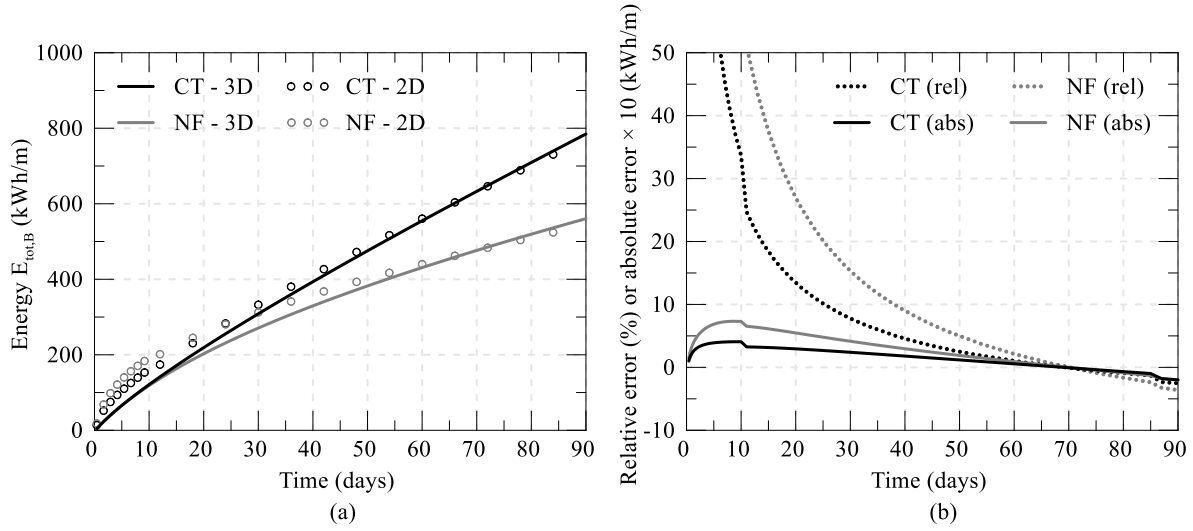

Figure 5-15: Comparison between 3D and 2D analyses for reference case with NF and CT boundary condition on the exposed face of the wall – correction Y 3 months (a) energy with time and (b) relative and absolute error with time

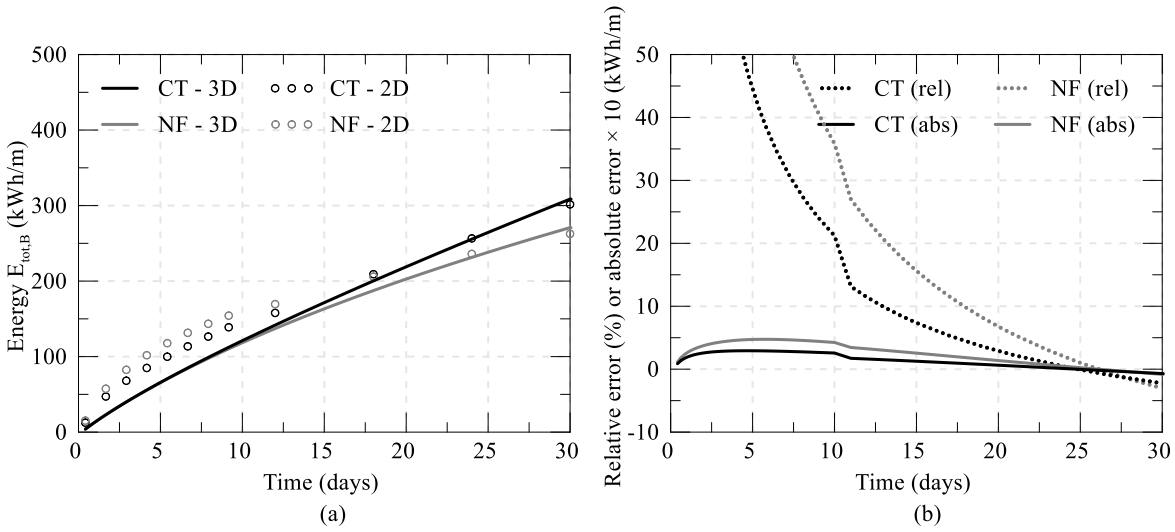

Figure 5-16: Comparison between 3D and 2D analyses for reference case with NF and CT boundary condition on the exposed face of the wall – correction Y 1 month (a) energy with time and (b) relative and absolute error with time

Figure 5-17 compares the changes in ground temperature at different distances from the wall within the retained side at 11.0 m depth for the analyses with correction factor *Y* for 6 months of operation. Given the lower temperatures in the 2D analyses for both NF and CT with respect to the previous approximation (for changes in ground temperature see Figure 5-13), lower temperatures are evaluated in both cases. For the NF case, with the application of correction factor *Y*, the changes in ground temperature are closer to the ones predicted in 3D. However, there are still considerable differences in the short term, which are due to the geometric simplification of a 2D plane-strain analysis. For the CT analysis, the ground temperatures are underestimated and slightly lower to those evaluated when applying the correction factor *X* for the long-term heat flux. Indeed, the differences between the two analyses are small since the computed correction factors *X* and *Y* for this case are similar (0.64 and 0.60, respectively). It is therefore considered that when evaluating changes in ground temperature through 2D plane-strain analyses in the long term, it is conservative to employ the corrections proposed to match the long-term heat flux for both CT and NF analyses.

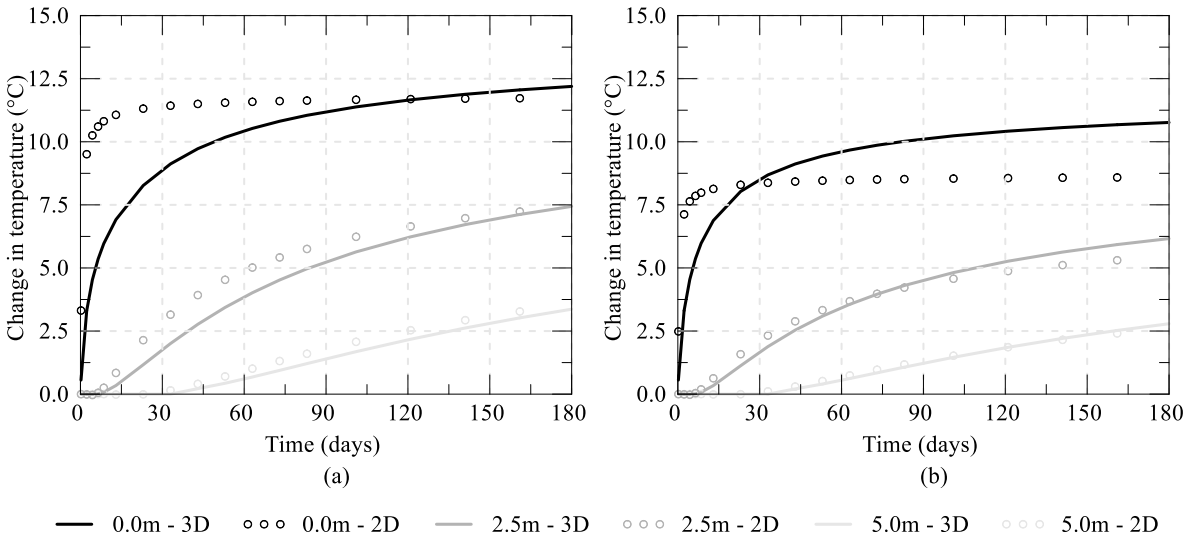

Figure 5-17: Comparison between 3D and 2D of temperature change with time at different distances from the wall within the retained side for reference case with correction Y for 6months (a) NF analysis and (b) CT analysis

5.2.4 Two-dimensional analyses adopting modelling approach 2

Modelling approach 2, which is described in detail in Chapter 4 and schematically represented in 3D and 2D in Figure 5-2, prescribes a nodal heat flux boundary condition to simulate the heat exchange. In the 3D analyses presented in Chapter 4, the magnitude of the heat flux was determined such that a target inlet temperature (or, equivalently, a target temperature change at the pipe inlet $\Delta T_{in,3D}$=$T_{in,3D} - T_0$) is achieved during a given operation period. However, as seen from the results obtained when simulating thermo-active walls in 2D plane-strain analyses employing MA1, in order to simulate the same heat transfer, the inlet temperatures in 2D may differ with respect to those applied in a 3D analysis, given the faster heat transfer rate occurring in a 2D plane-strain analysis.

In order to identify if any correction is required when simulating thermo-active walls employing MA2 in 2D plane-strain analyses, the same analyses reported in Table 5-1 were performed in 3D adopting MA2, where the target temperature change at the pipe inlet in 3D, $\Delta T_{in,3D}$, after 6 months of operation was set to 15°C for all the analyses, except for analysis I, for which it was equal to 20°C. The details of the analyses and the computed values of the heat flux (HF) boundary condition for all the analyses with either an NF or CT boundary condition along the exposed face of the wall are summarised in Table 5-7. Figure 5-18 plots the computed values of the heat flux boundary condition for a better comparison.

Table 5-7: Values of heat flux (HF) boundary conditions for 3D analyses

Analysis	L_{exp} (m)	B (m)	n_p (-)	λ_c (W/mK)	$\overline{\lambda_s}$ (W/mK)	$\Delta T_{in,3D}$ (°C)	HF_{NF} (kW)	HF_{CT} (kW)
Ref	9.5	1.5	2	1.6	1.62	15°C	0.245	0.447
I	9.5	1.5	2	1.6	1.62	20°C	0.327	0.596
II	4.8	1.5	2	1.6	1.62	15°C	0.267	0.367
III	15.0	1.5	2	1.6	1.62	15°C	0.216	0.538
IV	9.5	1.5	4	1.6	1.62	15°C	0.266	0.557
V	15.0	1.5	4	1.6	1.62	15°C	0.232	0.690
VI	9.5	0.75	4	1.6	1.62	15°C	0.144	0.329
VII	9.5	1.5	2	2.4	1.62	15°C	0.270	0.602
VIII	9.5	1.5	2	1.2	1.62	15°C	0.225	0.365
IX	9.5	1.5	2	1.6	3.23	15°C	0.320	0.505
X	9.5	1.5	2	1.6	0.81	15°C	0.190	0.404
XI	9.5	1.5	4	1.6	3.23	15°C	0.360	0.644
XII	9.5	1.5	4	1.6	0.81	15°C	0.203	0.499

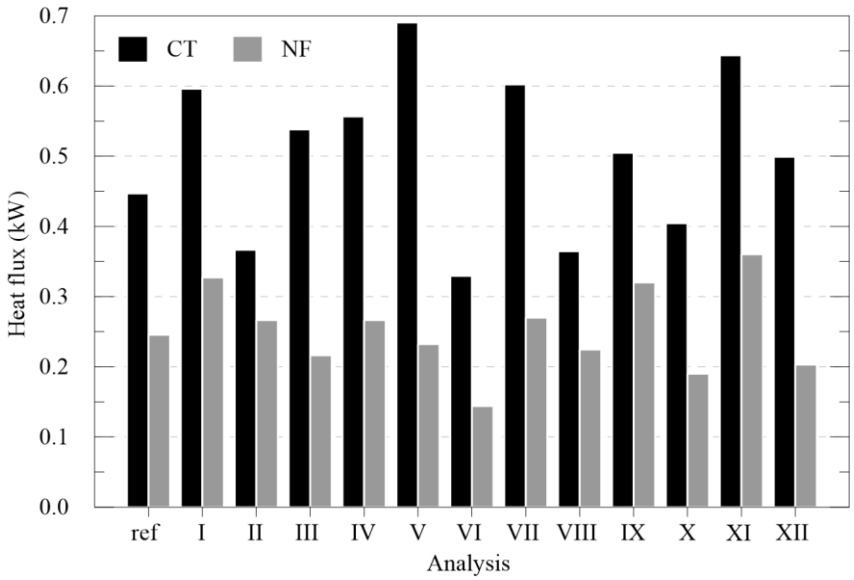

Figure 5-18: Values of heat flux (HF) boundary conditions computed for 3D analyses

After having established the magnitude of the heat flux boundary condition in 3D, 2D analyses were performed, including the adjustment of the area of the pipe according to Equation (5-6) to ensure an equivalent water flow rate in 2D and 3D. Furthermore, the applied value of the heat flux boundary condition was the same as that established in 3D normalised by the width of the wall (B), thus the same heat flux q_A is simulated in 2D and 3D. The analyses were run for 6 months and the temperature recorded at the pipe inlet in 2D at the end of the operation period was evaluated, which was compared

to the target temperature set in 3D. The results are depicted in Figure 5-19 and show that the temperature change at the pipe inlet in 2D ($\Delta T_{in,2D}$) is lower than the target temperature set in 3D ($\Delta T_{in,3D}$), highlighting the faster heat transfer in the former type of analysis. Furthermore, the obtained values are consistent with what was observed for MA1, e.g. larger temperatures are obtained for the NF cases and the difference between 2D and 3D is smaller as the spacing between the pipes reduces. This confirms that the actual target temperature cannot be employed when simulating thermo-active walls using MA2 in 2D plane-strain analyses, due to the larger heat transfer in the latter, which would lead to an overestimation of the energy performance.

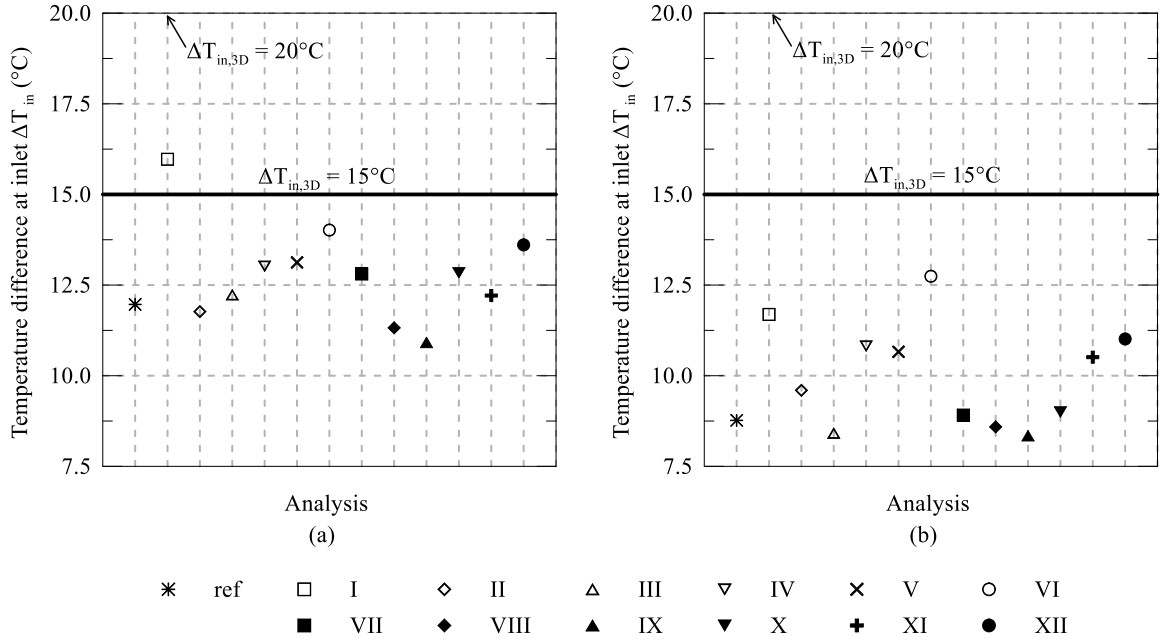

Figure 5-19: Temperature difference at pipe inlet (ΔT_{in}) for 3D and 2D analyses (a) NF an (b) CT. Note that all analyses except analysis I relate to $\Delta T_{in,3D} = 15°C$. Analysis I in 3D was performed with $\Delta T_{in,3D} = 15°C$.

In order to be able to establish the correct magnitude of the heat flux boundary condition to be applied in a 2D plane-strain analysis without performing 3D analyses, a target temperature change at the inlet $\Delta T_{in,2D}$ after 6 months is required (i.e. the values in Figure 5-19 for the considered geometries). Matching this temperature would mean that, after 6 months, the same heat transfer is modelled in the 2D and 3D representations of the same problem. To provide insight into how this target temperature in 2D could be calculated, the data shown in Figure 5-19 were used. In effect, the ratio $\Delta T_{in,2D}/\Delta T_{in,3D}$ was determined for each analysis and it was shown to assume values close to those of correction factor Y for MA1 (i.e. the correction factor that ensures that the same amount of energy is transferred over 6 months, see Table 5-5). This is perhaps unsurprising since the data in Figure 5-19 were obtained comparing 2D and 3D analyses characterised by the same amount of energy transferred over 6 months (i.e. the same criterion used to establish Y). This is further shown in Figure 5-20, which compares the values obtained for MA2 and MA1. A good agreement can be observed, with the values obtained for

MA2 diverging by less than ±10% of those evaluated for MA1. Therefore, when MA2 is adopted in 2D plane-strain analyses, the target temperature change, $\Delta T_{in,2D}$, can be estimated using Equations (5-9) and (5-10) with the coefficients reported in Table 5-5 corresponding to an operation of 6 months. The heat flux obtained iteratively to achieve this target temperature change will be equivalent to that required in the corresponding 3D analysis to achieve the uncorrected target temperature change $\Delta T_{in,3D}$. It should be noted, however, that this is valid only for 6 months of operation (i.e. the criterion adopted in the analyses above), and further analyses would be necessary to establish first the heat flux boundary condition required to achieve a certain $\Delta T_{in,3D}$ for shorter operation periods which could then be compared to what is obtained in 2D. Given the procedure described above, it is expected that these would correspond to the values of Y reported in Table 5-5 for the same period of operation.

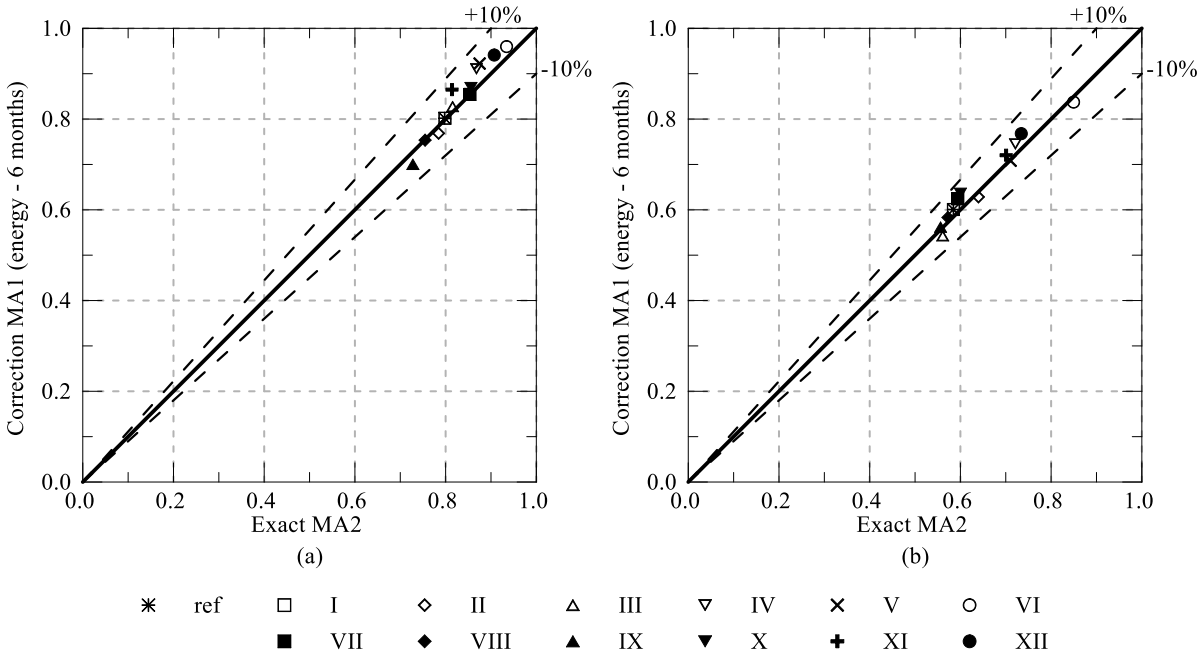

Figure 5-20: Comparison between correction factor Y for MA1 after 6 months of operation and exact solution for MA2

5.3 Factors controlling the long-term thermal performance of thermo-active retaining walls

Given the excellent agreement between the results computed in 3D and respective 2D analyses, the analyses presented in this section were carried out in 2D only. Indeed, a notable saving in computational time is obtained, with the analyses in 3D requiring 12h or 48h for a 6 months simulation period (respectively for n_p=2 and n_p=4), while the simulation time for each 2D analysis being limited to about 5min. In this section, a parametric study is performed to investigate the effect of varying problem parameters on the thermal performance of a thermo-active wall over a period of 6 months, where the influence of each parameter was assessed for both insulated walls (NF) and walls exposed to an environment exposed to a constant temperature (CT). The analyses presented in this section were performed using MA1, i.e. imposing a prescribed inlet temperature. Indeed, given the similar results obtained employing MA1 and 2 in Chapter 4, it is considered that the impact of the studied parameters for both modelling approaches will be similar.

5.3.1 Analyses

The parametric study investigates the influence of different geometrical parameters, such as the ratio of exposed length over total length (L_{exp}/L) and the number of pipes within a wall panel (n_p), the thermal conductivities of concrete (λ_c) and soil (λ_s), the water flow velocity (v), the initial (T_0) and inlet (T_{in}) temperatures and the operation mode. The different aspects analysed and corresponding values are summarised in Table 5-8, while the reference case is the same as that described in the previous section. Hence, for each analysis within the parametric study, one parameter at the time was varied with respect to the reference case in order to be able to assess the influence of each parameter independently.

The 2D approximation procedures outlined in Section 5.2.3 are applied, with the correction for the equivalent water flow rate being adopted for every analysis. When assessing the heat flux and changes in ground temperature, the approximation procedures described in section 5.2.3.2 are used for walls exposed to an environment at constant temperature (CT), whereas when computing the transferred energy the correction presented in Section 5.2.3.3 is employed for NF and CT boundary conditions. It should be noted that in this study only the energy after 6 months is evaluated, hence the corresponding constants for the correction factor for this operation period are used (see Table 5-5).

Table 5-8: Analyses for parametric study on thermal performance

Study (*)	Ref. case	Additional values analysed					
Ratio of exposed over total length ($\frac{L_{exp}}{L}$)	0.53	0.27			0.41		
Number of pipes (n_p)	2	4			6		
Thermal conductivity of concrete (λ_c)	1.6	$0.5\lambda_c$			$2.0\lambda_c$		
Thermal conductivity of soil ($\overline{\lambda_s}$)	1.62	$0.5\overline{\lambda_s}$			$2.0\overline{\lambda_s}$		
Water flow velocity (v)	0.5	0.2	0.4	0.6	0.8	1.0	1.2	1.4
Inlet temperature ($\Delta T_{in,3D}$)	15.0	10.0			20.0		
Operation mode	continuous	intermittent 6h					

(*) for each study, both boundary conditions (NF and CT) along exposed face of wall were considered

5.3.2 Results

Ratio of exposed over total length

The effect of different wall geometries was analysed by varying the ratio of the exposed over total length, i.e. L_{exp}/L, as summarised in Table 5-9, which also indicates the inlet temperature calculated for the 2D approximations for the long-term heat flux ($T_{in,2D,CT,HF}$) and energy transferred after 6 months ($T_{in,2D,\mathrm{NF},E}$ and $T_{in,2D,\mathrm{CT},E}$).

Table 5-9: Parameters used for 2D analyses simulating different ratios of exposed over total length

Analysis	L_{exp} (m)	L (m)	L_{exp}/L (-)	$\Delta T_{in,\mathrm{3D}}$ (°C)	$\Delta T_{in,2D,CT,HF}$ (°C)	$\Delta T_{in,2D,\mathrm{NF},E}$ (°C)	$\Delta T_{in,2D,\mathrm{CT},E}$ (°C)
Reference	9.5	18.0	0.53		9.7	12.0	9.0
L18	4.8	18.0	0.27	15.0	10.3	11.5	9.4
L23	9.5	23.0	0.41		10.1	11.8	9.2

When comparing the reference analysis and analysis L18, it should be noted that the walls have the same wall area in contact with the ground, but different exposed lengths. Conversely, analysis L23 presents the same exposed length as the reference analysis, though the total heat exchange area is larger for L23. Similarly, while the heat exchange area is different for L18 and L23, these two analyses have approximately the same embedded length.

Figure 5-21 shows the comparison of the heat flux per unit area for all the cases and the different boundary conditions on the exposed face.

For the NF boundary condition, a slightly larger (1.0 W/m^2) heat flux per unit area is achieved with configuration L18, because this geometry includes the insulated boundary with the least area, which

was shown to affect negatively the thermal performance when it is increased. Conversely, the heat injection rate in the long term is the same for the reference analysis and the L23 case. This reflects the fact that the thermal performance is being measured using a normalised metric (heat flux per metre squared of wall), which intrinsically compensates for the larger contact area of the latter analysis.

With a CT boundary condition, there is a larger difference in predicted thermal performance for the three different configurations. The highest heat flux is calculated for the reference analysis, being approximately 2.0 W/m^2 and 4.5 W/m^2 higher than those obtained for L23 and L18, respectively. This clearly reflects the fact that L_{exp}/L is largest for the reference analysis. Indeed, even though analysis L23 features the same exposed length as the reference analysis, the heat flux per metre squared of wall is smaller as it includes larger lengths of pipe in contact with the soil, which, as they are positioned within the embedded section, do not contribute as much to the overall thermal performance of the wall.

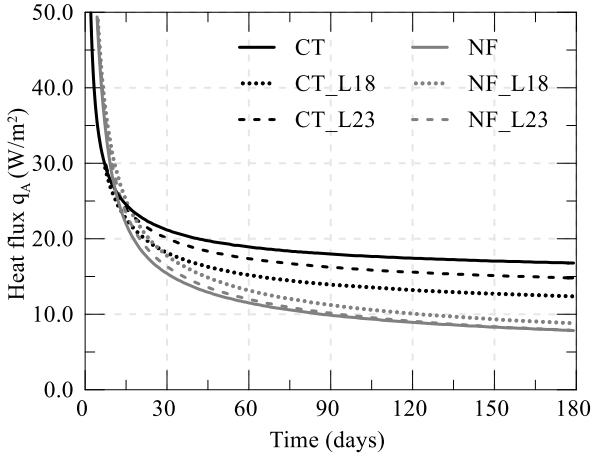

Figure 5-21: Influence of wall geometry on heat flux per unit area of wall with time

Figure 5-22 compares the proportions of heat flux corresponding to the two different sections (exposed and embedded) of the considered walls in terms of the ratio q_e, i.e. q_{exp}/q_A or q_{emb}/q_A, where q_{exp} and q_{emb} are calculated in 2D using:

$$q_{exp} = \frac{C_{v,w} v A_p (T_{in} - T_{exp})}{A_{wall}} \tag{5-11}$$

$$q_{emb} = \frac{C_{v,w} v A_p (T_{exp} - T_{out})}{A_{wall}} \tag{5-12}$$

where T_{exp} is the temperature recorded within the pipe at the depth of the top of the base slab.

In the short term, where the heat transfer takes place primarily within the concrete and temperature changes have not yet reached the exposed boundary, the ratio q_e is equal to L_{exp}/L and does not depend on the boundary condition along the exposed face. As observed in Chapter 4, for the NF case, the embedded section provides a larger contribution to the total heat flux. Considering the end of the

simulation (i.e. 6 months), for analysis L18, which has the smallest L_{exp}/L, 77% of the total heat flux is generated within the embedded section. For the wall geometry L23 and the reference case, this reduces to 68% and 59%, respectively. Although analyses L23 and L18 have a similar embedded length, proportionally this section has a greater contribution in the case of analysis L18. Conversely, for walls exposed to a constant temperature, the largest contribution to the total heat flux is provided by the exposed part of the wall. It is interesting to note that, although configuration L18 has a small area in contact with the environment at constant temperature (only 27% of L), 59% of the total heat flux is generated within the exposed part of the structure, further confirming that importance of this boundary to the transfer of heat in these structures.

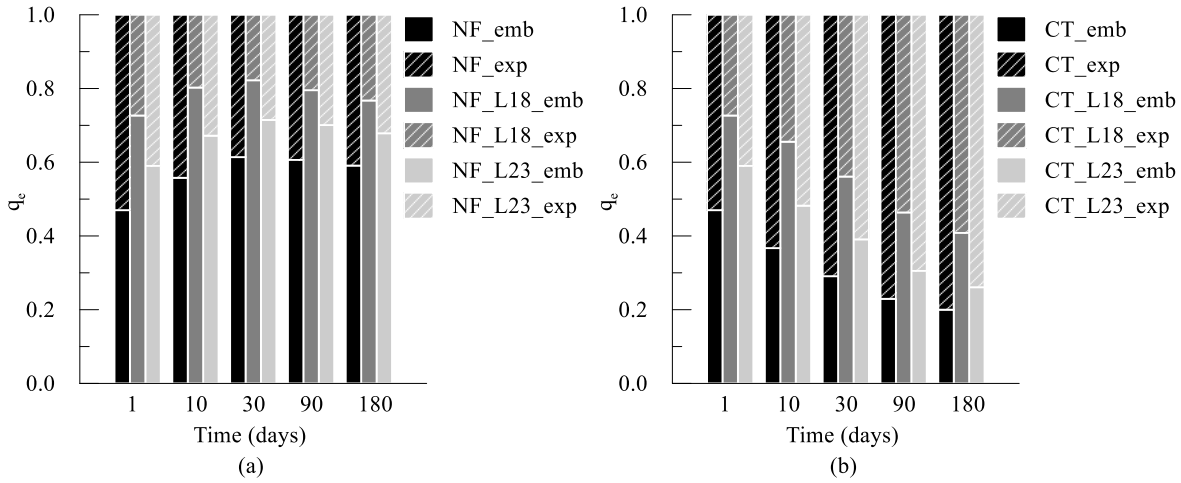

Figure 5-22: Comparison of heat flux ratio q_e for different wall geometries (a) NF and (b) CT

The effect of the different wall geometries is further investigated by comparing the energy per metre width, $E_{tot,B}$, transferred during the operation period. Clearly, a different scenario is now observed when comparing the energy per metre width of wall, $E_{tot,B}$, since the normalisation is different. Indeed, as can be observed from the results shown in Figure 5-23, for both boundary conditions, $E_{tot,B}$ is largest for analysis L23 as it has the largest heat exchange area. In effect, when compared to the reference case, an increase in energy of 62% and 52% is computed for the NF and CT cases, respectively. Furthermore, for the NF case, configuration L18 is slightly more efficient (5%) than the reference case due to the larger embedded section, while the contrary is valid for the CT case, with L18 transferring 17% less energy than the reference case, since the latter configuration is characterised by a larger exposed area, which favours heat transfer under CT conditions.

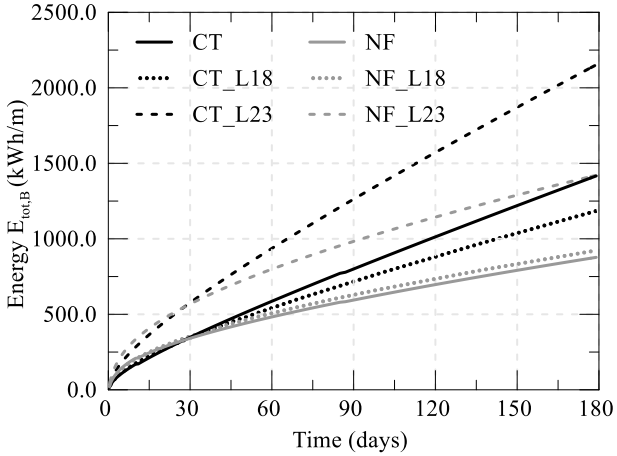

Figure 5-23: Influence of wall geometry on variation with time of energy per metre width of wall for different boundary conditions along exposed part of the wall

Number of pipes

Figure 5-24 (a) and (b) depict, respectively, the heat flux and energy computed for walls with different numbers of pipes in the out-of-plane direction (ranging from 2 to 6) within the 1.5 m wide wall panel. Naturally, this is equivalent to varying the pipe spacing B/n_pbetween 0.75m and 0.25m. In 2D, this is simulated by varying the cross-sectional area of the pipe, A_p^{2D}, calculated according to Equation (5-6), to achieve the same water flow rate per metre width as in a 3D problem. Furthermore, both the correction factor X and Y vary with the number of pipes, n_p (see Equations (5-8) and (5-10)). The parameters used in the 2D analyses are summarised in Table 5-10.

Table 5-10: Parameters used for 2D analyses simulating different numbers of pipes

Analysis	A_p^{2D} (m)	$\Delta T_{in,3D}$ (°C)	$\Delta T_{in,2D,CT,HF}$ (°C)	$\Delta T_{in,2D,NF,E}$ (°C)	$\Delta T_{in,2D,CT,E}$ (°C)
Ref. case (n_p = 2)	4.36×10^{-4}		9.7	12.0	9.0
n_p = 4	8.67×10^{-4}	15.0	11.9	13.7	11.2
n_p = 6	1.3×10^{-3}		12.8	14.1	12.1

For insulated walls, increasing the number of pipes does not affect the long-term heat injection rate and little gain in transferred energy is computed. This is attributed to the fact that, under these conditions, the wall heats up at such a fast rate that a further increase in the number of pipes does not contribute to improving heat exchange. Indeed, the increase in energy of 112 kWh/m (13%) and 156 kWh/m (18%) calculated for n_p=4 and n_p=6, respectively, is due to the larger heat transfer rate in the short term with larger number of pipes. Conversely, it has a beneficial effect on the thermal performance for walls exposed to a CT boundary condition, as was also concluded by Di Donna et al. (2017). In fact, in this case, a larger number of pipes enhances the heat transfer through this boundary, thus leading to lower

outlet temperatures. The computed heat injection rate after 6 months of operation for a panel with four pipes is 20.8 W/m^2 (i.e. 4.0 W/m^2 (24%) more than in the case of n_p=2) and with six pipes is 22.3 W/m^2 (i.e. 5.5 W/m^2 (33%) more than in the case of n_p=2), with the gains in the transferred energy being slightly higher (28% and 38% for four and six pipes, respectively) due to the short-term effects. The limited increase in heat injection rate between n_p=4 and n_p=6 of 1.5 W/m^2 and of transferred energy of 137 kWh/m indicates that increasing the number of pipes beyond a certain point may only lead to marginal gains in energy performance. This has to be balanced with the fact that a reduced number of pipes will be more economical in terms of material and installation costs. Furthermore, considering that the behaviour of real walls lies in between the two considered boundary conditions, it can be stated that the increase in thermal performance with a larger number of pipes is limited and highly dependent on the heat transfer mechanism assumed for the excavated face, further reinforcing the need to characterise accurately this aspect of thermo-active retaining walls.

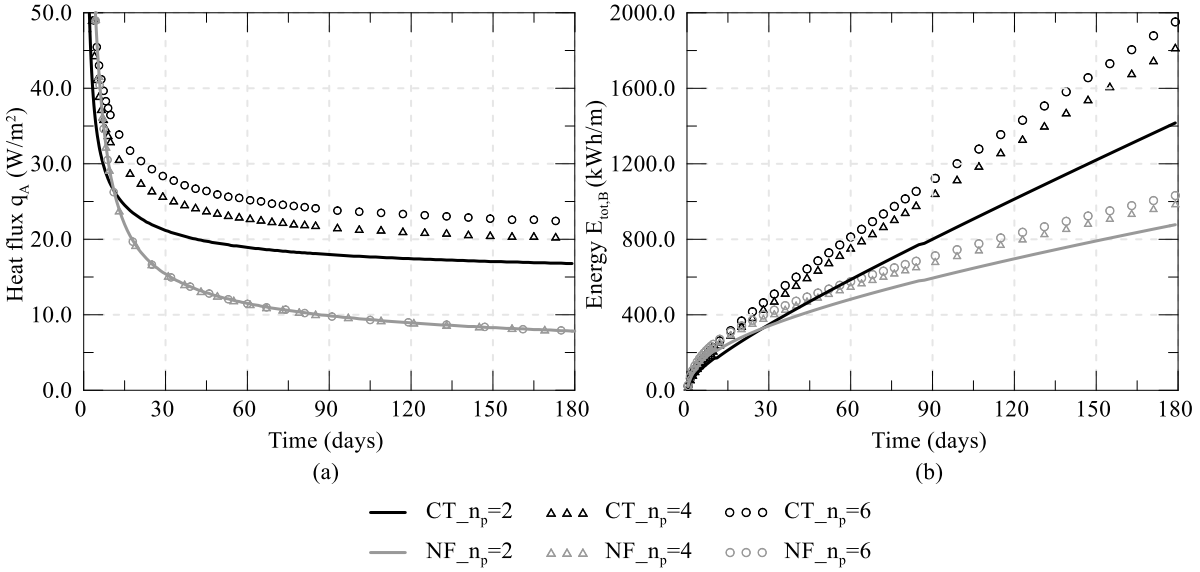

Figure 5-24: Effect of number of pipes n_p on evolution with time of (a) heat flux per unit area of wall with time and (b) energy per metre width

Concrete and soil thermal conductivity

The influence of the concrete thermal conductivity (λ_c) and soil thermal conductivity ($\overline{\lambda_s}$) is investigated by performing analyses using half and double the values employed in the reference analysis (see Table 4-1). Table 5-11 summarises the input parameters, since the concrete and soil thermal conductivities affect the correction factor Y. Figure 5-25 and Figure 5-26 show, respectively, the variation of the heat flux and transferred energy with time for the analyses with different λ_c and $\overline{\lambda_s}$.

Table 5-11: Parameters used for 2D analyses simulating different concrete and soil thermal conductivity

Analysis	λ_c (W/mK)	$\overline{\lambda_s}$ (W/mK)	$\Delta T_{in,3D}$ (°C)	$\Delta T_{in,2D,NF,E}$ (°C)	$\Delta T_{in,2D,CT,E}$ (°C)
Reference case	1.60	1.62		12.0	9.0
$2.0\lambda_c$	3.20	1.62		13.3	9.6
$0.5\lambda_c$	0.80	1.62	15.0	10.0	8.4
$2.0\overline{\lambda_s}$	1.60	3.23		13.5	8.4
$0.5\overline{\lambda_s}$	1.60	0.81		13.0	9.5

When an insulated wall is simulated (NF), the difference in heat flux with different λ_c is limited to ±3% of the one computed for the reference case (in Figure 5-25 (a) the three analyses appear to plot on a single line). As noted earlier, the heat transfer in these analyses occurs mainly towards the soil, therefore changing the thermal conductivity of the concrete will not affect greatly the results in the long term. However, it does affect the short-term heat exchange rate (see Appendix F for details), with different inlet temperatures computed as λ_c is varied, with the correction factor Y decreasing with decreasing λ_c (see Equation (5-10)). Thus, a slightly larger energy (11%) is computed when a high concrete conductivity is employed, while decreasing the conductivity by 50% leads to a reduction in the calculated energy of about 23%. Conversely, varying the thermal conductivity of the concrete has clearly a large effect for walls exposed to an environment at constant temperature (CT), since, for such a condition, the heat transfer takes place mainly through the wall-air interface, and, thus, through the concrete. In fact, for the analysis with a concrete conductivity twice as large as that in the reference analysis, the heat flux computed after 6 months is 28.2 W/m^2 (+68%), whereas a heat flux of 10.7 W/m^2 (-36%) is calculated for the analysis with half the concrete conductivity, with similar differences computed for the transferred energy (see Figure 5-26 (a)).

As expected, observing Figure 5-25 (b), varying the soil thermal conductivity has a more pronounced effect on the heat flux computed for insulated walls (NF), because of the heat transfer taking place mainly through the wall-soil interfaces. Compared to the reference analysis, halving or doubling $\overline{\lambda_s}$ leads to differences in heat flux after 6 months of 2.6 W/m^2 (-34%) and 4.5 W/m^2 (+58%), respectively, while, in terms of energy, differences of 195 kWh/m (-22%) and 163 kWh/m (+18%) are obtained for the two extreme values. A smaller difference is calculated for walls exposed to a constant temperature (CT): for soils with high thermal conductivity the heat flux and energy increase, respectively, by 17% and 11%, whereas they decrease by 10% and 5% for low conductivity soils.

It is interesting to note that, as can be clearly observed when comparing Figure 5-26 (a) and (b), the impact of the concrete conductivity on the transferred energy is visible in the very short term, while, when $\overline{\lambda_s}$ is varied, its effect arises much later in time (>30days), confirming that the concrete

conductivity has a major impact in the short term, while the soil conductivity affects the long term. This observation raises concerns over the suitability of performing small duration thermal response tests in thermo-active walls, since it is likely that the performance inferred from these field tests will be more affected by the thermal conductivity of the concrete, rather than by that of the soil.

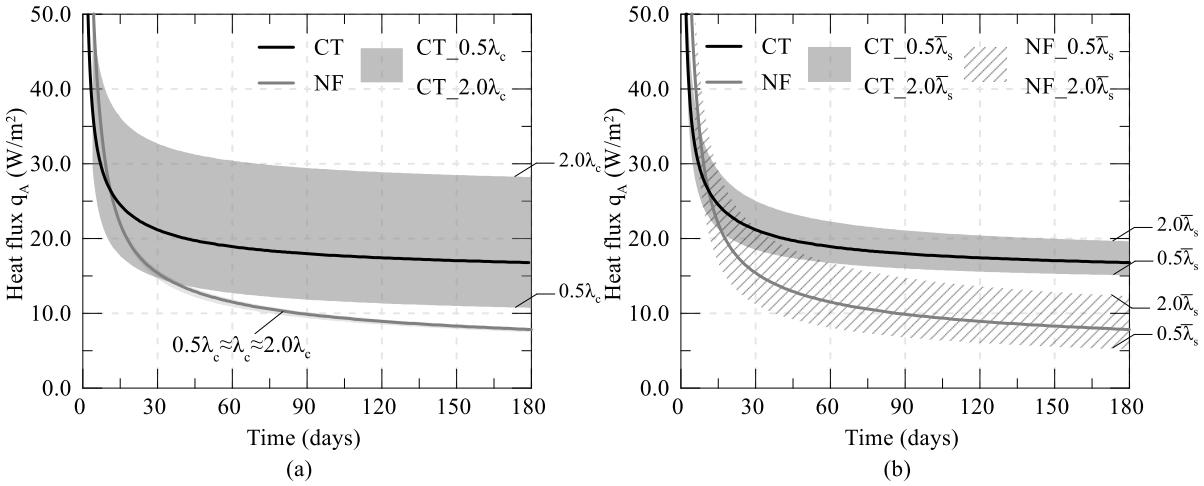

Figure 5-25: Heat flux with time for different (a) concrete thermal conductivity and (b) soil thermal conductivity

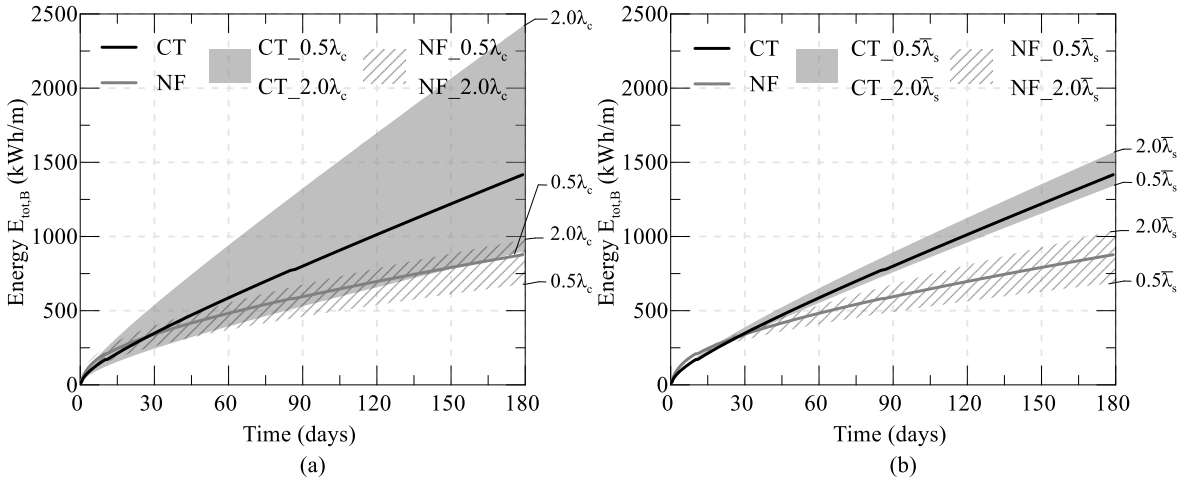

Figure 5-26: Energy with time for different (a) concrete thermal conductivity and (b) soil thermal conductivity

Varying the concrete conductivity has almost no effect on the changes in ground temperature, with differences <0.25°C for all of the analysed scenarios. However, the concrete thermal conductivity does control the temperatures within the wall, with higher values recorded for a small thermal conductivity, which is consistent with the heat dissipating at a slower rate. Conversely, the soil thermal conductivity affects greatly the temperature distributions within the ground. Figure 5-27 shows the development of changes in temperature within the ground on the retained side at 11.0 m depth for different soil thermal conductivities. Given the larger heat flux and transferred energy, a larger amount of heat is transferred to the soil with a high $\overline{\lambda_s}$. While this does not affect the temperatures at the wall-soil interface, it leads to considerable differences in the computed temperature at large distances from the wall with respect

to the reference case. At a distance of 5.0 m, with a high soil thermal conductivity, the changes in ground temperature increase by 1.8°C and 1.1°C, respectively for the NF and CT case. For a low $\overline{\lambda_s}$, the changes in ground temperature reduce by 2.1°C and 1.4°C for NF and CT, respectively. It should be noted that the relative difference between the values computed at all distances is not affected by the boundary condition. Indeed, doubling or halving the soil thermal conductivity leads to a difference of +40% and -47% at 5.0 m distance for both cases. This indicates that, as expected, the boundary condition does not affect the rate of heat transfer from the wall towards the soil, which, in effect, is controlled by the thermal diffusivity of the soil only (α_T).

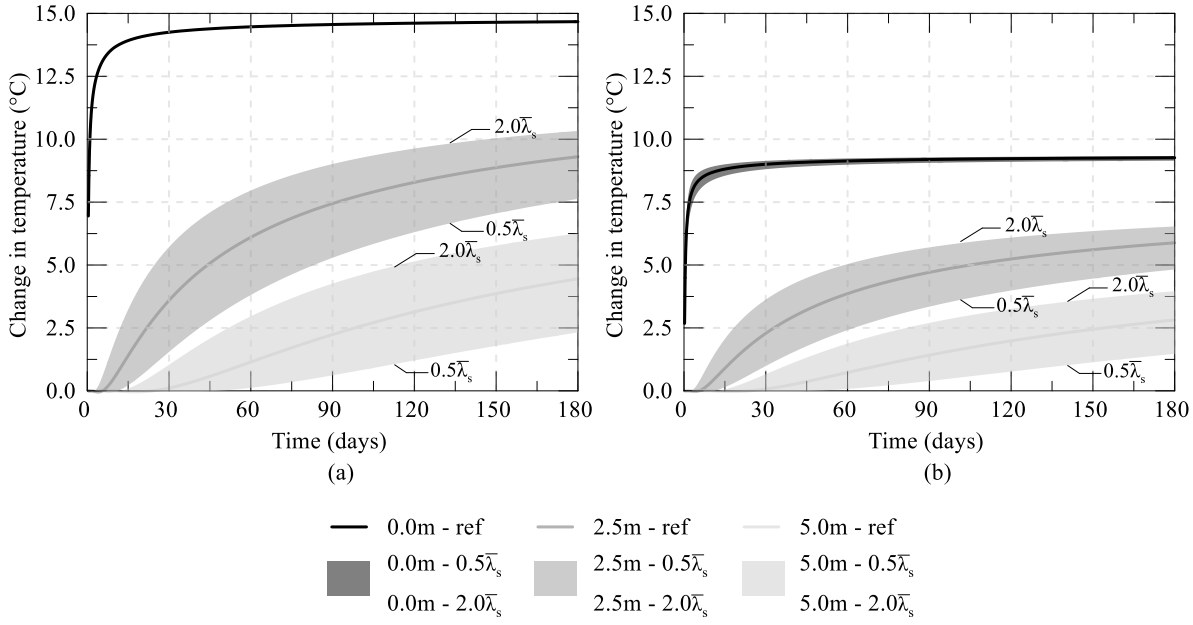

Figure 5-27: Changes in ground temperature at 11m depth behind the wall within the retained side for different soil thermal conductivity (a) NF and (b) CT

Water flow velocity

The effect of the water flow velocity on the heat extraction rate was analysed by modelling velocities ranging from 0.2 to 1.4 m/s, where the same water flow rate as simulated in the 3D analyses is ensured by calculating the pipe area in the 2D analyses (A_p^{2D}) through Equation (5-6). Considering the geometry of the reference analysis (i.e. 2 pipes spaced 0.75 m apart with A_p^{3D}= 3.27×10^{-4} m^2), A_p^{2D} is equal to 4.36×10^{-4} m^2. Furthermore, it should be noted that the correction for the long-term heat flux is not affected by the water flow velocity.

Figure 5-28 (a) and (b) depict, respectively for the NF and CT boundary condition, the variation of the heat flux for different water flow velocities at different time instants. The results show that the water flow velocity has an impact only in the very short term (<5h), whereas, after this period of time, the same heat extraction rate is computed in all the cases. Indeed, the fluid flow velocity controls merely the time to thermal breakthrough (i.e. when changes in temperature at the outlet are first measured)

where this is reached earlier with a higher water flow velocity, leading to a lower ΔT_p. However, this reduction in ΔT_p is not as large as the increase in water flow rate arising from the larger flow velocity, meaning that the product between these two quantities, and hence the heat flux, increases with water flow velocity. This agrees with what was observed by Xia et al. (2012) in the field test performed on thermo-active wall panels within the Natural History Museum of Shanghai. According to their observations, they suggest a water flow velocity ranging between 0.6 and 0.9 m/s, in order to balance energy efficiency and costs associated with the circulation pumps required to increase the flow rate. However, this conclusion is based on tests that lasted only 48h, thus the long-term effect of this parameters was not investigated. According to the results presented herein, it could be concluded that, for uniform operational regimes, even lower water flow velocities may be employed, without sacrificing the energy efficiency, while cutting the costs of the operation of the circulation pump. Additional research would be required to establish the validity of this conclusion for more realistic operational modes (i.e. intermittent operation).

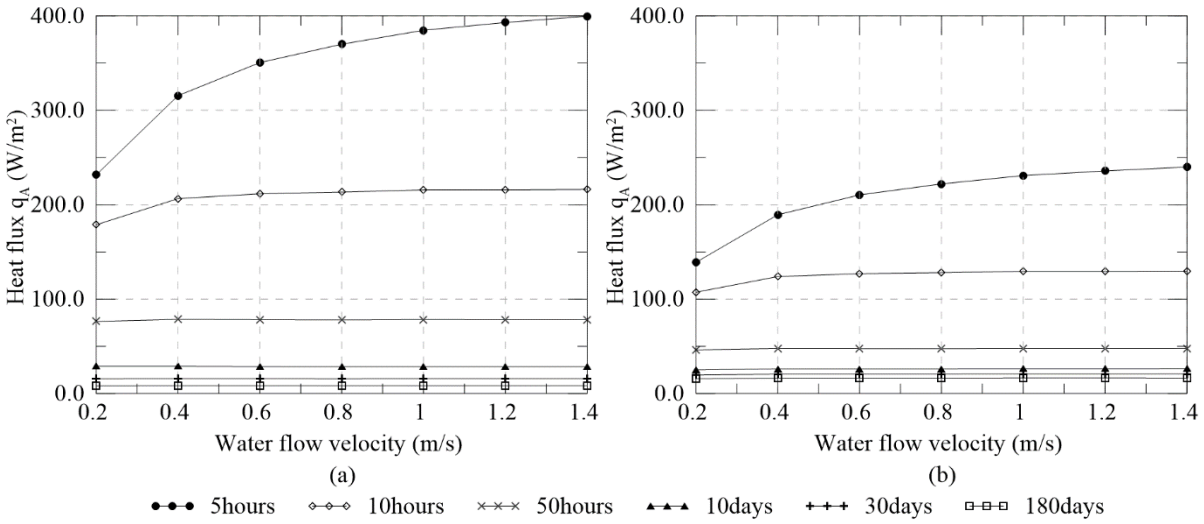

Figure 5-28: Heat flux for different water flow velocities and time instants for (a) NF and (b) CT

This conclusion agrees with the results presented in Di Donna et al. (2017), while Sterpi et al. (2017) found that the fluid flow velocity considerably affects the heat transfer rate. However, as detailed in Section 2.4.4, the values employed by Sterpi et al. (2017) are one to two orders of magnitude smaller than those analysed in this section and thus not directly comparable. Therefore, an additional analysis was carried out employing a water flow velocity of 0.01 m/s, which leads to a water flow rate similar to that presented in Sterpi et al. (2017). As previously mentioned, the calculation of the heat flux depends on the water flow rate, which affects the development of the temperatures within the pipes, where a smaller water flow rate leads to a slower increase with time of the temperatures within the pipes. Figure 5-29 (a) and (b) show respectively the calculated heat flux and the computed outlet temperatures for three different water flow velocities. As concluded from the results shown above, little difference is obtained when velocities of 0.2 m/s or 1.0 m/s are employed, with the long-term behaviour

being the same. The case with v=0.2 m/s predicts slightly lower outlet temperatures, though the increase in ΔT_p (which would lead to a higher heat flux) is compensated by a reduced water flow rate when q_A is calculated. On the other hand, a very different behaviour is observed with v=0.01 m/s. Clearly, as shown in Figure 5-29 (b), the time to thermal breakthrough is delayed and much lower outlet temperatures are obtained. However, the heat flux is lower than that computed for the other two analyses, reflecting the fact that, even with a large temperature difference between inlet and outlet, with such a low water flow rate the calculated q_A will be small. Furthermore, the effect of the boundary condition along the exposed face of the wall is very small, with CT and NF presenting almost the same long-term heat flux for this very low flow velocity. This indicates that the effect of the boundary condition reduces as the heat transfer occurs at a slower pace.

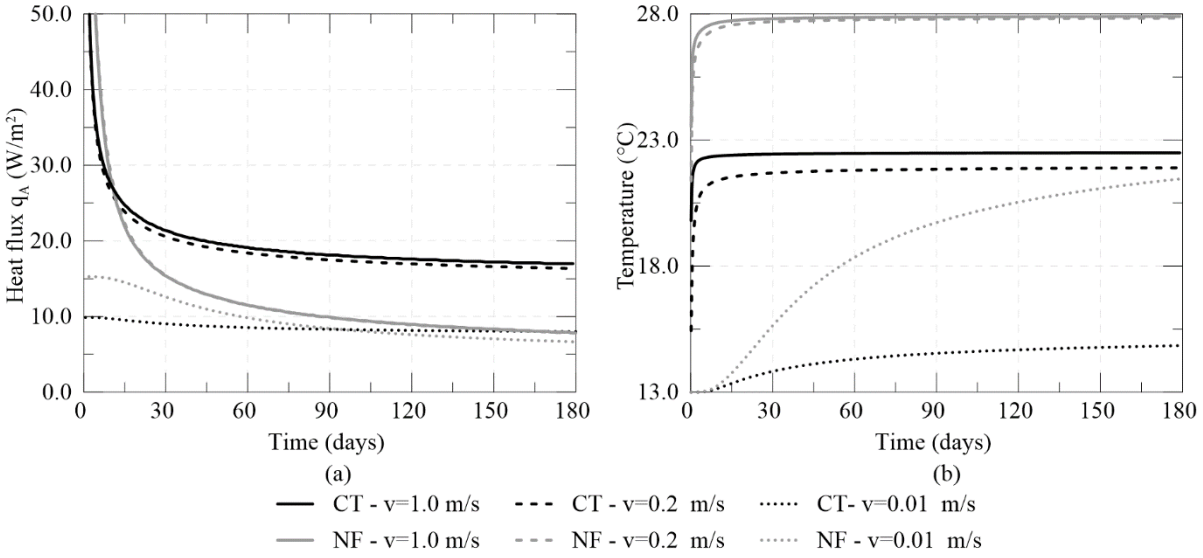

Figure 5-29: Impact of different water flow velocities on (a) heat flux and (b) outlet temperature

Inlet temperature

The effect of the temperature change at the pipe inlet ΔT_{in} (i.e. $T_{in} - T_0$) was analysed varying this quantity between 10°C and 20°C (note that 15°C was the value applied at the reference case and hence this represents a variation of ±1/3). Since both correction factors X and Y are not affected by ΔT_{in}, only the long-term heat flux is analysed, with X being equal to 0.6 for all cases.

Figure 5-30 shows the obtained results, demonstrating that, as expected, increasing the temperature at the pipe inlet increases the heat flux, due to the larger potential for exchanging heat. Perhaps unsurprisingly, the effect is independent of the boundary condition along the exposed face, with the heat flux for both cases varying proportionally to the change in temperature applied at the inlet (i.e. ±1/3). Indeed, if the values were to be plotted as the ratio of $q_A/\Delta T_{in}$, the results would plot on top of each other. This is because the heat transfer within the concrete and soil is simulated as purely conductive.

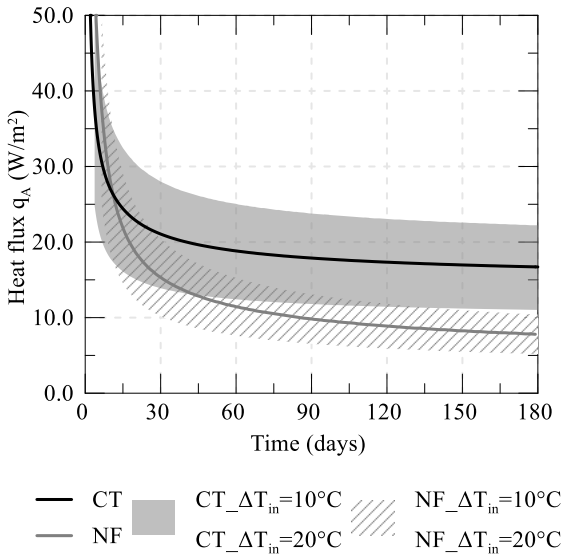

Figure 5-30: Effect of temperature change at pipe inlet on heat flux with time

Operation mode

The analyses presented so far simulated heat exchange with a continuous operation mode, i.e. the heat pump was constantly operating for 24h/day. In real applications, this is unlikely to be the case, with the exception perhaps of periods corresponding to the peak heating/cooling load. Indeed, heat pumps usually operate following an intermittent pattern, meaning the heat pump is likely to be switched off for substantial periods of time. The analyses representing the reference case were repeated simulating an intermittent operation mode (IOM) by alternating 6h of operation and 6h of idling, for a period of 6 months. The same 2D approximations as for a continuous operation mode were adopted which assumes that the heat transfer mechanisms do not change significantly and both 2D and 3D models would recover in a similar manner during the idling periods. However, if IOM would be idealised as a sequence of short-term operations alternating between injection and idling, then the assumption above is an important one, since the 3D to 2D approximations appear to perform with smaller accuracy in the very short term. Clearly, the only form of verifying whether this idealisation is correct would be to perform a 3D analysis featuring IOM. However, the study carried out by Pang (2018) demonstrated that a 2h timestep is required to model a 6h IOM with sufficient accuracy (while all the analyses so far used timesteps up to 48h), meaning that such simulation would require a much larger amount of time steps, rendering 3D analysis impractical due to the required computational resources.

The results for the reference analyses adopting a continuous operation mode are compared to those obtained when simulating an intermittent operation mode (IOM) and are displayed in Figure 5-31. Clearly, the simulation of an intermittent operation mode leads to a noticeable increase in the heat injection rate, as shown in Figure 5-31 (a). Indeed, on average, the modelled heat flux is almost twice the one computed with a constant operation mode, for both NF and CT boundary conditions. This increase in heat flux is due to the fact that during the idling periods (i.e. when the heat pump is switched

off) the temperature in the concrete and surrounding ground (i.e. the storage media) is allowed to recover, thus leading to a reduction in the overall temperature of the system. Therefore, when the operation is resumed, the gradient between the heat carrier fluid and the storage media is higher, enhancing heat transfer from the former to the latter. However, it is important to note that the total energy extracted over 6 months using the two different operation modes is approximately the same, as can be observed from Figure 5-31 (b). Indeed, only a slightly larger amount of energy (6% for both boundary conditions) is transferred when a continuous operation mode is simulated. This suggests that the intermittent operation mode is more efficient, since the same energy is exchanged in half the operation time, reducing the costs associated with system operation.

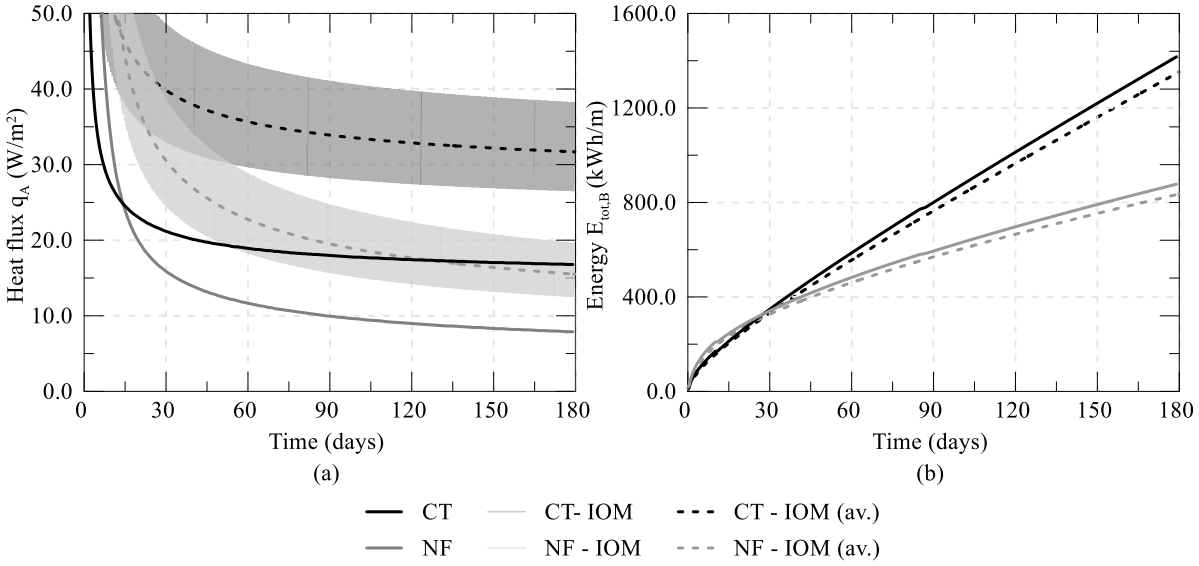

Figure 5-31: Comparison between continuous and intermittent operation mode (a) heat flux and (b) transferred energy

The changes in ground temperature at different distances behind the wall at a depth of 11.0 m within the retained side for the two operation modes are compared in Figure 5-32. The operation mode affects slightly the temperatures at the wall-soil interface, with the IOM predicting smaller changes in temperature due to the resting periods which allow the temperature to dissipate. In effect, the differences in the long term are less than 0.5°C for both cases. At larger distances from the wall, even smaller differences are computed. Hence, it can be concluded that adopting a continuous operation mode enables an accurate modelling of the temperature changes within the ground, even if the real operation mode is different, while performing simpler and more computationally efficient analyses.

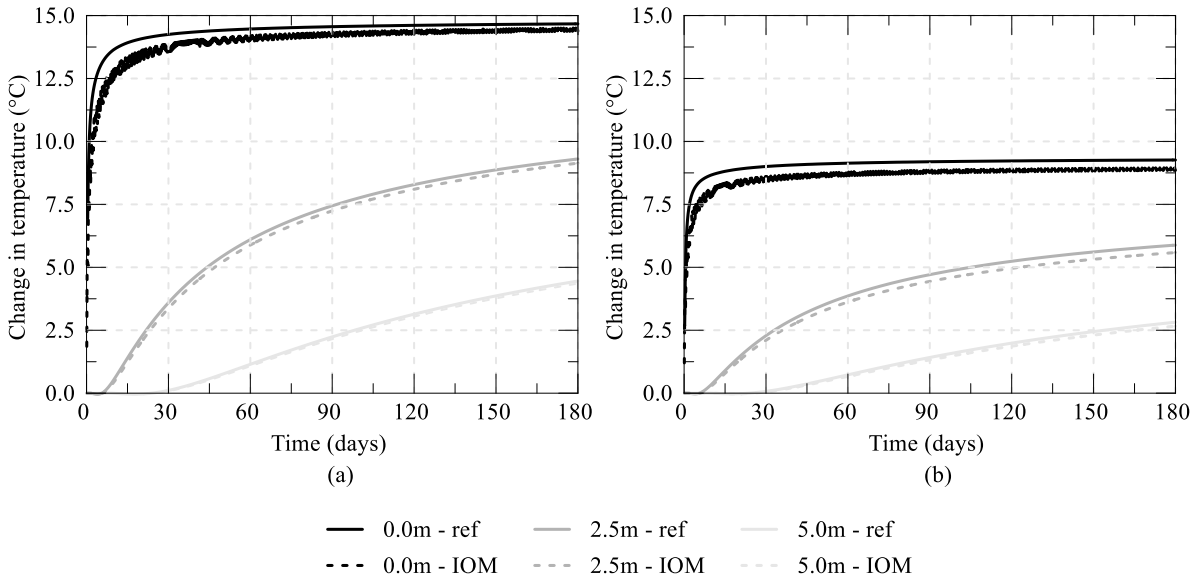

Figure 5-32: Impact of operation mode on changes in ground temperature (a) NF and (c) CT

5.4 Long-term efficiency

In this section, the long-term efficiency of thermo-active walls is analysed by simulating different scenarios over an operation period of 10 years, where, for each case, walls with a NF or CT boundary condition along the excavated wall were simulated. The analyses carried out aim at investigating the long-term effect of cyclic heating and cooling on the thermal performance of a retaining wall and of the recorded changes in ground temperature, with their magnitude and extent to which ground temperatures are affected around the structure being assessed. Indeed, this is an aspect that should be considered during the design of these structures, especially if they are installed in a densely-built urban environment. In such a scenario, the changes in temperature occurring due to the heat exchange may affect nearby underground infrastructure (see e.g. the numerical study reported in Sailer et al. (2019a)) and they should be assessed to evaluate possible system interactions.

5.4.1 Analyses

Table 5-12 summarises the assessed scenarios, where it should be noted that the terminology employed to describe the operation mode (i.e. heating and cooling) denotes the effect the above-ground circuit has on the soil-side system (i.e. in heating, heat is transferred to the ground to cool the building, and the opposite is true for cooling). Four different operation modes were assumed: a balanced operation of 6 months of heating (heat injection) and 6 months of cooling (heat extraction); 6 months of heating followed by 6 months of idling; 9 months of cooling and 3 months of heating; 9 months of cooling and 3 months of idling. It should be noted that the last two scenarios are likely to be representative of the use of ground source energy systems for residential buildings in temperate climates such as those of northern Europe, where heating needs prevail over the year and cooling may even be absent.

Table 5-12: List of performed analyses for effect of long-term cyclic loading on thermal performance

Analysis	Heating (heat injection)	Cooling (heat extraction)
Scenario (1)	6 months	6 months
Scenario (2)	6 months	N/A
Scenario (3)	3 months	9 months
Scenario (4)	N/A	9 months

The analyses were performed on the same reference geometry outlined in the previous section. However, due to the larger simulation time, the distances between the structure and the right-hand side and bottom mesh boundaries were increased in order to avoid boundary effects on the temperature distributions, while the left-hand side boundary was kept unchanged, simulating an excavation width of 30.0 m. The employed mesh, which is shown in Figure 5-33, extends to 100.0 m from the back of the wall and 45.0 m below the toe of the wall. The same type of elements and boundary conditions as in the previous analyses described in Section 5.2.2 were applied. While towards the end of each cycle the size of the time step could be increased since smaller changes in temperature occur, at the beginning of each cycle the time step has to be reduced in order to accurately capture the higher gradients in temperature at those time instants.

The temperature change at the pipe inlet, $\Delta T_{in,3D}$, was assumed to be 15°C both in heating and cooling. Since the aim of this study is the evaluation of the long-term thermal performance and changes in ground temperature, the analyses are carried out employing only the 2D approximations required to match the long-term heat flux, i.e. those described in Sections 5.2.3.1 and 5.2.3.2. Hence, for the NF boundary condition, the inlet temperature in heating (i.e. heat injection) was 28°C (i.e. T_0 + $\Delta T_{in,3D}$= 13°C + 15°C) while in cooling (i.e. heat extraction) it was -2°C (i.e. T_0 - $\Delta T_{in,3D}$= 13°C - 15°C), which is still an allowable temperature for GSHP systems, provided that antifreeze solutions are employed for the heat carrier fluid. For the CT boundary condition, the calculated inlet temperatures according to Equations (5-7) and (5-8) were of 22.7°C (i.e. T_0 + $\Delta T_{in,3D}$= 13°C + 0.65×15°C) and 3.3°C (i.e. T_0 + $\Delta T_{in,3D}$= 13°C + 0.65×15°C), for heating and cooling mode, respectively.

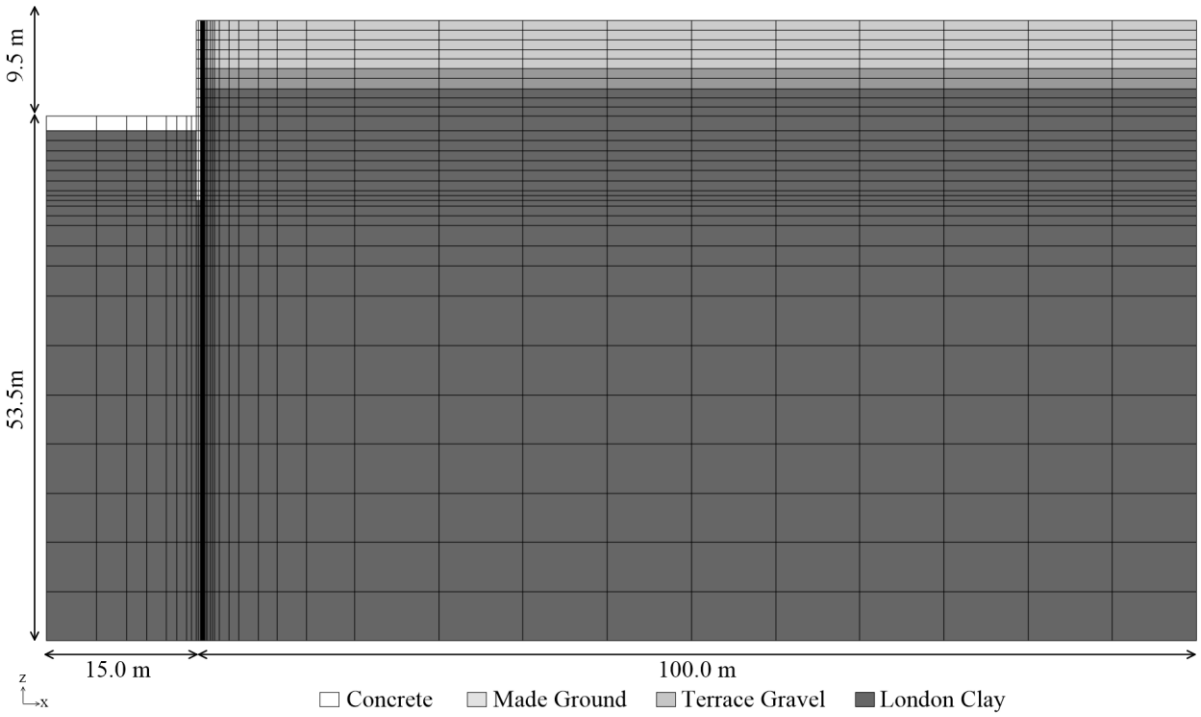

Figure 5-33: Finite element mesh for long-term simulations of thermal performance

5.4.2 Results

Scenario (1)

The evolution of the calculated heat flux per unit area, q_A, over 10 years of operation for both boundary conditions is displayed in Figure 5-34 for the case of 6 months of heating followed by 6 months of cooling.

Figure 5-35 plots the calculated heat flux at the end of each heating/cooling cycle (i.e. the minimum thermal performance for that cycle). It can be noted that the long-term heat flux remains approximately constant over the whole duration of the operation, with only marginal changes in the first two years, after which constant long-term heat extraction/injection rates are evaluated. This indicates that the problem has reached thermal equilibrium. This is a consequence of the balanced heating and cooling cycles being simulated, meaning that in each cycle the same energy is extracted and injected, allowing the soil to undergo little permanent temperature changes.

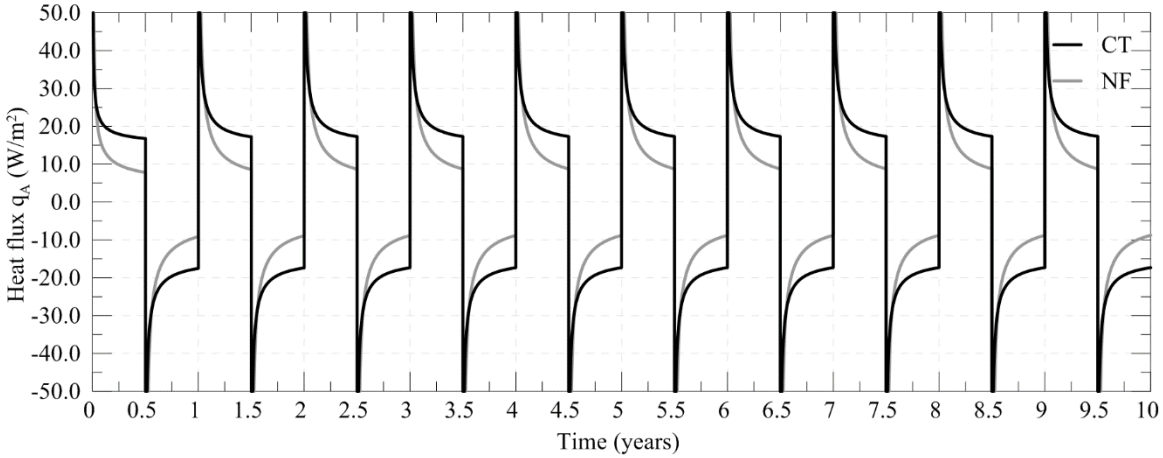

Figure 5-34: Scenario 1 - Heat flux versus time

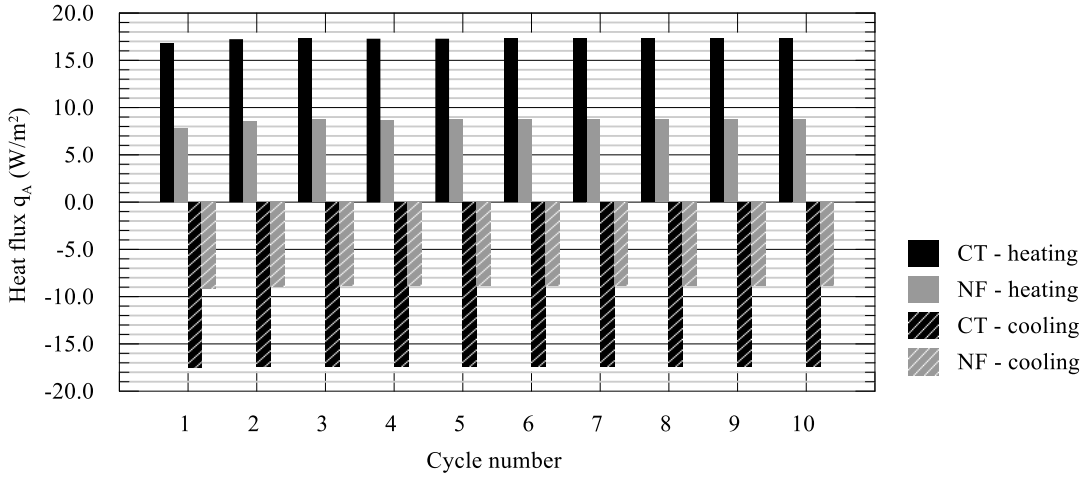

Figure 5-35: Scenario 1 - Heat flux at the end of each cycle versus cycle number

This is confirmed when observing the changes in temperature within the soil during the operation period. Figure 5-36 depicts the changes in temperature within the retained and excavated sides of the wall at different distances from the wall, while Figure 5-37 and Figure 5-38 show the contours of changes in temperature at the end of selected heating/cooling cycles for the NF and CT boundary conditions, respectively, along the exposed face. As expected, larger temperatures are computed for the NF case due to the insulated boundary along the exposed face. The temperatures within the soil in close proximity of the wall fluctuate considerably during each cycle, with the peaks being of ±12.0°C and ±7.5°C at 1.0 m from the wall, for the NF and CT case, respectively. At larger distances, considerably smaller temperature changes are recorded, with variations of approximately ±3.0°C and ±2.0°C at 5.0m from the wall for NF and CT, respectively. For both cases, no changes in temperature can be observed at distances from the wall above 10.0 m in the long term. This can also be clearly observed by the contour plots in Figure 5-37 and Figure 5-38, with the temperature changes in heating being approximately the same as in cooling, with opposite sign. Thus, there is no permanent drift of temperature change. Indeed, from Figure 5-38 and Figure 5-37 it is evident that a relatively small portion of soil around the wall is affected by temperature changes, which is beneficial in terms of long-

term efficiency and of interaction with surrounding underground structures. The changes in temperature within the excavated side are for all cases and at all distances smaller than on the retained side, since the pipes are located towards the retained side of the wall. Thus, a larger amount of time is required for the temperature changes to reach the monitored locations within the excavated side. Furthermore, it is evident from Figure 5-37 and Figure 5-38 that the changes in ground temperature have not reached the axis of symmetry (i.e. the left-hand boundary) and are thus not affected by the simulated adiabatic boundary condition. This suggests that there is a minimum value for the width of excavation, above which this quantity stops affecting the performance of the system, i.e. the opposite walls work as independent heat exchangers. For the considered operation mode and geometric characteristics of the retaining wall, the obtained contours indicate that the simulated width of 30 m is larger than that minimum value.

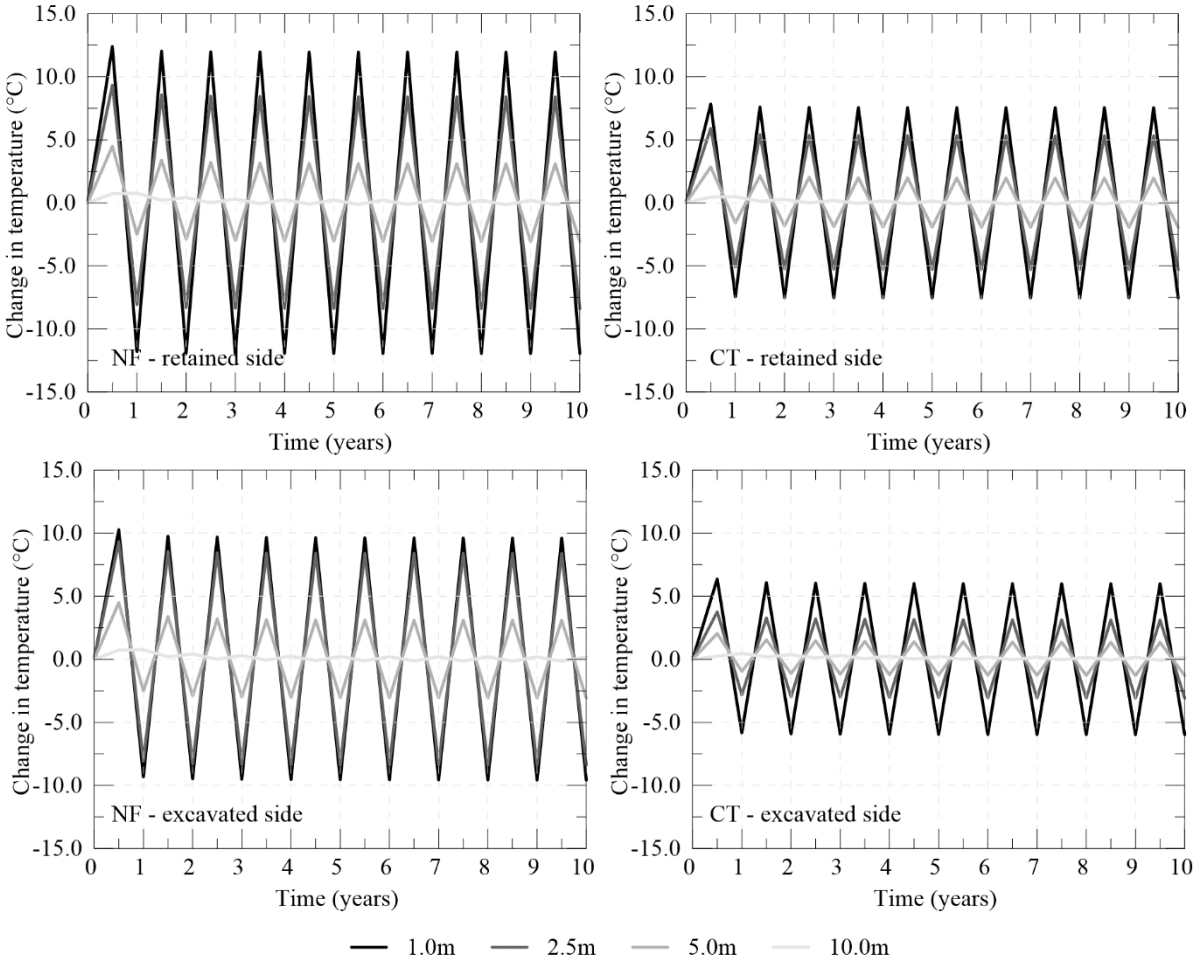

Figure 5-36: Scenario 1 - Change in soil temperature with time at different distances from the wall on the retained (11.0 m depth) and excavated side (15.0 m depth)

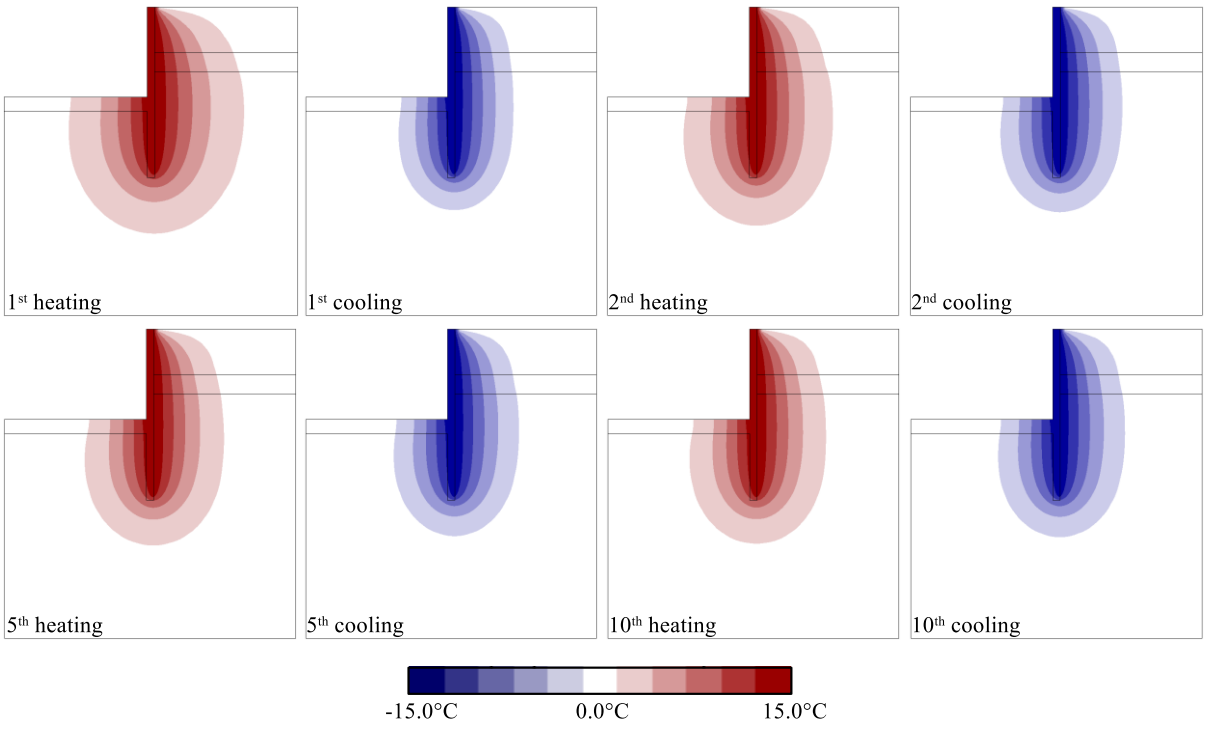

Figure 5-37: Scenario 1 - Contours of changes in temperature – NF

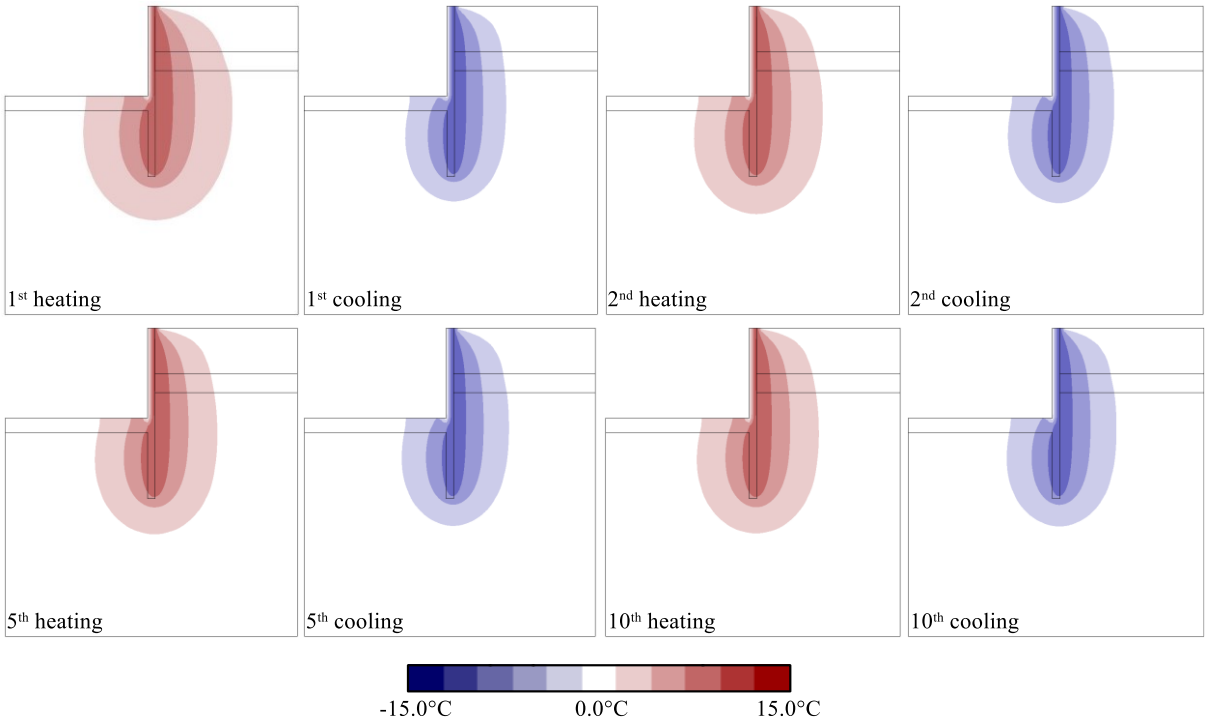

Figure 5-38: Scenario 1 - Contours of changes in temperature – CT

Scenario (2)

The development of the heat flux with time calculated for the analyses consisting of 6 months of heating and 6 months of idling is shown in Figure 5-39. As can be noted from the computed long-term heat flux after each cycle depicted in Figure 5-40 for this scenario, the heat flux steadily reduces with each cycle and this effect is more pronounced for the NF case. During the idling phase, the temperature is allowed to dissipate; however, this phenomenon does not take place at a sufficiently fast rate to allow the soil to completely recover from the temperature changes induced by the heat exchange. Hence, at the beginning of each subsequent cycle, the ground temperature is higher than at the previous cycle, which decreases the potential of heat transfer since the inlet temperature remains unchanged. For the NF case, after the 10th heating cycle, the heat flux has reduced from 7.8 W/m^2 obtained at the end of the 1st cycle to 5.0 W/m^2, i.e. a reduction of 36% during 10 years of operation is computed. For the CT case, a smaller difference, of 1.3 W/m^2 (8%), is registered. This is because the constant temperature boundary condition simulated along the exposed face of the wall assists in dissipating the temperature changes within the soil. Furthermore, this aspect leads to a smaller time required to reach thermal equilibrium: as it can be observed in Figure 5-40, the heat flux has stabilised during the last 3 cycles for the CT case, while it is still slightly decreasing for the NF case.

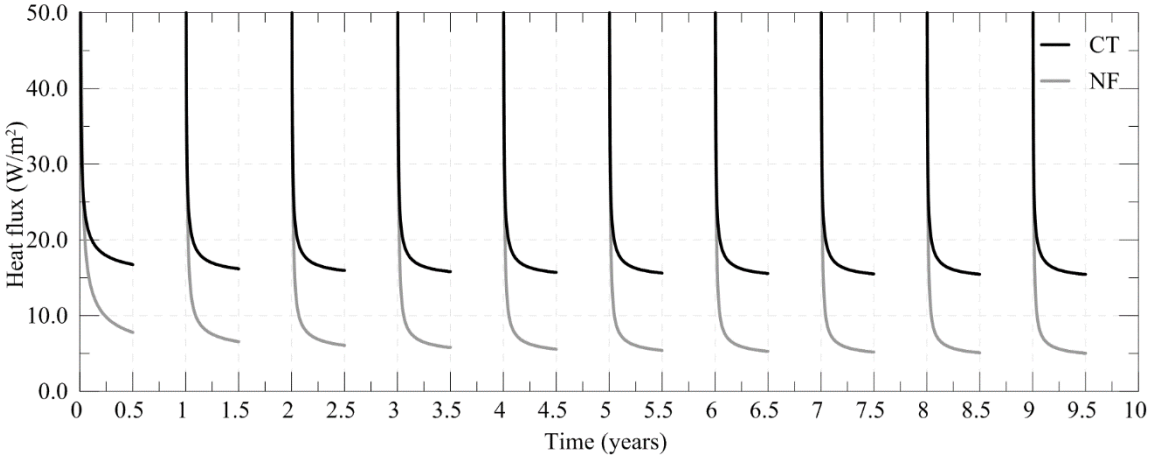

Figure 5-39: Scenario 2 - Heat flux versus time

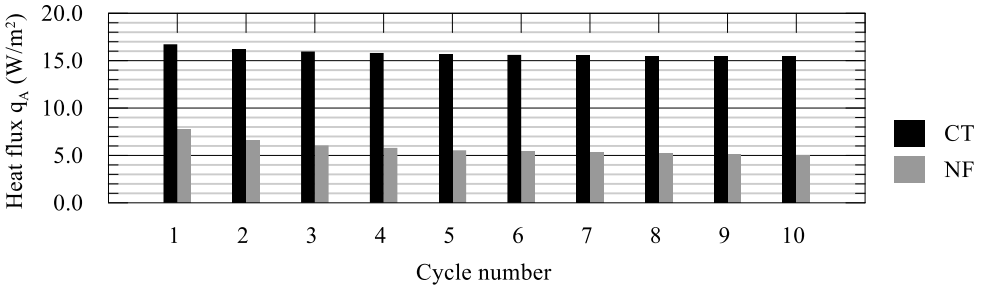

Figure 5-40: Scenario 2 - Heat flux at the end of each cycle versus cycle number

The use of an unbalanced operation leads to permanent changes in ground temperatures, as can be observed from Figure 5-41. Noticeable fluctuations are computed close to the wall (1.0m), where the

largest changes in temperature occur within the retained side and reach values of 13.4°C and 8.3°C for the NF and CT case, respectively. Moreover, only part of the temperature change is recovered during each idling period: from the end of the first heating cycle to the end of the last one, the system temperature increases by 1.0°C and 0.5°C, respectively for the NF and CT cases. Furthermore, during the idling period, the temperature increases with time after each cycle: from the end of the first idling period to the end of the last idling period, the temperature increases by 3.0°C and 1.1°C, for the NF and CT cases, respectively. A permanent change in temperature can also be observed at larger distances from the wall on the retained side: at a distance of 10.0 m, at the end of the simulation period, the recorded ground temperature changes are equal to 5.1°C and 2.7°C for NF and CT, respectively. Within the excavated side, smaller temperature changes are recorded initially. However, with time, at large distances from the wall, higher temperatures develop, where at 10.0 m distance, these are equal to 8.4°C and 4.4°C. Indeed, as can be seen from the contour plots displayed in Figure 5-42 and Figure 5-43, respectively for NF and CT, the changes in temperature reach the axis of symmetry (i.e. left hand side boundary) and thus an accumulation of heat occurs due to the simulated insulation along this boundary. Therefore, in this operation mode the width of the excavation appears to be a more significant factor in the performance of the system since for a 30 m excavation, as the one simulated, the two retaining walls do not function as independent heat exchangers.

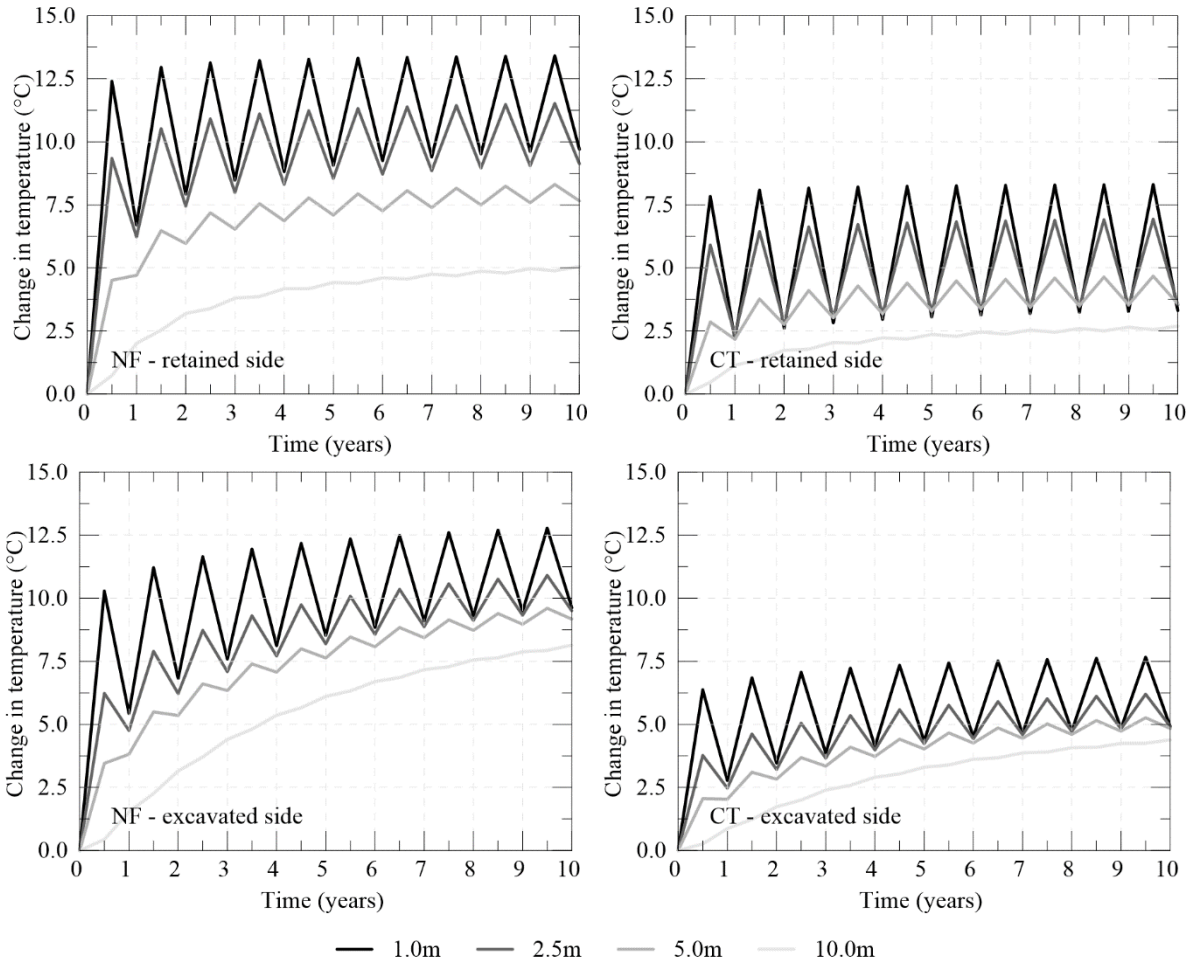

Figure 5-41: Scenario 2 - Change in soil temperature with time at different distances from the wall on the retained side (11.0 m depth) and excavated side (15.0 m depth)

Furthermore, it is evident from the temperature contours that the boundary condition along the exposed face noticeably affects the long-term temperature distribution within the ground. For the NF case, the temperatures can only dissipate through the ground surface, where a constant temperature is applied, and within the soil towards regions further away which are at a lower temperature. For the CT case, during the idling period, the heat within the ground dissipates also through the exposed face, and hence the temperatures within the upper part of the wall on the retained side are significantly lower than those calculated for the lower part of the wall and the excavated side. Hence, the extent of the area for which changes in ground temperature are determined is largely affected by the boundary condition. For the NF case, changes in temperature greater than 1.0°C are evaluated up to 30.0 m around the wall, whereas the size of the affected region reduces to 24.0 m for the CT case.

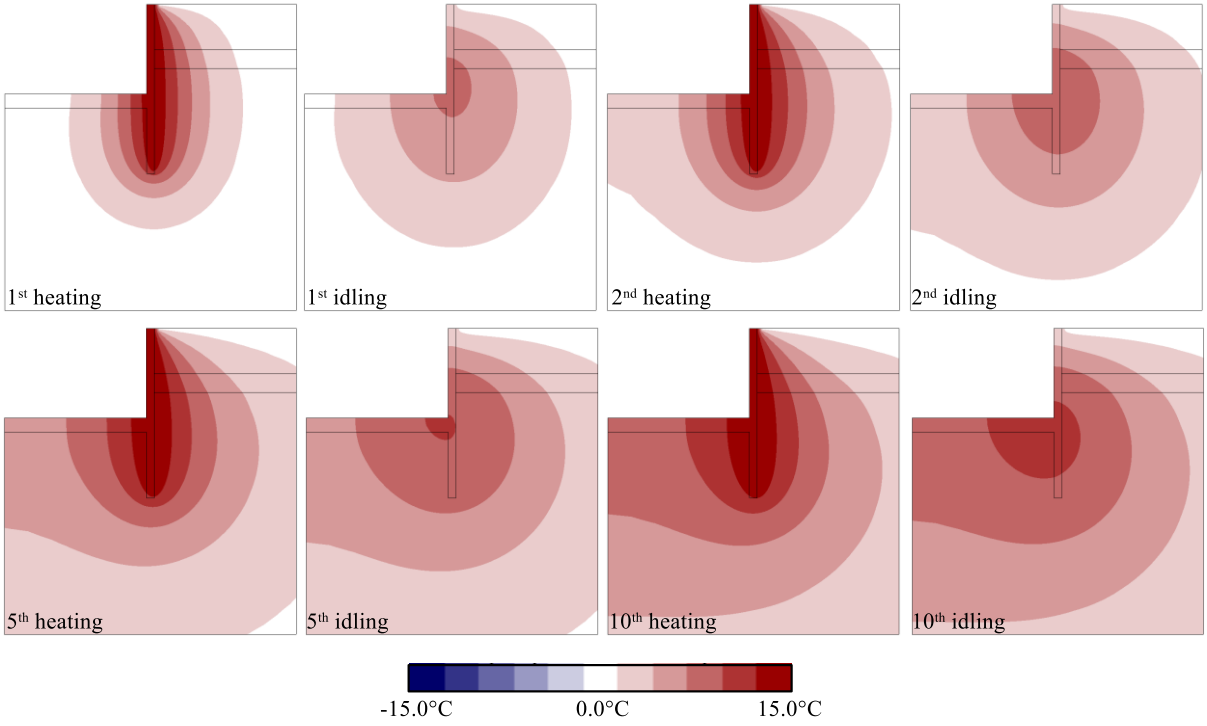

Figure 5-42: Scenario 2 - Contours of changes in temperature – NF

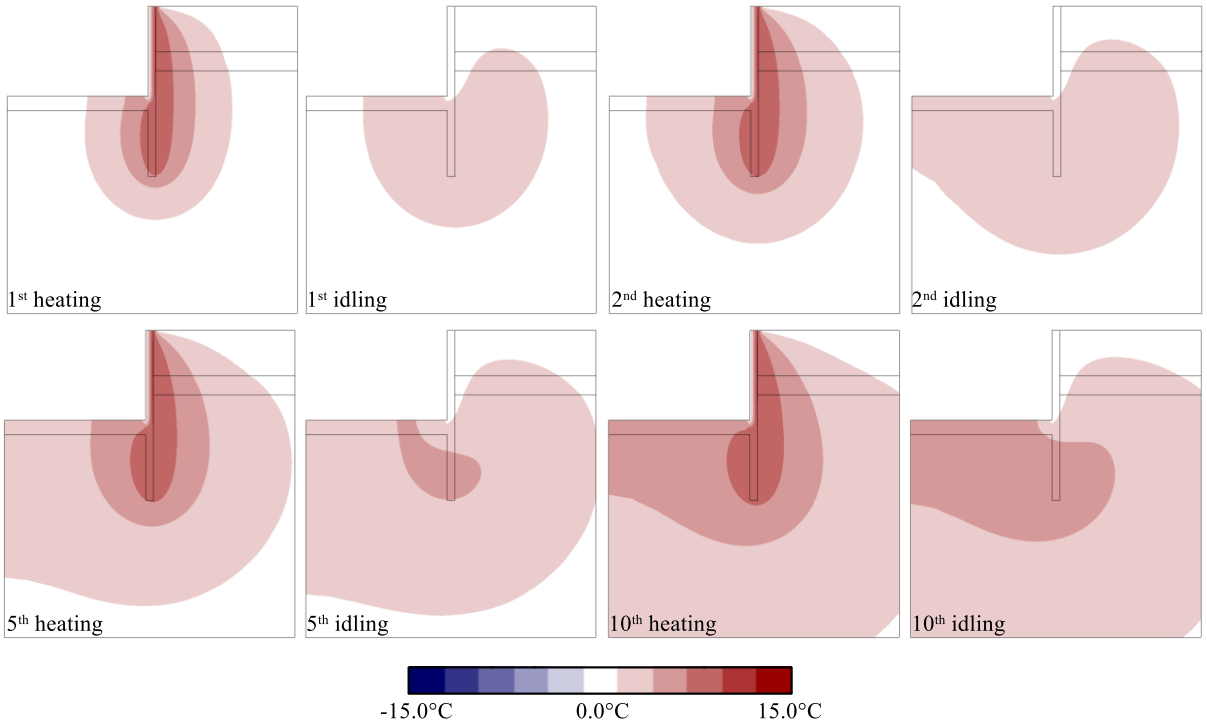

Figure 5-43: Scenario 2 - Contours of changes in temperature – CT

Scenario (3)

Figure 5-44 shows the development with time of the heat flux when 9 months of cooling and 3 months of heating are simulated, while the values of the heat flux at the end of each cycle are plotted in Figure 5-45. Due to the longer period of heat extraction with respect to heat injection, the thermal performance slightly reduces for the former, while it increases for the latter. Indeed, with this operation pattern, the ground temperatures drop with time, which is beneficial for heating mode as the difference between the inlet and ground temperatures grows larger after each cycle. The change in efficiency during the cooling phase is less pronounced than in the case where 6 months of heating only was simulated. Indeed, although the cooling phase lasts for a longer period of time, it is followed by a period of heat injection which allows the soil temperature to recover at a faster rate when compared to an idling phase. For the NF case, during the 10th cooling cycle, the heat flux has reduced to -6.1 W/m^2, i.e. a reduction of 12% in comparison to the heat flux obtained after the 1st cycle. For the CT case, a smaller difference – 3% – is registered. In heating mode, the energy efficiency increased by 6% and 2% for NF and CT, respectively. It should be noted that, when observing the values reported in Figure 5-45, it is clear that the heat flux stabilises after the 4th cycle for both boundary conditions, indicating that the system has reached thermal equilibrium. A larger amount of time than that observed in the case of a balanced heating and cooling operation (scenario 1) is required, due to the development of larger changes in ground temperature in the present case.

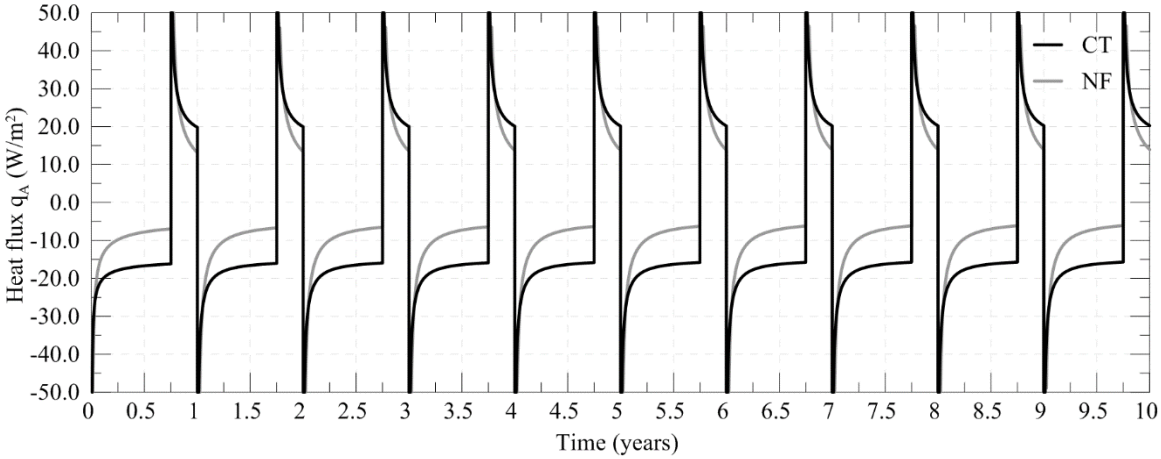

Figure 5-44: Scenario 3 - Heat flux versus time

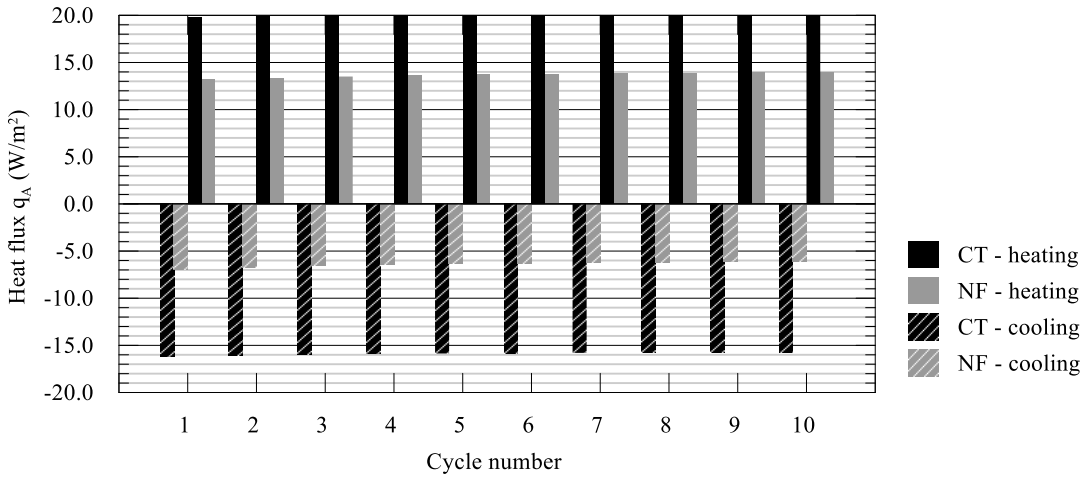

Figure 5-45: Scenario 3 - Heat flux at the end of each cycle versus cycle number

In terms of ground temperatures, peaks of -13.0°C (NF) and -8.2°C (CT) are recorded close to the wall on the retained side during the cooling cycles. Conversely, during heating cycles, the temperature increases by a maximum of 6.0°C (NF) and 10.0°C (CT). At larger distances, a permanent temperature change is recorded, as can also be clearly observed from the contour plots shown in Figure 5-47 and Figure 5-48. At a distance of 10.0 m from the wall on the retained side, after 10 years of operation, the temperature changes are of -3.4°C for NF and -2.2°C for CT. The temperature changes are larger within the excavated side, where these are equal to -5.1°C (NF) and -3.0°C (CT) at a distance of 10.0 m. These temperature changes are, in absolute values, 30 to 40% lower than those determined for scenario 2. Similarly, the area around the structure affected by changes in temperature is smaller, with changes of -1°C reaching distances of 24.0 m and 19.0 m for the NF and CT case, respectively. Furthermore, the rate at which the temperature changes take place reduces noticeably with time, confirming that the problem has reached thermal equilibrium.

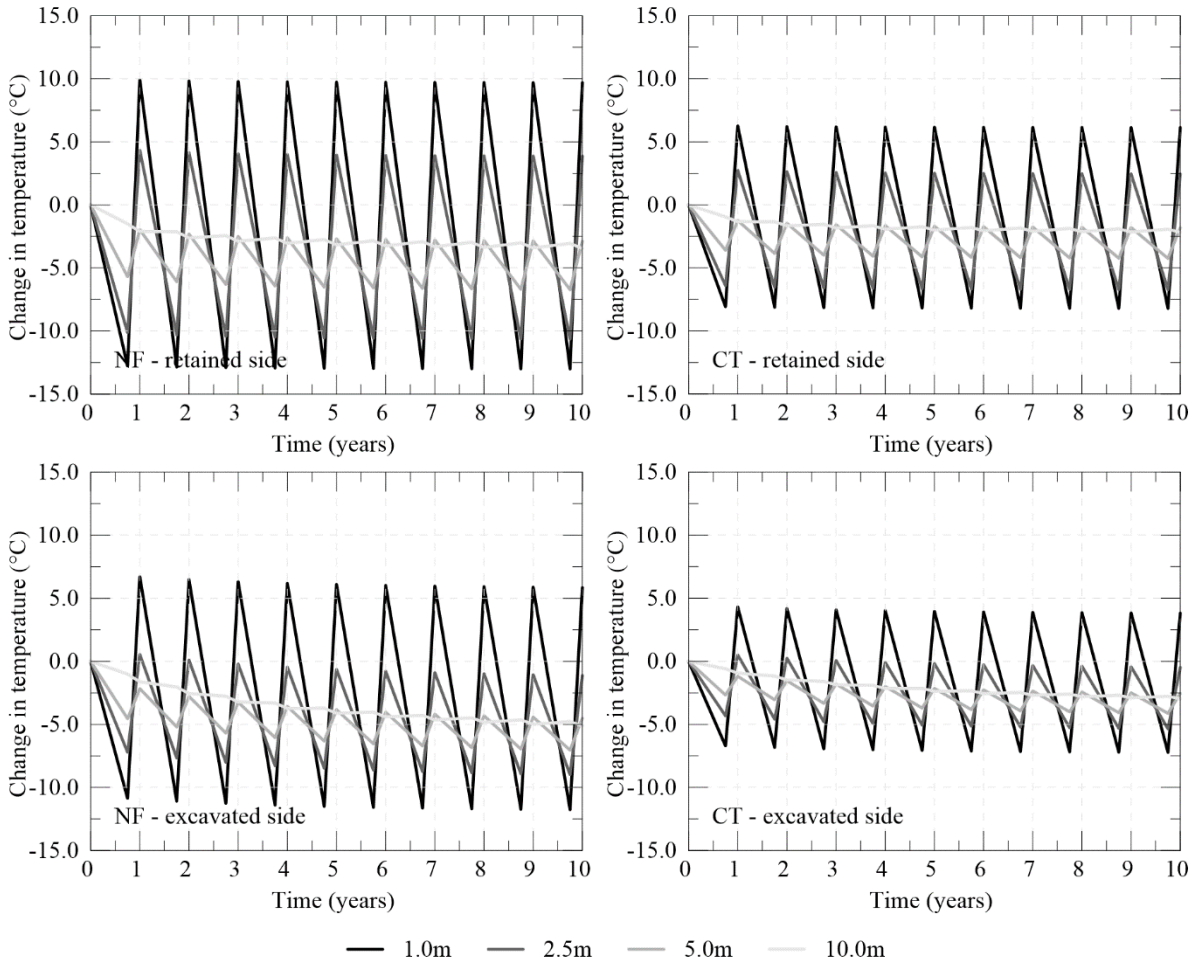

Figure 5-46: Scenario 3 - Change in soil temperature with time at different distances from the wall on the retained side (11.0 m depth) and excavated side (15.0 m depth)

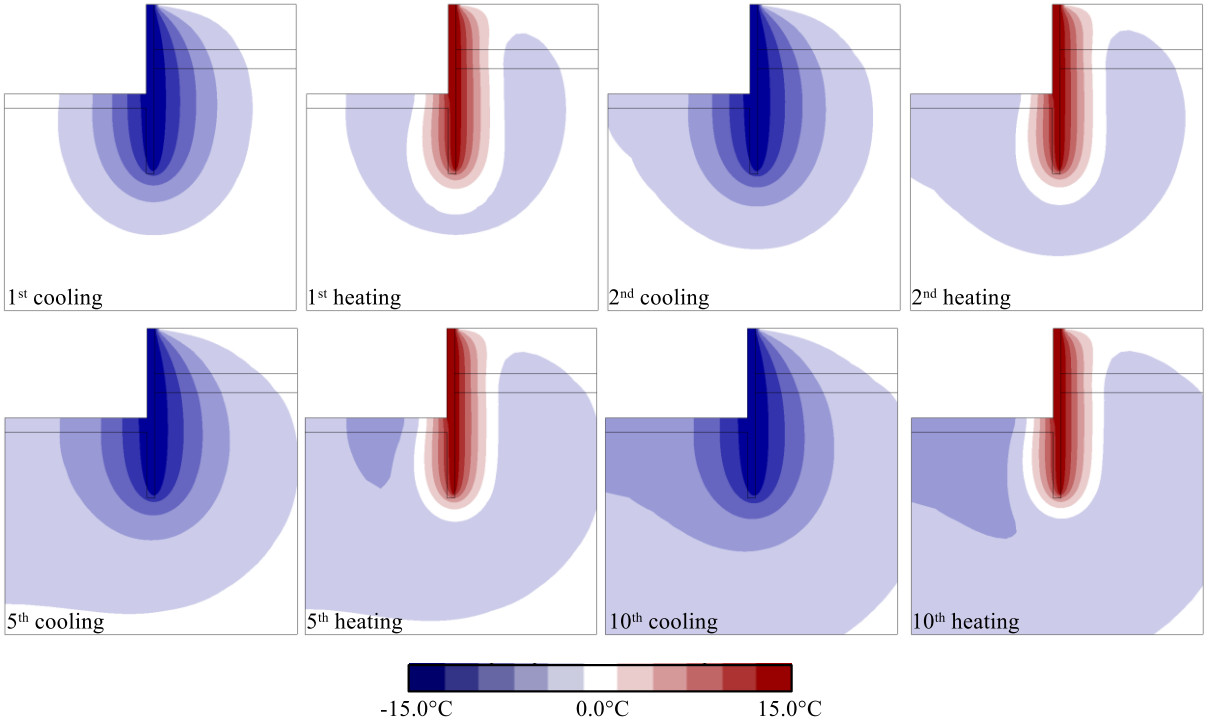

Figure 5-47: Scenario 3 - Contours of changes in temperature – NF

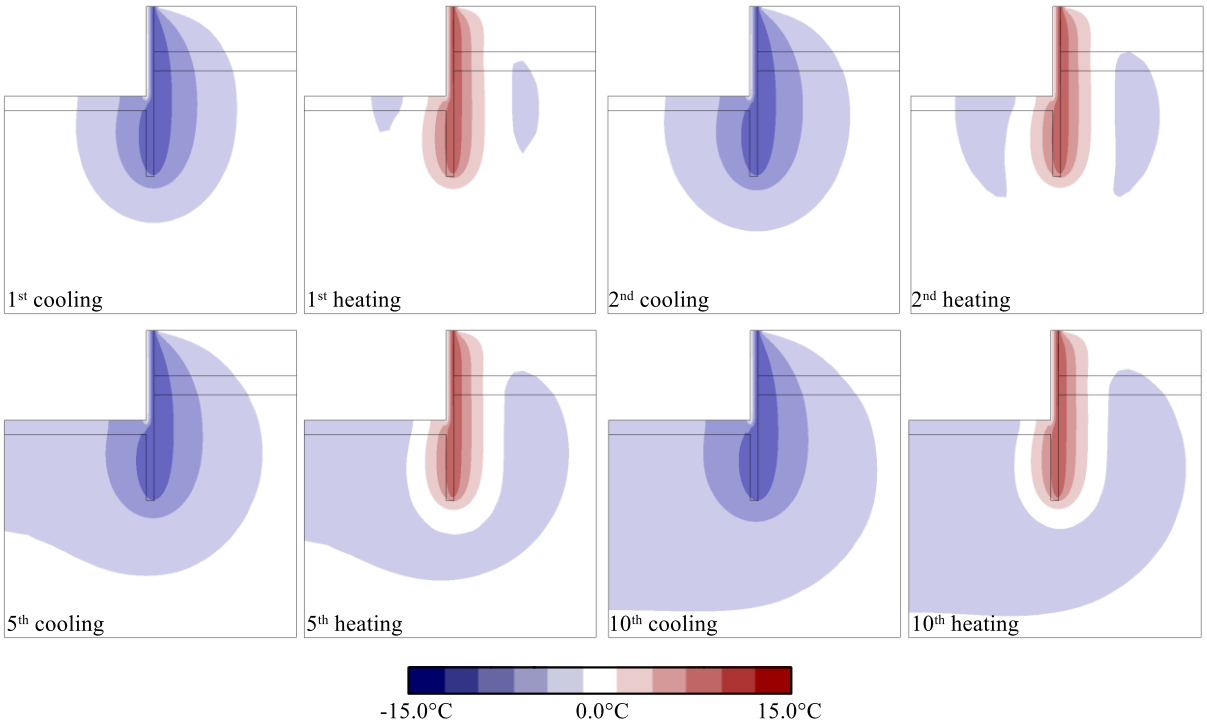

Figure 5-48: Scenario 3 - Contours of changes in temperature – CT

Scenario (4)

The heat flux calculated for the analyses consisting of 9 months of cooling and 3 months of idling is shown in Figure 5-49. Similar to the case of heating only (scenario 2), the heat flux steadily reduces with each cycle, since the soil is unable to recover fully during the idling phase. Although a shorter idling period than in the previous analysis of heating only (scenario 2) is simulated, the reduction in the efficiency observed for this operation mode is very similar. As can be seen from Figure 5-50, for the NF analysis, the heat flux has reduced from -6.9 W/m^2 to -4.5 W/m^2 within 10 years of operation, which corresponds to a reduction of 35%. For the CT case, the heat exchange rate reduces only by 8%.

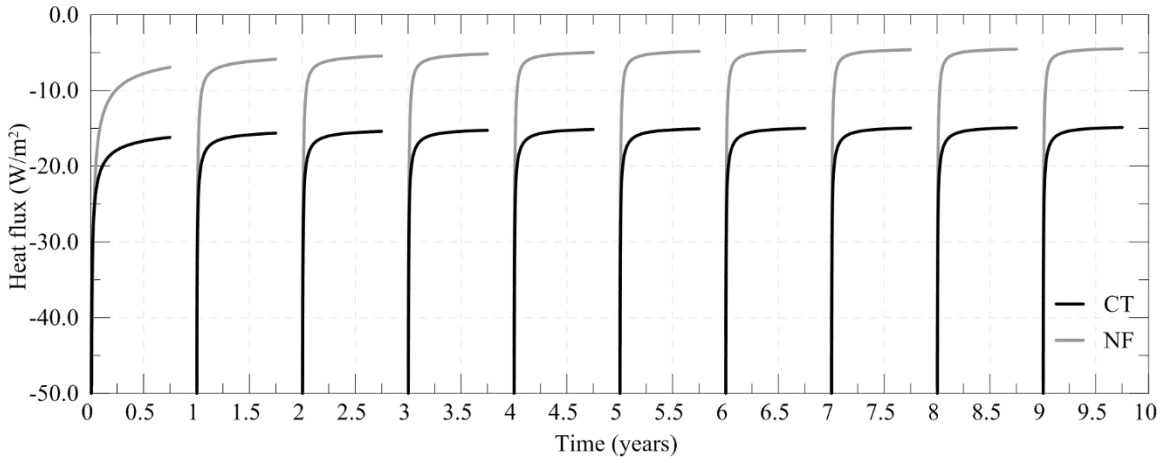

Figure 5-49: Scenario 4 - Heat flux versus time

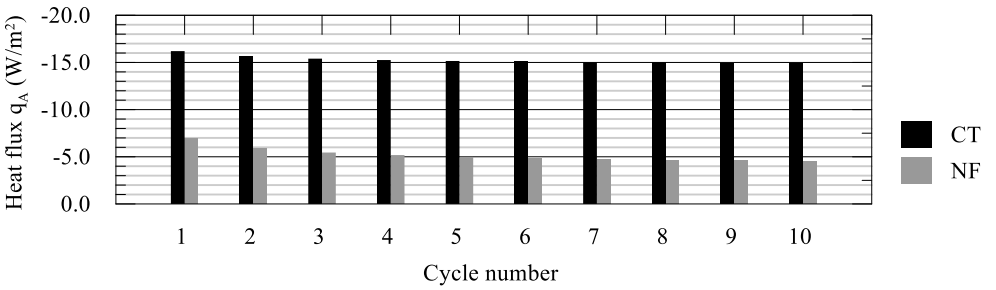

Figure 5-50: Scenario 4 - Heat flux at the end of each cycle versus cycle number

As expected, the largest temperature changes are evaluated for this scenario. As shown in Figure 5-51, close to the wall, only a small amount of the temperature changes is recovered during each idling period, with the accumulated temperature change increasing in each cycle. Indeed, while the first period of idling results in the recovery of 2.3°C, in the last period of idling this recovery is reduced to 1.3°C. The permanent drift of temperatures is clearly observed at larger distances from the wall, both within the excavated and retained sides. At a distance of 10 m, at the end of the simulation period, the recorded changes in ground temperatures are equal to -5.6°C for NF and -3.3°C for CT on the retained side and -9.0°C for NF and -5.9°C for CT on the excavated side. In terms of magnitude, these are slightly higher than those evaluated for the case of 6 months of heating followed by 6 months of idling (scenario 2).

However, the region affected by changes in temperature (see Figure 5-52 and Figure 5-53 for temperature contours) is similar in both cases.

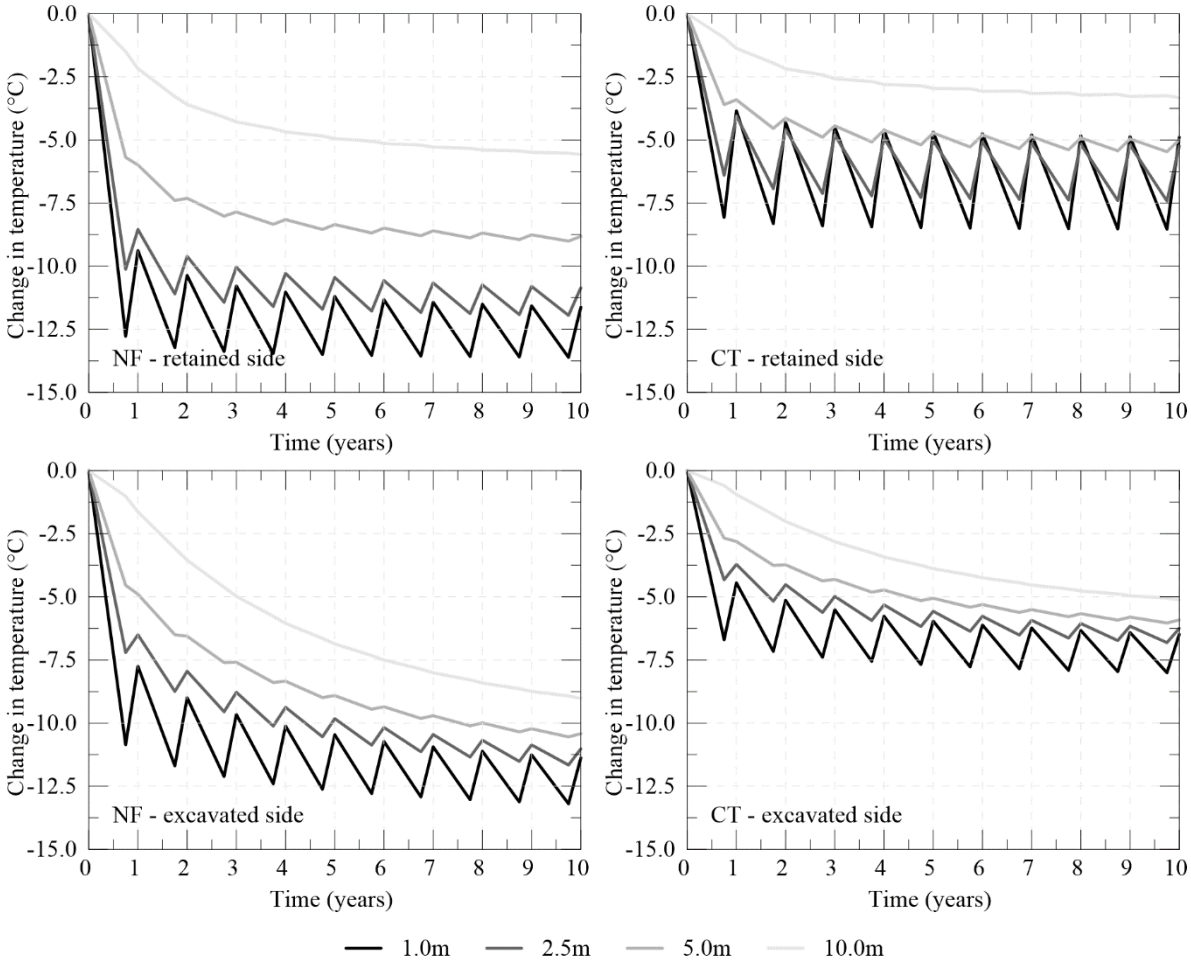

Figure 5-51: Scenario 4 - Change in soil temperature with time at different distances from the wall on the retained side (11.0 m depth) and excavated side (15.0 m depth)

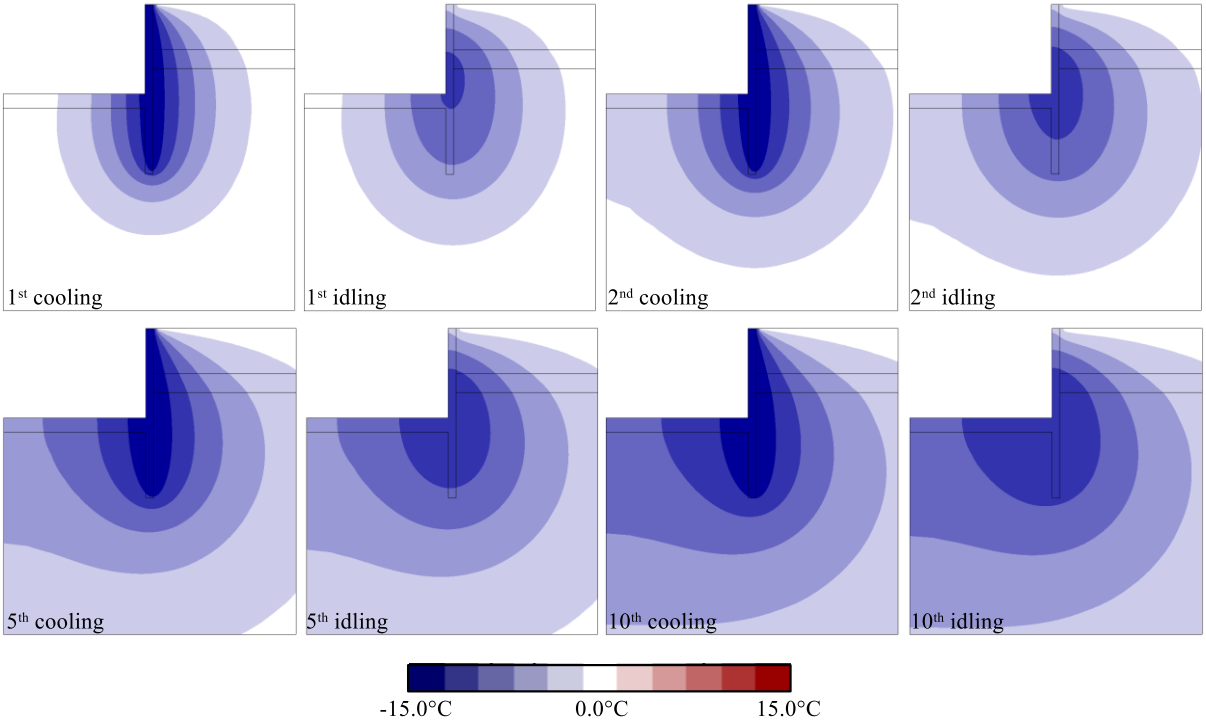

Figure 5-52: Scenario 4 - Contours of changes in temperature – NF

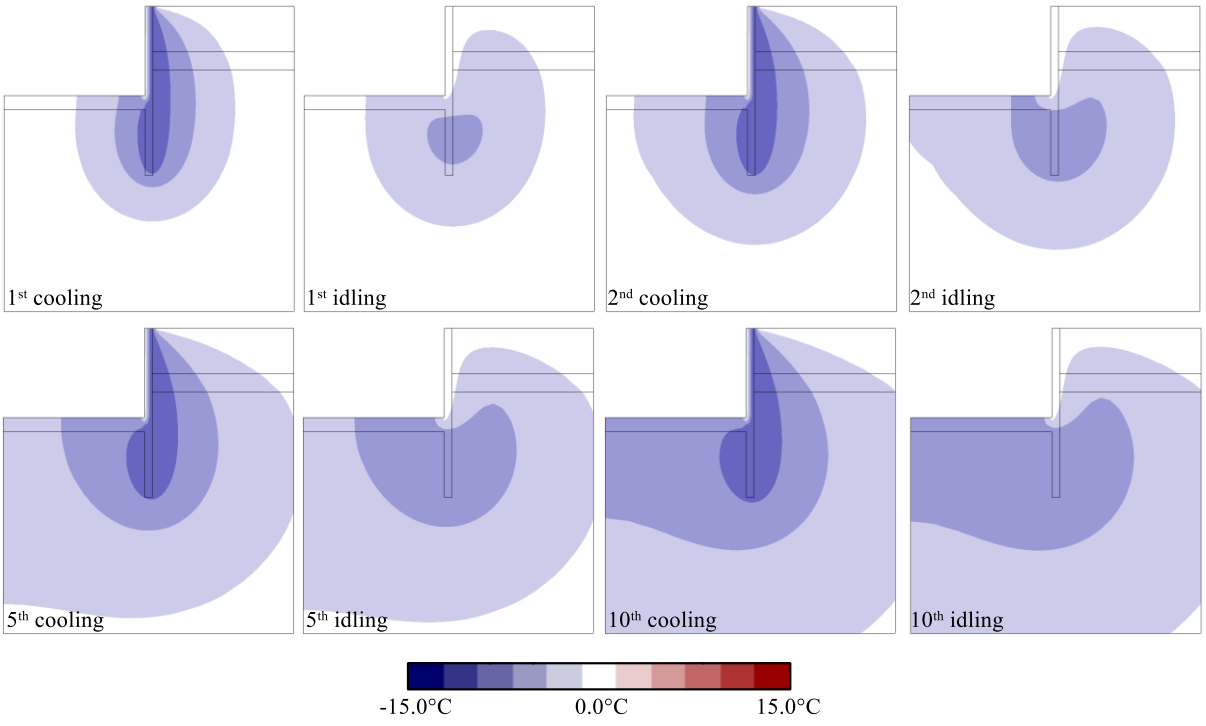

Figure 5-53: Scenario 4 - Contours of changes in temperature – CT

Energy considerations

The variations in the thermal performance for the different scenarios are related to the capability of the soil to store heat during a given operation period and to recharge during the idling periods. These aspects can be analysed by evaluating the changes in energy within the ground calculated through Equation (4-6), which accounts for the changes in temperature and heat content of the different materials within the problem.

For scenario 1 (i.e. balanced operation), the energy transferred to the ground remains constant after the 3rd cycle for both boundary conditions and is approximately the same during heat extraction and injection. For scenario 3, a longer period of heat extraction than that where injection takes place is simulated. The obtained results show that, as expected, a slightly larger amount of energy is being transferred during the former period (for example, during the last cycle, 10% more energy is computed during the heat extraction period when compared to the heat injection period, for both boundary conditions). A different pattern is observed for scenario 2. Figure 5-54 depicts the energy transferred during each heating (i.e. energy injection into the ground) and idling periods (i.e. at the end of each operation period of duration of 6 months each). It is evident that, as expected, the energy lost during the idling period is lower than that transferred during heating, suggesting that there is a reasonable efficiency of the storage medium to retain thermal energy. Thus, the transferred energy during each heating operation decreases as the average temperature of the system increases (see Figure 5-42 and Figure 5-43 for the NF and CT cases, respectively), allowing for a larger amount of recharge to occur during idling in subsequent cycles, until equilibrium is eventually reached. During idling, a larger change in energy within the ground occurs for the CT case, where additional energy is lost across the wall-air boundary when compared to the NF case. At the end of the idling period, a maximum of 40% and 63% of the injected energy during heating is lost to the environment, for the NF and CT cases respectively, which occurs during the last cycle.

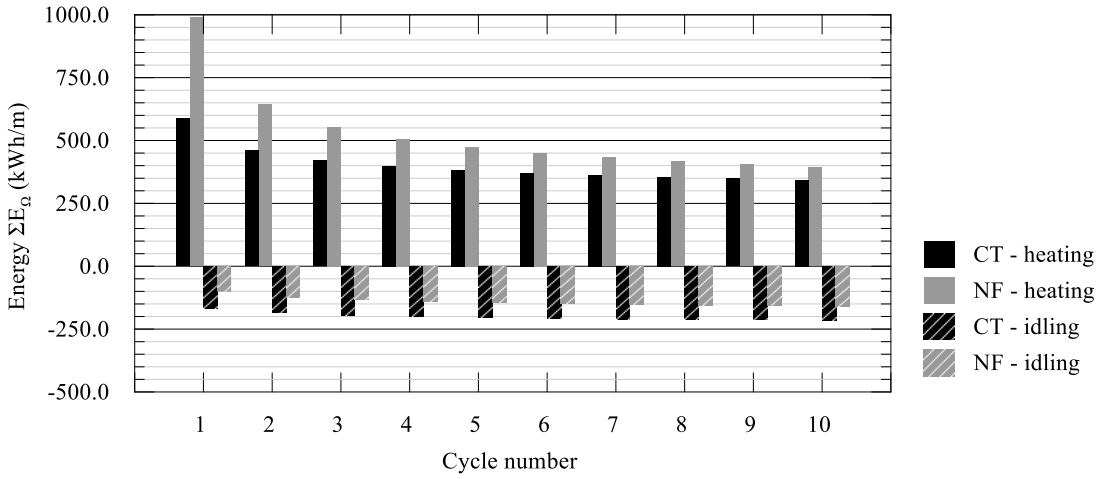

Figure 5-54: Scenario 2 - Variation in energy with cycle number at the end of heating and idling periods

Figure 5-55 shows the variation in energy during the idling periods at different time instants as a percentage of the change in energy at the end of the respective idling period for each cycle. It can be observed that the rate at which energy is lost differs according to the boundary condition along the exposed face. Indeed, for the NF case this occurs at a slower pace when compared to the CT case, with most of the changes occurring after 2 months of idling. The energy lost during the first 2 months of idling corresponds to 40% of the total energy change during a given idling period. For the CT case, the same percentage change occurs during the first month of idling. Furthermore, it can be noted that the rate at which energy is lost is approximately constant for each cycle.

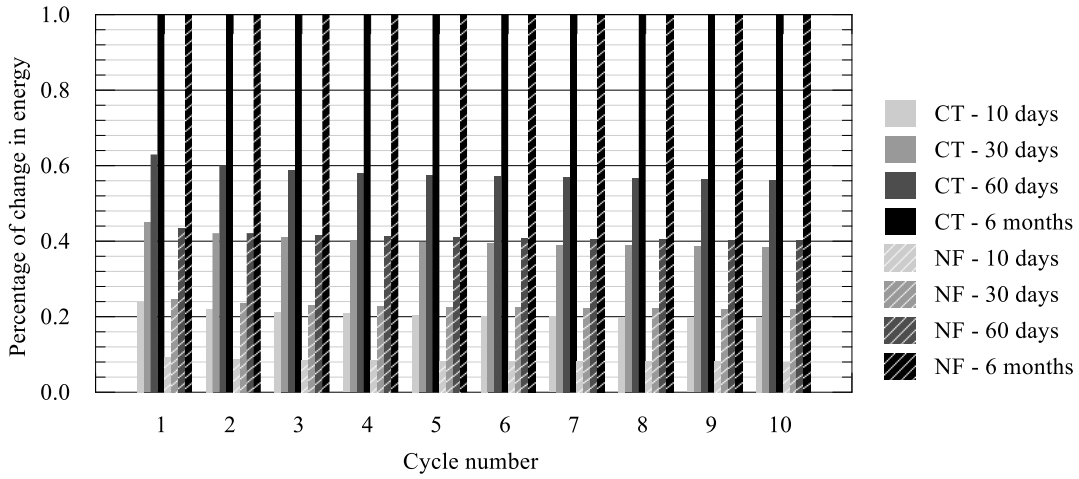

Figure 5-55: Scenario 2 – Variation of energy during idling periods with cycle number as a percentage of the total energy change during the corresponding idling period

Similar conclusions are obtained for scenario 4. However, given the shorter idling period, the maximum energy lost to the environment during the idling period corresponds to 28% and 52% of the energy extracted during the previous cooling period. Hence, a larger impact of the shorter idling period is computed for the NF case since the rate of change in energy is slower in this case, as previously discussed.

5.5 Summary and conclusions

In this chapter, the assessment of the thermal performance of thermo-active walls is carried out by performing two-dimensional (2D) plane-strain analyses, with the inclusion of one-dimensional elements to simulate the heat exchanger pipes and the advective-conductive heat transfer. Modelling thermo-active walls in 2D analyses allows considerable savings in terms of computational effort, given the reduced size of the problem. However, due to the geometric simplification introduced by modelling this type of problems in plane-strain conditions, the heat transfer mechanisms differ from those occurring in a full three-dimensional (3D) analysis. Indeed, in a 2D analysis the heat exchanger pipes, which are positioned at discrete locations within a wall panel in a 3D analysis, are replaced by a continuous “wall” of water flowing within a unit width of wall. As a consequence, the heat transfer is

fundamentally planar and occurs at a faster rate than in 3D. Therefore, approximations are required to take into account these effects when simulating thermo-active walls in 2D plane-strain analyses.

The conversion procedures were established assuming that, in the real problem, U-shaped pipe loops are installed within wall panels. Moreover, approximations are evaluated for both insulated walls (NF) and walls exposed to an environment maintained at constant temperature (CT). Firstly, approximations are derived for modelling approach 1 (MA1), i.e. the heat exchange is simulated by applying a constant inlet temperature, and subsequently an assessment of 2D analyses performed with modelling approach 2 (MA2), where a nodal heat flux boundary condition is applied to simulate the heat transfer, was also carried out.

When developing the approximations for MA1, different criteria were assessed, namely the long-term heat flux, the transferred energy during different operation periods and the changes in ground temperature. A first approximation is required to ensure that the same water flow rate per unit width is simulated in 3D and 2D analyses. This is achieved by altering the cross-sectional area of the pipe in 2D. It was shown that when this procedure was adopted and the same inlet temperature as in 3D was applied, a good match of the long-term heat flux for the NF case was obtained. However large discrepancies were recorded for the CT case, due to the larger heat exchange taking place through the exposed face in 2D. Hence, an additional correction was established to simulate the correct long-term heat flux in 2D. The correction, which reduces the inlet temperature in the 2D analysis according to the calculated factor X (expressed as the ratio $\Delta T_{in,2D}/\Delta T_{in,3D}$), depends on the ratio of exposed length of the wall over its total length, L_{exp}/L, and the spacing between the pipes, B/n_p, since these parameters affect the heat transfer through the exposed face. A similar correction was required when aiming to model the same transferred energy in 3D and 2D. The reduction in the inlet temperature, estimated with the correction factor Y, was required for both NF and CT conditions, since for both cases a high heat flux is generated in 2D in the short term. For this reason, the correction also differs according to the length of the operation period during which the energy is to be estimated and was established for 6 months, 3 months and 1 month of operation. Lower temperatures are required for shorter operation periods, in order to take into account the increased heat transfer in 2D in the short term. Similar to the correction factor X, the correction factor for estimating the transferred energy, Y, depends on the values of L_{exp}/L, and B/n_p. It also depends on the thermal conductivities of concrete (λ_c) and soil (λ_s) since these parameters affect substantially the short-term response.

To assess the performance of a 2D analysis when MA2 is adopted, the heat flux boundary condition to achieve a target temperature change at the pipe inlet in 3D, $\Delta T_{in,3D}$, was established first. Two-dimensional analyses were then simulated employing the conversion for the equivalent water flow rate. Furthermore, the magnitude of the heat flux boundary condition applied was obtained by normalising the heat flux simulated in 3D by the width of the panel. Comparing the inlet temperatures in 3D, $\Delta T_{in,3D}$,

and 2D, $\Delta T_{in,2D}$, it was shown that lower values are obtained in 2D. Therefore, it is suggested that when determining the nodal heat flux to be applied in 2D, the target temperature should be lower than that in 3D to ensure equivalent results. Moreover, the ratios between the temperature change at the pipe inlet in 2D and 3D, i.e. $\Delta T_{in,2D}/\Delta T_{in,3D}$, were compared to the correction factor Y after 6 months and a good agreement was observed, suggesting that the target temperature in 2D can be estimated employing this correction. However, further analyses are required to establish corrections for different time periods, since only a 6 months operation period was analysed.

After demonstrating the suitability of the 2D approximations to replicate the 3D behaviour, an extensive parametric study on the effect of different factors influencing the thermal performance of a thermo-active wall was carried out. 2D plane-strain analyses adopting the proposed 3D to 2D approximations and employing MA1 were used, which led to a considerable saving in computational effort. The study focuses on the thermal performance of thermo-active walls operating continuously in cooling mode (i.e. heat injection) over a period of 6 months and investigates the influence of the ratio of exposed length over total length (L_{exp}/L), the number of pipes within a wall panel (n_p), the thermal conductivities of concrete (λ_c) and soil ($\overline{\lambda_s}$), the water flow velocity (v), and inlet temperature (T_{in}) and the operation mode. For the latter study, the effect of simulating a system working for 6h followed by 6h of idling over a period of 6 months is compared to a continuous operation of 6 months. Furthermore, for all cases, the impact of the conditions simulated along the exposed part of the wall is analysed. The main conclusions are listed below and summarised in Table 5-13:

- the effect of changing the ratio of exposed length over total length L_{exp}/L depends on the boundary condition applied along the exposed face and on the normalisation of the analysed quantity: when the heat flux per unit area is compared, a small ratio of L_{exp}/L is favourable when a NF boundary condition is simulated, whereas the opposite has been observed for walls exposed to an environment at constant temperature; however when the energy normalised by unit width is analysed, the wall having a larger heat exchange area delivers more energy when compared to shorter walls;
- increasing the number of pipes (i.e. reducing the pipe spacing in the out-of-plane direction) affects the thermal performance when CT conditions are simulated along the exposed face of the wall. No impact of this variable in the long-term heat flux is computed for the NF case, while the transferred energy is observed to increase only marginally. Furthermore, the additional gains in thermal performance decrease as the number of pipes increases (i.e. a larger difference is computed between n_p=2 and 4 than between n_p=4 and 6). Considering that walls behave somewhere in between the two simulated extreme conditions, it can be estimated that increasing the number of pipes does not affect greatly the thermal performance of the system and an evaluation of cost-effectiveness should be carried out when designing it;

- a large effect of concrete thermal conductivity has been established for walls exposed to a constant temperature, where a high concrete thermal conductivity (+100%) increased the heat flux by 11.4 W/m^2 (+68%). Conversely, very little difference has been observed for different concrete conductivities for insulated walls (+3% for the same +100% variation in λ_c). The impact of the thermal conductivity of soil on the thermal performance is larger for insulated walls, with a maximum increase in heat flux of 4.5 W/m^2(58%) for high conductivity soils (+100%). In terms of changes in ground temperature, it was shown that the concrete conductivity has no effect on the temperature changes at larger distances. Conversely, increasing the soil thermal conductivity increased substantially the calculated temperature changes;
- the water flow velocity affects the heat transfer only in the very short term (<5h), with a higher water flow velocity providing a larger amount of energy. However, for longer durations, the same heat extraction rate is computed for all the analysed velocities (ranging from 0.2 m/s to 1.4m/s). Thus, when designing a geothermal system, it is considered that the water flow velocity should be chosen within this range and a value should be adopted that enables the operational costs to be minimised;
- applying different magnitudes of the temperature change at the inlet ΔT_{in} produces results which increase or decrease proportionally with this value;
- simulating an intermittent operation mode (IOM), where the system is switched on and off every 6h, leads to a larger heat flux, which, on average, is approximately twice the one computed when a continuous operation mode is simulated (for both NF and CT). Furthermore, the transferred energy is very similar for the two cases, indicating that the IOM is more efficient, since the same energy is transferred in half the operation time. It was shown that the ground temperatures are marginally affected by the type of operation simulated, indicating that, if these are to be evaluated, a continuous operation mode can be adopted, providing a simpler and more computationally efficient approach.

Table 5-13: Summary of effect of parameters on thermal performance

Parameter	Effect of parameter	
	NF	CT
Ratio of exposed over total length ($\frac{L_{exp}}{L}$)	-	++
Number of pipes (n_p)	+	++
Thermal conductivity of concrete (λ_c)	+	+++
Thermal conductivity of soil ($\overline{\lambda_s}$)	+++	++
Water flow velocity (v)	N/E	N/E
Inlet temperature ($\Delta T_{in,3D}$)	+++	+++
Operation mode	+++	+++

Key: + limited increase with property, ++ moderate increase with property, +++ substantial increase with property
- limited decrease with property, N/E no effect of property

In the last part of this chapter, the long-term thermal performance of thermo-active retaining walls was analysed by performing simulations of different operation patterns over a period of 10 years, assessing the variation in heat flux and the changes in ground temperature with time. The four analysed scenarios were: (1) balanced operation of 6 months of heating (heat injection) and 6 months of cooling (heat extraction), (2) 6 months of heating followed by 6 months of idling, (3) 9 months of cooling and 3 months of heating and (4) 9 months of cooling and 3 months of idling. The study showed that with a balanced operation (scenario 1), the thermal performance remains constant during the 10 years of operation and no permanent temperature changes are observed. Conversely, scenarios 2 and 4 are the most detrimental for the thermal performance, which reduces by 35% (NF) and 8% (CT) after 10 years of operation. This is due to permanent changes in ground temperature arising from the unbalanced heat extraction/injection, which reduces the energy potential, and the slow rate of recharge during the idling period. For the NF case a maximum of 40% and 28% of energy is recovered during idling, respectively for scenarios 2 and 4. A larger change in energy occurs during idling in the CT case due to the possibility of exchanging heat through the wall-air interface, leading to a maximum of 63% and 52% of the energy transferred during the heating/cooling operations to be recovered. In the most severe case (scenario 4), the changes in ground temperature at 10.0 m distance were equal to -5.6°C (NF) and -3.3°C (CT), whereas the region affected by changes in temperature >1.0° extended up to 30.0 m around the structure. These are considered significant when designing thermo-active structures in densely-built environments. For such conditions, the temperature changes should be taken into account during the design to assess the effects on nearby structures. However, it should be noted that the large permanent changes in temperature are a consequence of the extreme operation mode simulated, suggesting that more balanced systems may be preferable..

Chapter 6
Advanced modelling of the thermo-mechanical behaviour

6.1 Introduction

In this chapter, the thermo-mechanical response of thermo-active retaining walls is investigated by performing three-dimensional analyses which include heat exchanger pipes. Thus, it is possible to take into account the three-dimensional (3D) nature of this type of problems (as outlined in Chapter 4) and the time-dependent temperature changes, providing a more accurate modelling when compared to the preliminary analyses presented in Chapter 3. However, modelling such problems in fully coupled thermo-hydro-mechanical (THM) analyses in three dimensions is computationally very expensive, given the large dimensions of the finite element model required when assessing the mechanical performance and hence the increased number of degrees of freedom, especially when the hydraulic coupling is also considered within the soil domain. Therefore, in this chapter, an efficient modelling approach to simulate accurately the response of thermo-active retaining walls in two-dimensional (2D) plane-strain analyses is developed and compared to the behaviour obtained in the original 3D analyses.

The first part of this chapter outlines the results obtained in a 3D analysis of a wall panel and explains in detail the observed behaviour in terms of structural forces and wall displacements. In addition, a parametric study is carried out to investigate the impact of geometrical and thermal parameters on the thermo-mechanical behaviour of thermo-active walls in 3D. Subsequently, the effectiveness in reproducing the observed 3D behaviour of different approaches to simulate thermo-active walls in 2D (including that presented in Chapter 5 for the thermal response) is evaluated. Since the obtained results are not satisfactory, a new method to simulate thermo-active walls in 2D, which captures the average thermo-mechanical behaviour of thermo-active walls, is proposed and validated against numerous 3D

analyses. To account for the out-of-plane effects inherent to 3D analyses, an additional approximation procedure is proposed. In the last part of this chapter, the long-term response of walls under different scenarios of cyclic heating and cooling is evaluated. Parts of the content of this chapter were published in Sailer et al. (2020a).

It should be noted that all the results presented herein are taken as changes from the start of thermal loading. Furthermore, the sign convention in such that positive values refer to tensile excess pore water pressures, tensile axial forces, bending moment as a consequence of tension on the excavated side, upward vertical movements and horizontal movements towards the retained side of the wall.

6.2 Behaviour in three-dimensional analyses

In this section, 3D analyses with inclusion of heat exchanger pipes are presented in order to characterise the thermo-mechanical response of thermo-active retaining walls. The simulation of the presence of the heat exchanger pipes allows the time-dependent behaviour as a consequence of the heat transfer occurring from the pipes to the concrete and soil to be taken into account. This clearly occurs at a slower rate compared to changing simultaneously the temperature of all the elements of the wall, as was performed in the preliminary analyses reported in Chapter 3. Furthermore, it enables the simulation of different conditions along the exposed face, which affect the temperature distribution within the wall panel. Lastly, the effect of the non-uniform temperature distribution across the width of the wall can be assessed. Clearly, the response to the THM interactions observed in the simpler analyses performed in Chapter 3 are still valid.

Firstly, the wall problem presented in Chapter 3 is analysed in 3D and the effect of the boundary condition along the exposed face of the wall is assessed. To assess further the 3D behaviour of thermo-active walls, a parametric study is performed on an idealised wall geometry, varying geometrical and thermal parameters. All these analyses are carried out adopting modelling approach 1 (MA1) to simulate the heat exchange (refer to Chapter 4). In the last part of this section, a comparison between MA1 and MA2 in terms of the mechanical response is outlined.

6.2.1 Influence of boundary condition along exposed face

In this section, the wall problem presented in Chapter 3, i.e. a wall geometry based on that presented in Wood & Perrin (1984b), is modelled within a fully coupled THM analysis in 3D to evaluate the complex behaviour of walls during 6 months of heat injection. Firstly, the simulation procedure is outlined and subsequently the results are presented in terms of both the average wall behaviour (structural forces, displacements, excess pore water pressures) and the variation of the structural forces in the out-of-plane direction.

6.2.1.1 Modelling procedure

Problem description

Figure 6-1 depicts the finite element mesh, where the basement geometry and the soil stratigraphy are the same as those described in Chapter 3. The Thanet Sand layer has not been included in the finite element model, where instead a hydraulic boundary condition of zero change in pore water pressures with respect to the initial value was applied at the bottom boundary. It is assumed that the wall consists of 1.5 m wide panels, in which heat exchanger pipes are installed to form vertical U-loops. These are placed at 0.1 m from the concrete edge on the retained side and consist of two vertical pipe segments, 17.5 m in length, with a pipe-to-pipe spacing of 0.75 m, connected at the bottom by a horizontal pipe. The pipes are assumed to have an internal diameter of 20.4 mm. The initial conditions, i.e. pore water pressure, K_0 profile and initial temperature (13°C), are the same as those outlined in Chapter 3 (see Figure 3-3).

Material properties

Twenty-noded hexahedral solid finite elements were used to model all soils and the structural components. For the elements discretising all soil layers and the wall, displacement and temperature degrees of freedom were assigned at all the nodes, while, for the consolidating materials (i.e. London Clay and Lambeth Group Clay), pore water pressure degrees of freedom were added at the corner nodes. The elements used to simulate the structural components, i.e. slabs and columns, have only displacement degrees of freedom. The material models and properties for all soils and concrete were the same as those employed for the analyses carried out in Chapter 3, which are detailed in Section 3.2.4, with exception for the thermal parameters of concrete (i.e. thermal conductivity and heat capacity). For this material, the adopted parameters are equal to those employed in Chapter 4 (see Table 4-2). The heat exchanger pipes were modelled with one-dimensional elements (see Section 2.3.4 and Gawecka et al. (2018)). These elements have three nodes, with displacement and temperature degrees of freedom at each node and pore water pressure degrees of freedom at the nodes on their extremities. The pipe elements were modelled as linear-elastic materials, with a low stiffness in order not to affect the mechanical behaviour of the wall. Similarly, to avoid differential thermal expansion between the pipe elements and the concrete, the same thermal expansion coefficient of the concrete has been assigned to the pipes. The material properties employed for the one-dimensional pipe elements are outlined in Table 6-1. It should be noted that the TEM (refer to Section 2.3.5 for details) was not included in these analyses. Preliminary results have shown a small effect of the presence of the TEM on the mechanical response, since, as was discussed in Chapter 4 and demonstrated in Appendix F, the long-term temperature changes are not substantially affected by its presence.

Table 6-1: Material properties for heat exchanger pipe elements

Young's Modulus (kN/m^2)	E	10000.0
Poisson's ratio (-)	ν	0.0
Coefficient of thermal expansion (m/mK)	α	8.5×10^{-6}
Bulk modulus of water (kN/m^2)	K_f	0.0
Thermal conductivity of water (W/mK)	λ	0.4
Volumetric heat capacity of water (kJ/m^{3}K)	C_v	4200.0

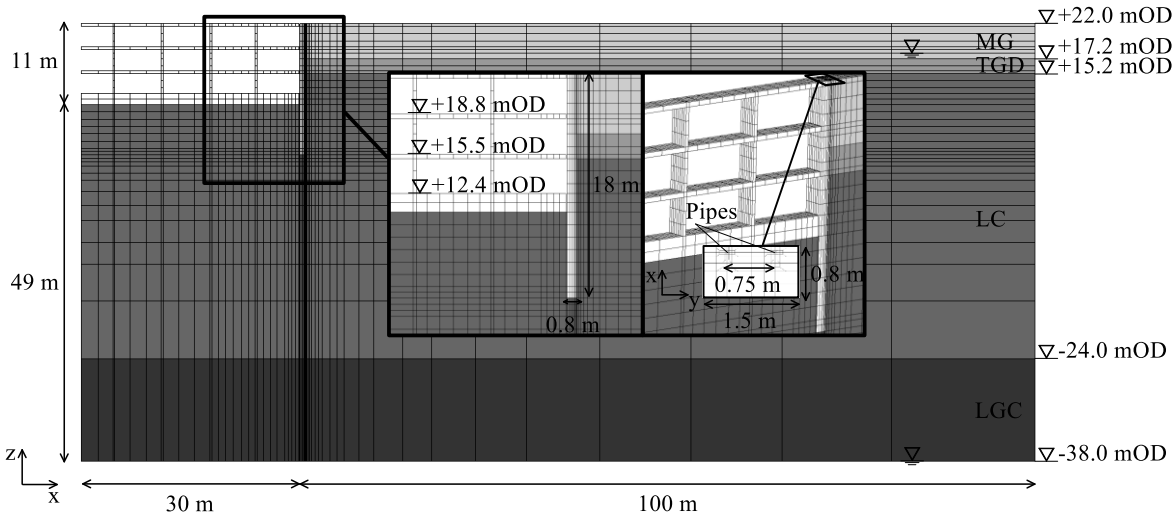

Figure 6-1: Finite element mesh for 3D analysis of basement geometry described in Wood & Perrin (1984b)

Simulation sequence

The bottom mesh boundary was restrained from moving in the vertical direction (z-direction) and, at each lateral boundary, the movement normal to its direction, i.e. either in the x-direction or y-direction, was restrained. The modelling of excavation and construction follows the same sequence as that outlined in Chapter 3 (see Section 3.3 for details). The temporary props were simulated as a nodal spring applied at the middle of the wall panel, with a stiffness adjusted to take into account the width of the wall panel. Similar to the analyses presented in Chapter 3, once construction of the permanent structures was completed, the generated excess pore water pressures were allowed to fully dissipate before the commencement of the heat exchange in order to isolate the effects of changes in temperature, thus allowing a clearer interpretation of the results. Furthermore, at the start of the heat injection, the stiffness of all soils was reset to its maximum value.

The operation of the geothermal system was simulated by adopting MA1 described in Chapter 4, i.e. the heat exchange was modelled by imposing a constant temperature at the inlet node of the pipe loop. The applied temperature, $T_{in,3D}$, was equal to 28.0°C, thus corresponding to a temperature difference from the initial temperature ($\Delta T_{in,3D}$) of 15.0°C. The remaining boundary conditions at the pipes are

identical to those adopted in Chapter 4 (see Section 4.4.2). Throughout the analysis, the temperature at the ground surface was not allowed to vary from its initial temperature of 13°C. All other boundaries were considered to be insulated, since they are either planes of symmetry (i.e. those perpendicular to the y-direction and the one positioned at half-width of the excavation), or far field boundaries, where the simulated boundary condition would not affect the results given that, considering the simulated period of time, substantial distances between the structure and the boundaries were adopted. Exception is made for the exposed part of the thermo-active retaining wall, which was shown to affect considerably the thermal-performance of thermo-active retaining walls (see Chapter 4 and Chapter 5). Hence, along this boundary, two different conditions are simulated, i.e. an insulated wall (or no heat flux across this boundary, NF) and a wall maintained at a constant temperature (CT) equal to the initial temperature, which were previously shown to be the two extreme cases for wall-air interaction.

Six months of heat injection were simulated and appropriate time steps were employed to avoid thermal and hydraulic shock problems (see Section 2.3.5, Cui et al. (2016b) and Cui et al. (2019)).

6.2.1.2 Average wall behaviour

The effect of the boundary condition along the exposed face is evaluated by presenting the evolution of excess pore water pressures, wall displacements and structural forces. The latter quantities are computed as the average value across the whole width of the wall panel. Out-of-plane effects in terms of structural forces are subsequently investigated in Section 6.2.1.3.

Excess pore water pressures

Figure 6-2 and Figure 6-3 show the contours of changes in pore water pressure at different time instances, respectively for the NF and CT analyses. Figure 6-4 shows the development of change in pore water pressure with time at mid-depth of the embedded section of the wall (i.e. 14.0m depth) and different distances from the wall within the retained side. As the temperature in the soil increases, compressive excess pore water pressures develop. Initially, these are concentrated on the retained side of the wall, where greatest temperature changes occur due to the pipes being located towards this side of the wall. As can be observed from Figure 6-4, they first increase with time close to the wall, while towards the end of the operation period they have started decreasing due to the consolidation process, indicating that limited changes in temperature are occurring close to the wall in the long term. Simultaneously, excess pore water pressures develop in regions further away from the structure, due to both changes in temperature and the time-dependent water flow. The changes in pore water pressures are slightly larger for the NF case in the medium to long term due to higher temperatures as a consequence of the modelled insulation along the wall-air interface (see Chapter 4). Furthermore, due to the lower temperatures simulated in the CT case, the dissipation of excess pore water pressures commences at a slightly earlier time instant when compared to the NF case. The maximum change is in the order of -60.0 kPa.

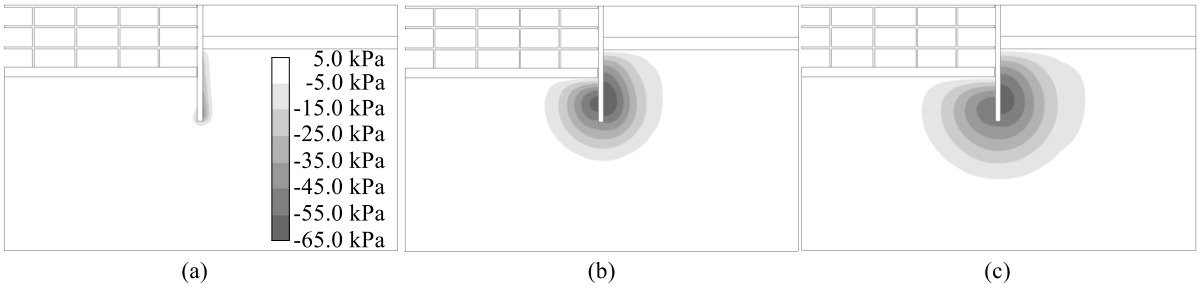

Figure 6-2: Contours of excess pore water pressures with NF boundary condition (a) 3 days, (b) 30 days and (c) 6 months

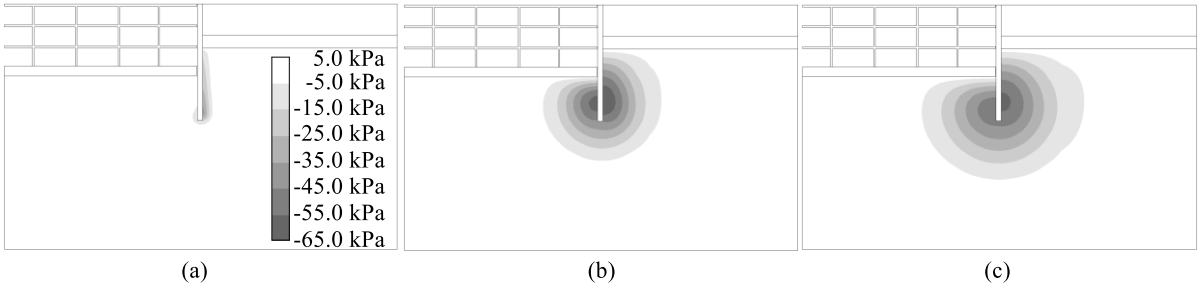

Figure 6-3: Contours of excess pore water pressures with CT boundary condition (a) 3 days, (b) 30 days and (c) 6 months

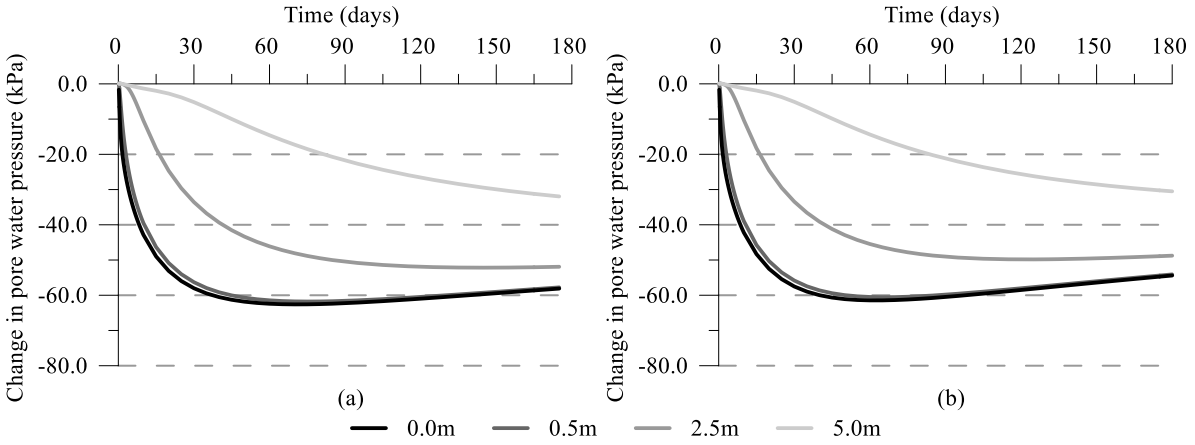

Figure 6-4: Change in pore water pressure with time at a depth of 14.0m (a) NF and (b) CT

Axial forces

The profiles of changes in average axial force per metre width of wall at two different time instants is shown in Figure 6-5 (a) and (b) for NF and CT cases, respectively. Furthermore, Figure 6-6 shows the change in axial force with time at a depth of 14.0 m (the approximate location of the peak in this quantity throughout the analysis).

The change in axial forces in the short term is not affected by the boundary condition along the exposed face since the temperatures are very similar (see Chapter 4). Indeed, the initial compression due to the restriction against the thermal expansion is the same for both analyses, with a maximum compressive force of approximately -20.0 kN/m. With time, the soil heats up and expands, inducing tension into the wall. The different heat transfer rate occurring in the NF and CT cases affects, as previously discussed, the development of excess pore water pressures and the consequent volumetric strains. Indeed, it can

be noted from Figure 6-6 that the decrease in the tensile axial force (which is due to consolidation, see Chapter 3) occurs sooner for the CT case, since the lower temperatures (and thus lower excess pore water pressures) accelerate the hydraulic equilibration.

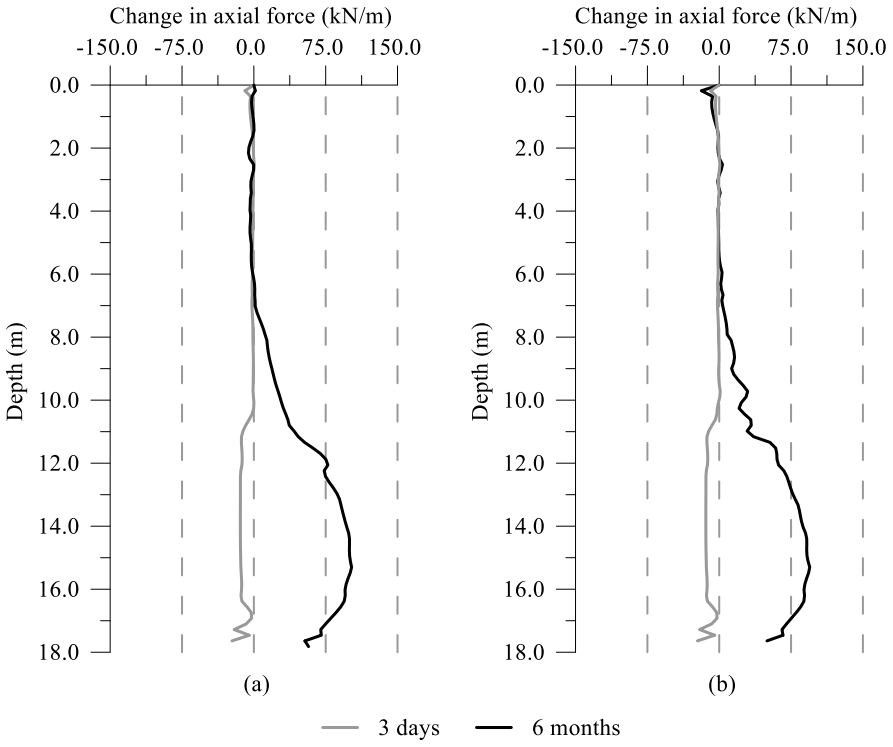

Figure 6-5: Change in axial force with depth at different time instants (a) NF and (b) CT

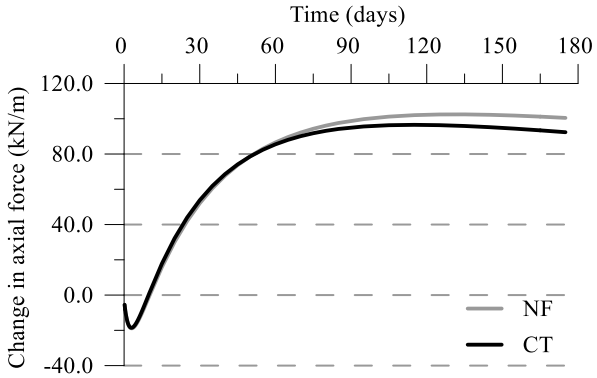

Figure 6-6: Development of change in axial force with time at depth of 14.0 m

Bending moments and horizontal displacements

As can be seen from Figure 6-7, which shows the profiles with depth of the average change in bending moment per unit width, the NF and CT cases display the same response in the short term, since the temperatures are very similar. However, as shown clearly in Figure 6-8, which depicts the development of the change in bending moment with time at a depth of 6.5 m, the two cases behave differently in the long term. Furthermore, it should be noted that the sign of the bending moment, with positive values corresponding to tension along the excavated side of the wall, does not correspond to what would be

expected by observing the horizontal displacements depicted in Figure 6-9 (which would suggest tension along the retained side of the wall). Indeed, this specific aspect of the thermo-mechanical behaviour of the wall arises from the non-uniform temperature across its thickness, H, caused by the presence of the heat exchanger pipes.

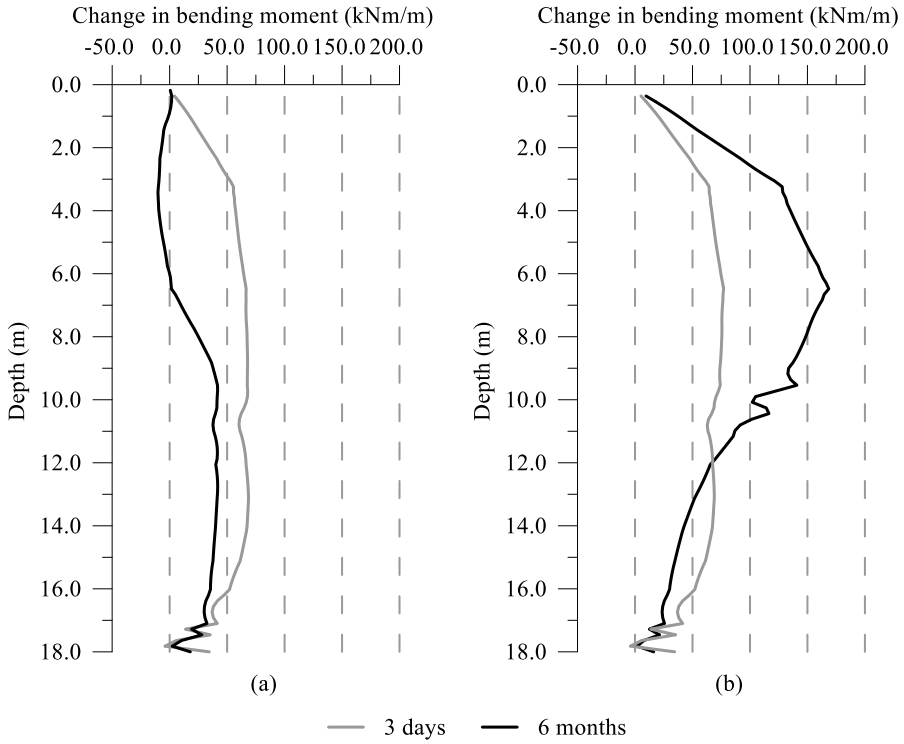

Figure 6-7: Change in bending moment with depth at different time instants (a) NF and (b) CT

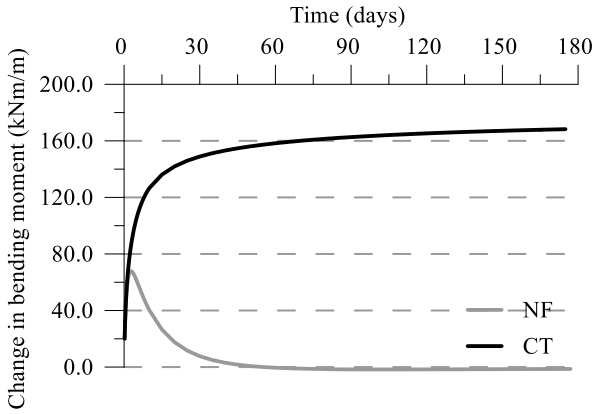

Figure 6-8: Development of change in bending moment with time at depth of 6.5m

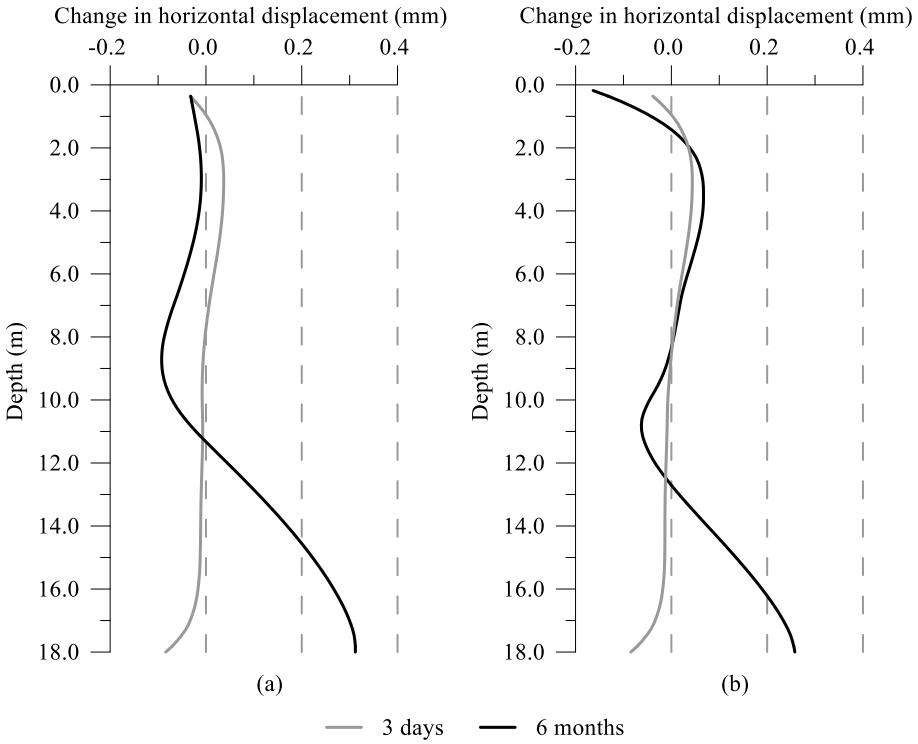

Figure 6-9: Change in horizontal displacement with depth at different time instants (a) NF and (b) CT

Indeed, as thermal loading is applied and the temperature difference between the pipes and the exposed face of the wall increases (see Figure 6-10 (a)), larger thermal strains are generated on the retained side, leading to the wall bending towards the retained side, as schematically depicted in Figure 6-11 (where the deformed shape is similar to that observed in the analyses in the short term). However, due to the large stiffness of the concrete, an internal reaction, which leads to a reduction of the curvature experienced by the wall, arises. This opposing reaction takes the form of mechanical strains which, when added to the thermal strains, result in significantly lower values of curvature (see Figure 6-10 (b) for variations across the wall width of the different components of strain, noting that $\varepsilon_{tot} = \varepsilon_{mech} + \varepsilon_{th}$). Clearly, while the observed deformed shape is connected to the distribution of total strains, the bending moment of the wall is related to that of the mechanical strains. Hence, the tensile mechanical strains observed on the excavated side lead to a positive bending moment according to the adopted sign convention, which, as previously highlighted, is in contradiction with the sign expected from the deformed shape. As a result, for thermally-loaded retaining walls, it can be concluded that there is a break in the link between the deformed shape and the sign of the bending moment, meaning that the former can no longer be employed to assess the variation of the latter.

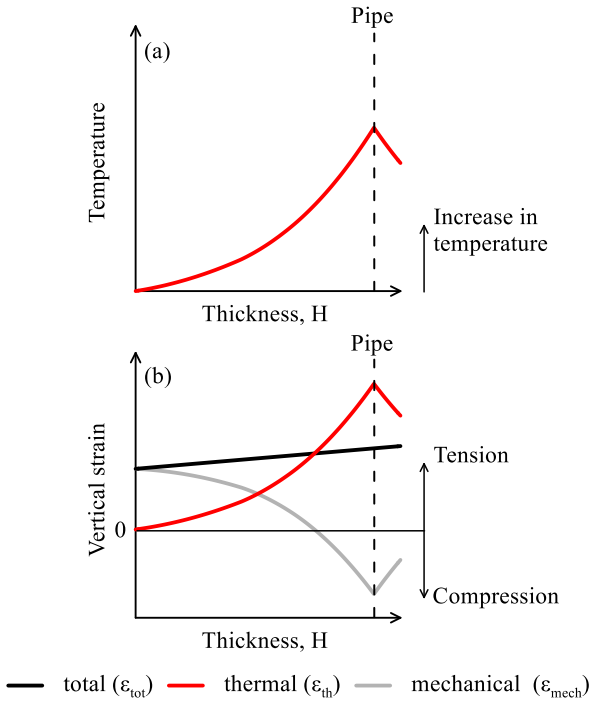

Figure 6-10: Schematic representation of (a) change in temperature and (b) vertical strains induced by temperature changes across thickness of wall

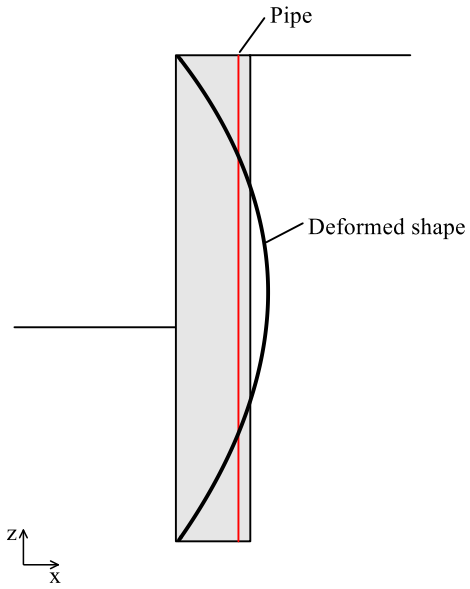

Figure 6-11: Schematic representation of deformed shape for thermo-active walls with heat injected into pipes located on the retained side (i.e. $T_{in} > T_0$)

Since the development of the bending moment is related to the temperature difference across the thickness of the wall, the different variations with time for each boundary condition can be easily explained: for the NF case, the temperature difference across the thickness reduces with time since the wall saturates with heat and, thus, in the longer term, the bending moment reduces; conversely, in the CT case, given the boundary condition along the exposed face, there is a permanent temperature gradient across the thickness and, hence, the bending moment increases with time as the temperature

within the pipes increases. The maximum change in bending moment computed for the CT case is 170.0 kNm/m, which corresponds to an increase of about 20% with respect to the maximum experienced during construction (and represents a much larger change when compared to that computed for the simpler 2D analyses presented in Chapter 3, which was of about 80.0 kNm/m).

The horizontal displacements depicted in Figure 6-9, similar to what was observed in the preliminary analyses outlined in Chapter 3, are very small and negligible when compared to those evaluated during construction (see Figure 3-5).

Vertical wall displacements

Figure 6-12 displays the variation with time of the vertical displacement of the top of the wall. Since the wall and the surrounding soil gradually heat up, the wall moves upwards with time. A larger displacement is computed for the NF case when compared to the CT case, since larger temperatures develop within the system. Thus, both the expansion of the wall and the soil mass is larger for the NF case, leading to a maximum vertical movement of 4.1 mm (1.0 mm larger than for the CT case) after 6 months.

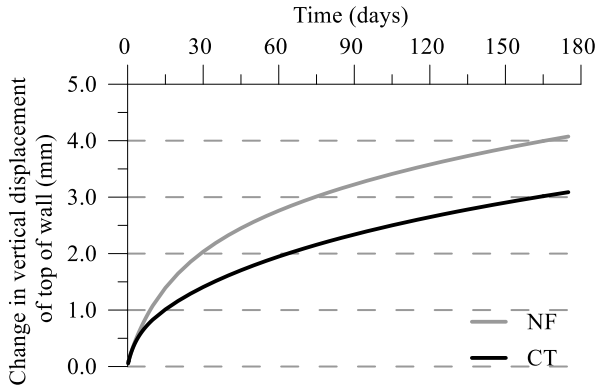

Figure 6-12: Change in vertical movement of top of wall with time

6.2.1.3 Evaluation of three-dimensional effects

As previously discussed, when simulating heat exchanger pipes in 3D analyses, non-uniform temperatures across the width of the wall panel develop. These affect the distribution of forces across the width of the wall panel (as observed by Sterpi et al. (2017), see Section 2.4.4), while negligible differences are computed for the horizontal and vertical displacements due to the wall's large stiffness.

The out-of-plane behaviour is analysed in terms of axial forces and bending moments for two different portions of wall across the width of the panel, i.e. the one containing the inlet pipe ("inlet section") and the middle portion of the panel ("mid-section"), as depicted in Figure 6-13. The structural forces are computed based on the normal stress distributions within each portion of the wall and are subsequently divided by the portion's width to obtain values per metre width of wall. Such normalisation means the

final values are independent of the width of the considered portion and allows direct comparisons with the average forces calculated for the whole panel.

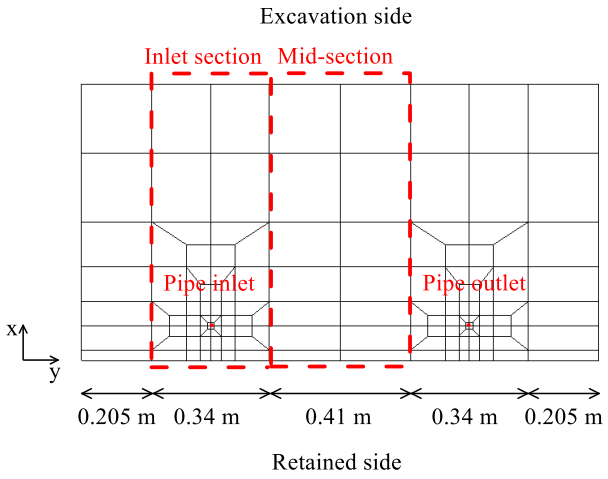

Figure 6-13: Mesh of wall panel in plan view with indication of sections employed to analyse out-of-plane effects

Axial forces

Figure 6-14 and Figure 6-15 show the change in axial force per metre width of wall for the NF and CT cases, respectively, calculated for the two portions of wall illustrated in Figure 6-13, and two different time instants. For reference, the average force of the whole panel is also displayed.

The changes in axial force evaluated within the inlet and mid-section are considerably different from the average change in axial force of the whole panel, particularly in the short term. This is a consequence of the non-uniform temperatures in the out-of-plane direction (i.e. the y-direction). Indeed, the inlet section is characterised by larger temperatures when compared to the mid-section, due to the presence of the heat exchanger pipe. This temperature difference leads to the development of internal forces due to the differential thermal expansion between the two portions of the wall. In effect, the thermal expansion of the inlet section is partly restricted by the adjacent portions at lower temperature which expand less, inducing mechanical compressive stresses. As expected, the opposite is true for the mid-section of the wall, which is subjected to tensile forces.

These out-of-plane effects are most significant when large temperature differences exist across the width of the wall. For the analysed case, this occurs at the beginning of the analysis. Observing Figure 6-14 (a) and Figure 6-15 (a), it can be noted that the inlet section experiences an average increase in compression of -90.0 kN/m (which is four times greater than the maximum average compressive force), while the mid-section is subjected, on average, to 50.0 kN/m of tension. Furthermore, the CT and NF analyses behave in a similar manner, since the temperatures within the wall in the short term are unaffected by the boundary condition along the exposed face. With time, for the NF case, the temperatures become more uniform and hence the difference in forces between the different sections of the wall decreases (see Figure 6-14 (b)). Conversely, for the CT case, the temperatures remain non-

uniform with time due to the constant temperature enforced along the exposed face (see Figure 4-22). Thus, larger out-of-plane effects are observed in the long term (Figure 6-15 (b)).

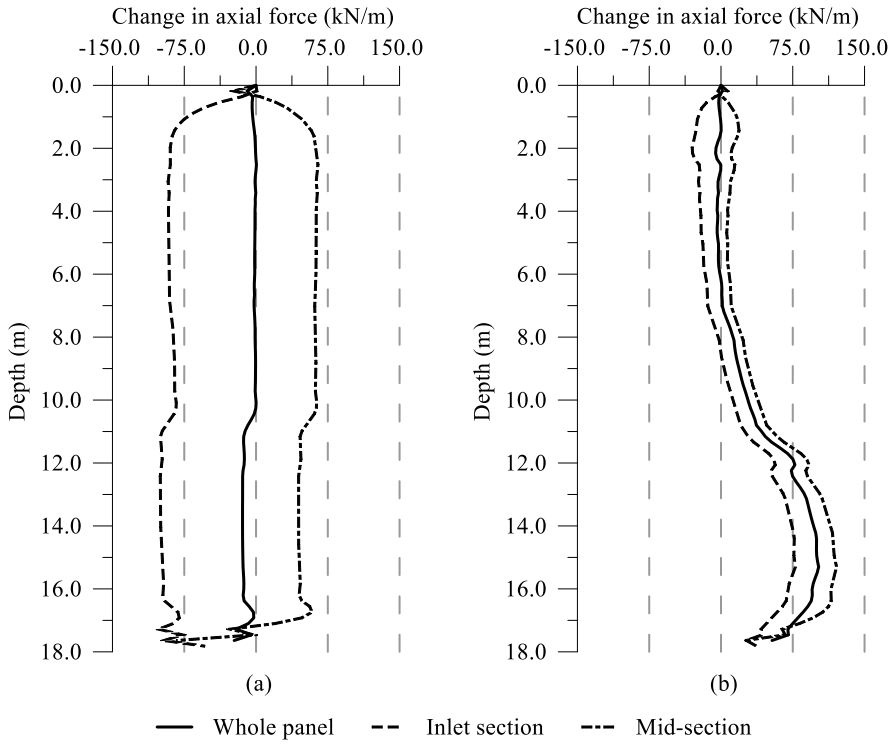

Figure 6-14: Out-of-plane effects – Change in axial force with depth for NF boundary condition (a) 3 days and (b) 6 months

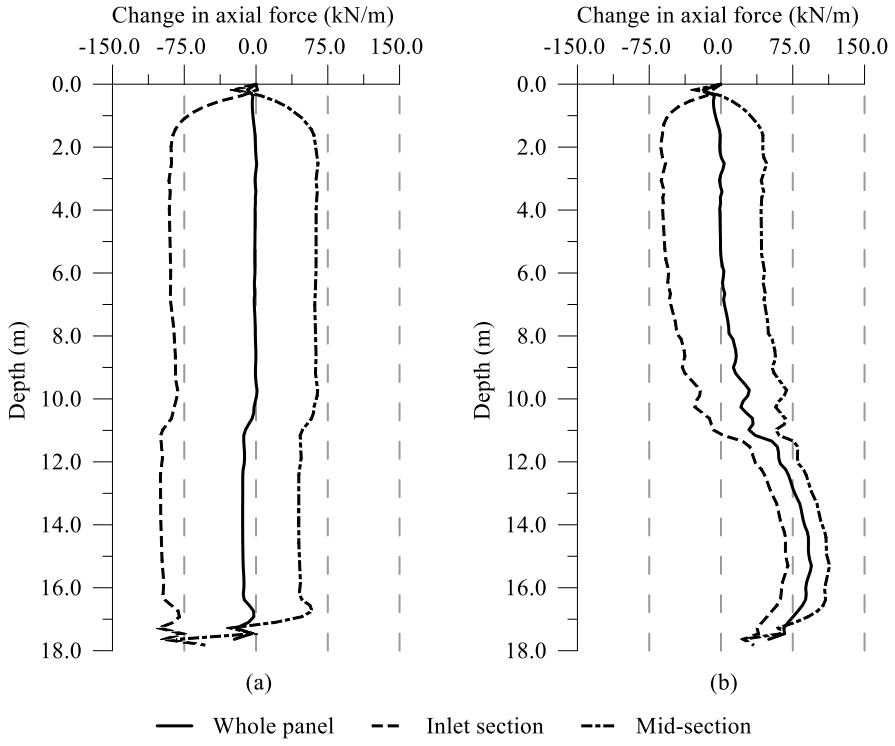

Figure 6-15: Out-of-plane effects – Change in axial force with depth for CT boundary condition (a) 3 days and (b) 6 months

Bending moments

Figure 6-16 and Figure 6-17 show the change in bending moment per metre width of wall for the NF and CT cases, respectively, and for two different time instants.

As was observed in the previous section, the bending moment induced by a change in temperature is affected by the magnitude of the temperature differential across the thickness of the panel, H (i.e. distance between the retained and excavated sides of the wall), which induces mechanical strains. Naturally, a smaller temperature difference between the retained and excavated sides of the wall leads to lower bending moments. It is therefore unsurprising that, as can be noted in Figure 6-16 (a) and Figure 6-17 (a), the inlet section is subjected to a larger change in bending moment, since the temperature differential is higher within this portion of the wall. Indeed, the maximum change in bending moment within the inlet section is 20 kNm/m larger when compared to the average one, while the one in the mid-section is 10 kNm/m smaller.

Similar to the axial forces, the difference in bending moments between the various wall portions reduces with time for the NF case, as the temperatures become more uniform. As previously observed, the bending moment in the long term for the NF case is driven by soil deformation rather than temperature gradients within the wall; thus, at the end of the analysis, the out-of-plane effects are negligible. Conversely, for the CT case, the temperature differential between the excavated and retained sides of the wall remains large due to the applied boundary condition along the excavated face. Hence out-of-plane effects are still present in the long term (Figure 6-17 (b)) and are only slightly smaller than those evaluated in the short term.

In absolute terms, the out-of-plane effects evaluated for bending moments are more limited when compared to those observed for the axial forces and are mainly relevant for walls subjected to a constant temperature along the exposed face.

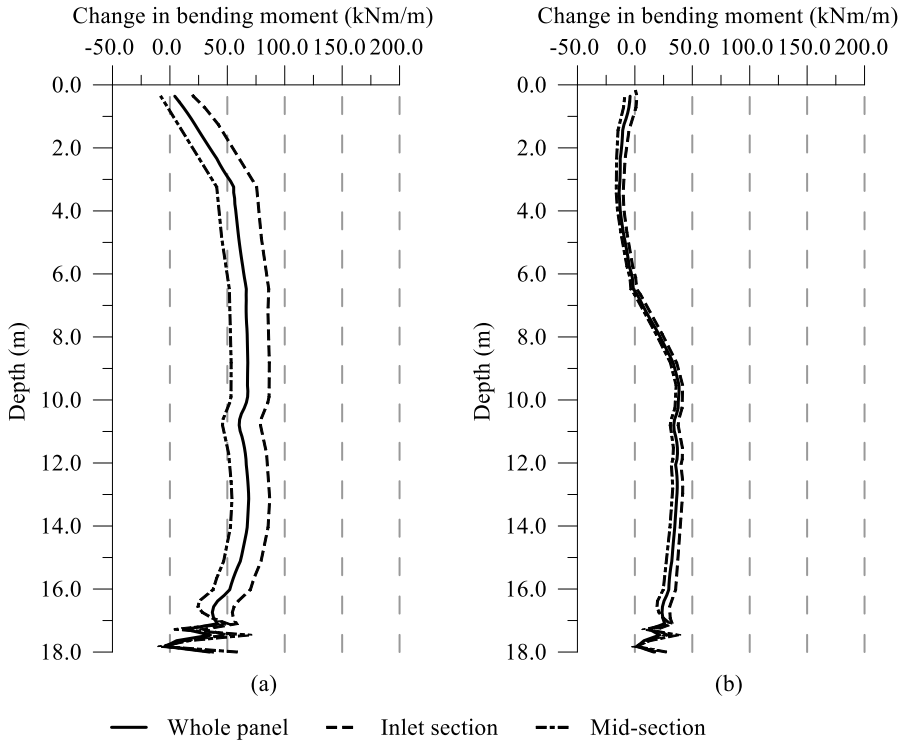

Figure 6-16: Out-of-plane effects – Change in bending moment with depth for NF boundary condition (a) 3 days and (b) 6 months

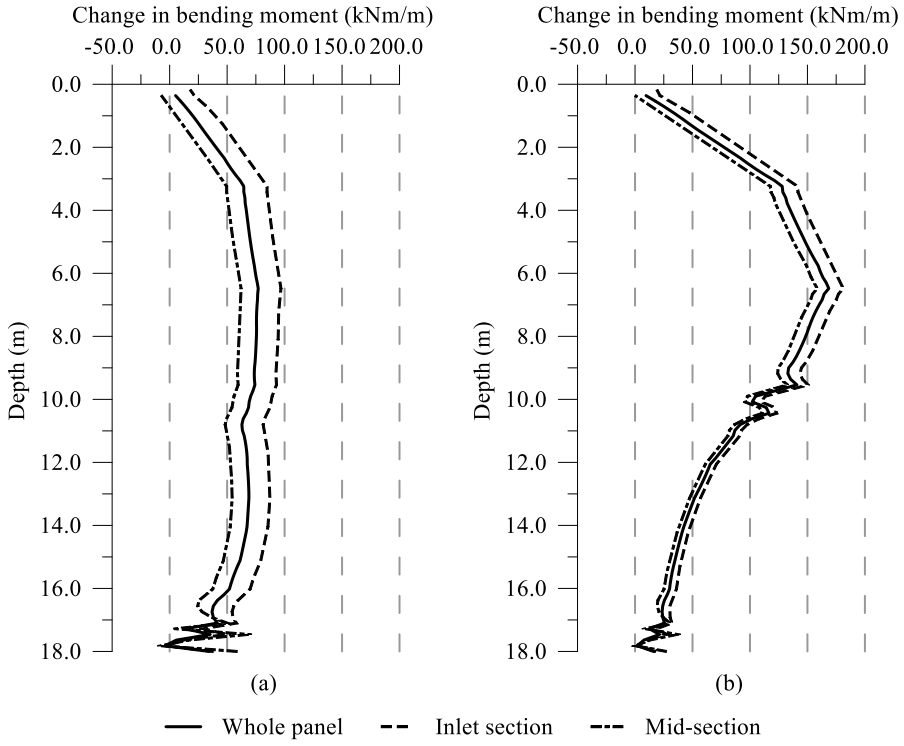

Figure 6-17: Out-of-plane effects – Change in bending moment with depth for CT boundary condition (a) 3 days and (b) 6 months

6.2.2 Parametric study on idealised wall geometry

In this section, a parametric study is carried out to assess the effect of geometric parameters (i.e. width of panel – or, equally, spacing between pipes – and depth of excavation) and thermal parameters (thermal conductivity of concrete and thermal diffusivity of soil) on the thermo-mechanical behaviour of thermo-active walls. Furthermore, for each case, the boundary condition along the exposed face was varied, imposing either a NF or CT condition, to investigate the influence of the analysed parameters for these two extreme scenarios. For this purpose, numerous 3D analyses of an idealised wall geometry, embedded in a uniform soil layer consisting of London Clay, were carried out. The list of the performed analyses is reported in Table 6-2. For all cases, the wall is 20.0 m long (L) and 1.0 m thick (H), while the width (B) varies between 2.0 m and 1.0 m. Since one single U-loop is modelled in each case, the spacing between the pipes varies with the width of the panel being respectively equal to 1.0 m and 0.5 m. The simulated excavation depth, L_{exp}, is 16.0 m or 4.0 m, to investigate two extreme cases of embedment depth (or, equivalently, of the ratio L_{exp}/L). The thermal conductivity of concrete was taken as 1.6 W/mK for most of the cases, while its effect was analysed by either doubling or halving this value in analyses C and D, respectively. Regarding the thermal parameters of the soil, either those of London Clay employed by Gawecka et al. (2017) or those adopted in Sailer et al. (2018a) were used in the analyses, leading, respectively, to a thermal diffusivity, $\alpha_{T,s}$, of 9.8×10^{-7} m^2/s or 6.7×10^{-7} m^2/s (see Table 6-3 for details).

Table 6-2: List of analyses carried out for parametric study

Analysis	L (m)	L_{exp} (m)	L_{exp}/L (m)	H (m)	B (m)	BC exp. face	$\alpha_{T,s}$ (m^2/s)	λ_c (W/mK)
A1	20.0	16.0	0.8	1.0	2.0	NF	9.8×10^{-7}	1.6
A2	20.0	16.0	0.8	1.0	2.0	CT	9.8×10^{-7}	1.6
B1	20.0	16.0	0.8	1.0	1.0	NF	9.8×10^{-7}	1.6
B2	20.0	16.0	0.8	1.0	1.0	CT	9.8×10^{-7}	1.6
C1	20.0	16.0	0.8	1.0	2.0	NF	9.8×10^{-7}	3.2
C2	20.0	16.0	0.8	1.0	2.0	CT	9.8×10^{-7}	3.2
D1	20.0	16.0	0.8	1.0	2.0	NF	9.8×10^{-7}	0.8
D2	20.0	16.0	0.8	1.0	2.0	CT	9.8×10^{-7}	0.8
E1	20.0	4.0	0.2	1.0	2.0	NF	6.7×10^{-7}	1.6
E2	20.0	4.0	0.2	1.0	2.0	CT	6.7×10^{-7}	1.6
F1	20.0	4.0	0.2	1.0	1.0	NF	6.7×10^{-7}	1.6
F2	20.0	4.0	0.2	1.0	1.0	CT	6.7×10^{-7}	1.6
G1	20.0	4.0	0.2	1.0	2.0	NF	9.8×10^{-7}	1.6
G2	20.0	4.0	0.2	1.0	2.0	CT	9.8×10^{-7}	1.6

6.2.2.1 Numerical analysis

Problem description

The analysed thermo-active wall supports a 30.0 m wide excavation and is embedded in London Clay. The heat exchanger pipes (internal diameter of 27.33 mm) are located at a distance of 0.1 m from the concrete edge on the retained side and reach a depth of 19.5 m, where they are connected by a horizontal pipe segment. As shown in Figure 6-18, which depicts the finite element mesh, only half of the domain is modelled due to the symmetry of the problem in the x-direction. In the out-of-plane direction (y-direction in Figure 6-18), an entire panel was simulated as a form of representing a wall characterised by a significant length. The wall is supported by horizontal slabs, where the floor slabs and the base slab were assumed to have thicknesses of 0.3 m and 1.0 m, respectively (see Figure 6-18 for details on their position – note that for the 4.0 m deep excavation, only the top two slabs were modelled, with the bottom one considered as base slab). Two different conditions were assumed for the wall-air interface: an insulated wall (i.e. no heat flux (NF) takes place across this boundary), and a wall face maintained at constant temperature (CT) equal to the initial temperature (T_0) of 15°C, denoted by the number used in the names of the analyses listed in Table 6-2 (1 for NF and 2 for CT). The initial ground conditions are characterised by a hydrostatic pore water pressure profile, where the water table is located at the ground surface, and a coefficient of earth pressure at rest, K_0, of 1.0, with the soil having a bulk unit weight, γ, of 20 kN/m^3.

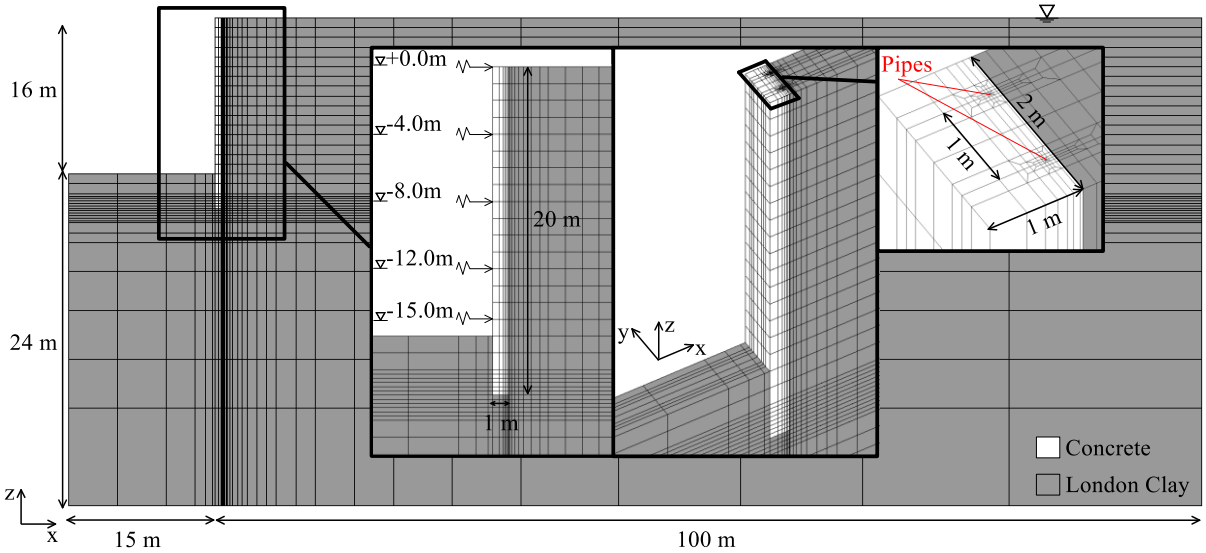

Figure 6-18: Finite element mesh for idealised geometry

Material properties

Concrete and pipes were modelled as linear-elastic materials. The former is characterised by a Young's modulus, E, of 30 GPa and a Poisson's ratio, ν, of 0.3. The pipes have a sufficiently low stiffness such that their presence will not affect the behaviour of the wall (see Table 6-1 for their mechanical

properties, with the coefficient of thermal expansion being equal to that of the concrete employed in the analyses of this study, i.e. 1.2×10^{-5} m/mK, see Table 6-3).

The soil was modelled as a non-linear elasto-plastic material, with a Mohr-Coulomb failure surface (c'=5.0 kPa, φ'=25.0°, ψ'=12.5°) coupled with the IC.G3S non-linear elastic stiffness model (Taborda et al., 2016). The model's equations and employed parameters for London Clay are reported in Chapter 3. The soil has a permeability of 1.0×10^{-10} m/s and the coefficient of expansion of water, α_w, is equal to 6.9×10^{-5} m/mK. The other thermal properties are outlined in Table 6-3, where the linear coefficient of thermal expansion of concrete, soil and pipe are assumed to be the same, in order to remove any effects of differential thermal expansion between the various materials (see e.g. Bourne-Webb et al. (2016b) and Sailer et al. (2018a) for analyses quantifying these effects in thermo-active retaining walls).

Table 6-3: Thermal material properties for analyses on idealised geometry

Material	α (m/mK)	C_v (kJ/m^{3}K)	λ (W/mK)
Concrete ([1])	1.2×10^{-5}	2160	1.60
London Clay (analyses A-D and G)	1.2×10^{-5}	1820 ([2])	1.79 ([2])
London Clay (analysis E and F)	1.2×10^{-5}	3000 ([3])	2.00 ([3])
Pipe/Geothermal fluid	1.2×10^{-5}	4180	0.60

([1]) see Table 6-2 for variation of this parameter
([2]) adopted from Gawecka et al. (2017)
([3]) adopted from Sailer et al. (2018a)

Modelling procedure

The details of the performed numerical analyses – element type, thermo-hydro-mechanical boundary conditions, heat exchanger pipes, use of Petrov-Galerkin and choice of timestep – are identical to those of the reference analysis described in Section 6.2.1. An undrained excavation was modelled adopting short time periods, where the final depth was reached by excavating layers of 2.0 m in thickness. The wall was supported by temporary props placed at depths of 3.0 m, 7.0 m and 11.0 m (for the 4.0 m deep excavation, no temporary props were employed). These were simulated as a nodal spring with a stiffness of 100 MN/m acting in the middle of the panel (i.e. y = 1.0 m, see Figure 6-18). Once excavation was completed, the temporary props were removed releasing the nodal reaction forces while the permanent slabs were constructed. These were simulated as normal springs applied along the whole width of the wall panel. The assigned stiffness was such that the springs would simulate the presence of concrete slabs (E=28.0 GPa), the thicknesses of which were given when describing the geometry of the problem. Once construction was completed, a pore water pressure of 0.0 kPa was imposed at the base of the excavation to simulate the presence of a drainage layer. Before the application of the thermal boundary conditions, the pore water pressures generated during excavation were fully dissipated to allow the

thermal effects on the behaviour of the wall during the following THM analyses to be isolated from those arising from the construction stages. Furthermore, before the application of the thermal load, the soil's stiffness was reset to its maximum value to account for the increase in stiffness given by the reversal in the load direction induced by the application of temperature (Gawecka et al., 2017; Schroeder et al., 2004). Six months of heat injection were simulated by applying a constant temperature of 30°C at the inlet node of the pipes ($T_{in,3D}$), i.e. $\Delta T_{in,3D}$=15.0°C.

6.2.2.2 Results

Effect of depth of excavation

The following results present the comparison of analyses A and G to assess the effect of the depth of excavation (L_{exp}) on the thermo-mechanical behaviour of the wall. The depth of excavation determines the area of contact between soil and wall, thus affecting the restriction the soil applies against the thermal expansion of the wall in the short term and the tensile actions induced in the long term as the heat is transferred to the soil and it expands. This is clearly visible in the development of the axial force depicted in Figure 6-19 and Figure 6-20. Overall larger changes in axial force are evaluated for the large embedment depth (i.e. shallow excavation), with a larger initial compression and larger tensile forces in the long term when compared to a smaller embedment depth (i.e. deep excavation). Regarding the variation in structural forces in the out-of-plane direction, the calculated pattern is not affected by the depth of excavation in the short term since this factor does not influence the temperatures within the wall. In the long term, larger out-of-plane effects are registered for the NF case when a shorter excavation is modelled, while the contrary is observed for the CT case, due to different relative differences in temperature across the width of the panel.

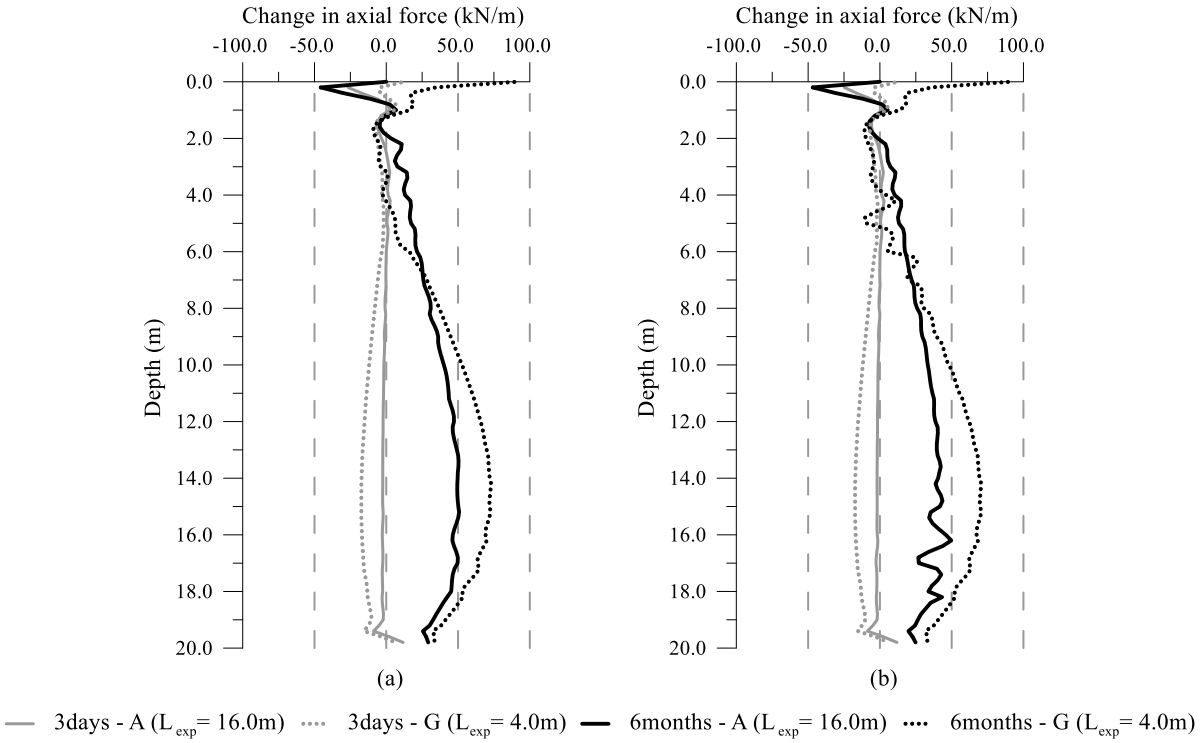

Figure 6-19: Effect of excavation depth on change in axial force with depth for different time instants (a) NF and (b) CT

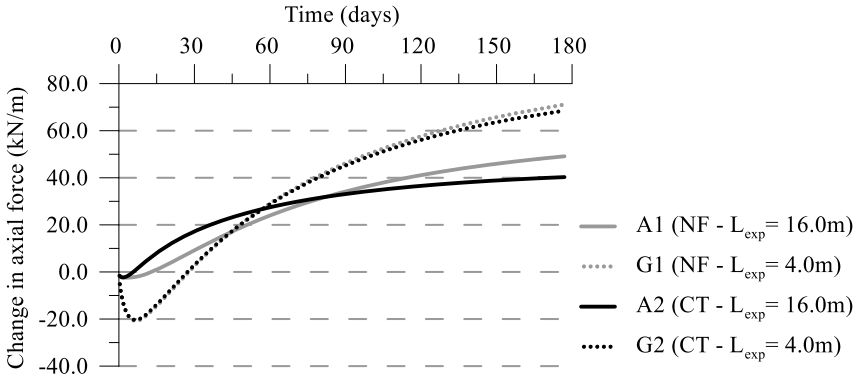

Figure 6-20: Effect of excavation depth on development of axial force with time at depth of 14.0m

The excavation depth clearly affects the distribution of the temperatures within the wall. Indeed, with a short excavation depth, a large part of the heat is dissipated to the soil, whereas with a large L_{exp} the temperatures of the wall are highly dependent on the boundary condition along the exposed face. Since the bending moment largely depends on the changes in temperature within the wall, its magnitude and evolution with time are influenced by the depth of excavation. As shown in Figure 6-21, no effect of the excavation depth is observed in the short term since the temperatures are the same for all the analyses, with the properties of concrete being the only important factor. However, as can be clearly observed in Figure 6-22, the development of the bending moment with time varies greatly for the different values of L_{exp}. For the NF case, a larger reduction of positive bending moment is observed in the long term for a large L_{exp}. This is due to more uniform temperatures within the wall due to the insulated boundary extending for a large length of the wall. Conversely, for the CT case, considerably

larger bending moments develop for a large L_{exp} given the higher temperature gradient across the thickness of the wall.

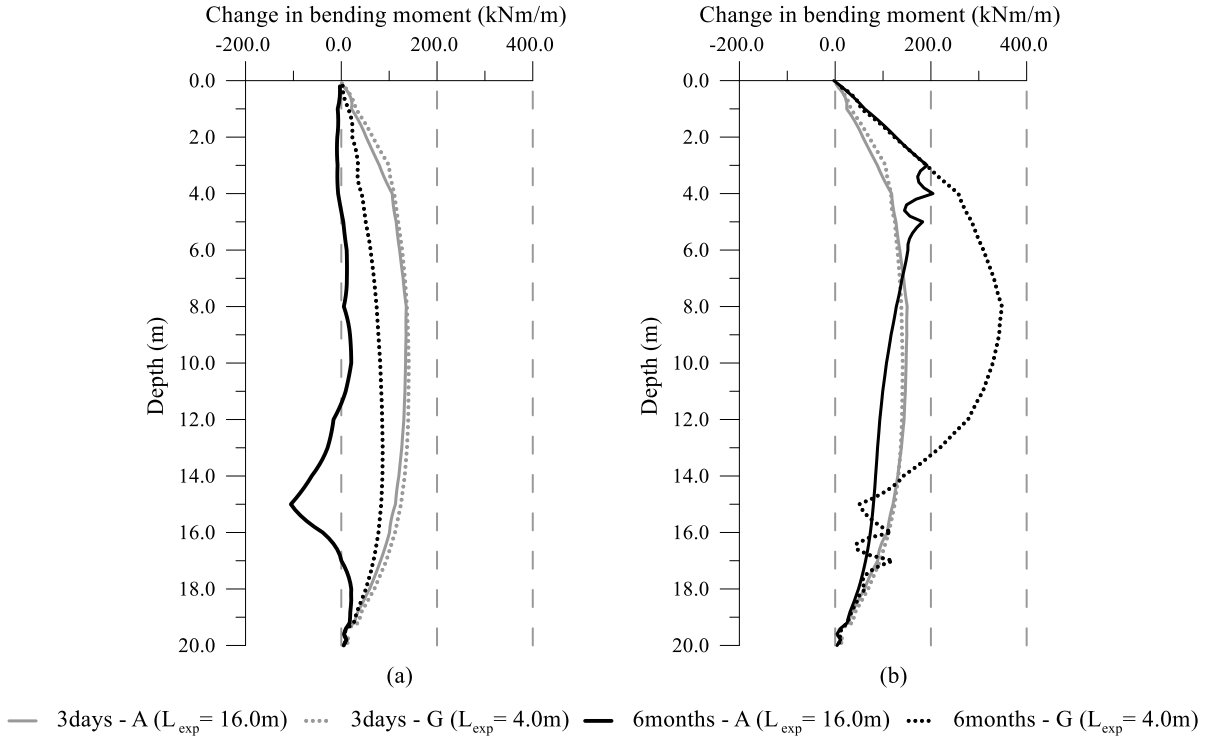

Figure 6-21: Effect of excavation depth on change in bending moment with depth for different time instants (a) NF and (b) CT

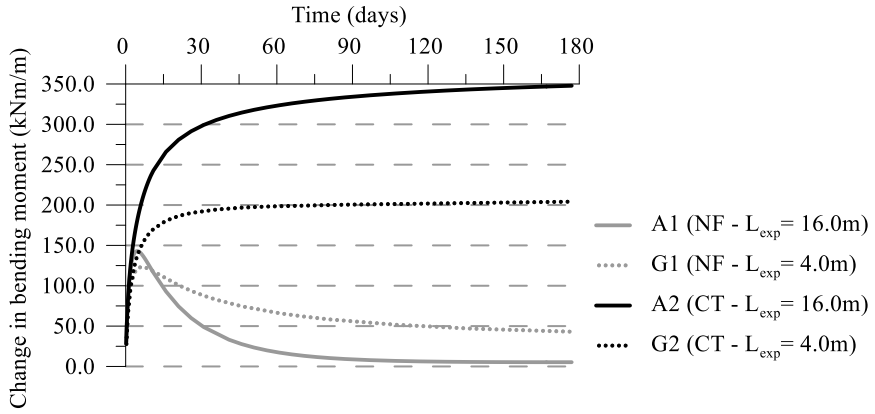

Figure 6-22: Effect of excavation depth on development of bending moment with time at depth of 8.0m

The evolution with time of the vertical movement of the top of the wall is illustrated in Figure 6-23. A similar long-term movement is computed for the two NF cases regardless of the excavation depth, with only slightly different variations with time being observed. Indeed, with a larger excavation depth the average temperature of an insulated wall is larger and hence a greater thermal expansion takes place in the short term. A significant difference in the movement is computed for the CT cases, with the wall supporting a shallower excavation (L_{exp}= 4.0 m) expanding almost twice as the one simulating an L_{exp}=

16.0 m. This is attributed to the lower temperatures developing in the latter case, since a larger part of the wall (80%) is maintained at a constant temperature along the exposed face.

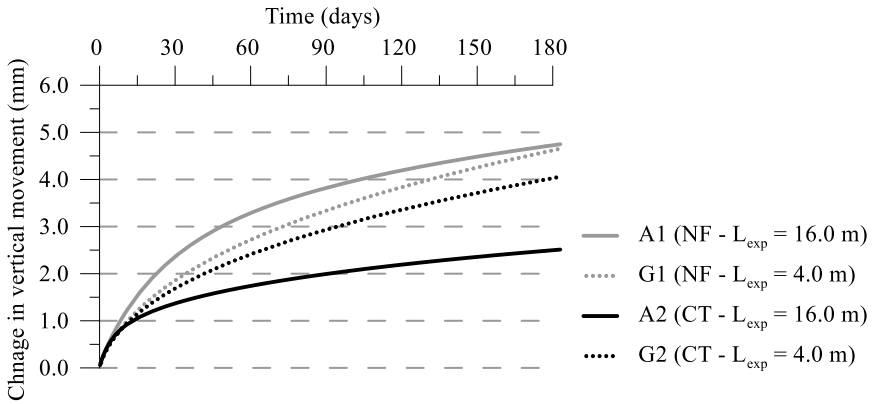

Figure 6-23: Effect of excavation depth on development of vertical movement of top of wall with time

Effect of panel width

The effect of the panel width (B) is analysed comparing analyses A and B (for a 16.0 m deep excavation). Reducing the width of the panel decreases the spacing between the pipes. Thus, for a smaller width, higher temperatures develop within the wall and a faster heat transfer to the soil occurs. It should be noted that the same conclusions can be drawn comparing analyses E and F (i.e. for a 4.0 m deep excavation), however the effects are less pronounced due to the smaller effect of the boundary condition along the exposed face.

As shown in Figure 6-24, which displays the axial force with depth, and in Figure 6-25, which plots the development of axial force with time at a depth of 14.0 m, the width of the panel marginally affects the distribution of the axial force. The simulations involving a smaller wall panel display a quicker reduction in the axial force with time due to the larger changes in temperature occurring with a smaller spacing between the pipes, which are more pronounced for the CT case. This leads to a greater expansion of the soil, which induces tensile changes in axial force in the wall. However, the differences are not very significant. The variation of axial forces in the out-of-plane direction depend on the temperature distribution across the width of the wall. It is therefore unsurprising that a larger variation in forces is registered for the larger wall panel, since greater differences in temperature amongst different wall sections develop. The differences reduce with time as the wall warms up.

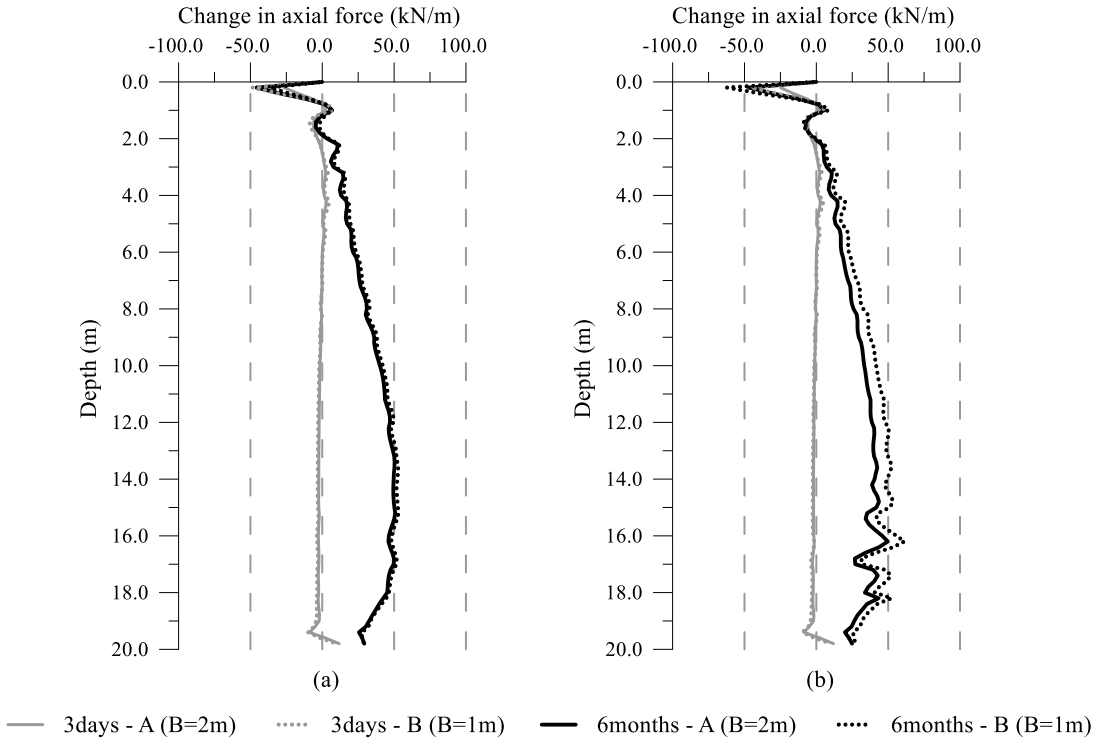

Figure 6-24: Effect of width of wall panel on change in axial force with depth for different time instants for 16 m deep excavation (a) NF and (b) CT

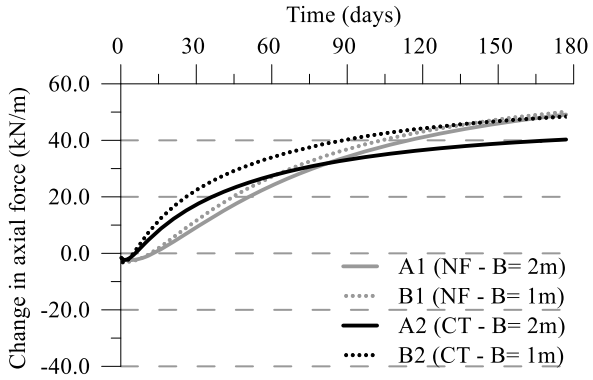

Figure 6-25: Effect of width of wall panel on development of axial force with time at depth of 14.0 m for 16 m deep excavation

The larger temperatures experienced in the analyses simulating a smaller panel width clearly affect the distribution of the bending moment, with larger values experienced for such cases due to the higher temperature difference across the wall's thickness, as can be observed from Figure 6-26 and Figure 6-27. This is applicable to the short term regardless of the boundary condition along the exposed face, where the bending moment increases by 68% as B is reduced from 2.0 m to 1.0 m. In the long term, it mainly affects the CT case, with an increase in bending moment of 50% when analysis B2 is compared to A2. For the NF analysis, the long-term bending moment is less affected by the width of the wall panel, indicating that a small difference in temperature is computed. This can be related to the observations in Chapter 5 where changing the spacing between the pipes does not affect the thermal performance because of the insulated boundary leading to uniform temperatures.

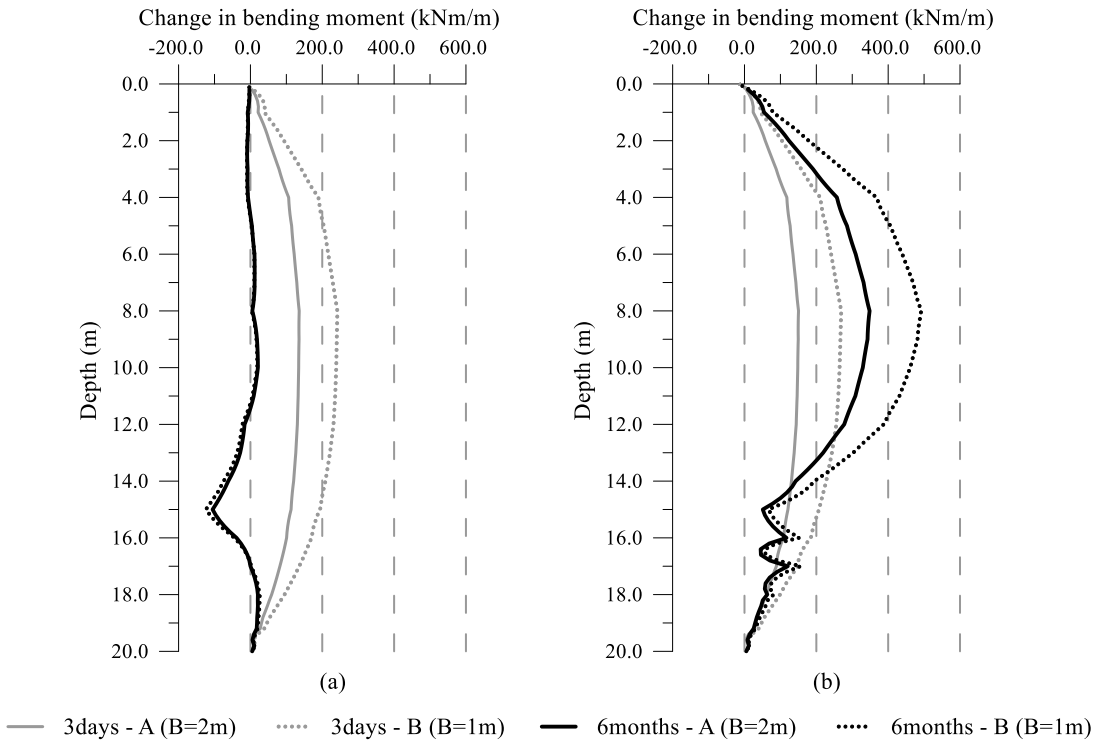

Figure 6-26: Effect of width of wall panel on change in bending moment with depth for different time instants for 16 m deep excavation (a) NF and (b) CT

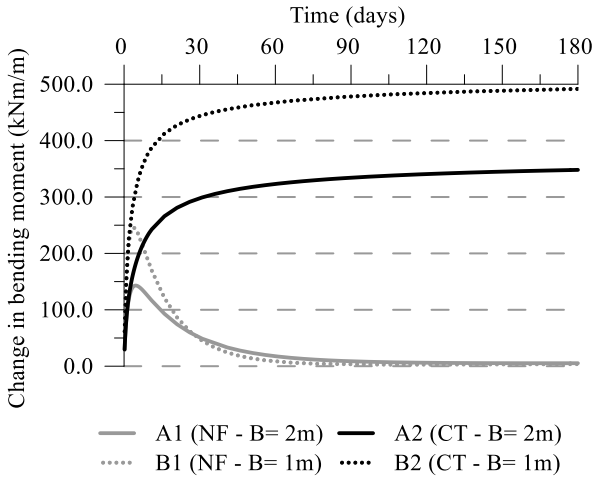

Figure 6-27: Effect of width of wall panel on development of bending moment with time at depth of 8.0 m for 16 m deep excavation

The smaller spacing between pipes and the consequent increase in temperature within the wall leads to larger vertical wall movements, as plotted in Figure 6-28. A similar relative difference is computed for both NF and CT cases, where the vertical movements recorded for the analyses simulating a smaller panel width are 25-30% larger than those evaluated for the equivalent analyses with a larger panel.

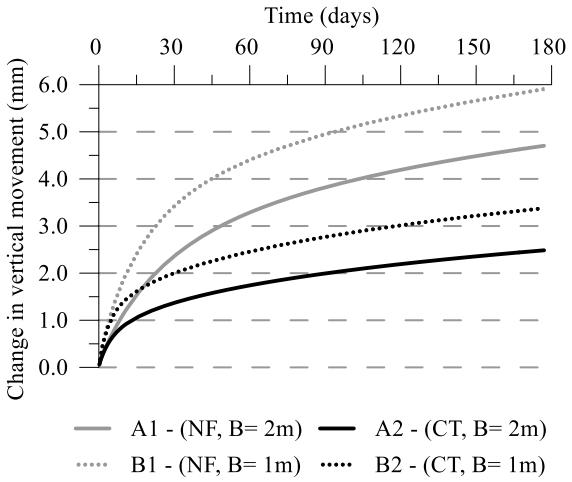

Figure 6-28: Effect of width of wall panel on development of vertical movement of top of wall with time for 16 m deep excavation

Effect of concrete thermal conductivity

The effect of the thermal conductivity of concrete is assessed comparing analyses A, C and D, with the two latter corresponding to twice and half the thermal conductivity of the concrete employed in analysis A, respectively. As discussed in Chapter 5, the thermal conductivity of the concrete affects the temperatures within the wall panel, despite not influencing in a substantial manner the temperatures within the soil. Furthermore, a faster heat transfer rate is experienced when a higher thermal conductivity is employed, meaning that larger initial temperatures are expected for such cases. However, as can be observed from Figure 6-29 and Figure 6-30, the axial force is marginally affected when different values of concrete thermal conductivity are employed. Indeed, only a small change in the initial compression is observed, which increases for the analyses with a higher thermal conductivity, given the higher temperatures within the wall and thus the larger restriction applied by the soil.

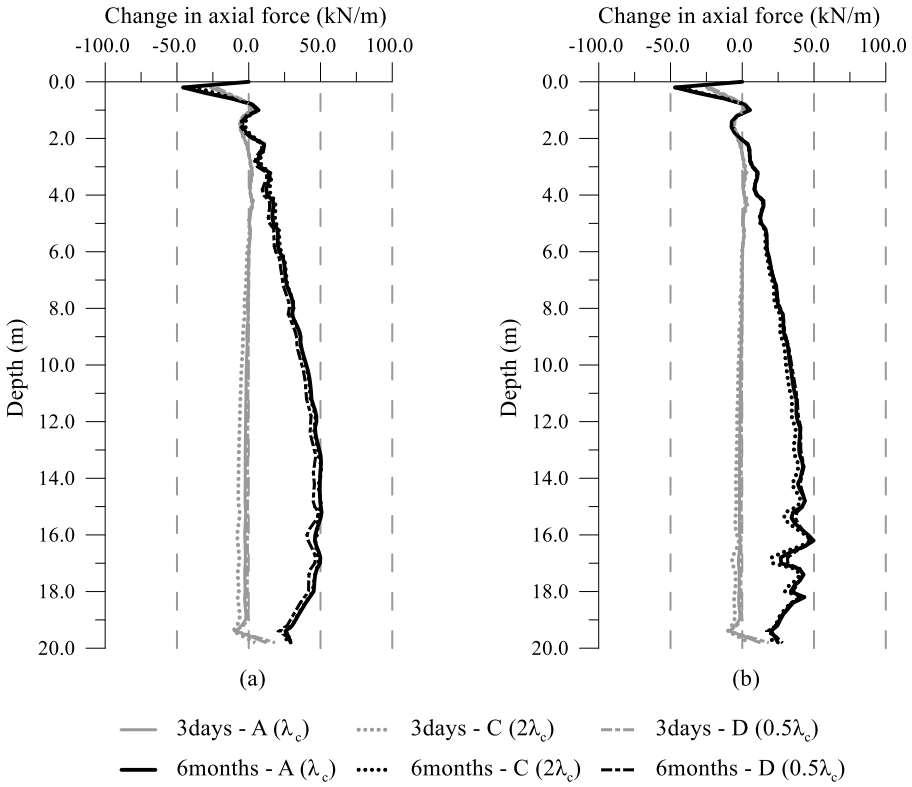

Figure 6-29: Effect of thermal conductivity of concrete on change in axial force with depth for different time instants (a) NF and (b) CT

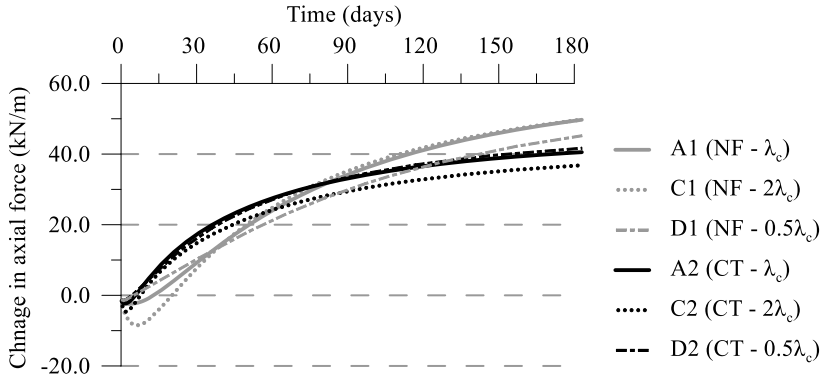

Figure 6-30: Effect of thermal conductivity of concrete on development of axial force with time at depth of 14.0 m

Similarly, the thermal conductivity of the concrete affects mainly the distribution of the bending moments in the short term, since similar temperatures are computed in the long term. As can be observed from Figure 6-31 and Figure 6-32, the largest changes, as expected, are evaluated for the CT case in the short term. Thus, while largely affecting the thermal performance, the concrete thermal conductivity has little effect on the distribution of forces for the CT case.

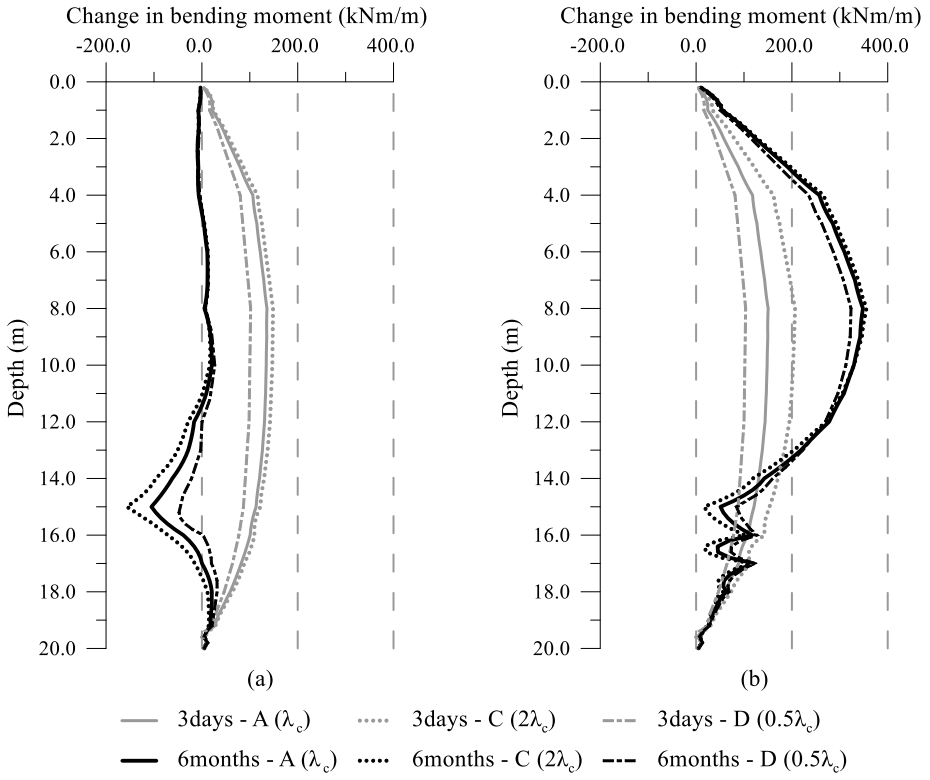

Figure 6-31: Effect of thermal conductivity of concrete on change in bending moment with depth for different time instants (a) NF and (b) CT

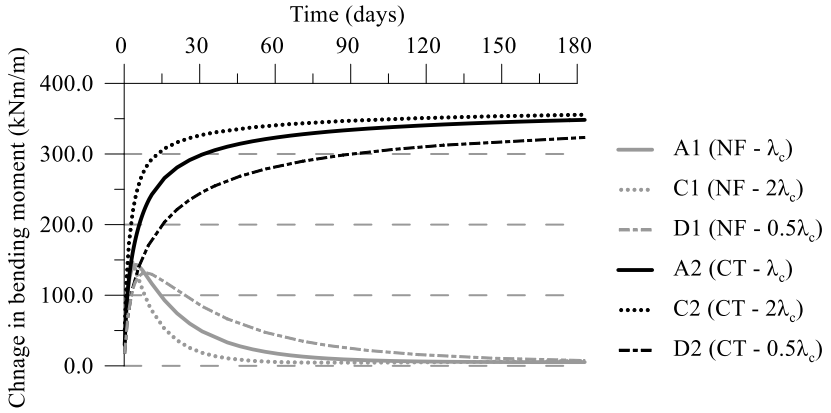

Figure 6-32: Effect of thermal conductivity of concrete on development of bending moment with time at depth of 8.0 m

Conversely, the vertical wall displacement is noticeably affected by the thermal conductivity, as shown in Figure 6-33. As previously mentioned, this parameter affects the temperature within the wall and the rate at which its increase takes place. For the NF case, after 3 days, when compared to analysis A1 the average wall temperature is 0.9°C (82%) higher when twice the concrete thermal conductivity is adopted (analysis C1) and 0.5°C (45%) lower for half the concrete thermal conductivity (analysis D1). For the CT case, the differences are, respectively, +0.7°C (68%) and -0.5°C (-44%). Thus, the analyses with a higher concrete thermal conductivity predict a larger displacement from the beginning of the analysis. With time, both the wall and soil temperatures gradually increase, with higher temperatures computed for a high thermal conductivity. The differences in the average temperature of the wall in the

long term for different concrete conductivities are larger for the NF case (+1.5°C (13%) and -2.2°C (19%) for $2\lambda_c$ and $0.5\lambda_c$, respectively) when compared to the CT case (+0.34°C (9%) and -0.6°C (13%) for $2\lambda_c$ and $0.5\lambda_c$, respectively) since the wall heats up quicker in the former case. Hence, doubling or halving the concrete conductivity leads to a larger difference in the wall movement for the NF case ($\pm$1.0 mm), while the effect of the concrete conductivity for the CT analyses is limited to $\pm$0.5 mm. It should be noted that the relative difference is similar for both analyses and corresponds to approximately $\pm$20% of the values computed for analyses A.

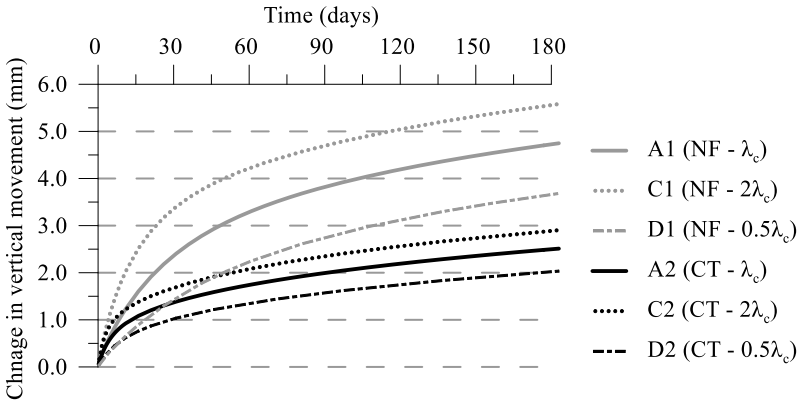

Figure 6-33: Effect of thermal conductivity of concrete on development vertical movement of top of wall with time

Effect of soil thermal diffusivity

To investigate the effect that soil thermal diffusivity ($\alpha_{T,s}$) has on the thermo-mechanical behaviour, analyses E and G are compared. These were carried out, respectively, with $\alpha_{T,s}$ of 6.7×10^{-7} m^2/s and 9.8×10^{-7} m^2/s, which are obtained by a different combination of both the thermal conductivity and heat capacity as detailed in Table 6-3. As explained in detail in Chapter 3, the thermal diffusivity affects the rate of heat transfer, with a higher value corresponding to a faster heat transfer rate. Indeed, although analyses E present a higher thermal conductivity of the soil, the fact that a much higher value of volumetric heat capacity is used means that the increase in soil temperature is slower than that for analyses G, where the combination of a lower thermal conductivity and heat capacity is such that a higher diffusivity is obtained. This is evident when comparing the evolution of the axial forces in the long term, which is governed by the thermal expansion of the soil (see Figure 6-34 and Figure 6-35). This is larger for analyses G, which, for both boundary conditions, display a larger tensile force in the long term (increase of 20 kN/m when compared to analysis E). Conversely, the short-term response is unaffected since, in that time frame, it depends mainly on the wall temperatures, which are not affected by the thermal parameters of the soil. This can also be seen in the development of the bending moment (Figure 6-36 and Figure 6-37), for which negligible effects of soil thermal diffusivity are observed.

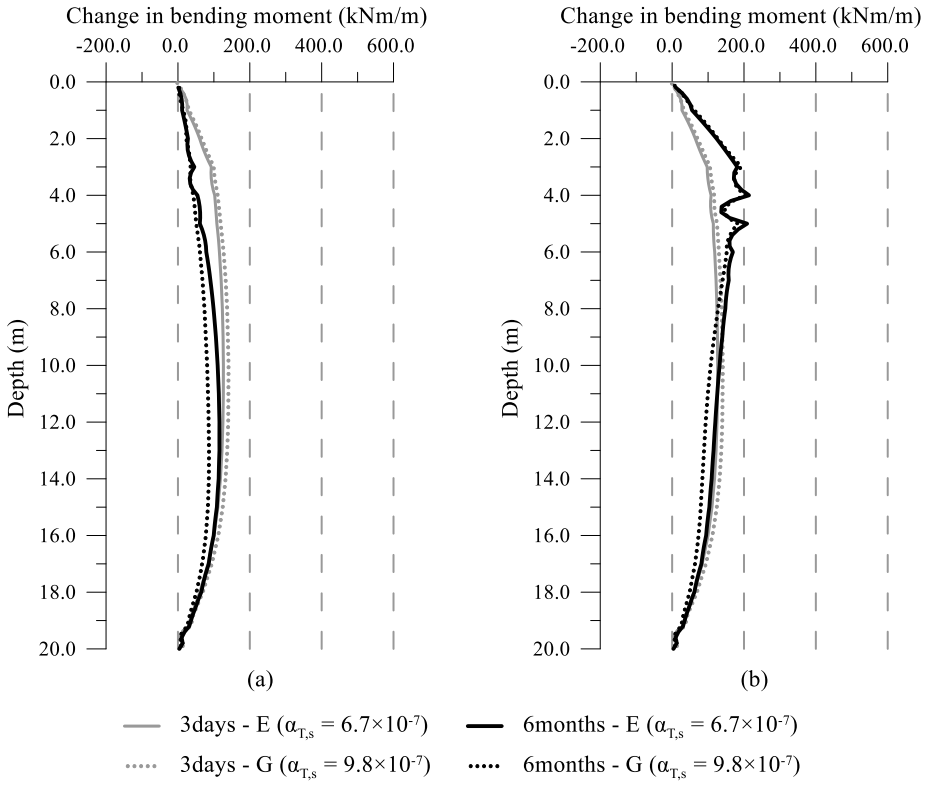

Figure 6-34: Effect of thermal diffusivity of soil on change in axial force with depth for different time instants a) NF and (b) CT

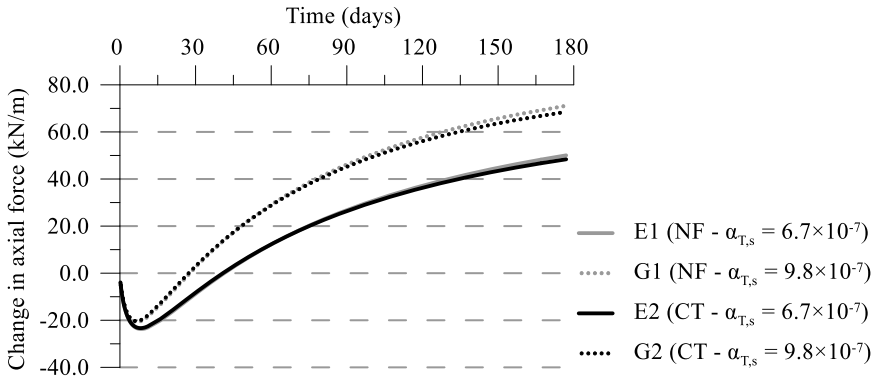

Figure 6-35: Effect of thermal diffusivity of concrete on development of axial force with time at depth of 14.0 m

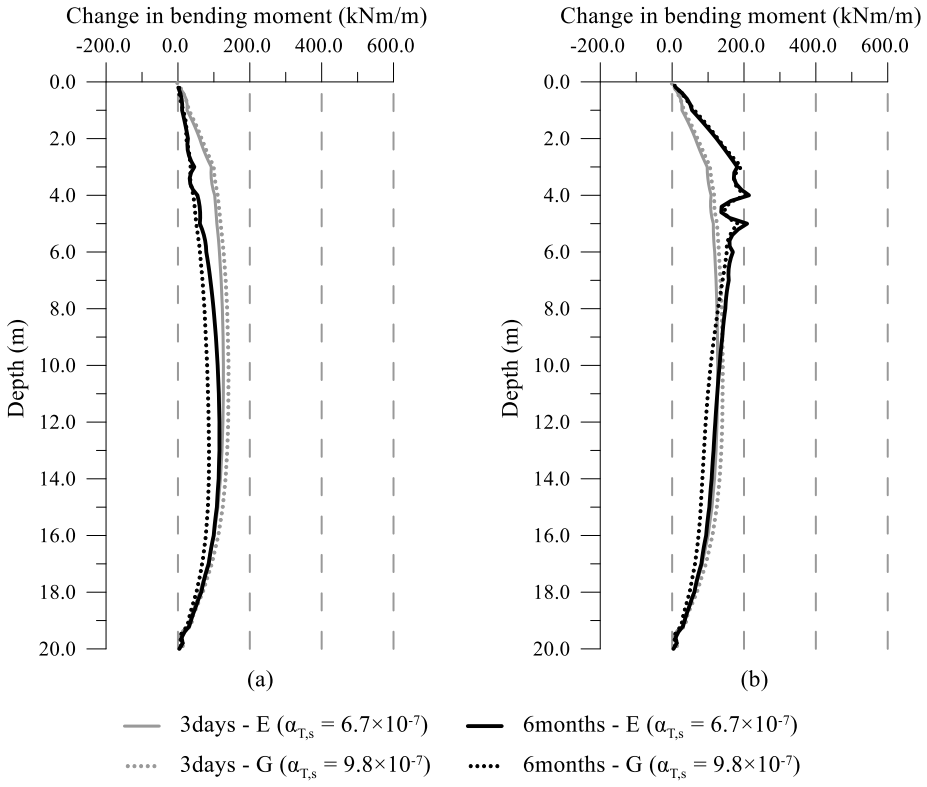

Figure 6-36: Effect of thermal diffusivity of soil on change in bending moment with depth for different time instants (a) NF and (b) CT

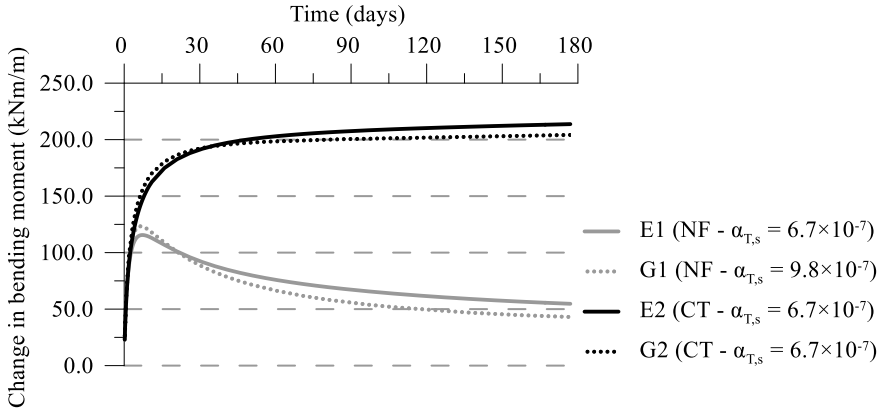

Figure 6-37: Effect of thermal diffusivity of soil on development of bending moment with time at depth of 8.0 m

With larger temperatures within the soil, a larger thermal expansion occurs affecting the vertical wall movement in the long term. Indeed, no difference is observed in the short term (<15 days), where the heat transfer takes place mostly within the concrete (as was previously observed when analysing the effect of the concrete thermal conductivity). In the long term, a larger displacement is computed for analyses G, which is 0.8 mm (21% for CT, 24% for NF) larger than that computed for analysis F, for both boundary conditions.

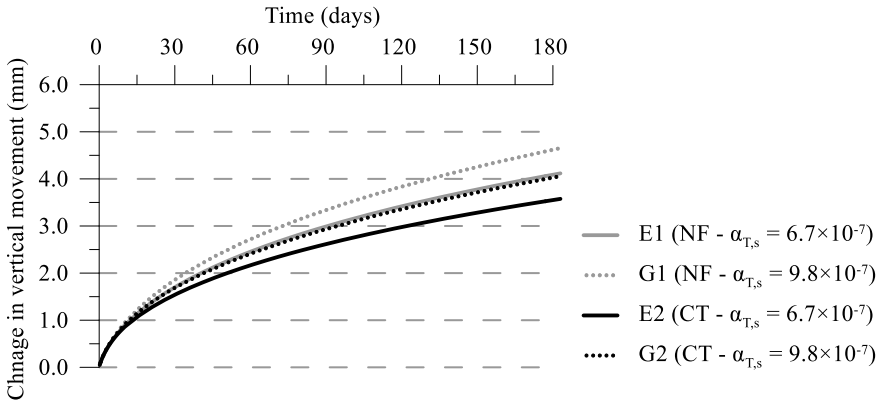

Figure 6-38: Effect of thermal diffusivity of soil on development vertical movement of top of wall with time

6.2.3 Effect of modelling approach in 3D analysis

In this section, the effect of the adopted modelling approach to simulate the heat transfer is investigated for the wall case A2 described in Table 6-2 (i.e. 20.0 m long, 2.0 m wide and 1.0 m thick wall panel, 16.0 m deep excavation, embedded in London Clay, with a constant temperature boundary condition along the exposed face of the wall). The modelling approach employed in the analyses so far applied a prescribed temperature at the pipe inlet and was named modelling approach 1 (MA1) in Chapter 4. The other modelling approach employed herein, termed modelling approach 2 (MA2), applies a nodal heat flux boundary condition at the pipe inlet, prescribing therefore the temperature difference between the inlet and outlet of the pipes. This approach is described in detail in Chapter 4, where it was shown that, if the adopted threshold criterion on temperature changes is applied to the inlet temperature, the main difference between the results obtained by the two approaches lies in the transient temperature changes, both in the wall and the ground. These are more rapid for MA1 given the higher temperature simulated at the pipe inlet in the short term.

Modelling procedure for modelling approach 2

The initial conditions, mechanical and hydraulic boundary conditions and construction sequence are the same as those outlined in Section 6.2.2.1 for MA1. Similarly, the same thermal boundary conditions are applied at the mesh boundaries, with the exception to those on the one-dimensional elements used to simulate heat exchanger pipes. The heat transfer is modelled by applying a nodal heat flux boundary condition at mid-length of the protruding pipe element of the inlet branch. The value of the heat flux boundary condition was such that the same temperature difference at the pipe inlet ($\Delta T_{in,3D}$) as that applied in the analysis simulated with MA1, i.e. $\Delta T_{in,3D}$ = 15°C, is obtained after 6 months of operation. To achieve such a change in temperature, for the given geometry and boundary condition along the exposed face, the magnitude of the heat flux boundary condition was equal to 0.56 kW. At the top nodes of the inlet and outlet branches, the temperature degrees of freedom were tied.

Comparison of results for different modelling approaches

Figure 6-39 and Figure 6-40 compare the development of axial forces and bending moment with depth and time, respectively. As discussed in Chapter 4, the different modelling approaches affect the temperature distributions in the short term, with higher temperatures computed for MA1, while the long-term temperature of the soil-wall system are very similar for both cases.

Even though slightly different temperatures are computed in the wall in the short term (the average wall temperature is 0.4°C lower for MA2), the contribution of the restriction by the soil is very limited in this case due to the short embedded depth, meaning that changes in axial force are almost identical for MA1 and MA2. Conversely, its effect is noticeable in the computed bending moment in the short term, which is smaller when MA2 is adopted. Furthermore, in this case, the increase with time is slower due to the slower rate of heat transfer. However, at the end of the simulation period, negligible differences are computed for the two approaches. This was expected, since the calibration criterion for MA2 was that the inlet temperature should be similar for both analyses after 6 months.

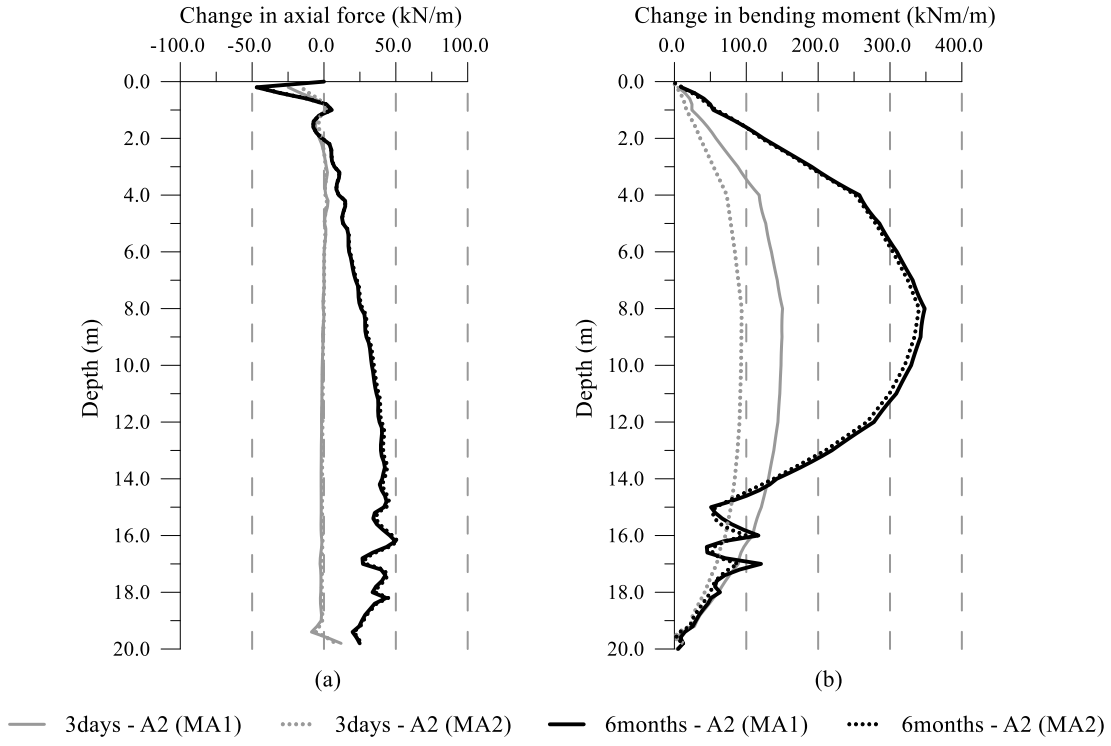

Figure 6-39: Effect of modelling approach on distribution of (a) axial force and (b) bending moment with depth

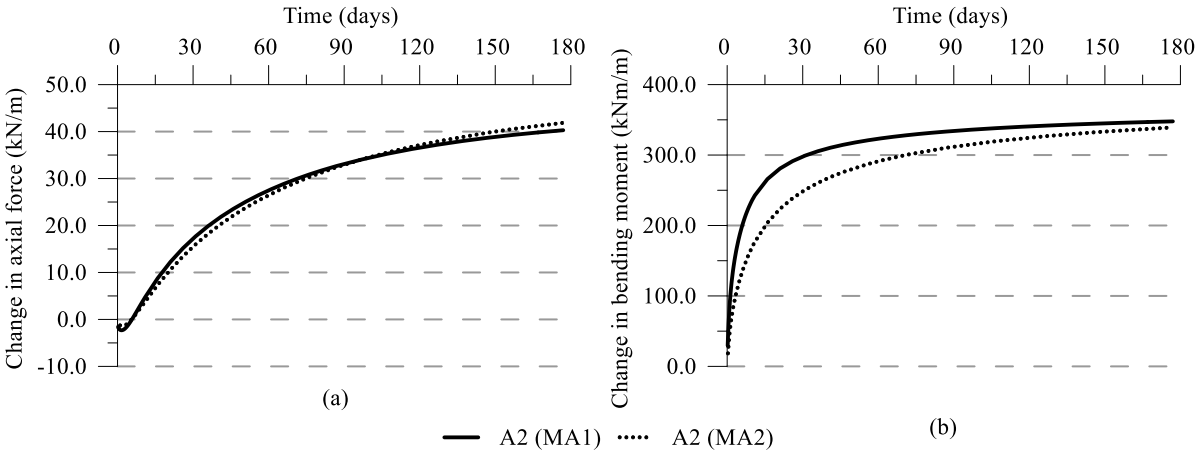

Figure 6-40: Effect of modelling approach on development of (a) axial force at depth of 14.0 m and (b) bending moment at depth of 8.0 m with time

As expected given the lower temperatures, a slightly smaller wall movement is computed for MA2, especially in the short term, as shown in Figure 6-41. Furthermore, the slower rate at which the temperatures increase in MA2 can be clearly observed. A negligible difference is recorded in the long term, since the temperatures are very similar (e.g. the difference in average wall temperature is limited to 0.03°C).

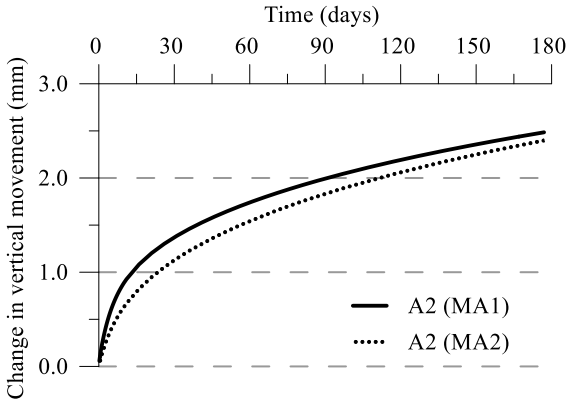

Figure 6-41: Effect of modelling approach on development of vertical movement of top of wall with time

6.3 Assessing two-dimensional modelling approaches

As highlighted throughout this research project, thermo-active wall problems simulated in 3D analyses with the inclusion of heat exchanger pipe elements to model the advective-conductive heat transfer require a significant computational effort, especially when performing fully coupled THM analyses. Furthermore, when simulating advection-dominated heat fluxes, such as those occurring in pipes, advanced numerical methods to overcome the instabilities occurring in such problems are required (Cui et al., 2018c; Gawecka et al., 2020). For this reason, in this section, the use of two-dimensional (2D) plane-strain analyses to simulate the THM response of thermo-active walls is investigated. According to the studies presented in Section 2.4.4, when vertically installed U-loops were assumed, the heat exchange was generally modelled by applying a constant temperature along a line within the wall (e.g.

Bourne-Webb et al. (2016b); Rui & Yin (2018); Yin & Rui (2019); Dai & Li (2019)). However, none of these publications have verified whether the modelling approach in 2D is able to capture the behaviour simulated in a 3D problem.

In this section, the response of the wall problem described in Section 6.2.1 (i.e. based on the Wood & Perrin (1984b) geometry and ground profile – see Chapter 3 for details) is simulated using two different modelling approaches in 2D plane-strain analysis. The two approaches consist of simulating the heat exchange by either prescribing a constant temperature along a line or following the modelling approach developed in Chapter 5 to approximate the thermal performance using 2D plane-strain analyses. Thus, the latter methodology includes one-dimensional pipe elements to simulate the heat transfer and a series of corrections are applied to properly model the heat exchange in plane-strain analyses. The results obtained by these analyses are compared to those obtained by the 3D analysis outlined in Section 6.2.1. Since the effect of the boundary condition is to be taken into account and was shown previously to affect the mechanical response of the wall, the modelling approach adopted in Chapter 3, i.e. changing the temperature of all elements of the wall simultaneously, was not considered in this study.

6.3.1 Numerical analysis

The wall geometry, initial ground conditions, material properties, the mechanical and hydraulic boundary conditions and construction sequence are detailed in Section 3.2 for the 2D analyses. Herein, only the details of the thermal modelling for the different 2D analyses are provided. All the details for the 3D analyses are reported in Section 6.2.

Two different analyses in plane strain were performed to evaluate the capabilities of different modelling approaches to replicate the behaviour of thermo-active walls modelled in 3D:

(1) Analysis labelled “LINE”: the heat exchange is simulated by applying a change in temperature of 15°C (i.e. equal to the temperature applied in the 3D analysis at the pipe inlet, $\Delta T_{in,3D}$) along a line at 0.1 m from the concrete edge (i.e. where the pipes are located in the 3D analysis) and this is kept constant for 6 months;
(2) Analysis labelled “PIPE”: this is performed by including a pipe element in the 2D analysis, which are characterised by the same material properties as those employed in the 3D problem (see Table 6-1). The thermal loading is applied adopting the 3D to 2D approximation procedures to match the long-term heat flux outlined in Chapter 5, where the input parameters in 2D are those employed for the reference case outlined in Section 5.2.3.2 (i.e. the 2D inlet temperatures for the NF and CT analyses were respectively 28.0°C and 22.7°C, as calculated through Equation (5-7), and the area of the pipe was changed according to Equation (5-6) to achieve the same water flow velocity as in the 3D analysis).

6.3.2 Results

Temperatures

The evolution of temperatures within the retained side at mid-depth of the wall are displayed in Figure 6-42 for different distances from the wall and for the two boundary conditions along the exposed face.

For the NF case, similar temperatures are computed for both 2D analyses, because the temperature applied in the LINE analysis is the same as that prescribed at the pipe inlet for the PIPE analysis. Furthermore, as shown in Chapter 4 and Chapter 5, the thermal performance of the NF case is quite low, hence this indicates that the temperature differential between the pipe inlet and outlet is not large. It can therefore be assumed that the temperatures along the pipes vary within a very limited range and are similar to the inlet temperature. Thus, it is not surprising that the temperatures within the soil are similar for both cases. As was shown in Chapter 5, these are larger than those computed in the 3D analysis, even at considerable distances from the wall.

Conversely, for the CT case, different temperatures are evaluated for the 2D analyses simulated applying a thermal boundary condition or employing the pipe elements. This is due to the reduced inlet temperature at the pipe inlet (22.7°C) resulting from the conversion procedure outlined in Section 5.2.3.2. As was shown in Chapter 5, the temperature obtained by the PIPE analysis compares very well to that computed in 3D at larger distances from the wall, whereas a larger discrepancy is evaluated at the soil-wall interface. Conversely, the LINE analysis, as expected, overestimates the temperature changes at all distances (e.g. at 2.5 m, a difference of 4.3°C is evaluated).

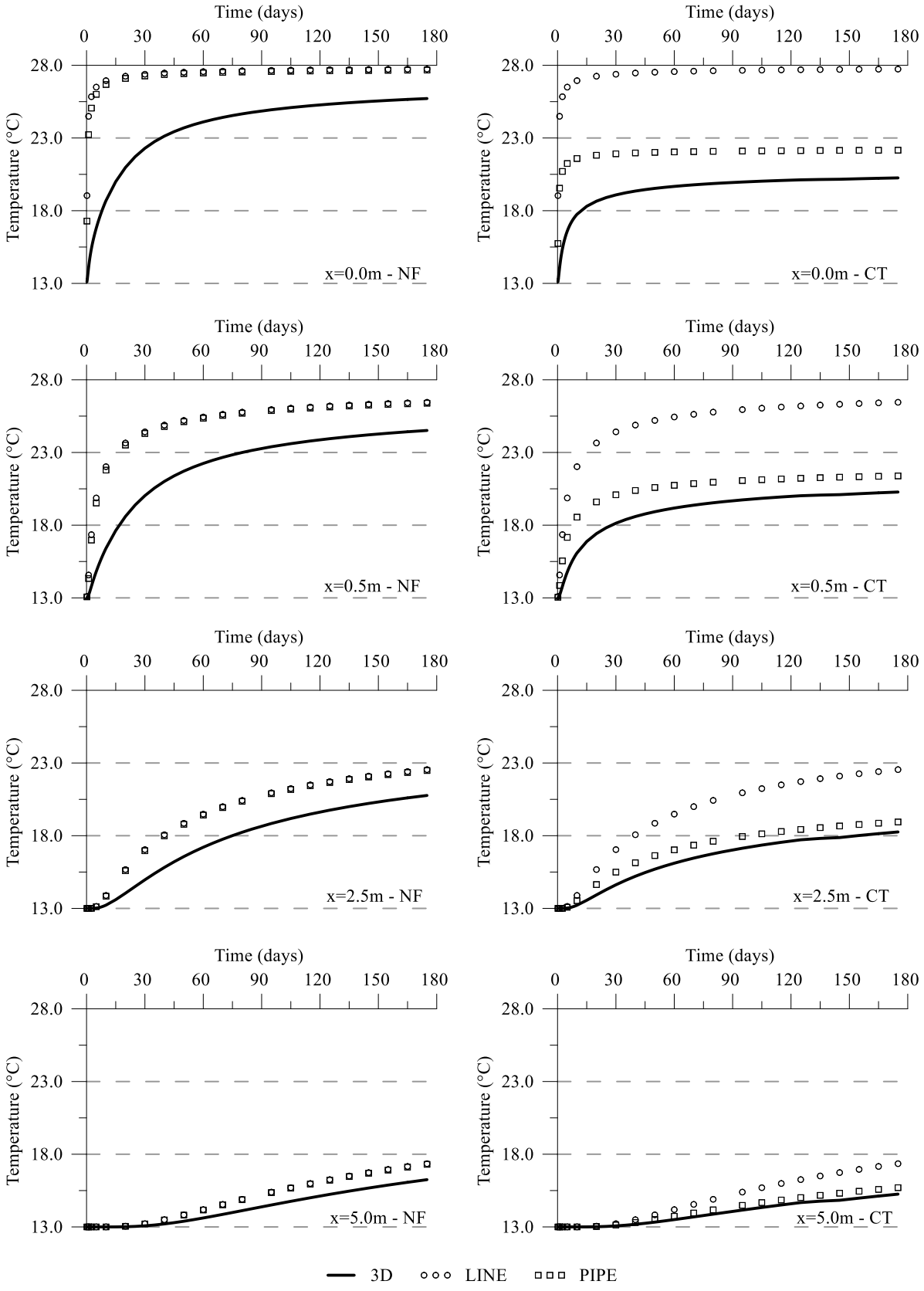

Figure 6-42: Comparison between 3D and 2D analyses with different modelling approaches – Temperature with time at different distances from the edge of the wall on the retained side and for different boundary conditions

Axial force

The distributions of changes in axial force with depth for all the analyses are displayed in Figure 6-43, where Figure 6-43 (a) depicts the forces for the wall simulated with a NF boundary condition along the exposed face and Figure 6-43 (b) with a CT boundary condition. Figure 6-44 (a) and (b) show the development with time of the axial force at depth of 14.0 m for NF and CT cases, respectively. Note that, for the 3D analysis, the average axial force for the entire section is shown.

Since the 2D analyses simulate larger temperatures within the wall in the short term, a larger initial compressive axial force is computed. This is largest for the LINE analysis for both boundary conditions, since the thermal loading is slightly slower for the PIPE analyses and hence a more transient behaviour is simulated in terms of temperature changes within the wall. Smaller differences between the two 2D analyses are observed for the NF case when compared to the CT case, due to the previously mentioned differences in inlet temperature for the PIPE analysis for the CT case. The 2D LINE analyses overestimate the peak in compressive axial force by 45 kN/m for both CT and NF conditions, thus computing a force which is three times larger than the one obtained in 3D. A similar value is obtained for the PIPE analysis with an NF boundary condition, while for the CT case, a smaller difference, of 15.5 kN/m (89%) is computed. It should also be noted that the peak does not occur at the same time instant as in the 3D analysis, but slightly earlier, due to the faster heat transfer in 2D.

In the medium term (10-90 days) the 2D analyses replicate the 3D behaviour reasonably well. However, at the end of the simulation period (6 months) the 2D analyses underestimate the tensile forces within the wall for both cases. As can be seen from Figure 6-44, the 2D analyses simulate a compressive action towards the end of the analysis, attributed to the dissipation of compressive excess pore water pressures (refer to Section 3.5 for details). This is because in the 2D analyses thermal steady state is reached earlier when compared to the 3D case. This is confirmed when observing Figure 6-42, which show that little change in temperature occurs at the wall-soil interface after 30 days, while the temperatures are still increasing for the 3D analyses. This implies a different transient soil behaviour in terms of development of excess pore water pressures. This behaviour is accelerated for the PIPE analysis with a CT boundary condition, because lower excess pore water pressures develop at lower temperatures, hence the dissipation occurs at a faster pace.

For the NF case, the tensile actions within the wall are underestimated by 19.0 kN/m (20%) and 14.5 kN/m (15%) for the LINE and PIPE analyses, respectively. For the CT case, the differences are 9.0 kN/m (10%) and 32.0 kN/m (35%) for the LINE and PIPE analyses, respectively.

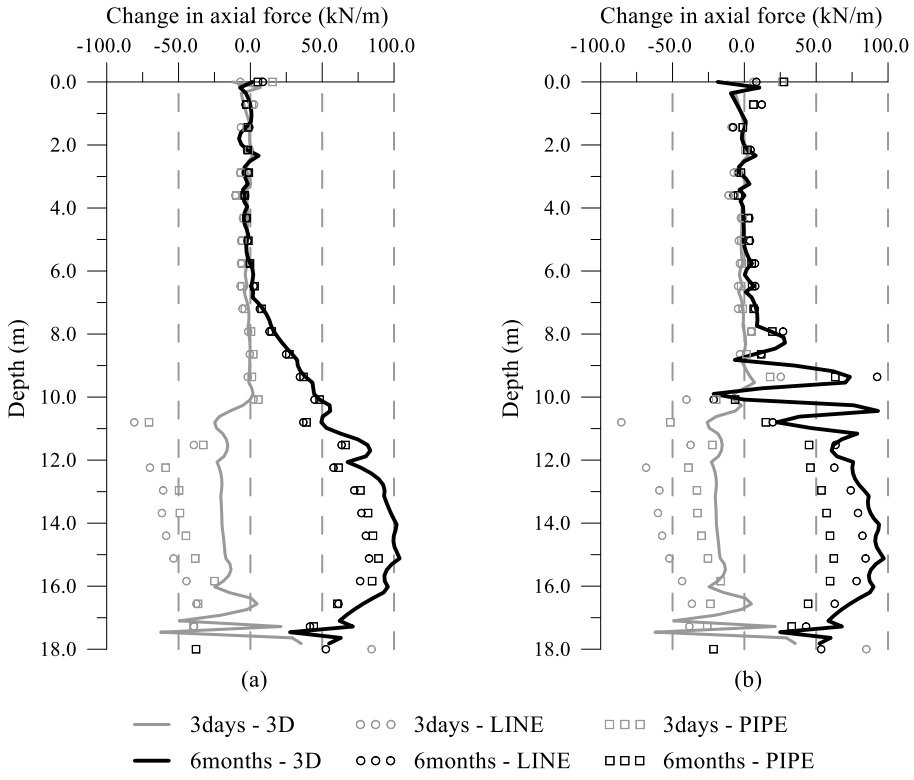

Figure 6-43: Comparison between 3D and 2D analyses with different modelling approaches – Axial force with depth for different time instants (a) NF and (b) CT

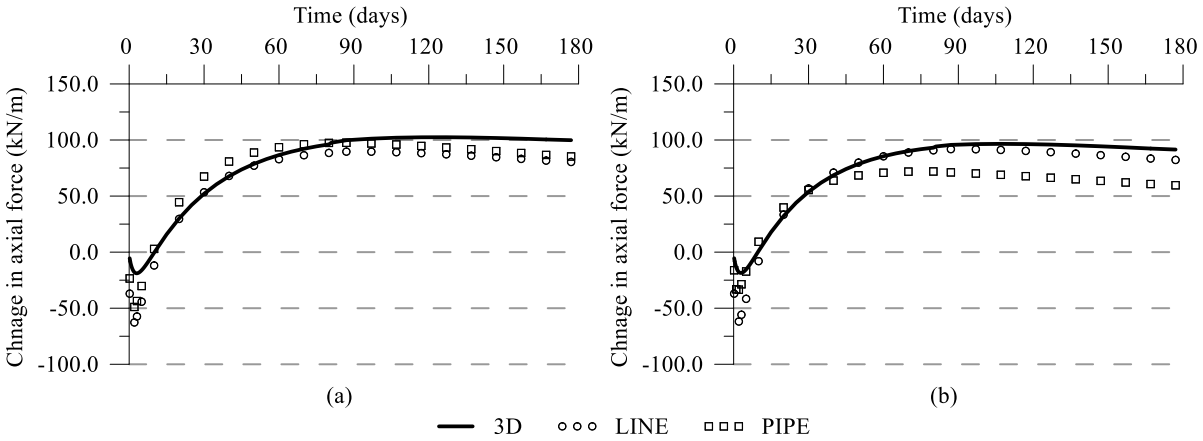

Figure 6-44: Comparison between 3D and 2D analyses with different modelling approaches – Axial force with time at depth of 14.0m (a) NF and (b) CT

Bending moment

The development of the bending moment with depth is displayed in Figure 6-45 (a) and (b) for the NF and CT cases, respectively. The change of bending moment with time at depth of 6.5 m is shown in Figure 6-46.

In the short term, the 2D analyses display a large immediate increase in bending moment which highly overestimates the bending moment calculated in 3D. The difference reaches values of 275.0 kNm/m for all LINE analyses and the PIPE analysis with an NF boundary condition (i.e. approximately 7 times

larger than the one computed in 3D). A smaller difference, of 145.0 kNm/m (which is 2.5 times the one computed in 3D), is obtained for the PIPE analysis with a CT boundary condition due to the lower inlet temperature). This is due to the large temperatures imposed in these analyses, which do not reflect the actual temperatures developing in the 3D analyses.

In the long term, the NF cases display a similar behaviour to the one obtained in 3D. Since the temperature distribution within the wall in 3D becomes uniform with time, the bending moment calculated in 2D is similar to that computed in 3D. Conversely, for the CT cases, larger bending moments are computed in the 2D analyses (difference of 160 kNm/m (94%) and 40 kNm/m (22%) for the LINE and PIPE analyses, respectively), because of the larger temperatures within the wall and hence the larger temperature gradient across the wall's thickness. Clearly, this is less pronounced for the PIPE analysis, given the lower temperature applied in this analysis. Furthermore, the transient behaviour of the 2D analyses is different from that observed in 3D: for the former, the bending moment remains approximately constant, because the temperatures hardly change with time; in the latter, the wall portions between the pipes heat up and lead to a gradual increase in bending moment.

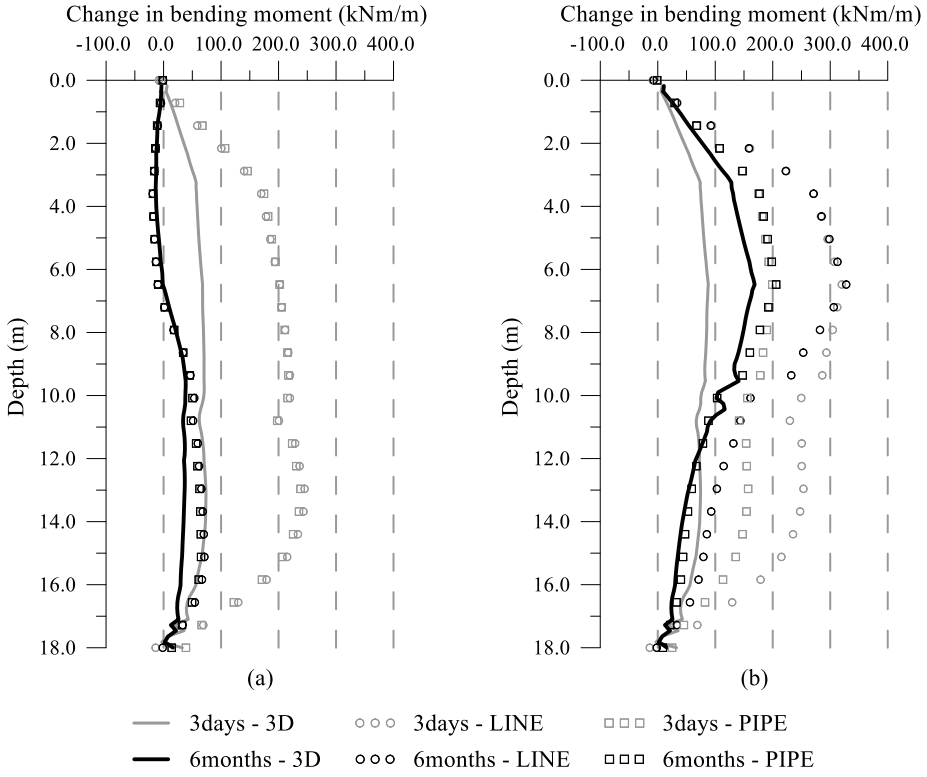

Figure 6-45: Comparison between 3D and 2D analyses with different modelling approaches – Bending moment with depth for different time instants (a) NF and (b) CT

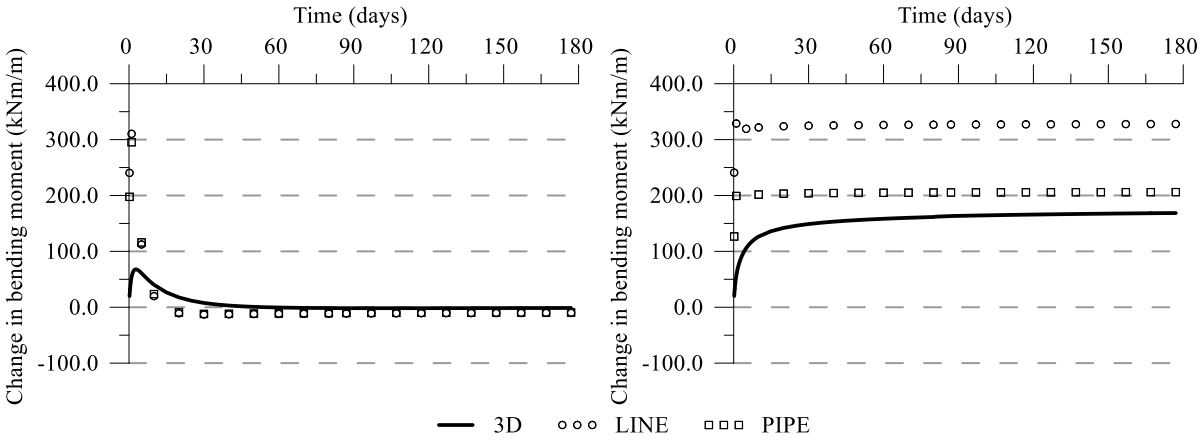

Figure 6-46: Comparison between 3D and 2D analyses with different modelling approaches – Bending moment with time at depth of 6.5m (a) NF and (b) CT

Vertical wall displacement

The evolutions of the vertical displacement of the top of the wall with time are shown in Figure 6-47. Similar to what was observed for temperatures and forces, larger displacements are computed for the 2D analyses, with these being largest for the LINE analyses, due to the larger temperatures applied. When compared to the 3D analysis, the long-term displacement is overestimated by 1.9 mm (45%) for the NF case and by 2.4 mm (76%) for the CT case. The PIPE analysis in the CT case matches the long-term displacement observed in the 3D analysis quite well, while for the NF case a similar difference to the LINE analysis, of 1.5 mm (37%), is computed.

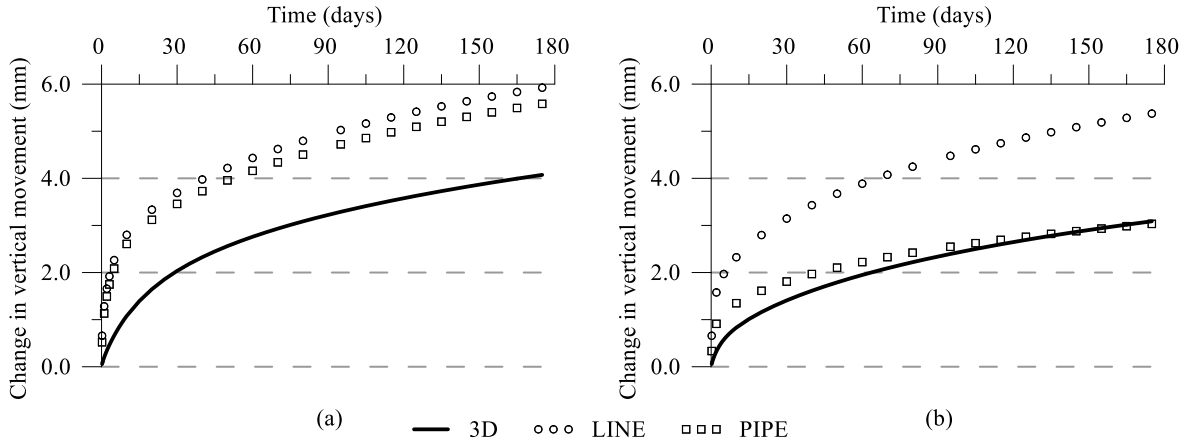

Figure 6-47: Comparison between 3D and 2D analyses with different modelling approaches – Vertical displacement of top of the wall with time (a) NF and (b) CT

6.4 A new method for modelling thermo-active retaining walls in two dimensions

The analyses shown in the previous section demonstrate that a new methodology is necessary to be able to capture the 3D thermo-mechanical behaviour of thermo-active walls and the effect of the boundary condition on the exposed face. In this section, a new approach to model thermo-active walls in two-dimensional plane-strain analyses is presented, which aims at reproducing the average transient behaviour of thermo-active walls per metre width of wall panel. The key objective is to model this type of structure without the inclusion of elements simulating pipes as these require advanced numerical methods (Cui et al., 2018c). Instead, the problem should be solved by performing relatively simple analyses which require solely the application of thermal boundary conditions. Furthermore, in order to evaluate the observed out-of-plane effects on the distribution of forces (see Section 6.2.1.3), an analytical procedure is developed and outlined in the last part of this section.

6.4.1 Method to simulate the average wall behaviour

6.4.1.1 Method description

The assumptions of the method are the following:

(1) the pipes in the 3D problem are installed vertically and form U-shaped loops within the panel (as is common practice, see e.g. Amis et al. (2010)), where the presence of the horizontal pipe segment connecting the vertical pipes is neglected, since limited change in temperature occurs within this portion of pipe;
(2) the temperature differential between pipe inlet and outlet within a U-loop, ΔT_p, should be characteristic of the heat extraction/injection rates reported for thermo-active walls in literature (i.e. 10 to 30 W/m^2, see Brandl (2006), Angelotti & Sterpi (2018) and Sterpi et al. (2020), values which are consistent to those evaluated in Chapter 4 and Chapter 5);
(3) a linear variation in temperature between the inlet and outlet is considered, similar to other thermo-active structures (Loveridge et al., 2013).

The proposed method is schematically represented in Figure 6-48 and consists of determining an equivalent temperature, $T_{i,2D}$, to be applied as a time-dependent boundary condition in a 2D coupled THM plane-strain analysis along the corresponding position of the pipes in the original geometry (i.e. along line C-D in Figure 6-48 (c)). $T_{i,2D}$ is evaluated as the average temperature across the width of the panel (B) (y-direction in Figure 6-48) where the pipes are located (i.e. along line A-B in Figure 6-48 (a) and (b)) and takes into account the different temperature distributions above and below the excavation level using a weighted average:

$$T_{i,2D} = \frac{L_{exp}}{L}\,\bar{T}_{i,exp} + \frac{L_{emb}}{L}\,\bar{T}_{i,emb} \tag{6-1}$$

where L_{exp} and L_{emb} are the exposed and embedded lengths of the wall (m), respectively, L is the total length of the wall (m) and $\bar{T}_{i,exp}$ and $\bar{T}_{i,emb}$ are the average temperatures at time instant $t = t_i$ across the width of the panel (B) where the pipes are located (i.e. along line A-B in Figure 6-48 (a) and (b)) for the exposed and embedded sections of the wall, respectively.

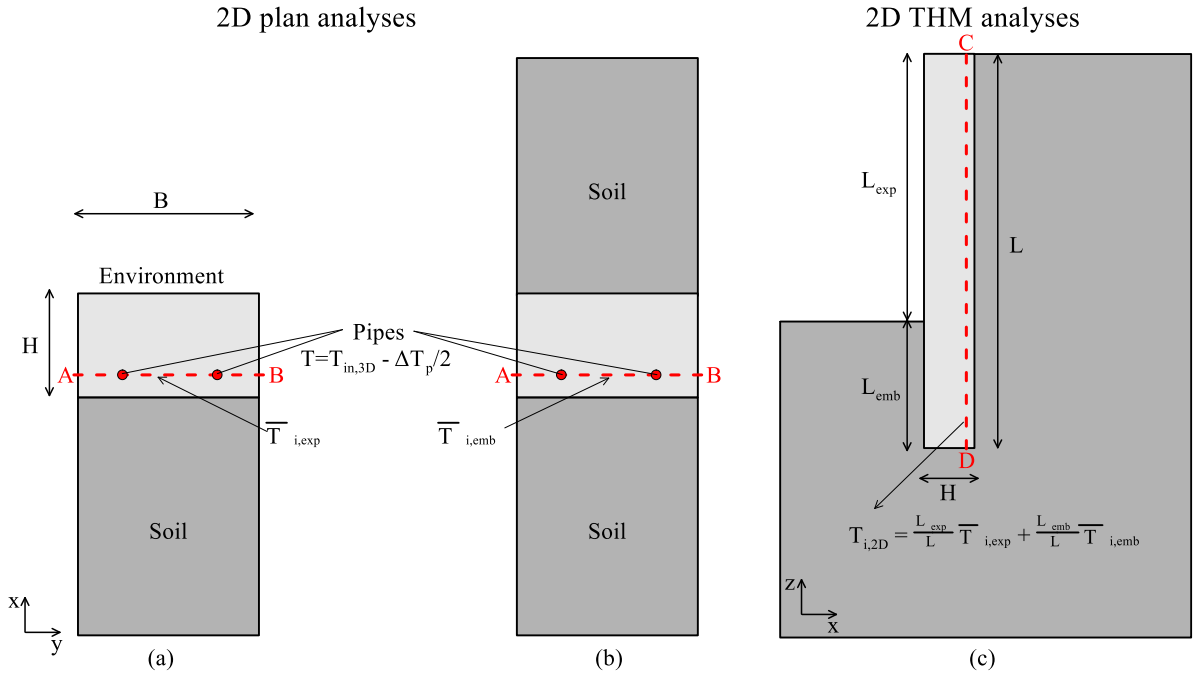

Figure 6-48: Schematic representation of the proposed method (a) 2D plan analysis for exposed section, (b) 2D plan analysis for embedded section and (c) 2D THM analysis simulated with temperature boundary condition

The average temperatures $\bar{T}_{i,exp}$ and $\bar{T}_{i,emb}$ are computed by performing simple two-dimensional plane-strain analyses of the wall problem in plan view, designated hereafter as "2D plan analysis". It is important to note that these analyses are thermal-only (i.e. the simulation of the HM response of soil, and its coupling with the thermal behaviour, is not required). As depicted in Figure 6-48 (a), for the exposed section, the problem consists of a wall panel with soil only on one side, while along the face of the wall a boundary condition is prescribed that best represents the conditions within the underground space. For the embedded section (Figure 6-48 (b)), the wall panel is surrounded by soil on both sides.

The 2D plan analyses are performed by applying a constant temperature boundary condition at the nodes corresponding to the positions of the pipes in the real problem (which are vertical according to assumption (1)). As per assumption (2) and (3), the average value of the temperature at these points can be estimated as $T_{in,3D} - \Delta T_p/2$ (see Figure 6-48 (a) and (b)), where $T_{in,3D}$ is the design inlet temperature. Clearly, in a real problem involving cooling operation mode (i.e. hotter-than-the-ground fluid is circulated through the ground circuit), the two pipe branches would register different

temperatures, with the pipe where the fluid is circulating downwards being hotter than the pipe where the fluid is circulating upwards, with the opposite being true for heating operation modes. Moreover, the temperature at the pipes would also vary with depth. However, as a simplification, which, in comparison with the other assumptions of the method, is expected to have only minor consequences to its accuracy, the same temperature, equal to the average temperature along the pipes, is applied to the nodes representing the pipes. The 2D plan analyses, for the excavated and embedded sections of the wall, are carried out for the required simulation time and, for each step of the analysis, $\bar{T}_{i,exp}$ and $\bar{T}_{i,emb}$ are evaluated. Equation (6-1) is then employed to calculate the temperature to be applied in the 2D plane-strain analysis of the wall to be analysed (Figure 6-48 (c)).

The following observations regarding the proposed method should be considered:

- The temperature applied in the 2D plane-strain analysis, $T_{i,2D}$, is constant with depth. This assumption is considered to negligibly affect the results since the variation in temperature across the length of the pipe in a 3D problem is limited;
- If the characteristics of the environment in front of the wall are not known, it is suggested that the temperatures are evaluated in 2D plan analyses for the two extreme scenarios, i.e. an insulated wall (i.e. no heat flux (NF) occurs across the wall-air interface) and a wall face maintained at constant temperature (CT), equal to the initial temperature. Hence, two different 2D plan analyses for the exposed part are to be carried out to evaluate $T_{i,2D}$ for the different boundary conditions along the exposed face of the wall and two separate THM analyses should be performed to evaluate the impact of these boundary conditions on the mechanical behaviour of the wall;
- The mesh refinement in proximity of the pipes in the 2D plan analysis needs to be sufficiently fine to avoid mesh effects (see Appendix D) and the boundaries should be far enough to avoid boundary effects on the temperature distribution;
- The adopted methodology is sufficiently general to be extended to problems involving walls embedded in layered soils (hence for cases with a variation in the thermal parameters of the soil in the vertical direction). For such scenarios, additional 2D plan analyses can be performed and weighting factors can be applied to take into account the thickness of the soil layer when evaluating $T_{i,2D}$;
- While the TEM is not included in the analyses, and it was shown in Appendix F to have little influence in the response of a wall simulated in 2D plane strain, its presence can be taken into account when performing the 2D plan analyses, by setting the elements next to the pipes to have the properties of the TEM. This will result in different temperature distributions used to evaluate $T_{i,2D}$ and hence its effect is intrinsically accounted for even without adding the TEM in the 2D plane-strain analyses in cross-section.

6.4.1.2 Validation of the method for a reference case

The proposed method is validated herein by comparing the results obtained by the 3D analyses listed in Table 6-2 to those obtained by 2D analyses simulated with the proposed method. First, a detailed assessment of the method is reported for Analyses A1 and A2 (i.e. 16.0 m deep excavation, wall panel 2.0 m in width, with respectively NF and CT boundary conditions along the exposed face of the wall. Subsequently, key quantities for all the analysed cases are evaluated. A further case is analysed in Appendix G, consisting of a whole year of operation (with 6 months of heat injection followed by 6 months of heat extraction)

Modelling procedure for 2D analysis

2D plan analysis

The 2D plan analyses were performed with a 2D mesh consisting of 8-noded quadrilateral elements, with the same mesh discretisation in the x-y plane of the 3D analysis (see Figure 6-18) being adopted. Since 2D plan analyses are solely required to evaluate temperatures (hence the mechanical behaviour is not considered), the elements include only displacements and temperature degrees of freedom at all nodes (while only temperatures are evaluated, displacement degrees of freedom cannot be deactivated in ICFEP). The initial temperature of all the elements was 15°C. The temperature differential between the pipe inlet and outlet, ΔT_p, was assumed to be 1.0°C, as this is considered to be an average temperature change per U-loop over the period of six months, corresponding to a heat flux of approximately 20 W/m^2 according to Equation (4-5) (it should be noted that this temperature difference does not necessarily represent the temperature difference at the heat pump, since more than one U-loop is typically connected to a heat pump). Thus, a constant temperature of 29.5°C (given that $T_{in,3D}$=30°C) was imposed at the nodes corresponding to the position of the pipes in the 3D analysis. Clearly, the value of ΔT_p across the pipes and hence of the temperature applied in the 2D plan analysis, depends on a variety of factors. However, as demonstrated subsequently in the last part of this section, the impact of the choice of this parameter on the response of the analysed thermo-active wall is limited, provided that a reasonable assumption is made. Three separate analyses were carried out, i.e. one for the embedded section and two for the exposed section with either a NF or a CT boundary condition. These analyses were run for 6 months with the same time discretisation employed in the thermal phase of the 3D analysis and, for each step of the analysis, the average temperatures $\overline{T}_{i,exp}$ and $\overline{T}_{i,emb}$ were evaluated and the weighted average $T_{i,2D}$ was calculated for the two cases, as shown in Figure 6-49. As expected, the NF analysis is characterised by substantially larger average temperatures.

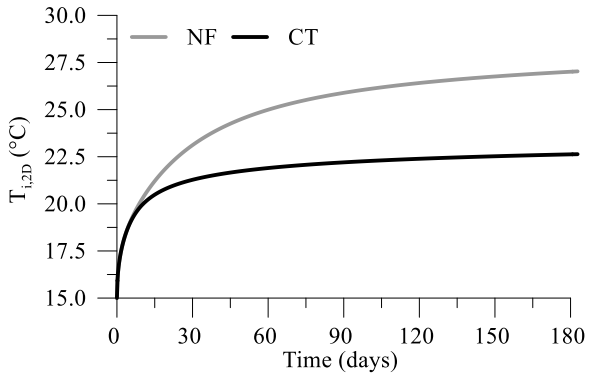

Figure 6-49: Temperature values for boundary condition in 2D plane-strain THM analysis with NF and CT boundary condition

2D plane-strain analysis

The finite element mesh employed for the 2D plane-strain THM analysis consists of 8-noded quadrilateral elements, with displacement and temperature degrees of freedom at each node and pore water pressure degrees of freedom associated to the corner nodes of the elements discretising the soil. The mesh refinement in the z-direction is equal to that of the 3D mesh (Figure 6-18), while in the x-direction, the refinement of the 3D mesh within the plane containing the pipe elements (i.e. y=0.5 m) was adopted.

The initial conditions (i.e. pore water pressure profile, K_0 and temperature) as well as the mechanical and hydraulic boundary conditions were the same as in the 3D analysis (see Section 6.2.2.1). Similarly, the same construction sequence was modelled for the stages prior to the application of changes in temperature.

The heat exchange was simulated by applying a prescribed temperature boundary condition along a vertical line located at 0.1 m from the concrete edge on the retained side, i.e. where the pipes are located in the 3D model. The values of temperature applied, $T_{i,2D}$, vary with time and boundary condition along the exposed face, as shown in Figure 6-49.

Comparison between 3D and 2D analyses

The results obtained by the 3D and 2D analyses of the problem described above are presented for the two extreme boundary conditions along the exposed face. The average soil and wall behaviour are analysed in terms of temperatures, heat flux, excess pore water pressures, structural forces and movements.

Temperatures and heat flux

Figure 6-50 shows the change in temperature with time computed at mid-depth of the wall (i.e. 10.0 m below ground surface) and at three different distances from the wall on the retained side, i.e. at the soil-wall interface (0.0 m), 1.0 m and 4.0 m from the edge of the wall.

The 2D analysis predicts a slightly lower temperature than the 3D analysis for the NF case (Figure 6-50 (a)), with a maximum difference of 0.5°C at the soil-wall interface. However, the difference in temperature reduces with the distance from the wall: at a distance of 4.0 m, the difference between 3D and 2D reduces to 0.1°C. Conversely, the 2D analysis slightly overpredicts the change in temperature for the CT case ((Figure 6-50 (b)), with a maximum difference of 0.7°C at the soil-wall interface, while at larger distances negligible differences are observed. In general, it can be said that the proposed simplified 2D method is capable of reproducing the temperature field accurately, particularly when the considerable approximations in terms of modelling heat sources are taken into account.

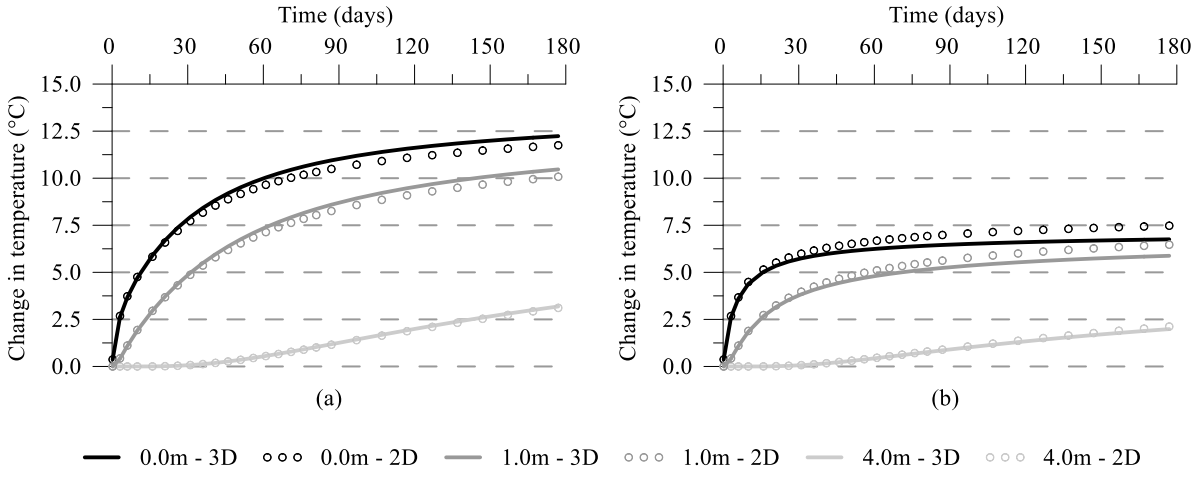

Figure 6-50: Comparison between 3D and 2D analyses with new approach – temperature change with time at different locations at mid-depth of wall within the retained side (a) NF analysis and (b) CT analysis

The comparison between the calculated heat flux with time in 3D and 2D for both boundary conditions is plotted in Figure 6-51. For the 3D analyses, this is computed employing Equation (4-5) with the recorded outlet temperature. Since in 2D no pipe elements are employed, the heat flux is computed as follows: the heat flux rates across the edges (i.e. the energy crossing a given line per second in a plane-strain analysis, kJ/(sm)) of the elements either side of where the prescribed temperature boundary condition is applied are recorded. These are then integrated along the length of the wall, summed, and normalised by the length of the wall, resulting in a heat flux per unit area of wall. It should be noted that this procedure neglects the energy required to heat up the elements between the two lines where the heat flux rates are recorded. However, it is considered that this negligibly affects the results since the elements have a very small thickness. The results match the heat flux computed in 3D very well, apart from the beginning of the analysis, where the heat flux is underestimated by the 2D analysis. This may be due to the aforementioned simplification. The difference at the end of operation is equal to 0.5 W/m^2 and 0.8 W/m^2 for the NF and CT cases, respectively. This suggests that the proposed method can also be employed to estimate the long-term thermal performance of thermo-active walls.

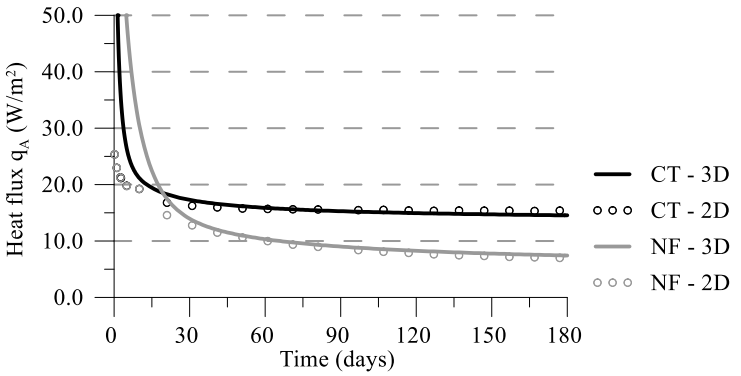

Figure 6-51: Comparison between 3D and 2D analyses with new approach –heat flux with time

Pore water pressures

Given the good match observed for temperature changes, it is expected that also the changes in pore water pressures are similar in 3D and 2D. This is confirmed when observing Figure 6-52, which compares the evolution with time of excess pore water pressures computed at mid-depth of the wall at different distances from the wall on the retained side. Indeed, the changes in pore water pressures with time are very similar in 3D and 2D, with the largest differences being computed further away from the wall, where the 2D analysis underestimates the excess pore water pressures by 3.8 kPa and 2.2 kPa for the NF and CT cases, respectively.

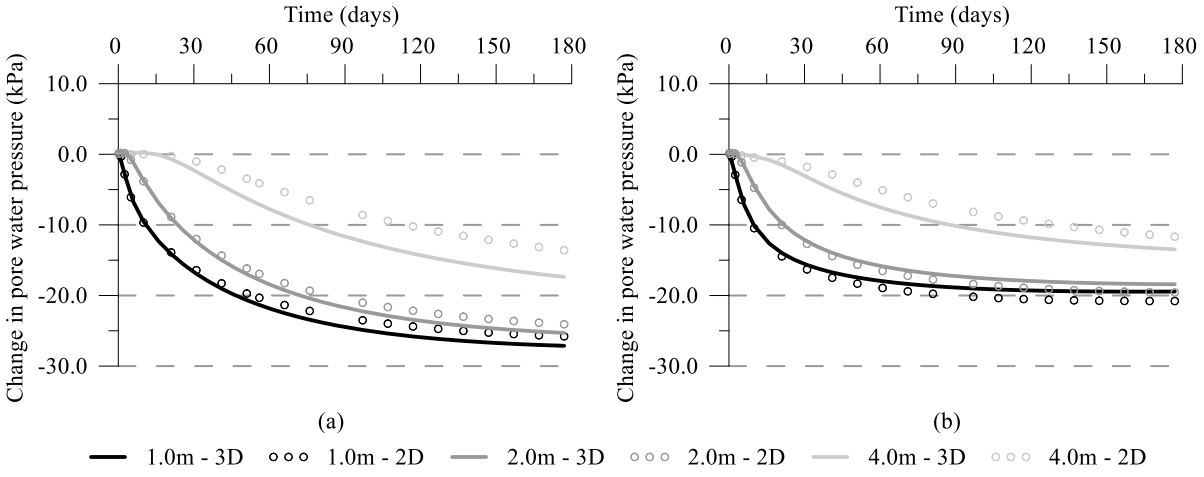

Figure 6-52: Comparison between 3D and 2D analyses with new approach –changes in pore water pressure with time at different locations at mid-depth of wall within the retained side (a) NF analysis and (b) CT analysis

Axial force

The profiles of changes in average axial force per metre width of the wall at two different time instants are shown in Figure 6-53 (a) and (b) for NF and CT cases, respectively. Furthermore, Figure 6-54 shows the change in axial force with time at a depth of 14.0 m (the approximate location of the peak in this quantity throughout the analysis).

The change in axial forces resulting from the 2D analyses compare very well with those computed by the 3D model, both in terms of variations with depth and time. The initial compression is very well

simulated in the 2D analyses, where the difference in the peak, occurring approximately after 1 day of operation, is of less than 1.0 kN/m for both boundary conditions. Similar levels of agreement are computed in the long term, with the differences in tensile changes in axial force between the 2D analyses and the 3D response being limited to ±1.5 kN/m. It should be noted that the thermally-induced changes in axial forces are quite small, as expected given the short embedment depth of the wall, which leads to a limited restraint of the soil against the thermal expansion of the wall.

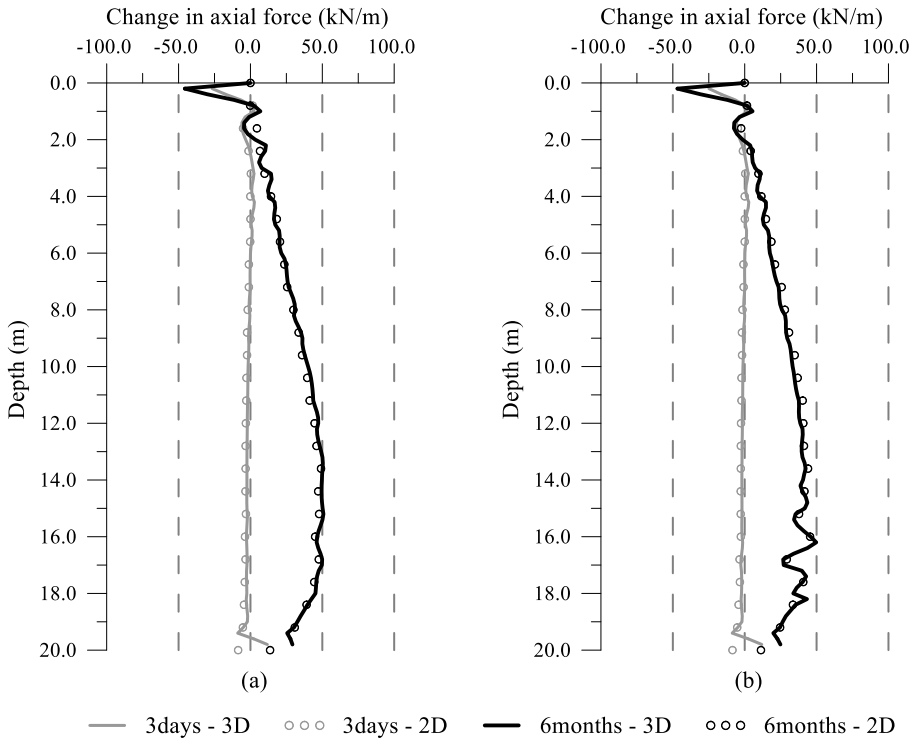

Figure 6-53: Comparison between 3D and 2D analyses with new approach – change in axial force with depth (a) NF and (b) CT

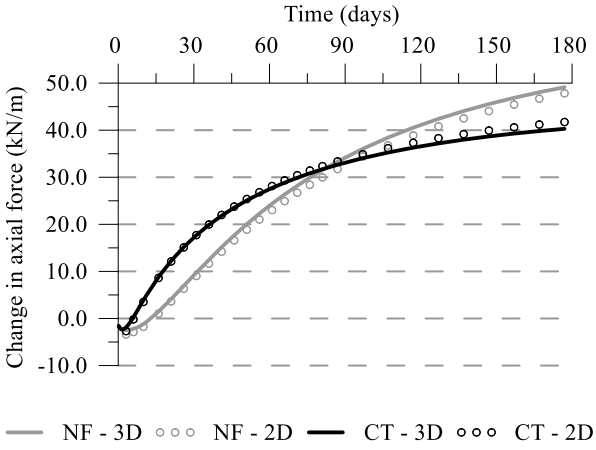

Figure 6-54: Comparison between 3D and 2D analyses with new approach – change in axial force with time at a depth of 14.0m

Bending moment

The development of the average bending moment per unit width with depth after 3 days and 6 months from the beginning of operation is shown in Figure 6-55 (a) and (b) for the NF and CT cases, respectively. Furthermore, Figure 6-56 depicts the change in bending moment with time at a depth of 8.0 m. It can be observed that the average bending moment with depth and its development with time compare well. In the short term, negligible differences are computed; in the long term, for the CT case, the 2D analysis overestimates the bending moment within the exposed part of the wall by a maximum of 30 kNm/m (9%), while, for the NF case, the largest difference occurs at the position of the base slab, where the 2D analysis predicts a slightly larger negative change in bending moment.

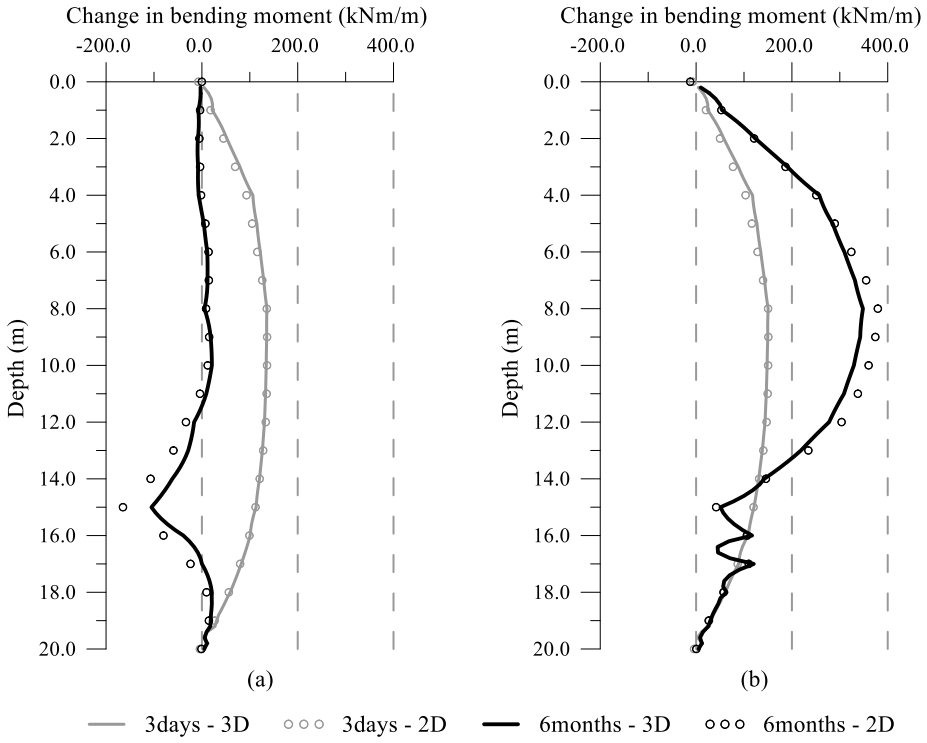

Figure 6-55: Comparison between 3D and 2D analyses with new approach – change in bending moment with depth (a) NF and (b) CT

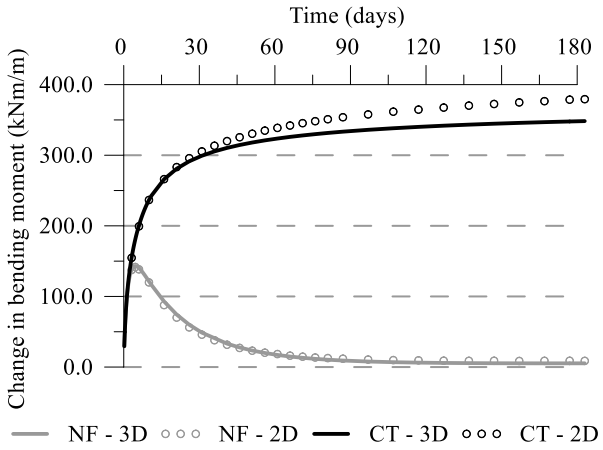

Figure 6-56: Comparison between 3D and 2D analyses with new approach – change in bending moment with time at a depth of 8.0m

Vertical wall movements

Figure 6-57 shows the development of the change in vertical displacement measured at the top of the wall with time for both boundary conditions. The displacement, which is due to the thermal expansion of concrete and soil upon changes in temperature, is largest for the NF analysis, where the computed temperature changes are larger (see Figure 6-49 and Figure 6-50). The 2D analyses are able to capture both magnitude and changes with time to a high degree of accuracy, with differences of less than 0.5 mm (9%).

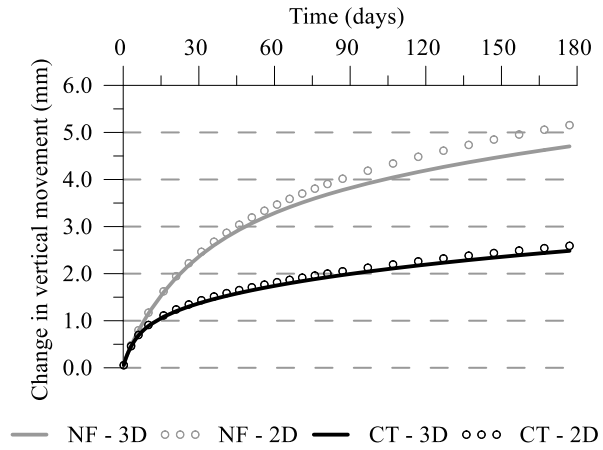

Figure 6-57: Comparison between 3D and 2D analyses with new approach – change in vertical movement of top of wall with time

Effect of the choice of ΔT_p

The proposed simplified modelling approach to model thermo-active retaining walls in 2D plane-strain analyses requires the assumption of a variation of temperature, ΔT_p (equal to the temperature differential between the temperature at the pipe inlet (T_{in}) and outlet (T_{out})), along the pipe loop installed within the retaining wall. This parameter determines the estimated heat flux, q_A (W/m^2), according to Equation (4-5), which, rearranged, yields:

$$\Delta T_p = \frac{q_A \cdot A_{wall}}{C_{v,w} Q_w} \tag{6-2}$$

As shown in Chapter 4 and Chapter 5, the heat flux, q_A, varies with time and depends on a large number of factors, including, but not limited to, the embedment depth, the thermal parameters of soil and concrete, and the boundary condition along the exposed face of the wall, with values ranging between 10 and 30 W/m^2 reported in the literature. For analyses A described in Section 6.2.2, the values to be used in Equation (6-2) are: A_{wall}= 40 m^2, $C_{v,w}$= 4180 kJ/m^{3}K and Q_w = 2.05×10^{-4} m^3/s.

In this study, the impact of varying ΔT_p on the mechanical response of the wall is analysed. Two additional scenarios are compared to the one presented in the previous study (i.e. ΔT_p = 1.0°C, hence $q_A \cong$ 20 W/m^2): (1) a $\Delta T_p$of 0.0°C, resulting in a heat flux, q_A, of 0 W/m^2; (2) a ΔT_p of 2.0°C, which translates into a heat flux of approximately 40 W/m^2 according to Equation (6-2). The computed average temperatures resulting from the 2D plan analyses, $T_{i,2D}$, and used as input in the 2D THM analyses are depicted in Figure 6-58. As expected, these are higher when a ΔT of 0.0°C is assumed. It should be noted that case (1), i.e. ΔT_p = 0.0°C ($T_{in} = T_{out}$), is considered an extreme case where the maximum possible temperatures within the pipes are employed as a boundary condition in the 2D analyses. Even though in such case the estimated heat transfer rate according to Equation (6-2) is equal to 0 W/m^2, this does not necessarily imply that no heat transfer occurs within the system, since the problem is simulated by applying a prescribed temperature boundary condition, rather than a heat flux boundary condition. Hence, although in this hypothetical scenario no heat is transferred to the above-ground circuit, changes in temperature occur within the wall and the soil due to the simulated prescribed temperatures.

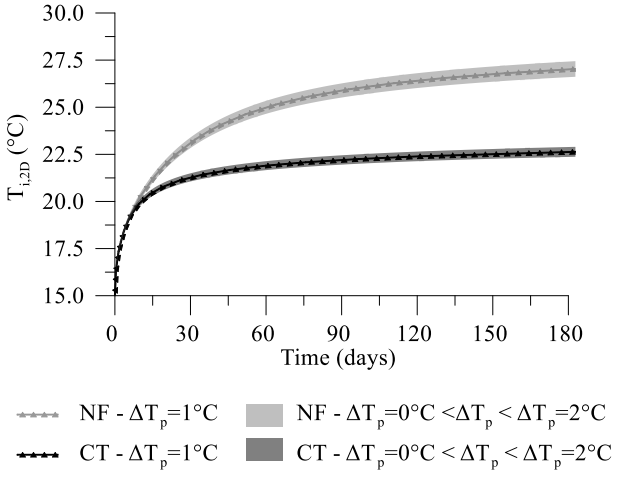

Figure 6-58: Temperature values for boundary condition in 2D plane-strain THM analysis with NF and CT boundary condition

The results in terms of changes in temperature, axial force and bending moment, and vertical displacement of the top of the wall with time are displayed in Figure 6-59, Figure 6-60 and Figure 6-61, respectively.

It can be observed that, in general, the value of ΔT_p assumed to perform the 2D plan analyses has a limited effect on the mechanical response of the wall in 2D and the temperature changes evaluated within the soil. Indeed, all the analysed quantities vary within a range of ±4% of the values computed with a ΔT_p of 1.0°C. Furthermore, it can be noted that the assumed ΔT_p does not affect the time dependent behaviour, since the development with time of forces and displacements is the same (i.e. peaks occurring at the same time instants). Thus, it is considered that, provided that the chosen value of ΔT_p lies within a reasonable range, it does not affect the validity of the proposed methodology. Furthermore, assuming a ΔT_p of 0.0°C provides more conservative results, since larger temperature changes are predicted.

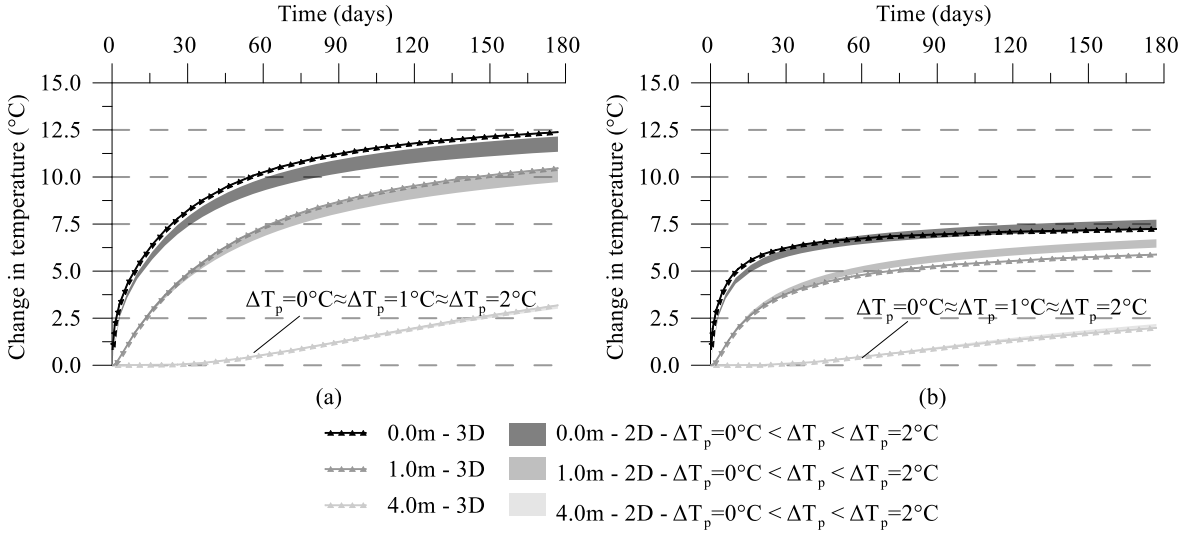

Figure 6-59: Comparison between 3D and 2D analyses with new approach for different ΔT_p at different locations at mid-depth of wall within the retained side (a) NF analysis and (b) CT analysis

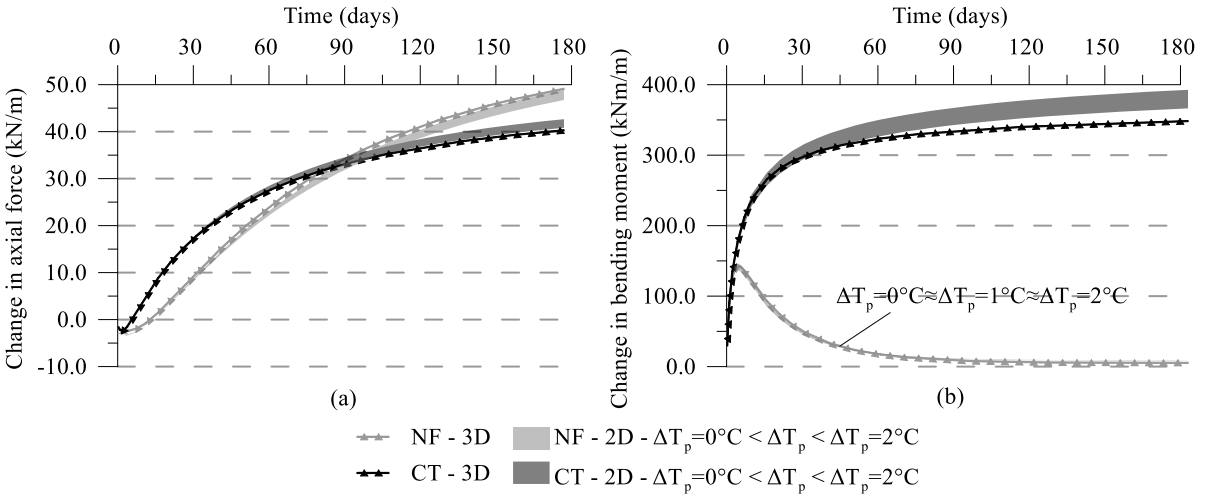

Figure 6-60: Comparison between 3D and 2D analyses with new approach for different ΔT_p (a) change in axial force with time at a depth of 14.0m and (b) change in bending moment with time at a depth of 8.0m

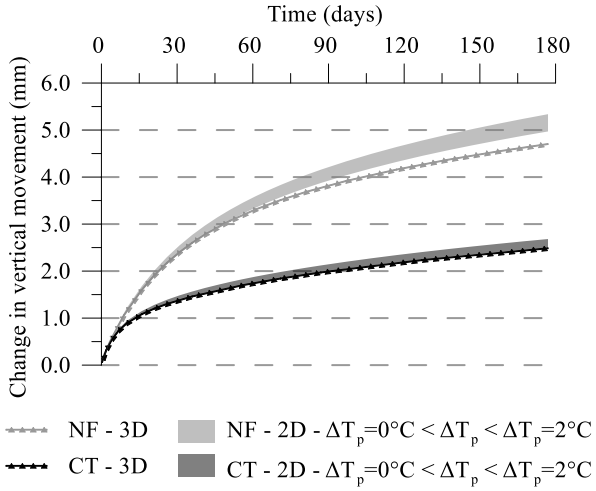

Figure 6-61: Comparison between 3D and 2D analyses with new approach for different ΔT_p – change in vertical movement of top of wall with time

6.4.1.3 Performance of the method

Based on the wall problem described in the previous section, the performance of the proposed method was analysed for additional cases.

To characterise the capabilities of the proposed method, the procedure described in the Section 6.4.1.1 was applied to all the analyses listed in Table 6-2. For all the cases, a ΔT_p of 1.0°C has been assumed when performing the 2D plan analyses.

The behaviour simulated by the 3D analyses listed in Table 6-2 and the respective 2D analyses modelled with the proposed method is compared in terms of a wide range of key quantities for thermo-active walls, such as the maximum changes in compressive and tensile axial force, positive bending moment and vertical displacement at the top of the wall.

The results of all the analyses are displayed in Figure 6-62, where the full and empty symbols relate, respectively, to analyses with an NF and CT boundary conditions along the exposed face of the wall. The thick line indicates a 100% match between the 3D and 2D results, whereas the region bounded by the dashed lines contains results with a deviation of ±10%.

The results predicted by the 2D analyses using the proposed method approximate the behaviour of the 3D analyses to a high degree. Indeed, for all the analysed quantities, the majority of the 2D analyses display values which are within ±10% of the ones computed in the 3D analyses. Furthermore, in those cases where larger differences are observed, the 2D analyses generally overestimate the results given by the 3D analysis, thus ensuring that designing based on the results of the former is conservative. It can also be noted that there is no pattern suggesting that any of the investigated parameters or boundary conditions produces a greater deviation between the 2D and 3D analyses, confirming the applicability of the method to a wide range of cases. In addition to these analyses, a further verification for a whole year of operation (with 6 months of heat injection followed by 6 months of heat extraction) was carried out and is reported in Appendix G. The excellent agreement between the 3D and 2D results provides confidence in the proposed methodology, allowing a more accurate simulation in comparison to other approaches used in literature, which were previously shown to lead to larger discrepancies. Thus, the proposed method enables the analysis of thermo-active retaining walls using 2D plane-strain analyses, which require a reduced computational effort. Furthermore, Liu et al. (2020) adapted the proposed method for the simulation of single thermo-active piles in 2D axi-symmetric analyses, obtaining equally excellent results for different pile diameters and numbers of U-loops installed.

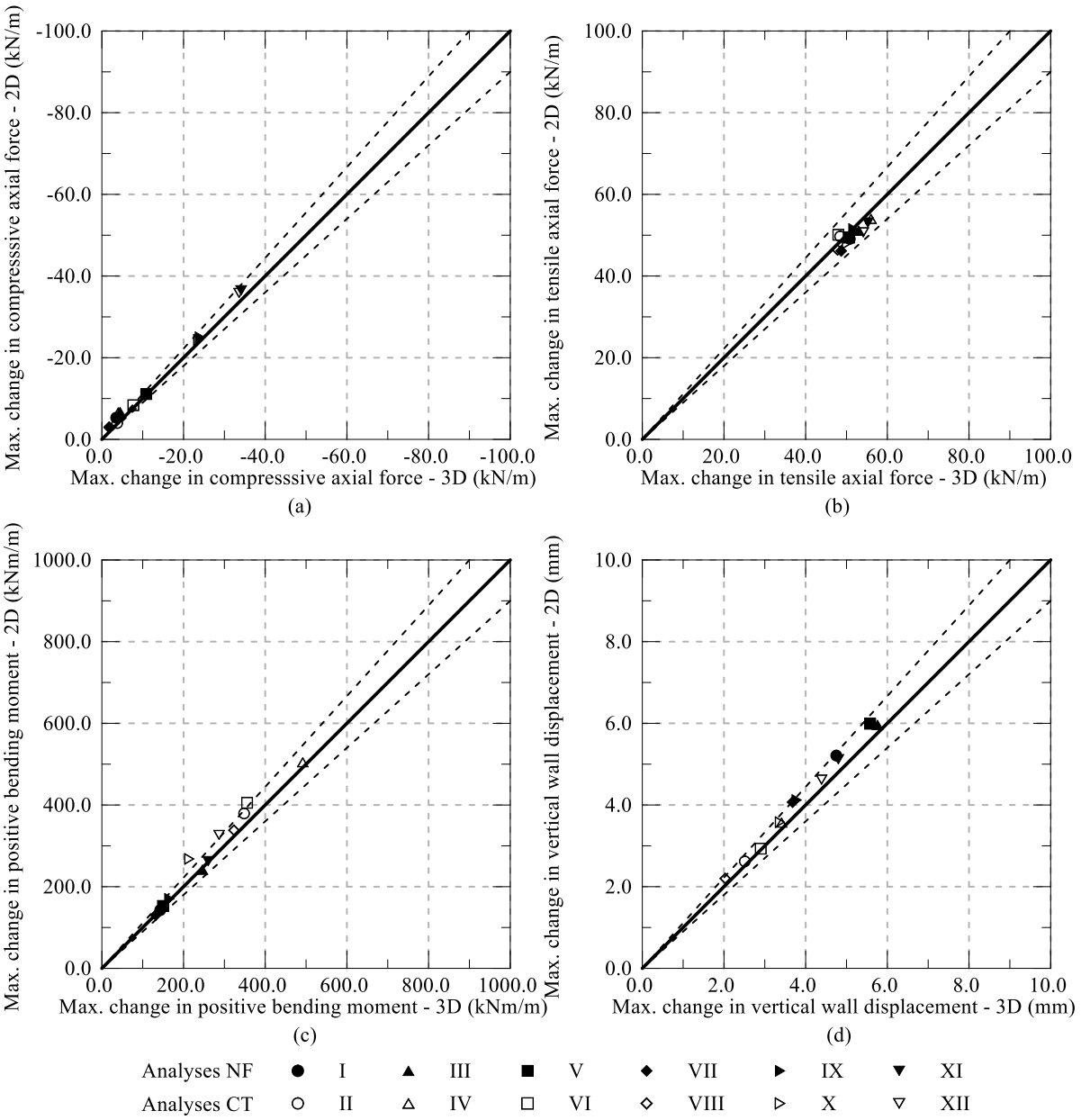

Figure 6-62: Summary of the results of the comparison between 3D and 2D analyses (a) maximum change in compressive axial force, (b) maximum change in tensile axial force, (c) maximum change in positive bending moment and (d) maximum change in vertical wall displacement

6.4.2 Approximation to evaluate out-of-plane axial forces

As discussed in Section 6.2.1.3, a variation in the forces in the out-of-plane direction is computed in 3D analyses due to the non-uniform temperature distributions across the wall panel's width (B). Furthermore, the variation was shown to be more significant for axial forces than bending moments. Since a 2D analysis cannot account for such variation in temperature, an additional analytical procedure was developed to evaluate the variation in axial force across the width of the wall (i.e. y-direction in Figure 6-1 and Figure 6-18). No additional procedure is considered to be required for the bending moment, since it was observed that the 2D analysis generally overestimated these, when compared to the results of the 3D analysis.

Method

In Section 6.2.1.3 it was explained that the changes in axial forces across the width of the wall panel are due to internal actions and reactions that result from the differential expansion of portions of wall that are subjected to different temperatures. To account for such phenomena, the problem is simplified by idealising the wall as a series of n adjacent blocks, each at a given uniform temperature, T_i, of width B_i, thickness H and 1.0 m in height, as schematically represented in Figure 6-63. To evaluate the interaction between the different blocks and estimate the resulting changes in axial forces, the following assumptions are introduced:

(1) The blocks are unrestrained in the z-direction and the strain in this direction is equal for all the blocks;
(2) The blocks are restrained in the x-direction;
(3) The extremities of the blocks i=1 and i=n are restrained in the y-direction (i.e. the average strain across the entire block arrangement is 0 in this direction, but this component of strain in each block is not necessarily equal to 0);
(4) The temperature of a single block is the average temperature of a considered portion of wall;
(5) The blocks are made of concrete, with a linear elastic behaviour following Hooke's law.

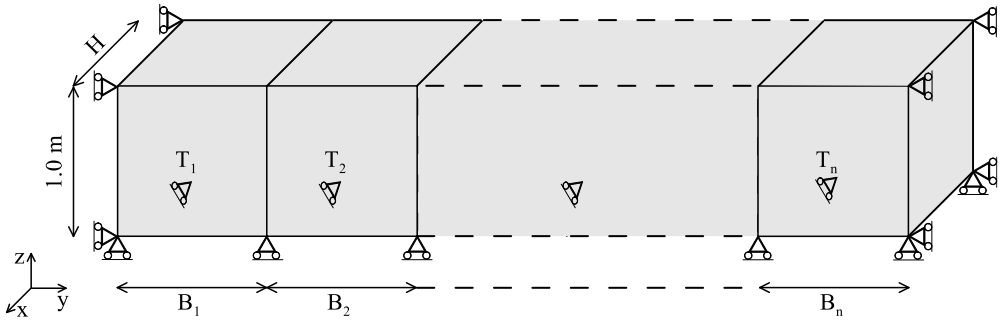

Figure 6-63: Schematic of the problem for evaluation of variation in axial forces across the width of the wall

Assumption (1) indicates that the structure is free to expand in the vertical direction (i.e. the total reaction along z is equal to zero), which does not consider any restriction induced by the soil

surrounding the wall. Furthermore, assuming equal strains in this direction for all blocks, while not entirely accurate, allows the problem to be solved analytically, producing conservative results. Assumption (2) results from the fact that the wall panel is assumed to be restrained along its thickness (x-direction) by the presence of soil within the embedded part and the horizontal structures in the excavated section of the wall, while assumption (3) introduces a restraint in the out-of-plane direction (y-direction) since it is regarded that walls have a considerable length in this direction, though it neglects the contribution of joints between panels (see Zdravković et al. (2005) for details). The average temperatures of the blocks are determined from the 2D plan analyses outlined in Section 6.4.1.1. These are calculated by numerical integration over the different portions of the mesh according to the equations outlined in Appendix C.

Noting that:

- the total strain (ε_{tot}) is equal to $\varepsilon_{tot} = \varepsilon_{mech} + \varepsilon_{th}$, where ε_{mech} and ε_{th} are respectively the mechanical and thermal strains;
- the mechanical strain, for example in direction x, $\varepsilon_{mech,x}$, is calculated according to the Hooke's law for isotropic elastic materials as $\varepsilon_{mech,x} = \frac{1}{E}\left[\sigma_x - \nu\left(\sigma_y + \sigma_z\right)\right]$, where E is the Young's modulus and σ_x, σ_y and σ_z are the stresses in the x, y and z directions, respectively, and ν is the Poisson's ratio;
- the thermal strain in each direction is defined as $\varepsilon_{th} = \alpha T$, with α being the linear coefficient of thermal expansion.

The following equations can be established to evaluate the stresses in each direction generated by n adjacent blocks at different temperatures for a specific time instant.

From assumption (1) it can be established that the sum of the forces in the z-direction, F_z, is equal to zero:

$$\sum_{i=1}^{n} F_{z,i} = 0 \quad i = 1, \dots, n \tag{6-3}$$

which can be rewritten as:

$$\sum_{i=1}^{n} \sigma_{z,i} A_{z,i} = 0 \quad i = 1, \dots, n \tag{6-4}$$

Furthermore, assuming that the total strain in the z-direction is equal for all adjacent blocks leads to:

$$\varepsilon_{tot,z,i} = \varepsilon_{tot,z,(i+1)} \quad i = 1, \dots, (n-1) \tag{6-5}$$

which can be expressed as:

$$\begin{aligned}&\frac{1}{E}\left[\sigma_{z,i}-\nu\left(\sigma_{x,i}+\sigma_{y,i}\right)\right]+\alpha T_i\\&-\frac{1}{E}\left[\sigma_{z,(i+1)}-\nu\left(\sigma_{x,(i+1)}+\sigma_{y,(i+1)}\right)\right]-\alpha T_{(i+1)}=0\quad i=1,\dots,(n-1)\end{aligned}\tag{6-6}$$

Assumption (2) indicates that the total strain of each block in the x-direction is equal to zero:

$$\varepsilon_{tot,x,i}=0\quad i=1,\dots,n\tag{6-7}$$

which is equivalent to:

$$\frac{1}{E}\left[\sigma_{x,i}-\nu\left(\sigma_{y,i}+\sigma_{z,i}\right)\right]+\alpha T_i=0\quad i=1,\dots,n\tag{6-8}$$

Assumption (3) implies that the force in the y-direction, F_y, of each block is the same:

$$F_{y,i}=F_{y,(i+1)}\quad i=1,\dots,(n-1)\tag{6-9}$$

Hence:

$$\sigma_{y,i}A_{y,i}-\sigma_{y,(i+1)}A_{y,(i+1)}=0\quad i=1,\dots,(n-1)\tag{6-10}$$

In addition, the displacement in this direction, δ_y, is equal to zero:

$$\delta_y=0\tag{6-11}$$

which can be expressed as the sum of the total strain along y occurring in each of the blocks multiplied by its width B:

$$\sum_{i=1}^{n}B_i\varepsilon_{tot,y,i}=0\quad i=1,\dots,n\tag{6-12}$$

which equates to:

$$\sum_{i=1}^{n}B_i\left\{\frac{1}{E}\left[\sigma_{y,i}-\nu\left(\sigma_{x,i}+\sigma_{z,i}\right)\right]+\alpha T_i\right\}=0\quad i=1,\dots,n\tag{6-13}$$

According to this procedure, a system of $3\times n$ equations with $3\times n$ unknowns has to be solved, where these are the stresses within each of the n blocks in the three directions. In the equations above, $A_{j,i}$ indicates the the area of the face of block i which is normal to the direction j.

Once the stresses are computed, the force per metre width in the z-direction in each block i is evaluated as:

$$\frac{F_{z,i}}{B_i} = \frac{\sigma_{z,i} A_{z,i}}{B_i} \tag{6-14}$$

This is summed to the axial force per metre width computed in the 2D analysis, P_{2D}, to obtain the variation of axial force, P, in the out-of-plane direction:

$$P_i = \frac{F_{z,i}}{B_i} + P_{2D} \tag{6-15}$$

which is equally expressed as:

$$P_i = \frac{\sigma_{z,i} A_{z,i}}{B_i} + P_{2D} \tag{6-16}$$

Application

The variation in axial force across the width of the wall calculated by means of the proposed approximation procedure is evaluated for Analysis A2 listed in Table 6-2 (i.e. with a constant temperature boundary condition along the exposed face of the wall, since larger 3D effects are evaluated for this case). It should be noted that this procedure was applied to all the cases outlined in Table 6-2 and similar conclusions were found.

The wall panel shown in Figure 6-64 (a) was divided into five blocks, as schematically represented in Figure 6-64 (b) with indication of their dimensions, while the material properties of concrete are those outlined in Section 6.2.2.

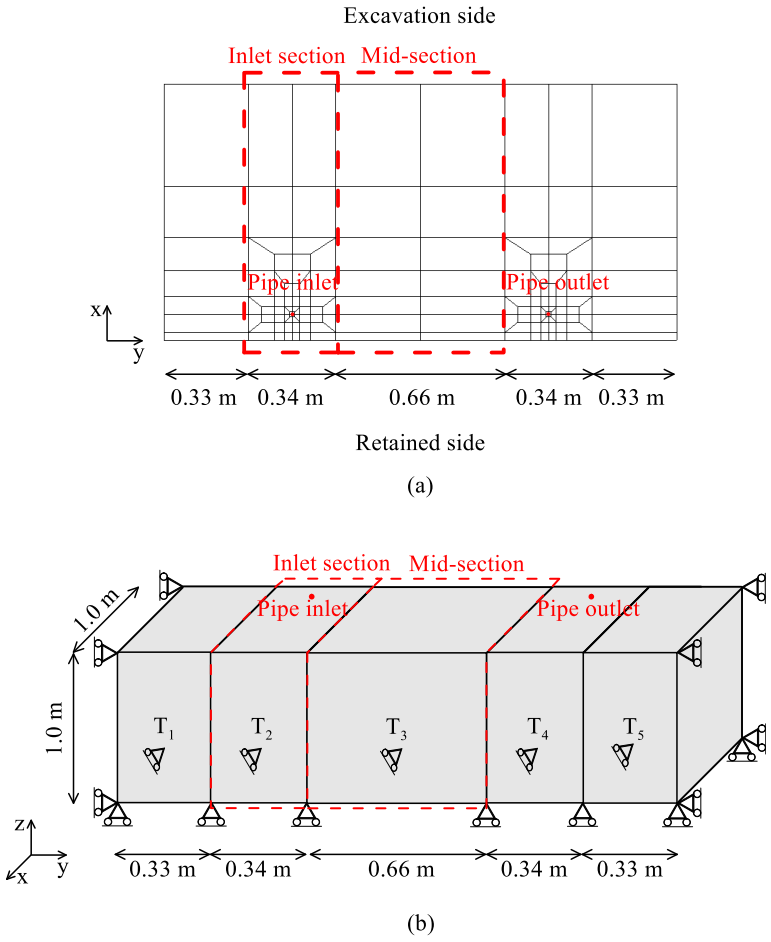

Figure 6-64: Evaluation of out-of-plane axial forces (a) finite element mesh of wall panel and (b) Schematic of the system of blocks

Figure 6-65 (a) and (b) show the changes in axial force per metre width after 3 days and 6 months of operation. The changes in axial force computed in the 3D analyses for the inlet section and mid-section shown in Figure 6-64 (a) (i.e. blocks 2 and 3 in Figure 6-64 (b)) are compared to those evaluated through the analytical procedure outlined above.

After 3 days, the average changes in temperatures of the inlet section and mid-section were evaluated to be 1.47°C and 0.79°C, respectively; after six months, these have increased to 5.23°C and 4.84°C, respectively. Given the larger temperature difference between the two wall portions in the short term, a larger variation in axial force across the width of the wall is estimated for this time instant. Indeed, the analytical procedure yields a compressive force within the inlet section, $F_{z,2}/B_2$, of -231.0 kN/m and a tensile force within the midsection, $F_{z,3}/B_3$, of 119.0 kN/m; after 6 months these decrease to -134.0 kN/m and 69.0 kN/m, respectively. As can be seen in Figure 6-65, when summed to the axial force computed in the 2D analysis, the corrected axial forces approximate very well the variation in axial force across the width of the panel registered in the 3D analysis. Larger differences are predicted in the short term, where the axial force calculated through the analytical procedure exceeds the one computed in 3D, on average, by 50 kN/m. In the long term, excellent accuracy is obtained.

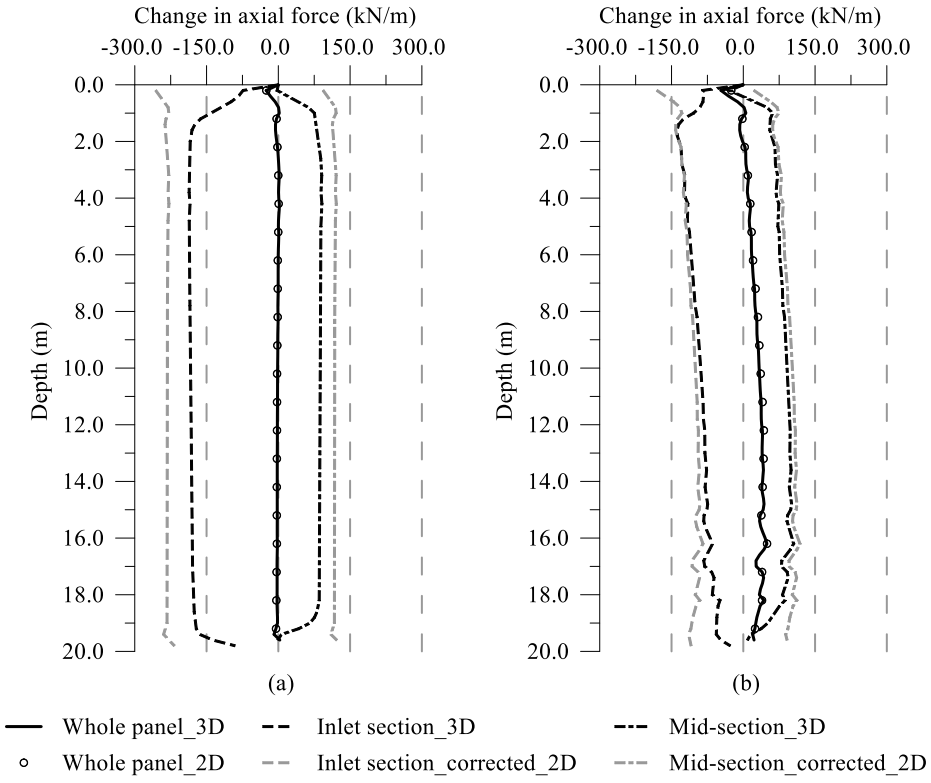

Figure 6-65: Axial force with depth – comparison between out-of-plane forces in 3D (CT case) and corrected forces (a) after 3 days and (b) after 6 months

6.5 Thermo-hydro-mechanical response under cyclic thermal loading

This section investigates the long-term behaviour of a thermo-active retaining wall subjected to different scenarios of cyclic heating and cooling in 2D employing the new modelling approach presented in the previous section, which allows to save considerable computational effort when compared to full 3D analyses. Indeed, analyses performed as part of this research suggested that 6 months of operation lead to approximately 3000 times larger computational running time in 3D than the equivalent analysis in 2D. The wall geometry employed in this study is that corresponding to the Wood & Perrin (1984b) case described in Chapter 3 and reproduced in 3D within this chapter in Section 6.2.1 (see Figure 6-1). Hence, the initial conditions, construction sequence and boundary conditions are the same as previously described, where it should be noted that the initial temperature was 13.0°C. The analysed scenarios are similar to those simulated in Chapter 5 and are (as summarised in Table 6-4):

- Scenario (1) simulates 6 months of heating followed by 6 months of cooling;
- Scenario (2) consists of 6 months of heating followed by 6 months of idling;
- Scenario (3) investigates the effect of unbalanced thermal loading with a 9 months cooling followed by 3 months of heating.

It should be noted that the designation of the operation mode (i.e. heating and cooling) refers to the soil side of the system (i.e. in heating, heat is injected to the ground to provide cooling to the building, and the opposite is true for cooling). For each case, 5 years of operation were simulated and both NF and CT boundary conditions along the exposed face of the wall were applied. It should be noted that temperature independent parameters, such as the coefficient of expansion of water and the soil's permeability, have been adopted in this study. This aspect affects the changes in excess pore water pressures (see Chapter 2 and Cui et al. (2020)) and is part of further research to be carried out.

Table 6-4: List of performed long-term THM analyses

Analysis	Heating	Cooling	$T_{in,3D}$ (°C)	ΔT_p (°C)
Scenario (1)	6 months	6 months	+28.0/-2.0	1.0
Scenario (2)	6 months	N/A	+28.0	1.0
Scenario (3)	3 months	9 months	+28.0/-2.0	1.0

6.5.1 Modelling procedure

The procedure to model the heat exchange follows the new proposed method described in Section 6.4. Hence, for each case, 3 analyses in plan view were carried out to simulate the embedded section and

the exposed section with either a NF or CT boundary condition along the exposed face. Since a large part of the wall is embedded in London Clay and the thermal properties for the soil layers are relatively similar (see Table 3-5), for simplicity, the 2D plan analyses were carried out with soil properties of this material only. It is expected that simulating the exposed section also with properties of Made Ground and Terrace Gravel and evaluating the average temperature as a weighted average according to the thickness of the soil layers could provide a more accurate modelling. The values of temperatures applied are calculated through the assumed design inlet temperature, $T_{in,3D}$, and temperature differential between the pipe inlet and outlet, ΔT_p, both reported in Table 6-4. Thus, the temperature applied in the 2D plan analysis was 27.5°C during heating and -1.5°C during cooling. For each time step of the analysis, the equivalent temperature, $T_{i,2D}$, to be applied in the plane-strain analysis of the wall in cross section was determined according to Equation (6-1), with L_{exp} and L_{emb} equal to 9.6 m and 8.4 m, respectively (see Figure 6-1). For scenario (2), the same procedure was followed during the idling phase, with no temperatures being prescribed in the 2D plan analyses. Figure 6-66 depicts the computed $T_{i,2D}$ for the three analysed scenarios. As expected from the results presented in Chapter 5, for scenario (1) and (3) the temperatures do not vary greatly with increasing number of cycles, indicating that the problems reach thermal equilibrium after few number of cycles. Conversely, scenario (2) displays a continuous increase in $T_{i,2D}$, with the amount of heat dissipated during each subsequent idling phase decreasing with time. It should be noted that, at the beginning of each new operation period (i.e. heating, cooling or idling), the stiffness of all soils was reset to its maximum value due to the loading reversal induced by the change in temperature (see Section 2.3.5 and Gawecka et al. (2017) for details on this procedure in thermal analyses).

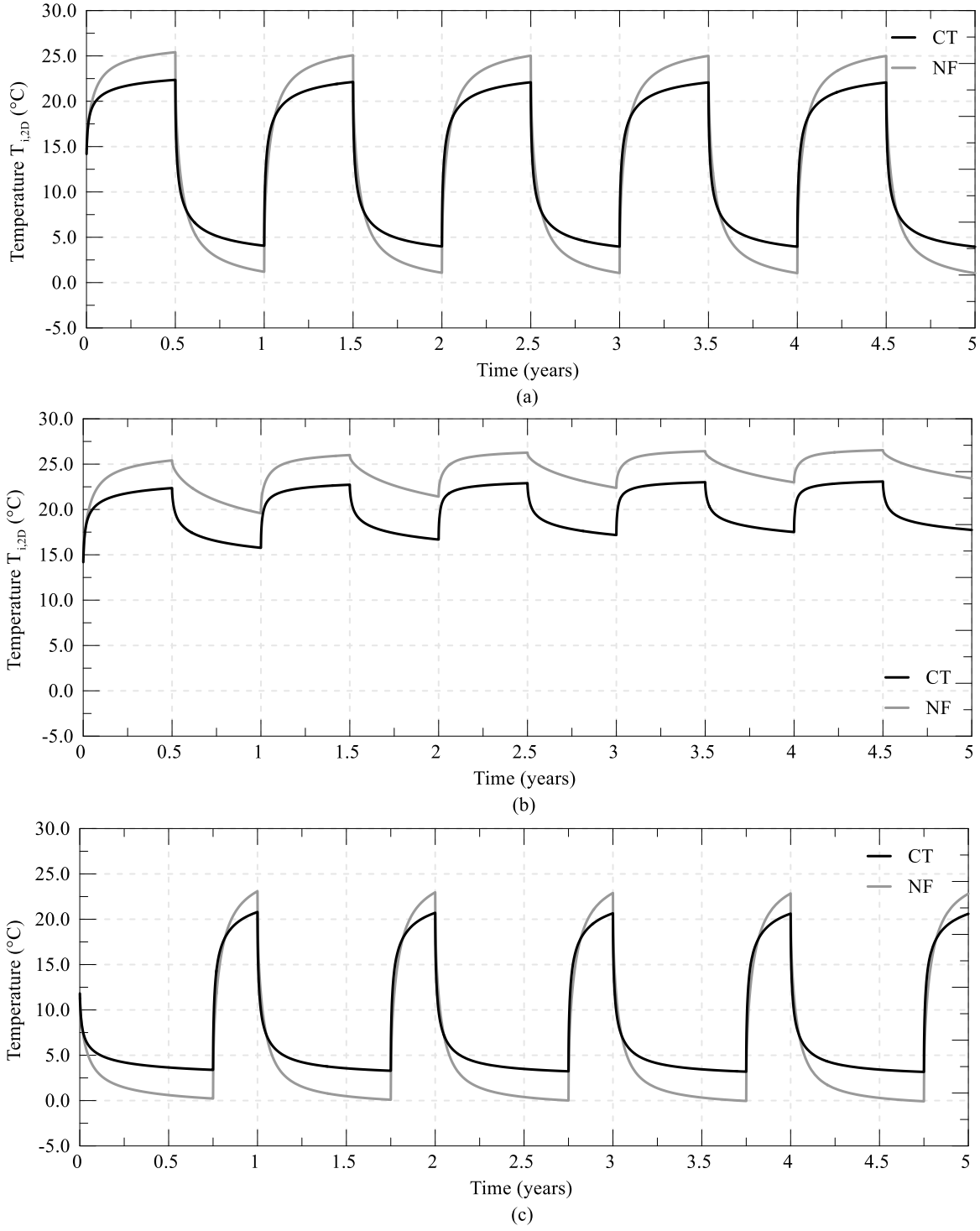

Figure 6-66: Temperature applied in 2D analyses (a) scenario (1), (b) scenario (2) and (c) scenario (3)

6.5.2 Scenario (1)

Temperatures and pore water pressures

Figure 6-67 and Figure 6-68 show the contours of temperature changes computed at different time instants during the 5 years of operation. Due to the balanced heating and cooling cycles, limited permanent temperature changes occur, with the area of ground affected in each cycle being approximately the same, with slightly higher values computed for the NF case.

Figure 6-69 and Figure 6-70 illustrate the contours of changes in pore water pressure around the wall. During the first six months of heating, compressive excess pore water pressures develop as previously described in Section 6.2.1.2. The subsequent cooling period leads to an initial reduction in the compressive excess pore water pressures around the wall, with an increase in the regions further away. At the end of the first cooling cycle, tensile pore water pressures have developed around the wall, while compressive excess pore water pressures are registered at considerable distances from the wall. Since it was shown that the temperature changes do not extend for a large distance around the wall, these are due to the time-dependent water flow and are thus "hydraulically-induced" (see Chapter 3). During the subsequent years of alternating heating and cooling, similar changes are observed, however the extent of the area influenced by changes in pore water pressure reduces as thermal equilibrium is reached. It should also be noted that slightly higher excess pore water pressures develop at the beginning of each heating/cooling period within the excavated side, due to the mechanical restriction applied by the base slab. The maximum change in excess pore water pressures varies between $\pm$60.0 kPa and $\pm$50.0 kPa, for the NF and CT cases, respectively.

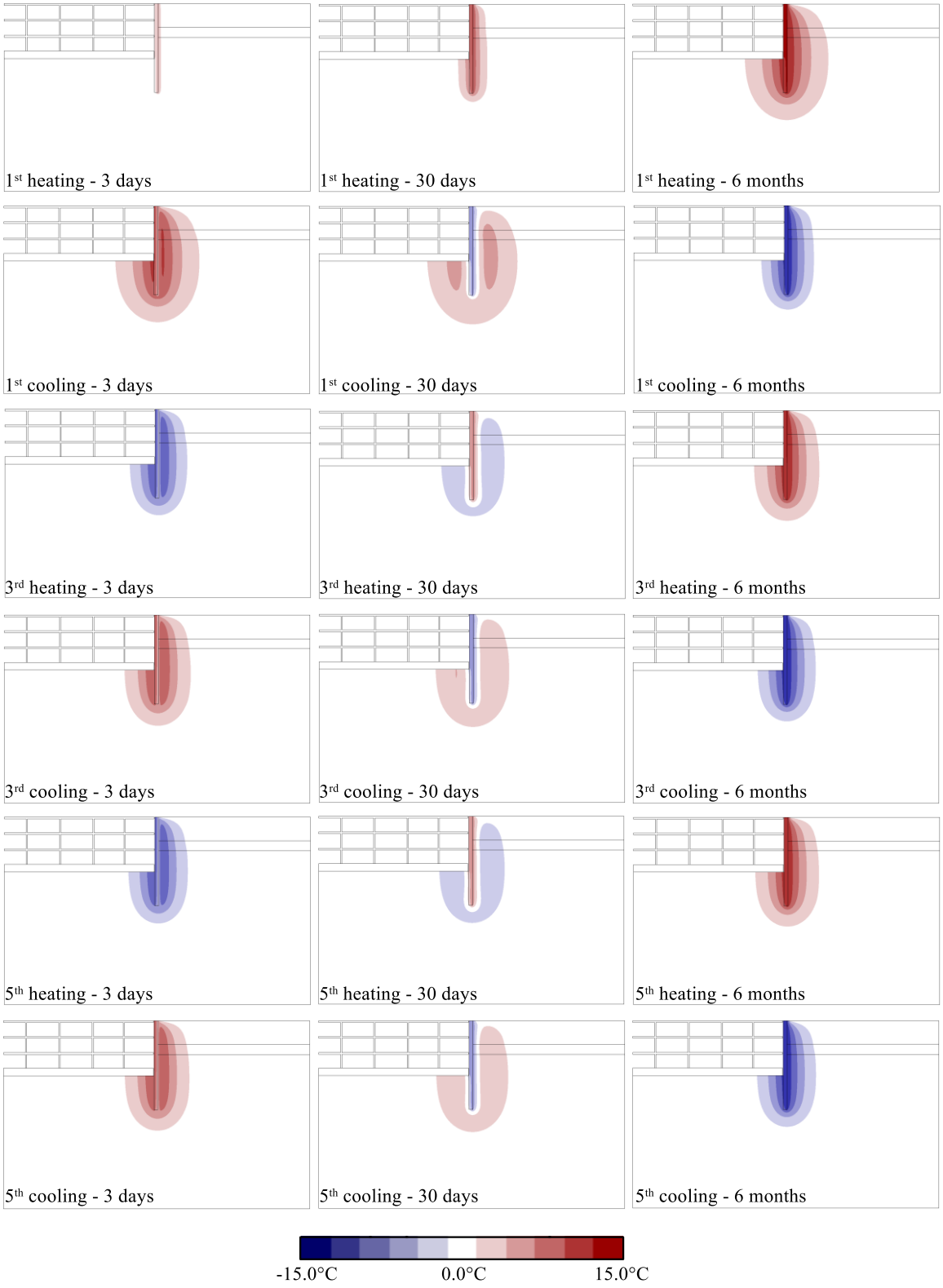

Figure 6-67: Scenario (1) - Contours of temperature changes at different time instants - NF

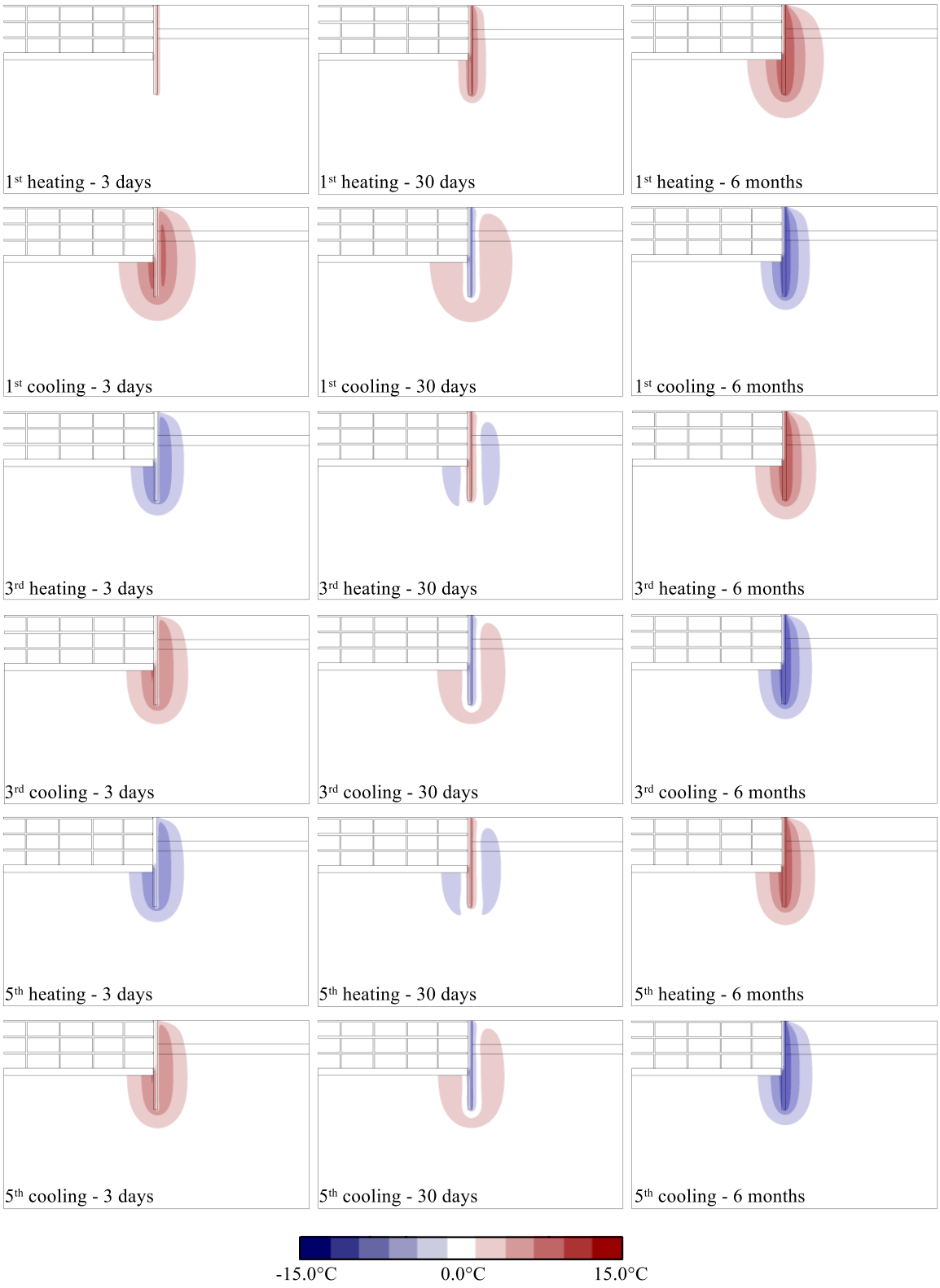

Figure 6-68: Scenario (1) - Contours of temperature changes at different time instants for scenario - CT

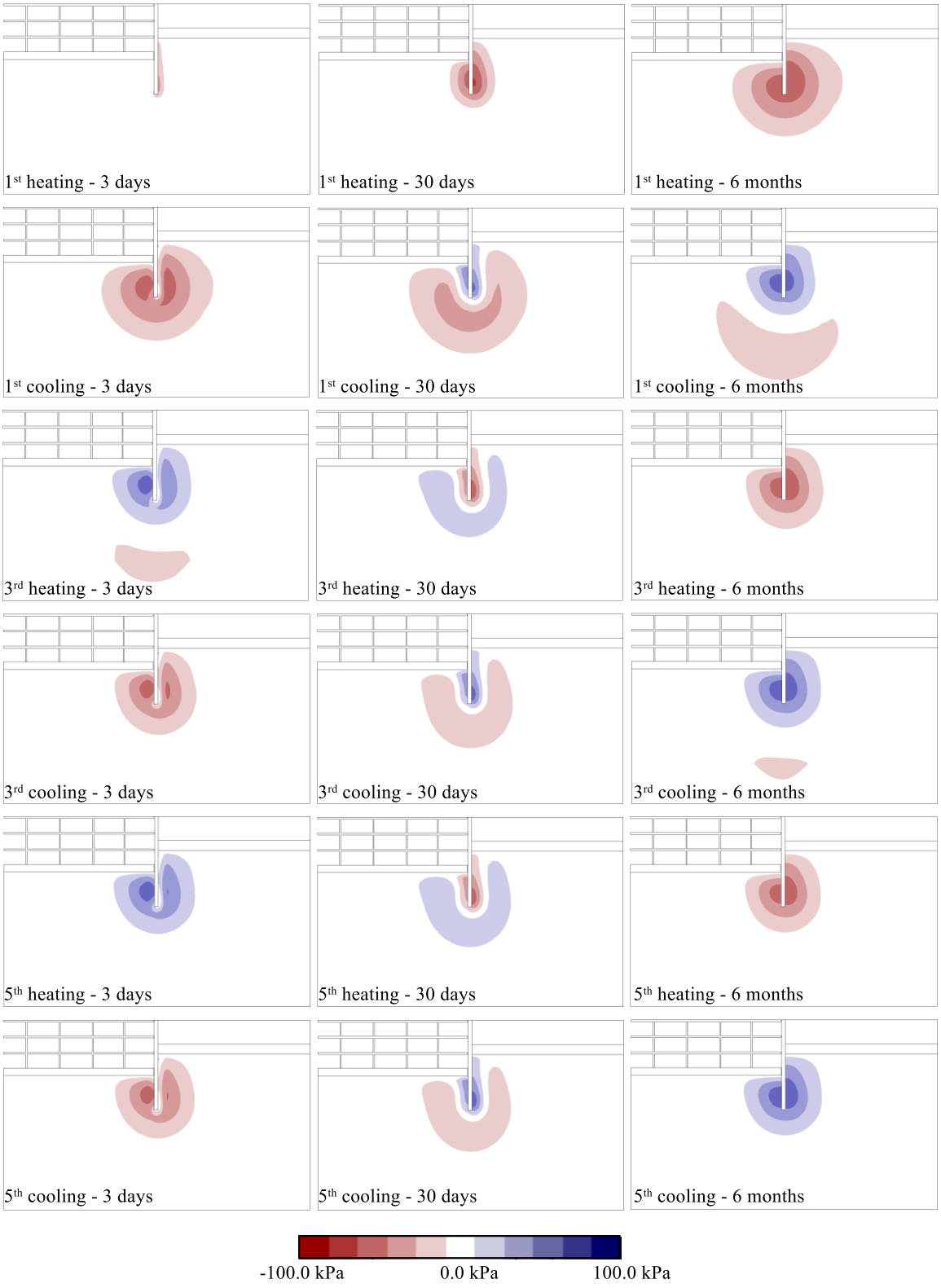

Figure 6-69: Scenario (1) - Contours of changes in excess pore water pressures at different time instants - NF

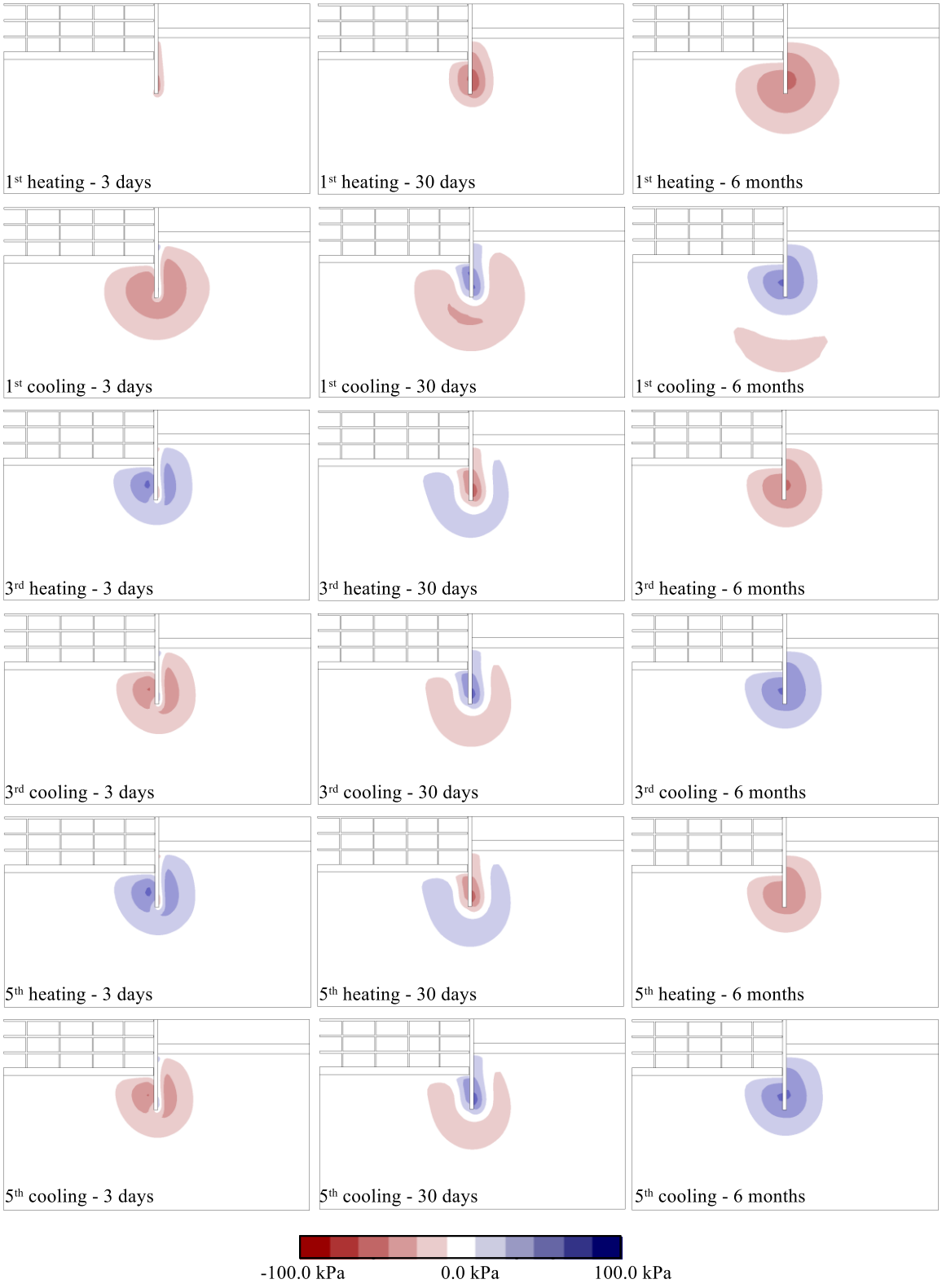

Figure 6-70: Scenario (1) - Contours of changes in excess pore water pressures at different time instants for - CT

Axial forces and bending moments

Figure 6-71 and Figure 6-72 show the development of the axial force with depth and time, respectively. In Figure 6-71, the profiles of axial force for peak values (which occur after 3 days from the commencement of heating/cooling) and at the end of cooling/heating periods (6 months) are plotted. As previously observed, heating induces an initial compression of the wall (point A in Figure 6-72), followed by tensile actions as the soil expands due to the various coupled phenomena associated with the increase in temperature (i.e. point A to A' in Figure 6-72). During cooling, the temperatures of the wall decrease, which leads to thermal contraction. Since this thermal deformation is initially restricted by the soil, a peak in tensile axial force is observed at the beginning of the cooling period. Furthermore, the accentuated increase in tensile force (e.g. point B in Figure 6-72) is also due to the reset of the stiffness simulated as the temperature is decreased. This tensile action is followed by a compression of the wall as the soil contracts (i.e. from point B to B' in Figure 6-72). Although the applied temperatures are very similar for each year of operation (see Figure 6-66 (a)), the development of axial forces are not symmetrical in each cycle. As can be noted clearly from Figure 6-72, with time, the axial force becomes more compressive, with the peaks in each cycle displaying a lower value. This is attributed to slight changes in excess pore water pressure during each cycle, with higher tensile excess pore water pressures developing close to the wall during subsequent cooling periods (see Figure 6-69 and Figure 6-70), thus leading to an overall compressive action. Furthermore, it can be noted that a noticeable increase in the compressive force during the heating period is observed between the 1st and 2nd year of operation, due to the simulated cooling phase in between which leads to larger changes in temperature. The seasonal changes in axial force during the first six months of heating (i.e. between points A and A' in Figure 6-72) are equal to 110.0 kN/m and 86.0 kN/m, for the NF and CT cases, respectively. These values increase, respectively, to 190 kN/m and 155 kN/m in subsequent heating cycles (e.g. between points C and C') and remain approximately constant (similar variations in axial forces are computed during the cooling cycles, given the similar temperature changes), suggesting that thermal equilibrium is achieved (as was observed in Chapter 5). These observations demonstrate the need of simulating more than one year of operation to capture a response of the wall which is more representative of its long-term behaviour.

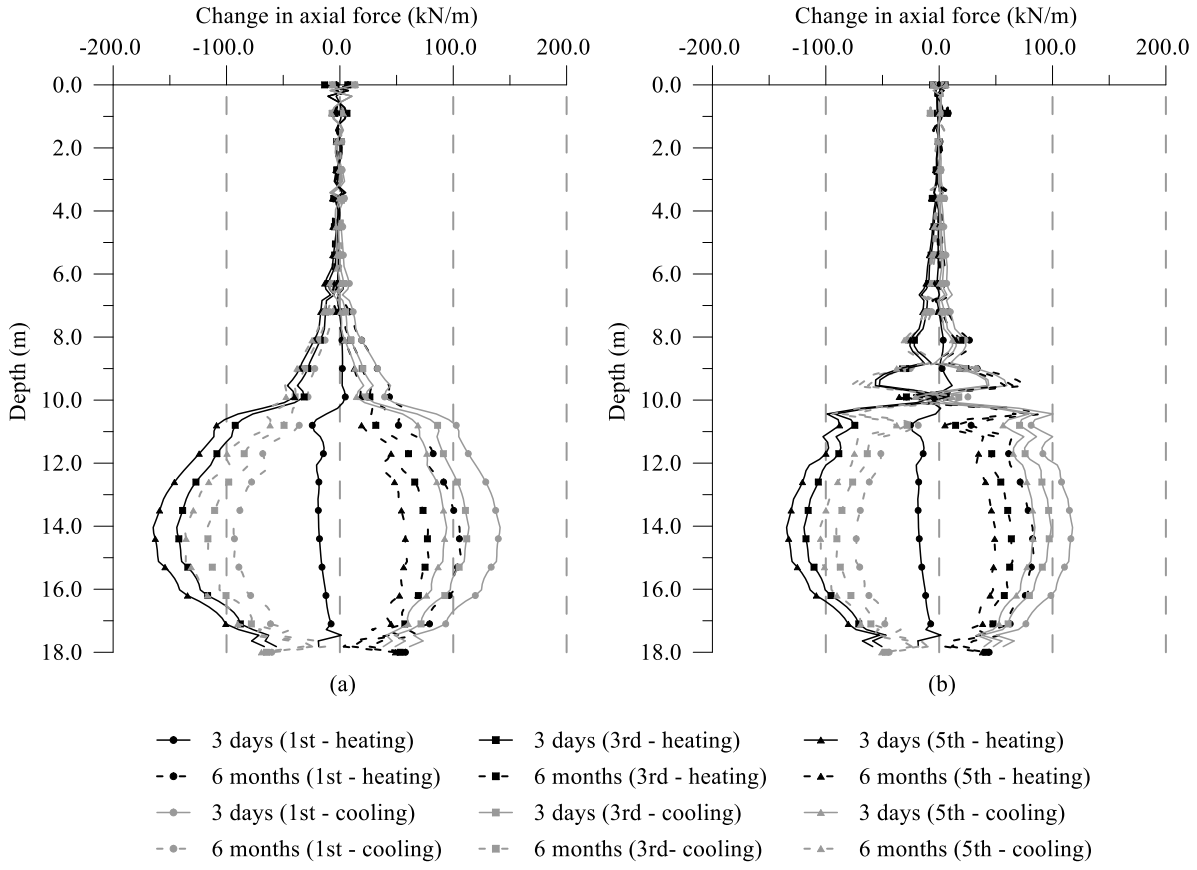

Figure 6-71: Scenario (1) - Change in axial force with depth at different time instants (a) NF and (b) CT

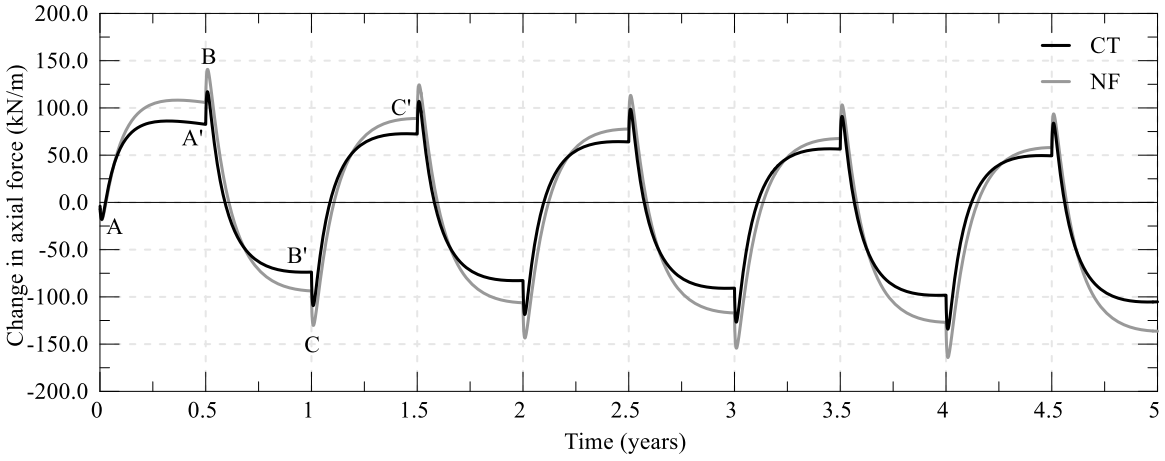

Figure 6-72: Scenario (1) - Change in axial force with time at depth of 14.0m

Contrary to the development of the axial forces, the bending moments display a rather symmetrical behaviour, with limited changes between different operation periods, as can be noted from Figure 6-73 and Figure 6-74. As previously observed, the thermally-induced changes in bending moment mainly depend on the distributions of temperatures across the thickness of the wall. As a consequence, a different effect associated to the cyclic temperature variations is observed for the NF and CT cases. To analyse the observed behaviour, the first period of cooling after heating is considered in detail (for the behaviour during heating refer to Section 6.2.1). For the NF case, a fairly uniform temperature field had

been reached within the wall during the previous heating period (see Chapter 4). As the temperature along the pipes is reduced at the beginning of the cooling period, a large gradient in temperature across the wall thickness develops. This leads to a substantial change in bending moment with opposite sign with respect to the heating period (point A in Figure 6-74). As the temperatures within the wall become more uniform, the bending moment reduces at the end of the cooling period (point A' in Figure 6-74). A very different pattern is observed for the CT case: decreasing the temperature leads to an immediate reduction of the bending moment (point B in Figure 6-74), a process which carries on with time as the temperature along the pipes decreases further (thus increasing the temperature gradient across the wall's thickness), eventually becoming as large as during the previous heating phase (point B' in Figure 6-74), but with opposite sign. The profiles of bending moment at the end of each phase are approximately symmetrical since the same absolute value of $\Delta T_{in,3D}$ is applied in both heating and cooling (i.e. $\pm$15°C). The maximum changes in bending moment vary between $\pm$130.0 kNm/m and $\pm$200.0 kNm/m, for the NF and CT cases, respectively.

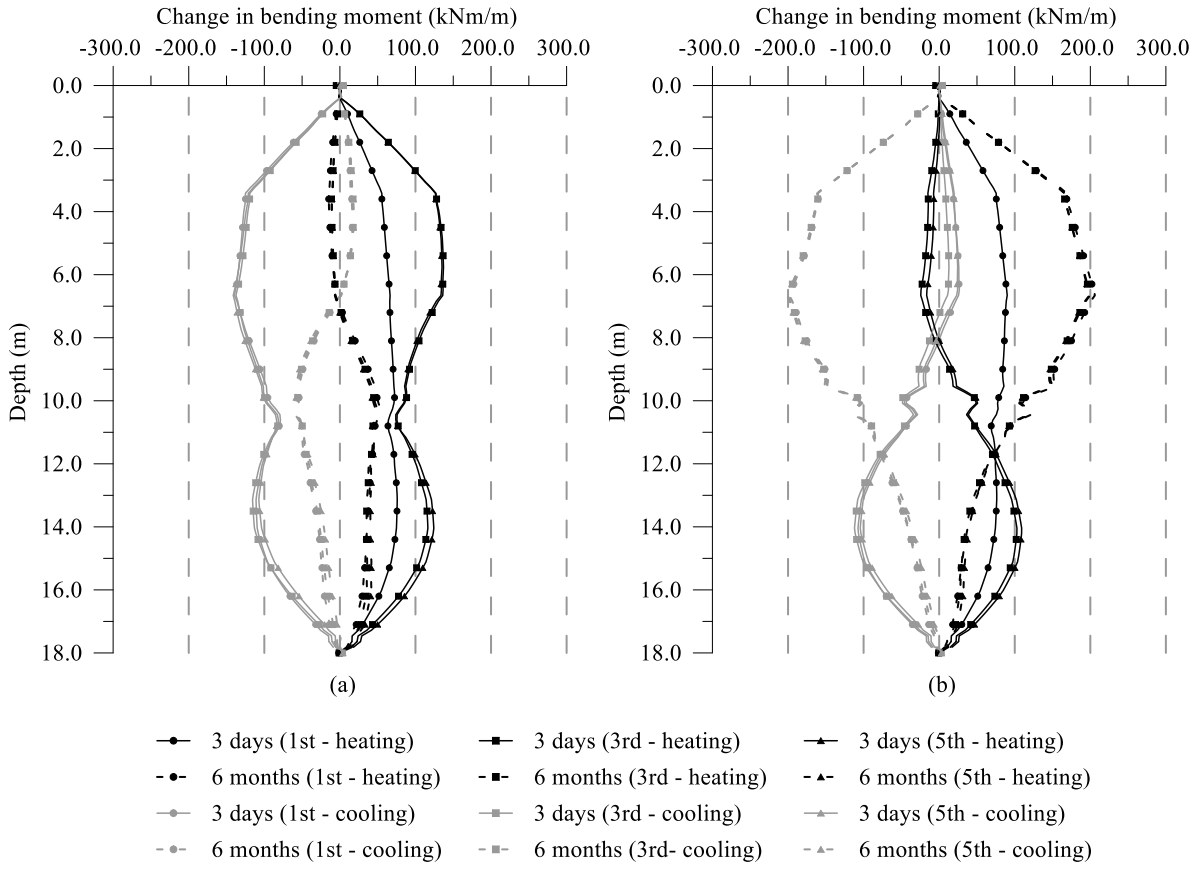

Figure 6-73: Scenario (1) - Change in bending moment with depth at different time instants (a) NF and (b) CT

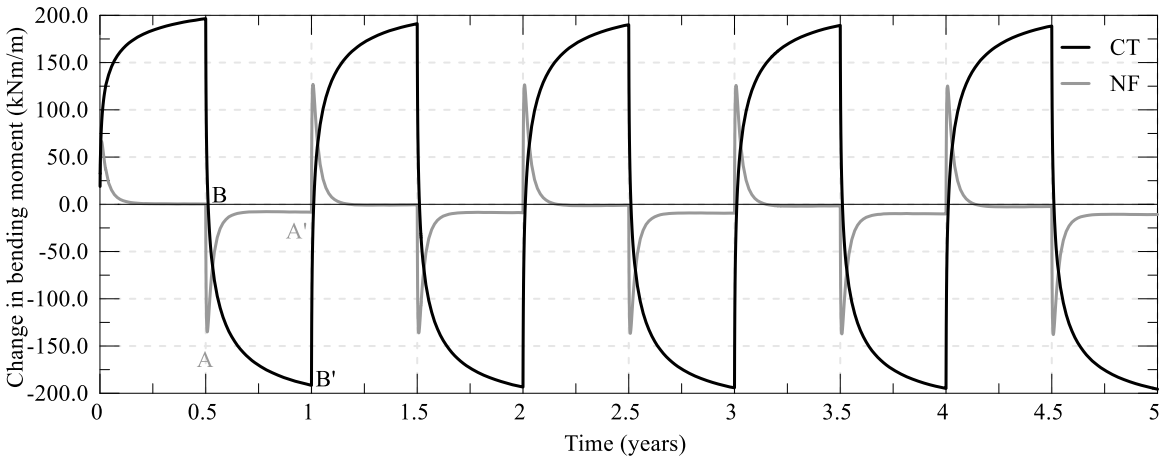

Figure 6-74: Scenario (1) - Change in bending moment with time at depth of 6.5m

Wall and ground movements

Figure 6-75 shows the vertical movement of the top of the wall with time. The vertical movement of the wall displays an average downward movement with time, which is largest in the first 2 years, after which it stabilises. The movement recorded at the end of the first and last heating period decreased by 1.0 mm and 0.7 mm for the NF and CT analyses, respectively. The seasonal changes recorded are largest in the first cooling period, corresponding to 8.0 mm and 5.5 mm, respectively for the NF and CT analyses, while they reduce slightly with time (in the last cooling period, the change in vertical movement is respectively equal to 7.7 mm and 5.2 mm).

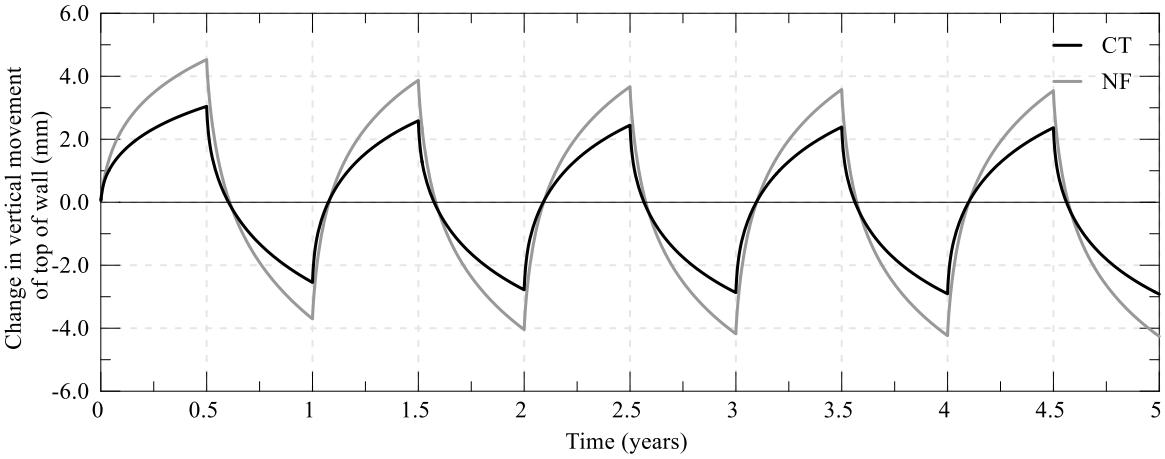

Figure 6-75: Scenario (1) - Change in vertical movement of top of wall with time

Figure 6-76 and Figure 6-77 display the contours of horizontal displacements together with the deformed shape for the NF and CT cases, respectively. The deformed shape shows clearly the soil expansion and contraction upon heating and cooling of the soil. This involves the soil mass next to the wall, as well as the horizontal structures inside the basement, which move up and down as the wall expands and contracts. The ground surface behind the wall is subjected to cyclic heave and settlement induced by the heat exchange. At a distance of 5.0 m, the ground surface experiences seasonal changes in vertical movement in the order of 6.5 mm and 4.0 mm for the NF and CT cases, respectively.

The horizontal displacements of the soil are limited to ±3.0 mm for both cases, with lower values computed for the CT case due to the lower temperatures in the wall-soil system. Furthermore, it is interesting to note that the soil undergoes changes in horizontal movements mainly within the retained side of the wall, while almost no change is recorded within the excavated side. This is attributed to the larger restriction in the horizontal direction imposed by the presence of the permanent building structures and the vicinity of the axis of symmetry, where the horizontal movement is restricted. It can also be seen, as noted in Section 6.2.1.2, that the wall itself is subjected to very limited horizontal movements, with the highest values experienced at the toe of the wall.

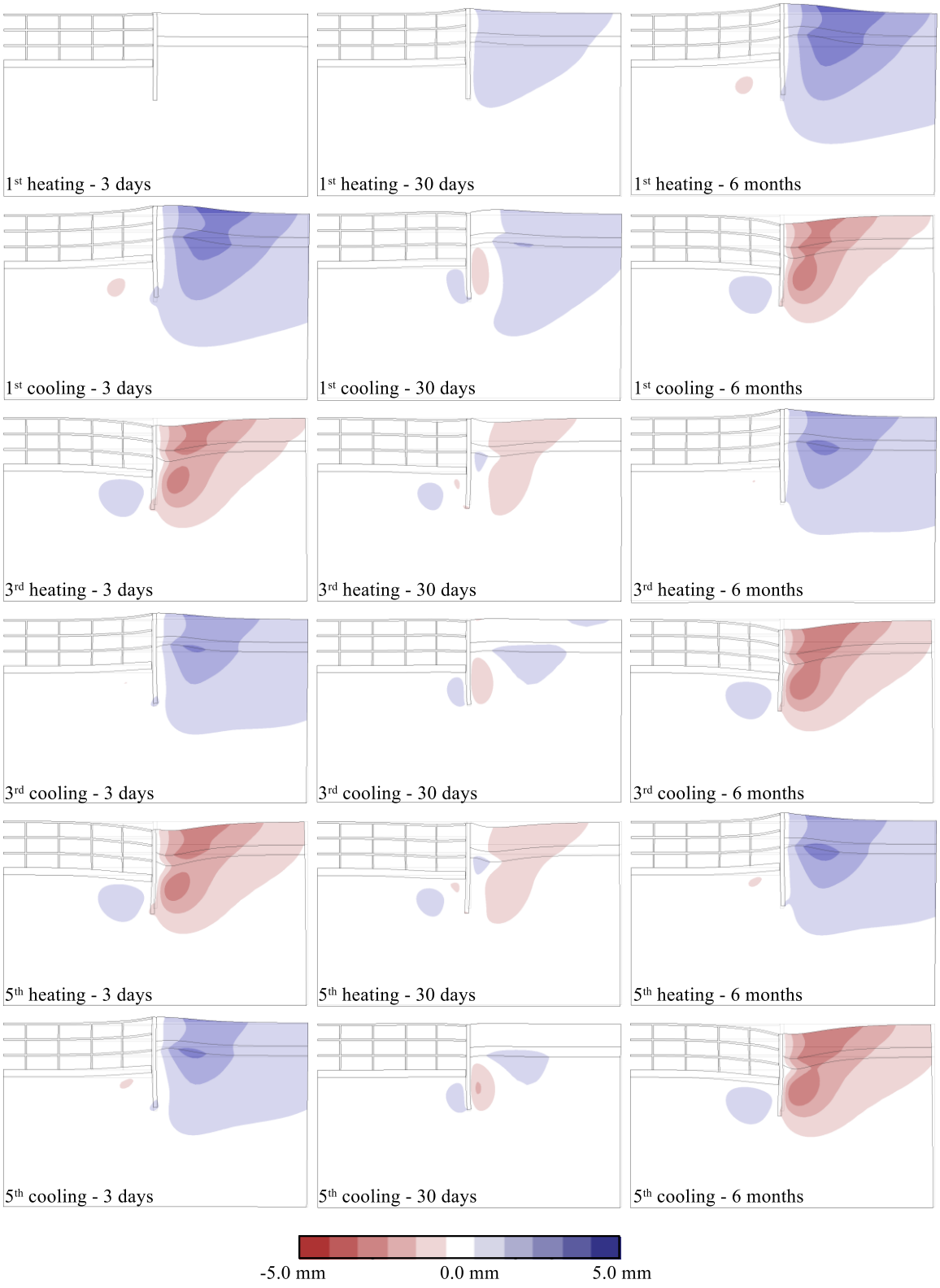

Figure 6-76: Scenario (1) - Contours of changes in horizontal movement at different time instants and deformed shape (exaggeration factor 500) - NF

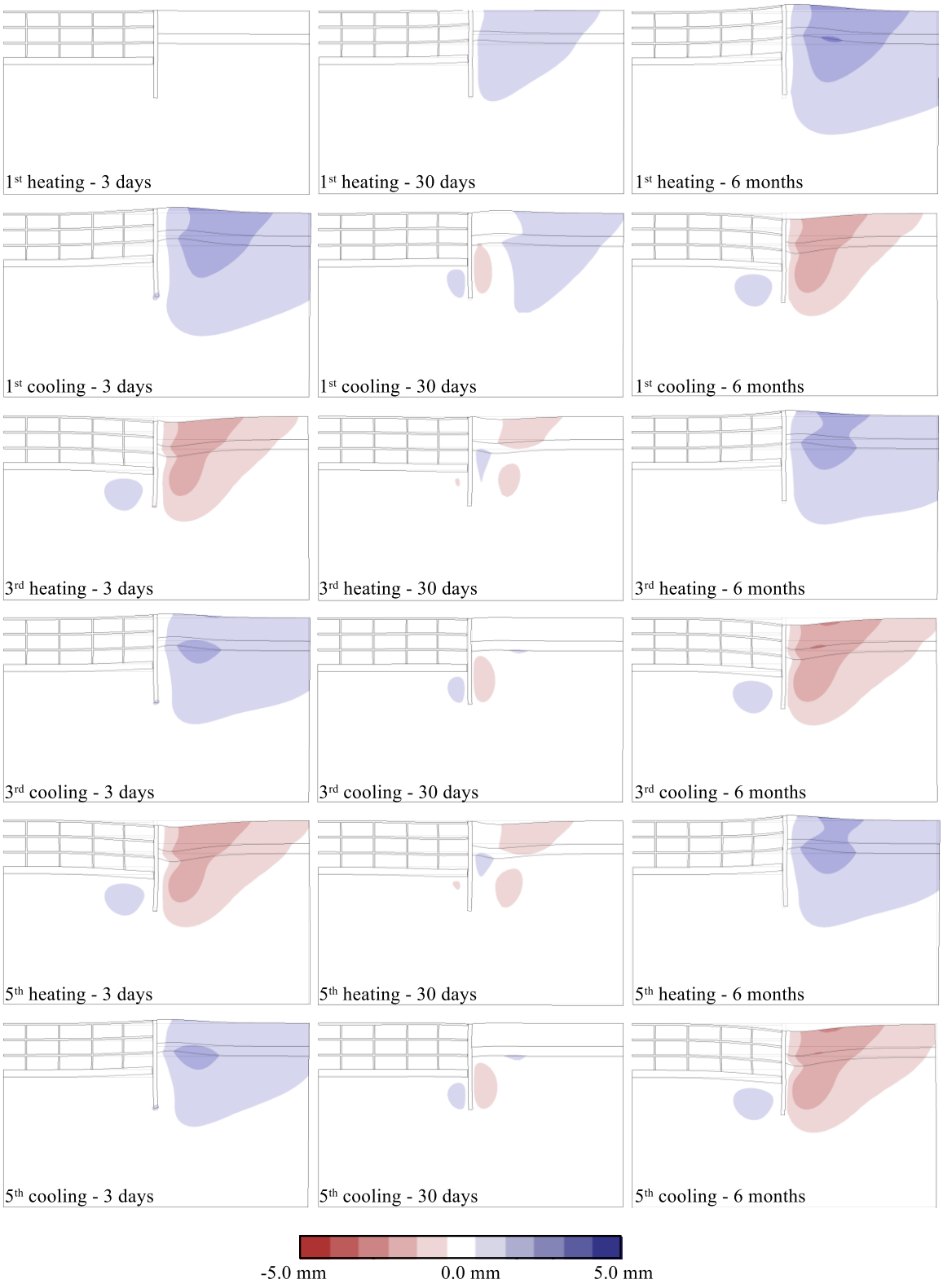

Figure 6-77: Scenario (1) - Contours of changes in horizontal movement at different time instants and deformed shape (exaggeration factor 500) – CT

6.5.3 Scenario (2)

Temperatures and pore water pressures

In this scenario 6 months of heating are followed by 6 months of idling. The calculated temperatures imposed as a boundary condition in the analysis, $T_{i,2D}$, show that during each idling phase, a part of the temperature changes is not recovered and the temperatures in the wall increase steadily (see Figure 6-66 (b)). This can also be clearly observed in Figure 6-78 and Figure 6-79, which plot the contours of changes in temperature for the NF and CT analyses, respectively. Part of the heat is dissipated during the idling phase, though an accumulation of temperature is observed in the long term, with an increasingly larger area of soil subjected to permanent temperature changes.

This clearly affects the distributions of excess pore water pressures, which are depicted in Figure 6-80 and Figure 6-81 for the NF and CT analyses, respectively. Increasing the temperature of the soil leads to the generation of compressive excess pore water pressures which, as previously seen, begin to dissipate during the heating period. The consolidation process continues during the idling phase, with the excess pore water pressures slowly dissipating towards the drainage boundary at the bottom of the mesh. During subsequent heating periods, additional compressive excess pore water pressures develop close to the wall. Since the excess pore water pressures do not fully dissipate during the idling phase and because during each heating period a larger area of soil is subjected to changes in temperature, the area affected by changes in pore water pressures increases noticeably with time. However, the excess pore water pressures close to the wall due to each heating period reduce, as smaller changes in temperature are observed in this region. Indeed, for the NF case, during the first heating period, the maximum excess pore water pressure is equal to -65.0 kPa, reducing to -40.0 kPa during the last heating period. A similar reduction, though with overall lower values, is computed for the CT case.

Figure 6-78: Scenario (2) - Contours of temperature changes at different time instants - NF

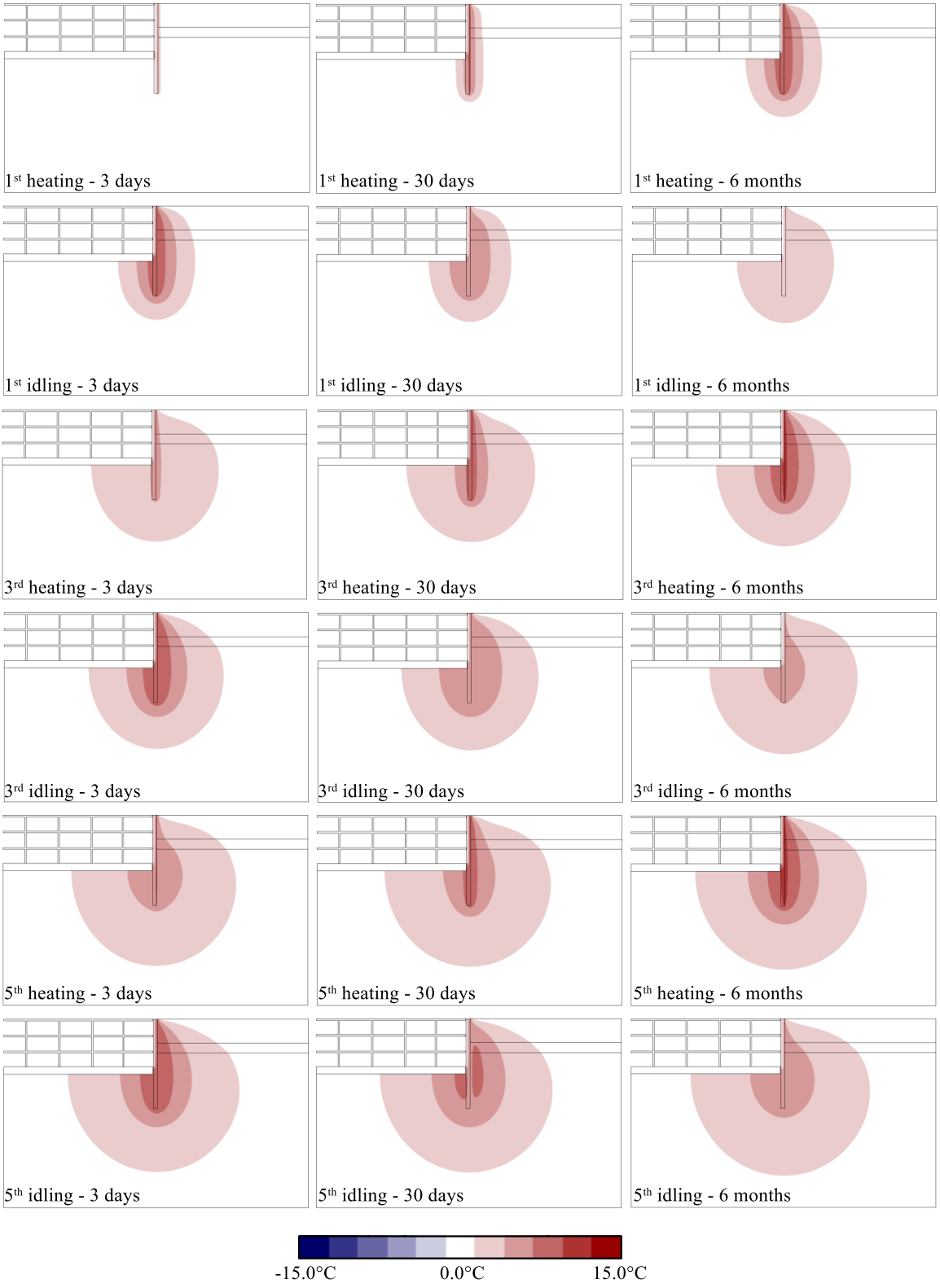

Figure 6-79: Scenario (2) - Contours of temperature changes at different time instants – CT

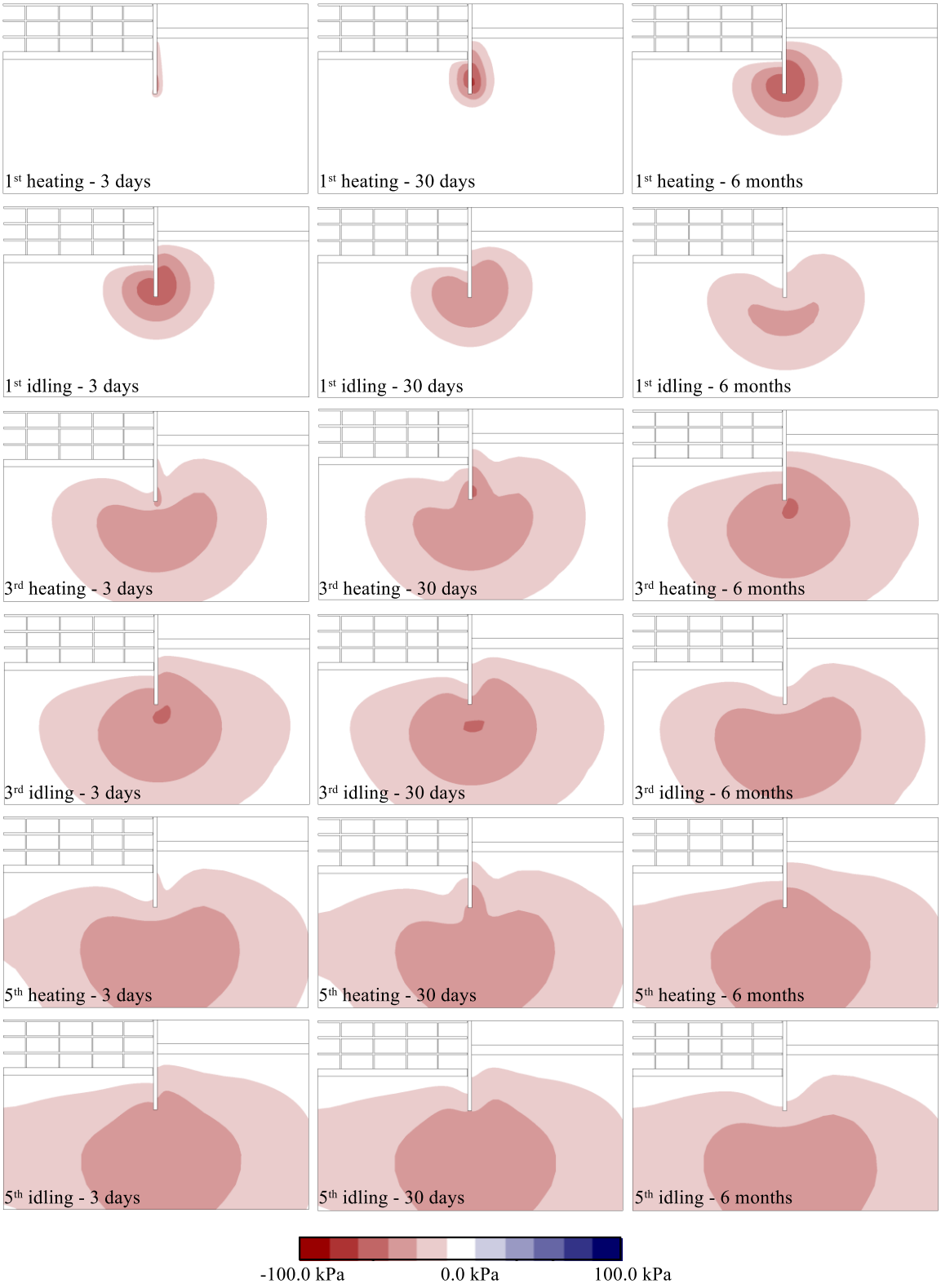

Figure 6-80: Scenario (2) - Contours of changes in excess pore water pressures at different time instants - NF

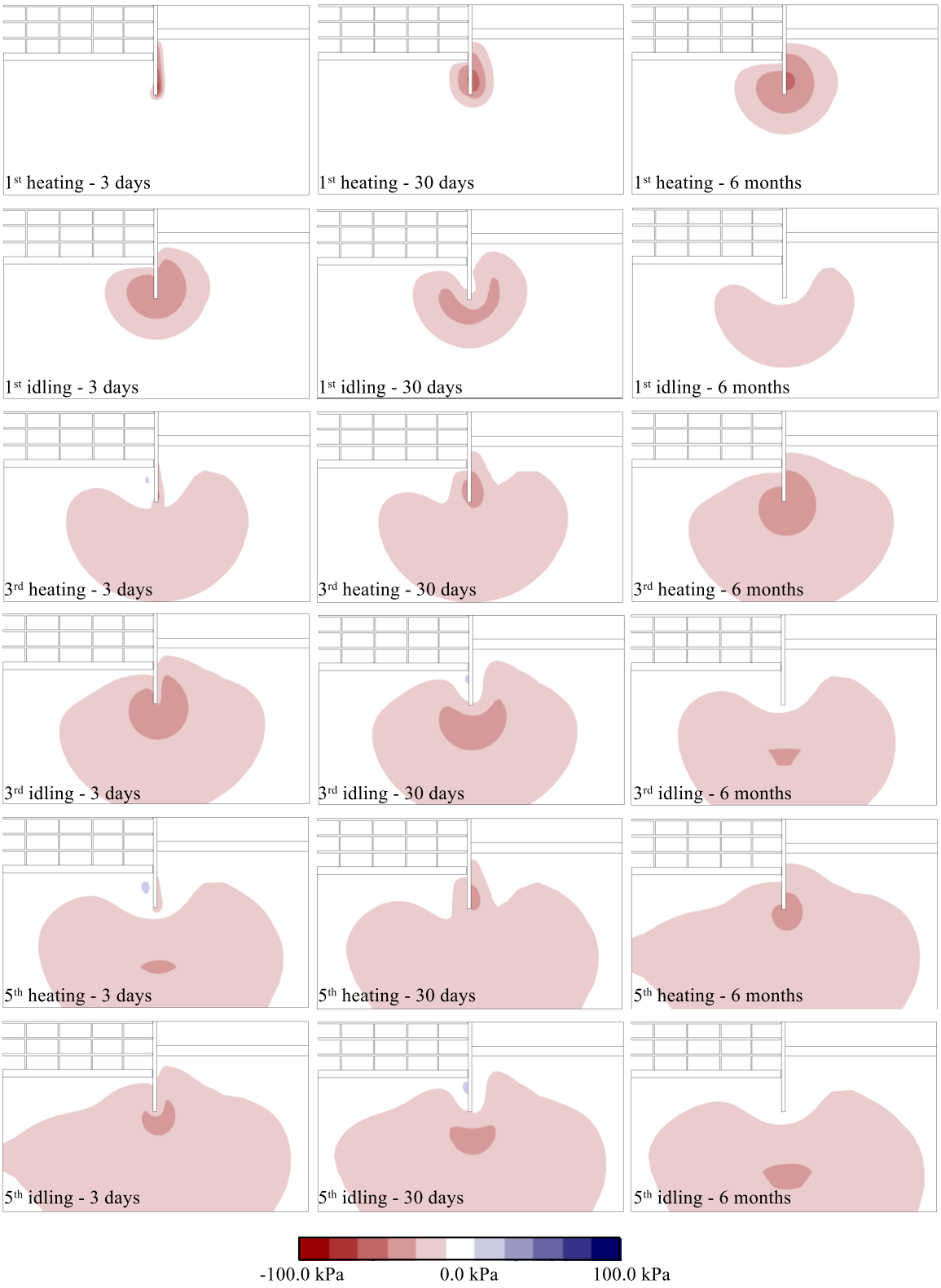

Figure 6-81: Scenario (2) - Contours of changes in excess pore water pressures at different time instants – CT

The changes in axial force are illustrated in Figure 6-82 and Figure 6-83. During the idling phase, the soil temperature decreases, though at a slower pace when compared to the cooling period in scenario (1). Thus, the compressive action due to soil contraction is lower than in the latter case. At the same time, since the soil temperatures remain with larger values and the thermal loading is applied by prescribing a given value of temperature, smaller temperature changes occur close to the wall during each subsequent period of heating, which also reduces the overall soil expansion and the tensile action during heating. Furthermore, the development of compressive excess pore water pressures generated during heating and their subsequent dissipation leads to soil settlement, inducing further compression within the wall. Consequently, in this scenario, the development of axial force during each cycle becomes increasingly more compressive, as can be clearly observed in Figure 6-83. The peak in compression during the last heating phase (point B in Figure 6-83) is equal to -30.0 kN/m and -60.0 kN/m, respectively for the NF and CT cases, indicating a large increase with respect to the first heating period (where the computed compressive axial force is approximately -20.0 kN/m for both cases – point A in Figure 6-83). After the first heating period, larger compressive axial forces and seasonal changes (e.g. changes from point B to B' in Figure 6-83) are evaluated for the CT case when compared to the NF case since larger temperature changes occur when such interaction is simulated along the wall-air interface. For both cases, it can be seen that the development of axial forces has not stabilised, indicating that the system is not in thermal equilibrium.

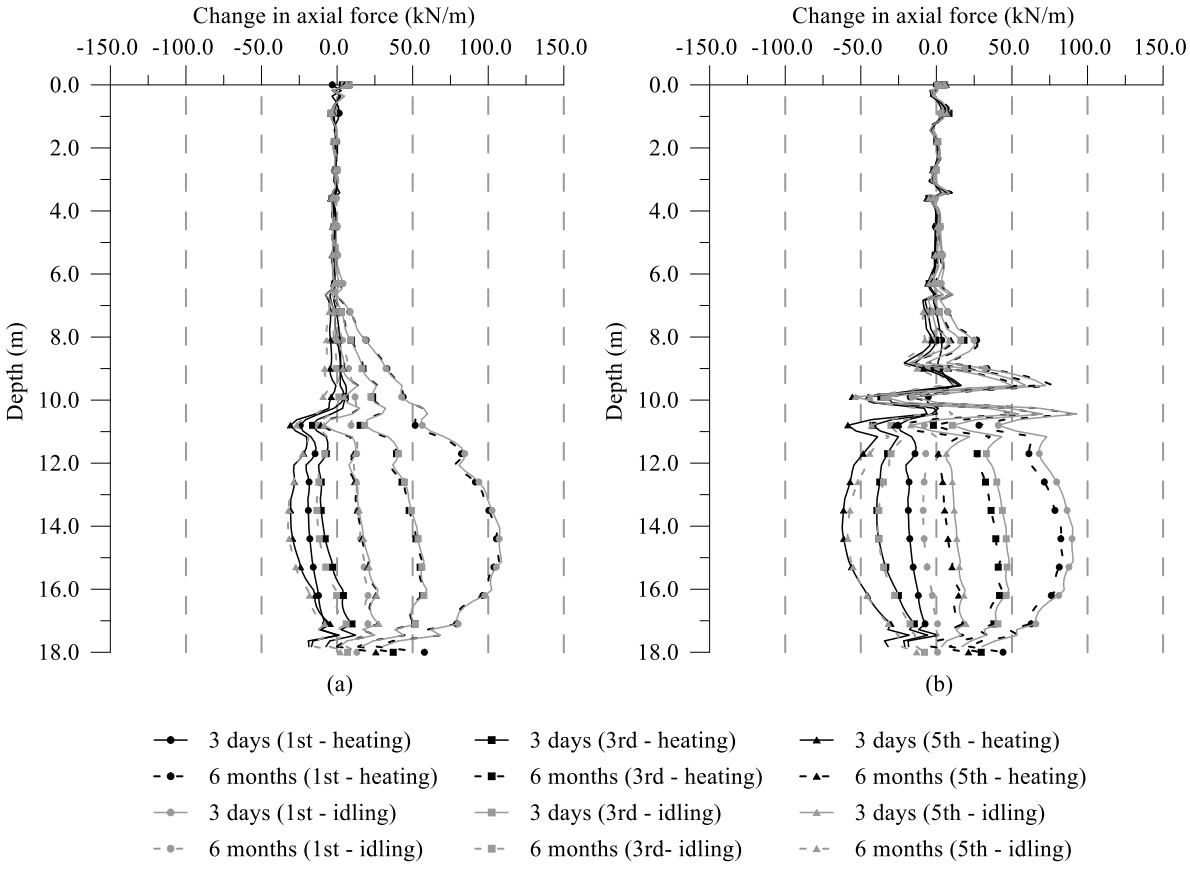

Figure 6-82: Scenario (2) - Change in axial force with depth at different time instants (a) NF and (b) CT

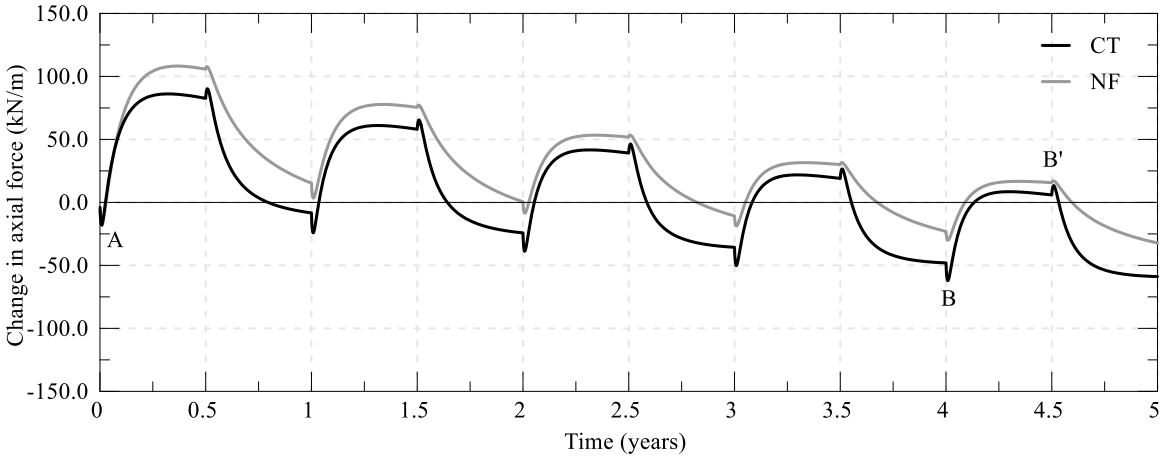

Figure 6-83: Scenario (2) - Change in axial force with time at depth of 14.0m

The changes in bending moment are displayed in Figure 6-84 and Figure 6-85. A different response is observed when comparing the NF and CT analyses, while the mechanism is the same as discussed for scenario (1). In the NF case, with time, the changes in bending moment reduce noticeably due to the uniform temperatures developing within the wall. Indeed, the temperatures prescribed during the heating and idling phases increase with each cycle, with the difference in temperature in the two periods decreasing with time, as shown in Figure 6-66 (b). Thus, the peak in bending moment developing at the beginning of each heating phase reduces with time (points A in Figure 6-85), since the temperature

change across the thickness of the wall reduces after each cycle and hence leads to limited seasonal changes. During the last heating phase, the peak in bending moment is equal to 20.0 kNm/m (a reduction of 45.0 kNm/m with respect to the first heating period). For the CT case, due to the constant temperature applied along the excavation boundary, a permanent temperature gradient exists, leading to an increase in positive bending moment during heating and a reduction during idling, since the temperatures are dissipated through the wall-air interface. In the first three cycles, the maximum bending moment during heating (points A' in Figure 6-85) increases since slightly larger temperatures are applied when compared to the first heating period of the CT case (see Figure 6-66 (b)), while it stabilises during the last two cycles, with a maximum change in bending moment of 210.0 kNm/m being computed. The reduction in bending moment during each idling phase reduces with time, since the changes in temperature are smaller during each subsequent cycle, as can be clearly seen from the temperature contours in Figure 6-79.

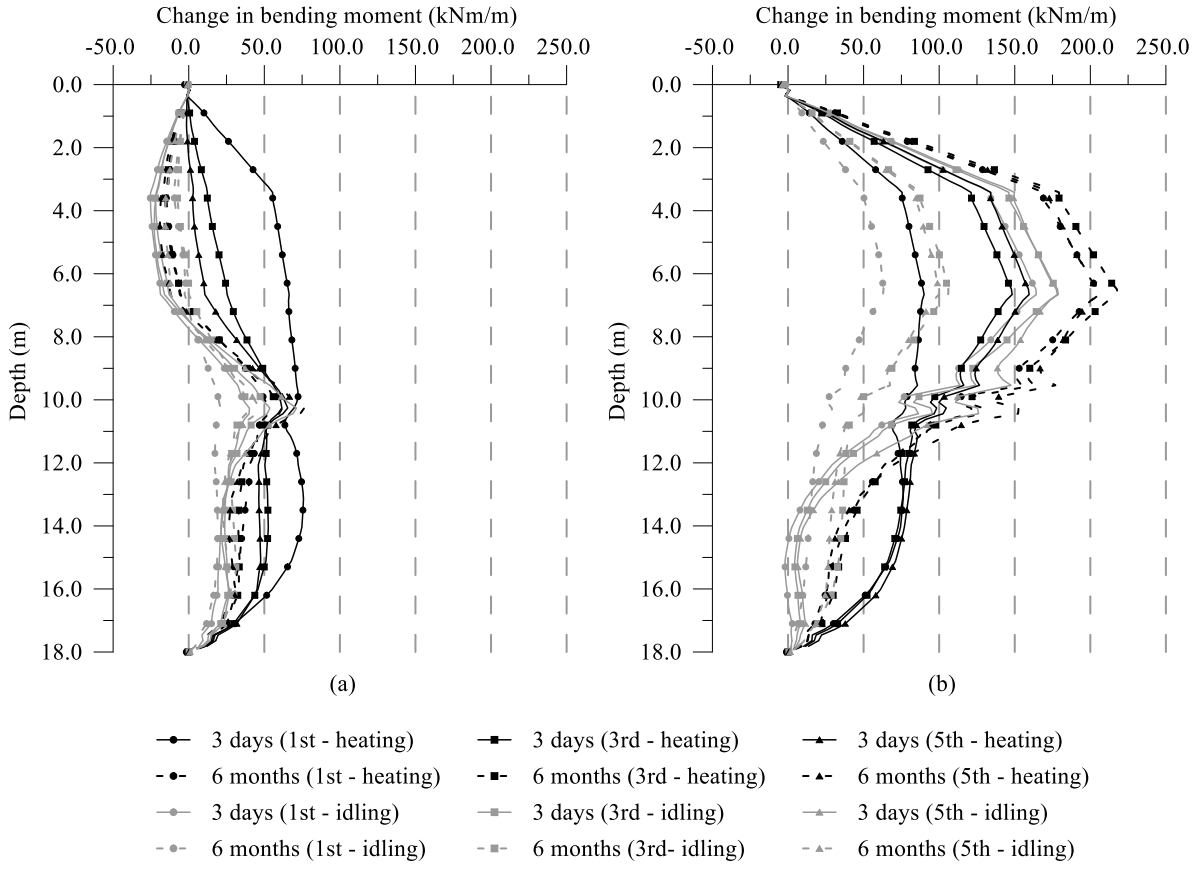

Figure 6-84: Scenario (2) - Change in bending moment with depth at different time instants (a) NF and (b) CT

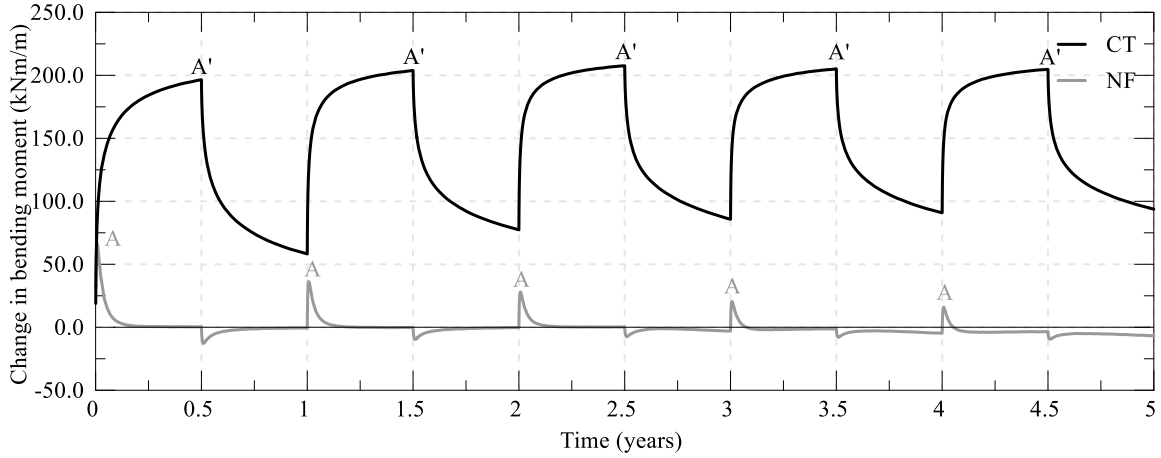

Figure 6-85: Scenario (2) - Change in bending moment with time at depth of 6.5 m

Wall and ground movements

The change in vertical movements of the wall with time is displayed in Figure 6-86. As the temperature in the wall and soil increases after each year of operation, an increase in upward vertical displacement is computed, reaching a maximum value of 7.3 mm and 4.7 mm at the end of the last heating period. This corresponds to an increase of 2.8 mm and 1.7 mm with respect to the maximum registered during the first heating period. Furthermore, the reduction in displacement observed during each idling phase decreases with time, as the slow recovery during this stage means that the average temperature of the soil steadily increases with time, with the dissipation of excess pore water pressures occurring at a slower pace. The movement of the wall has not stabilised yet, displaying an increase of 0.3 mm between the 4th and 5th year of operation.

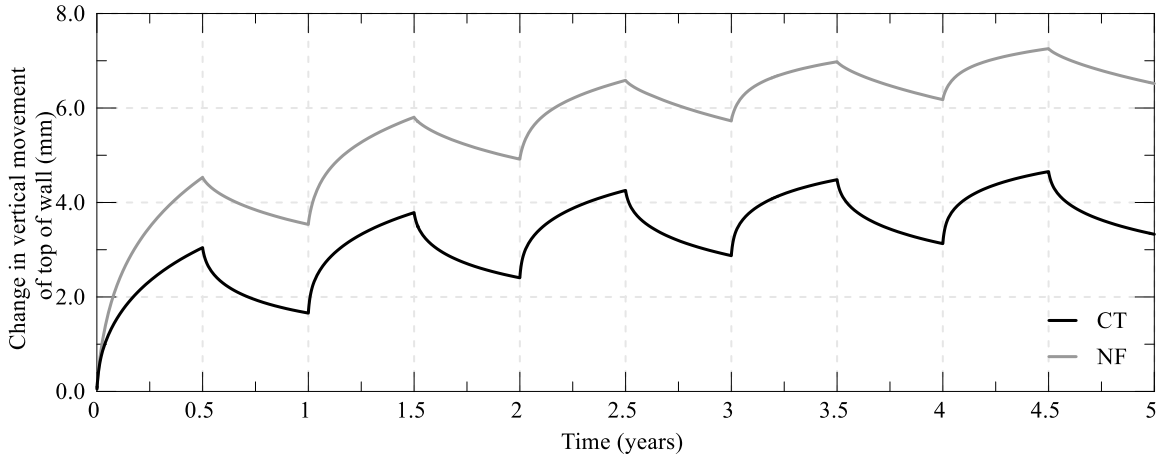

Figure 6-86: Scenario (2) - Change in vertical movement of top of wall with time

Figure 6-87 and Figure 6-88 display the changes in horizontal movement and the deformed shape for different time instants for the NF and CT cases, respectively. Similar to the previous case, the horizontal ground movements are highest on the retained side where the soil mass is less constrained, reaching values of up to 5.0 mm at the ground surface. During heating, the soil expands laterally towards the far field boundaries. The movements increase after each year of operation as a consequence of the general

increase in temperature. Within the excavation side, starting from the 3rd year, during the idling period a negative horizontal movement (i.e. towards the axis of symmetry) is registered at some distance below the base slab. This is attributed to the increase in temperature in this region in the long term. Furthermore, additional compressive excess pore water pressures, which lead to soil expansion, develop in the area where the movement is observed.

The deformed shape indicates an overall upward movement of the wall, the soil and the internal horizontal structures. These latter deform with the wall and are expected to be subjected to additional forces as a consequence of the upward movement and imposed deflection. Compared to the previous scenario, a much larger soil mass undergoes thermal expansion, where, along the ground surface, vertical movements larger than 1.0 mm are computed up to 30.0 m behind the wall, for both cases.

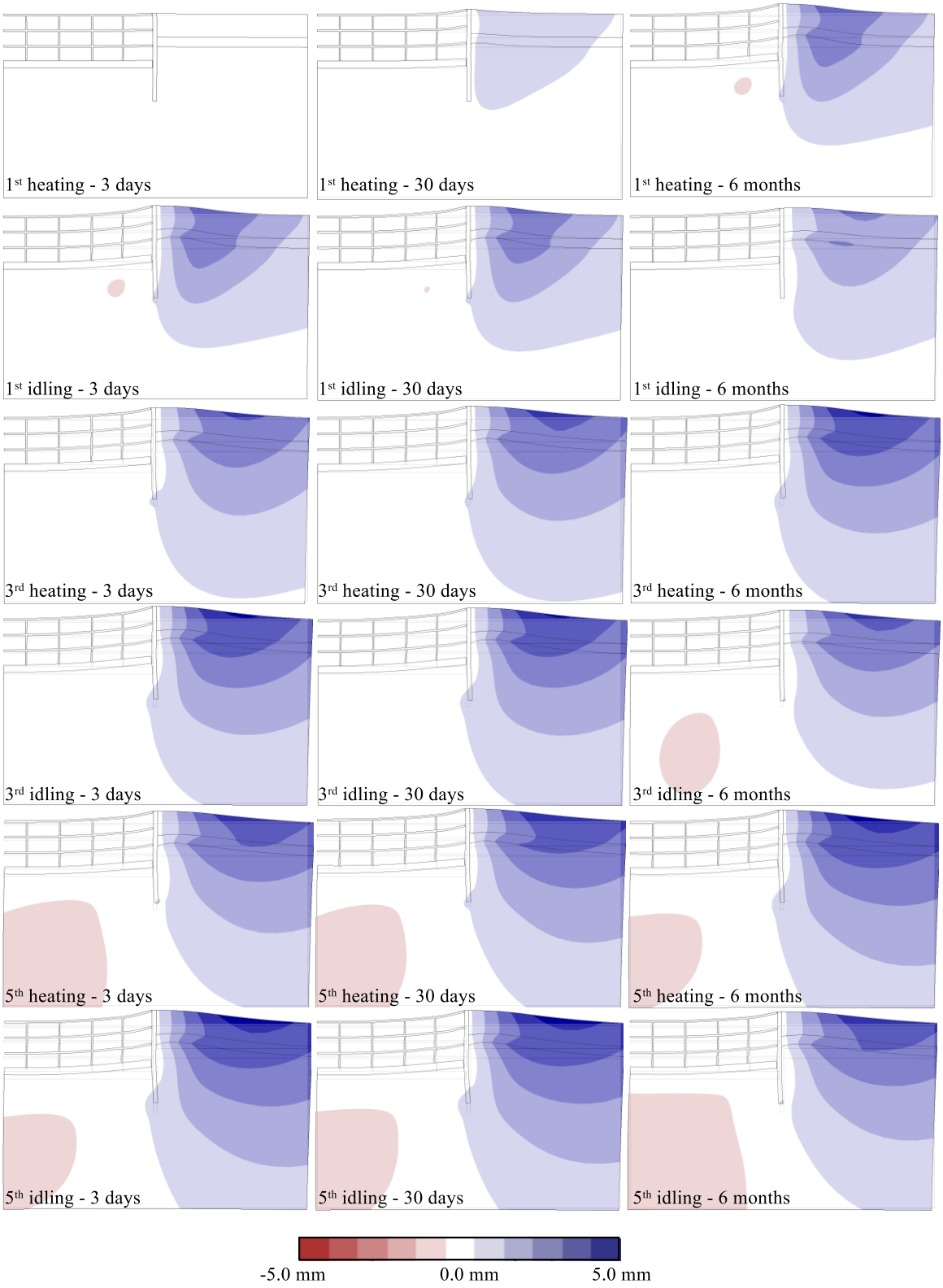

Figure 6-87: Scenario (2) - Contours of changes in horizontal movement at different time instants and deformed shape (exaggeration factor 500) - NF

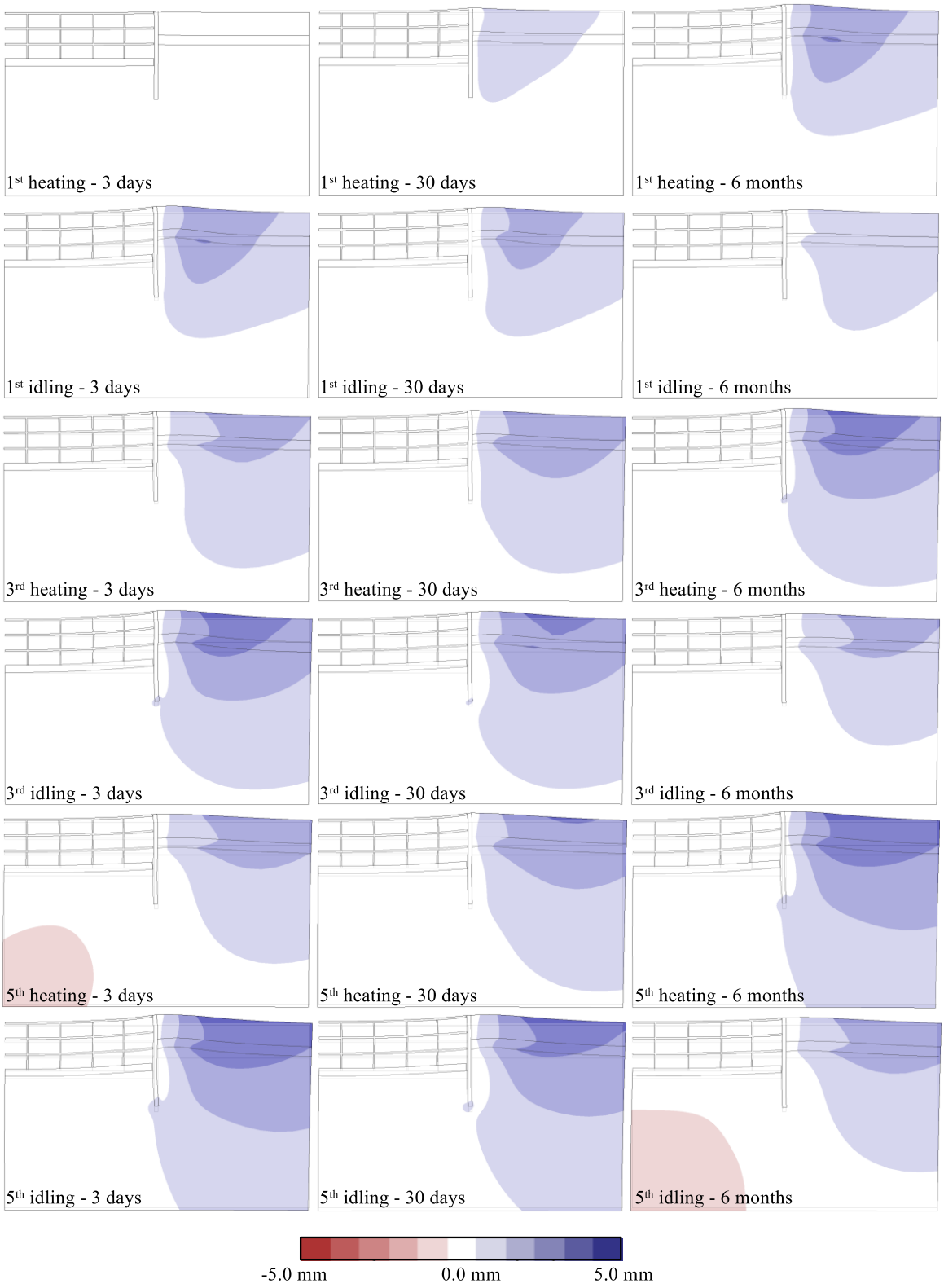

Figure 6-88: Scenario (2) - Contours of changes in horizontal movement at different time instants and deformed shape (exaggeration factor 500) – CT

6.5.4 Scenario (3)

Temperatures and pore water pressures

In scenario (3) 9 months of cooling followed by 3 months of heating are simulated. Since cooling prevails over heating, a permanent reduction in ground temperature develops close to the wall, as can be seen from the temperature contours displayed in Figure 6-89 and Figure 6-90, respectively for the NF and CT cases.

Figure 6-91 and Figure 6-92 show the contours of changes in pore water pressure for the NF and CT analyses, respectively. Initially (i.e. during the first 9 months), cooling induces tensile excess pore water pressures. With time, close to the wall, these reduce as they equilibrate. During heating, compressive excess pore water pressures develop, which steadily increase during the 3 months operation period as it lasts for a shorter amount of time when compared to cooling (and hence dissipation does not commence). In subsequent cooling periods, the tensile excess pore water pressures close to the wall are smaller in magnitude in comparison to the first period, since lower changes in temperature take place close to the wall and because of the compressive excess pore water pressures generated during the previous heating phases. However, tensile excess pore water pressures increase in regions further away from the wall, because they do not fully dissipate during the heating phases and concurrently the cold front moves further away. Furthermore, the time-dependent water flow leads to hydraulically-induced excess pore water pressures in regions where no change in temperature has taken place (i.e. towards the bottom of the mesh, see Chapter 3 for a detailed analysis of this phenomenon), leading to a large area of soil being subjected to changes in pore water pressure. Conversely, during heating, the compressive excess pore water pressures close to the wall increase during each subsequent heating period, reaching a maximum of -80.0 kPa and -65.0 kPa, for the NF and CT cases, respectively. The increase is attributed to the concurrent equilibration of the tensile excess pore water pressures generated during the previous cooling phase, which results in additional compressive excess pore water pressures. Indeed, as can be seen from the applied temperatures within the wall during the heating phases depicted in Figure 6-66 (c), these do not greatly change with time, hence the observed changes in pore water pressures are not related to higher temperatures.

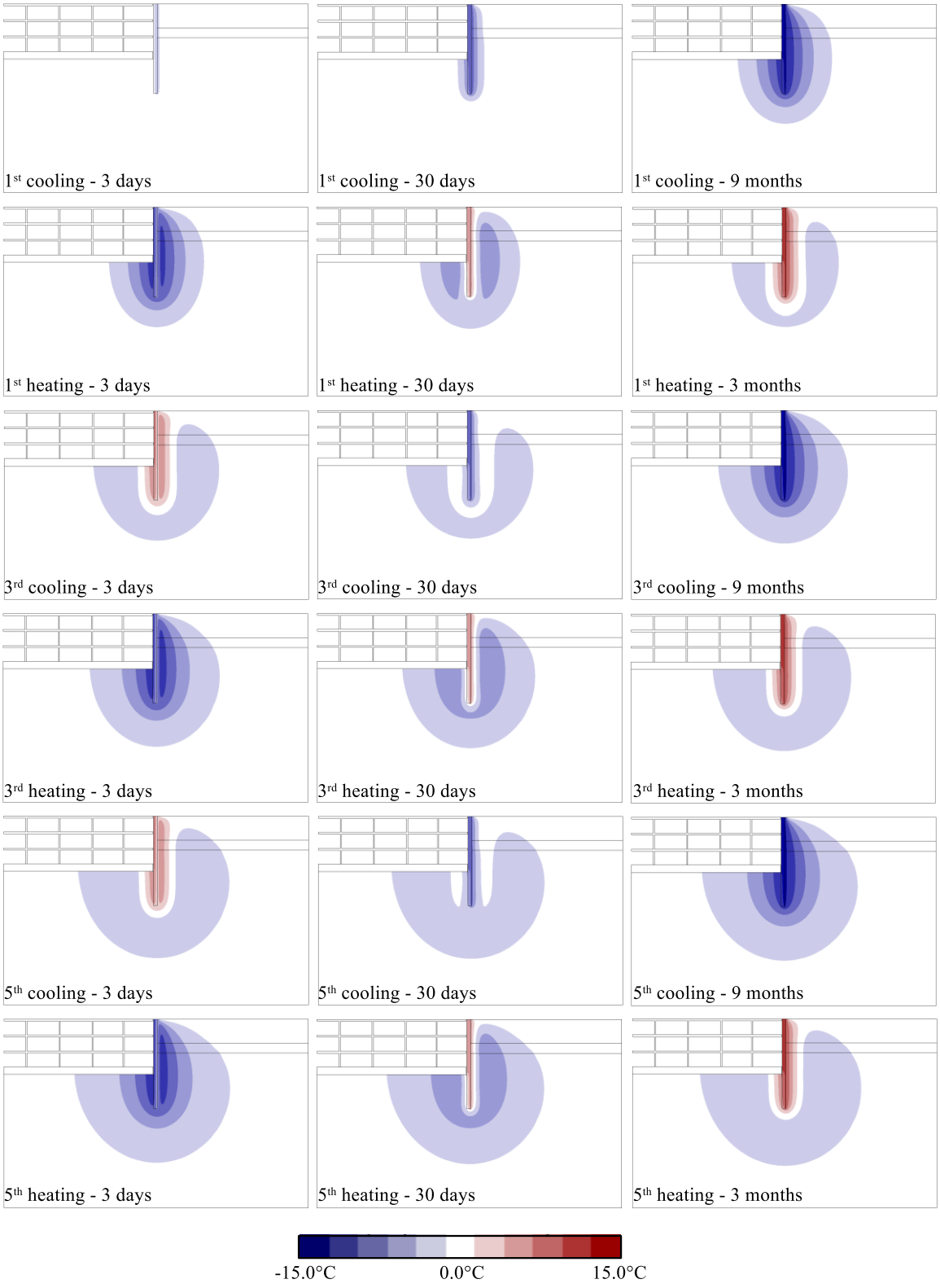

Figure 6-89: Scenario (3) - Contours of temperature changes at different time instants - NF

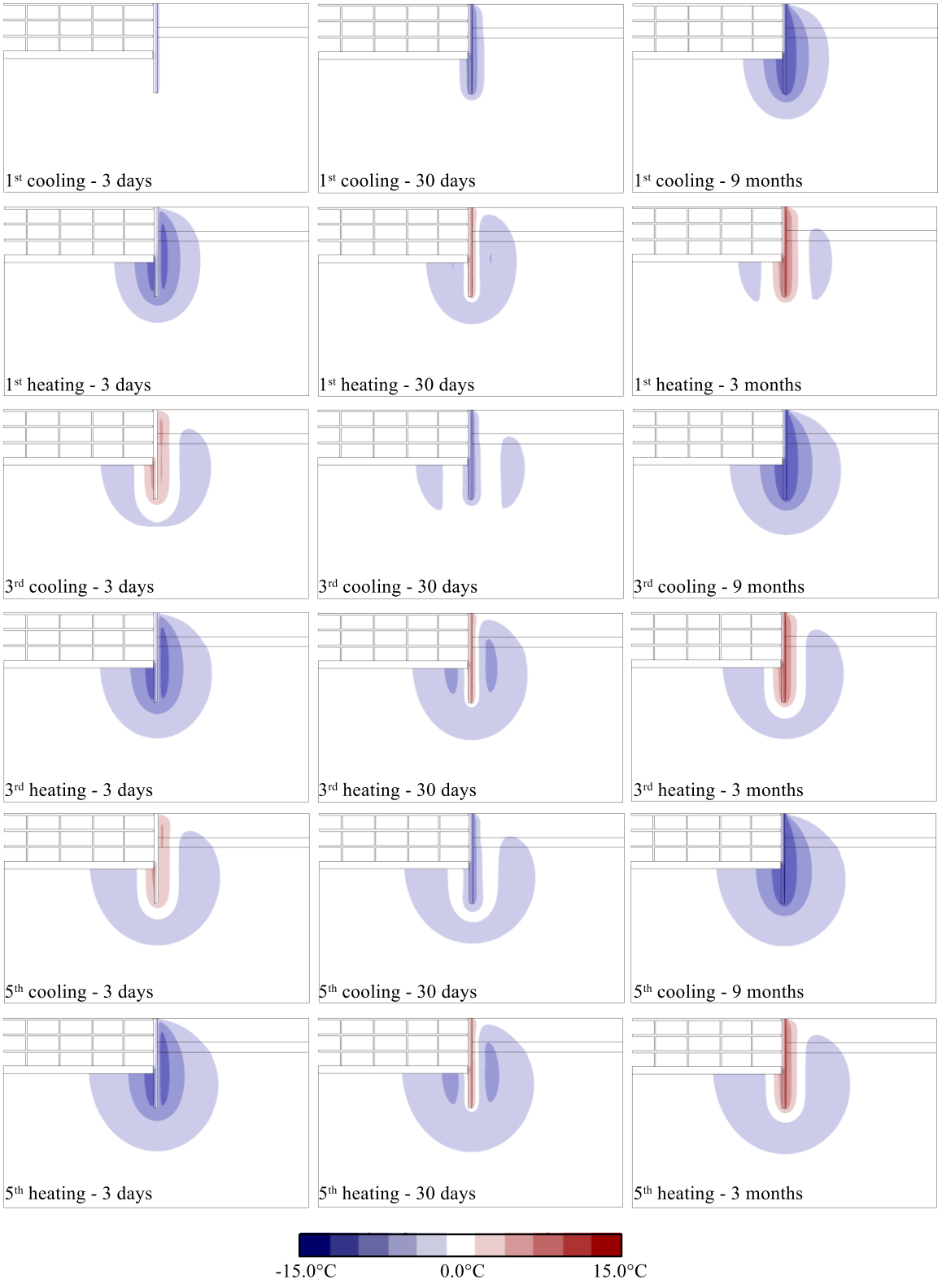

Figure 6-90: Scenario (3) - Contours of temperature changes at different time instants - CT

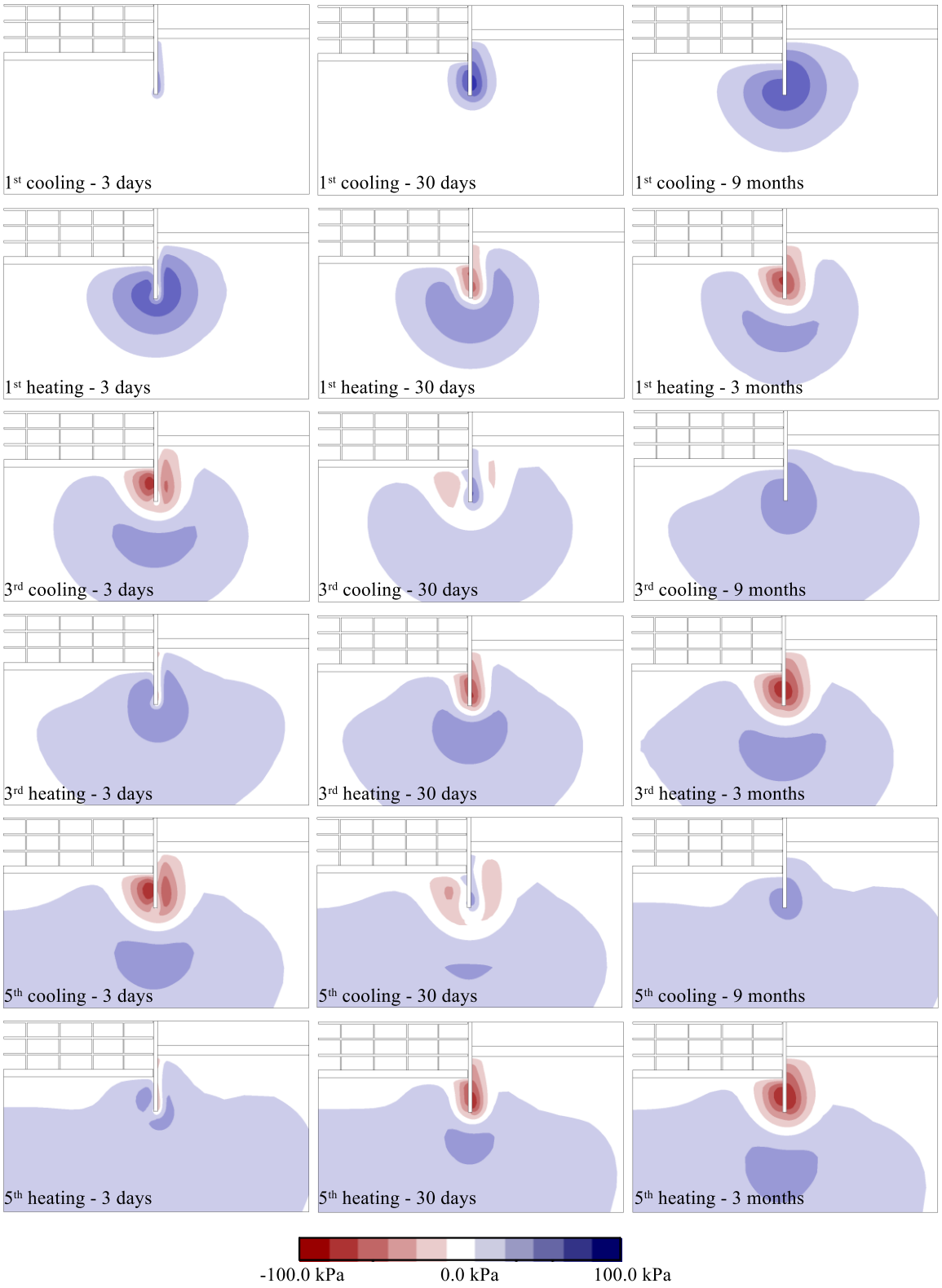

Figure 6-91: Scenario (3) - Contours of changes in excess pore water pressures at different time instants - NF

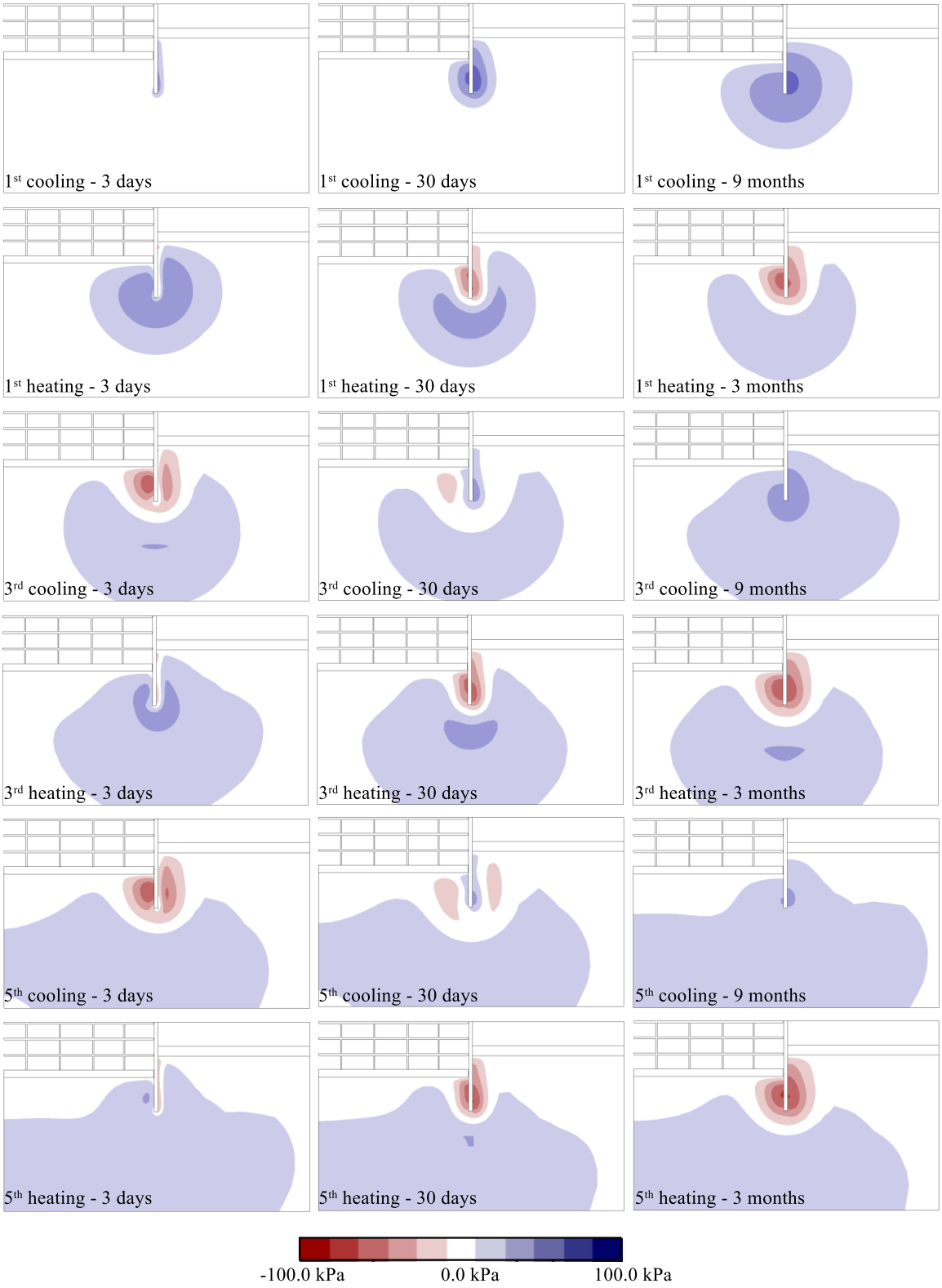

Figure 6-92: Scenario (3) - Contours of changes in excess pore water pressures at different time instants – CT

Axial forces and bending moments

Overall, since in this scenario cooling is simulated first, the opposite behaviour than that observed in scenario (1) is expected. Furthermore, as the cooling period is longer, its effect prevails when the response of the wall is analysed. This can be observed by examining the development of axial forces, depicted in Figure 6-93 and Figure 6-94. At the beginning of the cooling period, the wall is subjected to tensile axial forces (e.g. point A in Figure 6-94) due to the restriction the soil applies against thermal contraction of the wall induced by the reduction in temperature. This is then followed by a compressive action as the soil cools down (from point A to A' in Figure 6-94), while the opposite occurs during heating (i.e. change from point B to B' in Figure 6-94). A cyclic behaviour is observed similar to scenario (1), with peaks of compressive and tensile forces of ranging between -135.0 kN/m and 120.0 kN/m, with larger changes computed in the NF case due to larger temperature changes.

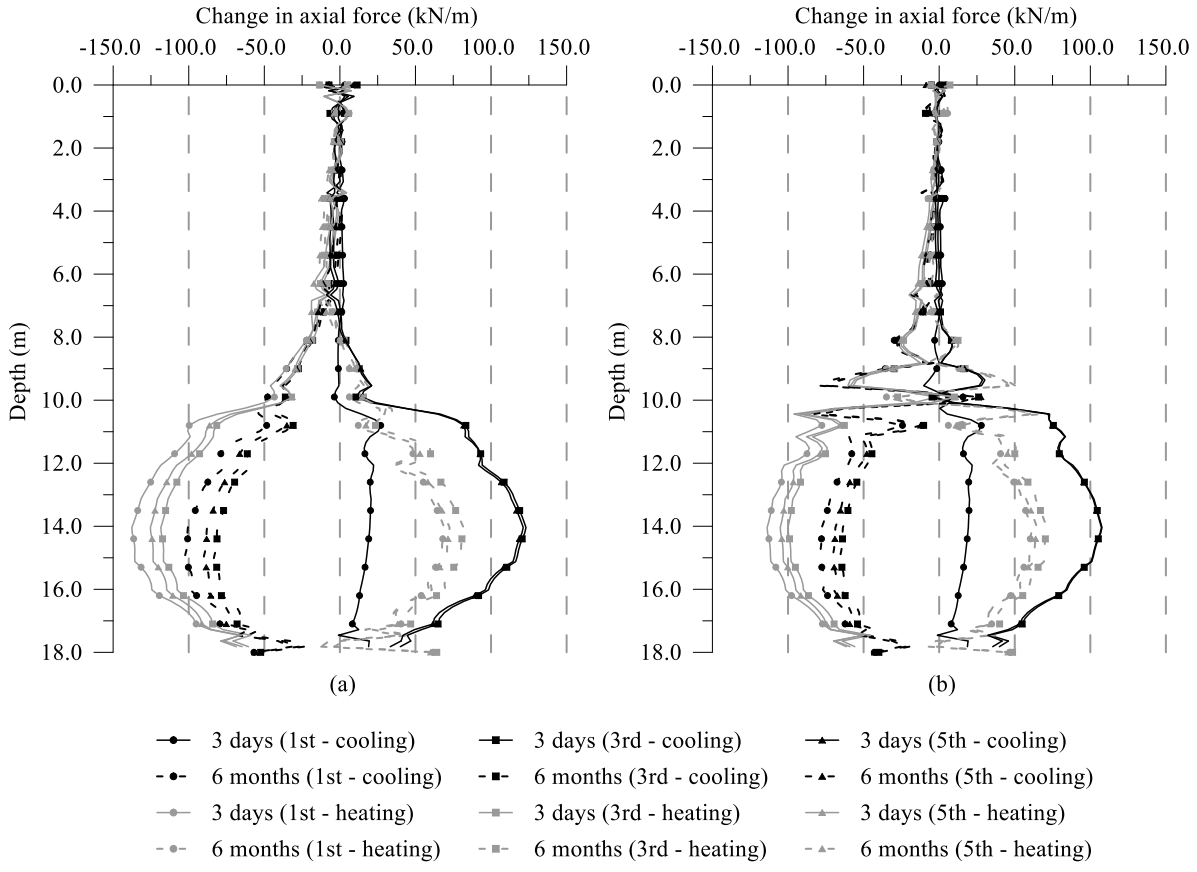

Figure 6-93: Scenario (3) - Change in axial force with depth at different time instants

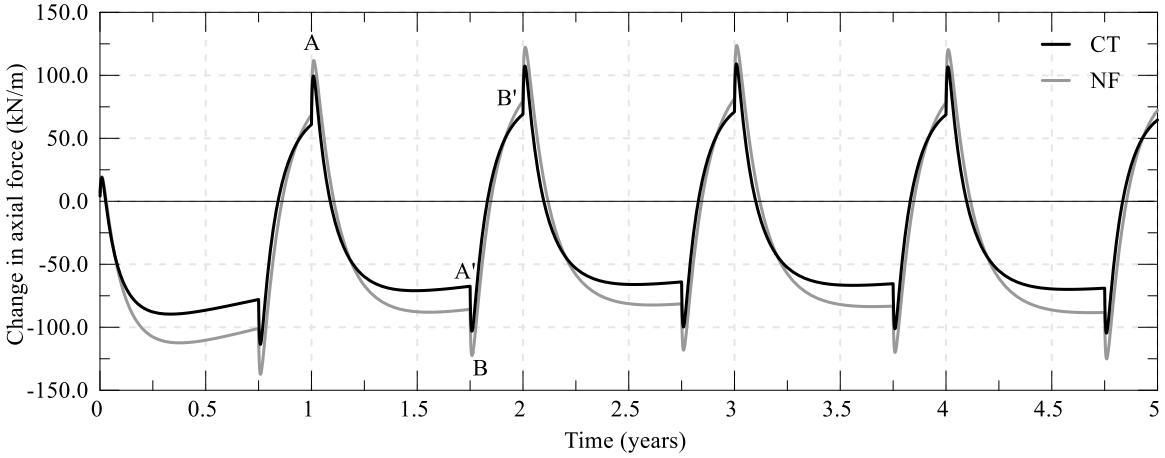

Figure 6-94: Scenario (3) - Change in axial force with time at depth of 14.0m

The development of the bending moment, reported in Figure 6-95 and Figure 6-96, is similar to that observed in scenario (1) given the similar magnitudes of applied temperatures (see Figure 6-66). For the NF case, the peak values registered during cooling and heating have a similar magnitude, of approximately ±125.0 kNm/m. Furthermore, the reduction in bending moment computed during cooling and heating (i.e. respectively points A-A' compared to B-B' in Figure 6-96) is also similar since the temperatures within the wall become quickly uniform. Conversely, for the CT case, a larger peak value is computed during the cooling phase since this lasts for a longer period of time and hence a higher temperature difference across the wall develops (e.g. compare point C and D in Figure 6-96). The maximum change in bending moment recorded is equal to -200 kNm/m and 165.0 kNm/m, respectively during cooling and heating.

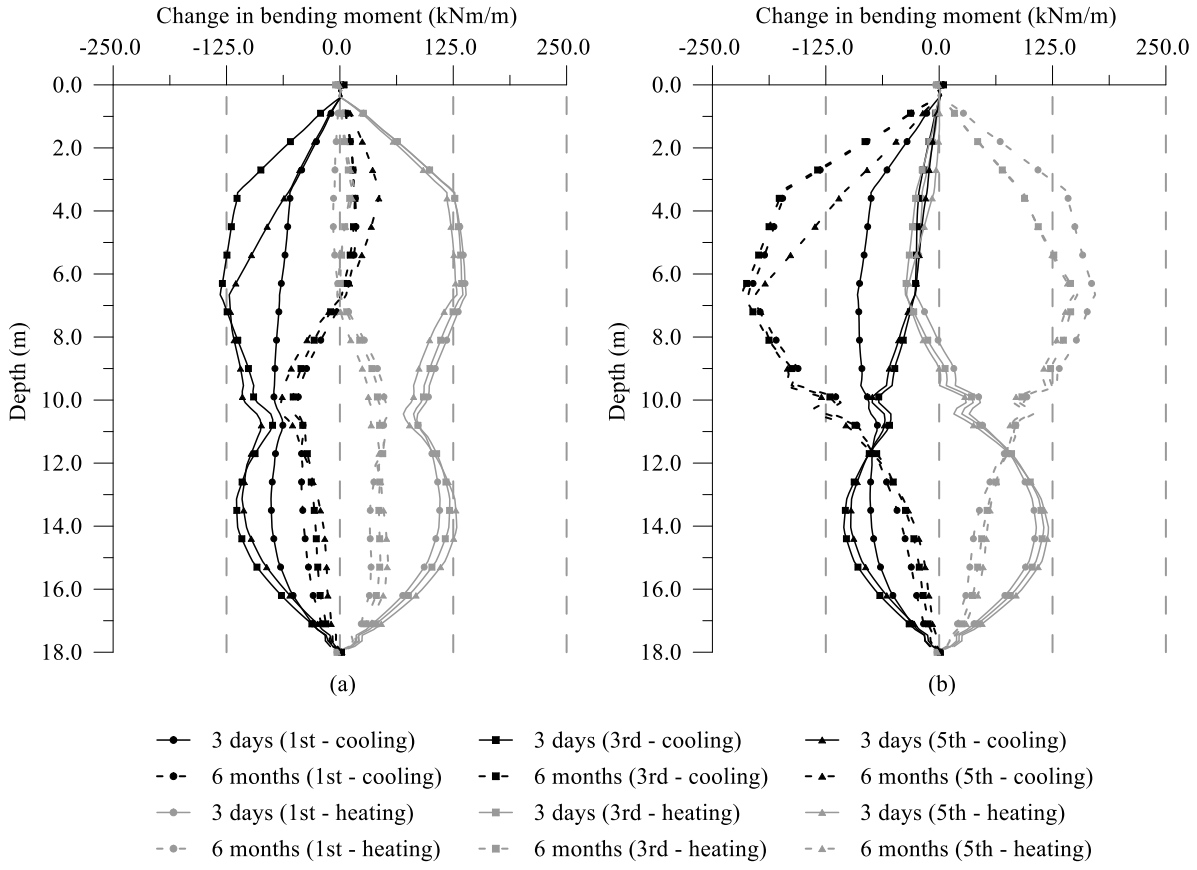

Figure 6-95: Scenario (3) - Change in bending moment with depth at different time instants (a) NF and (b) CT

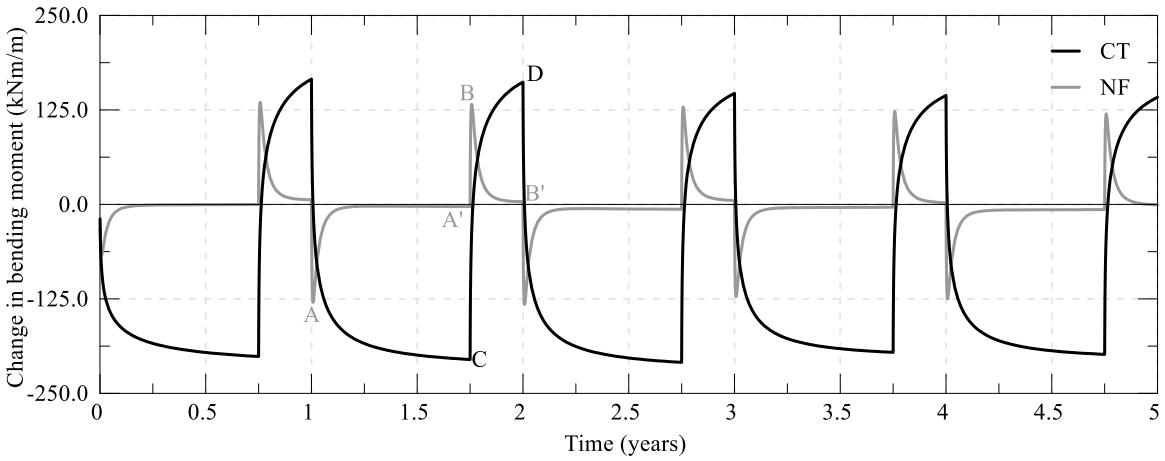

Figure 6-96: Scenario (3) - Change in bending moment with time at depth of 6.5 m

Wall and ground movements

The unbalanced operation pattern and permanent temperature changes clearly lead to a downward long-term movement of the wall, as shown in Figure 6-97. The maximum change recorded is equal to -6.8 mm and -4.6 mm at the end of the last cooling phase, for the NF and CT analyses respectively. Thus, an increase of respectively 1.8 mm and 1.2 mm with respect to the first cooling period is registered. The upward movement during heating is similar in each subsequent year, leading to a change

of 6.5 mm and 4.5 mm in one season, for the NF and CT cases, respectively. Thus, while the seasonal changes are lower when compared to scenario (1), the accumulated movement is larger.

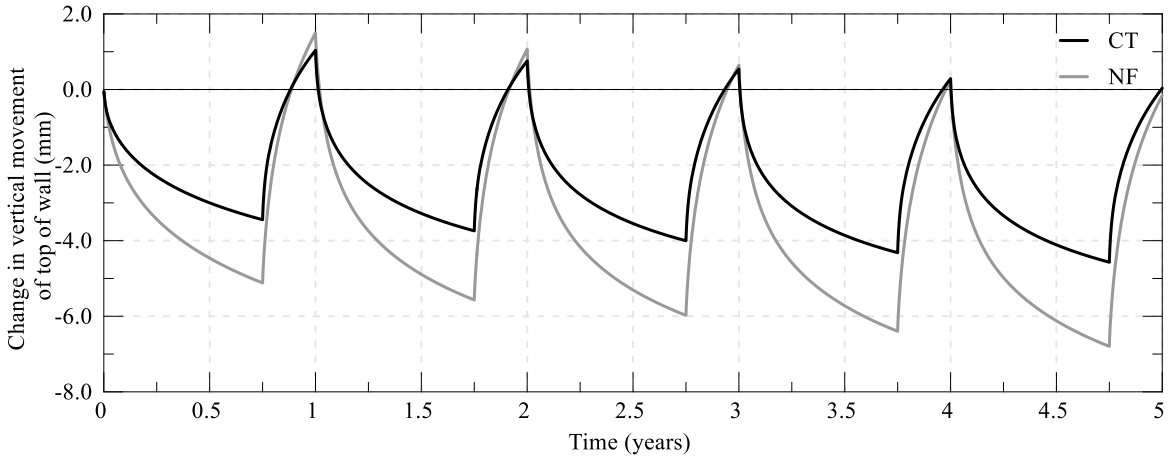

Figure 6-97: Scenario (3) - Change in vertical movement of top of wall with time

The contours of horizontal movement together with the deformed shape are illustrated in Figure 6-98 and Figure 6-99, respectively for NF and CT cases. During cooling, the soil contracts and hence the soil on the retained side displaces towards the wall, while the opposite occurs during heating. The magnitude and extent of horizontal movements are clearly larger during cooling since it lasts for a longer period of time. At the end of each heating period, the largest horizontal movements occur close to the wall. Different from the other scenarios, these take place also within the excavated side in proximity of the wall. These may be related to the development of significant compressive excess pore water pressures, due to the large difference between the reduced soil temperature after 9 months of cooling and the applied heating at the wall, which induce soil expansion. Similar to the vertical movements of the wall, the vertical movement of the ground surface displays settlement during each cooling period and heave during each heating period. With time, a permanent settlement is registered. The area affected by movements >5.0 mm extends up to 10.0 m and 5.0 m from the wall, respectively for the NF and CT analyses.

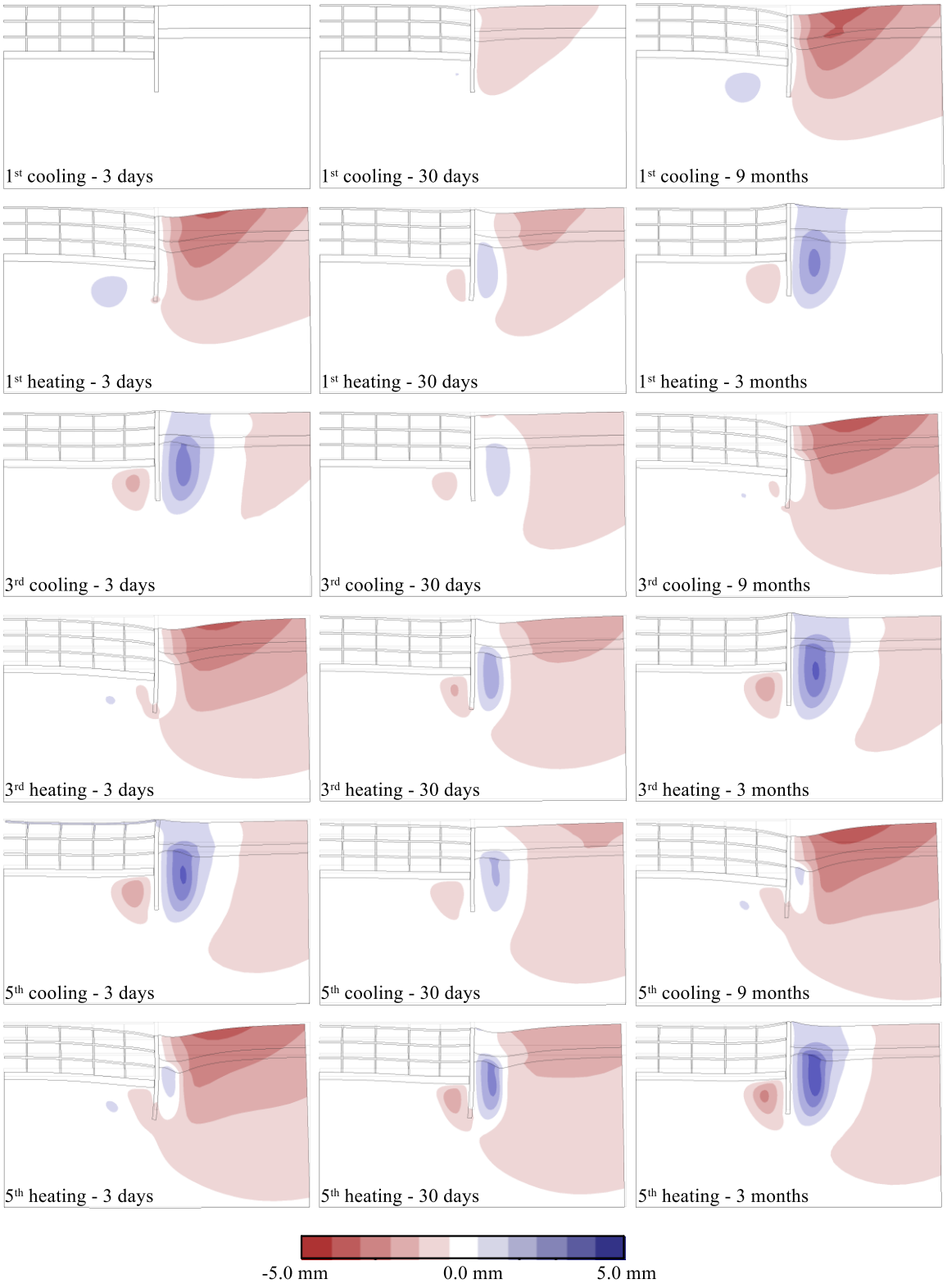

Figure 6-98: Scenario (3) - Contours of changes in horizontal movement at different time instants and deformed shape (exaggeration factor 500) - NF

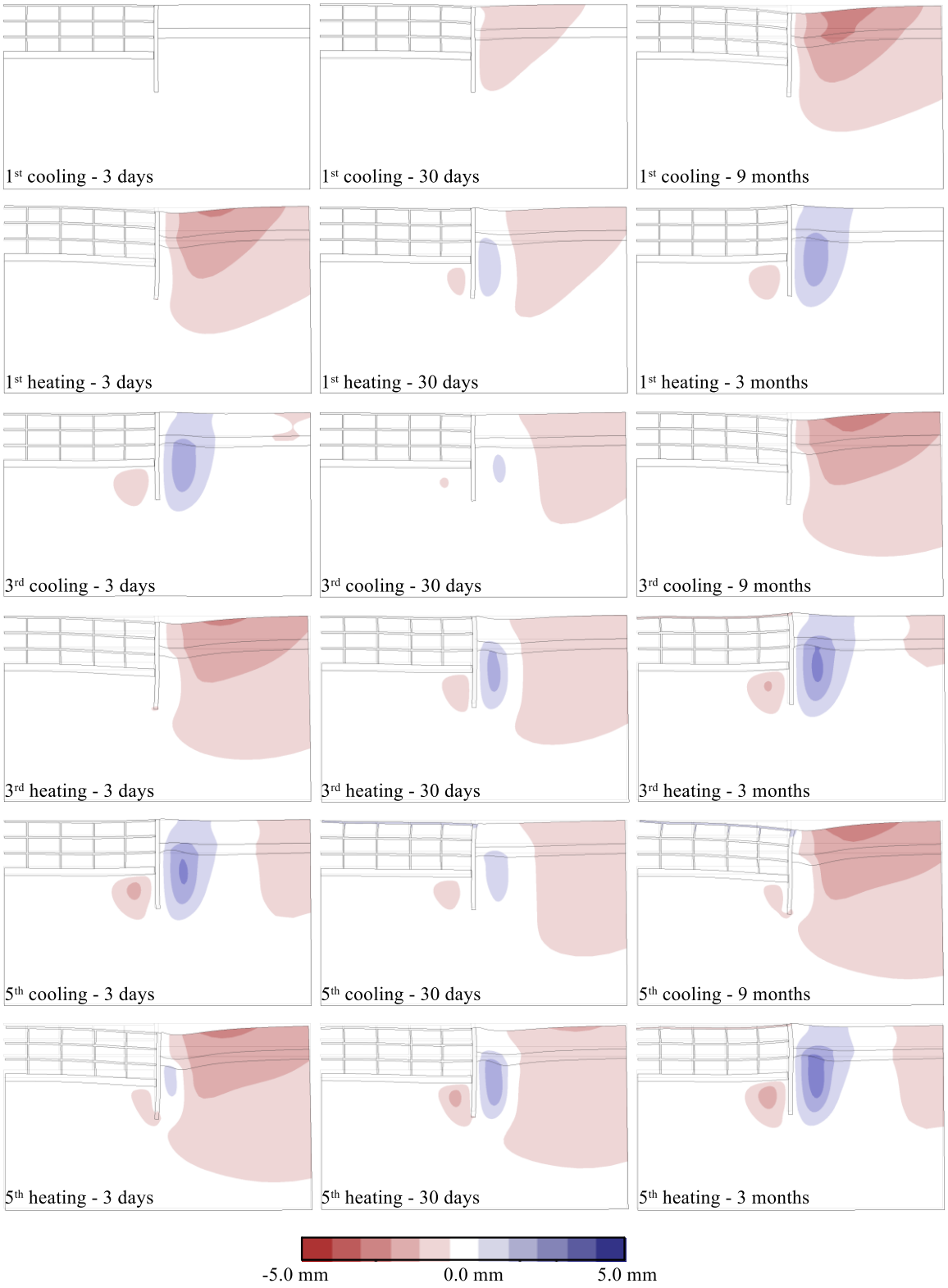

Figure 6-99: Scenario (3) - Contours of changes in horizontal movement at different time instants and deformed shape (exaggeration factor 500) - CT

6.6 Summary and conclusions

The first part of this Chapter investigates the behaviour of thermo-active retaining walls modelled in three-dimensional (3D) fully coupled THM analyses, to provide insights into the behaviour of these structures when the heat exchanger pipes are included. Furthermore, it allows the evaluation of 3D effects occurring due to the non-uniform temperature across the width of the wall, as well as providing benchmark results to assess thermo-active walls modelled in two-dimensional (2D) plane-strain analyses.

The first study presented in Section 6.2 carried out in 3D is based on the deep basement presented in Wood & Perrin (1984b) and analysed in Chapter 3 and aims at identifying the main mechanisms occurring in thermo-active walls simulated in 3D and at evaluating the effect of the boundary condition along the exposed face of the wall. Subsequently, a parametric study on an idealised problem of a 20.0 m long wall embedded in London Clay was carried out to evaluate the effect of geometric characteristics (excavation depth and panel width) and thermal parameters (thermal conductivity of concrete and soil diffusivity) on the thermo-mechanical response of the wall. Lastly, the effect of the adopted modelling approach to simulate the heat exchange (i.e. modelling approach 1 or 2 outlined in Chapter 4) is investigated. For each analysis, the wall-air interaction was varied to simulate both insulated walls (NF) and walls maintained at a constant temperature (CT). Furthermore, these analyses comprise 6 months of heating, i.e. heat injection. The main conclusion of these studies can be summarised as follows (if not specified, the forces are intended as average across the wall panel):

- the axial forces are not largely affected by the boundary condition along the exposed face and generally follow the same mechanisms outlined in Chapter 3, with slightly lower changes in forces computed when compared to the preliminary 2D THM analyses presented in Chapter 3. This is due to the slower heat transfer rate simulated when heat exchanger pipes are included in the model;
- bending moments due to temperature changes are no longer related to the deformed shape of the wall due to the development of mechanical strains as a consequence of temperature differentials across the wall's thickness. The magnitude of the change in bending moment is largely affected by the boundary condition along the exposed face of the wall, where this is significantly larger when a constant temperature is simulated, especially in the long term;
- larger temperatures and thus a larger soil thermal expansion is computed for insulated walls. This translates into larger vertical wall movements;
- out-of-plane effects exist due to non-uniform temperatures across the width of the wall which affect the distribution of forces. These are more significant in the short term, where larger temperature differences are registered, and lead to important variations in the distribution of changes in axial forces in the out-of-plane direction. These are affected by the boundary condition along the exposed face of the wall and are larger when a constant temperature is simulated;

- the excavation depth influences the magnitude of forces and displacements of the wall. A larger excavation depth leads to smaller axial forces, but to larger bending moments, which increase significantly when a constant temperature is simulated. For this case, given the differences in temperature, larger wall displacements are computed for a smaller depth of excavation;
- decreasing the width of the panel reduces the spacing between the heat exchanger pipes and thus leads to higher temperatures within the wall. These marginally affect the development of axial forces, despite leading to larger bending moments, especially for the CT case. Furthermore, larger vertical wall movements are computed;
- changing the concrete thermal conductivity affects mainly the vertical movements of the wall, where larger movements are computed for a larger thermal conductivity. Indeed, this parameter leads to higher temperatures and thus a larger thermal expansion. Furthermore, its effect is more pronounced for the NF cases, although the relative difference is equal for both boundary conditions;
- adopting different thermal parameters for the soil affects the temperature distribution within it and thus its thermal expansion. Hence, larger changes in axial forces are computed for a higher soil thermal diffusivity. Furthermore, this leads to larger wall vertical movements;
- the modelling approach employed to simulate the heat exchange in 3D analyses marginally affects the wall's response since similar temperatures develop in the long term. Indeed, it mainly affects the development of the bending moment and wall movement with time, which increase at a slower pace when modelling approach 2 is adopted, although similar values are reached at the end of operation.

In Section 6.3, two different modelling approaches to simulate thermo-active walls in two-dimensional analyses are explored and the results compared to those obtained in 3D by simulating the Wood & Perrin (1984b) geometry. The two approaches, named LINE and PIPE, consist of applying either a prescribed temperature along a line equal to the inlet temperature in 3D or simulating the presence of a heat exchanger pipe and adopting the approximation procedures described in Chapter 5 for estimating the thermal performance of thermo-active retaining walls. It is shown that both approaches overestimate the changes in forces and displacements and are not able to reproduce the transient behaviour with acceptable levels of accuracy. Smaller differences are computed for the PIPE analyses with a constant temperature along the exposed face of the wall, since lower inlet temperatures are applied. Given the large discrepancies obtained with these approaches, it was deemed necessary to establish a new method to enable a closer approximation to the response observed in 3D. Furthermore, since the 2D analyses do not allow to take into account the aforementioned variation in forces in the out-of-plane effects, an analytical procedure was developed to evaluate the variation in axial forces due to temperature variations in the out-of-plane direction.

The proposed method is presented in Section 6.4 and replaces the use of special one-dimensional elements for simulating the presence of heat exchanger pipes with the use of thermal boundary

conditions, which are readily available in most FE codes. Indeed, the proposed methodology consists of performing first 2D analyses in plan view (termed herein 2D plan analyses), through which the temperature to be applied in the 2D THM plane-strain analyses, $T_{i,2D}$, of the wall are evaluated. The main assumption of this method lies in the applied temperature within the 2D plan analyses, which require an estimation of the temperature differential between the pipe inlet and outlet, ΔT_p. A study on this parameter has shown that its effect is small provided that sensible values are employed. The applicability of the proposed approach has been validated for numerous cases, which included varying the wall geometry, the depth of excavation, the thermal parameters of soil and concrete and the thermal boundary condition along the exposed face of the wall. It was shown that the 2D analyses are able to reproduce with a high level of accuracy the average wall behaviour computed by the original analyses in 3D. Similarly, a good estimate of the additional forces due to out-of-plane effects within a 3D problem is provided by the proposed analytical procedure. Thus, a useful and practical methodology for the design of thermo-active walls was established, enabling a reduction of the required computational effort associated with the accurate modelling of these complex structures.

After having established a consistent modelling approach in 2D, the long-term THM response under different scenarios of cyclic thermal loading is evaluated in Section 6.5. The three scenarios analysed are (1) 6 months of heating followed by 6 months of cooling, (2) 6 months of heating followed by 6 months of idling and (3) 9 months of cooling followed by 3 months of heating. It should be noted that heating and cooling refer to the soil circuit and are therefore intended as heat injection and extraction, respectively. For each case, 5 years of operation are simulated. The analyses show the influence of the complex coupled THM behaviour, with changes in temperature and pore water pressures affecting substantially the results. Indeed, even if in scenario (1) the temperature changes do not vary greatly during subsequent cycles, the changes in pore water pressures differ from the first to the last cycle, inducing an overall compressive action into the wall and a downward vertical movement with time. Clearly, when an unbalanced system is simulated, these phenomena are accentuated, which is the case for scenario (2) and (3). In such cases, a much larger soil mass undergoes permanent changes in temperatures and pore water pressures, which leads to the vertical ground movements extending for a significant distance behind the wall and large changes in wall displacement being computed. The heat exchange leads to changes in structural forces of approximately $\pm$20% of the values recorded at the start of the operation. Furthermore, significant seasonal changes in vertical wall movement, of up to 8.0 mm, are recorded. Lastly, the study showed that, especially when an unbalanced system is to be designed, multiple years of operation should be simulated to account for the long-term behaviour of the wall, as large changes may occur after subsequent cycles of cooling and heating. This is particularly important in the case of the serviceability of the wall itself and any nearby structures, since it was observed that long-term movements develop in such cases, which cannot be taken into account if only one year of operation is simulated.

Chapter 7
Conclusions and future research

7.1 Introduction

The objective of the research presented in this thesis was to assess the energy efficiency and structural behaviour of thermo-active retaining walls through numerical analyses using the Imperial College Finite Element Program (ICFEP, Potts & Zdravković, 1999). For this purpose, numerous studies were performed to establish appropriate modelling procedures, both in three-dimensional (3D) and two-dimensional (2D) analyses, and to investigate in detail the influence of a variety of parameters on these structures' thermal performance and structural response.

In an extensive literature review (Chapter 2), the lack of field and laboratory studies undertaken to assess the behaviour of thermo-active retaining walls was highlighted. Furthermore, the need for consistent modelling approaches in terms of numerical analyses, together with a sound understanding of the complex phenomena taking place within fully coupled thermo-hydro-mechanical (THM) analyses was outlined. Thus, increasingly complex analyses were performed to improve the understanding of the structural response and thermal performance of thermo-active retaining walls. The preliminary studies presented in Chapter 3 investigated in detail the development of the THM interactions in simple, one-dimensional problems and the results were employed to establish an interpretative framework, which is subsequently used throughout this thesis to evaluate and assess boundary value problems simulating thermo-active walls. The effect of the THM interactions on the transient response of the wall was explored in Chapter 3 by performing analyses with different modelling approaches, where one or more components of the THM formulation were inactive and hence the effect of different phenomena could be isolated. These analyses were modelled in 2D with the heat

transfer being modelled employing a simple thermal boundary condition to assess the fundamental aspects of the behaviour of thermo-active retaining walls. In Chapter 4, the modelling procedure for 3D analyses, including the explicit simulation of the heat exchanger pipes, was explained in detail and validated against field data. Furthermore, the effect of the boundary condition along the exposed face of the wall on temperature distributions with time and the heat transfer mechanisms from the structure to the ground was assessed. These aspects were further investigated in Chapter 5, in which approximations for the estimation of the energy efficiency of thermo-active retaining walls by means of 2D plane-strain analyses were established. The thermo-mechanical behaviour in 3D, fully coupled THM analyses and the implication of non-uniform temperature distributions across the thickness and width of the wall on the structure's response was subsequently investigated in Chapter 6. A new method to capture the transient thermo-mechanical behaviour of thermo-active retaining walls was also established, which was shown to produce more accurate results when compared to the conventional approaches employed in literature. Throughout this thesis, the effect of problem parameters, such as thermal and thermo-mechanical properties of soil and concrete, the geometry of the wall and the configuration of heat exchanger pipes, on the development of the THM interactions (Chapter 3), the thermal performance (Chapter 5) and the thermo-mechanical response (Chapter 6) was examined. Furthermore, long-term analyses with different scenarios of cyclic heating and cooling were carried out to evaluate the effect on the energy efficiency (Chapter 5) and the structural response (Chapter 6) of thermo-active retaining walls.

In the following sections, the main conclusions of this research are presented and, within the last part of this chapter, topics for future research are proposed.

7.2 Thermo-hydro-mechanical interactions and impacts on thermo-active wall behaviour

Problems involving thermo-active structures imply that changes in temperature occur both within the structure and the surrounding soil. Since the latter, when saturated, is a two-phase material, fully coupled THM analyses are required to capture the transient phenomena taking place, some of which occur simultaneously. Indeed, changes in temperature of a material lead to its thermal expansion/contraction, which may be mechanically restrained, inducing additional stresses. Within soils, excess pore water pressures develop as a consequence of changes in temperature. These are mainly related to the differential thermal expansion between water and soil (i.e. $\alpha_w - \alpha_s$), while their development with time is affected by the thermal, hydraulic and mechanical boundary conditions as well as the soil properties. The generation and dissipation of excess pore water pressure lead to important THM interactions which affect the transient response of thermo-active retaining walls. According to the hydraulic equation implemented in ICFEP, there are three main processes that contribute to the development of excess pore water pressures in fully coupled THM problems: changes

in temperature (designated as "thermally-induced"), water flow (termed "hydraulically-induced") and mechanical actions (named "mechanically-induced"). The first are due to the difference between α_w and α_s; hydraulically-induced excess pore water pressures are due to the time-dependent water flow and were shown to occur also without changes in temperature; the latter are due to the variations in mechanical volumetric strains, hence depending on the mechanical restrictions. Furthermore, it was shown that the THM interactions are controlled by the relative rate at which heat transfer and water flow occur, which was measured by the dimensionless parameter α_{TH}, expressed as the ratio between the thermal diffusivity (α_T) and hydraulic diffusivity (α_H), i.e. the higher its value, the faster the rate of heat transfer with respect to water flow. Analyses on simple, one-dimensional problems have identified a direct correlation between α_{TH} and the thermally-induced excess pore water pressures developing close to the application of a thermal boundary condition, with higher excess pore water pressures observed for large values of α_{TH}, since in such case water flow, and thus the dissipation of pore water pressures, occurs at a comparatively slow pace.

The preliminary analyses carried out on the response of a thermo-active retaining wall consisted of 2D plane-strain analyses, where a uniform change in temperature over the whole cross-section of the wall was applied. This was kept constant for a long period of time (10 years) to evaluate the transient thermo-mechanical response of the wall and the effect the THM interactions have on the development of forces and displacements. Given the time-dependent nature of the THM interactions, the response of thermo-active retaining walls was shown to be controlled by different phenomena prevailing over different time periods, namely thermal soil expansion, volumetric deformations due to excess pore water pressure generation and dissipation, and interactions with mechanical boundary conditions. For example, when the wall is heated, compressive axial forces develop as a consequence of the restriction the soil applies against the thermal expansion of the wall. Subsequently, as the heat transfers to the soil and this consequently expands, it induces tension within the wall. Concurrently, the increase in soil temperature leads to the generation of compressive excess pore water pressures. As these dissipate, the soil settles and applies a compressive action within the wall. The changes in bending moment are governed by the volumetric changes of the soil upon changes in temperature and pore water pressures and, depending on the geometry of the problem, may be affected by interactions with the mechanical boundary conditions.

Clearly, some of these aspects cannot be captured if one or more coupled processes are ignored when adopting simpler modelling approaches. It was shown that such simplifications, when compared to fully coupled THM analyses, generally produce conservative results in terms of structural forces. However, they tend to highly underestimate wall and ground movements in the long term. Hence, it is considered that fully coupled THM analyses should be undertaken when analysing thermo-active structures. Furthermore, the results obtained by the fully coupled THM analysis indicated that relatively low magnitudes of forces and horizontal wall displacements were induced by changes in temperature when

compared to those evaluated during construction. However, the predicted vertical wall displacements and ground movements were shown to be significant. This highlights that adequate assessments are required to ensure the serviceability of the structure and evaluate possible interactions occurring with nearby underground structures and services. A further study was conducted to assess the effect of different values of α_{TH} on the response of thermo-active retaining walls. The variation of α_{TH}, as previously outlined, alters the THM response of the soil and this was shown to significantly change the magnitude of thermally-induced forces and movements as well as the time-dependent behaviour, demonstrating the importance of estimating accurately the soil parameters in order to ensure a safe and reliable design of thermo-active retaining walls.

7.3 Heat transfer and thermo-mechanical behaviour in three-dimensional analyses

In order to model accurately the heat transfer from the heat exchanger pipes to the structure and then to the surrounding soil, 3D analyses with inclusion of special one-dimensional elements, which enable the simulation of the advective-conductive heat transfer within the pipes, are required. Indeed, modelling thermo-active retaining walls in 3D with explicit simulation of the heat exchanger pipes allows the variation in temperature across the width and thickness of the panel to be taken into account and its effect on the heat transfer mechanisms and the thermo-mechanical behaviour to be assessed. In this respect, three main aspects were analysed within this research: (1) establishing an accurate modelling approach by validating it against field data; (2) assessing the long-term thermal performance and heat transfer mechanisms and (3) investigating the thermo-mechanical response of walls modelled in complex THM analyses. Furthermore, the effect of the interaction between the wall and the environment to which it is exposed was evaluated. The two extreme scenarios that characterise the wall-air interaction correspond to an insulated wall (i.e. no heat flux (NF) takes place along the wall-air interface) and a wall face maintained at a constant temperature (CT). These cases describe surfaces characterised by a convective heat transfer coefficient, h, of 0 and ∞ W/m^{2}K, respectively.

Modelling approach

The general approach to simulate thermo-active retaining walls in 3D analyses follows the same principles as those outlined in Gawecka et al. (2020), where the heat exchanger pipes are simulated employing one-dimensional elements (Gawecka et al., 2018), which present a coupled THM formulation allowing the simulation of the conductive-advective heat transfer. Due to the high water flow simulated within these elements (i.e. the problem is advection-dominated), the Petrov-Galerkin FE method (Cui et al., 2018c) is required to ensure numerical stability. Furthermore, to account for the zero lateral contact area of the pipes when simulated with one-dimensional elements, these need to be surrounded by a Thermally Enhanced Material (TEM), i.e. a material of higher conductivity than concrete, through which only conduction is simulated and heat transfer is enhanced. In addition, it was

highlighted that an adequate spatial mesh discretisation is required for an accurate simulation of the temperature distributions. It was shown that, as expected, when small elements are employed next to the heat exchanger pipes, more accurate results are obtained.

Two different modelling approaches have been assessed within this research. The first modelling approach (MA1) consists of specifying the inlet temperature at the heat exchanger pipes, with the heat flux being calculated through the computed outlet temperature. This approach is commonly used in literature. The second modelling approach (MA2) simulates the heat transfer through the application of a nodal heat flux boundary condition, thus mimicking the presence of a heat pump. In order to determine the magnitude of the applied heat flux boundary condition, a threshold criterion on the temperature changes has to be defined. Within this research, a target change in temperature at the pipe inlet was imposed, enabling the value of the heat flux boundary condition to be estimated iteratively.

The two modelling approaches were validated by reproducing thermal performance tests on two different pipe layouts reported in Xia et al. (2012). Generally, a very good agreement between the measured data and the computed results for both modelling approaches was obtained, particularly when considering the substantial uncertainties regarding the simulated field test (e.g. initial conditions and material properties). Thus, this validation exercise demonstrated the suitability of the general modelling approach adopted for thermo-active retaining wall problems in 3D analyses, highlighting the importance of the TEM and mesh discretisation on the obtained results. It should be noted that, while the presence of the TEM was shown to significantly affect the results in the short term, it has small effects on the temperature distributions in the long term and was therefore not included in subsequent long-term analyses. In addition, its absence provides conservative results in terms of thermal performance.

Heat transfer

A first set of 3D analyses explored the effect of the employed modelling approach and of the simulated boundary condition along the exposed face of the wall on the heat transfer mechanisms and calculated heat flux and transferred energy. In these analyses, the mechanical behaviour was not evaluated. In order for the two modelling approaches to be compared, the threshold criterion defined to determine the heat flux boundary condition for MA2 was such that the long-term temperature change at the pipe inlet was the same as that applied in MA1. This implies that similar heat transfer rates are simulated with both approaches. Three wall-air interactions were assumed, namely an insulated wall (NF), a wall maintained at a constant temperature (CT) equal to the initial temperature and a wall characterised by a convective heat transfer coefficient, h, of 2.5 W/m^{2}K (CH).

The boundary condition along the exposed face of the wall noticeably affects the temperature distributions within the wall and the ground in the long term, with higher temperatures computed for the NF analysis since no heat transfer can occur along the exposed face. Consequently, a considerably

lower heat flux is obtained for this condition when compared to the CT analysis (i.e. 50% less). Thus, it is considered that the characterisation of the wall-air interaction is a fundamental aspect for the thermal design of thermo-active retaining walls. The different interactions along the wall-air interface also lead to different heat transfer mechanisms. Indeed, for the NF case, most of the heat exchange occurs within the embedded section through the wall-soil interfaces; conversely, for the CT and CH cases, where heat can be exchanged across the wall-air interface, a larger contribution of the exposed section is provided to the total heat flux, with these conclusions being independent of the adopted modelling approach. Hence, the choice of the configuration and position of the pipes within a wall panel depend on the conditions along the exposed part of the wall as well as the operation mode of the geothermal system.

When comparing the results obtained with MA1 and MA2, the main difference lies in the development with time of the temperature changes within the pipes, the structure and the soil. As expected, the changes in temperature occur at a faster rate when MA1 is adopted. For MA2, the applied magnitude of the heat flux boundary condition depends on the simulated wall-air interaction and is highest for the CT case. Consequently, in the short term, higher temperatures develop for the CT case, while the lowest temperatures are evaluated for the NF case. With time, similar changes in temperature as those evaluated for MA1 are computed and thus larger changes are evaluated for the NF case. In conclusion, the study showed that two different modelling approaches based on similar assumptions produce comparable results. While MA1 is a simpler approach, and thus widely used in literature, it is considered that MA2 should be further explored since it represents the operation pattern of heat pumps with greater accuracy.

Thermo-mechanical behaviour

Fully coupled 3D THM analyses with inclusion of one-dimensional heat exchanger pipes were performed to assess the mechanical response of thermo-active retaining walls modelled in a more accurate way in comparison to the initial preliminary analyses. These allowed the investigation of the impact of the simulated boundary condition along the exposed face of the wall (either NF or CT) on the thermo-mechanical behaviour as well as evaluating the impact of non-uniform temperatures across the panel's width and thickness on the distribution of forces. Compared to the preliminary analyses where the temperature of the whole wall was changed at the same time, the inclusion of heat exchanger pipes leads to a slower heat transfer rate and hence to smaller changes in excess pore water pressures, however the same mechanisms outlined in Section 7.2 are still applicable.

While the simulated wall-air interaction was shown to marginally affect the change in axial force with time, it influenced substantially the change in bending moment and vertical wall movements. It was observed that the magnitude and evolution of changes in bending moment with time depend on the temperature gradient across the thickness of the wall panel. Indeed, this leads to the development of mechanical strains which contribute to changes in bending moment. Clearly, a larger temperature

gradient across the wall's thickness, and thus larger changes in bending moment, occur for the CT case when compared to the NF case, for which the temperatures within the wall become uniform in the long term. It was also observed that the mechanical strains which contribute to changes in bending moment do not necessarily relate to the deformed shape of the wall and, hence, the sign of the bending moment can no longer be determined by the horizontal wall deflections. The vertical movements of the wall are directly related to the temperature changes of the wall and are thus larger for insulated walls (NF). The non-uniform temperatures across the width of the wall affect the distribution of forces along this dimension, leading to significant variations in the distribution of changes in axial forces (particularly in the short term where larger temperature differences exist), while smaller changes in bending moment were observed. As previously mentioned, the two modelling approaches adopted to simulate the heat exchange in 3D analyses lead to similar temperatures in the long term. Thus, the wall's mechanical response is only marginally affected, leading to a slightly different transient response in terms of changes in bending moment and wall movement with time, which increase at a slower pace when MA2 is adopted.

7.4 Modelling thermo-active walls in two-dimensional analyses

While performing 3D analyses enables the modelling of thermo-active walls in a more realistic manner when compared to 2D analyses, the simulations are computationally very expensive due to the large number of degrees of freedom within the model. However, due to the geometric simplification introduced by the plane-strain assumptions (i.e. the discrete position of the heat exchanger pipes within a wall panel cannot be accounted for), the heat transfer differs from that occurring in a full 3D analysis. Therefore, new methods and approximations had to be established to simulate accurately the response of thermo-active retaining walls in 2D plane-strain analyses, an aspect that has not yet been investigated in the literature. The aim was to establish simple and practical methodologies for the design of thermo-active walls, in order to allow a reduction of the required computational effort while ensuring that the obtained results are comparable to those computed in 3D.

Thermal performance

In order to enable the prediction of the thermal performance of thermo-active retaining walls by means of 2D plane-strain analyses, the proposed modelling approach includes one-dimensional elements to simulate the water flow and heat flux through the heat exchanger pipes. Thus, in 2D, the heat exchanger pipes are represented by a continuous, 1 m wide, zero-thickness "sheet" of water flowing along the depth of the wall. As a consequence, a higher heat transfer occurs in 2D and thus approximations are required. These were developed assuming that, in the real problem, U-shaped pipe loops are installed within wall panels, and were established for both extreme scenarios of wall-air interaction (i.e. NF and CT). The appropriateness of the approximations was evaluated by comparing the results in 2D to those

obtained for numerous cases simulated in 3D. Furthermore, they were firstly derived for MA1, while the simulation in 2D adopting MA2 was subsequently assessed.

The design criteria employed to derive the 2D approximations were the long-term heat flux, the transferred energy during different operation periods and the changes in ground temperature. It was shown that different approximations are required depending on the boundary condition along the exposed face and on whether the 2D analysis aims at reproducing the long-term heat flux or the transferred energy computed in 3D. The established approximations for MA1 were the following:

(1) in order to ensure an equivalent energy input between 3D and 2D, the same water flow rate per unit width in both problems has to be modelled. This aspect is independent of the design criterion to be met and on the modelling approach adopted to simulate the heat transfer (hence, it is also valid for MA2). This was achieved by altering the area of the pipe in 2D according to the number of vertical pipe segments that are present in the 3D problem;

(2) when adopting the above procedure and applying the same inlet temperature as in 3D, a good match of the long-term heat flux for the NF cases was obtained, however significantly larger errors were calculated for the CT cases. Indeed, in such case, the wall-air interaction is overestimated in 2D due to the continuous pipe element in the out-of-plane direction and thus an additional correction was established. The proposed correction reduces the inlet temperature in the 2D analysis according to a correction factor X, expressed as the ratio between the change in temperature at the pipe inlet in 2D and 3D ($\Delta T_{in,2D}/\Delta T_{in,3D}$). This correction factor was determined empirically and is calculated based on the ratio of exposed over total length of wall, L_{exp}/L, and the spacing between the pipes, B/n_p, since these parameters control the heat transfer through the exposed face. With this approximation, it was shown that a good estimate of the long-term heat flux is obtained in 2D, while a larger discrepancy between the heat flux computed in 3D and 2D is evaluated in the short term, due to the higher heat transfer rate simulated in 2D. A good match in the changes in ground temperature was also obtained;

(3) to simulate the same transferred energy in 3D and 2D, a similar correction was required. Due to the higher heat flux generated in 2D in the short term for both NF and CT conditions, corrections were required for both cases, according to which the inlet temperature in 2D is computed through the correction factor Y (also equal to $\Delta T_{in,2D}/\Delta T_{in,3D}$). Contrary to the correction factor X, Y depends not only on the values of L_{exp}/L, and B/n_p, but also on the thermal conductivity of concrete (λ_c) and soil (λ_s) since these parameters affect the heat transfer mechanisms in the short term. Furthermore, it varies according to the length of the operation period during which the energy is to be estimated and was established for 6 months, 3 months and 1 month of operation.

To establish 2D approximations when MA2 is adopted, numerous 3D analyses were first carried out to determine the correct heat flux boundary condition for a set target temperature change. Subsequently, 2D analyses were carried out adopting appropriate conversions of equivalent water flow (see (1) above) and applying the heat flux boundary condition established in 3D normalised by the width of the wall. It was found that the target temperature required to obtain comparable results is lower than in that employed in 3D. It was also shown that, when the ratios between the changes in temperature at the pipe inlet in 2D and 3D, i.e. $\Delta T_{in,2D}/\Delta T_{in,3D}$, are compared the correction factor Y after 6 months established for MA1, a good agreement is obtained. This indicates that the temperature threshold in 2D can be estimated employing this correction. However, this was established only for 6 months of operation, thus further analyses are required to determine corrections for different time periods.

Thermo-mechanical behaviour

To establish an accurate modelling of the THM behaviour of thermo-active walls, first, two different modelling approaches, consisting of either a prescribed temperature along a line equal to the inlet temperature in 3D (i.e. that commonly employed in literature) or simulating the presence of a heat exchanger pipe and adopting the approximation procedures for long-term heat flux described above (for MA1) were evaluated and the results compared to those obtained by equivalent 3D analyses. Both 2D approaches overestimated the changes in temperatures and, consequently, the changes in forces and displacements. Furthermore, the transient behaviour was not captured accurately due to the heat transfer in 2D taking place at a faster rate. For these reasons, a new method to enable a closer approximation to the THM response observed in 3D was developed. The scope was to provide a practical approach which requires the sole use of boundary conditions, thus replacing the use of special one-dimensional elements for simulating the presence of heat exchanger pipes and avoiding the need of advanced numerical methods (e.g. Petrov-Galerkin FE method).

The proposed method to model the average behaviour of walls in 2D plane-strain analyses consists of determining a time dependent temperature, $T_{i,2D}$, to be applied as a boundary condition to simulate the heat exchange. This temperature is determined by performing 2D thermal analyses in plan view (termed herein "2D plan analyses") of the embedded and exposed section, where the latter allows for different wall-air interactions to be taken into account. The average temperature across the width of the wall along the line containing the pipes is determined and weighted according to the exposed and embedded lengths of the wall. The main assumption of this method lies in the applied temperature within the 2D plan analyses, which requires an estimation of the temperature differential across the inlet and outlet of the heat exchanger pipes in the actual problem, ΔT_p. However, it was shown that, if sensible values are employed, this parameter has little effect on the results. This approach was validated for numerous cases varying the wall geometry, the thermal parameters of soil and concrete and the thermal boundary condition along the exposed face of the wall. The 2D analyses provide an excellent estimation of the average wall behaviour computed by the original analyses in 3D, thus providing confidence in the new

proposed approach. As described in the previous section, a variation in distribution of axial forces in the out-of-plane direction was observed in 3D analyses. This cannot be captured in 2D since no variation in temperature can be simulated in the out-of-plane direction. Thus, an analytical procedure was developed to account for the additional stresses induced by the differential expansion of portions of walls at different temperatures and was shown to lead to a good approximation of the axial forces for different time instants.

7.5 Influence of problem parameters

Given the many variables of a thermo-active retaining wall problem in terms of its geometry and material properties, several parametric studies have been carried out within this research to evaluate their effect on both the energy efficiency and the thermo-mechanical response of thermo-active retaining walls. These studies provide an estimation of the importance of these parameters and thus aid in design choices, especially in the presence of considerable uncertainties in the available data.

Thermal performance

For a continuous heat injection of 6 months and for both NF and CT conditions along the exposed face of the wall, a parametric study analysed the effect on the thermal performance of thermo-active walls of geometric parameters (the ratio of exposed over total length (L_{exp}/L), the number of pipes within a wall panel (n_p)), thermal parameters (thermal conductivity of concrete (λ_c) and soil ($\overline{\lambda_s}$)), the water flow velocity (v), inlet temperature (T_{in}) and the operation mode (intermittent operation of duration of 6h). The main conclusions of this study are summarised as follows:

- simulating larger number of U-loops within a panel (i.e. reducing the pipe spacing in the out-of-plane direction) affects the long-term heat flux only for walls simulated with a CT condition along the exposed face of the wall. Furthermore, as the number of pipes increased, smaller increases in thermal performance were observed. Consequently, since walls behave somewhere in between the two simulated extreme conditions, the design of the pipe layout should be based on the cost-effectiveness of additional pipe material and installation time versus gains in energy efficiency;
- employing a high concrete thermal conductivity increased substantially the heat flux for walls exposed to a constant temperature (CT), while almost no effect of this parameter was computed for insulated walls (NF). Changing the soil thermal conductivity had a higher relative impact for insulated walls, where higher values of $\overline{\lambda_s}$ were shown to be beneficial for the thermal performance. This parameter also affects considerably the changes in ground temperature. It is therefore considered that site specific parameters should be employed in design in order to provide an accurate assessment of the energy efficiency and changes in ground temperature;
- the water flow velocity, within the analysed range of 0.2 m/s to 1.4 m/s, does not affect the long-term thermal performance of thermo-active walls. For lower values (of one order of magnitude), a

decrease in the thermal performance was found. Thus, when designing a thermo-active retaining wall, the water flow velocity should be chosen within the abovementioned range, selecting a value that minimises the operation costs;

- when a system was simulated to work intermittently (IOM), i.e. switched on and off every 6h, approximately twice the heat flux was obtained when compared to a continuous operation mode (for both NF and CT). Since a similar transferred energy was calculated for continuous and intermittent operation modes, it was concluded that the IOM is more efficient, transferring the same amount energy in half the operation time. However, the development of ground temperatures is only marginally affected by the simulated operation pattern. Thus, if these are to be calculated, then simulating continuous operation provides a simpler and more computationally efficient approach.

Thermo-mechanical behaviour

A similar study was carried out to analyse the effect on the thermo-mechanical behaviour of thermo-active retaining walls of the excavation depth (expressed by the ratio L_{exp}/L), the width of the panel (which directly alters the spacing between the pipes), the concrete thermal conductivity and the soil diffusivity. The influence of these parameters on the evolution with time of forces and displacements was evaluated, concluding that:

- with a larger excavation depth, the contact area between the structure and the soil decreases and thus smaller changes in axial forces develop due to the decreased restriction provided by the soil. However, larger bending moments are computed for a higher L_{exp}/L, which increase significantly for the CT case. The wall displacements, being controlled by the changes in wall temperature, are only marginally affected by the excavation depth for the NF cases, whereas for CT conditions larger wall displacements are computed for a smaller depth of excavation;
- a smaller panel width (i.e. reduced spacing between the heat exchanger pipes), induces higher temperature changes within the wall. These lead to larger bending moments, especially for the CT cases, and to larger vertical wall movements;
- similarly, changing the concrete thermal conductivity affects the temperature changes within the wall, with higher values computed for a larger thermal conductivity. This translates into larger vertical movements of the wall. However, the development of forces is only marginally affected by this parameter;
- simulating a higher soil thermal diffusivity leads to a faster heat transfer and thus to larger changes in ground temperatures, which directly increase its thermal expansion. As a consequence, larger changes in axial forces and vertical wall movements are recorded in the long term (which are both controlled by the thermal expansion of the soil);

7.6 Response to long-term cyclic thermal loading

Thermo-active retaining walls, and ground source energy systems in general, are designed to provide thermal energy over a long period of time. They may operate in a single or dual operation mode, meaning that the system may be employed solely for heating or cooling, or for both. Consequently, both the structure and the soil are subjected to cyclic changes in temperature over multiple years. The geothermal system may be designed as balanced, i.e. the net energy exchanged with the ground during a year of operation is equal to zero, or it may be unbalanced, i.e. more energy is extracted than injected or vice versa. The latter scenario induces permanent temperature changes and more time is required for the system to reach thermal equilibrium. Furthermore, as previously discussed, temperature changes affect the development of excess pore water pressures which in turn influence the thermo-mechanical response of thermo-active retaining walls. As a result, to provide insight into the long-term behaviour of these structures, multiple years of cyclic thermal loading were explored. Different scenarios with varying operation patterns were analysed and their impact on the thermal performance and the THM response was assessed. In the following, the designation of the operation mode refers to the soil-side of the system, e.g. in heating, heat is transferred to the soil to provide cooling to a building, while the opposite is true for cooling.

Thermal performance

2D plane-strain analyses including heat exchanger pipes, adopting the approximations for the long-term heat flux described in Section 7.4, were carried out to assess the variation in heat flux and in ground temperatures with time over a period of 10 years. Four different scenarios were modelled, namely: (1) 6 months of heating followed by 6 months of cooling, (2) 6 months of heating followed by 6 months of idling, (3) 9 months of cooling followed by 3 months of heating and (4) 9 months of cooling followed by 3 months of idling. When a balanced operation was simulated (scenario (1)), no change in the long-term thermal performance was recorded during the 10 years of operation and no permanent temperature changes were computed at larger distances from the wall. For all other scenarios, permanent temperature changes developed around the wall, where these were larger for insulated walls (NF) compared to walls maintained at a constant temperature (CT). For example, in the worst case (i.e. scenario (4)) the changes in temperature evaluated at a distance of 10.0 m from the wall were equal to -5.6°C and -3.3°C, respectively for NF and CT, whereas the region affected by changes in temperature $>$1.0°C extended up to 30.0 m around the structure. These permanent changes in temperature led to a reduction in the thermal performance with time, hence highlighting the importance of simulating multiple years of operation. Furthermore, it should be noted that the changes in ground temperature and consequent ground movements should be taken into account during the design of thermo-active structures to assess any interaction with nearby underground structures which may be affected.

Thermo-mechanical behaviour

To evaluate the effect of cyclic thermal loading on the THM behaviour of thermo-active walls, the modelling approach based on establishing a time-dependent thermal boundary condition to simulate the thermo-mechanical behaviour in 2D plane-strain analyses described in Section 7.4 was adopted. The study consisted of evaluating the long-term response of a thermo-active retaining wall subjected to three different scenarios over a period of 5 years: (1) 6 months of heating followed by 6 months of cooling, (2) 6 months of heating followed by 6 months of idling and (3) 9 months of cooling followed by 3 months of heating. The results demonstrate the complexity of coupled THM problems. For scenario (1), as previously described, no permanent temperature changes were evaluated. Nonetheless, a variation in excess pore water pressures during the analysed operation period was computed and this induced an overall compressive action into the wall and a downward vertical movement with time. This is related to the different time-dependent behaviour of heat transfer with respect to water flow, where the former occurs at a faster pace than the latter. When an unbalanced system was simulated, i.e. scenario (2) and (3), a larger soil mass was subjected to permanent changes in average temperature and, consequently, in pore water pressures. These, together with the imbalance in the rate of heat transfer and water flow, induced in such cases even larger permanent effects on the structure and surrounding soil, especially in terms of ground and wall movements. The computed changes in structural forces were of the order of $\pm$20% of the values recorded at the start of the operation (i.e. after excavation and construction), while the changes in vertical wall movements within one season reached values of up to 8.0 mm, which is of similar magnitude experienced during loading of the structure and thus considered to be significant. The study concluded that, to account for the long-term behaviour of thermo-active retaining walls, multiple years of operation should be simulated in order to enable the prediction of the whole range of changes within the structural behaviour during the design life of the structure which cannot be taken into account if only one year of operation is simulated. While the changes in forces of the structure were shown not to be detrimental to its stability, the effects of temperature on its serviceability, as well as ground movement which may affect nearby structures, was highlighted.

7.7 Recommendations for future research

The work presented in this thesis provided new modelling approaches for the simulation and design of thermo-active retaining walls in 2D analyses and included results evaluating multiple aspects of the behaviour of thermo-active retaining walls offering an extensive overview and understanding of the problem. However, there are aspects that have not been considered during this research, with the following recommendations for future research.

Some aspects were simplified within this research. For example, the internal structures (slabs and columns) were considered either thermally-inactive or modelled as springs. Thus, the effect of temperature changes within these structures was ignored. Accounting for the heat transfer towards the

internal structures allows the effect of the heat exchange on these to be evaluated, as well as the impact of their thermal deformation on the thermo-active retaining wall to be determined. Indeed, it was shown that the thermal deformation of the wall induces deformations of the internal structures and additional forces are expected to develop, however these were not quantified. Simulating changes in temperature within these structures may induce additional deformations which can affect the forces and displacements of the thermo-active retaining wall. Clearly, these aspects will also be affected by the type of connection simulated between the retaining wall and the permanent horizontal structures, which, within this thesis, was simulated as a pinned connection. Full moment connections are expected to induce larger changes in forces, which need to be quantified to assess whether the thermal loading in such a scenario has a more detrimental effect when compared to those obtained with a pinned connection. Simulating the heat transfer through the internal structures also implies that, if solid elements are employed for their simulation, appropriate thermal boundary conditions to simulate the environment within the excavation have to be applied, which, as discussed throughout this thesis, are difficult to estimate. Another aspect that should be considered is the possibility of utilising the base slab or any foundation piles built to support the basement as heat exchangers in conjunction with thermo-active retaining walls. In such a scenario, their presence should be evaluated both from a thermal and structural perspective, since the temperature field around the wall will be altered, which can affect its thermal performance. Furthermore, the thermal expansion/contraction of the base slab or foundation piles as a consequence of the heat exchange can induce additional deformations and forces within the earth retaining structure and should be assessed.

A further feature that was not accounted for within this research is the different position of heat exchanger pipes within a wall panel. As explained in Chapter 2, these are generally installed towards the retained side of the structure to take advantage of the heat exchange towards the soil. However, these could also be installed on both sides of the thermo-active wall or only along the exposed face. This alters the temperature distribution within the wall and thus is expected that a different thermal and structural response would be evaluated. Furthermore, with pipes installed along the excavated side of the structure, the behaviour will be even more sensitive to the boundary condition employed to simulate the wall-air interaction. It is therefore suggested that these aspects should be investigated first in 3D analyses to evaluate the effects on the temperature distribution and subsequently assess the applicability of the proposed modelling approaches in 2D plane-strain analyses for different pipe configurations.

All the analyses conducted within this research assumed a constant temperature along the ground surface and within the excavation, when the thermal interaction was assumed to be characterised as such. Clearly, this is a simplification since the temperatures of the ground surface vary seasonally/monthly. Simulating seasonally-varying air temperatures implies that first a steady state temperature field has to be determined. The obtained variation of temperature with depth is then used as an input at the start of the analysis. A problem of "locked-in" stresses arises when a concrete structure

is wished in place, since the temperature field established in undisturbed conditions is not in equilibrium due to the introduction of a material of different thermal properties. This phenomenon was observed in the simulation of thermo-active pile problems by Grevers (2017) and requires further consideration. It should be noted that, within the current literature, although thermo-mechanical or thermo-hydro-mechanical analyses with varying surface temperature have been performed (e.g. Barla et al., 2020; Dai & Li, 2019), this problem has not been mentioned so far. Furthermore, if a varying ground surface temperature is to be simulated, the proposed methods for modelling thermo-active retaining walls in 2D plane-strain analyses need to be reassessed. Indeed, the time-dependent temperature along the ground surface and/or within the excavation may affect the obtained corrections for the approximations established for the thermal performance. Conversely, the method to simulate the thermo-mechanical behaviour requires the introduction of these features within the 2D plan analyses, since cyclic temperatures within the ground surface/face of excavation alter the temperature distribution within the wall. The effect on the exposed face can be easily accounted for, while that of the ground surface may require an additional plan analysis for the upper part of the soil affected by changes in ground temperature due to the cyclic temperature. Clearly, the temperature variations will have to be introduced also within the 2D THM analysis.

As pointed out throughout this thesis, the material properties employed are considered as temperature independent and the soil response to be thermo-elastic. As explained in Chapter 2 and extensively discussed in Gawecka (2017) and Cui et al. (2020), the properties of water vary greatly with temperature, with its coefficient of thermal expansion increasing with temperature, while its volumetric heat capacity and density decrease with temperature. Furthermore, the permeability of soils is also affected by changes in temperature, with an increase in permeability observed upon heating mainly due to the reduction of the fluid viscosity. These aspects can clearly affect the THM interactions within the soil, which were shown to be largely dependent on the changes in pore water pressures. Indeed, these are governed by the differential expansion between soil and water and the hydraulic diffusivity of the soil mass. Furthermore, numerous laboratory experiments on clays have shown that their volumetric response to cycles of heating and cooling may not be elastic. For this reason, Gawecka (2017) implemented a thermo-plastic constitutive model within ICFEP that allows to account for thermo-plasticity upon changes in temperature. The impact of both these features, i.e. temperature dependent material properties and thermo-plasticity, on the response of thermo-active walls should be evaluated. However, especially for the latter aspect, given the sometimes contradicting experimental evidence, more laboratory studies are required to confidently model the actual soil behaviour upon changes in temperature.

In general, as highlighted throughout this thesis, there is an urgent need for field work with regards to the thermo-mechanical response of thermo-active retaining walls. A comprehensive field monitoring scheme, including long-term measurements of temperature, strains, water and earth pressures, together

with a site-specific characterisation of the material properties, is required to advance the understanding of the actual behaviour of thermo-active retaining walls. Furthermore, such work would allow the validation and improvement of current modelling approaches and thus provide further confidence when designing these structures. Lastly, the inclusion of monitoring work within the soil surrounding a thermo-active structure and development of numerical tools able to reproduce the observed behaviour will aid in the assessment of the impact of thermo-active structures on surrounding infrastructure and buildings. Indeed, a necessary step to increase the deployment of thermo-active structures is the evaluation of the interaction between systems to ensure their long-term viability both from a thermal and structural perspective. Indeed, minimising the temperature effects and interaction between nearby structures will provide assurance to all the parties involved of the safe and efficient use of these systems.

References

Abuel-Naga, H., Raouf, A. M. I., Raouf, M. I. N. & Nasser, A. G. (2015) Energy piles: current state of knowledge and design challenges. *Environmental Geotechnics,* 2 (4), 195-210.

Abuel-Naga, H. M., Bergado, D. T., Ramana, G. V., Grino, L., Rujivipat, P. & Thet, Y. (2006) Experimental evaluation of engineering behavior of soft Bangkok clay under elevated temperature. *Journal of Geotechnical and Geoenvironmental Engineering,* 132 (7), 902-910.

Abuel-Naga, H. M., Bergado, D. T. & Bouazza, A. (2007a) Thermally induced volume change and excess pore water pressure of soft Bangkok clay. *Engineering Geology,* 89 (1-2), 144-154.

Abuel-Naga, H. M., Bergado, D. T., Bouazza, A. & Ramana, G. V. (2007b) Volume change behaviour of saturated clays under drained heating conditions: experimental results and constitutive modeling. *Canadian Geotechnical Journal,* 44 (8), 942-956.

Adam, D. & Markiewicz, R. (2009) Energy from earth-coupled structures, foundations, tunnels and sewers. *Géotechnique,* 59 (3), 229-236.

Akrouch, G. A., Briaud, J.-L., Sanchez, M. & Yilmaz, R. (2016) Thermal Cone Test to Determine Soil Thermal Properties. *Journal of Geotechnical and Geoenvironmental Engineering,* 142 (3),

Al-Khoury, R. (2012) *Computational Modeling of Shallow Geothermal Systems.* Multiphysics Modeling. Boca Raton, Taylor & Francis.

Amatya, B., Soga, K., Bourne-Webb, P. J., Amis, T. & Laloui, L. (2012) Thermo-mechanical behaviour of energy piles. *Geotechnique,* 62 (6), 503-19.

Amis, T. (2010) *Current and future research into Ground Source Energy.* [Research seminar] GSHPA, 21st January 2010.

Amis, T., Robinson, C. A. W. & Wong, S. (2010) Integrating geothermal loops into the diaphragm walls of the Knightsbridge Palace Hotel project. In: *Proceedings of 11th DFI/EFFC International Conference on Geotechnical Challenges in Urban Regeneration, 26-28 May 2010, London, UK.* Deep Foundations Institute. pp. 10-19.

Amis, T. & Loveridge, F. (2014) Energy piles and other thermal foundations for GSHP – developments in UK practice and research. *REHVA Journal,* 2014 (1), 32-35.

Angelotti, A. & Sterpi, D. (2018) On the performance of energy walls by monitoring assessment and numerical modelling: a case in Italy. *Environmental Geotechnics,* (ahead of print)

ASHRAE (2015) *Heating, ventilating, and air-conditioning applications.* 2015 ASHRAE handbook : HVAC applications (SI). Atlanta, GA, ASHRAE.

Atkinson, J. H., Richardson, D. & Stallebrass, S. E. (1990) Effect of recent stress history on the stiffness of overconsolidated soil. *Geotechnique,* 40 (4), 531-540.

Awbi, H. B. & Hatton, A. (1999) Natural convection from heated room surfaces. *Energy and Buildings,* 30 233-244.

Baldi, G., Hueckel, T. & Pellegrini, R. (1988) Thermal volume changes of the mineral-water system in low-porosity clay soils. *Canadian geotechnical journal,* 25 (4), 807-825.

Banks, D. (2012) *An Introduction to Thermogeology: Ground Source Heating and Cooling.* 2nd Edition. Chichester, Wiley-Blackwell.

Barla, M., Di Donna, A. & Santi, A. (2020) Energy and mechanical aspects on the thermal activation of diaphragm walls for heating and cooling. *Renewable Energy,* 147 2654-2663.

Batini, N., Rotta Loria, A. F., Conti, P., Testi, D., Grassi, W. & Laloui, L. (2015) Energy and geotechnical behaviour of energy piles for different design solutions. *Applied Thermal Engineering,* 86 199-213.

Beier, R. A., Smith, M. D. & Spitler, J. D. (2011) Reference data sets for vertical borehole ground heat exchanger models and thermal response test analysis. *Geothermics,* 40 (1), 79-85.

Bidarmaghz, A., Narsilio, G. A., Johnston, I. W. & Colls, S. (2016) The importance of surface air temperature fluctuations on long-term performance of vertical ground heat exchangers. *Geomechanics for Energy and the Environment,* 6 35-44.

Bouazza, A. (2011) Harnessing on site renewable energy through pile foundations. *Australian Geomechanics,* 46 (4), 79-89.

Bouazza, A. & Adam, D. (2012) Turning geostructures into sources of renewable energy. In: *11th Austraia-New Zeland Conference on Geomechanics Ground Engineering in a Changing World, 15-18 July 2012, Melbourne, Australia.* pp. 1051-1056.

Bourne-Webb, P. J., Amatya, B., Soga, K., Amis, T., Davidson, C. & Payne, P. (2009) Energy pile test at Lambeth College, London: geotechnical and thermodynamic aspects of pile response to heat cycles. *Géotechnique,* 59 (3), 237-248.

Bourne-Webb, P. J., Bernard, J.-B., Friedemann, W., von der Hude, N., Pralle, N., Uotinen, V. M. & Widerin, B. (2013a) Delivery of Energy Geostructures. In: Laloui, L. & Di Donna, A. (eds.) *Energy Geostructures: Innovation in Underground Engineering.* London, John Wiley & Sons, Inc., pp. 229-263.

Bourne-Webb, P. J., Soga, K. & Amatya, B. (2013b) A framework for understanding energy pile behaviour. *Proceedings of the Institution of Civil Engineers - Geotechnical Engineering,* 166 (2), 170-177.

Bourne-Webb, P. J., Burlon, S., Javed, S., Kürten, S. & Loveridge, F. (2016a) Analysis and design methods for energy geostructures. *Renewable and Sustainable Energy Reviews,* 65 402-419.

Bourne-Webb, P. J., Bodas Freitas, T. M. & da Costa Gonçalves, R. A. (2016b) Thermal and mechanical aspects of the response of embedded retaining walls used as shallow geothermal heat exchangers. *Energy and Buildings,* 125 130-141.

Bourne-Webb, P. J., Bodas Freitas, T. M. & Freitas Assunção, R. M. (2019) A review of pile-soil interactions in isolated, thermally-activated piles. *Computers and Geotechnics,* 108 61-74.

Bourne-Webb, P. J. & Bodas Freitas, T. M. (2020) Thermally-activated piles and pile groups under monotonic and cyclic thermal loading–A review. *Renewable Energy,* 147 2572-2581.

Brandl, H. (1998) Energy piles and diaphragm walls for heat transfer from and into the ground. In: Haegeman, V. I. (ed.) *Deep Foundations on Bored and Auguer Piles, 19-21 October 1998, Ghent, Belgium.* Balkema. pp. 37-60.

Brandl, H. (2006) Energy foundations and other thermo-active ground structures. *Géotechnique,* 56 (2) 81-122.

Brandl, H., Adam, D., Markiewicz, R., Unterberger, W. & Hofinger, H. (2010) Concrete absorber technology for earth coupled concrete structures using geothermal energy for the Vienna Undeground line U2. *Österreichische Ingenieur- und Architekten-Zeitschrift,* 155 (Heft 7-9/2010 und Heft 10-12/2010),

Brandl, H. (2013) Thermo-active Ground-Source Structures for Heating and Cooling. *Procedia Engineering,* 57 9-18.

Britto, A. M., Savvidou, C., Maddocks, D. V., Gunn, M. J. & Booker, J. R. (1989) Numerical and centrifuge modelling of coupled heat flow and consolidation around hot cylinders buried in clay. *Geotechnique,* 39 (1), 13-25.

Busby, J., Lewis, M., Reeves, H. & Lawley, R. (2009) Initial geological considerations before installing ground source heat pump systems. *Quarterly Journal of Engineering Geology and Hydrogeology,* 42 (3), 295-306.

Campanella, R. G. & Mitchell, J. K. (1968) Influence of temperature variations on soil behaviour. *ASCE Journal Soil Mechanics and Foundation Engineering Division,* 4 (3), 709-734.

Carslaw, H. S. & Jaeger, J. C. (1959) *Conduction of heat in solids.* 2nd Edition. Oxford, Clarendon Press.

Cekerevac, C. & Laloui, L. (2004) Experimental study of thermal effects on the mechanical behaviour of a clay. *International Journal for Numerical and Analytical Methods in Geomechanics,* 28 (3), 209-228.

Cekerevac, C., Laloui, L. & Vulliet, L. (2005) A Novel Triaxial Apparatus for Thermo-Mechanical Testing of Soils. *Geotechnical Testing Journal,* 28 (2), 161-170.

Çengel, Y. A. & Ghajar, A. J. (2011) *Heat and Mass Transfer: Fundamentals and Applications.* 4th Edition. New York, McGraw-Hill.

Chen, S., Zdravković, L. & Carraro, J. A. H. (2019) Thermally induced pore water pressure of reconstituted London clay. In: *7th International symposium on deformation characteristics of geomeaterials, 26-28 June 2019, Glasgow.*

Churchill, S. W. & Chu, H. H. S. (1975) Correlating equations for laminar and turbulent free convection from a vertical plate. *International Journal of Heat and Mass Transfer,* 18 (11), 1323-1329.

CIRIA (2007) *CIRIA C660*. Early-age thermal crack control in concrete. London, CIRIA

CIRIA (2017) *CIRIA C760*. Guidance on embedded retaining wall design. London, CIRIA

Committee on Climate Change (2019) *Reducing UK emissions – 2019 progress report to Parliament.*

Craig, R. F. (2004) *Craig's soil mechanics.* 7th Edition. London, Spon Press/Taylor Francis.

Cui, W. (2015) *Development, implementation and application of thermo-hydro-mechanical couplings in finite element analysis.* PhD thesis. Imperial College London.

Cui, W., Gawecka, K. A., Potts, D. M., Taborda, D. M. G. & Zdravković, L. (2016a) Numerical analysis of coupled thermo-hydraulic problems in geotechnical engineering. *Geomechanics for Energy and the Environment,* 6 22-34.

Cui, W., Gawecka, K. A., Taborda, D. M. G., Potts, D. M. & Zdravković, L. (2016b) Time-step constraints in transient coupled finite element analysis. *International Journal for Numerical Methods in Engineering,* 106 (12), 953-971.

Cui, W., Potts, D. M., Zdravković, L., Gawecka, K. A. & Taborda, D. M. G. (2018a) An alternative coupled thermo-hydro-mechanical finite element formulation for fully saturated soils. *Computers and Geotechnics,* 94 22-30.

Cui, W., Potts, D. M., Zdravković, L., Gawecka, K. A., Taborda, D. M. G. & Tsiampousi, A. (2018b) A coupled thermo-hydro-mechanical finite element formulation for curved beams in two-dimensions. *Computers and Geotechnics,* 103 103-114.

Cui, W., Gawecka, K. A., Potts, D. M., Taborda, D. M. G. & Zdravković, L. (2018c) A Petrov-Galerkin finite element method for 2D transient and steady state highly advective flows in porous media. *Computers and Geotechnics,* 100 158-173.

Cui, W., Gawecka, K. A., Taborda, D. M. G., Potts, D. M. & Zdravković, L. (2019) Time-step constraints for finite element analysis of two-dimensional transient heat diffusion. *Computers and geotechnics,* 108 1-6.

Cui, W., Tsiampousi, A., Gawecka, K. A., Potts, D. M. & Zdravkovic, L. (2020) Numerical modelling of time-dependent thermally induced pore pressures in a saturated soil. *ASCE Journal of Geotechnical and Geoenvironmental Engineering,* 146 (4),

Curtis, R., Busby, J., Law, R. & Adams, C. (2019) Geothermal energy Use, Country update for United Kingdom. In: *European Geothermal Congress, 11-14 June 2019, Den Haag, The Netherlands.*

Dai, Q. & Li, Z. (2019) Long-term mechanical performance of geothermal diaphragm walls in stiff clay. *Tunnelling and Underground Space Technology,* 94 103-113.

Dassault Systèmes (2019) *Abaqus Unified FEA* [Software] Paris, France. Avaliable from: www.3ds.com/products-services/simulia/products/abaqus.

Day, R. A. & Potts, D. M. (1990) Curved Mindlin beam and axi-symmetric shell elements - A new approach. *International Journal for Numerical Methods in Engineering,* 30 (7), 1263-1274.

Day, R. A. (1990) *Finite element analysis of sheet pile retaining walls.* PhD thesis. Imperial College London.

de Moel, M., Bach, P. M., Bouazza, A., Singh, R. M. & Sun, J. O. (2010) Technological advances and applications of geothermal energy pile foundations and their feasibility in Australia. *Renewable and Sustainable Energy Reviews,* 14 (9), 2683-2696.

Delage, P., Sultan, N. & Cui, Y. J. (2000) On the thermal consolidation of Boom clay. *Canadian Geotechnical Journal,* 37 (2), 343-354.

Delage, P. (2013) On the thermal impact on the excavation damaged zone around deep radioactive waste disposal. *Journal of Rock Mechanics and Geotechnical Engineering,* 5 (3), 179-190.

Di Donna, A. (2016) Energy walls for an underground car park. In: *25th European Young Geotechnical Engineers Conference, 21-24 June 2016, Sibiu, Romania.* pp. 133-138.

Di Donna, A. & Barla, M. (2016) The role of ground conditions on energy tunnels' heat exchange. *Environmental Geotechnics,* 3 (4), 214-224.

Di Donna, A., Cecinato, F., Loveridge, F. & Barla, M. (2017) Energy performance of diaphragm walls used as heat exchangers. *Proceedings of the Institution of Civil Engineers: Geotechnical Engineering,* 180 (3), 232-245.

Diersch, H. J. G., Bauer, D., Heidemann, W., Ruhaak, W. & Schatzl, P. (2011) Finite element modeling of borehole heat exchanger systems. Part 2. Numerical simulation. *Computers and Geosciences,* 37 (8), 1136-1147.

Diersch, H. J. G. (2014) *FEFLOW: Finite Element Modeling of Flow, Mass and Heat Transport in Porous and Fractured Media.* Berlin, Springer.

Dong, S., Li, X., Tang, A. M., Pereira, J. M., Nguyen, V. T., Che, P. & Xiong, Z. (2019) Thermo-mechanical behavior of energy diaphragm wall: Physical and numerical modelling. *Applied Thermal Engineering,* 146 243-251.

Environment Agency (2015) *Management of the London Basin Chalk Aquifer. Status Report 2015*. Bristol, Environment Agency

Eskilson, P. (1987) *Thermal analysis of heat extraction boreholes.* PhD thesis. University of Lund.

European Commission (2009) *2009/28/EC - Directive 2009/28/ec of the european parliament and of the council of 23 April 2009 on the promotion of the use of energy from renewable sources and amending and subsequently repealing Directives 2001/77/EC and 2003/30/EC*.

Fadejev, J., Simson, R., Kurnitski, J. & Haghighat, F. (2017) A review on energy piles design, sizing and modelling. *Energy,* 122 390-407.

Faizal, M., Bouazza, A. & Singh, R. M. (2016) Heat transfer enhancement of geothermal energy piles. *Renewable and Sustainable Energy Reviews,* 57 16-33.

Farouki, O. T. (1981) *Thermal properties of soils.* Hanover, United States Army Corps of Engineers, Cold Regions Research and Engineering Laboratory.

Fei, Y. (1995) Thermal Expansion. In: Ahrens, T. J. (ed.) *Mineral Physics and Crystallography: A Handbook of Physical Constants.* Washington DC, American Geophysical union, pp. 29-44.

Fujii, H., Okubo, H., Nishi, K., Itoi, R., Ohyama, K. & Shibata, K. (2009) An improved thermal response test for U-tube ground heat exchanger based on optical fiber thermometers. *Geothermics,* 38 (4), 399-406.

Gashti, E. H. N., Malaska, M. & Kujala, K. (2014) Evaluation of thermo-mechanical behaviour of composite energy piles during heating/cooling operations. *Engineering Structures,* 75 363-373.

Gawecka, K. A. (2017) *Numerical analysis of geothermal piles.* PhD thesis. Imperial College London.

Gawecka, K. A., Taborda, D. M. G., Potts, D. M., Cui, W., Zdravković, L. & Haji Kasri, M. S. (2017) Numerical modelling of thermo-active piles in London Clay. *Proceedings of the Institution of Civil Engineers: Geotechnical Engineering,* 170 (3), 201-219.

Gawecka, K. A., Potts, D. M., Cui, W., Taborda, D. M. G. & Zdravković, L. (2018) A coupled thermo-hydro-mechanical finite element formulation of one-dimensional beam elements for three-dimensional analysis. *Computers and Geotechnics,* 104 29-41.

Gawecka, K. A., Taborda, D. M. G., Potts, D. M., Sailer, E., Cui, W. & Zdravković, L. (2020) Finite element modelling of heat transfer in ground source energy systems with heat exchanger pipes. *ASCE International Journal of Geomechanics,* 20 (5), 1-14.

Georgiadis, K. (2003) *Development, Implementation and application of partially saturated soil models in finite element analysis.* PhD thesis. Imperial College London.

Grevers, C. (2017) *Modelling Single and Group Thermo-active Piles.* MSc thesis. Imperial College London.

GSHP Association (2012) *Thermal Pile - Design, Installation and Materials Standards.* Milton Keynes, GSHP Association.

Haehnlein, S., Bayer, P. & Blum, P. (2010) International legal status of the use of shallow geothermal energy. *Renewable and Sustainable Energy Reviews,* 14 (9), 2611-25.

Heinrich, J. C. & Zienkiewicz, O. C. (1977) Quadratic finite element schemes for two-dimensional convective-transport problems. *International Journal for Numerical Methods in Engineering,* 11 (12), 1831-1844.

Hight, D. W., Higgins, K. G., Jardine, R. J., Potts, D. M., Pickles, A. R., de Moor, E. K. & Nyirenda, Z. M. (1993) Predicted and measured tunnel distortions associated with construction of Waterloo International Terminal. In: Houlsby, G. T. & Schofield, A. N. (eds.) *Predictive soil mechanics.* London, Thomas Telford, pp. 317-338.

Hofinger, H. & Kohlböck, D. (2005) *Wirtschaftliche Optimierung Von Tunnelthermie®-Absorberanlagen.* iC-Consulenten. Report number: 12x05080 - Rev. 1.

Hueckel, T. & Baldi, G. (1990) Thermoplasticity of saturated clays: experimental constitutive study. *ASCE Journal of Geotechnical and Geoenvironmental Engineering,* 116 (12), 1778-1796.

Huyakorn, P. S. (1977) Solution of steady-state, convective transport equation using an upwind finite element scheme. *Applied Mathematical Modelling,* 1 (4), 187-195.

Institution of Civil Engineers (2007) *ICE specification for piling and embedded retaining walls.* 2nd Edition. London, Thomas Telford.

ISO (2017) *BS EN ISO 6946:2017 Building components and building elements - Thermal resistance and thermal transmittance - Calculation method*. British Standard Institution

Jardine, R. J. (1992) Some observations on the kinematic nature of soil stiffness. *Soils and Foundations,* 32 (2), 111-124.

Jorgensen, D. G. (1980) *Relationships between basic soils-engineering equations and basic ground-water flow equations.* United States Department of The Interior. Report number: 2064.

Kavanaugh, S. P. & Rafferty, K. D. (2014) *Ground-source heat pumps: design of ground source heat pump systems.* Atlanta, American Society of Heating, Refrigerating and Air-Conditioning Engineers.

Khalifa, A.-J. N. (2001) Natural convective heat transfer coefficient – a review: I. Isolated vertical and horizontal surfaces. *Energy Conversion and Management,* 42 (4), 491-504.

Khan, M. I. (2002) Factors affecting the thermal properties of concrete and applicability of its prediction models. *Building and Environment,* 37 607-614.

Kim, K., Jeon, S., Kim, J. & Yang, S. (2003) An experimental study on thermal conductivity. *Cement and Concrete Research,* 33 363-371.

King, W., Banks, D. & Findlay, J. (2012) Field determination of shallow soil thermal conductivity using a short-duration needle probe test. *Quarterly Journal of Engineering Geology and Hydrogeology,* 45 (4), 497-504.

Kürten, S., Mottaghy, D. & Ziegler, M. (2015) Design of plane energy geostructures based on laboratory tests and numerical modelling. *Energy and Buildings,* 107 434-444.

Lagioia, R., Puzrin, A. M. & Potts, D. M. (1996) A new versatile expression for yield and plastic potential surfaces. *Computers and Geotechnics,* 19 (3), 171-191.

Laloui, L., Nuth, M. & Vulliet, L. (2006) Experimental and numerical investigations of the behaviour of a heat exchanger pile. *International Journal for Numerical and Analytical Methods in Geomechanics,* 30 (8), 763-781.

Laloui, L. & Di Donna, A. (eds.) (2013) *Energy Geostructures: Innovation in Underground Engineering.* London, John Wiley & Sons, Inc.

Liu, H., Liu, H., Xiao, Y. & McCartney, J. S. (2018) Influence of Temperature on the Volume Change Behavior of Saturated Sand. *Geotechnical Testing Journal,* 41 (4), 747-758.

Liu, R. Y. W., Sailer, E., Taborda, D. M. G., Zdravković, L. & Potts, D. M. (2020) A practical method for determining thermally-induced stresses in pile foundations used as heat exchangers. *Computers and Geotechnics,* 126 1-16.

Loveridge, F., Holmes, G., Powrie, W. & Roberts, T. (2013) Thermal response testing through the Chalk aquifer in London, UK. *Proceedings of the Institution of Civil Engineers: Geotechnical Engineering,* 166 (2), 197-210.

Loveridge, F., Powrie, W. & Nicholson, D. (2014) Comparison of two different models for pile thermal response test interpretation. *Acta Geotechnica,* 9 (3), 367-384.

Loveridge, F., McCartney, J. S., Narsilio, G. A. & Sanchez, M. (2020) Energy geostructures: A review of analysis approaches, in situ testing and model scale experiments. *Geomechanics for Energy and the Environment,* 22 100173.

Makasis, N., Narsilio, G. A., Bidarmaghz, A. & Johnston, I. W. (2019) The Application of Retaining Walls and Slabs as Energy Structures in Underground Train Stations. In: Ferrari, A. & Laloui, L. (eds.) *Energy Geotechnics.* Berlin, Springer, pp. 535-50.

Markiewicz, R. (2004) *Numerical and Experimental Investigations for Utilization of Geothermal Energy Using Earth-Coupled Structures and New Developments for Tunnels.* PhD thesis. Vienna University of Technology.

Martinez Calonge, D. (2017) *Experimental investigation of the thermo-mechanical behaviour and thermal properties of London Clay.* PhD thesis. Imperial College London, UK.

Mimouni, T. & Laloui, L. (2015) Behaviour of a group of energy piles. *Canadian Geotechnical Journal,* 52 (12), 1913-1929.
Mitchell, J. K. (1993) *Fundamentals of soil behavior.* 2nd Edition. Chichester, New York, Wiley.
Murphy, K. D., McCartney, J. S. & Henry, K. S. (2015) Evaluation of thermo-mechanical and thermal behavior of full-scale energy foundations. *Acta Geotechnica,* 10 (2), 179-195.
Neville, A. M. (2011) *Properties of Concrete.* 5th Edition. Harlow, Prentice Hall
Ng, C. W. W., Wang, S. H. & Zhou, C. (2016) Volume change behaviour of saturated sand under thermal cycles. *Géotechnique Letters,* 6 (2), 124-131.
Ozudogru, T. Y., Olgun, C. G. & Senol, A. (2014) 3D numerical modeling of vertical geothermal heat exchangers. *Geothermics,* 51 312-324.
Palyvos, J. A. (2008) A survey of wind convection coefficient correlations for building envelope energy systems' modeling. *Applied Thermal Engineering,* 28 (8-9), 801-808.
Pang, M. H. (2018) *Numerical modelling of the thermal performance of the thermo-active retaining walls and its impact on their design.* MEng thesis. Imperial College London.
Peeters, L., Beausoleil-Morrison, I. & Novoselac, A. (2011) Internal convective heat transfer modeling: Critical review and discussion of experimentally derived correlations. *Energy and Buildings,* 43 (9), 2227-2239.
PLAXIS (2015) *Thermal and coupled THM analysis.* PLAXIS.
PLAXIS (2019) *PLAXIS* [Software] Delft, The Netherlands. Avaliable from: www.plaxis.com.
Pothiraksanon, C., Bergado, D. T. & Abuel-Naga, H. M. (2010) Full-scale embankment consolidation test using prefabricated vertical thermal drains. *Soils and Foundations,* 50 (5), 599-608.
Potts, D. M. & Zdravković, L. (1999) *Finite Element Analysis in Geotechnical Engineering: Theory.* London, Thomas Telford.
Potts, D. M. & Zdravković, L. (2001) *Finite Element Analysis in Geotechnical Engineering: Application.* London, Thomas Telford.
Preene, M. & Powrie, W. (2009) Ground energy systems: from analysis to geotechnical design. *Géotechnique,* 59 (3), 261-271.
Qi, H. (2015) *Thermal performance of the energy geotechncial structures.* PhD thesis. University of Cambridge.
Rammal, D., Mroueh, H. & Burlon, S. (2018) Thermal behaviour of geothermal diaphragm walls: Evaluation of exchanged thermal power. *Renewable Energy,*
Rawlings, R. H. D. & Sykulski, J. R. (1999) Ground source heat pumps: A technology review. *Building services engineering research & technology.,* 20 (3), 119-129.
Raymond, J. & Lamarche, L. (2014) Development and numerical validation of a novel thermal response test with a low power source. *Geothermics,* 51 434-444.
Raymond, J., Lamarche, L. & Malo, M. (2015) Field demonstration of a first thermal response test with a low power source. *Applied Energy,* 147 30-39.
Rees, S. J. & He, M. (2013) A three-dimensional numerical model of borehole heat exchanger heat transfer and fluid flow. *Geothermics,* 46 1-13.
Rees, S. W., Adjali, M. H., Zhou, Z., Davies, M. & Thomas, H. R. (2000) Ground heat transfer effects on the thermal performance of earth-contact structures. *Renewable and Sustainable Energy Reviews,* 4 (3), 213-265.
Rotta Loria, A. F. & Laloui, L. (2016) The interaction factor method for energy pile groups. *Computers and Geotechnics,* 80 121-137.
Rui, Y. (2014) *Finite element modelling of thermal piles and walls.* PhD thesis. University of Cambridge.
Rui, Y. & Yin, M. (2018) Thermo-hydro-mechanical coupling analysis of a thermo-active diaphragm wall. *Canadian Geotechnical Journal,* 55 (5), 720-735.
Sailer, E. (2014) *Design of closed loop ground source heat pump systems.* MSc thesis. Imperial College London.
Sailer, E., Taborda, D. M. G., Zdravkovic, L. & Potts, D. M. (2018a) Factors affecting the thermo-mechanical response of a retaining wall under non-isothermal conditions. In: *9th European Conference on Numerical Methods in Geotechnical Engineering, 25-28 June 2018, Porto, Portugal.* pp. 741-748.

Sailer, E., Taborda, D. M. G. & Zdravkovic, L. (2018b) A new approach to estimating temperature fields around a group of vertical ground heat exchangers in two-dimensional analyses. *Renewable energy,* 118 579-590.

Sailer, E., Taborda, D. M. G., Zdravković, L. & Potts, D. M. (2019a) Assessing the impact of vertical heat exchangers on the response of a retaining wall. In: *7th International Symposium on Deformation Characteristics of Geomaterials, 26-28 June 2019, Glasgow, UK.*

Sailer, E., Taborda, D. M. G., Zdravković, L. & Potts, D. M. (2019b) Fundamentals of the coupled thermo-hydro-mechanical behaviour of thermo-active retaining walls. *Computers and Geotechnics,* 109 189-203.

Sailer, E., Taborda, D. M. G., Zdravković, L., Potts, D. M. & Pang, M. (2019c) Long-term thermal performance of a thermo-active retaining wall. In: *17th European Conference on Soil Mechanics and Geotechnical Engineering 1-6 September 2019, Reykjavik, Iceland.* pp. 592-599.

Sailer, E., Taborda, D. M. G., Zdravković, L. & Potts, D. M. (2019d) Numerical modelling of thermo-active shafts. In: Ferrari, A. & Laloui, L. (eds.) *Energy Geotechnics.* Berlin, Springer, pp. 97-104.

Sailer, E., Taborda, D. M. G., Zdravković, L. & Potts, D. M. (2020a) A novel method for designing thermo-active retaining walls using two-dimensional analyses. *Proceedings of the Institution of Civil Engineers - Geotechnical Engineering,* (ahead of print)

Sailer, E., Taborda, D. M. G., Zdravković, L., Potts, D. M. & Cui, W. (2020b) Thermo-hydro-mechanical interactions in porous media: implications on thermo-active retaining walls. (under review)

Sani, A. K., Singh, R. M., Tsuha, C. d. H. C. & Cavarretta, I. (2019a) Pipe–pipe thermal interaction in a geothermal energy pile. *Geothermics,* 81 209-223.

Sani, A. K., Singh, R. M., Amis, T. & Cavarretta, I. (2019b) A review on the performance of geothermal energy pile foundation, its design process and applications. *Renewable and Sustainable Energy Reviews,* 106 54-78.

Sanner, B. (2019) Summary of EGC 2019 Country update reports on geothermal energy in Europe. In: *European Geothermal Congress, 11-14 June 2019, Den Haag, The Netherlands.*

Savvidou, C. & Britto, A. M. (1995) Numerical and experimental investigation of thermally induced effects in saturated clay. *Soils and Foundations,* 35 (1), 37-44.

Schroeder, F. C., Potts, D. M. & Addenbrooke, T. I. (2004) The influence of pile group loading on existing tunnels. *Geotechnique,* 54 (6), 351-362.

SIA (2005) *SIA D 0190.* Nutzung der Erdwärme mit Fundationspfählen und anderen erdberührten Betonbauteilen - Leitfaden zu Planung, Bau und Betrieb. Zürich, Schweizerischer Ingenieur- und Architektenverein.

Soga, K., Qi, H., Rui, Y. & Nicholson, D. (2014) Some considerations for designing GSHP coupled geotechnical structures based on a case study. In: *7th International Congress on Environmental Geotechnics, Melbourne, Australia.* pp. 24-41.

Sterpi, D., Angelotti, A., Corti, D. & Ramus, M. (2014) Numerical analysis of heat transfer in thermo-active diaphragm walls. *Numerical Methods in Geotechnical Engineering - Proceedings of the 8th European Conference on Numerical Methods in Geotechnical Engineering, NUMGE 2014,* 2 1043-1048.

Sterpi, D., Coletto, A. & Mauri, L. (2017) Investigation on the behaviour of a thermo-active diaphragm wall by thermo-mechanical analyses. *Geomechanics for Energy and the Environment,* 9 1-20.

Sterpi, D., Angelotti, A., Habibzadeh-Bigdarvish, O. & Jalili, D. (2018) Assessment of thermal behaviour of thermo-active diaphragm walls based on monitoring data. *Journal of Rock Mechanics and Geotechnical Engineering,* 10 (6), 1145-1153.

Sterpi, D., Tomaselli, G. & Angelotti, A. (2020) Energy performance of ground heat exchangers embedded in diaphragm walls: Field observations and optimization by numerical modelling. *Renewable Energy,* 147 2748-2760.

Suckling, T. P. & Smith, P. E. H. (2002) Environmentally friendly geothermal piles at KebleCollege, Oxford, UK. In: *9th International conference on piling and deep foundations Nice, France.* Deep Foundation Institute.

Sultan, N., Delage, P. & Cui, Y. J. (2002) Temperature effects on the volume change behaviour of Boom clay. *Engineering geology,* 64 (2-3), 135-145.

Sun, M., Xia, C. & Zhang, G. (2013) Heat transfer model and design method for geothermal heat exchange tubes in diaphragm walls. *Energy and Buildings,* 61 250-259.

Taborda, D. M. G., Potts, D. M. & Zdravković, L. (2016) On the assessment of energy dissipated through hysteresis in finite element analysis. *Computers and Geotechnics,* 71 180-194.

Tatro, S. B. (2006) Thermal properties. In: Lamond, J. F. & Pielert, J. (eds.) *Significance of tests and properties of concrete and concrete-making materials.* West Conshohocken, PA, ASTM International, pp. 226-237.

Tsiampousi, A. (2011) *Numerical analysis of slopes in unsaturated soils.* PhD thesis. Imperial College London.

Tsiampousi, A., Zdravković, L. & Potts, D. M. (2013) A new Hvorslev surface for critical state type unsaturated and saturated constitutive models. *Computers and Geotechnics,* 48 156-166.

UK Parliament (2008) *Climate Change Act*.

Vardon, P. J., Baltoukas, D. & Peuchen, J. (2019) Interpreting and validating the thermal cone penetration test (T-CPT). *Géotechnique,* 69 (7), 580-592.

VDI (2010) *VDI 4640 – Blatt 1.* Thermal use of the underground: fundamentals, approvals, environmental aspects. Düsseldorf, Verein Deutscher Ingegneure.

Vélez Márquez, M., Raymond, J., Blessent, D., Philippe, M., Simon, N., Bour, O. & Lamarche, L. (2018) Distributed Thermal Response Tests Using a Heating Cable and Fiber Optic Temperature Sensing. *Energies,* 11 (11),

Wallentén, P. (2001) Convective heat transfer coefficients in a full-scale room with and without furniture. *Building and Environment,* 36 743-751.

Williams, G. P. & Gold, L. W. (1976) Ground temperatures. *Canadian Building Digests,* CBD-180

Wood, L. A. & Perrin, A. J. (1984a) Monitoring of a deep basement in London. In: *International conference on Case Histories in Geotechnical Engineering, 6–11 May, Rolla, Missouri.* pp. 301–308.

Wood, L. A. & Perrin, A. J. (1984b) Observations of a strutted diaphragm wall in London clay: A preliminary assessment. *Geotechnique,* 34 (4), 563-579.

Wood, W. L. (1990) *Practical time-stepping schemes.* Oxford, Clarendon Press.

Xia, C., Sun, M., Zhang, G., Xiao, S. & Zou, Y. (2012) Experimental study on geothermal heat exchangers buried in diaphragm walls. *Energy and Buildings,* 52 50-55.

Yin, M. & Rui, Y. (2019) Investigation of long-term behaviour of thermal wall by finite element analysis. *Soils and Foundations,* 59 (5), 1182-1192.

You, S., Cheng, X., Guo, H. & Yao, Z. (2014) In-situ experimental study of heat exchange capacity of CFG pile geothermal exchangers. *Energy and Buildings,* 79 23-31.

You, S., Zhang, C. H., Cheng, X. H. & Zhu, M. (2019) Centrifuge Simulation of the Thermal Response of a Dry Sand-Embedded Diaphragm Wall. *Strength of Materials,* 51 (1), 62-68.

Zdravković, L., Potts, D. M. & St. John, H. D. (2005) Modelling of a 3D excavation in finite element analysis. *Geotechnique,* 55 (7), 497-513.

Ziegler, M., Koppmann, D., Peching, R. & Knapp, D. (2019) Energy sheet pile walls – Experimental and numiercal investigation of innovative energy geostructures. In: *XVII European Conference on Soil Mechanics and Geotechnical Engineering, 1-6 September 2019, Reykjavik, Iceland.* pp. 932-939.

Appendix A

Temperature distribution for solid of length L with constant temperature T_0 at x=0 and T_1 at x=L

The temperature distributions for different x-coordinates and time instants for a solid of length L, with temperature T_0 applied at $x = 0$ and temperature T_1 applied at $x = L$, can be calculated analytically using the following expression (Carslaw & Jaeger, 1959):

$$\begin{aligned} & T(x,t) \\ &= T_0 + (T_1 - T_0)\frac{x}{L} + \frac{2}{\pi}\sum_{n=1}^{\infty}\frac{T_1 \cos n\pi - T_0}{n}\sin\frac{n\pi x}{L}e^{-n^2\pi^2 Fo} \\ &+ \sum_{1}^{\infty} sin\frac{n\pi x}{L}e^{-n^2\pi^2 Fo}\int_0^L f(x')\, cos\frac{(2n+1)\pi x'}{2L} \end{aligned} \tag{A-1}$$

where $\int_0^L f(x')dx'$ is the function of the initial temperature distribution and F_o is the Fourier number (expressed as $\alpha_T t/L^2$). For the special case of a constant initial temperature distribution of 0°C or if changes in temperature from an initially constant temperature distribution wish to be calculated, Equation (A-1) reduces to:

$$T(x,t) = T_0 + (T_1 - T_0)\frac{x}{L} + \frac{2}{\pi}\sum_{n=1}^{\infty}\frac{T_1 \cos n\pi - T_0}{n}\sin\frac{n\pi x}{L}e^{-n^2\pi^2 Fo} \tag{A-2}$$

Temperature distribution for solid of length L with no heat flux at x=0 and constant temperature T_0 at x=L

The equation below (Carslaw & Jaeger, 1959) allows the calculation of the temperature distributions for a solid of length L where the boundary at $x = 0$ is insulated and at $x = L$ is kept at constant temperature T_0:

$$T(x,t) = T_0 + \frac{2}{L}\sum_{n=0}^{\infty} e^{-(2n+1)^2\pi^2 Fo/4} \cos\frac{(2n+1)\pi x}{2L}\left\{\frac{2L(-1)^{n+1}T_0}{(2n+1)\pi} + \int_0^L f(x')\cos\frac{(2n+1)\pi x'}{2L}dx'\right\} \quad \text{(A-3)}$$

For the special case of a constant initial temperature distribution of 0°C or if changes in temperature from an initially constant temperature distribution wish to be calculated, Equation (A-3) reduces to:

$$T(x,t) = T_0 + \frac{2}{L}\sum_{n=0}^{\infty} e^{-(2n+1)^2\pi^2 Fo/4} \cos\frac{(2n+1)\pi x}{2L}\left\{\frac{2L(-1)^{n+1}T_0}{(2n+1)\pi}\right\} \quad \text{(A-4)}$$

Appendix B

B.1 Additional parametric study on Problem A

A similar parametric study on the influence of α_{TH} to that presented in Section 3.4.3 is presented. The aim is to demonstrate the validity of the conclusions drawn for the same values of α_{TH}, though obtained with a different combination of parameters. Consequently, the analyses are performed on Problem A.

The same geometry and boundary conditions of Problem A are shown in Section 3.4.3 are employed. In Section 3.4.3 α_{TH} was varied by varying the permeability of the soil. The same values of α_{TH} are obtained herein by varying the thermal conductivity of the soil according to Table B-2, while all other problem parameters (see Table B-1) remained unchanged.

Clearly, the use of different values of thermal conductivity implies that for the same time instants different temperature distributions are obtained. For this reason, it is highlighted that analyses with equal α_{TH} present the same results only for an equal value of degree of heat transfer, R. It is specified that the analyses were carried out by varying the time-step, rather than the length of the analysis. This allowed to avoid oscillations in temperature due to the thermal-shock problem, since the critical time step increases with reducing thermal conductivity of the soil (see Cui et al. (2016b) for details). Hence, the time step used is inversely proportional to the thermal conductivity of the soil (i.e. larger time steps were used for analysis with low thermal conductivities). Furthermore, it is important to note that, to cover the same interval of values of α_{TH} as those analysed in Section 3.4.3 by varying the thermal conductivity, values which are outside the typical range for soils (e.g. VDI, 2010) were employed, for the sole purpose of proving the validity of the observed phenomena.

Table B-1: Material properties of one-dimensional problems

Bulk modulus of soil skeleton (MPa)	K_s	83.3
Poisson's ratio (-)	ν	0.3
Permeability (m/s)	k	1.0×10^{-10}
Thermal conductivity (W/mK)	λ	variable (*)
Volumetric heat capacity (kJ/m^{3}K)	C_v	3000.0
Coefficient of thermal expansion of soil (m/mK)	α_s	1.0×10^{-5}
Coefficient of thermal expansion of water (m/mK)	α_w	6.9×10^{-5}
Bulk modulus of fluid (GPa)	K_f	2.2
Porosity (-)	n	0.5

(*) see Table B-2

Table B-2: Performed analyses for parametric study on the influence of α_{TH}

α_H (m^2/s)	λ (m/s)	α_T (m^2/s)	α_{TH}
8.34×10^{-7}	2.0×10^{-8}	6.67×10^{-12}	8.0×10^{-6}
	2.0×10^{-5}	6.67×10^{-9}	8.0×10^{-3}
	2.0×10^{-3}	6.67×10^{-7}	8.0×10^{-1}
	2.0×10^{-1}	6.67×10^{-5}	8.0×10^{1}
	2.0×10^{1}	6.67×10^{-3}	8.0×10^{3}

The influence of α_{TH} is analysed in terms of excess pore water pressures developing at the heat source (in terms of $u^* = \Delta u_{FE}/\Delta u_{AN}$), both at the beginning of the analyses and their development with time, and of excess pore water pressures taking place ahead of changes in temperature, for different values of R.

The results obtained are depicted in Figure B-1, Figure B-2 and Figure B-3. When comparing to the results shown in Section 3.4.3, it can be noted that identical values are obtained. This demonstrates that indeed α_{TH} controls the rate at which THM interactions take place and, when evaluated at the same value of R, identical results are obtained for α_{TH} obtained with different combinations of parameters.

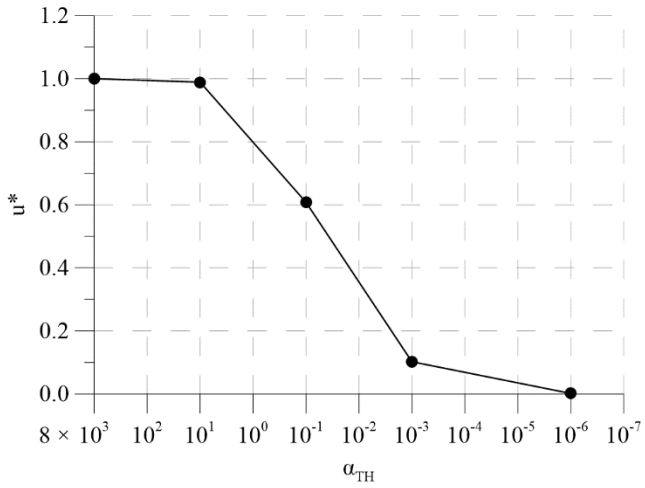

Figure B-1: Variation of u^* at the heat source at beginning of the analysis with α_{TH}

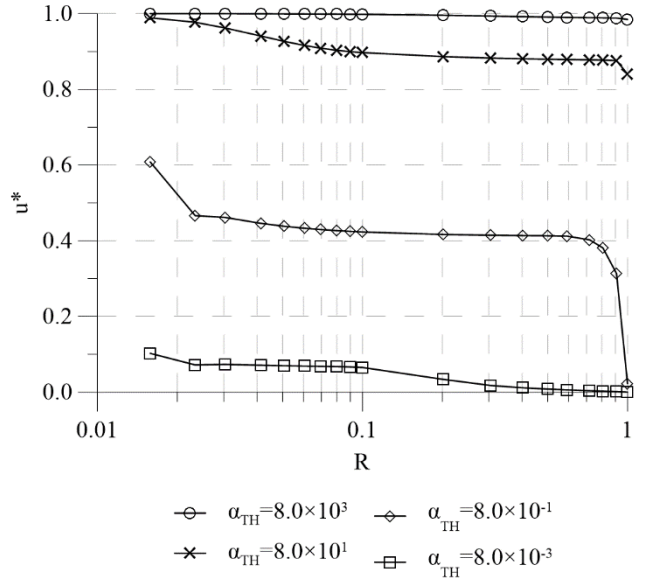

Figure B-2: Variation of u^* at heat source with R for different α_{TH}

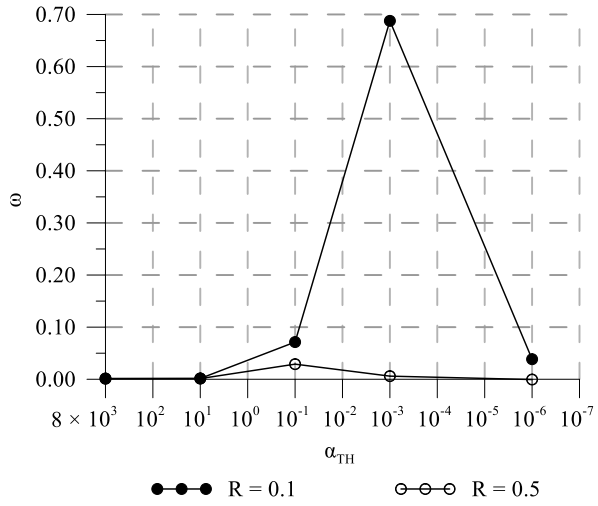

Figure B-3: Variation of ω with α_{TH} for R = 0.1 and R = 0.5

B.2 Additional parametric study on thermo-active wall problem

A similar exercise to the one described in the previous section was also performed for the thermo-active wall problem described in Section 3.5. The aim is to analyse the impact of different values of α_{TH} obtained with a different combination of parameters with respect to those shown in Section 3.5.3.

For this purpose, the same values of α_{TH} were used by varying the thermal conductivity of the soil, as shown in Table B-3, while all other parameters remained unchanged from those outlined in Section 3.2.4.

Table B-3: Parameters of parametric study for THM interactions in thermo-active retaining wall problem

Analysis	λ (W/mK)	α_T (m^2/s)	α_H (m^2/s)	α_{TH} (-)
High	2.0×10^{-2}	9.8×10^{-9}		2.6×10^{2}
Base case	2.0×10^{0}	9.8×10^{-7}	3.8×10^{-7}	2.6×10^{0}
Low	2.0×10^{2}	9.8×10^{-5}		2.6×10^{-2}

As for the previous problem, it should be highlighted that the use of different thermal conductivities implies that changes in temperature occur at a different rate. Thus, different time steps were employed for the three different analyses and the results are shown as changes against dimensionless time, i.e. Fourier number (F_o), calculated as $\alpha_T t/L^2$, where for L a nominal value of 1.0 m was employed.

The development of axial forces and bending moments with F_o are displayed in Figure B-4 (a) and (b), respectively, while the evolution of the vertical movement of the top of the wall against F_o is shown in Figure B-5. When comparing to the results shown in Section 3.5.3, it can be observed that the same behaviour is computed. This further proves that the THM interactions are controlled by the value of α_{TH} and that these affect the transient response of the wall.

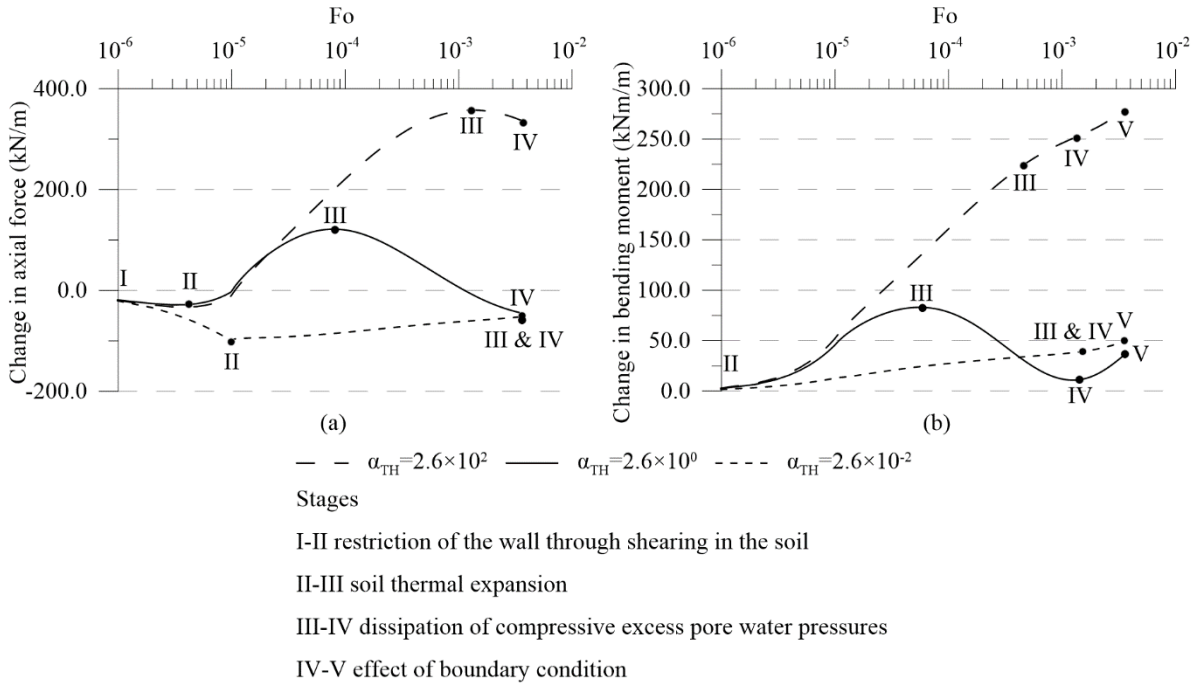

Figure B-4: Effect of α_{TH} on the development of structural forces with dimensioless time F_o (a) axial forces and (b) bending moments

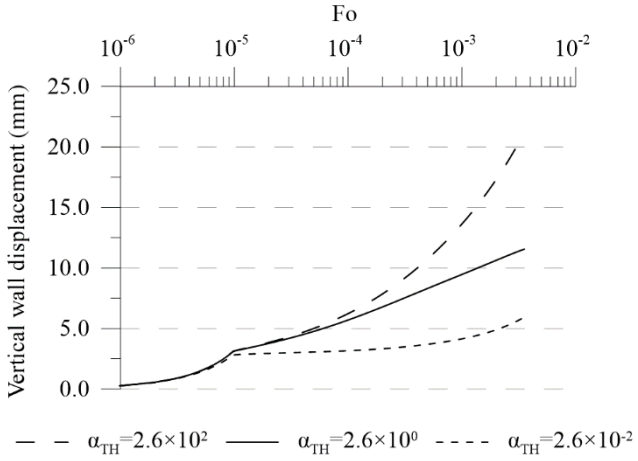

Figure B-5: Effect of α_{TH} of the vertical movement of top of wall with dimensioless time F_o

Appendix C

The average temperature of a section containing n elements is given by:

$$\bar{T}_{sect} = \frac{\sum_1^n \bar{T}_{el} \cdot V_{el}}{V_{sect}} \tag{C-1}$$

where the subscript el and $sect$ refer to element and section, respectively. The term $\bar{T}_{el} \cdot V_{el}$ represents the integral over the volume of the element of the temperatures within the element, the calculation of which varies according to the type of element (linear or quadratic), order of integration and type of analysis, i.e. whether it is a 3D element or a 2D element modelled in plane-strain or axi-symmetric conditions.

C.1 Average temperature for 2D elements

The general form of the volume integral is expressed by the following equation for plane-strain analyses:

$$\iiint T dx dy dz = \sum_{i=1}^{m} \left[\sum_{j=1}^{m} w_i \cdot w_j \cdot T\left(x(s_i, t_j), y(s_i, t_j)\right) \cdot \left|J(s_i, t_j)\right| \right] \tag{C-2}$$

where $T\left(x(s_i, t_j), y(s_i, t_j)\right)$ are the temperatures computed at the integration points of coordinates x and y expressed in terms of the parent element coordinate system s and t (see Figure C-1), $\left|J(s_i, t_j)\right|$ is the Jacobian determinant calculated for the integration point at coordinates (s_i, t_j), w_i and w_j are the weights applied to the integration points, and m is the number of integration points along one direction (either 2 or 3). The weights w_i and w_j depend on the integration scheme and those defined by the Gauss-Legendre quadrature are adopted (i.e. for a 2×2 integration, these are equal to 1.0; for a 3×3 integration, the weights are $w_1 = 5/9$, $w_2 = 8/9$ and $w_3 = 5/9$).

The volume integral for axi-symmetric analyses is equal to:

$$\iiint T dr dz d\theta = 2\pi \sum_{i=1}^{m} \left[\sum_{j=1}^{m} w_i \cdot w_j \cdot T\left(r(s_i, t_j), z(s_i, t_j)\right) \cdot |J(s_i, t_j)| \, r(s_i, t_j) \right] \quad \text{(C-3)}$$

where $T\left(r(s_i, t_j), z(s_i, t_j)\right)$ are the temperatures computed at the integration points of coordinates r and z expressed in terms of the parent element coordinate system s and t and $r(s_i, t_j)$ is the radial coordinate of the integration point, calculated as:

$$r(s_i, t_j) = \sum_{1}^{n} r_i N_i \quad \text{(C-4)}$$

where n is the number of nodes of an element, r_i is the global coordinate of node i and N_i is the associated shape function calculated with s and t coordinates of the considered integration point.

$|J|$ is the determinant of the Jacobian matrix, J, which is required when making a change of variables to evaluate a multiple integral of a function. In this case, the temperature is evaluated at the Gauss points and a change of variables between the global coordinate system and the natural coordinate system is required. The Jacobian matrix J contains the derivatives of the global coordinates with respect to the natural coordinates:

$$J = \begin{bmatrix} \frac{\partial x}{\partial s} & \frac{\partial y}{\partial s} \\ \frac{\partial x}{\partial t} & \frac{\partial y}{\partial t} \end{bmatrix} \quad \text{(C-5)}$$

$$J = \begin{bmatrix} \frac{\partial r}{\partial s} & \frac{\partial z}{\partial s} \\ \frac{\partial r}{\partial t} & \frac{\partial z}{\partial t} \end{bmatrix} \quad \text{(C-6)}$$

where Equation (C-5) and (C-6) refer to plane strain and axi-symmetric conditions, respectively.

Thus, the determinant is computed as:

$$|J| = \frac{\partial x}{\partial s}\frac{\partial y}{\partial t} - \frac{\partial y}{\partial s}\frac{\partial x}{\partial t} \quad \text{(C-7)}$$

or

$$|J| = \frac{\partial r}{\partial s}\frac{\partial z}{\partial t} - \frac{\partial r}{\partial s}\frac{\partial z}{\partial t} \quad \text{(C-8)}$$

where the derivatives are calculated as the product of the global coordinates of the nodes and the derivative of the shape function with respect to the natural coordinate.

For plane-strain analyses:

$$\frac{\partial x}{\partial s} = x_1 \frac{\partial N_1}{\partial s} + \cdots + x_n \frac{\partial N_n}{\partial s} \quad \text{(C-9)}$$

$$\frac{\partial x}{\partial t} = x_1 \frac{\partial N_1}{\partial t} + \cdots + x_n \frac{\partial N_n}{\partial t} \quad \text{(C-10)}$$

$$\frac{\partial y}{\partial s} = y_1 \frac{\partial N_1}{\partial s} + \cdots + y_n \frac{\partial N_n}{\partial s} \quad \text{(C-11)}$$

$$\frac{\partial y}{\partial t} = y_1 \frac{\partial N_1}{\partial t} + \cdots + y_n \frac{\partial N_n}{\partial t} \quad \text{(C-12)}$$

For axi-symmetric analyses:

$$\frac{\partial r}{\partial s} = r_1 \frac{\partial N_1}{\partial s} + \cdots + r_n \frac{\partial N_n}{\partial s} \quad \text{(C-13)}$$

$$\frac{\partial r}{\partial t} = r_1 \frac{\partial N_1}{\partial t} + \cdots + r_n \frac{\partial N_n}{\partial t} \quad \text{(C-14)}$$

$$\frac{\partial z}{\partial s} = z_1 \frac{\partial N_1}{\partial s} + \cdots + z_n \frac{\partial N_n}{\partial s} \quad \text{(C-15)}$$

$$\frac{\partial z}{\partial t} = z_1 \frac{\partial N_1}{\partial t} + \cdots + z_n \frac{\partial N_n}{\partial t} \quad \text{(C-16)}$$

where x_i and y_i are the global coordinates of the nodes in plane-strain analyses, r_i and z_i are the global coordinates of the nodes in axi-symmetric analyses and N_i are the shape functions associated to a node (see Potts & Zdravković (1999) for their equations), where the subscripts 1 to n denote the position of the nodes, which ranges from 1 to 4 for linear elements and from 1 to 8 for quadratic elements (see respectively Figure C-1 (a) and (b)).

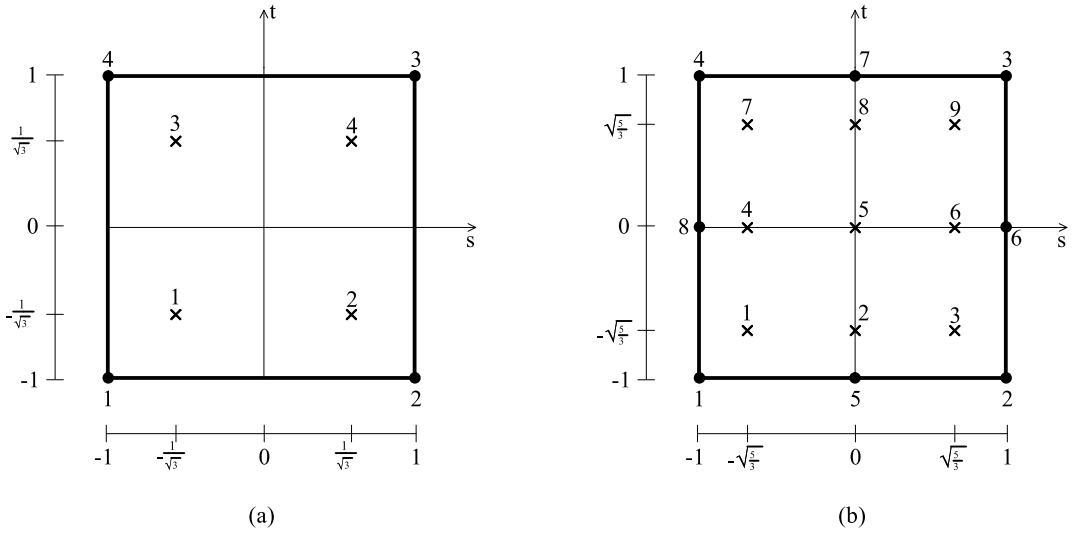

Figure C-1: Isoparametric two-dimensional element (a) linear with 2×2 integration and (b) quadratic with 3×3 integration

In Equation (C-1), V_{sect} is the total volume of the section containing n elements for which the average temperature is evaluated. This is calculated as the sum of the volumes of the elements, V_{el}, within the section:

$$V_{sect} = \sum_{1}^{n} V_{el,i} \tag{C-17}$$

The volume of a single element, which may have straight or curved sides, is calculated as follows for plane-strain conditions:

$$V_{el} = \iiint 1 dx dy dz = \sum_{i=1}^{m} \left[\sum_{j=1}^{m} w_i \cdot w_j \cdot \left| J(s_i, t_j) \right| \right] \tag{C-18}$$

The following equation is adopted for axi-symmetric conditions

$$V_{el} = \iiint 1 dr dz d\theta = 2\pi \sum_{i=1}^{m} \left[\sum_{j=1}^{m} w_i \cdot w_j \cdot \left| J(s_i, t_j) \right| \cdot r(s_i, t_j) \right] \tag{C-19}$$

C.2 Average temperature for 3D elements

For 3D elements, the general form of the volume integral is expressed as:

$$\iiint T dx dy dz$$
$$= \sum_{i=1}^{m} \left\{ \sum_{j=1}^{m} \left[\sum_{k=1}^{m} w_i \cdot w_j \cdot w_k \cdot T\left(x(s_i, t_j, u_k), y(s_i, t_j, u_k), z(s_i, t_j, u_k) \right) \cdot \left| J(s_i, t_j, u_k) \right| \right] \right\} \tag{C-20}$$

where $T\left(x(s_i, t_j, u_k), y(s_i, t_j, u_k), z(s_i, t_j, u_k) \right)$ are the temperatures computed at the integration points of coordinates x, y and z expressed in terms of the parent element coordinate system s, t and u, $\left| J(s_i, t_j, u_k) \right|$ is the Jacobian determinant calculated for the integration point at coordinates (s_i, t_j, u_k), w_i, w_j and w_k are the weights applied to the integration points, and m is the number of integration points along one direction (either 2 or 3).

$|J|$ is the determinant of the Jacobian matrix, J, containing the derivatives of the global coordinates with respect to the natural coordinates:

$$J = \begin{bmatrix} \frac{\partial x}{\partial s} & \frac{\partial y}{\partial s} & \frac{\partial z}{\partial s} \\ \frac{\partial x}{\partial t} & \frac{\partial y}{\partial t} & \frac{\partial z}{\partial t} \\ \frac{\partial x}{\partial u} & \frac{\partial y}{\partial u} & \frac{\partial z}{\partial u} \end{bmatrix} \tag{C-21}$$

The determinant is then expressed as:

$$|J| = \frac{\partial x}{\partial s}\left(\frac{\partial y}{\partial t}\cdot\frac{\partial z}{\partial u} - \frac{\partial z}{\partial t}\cdot\frac{\partial y}{\partial u}\right) - \frac{\partial y}{\partial s}\left(\frac{\partial x}{\partial t}\cdot\frac{\partial z}{\partial u} - \frac{\partial z}{\partial t}\cdot\frac{\partial x}{\partial u}\right) + \frac{\partial z}{\partial s}\left(\frac{\partial x}{\partial t}\cdot\frac{\partial y}{\partial u} - \frac{\partial y}{\partial t}\cdot\frac{\partial x}{\partial u}\right) \tag{C-22}$$

The derivatives required to calculate the Jacobian determinant are:

$$\frac{\partial x}{\partial s} = x_1\frac{\partial N_1}{\partial s} + \cdots + x_n\frac{\partial N_n}{\partial s} \tag{C-23}$$

$$\frac{\partial x}{\partial t} = x_1\frac{\partial N_1}{\partial t} + \cdots + x_n\frac{\partial N_n}{\partial t} \tag{C-24}$$

$$\frac{\partial x}{\partial u} = x_1\frac{\partial N_1}{\partial u} + \cdots + x_n\frac{\partial N_n}{\partial u} \tag{C-25}$$

$$\frac{\partial y}{\partial s} = y_1\frac{\partial N_1}{\partial s} + \cdots + y_n\frac{\partial N_n}{\partial s} \tag{C-26}$$

$$\frac{\partial y}{\partial t} = y_1\frac{\partial N_1}{\partial t} + \cdots + y_n\frac{\partial N_n}{\partial t} \tag{C-27}$$

$$\frac{\partial y}{\partial u} = y_1\frac{\partial N_1}{\partial u} + \cdots + y_n\frac{\partial N_n}{\partial} \tag{C-28}$$

$$\frac{\partial z}{\partial s} = z_1\frac{\partial N_1}{\partial s} + \cdots + z_n\frac{\partial N_n}{\partial s} \tag{C-29}$$

$$\frac{\partial z}{\partial t} = z_1\frac{\partial N_1}{\partial t} + \cdots + z_n\frac{\partial N_n}{\partial t} \tag{C-30}$$

$$\frac{\partial z}{\partial u} = z_1\frac{\partial N_1}{\partial u} + \cdots + z_n\frac{\partial N_n}{\partial u} \tag{C-31}$$

where x_i, y_i and z_i are the global coordinates of the nodes and N_i are the shape functions associated to a node (see Potts & Zdravković (1999) for their equations), where the subscripts 1 to n denote the number of the node and corresponding shape function (with n ranging from 1 to 8 for linear elements and from 1 to 20 for quadratic elements).

To calculate the total volume of the section containing n elements the volumes of the single elements within the section are summed according to Equation (C-17). The volume of a single element in 3D is computed as follows:

$$V_{el} = \iiint 1\,dx\,dy\,dz = \sum_{i=1}^{m}\left\{\sum_{j=1}^{m}\left[\sum_{k=1}^{m} w_i \cdot w_j \cdot w_k \cdot \left|J(s_i, t_j, u_k)\right|\right]\right\} \tag{C-32}$$

Appendix D

D.1 Effect of spatial discretisation on modelling heat conduction with different boundary condition types

D.1.1 Problem description

To assess the influence of spatial discretisation when modelling thermal problems, a 2D plane-strain analysis simulating transient radial heat conduction from a single point source was carried out. The geometry and the initial conditions of the problem are shown in Figure D-1, with the adopted material properties being a thermal conductivity, λ of 1.0 W/mK and a volumetric heat capacity, C_v, of 2656.0 kJ/m^{3}K.

The problem shown in Figure D-1 was discretised with meshes having two different element sizes in the radial direction, i.e. 0.025 m and 1.0 m, where the first mesh is termed as "fine mesh" (F), having an element size which is 40 times smaller than the second mesh, which is designated as "coarse mesh" (C). It should be noted that the difference in solutions could be hardly observed when an element size below 0.025 m was used (e.g. 0.01 m). Two boundary conditions (BCs), i.e. the Dirichlet-type BC, specifying a temperature increase of 1.0˚C and keeping the temperature constant throughout the analysis, and the Neumann-type BC, specifying a injected heat flux of 1.0 W throughout the analysis, were prescribed at point 1 in Figure D-1. These represent two commonly used approaches in modelling heat sources. In addition, the influence of element types (i.e. 4-noded linear and 8-noded quadratic elements) as well as integration schemes for the 8-noded quadratic element (i.e. 3×3 full integration and 2×2) were also studied. All the performed analyses are listed in Table D-1, where the letters "N" and "D" indicate a Neumann-type or a Dirichlet-type BC. The time-step was chosen so that oscillatory solutions in temperature at the initial stage of the simulation were avoided for all analyses (Cui et al., 2016b; Cui et al., 2019).

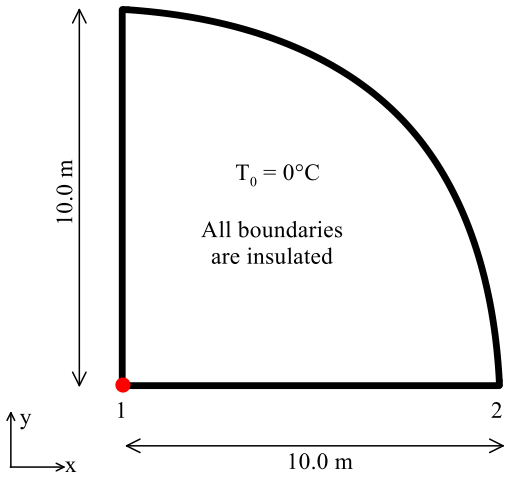

Figure D-1: Geometry and initial conditions

Table D-1: Analysed cases for demonstrating the effect of spatial discretisation on the modelling of heat conduction

Analysis	Element size in radial direction (m)	Boundary condition	Element type	Integration order
DF-I	0.025	Prescribed temperature change (Dirichlet-type)	4-noded	2×2
DF-II	0.025		8-noded	2×2
DF-III	0.025		8-noded	3×3
DC-I	1.0		4-noded	2×2
DC-II	1.0		8-noded	2×2
DC-III	1.0		8-noded	3×3
NF-I	0.025	Prescribed heat flux (Neumann-type)	4-noded	2×2
NF-II	0.025		8-noded	2×2
NF-III	0.025		8-noded	3×3
NC-I	1.0		4-noded	2×2
NC-II	1.0		8-noded	2×2
NC-III	1.0		8-noded	3×3

To quantify the impact of different mesh discretisation, the distribution of the nodal temperatures along line 1-2 in Figure D-1 were evaluated. In addition, the energy transferred per unit volume over the domain via the prescribed boundary condition is computed through Equation (D-1):

$$E_{i,\Omega} = C_v \cdot \left(\bar{T}_{i,\Omega} - T_0\right) \tag{D-1}$$

where $\bar{T}_{i,\Omega}$ is the average temperature over a region Ω of area A_Ω at a time instant $t = t_i$:

$$\bar{T}_{i,\Omega} = \frac{\iint_{\Omega} T_i \, dA}{A_{\Omega}} \tag{D-2}$$

which was evaluated through numerical integration according to Appendix C.

It should be noted that all the results are presented normalised by the value of either the applied prescribed temperature or heat flux, since the temperature distributions are directly proportional to the magnitude of the BC.

D.1.2 Dirichlet type boundary condition (prescribed temperature)

When the Dirichlet-type BC (i.e. prescribed nodal temperature, T, of 1.0°C) was applied, significant mesh effects were observed when comparing the results from analyses with element sizes of 1.0m (coarse, DC-I, DC-II) and 0.025 m (fine, DF-I, DF-II). Figure D-2 (a) shows the variation of the input energy per unit volume over the whole mesh, $E_{i,\Omega}$, normalised by the applied nodal temperature. It can be seen that the element size has a large impact on the energy being transferred into the mesh (e.g. DF-I vs DC-I). Clearly, the differences in the transferred energy imply substantial differences in transient temperature fields, with the coarse mesh displaying significantly larger temperatures than the fine mesh, as shown in Figure D-2 (b). Moreover, when larger elements (i.e. 1.0 m) are employed, quadratic elements (DC-II) perform better, with the solutions being closer to the reference ones using the fine mesh, due to a much shorter spacing between temperature degrees of freedom (see DC-I vs DC-II in both Figure D-2 (a) and 2(b)). For analyses with small elements (i.e. 0.025m), the difference induced by element types (see DF-I vs DF-II) is negligible. It is also noted that the integration order had no substantial impact (DF-II vs DF-III) and therefore is not shown for brevity.

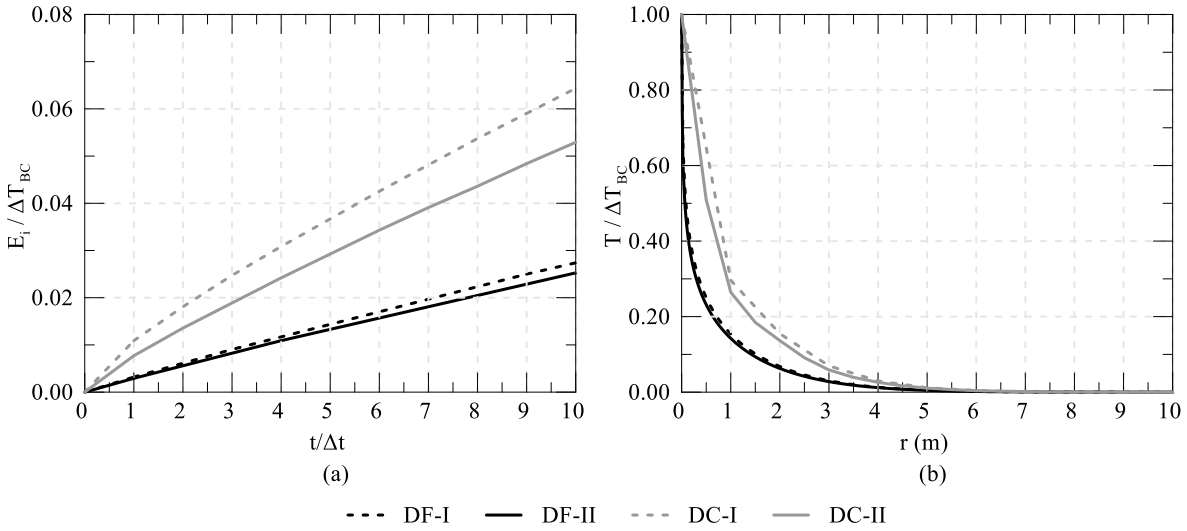

Figure D-2: Effect of mesh refinement and element type with Dirichlet-type BC on (a) variation of energy per unit volume and (b) distribution of the temperature along line 1-2 at $t/\Delta t = 10$

D.1.3 Neumann type boundary condition (prescribed heat flux)

With the Neumann-type BC (i.e. a constant heat flux, q, of 1.0 W), a different scenario is observed. The same transferred energy was obtained regardless of the employed mesh, as shown in Figure D-3 (a). It should be noted that the slope of the line in Figure D-3 (a) reflects the heat flux specified by the prescribed boundary condition. Similarly, a negligible difference in the nodal temperatures is evaluated, with the largest difference existing at the point where the boundary condition is prescribed (see NF-I vs NC-I and NF-II vs NC-II in Figure D-3 (b)), with this difference being confined to a very small region near the heat source. Similarly, the element type has an impact only for coarse meshes with NC-II being marginally closer to the reference case (NF-II) than NC-I in Figure D-3 (b), while the integration order had an negligible impact (NF-II vs NF-III) and is therefore not shown for brevity.

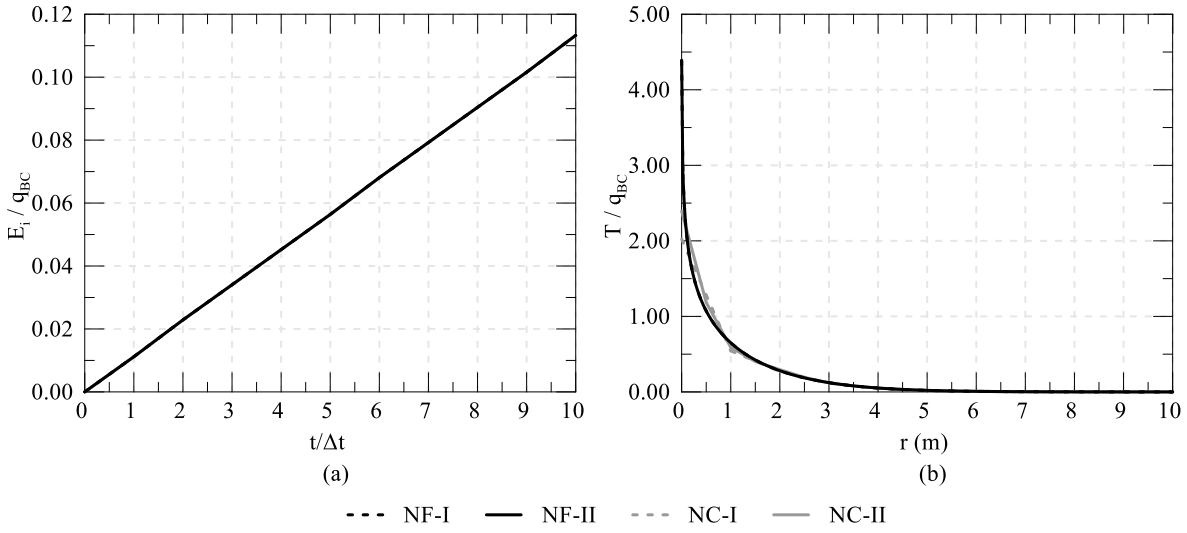

Figure D-3: Effect of mesh refinement and element type with Neumann-type BC on (a) variation of energy per unit volume and (b) distribution of the temperature along line 1-2 at $t/\Delta t = 10$

D.1.4 Concluding remarks

In conclusion, when the energy transferred to the soil is specified via the heat flux boundary condition (Neumann-type), the adopted spatial discretisation has a very limited impact on the results even when the difference in element size is substantial (40 times difference in the examples shown above). However, when using the specified temperature (Dirichlet-type) boundary condition, the difference in element sizes leads to different values of energy transferred to the mesh, which in turn results in significantly different temperature distributions around the heat source. Below, different strategies to mitigate the impact of the spatial discretisation on the temperature distributions obtained when the specified temperature (Dirichlet-type) boundary condition is employed are investigated.

D.2 Mesh refinement approach with Dirichlet type boundary condition

A high temperature gradient exists in the region close to where a prescribed temperature (i.e. Dirichlet-type BC) is specified. When a coarse mesh is employed in the analysis, errors in both the temperature distributions and the transferred energy are encountered, due to the difficulty in modelling accurately this steep slope within a large element. This is especially problematic within the first element next to the heat source, where the maximum gradient is observed. Therefore, the size of the elements around the heat source, especially the radial length of the first element next to the heat source, is thought to be important for overcoming the problems outlined above. Thus, two studies are carried out, focusing first on the effect of the size of the first element and, subsequently, on the size of the refined zone around the point of application of the BC. The results of these studies are used to propose an efficient mesh refinement approach, as represented in Figure D-4. Indeed, while it was shown that a fully refined mesh leads to accurate results, it is not computationally efficient given the increased number of elements and degrees of freedom.

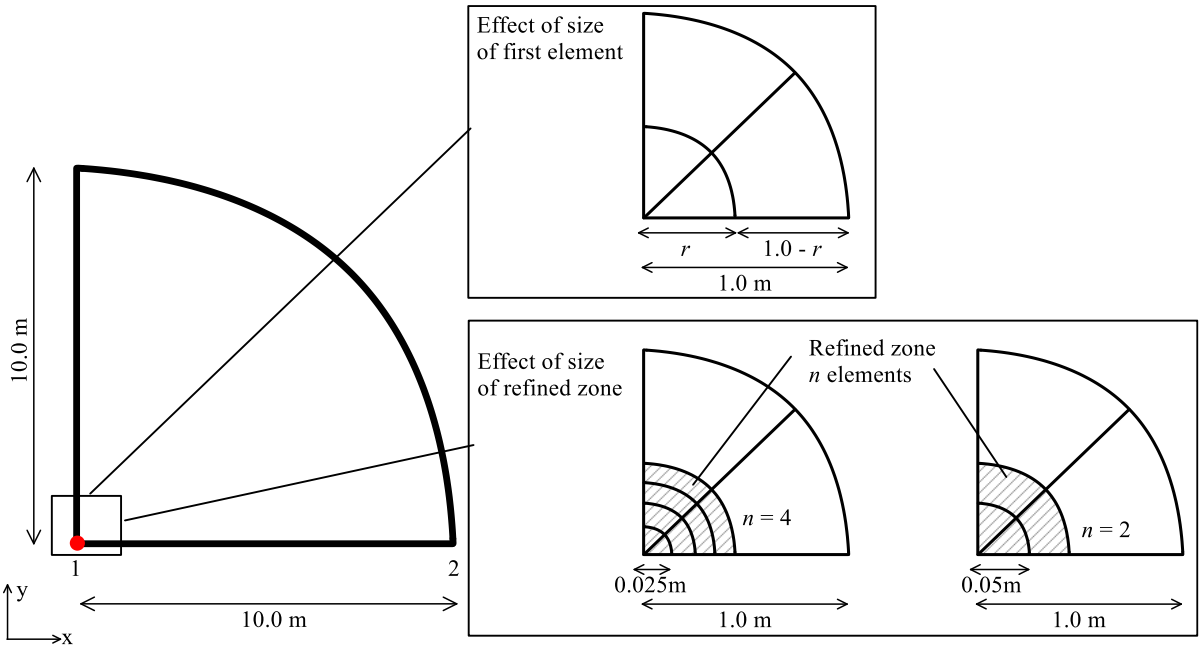

Figure D-4: Approaches for mesh refinement

D.2.1 Effect of the size of the first element around the heat source

To demonstrate the effect of the size of the first element next to the heat source where a Dirichlet-type BC is prescribed, the analysis previously described was performed adopting a coarse mesh with a 1.0 m element size in the radial direction. However, the elements which have point 1 as a corner node (i.e. elements next to the heat source) were split into two elements with sizes of r for the first element next to the heat source and 1.0-r for the second element, as shown in Figure D-4. Four cases were analysed

with values of r=0.01 m, 0.025 m, 0.05 m, 0.1 m. All analyses were performed with an integration order of 2×2, since it was previously demonstrated that the order of integration has a negligible influence on the results, and were repeated for both 4-noded elements and 8-noded elements (see Table D-2 for analysed cases).

As shown in Figure D-5 (a) and (b), using a mesh refined only by a small element next to the heat source improved significantly both the transferred energy and nodal temperatures obtained compared to those with the original uniform coarse mesh. To quantify the improvement obtained by adjusting the mesh, a metric is introduced in this study:

$$M_i(\%) = \frac{E_{i,\Omega,\text{coarse}} - E_{i,\Omega}}{E_{i,\Omega,\text{coarse}} - E_{i,\Omega,\text{fine}}} \times 100 \tag{D-3}$$

where $E_{i,\Omega,\text{fine}}$ and $E_{i,\Omega,\text{coarse}}$ are the values of input energy for the uniform mesh with, respectively, 0.025 m (DF-I for 4-noded elements and DF-II for 8-noded elements) and 1.0m (DC-I for 4-noded elements and DC-II for 8-noded elements), and i represents the increment number. A value of 0% represents no improvement over using a uniform coarse mesh, while a value of 100% means the results are now identical to those obtained using a uniform fine mesh. This improvement metric was arbitrarily evaluated after 10 increments of the analysis ($t/\Delta t$=10, i.e. M_{10}).

Table D-2 presents the metric M_{10} together with the average temperature measured over the area with a radial distance of 1.0 m at increment 10, $T_{10,1m}$. It is concluded that introducing a small element has a very large impact on the results even if its dimensions are relatively large, i.e. using a 0.1 m element leads to improvements corresponding to M_{10}=64% and 72% for 4-noded and 8-noded, respectively. As expected, smaller elements improve the obtained results, though the gains are relatively marginal especially for linear elements. Indeed, the solutions of analyses with r =0.1 m and r =0.01 m (i.e. r reduces by an order of magnitude) are improved by only 7% and 15%, for 4-noded and 8-noded elements, respectively.

Table D-2: Effect of using a small element next to the heat source

Mesh	Analysis	4-noded elements		Analysis	8-noded elements	
		$T_{10,1m}$	M_{10} (%)		$T_{10,1m}$	M_{10} (%)
Uniform 0.025m	DF-I	0.154	100.0	DF-II	0.142	100.0
r =0.01m	D10-4-1	0.206	71.0	D10-8-1	0.165	87.0
r =0.025m	D25-4-1	0.209	70.0	D25-8-1	0.169	84.0
r =0.05m	D50-4-1	0.213	68.0	D50-8-1	0.176	80.0
r =0.1m	D100-4-1	0.220	64.0	D100-8-1	0.187	72.0
Uniform 1.0 m	DC-I	0.296	0.0	DC-II	0.265	0.0

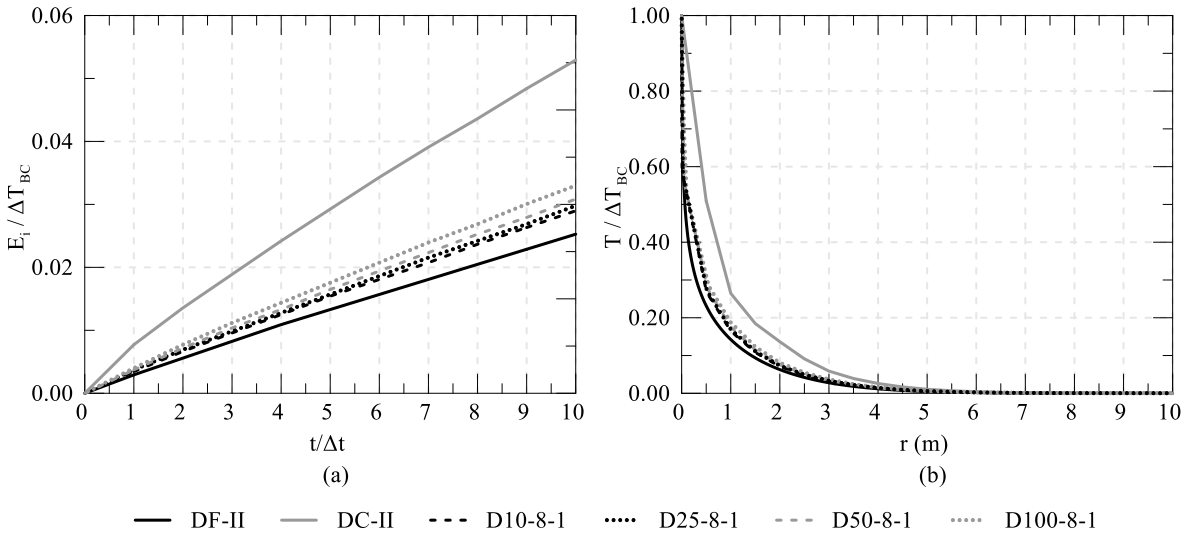

Figure D-5: Effect of size of first element for 8-noded elements on (a) variation of energy per unit volume and (b) distribution of the temperature along line 1-2 at $t/\Delta t = 10$

D.2.2 Effect of the size of the refined area around the heat source

The study above has demonstrated that the introduction of one small element around the heat source simulated by a Dirichlet-type BC can significantly improve the obtained results when compared to those obtained with a uniform coarse mesh. Therefore, a potential effective approach for minimising mesh effects is to refine a small zone around the heat source with more elements. To further investigate the effectiveness of this approach, two additional sets of analyses were performed where the size of the refined area (i.e. number of small elements for refinement, n) around the heat source was varied, as shown in Figure D-4. In the first set, elements with a size of 0.025 m were used, while in the second set, an element size of 0.05 m was adopted for the elements within the refined area. An integration order of 2x2 was adopted in this study and all analyses were repeated with both 4-noded and 8-noded elements.

Figure D-6 (a) and (b) compare the transferred energy over the mesh, E_i, and the temperature distribution in the radial direction, respectively, for analyses using 8-noded elements with coarse meshes refined by introducing n (i.e. 1, 2, 4 and 10) elements of 0.025 m around the heat source against those with uniform coarse (DC-II) and fine (DF-II) meshes. It is evident that even for a small number of elements (e.g. n=2), significant improvements are obtained. The same behaviour can also be observed in Figure D-7 (a) and (b) which present the comparison between analyses using n elements of 0.05 m and those using uniform coarse and fine meshes.

Table D-3 lists all analysed cases with the corresponding improvement metric and average temperature measured over the area with a radial distance of 1.0 m at increment 10 (i.e. M_{10} and $T_{10,1m}$) for each case. It is concluded that large gains are achieved by increasing the number of elements

in the refined zone, e.g. M_{10}=70% for n=1, M_{10}=82% for n=2, and M_{10}=97% for n=10 in analyses with 4-noded elements and 0.025 m elements. Moreover, gains are more modest with 8-noded elements because they are characterised by greater accuracy even prior to refinement, due to a shorter distance between each node. However, the results show that the area of the zone is not an important factor compared to the size of elements. For example, using 4×0.025 m elements yields the same refined area as that using 2×0.05 m elements and the gains are much larger for the former case. Similarly, adopting 10×0.025 m elements performs better when compared to the study with 5×0.05 m elements. This suggests that an improvement is achieved whenever large number of smaller elements are used, even if a smaller refined zone is obtained. (e.g. M_{10}=90% was achieved when using 4-noded elements for the cases with either 4×0.025m elements or 10×0.05m elements, even though the area of the refined zone is 25 times larger in the latter case).

Table D-3: Effect of size of refined area using element sizes of 0.025m and 0.05m

Mesh	n	4-noded elements			8-noded elements		
		Analysis	$T_{10,1m}$	M_{10} (%)	Analysis	$T_{10,1m}$	M_{10} (%)
Uniform 0.025m	N/A	DF-I	0.154	100.0	DF-II	0.142	100.0
0.025m elements in refined zone	1	D25-4-1	0.209	70.0	D25-8-1	0.169	84.0
	2	D25-4-2	0.181	82.0	D25-8-2	0.153	92.0
	4	D25-4-4	0.165	90.0	D25-8-4	0.146	97.0
	10	D25-4-10	0.153	97.0	D25-8-10	0.143	100.0
0.05m elements in refined zone	1	D50-4-1	0.213	68.0	D50-8-1	0.176	80.0
	2	D50-4-2	0.187	79.0	D50-8-2	0.162	87.0
	5	D50-4-5	0.172	87.0	D50-8-5	0.158	89.0
	10	D50-4-10	0.167	90.0	D50-8-10	0.157	89.0
Uniform 1.0m	N/A	DC-I	0.296	0.0	DC-II	0.265	0.0

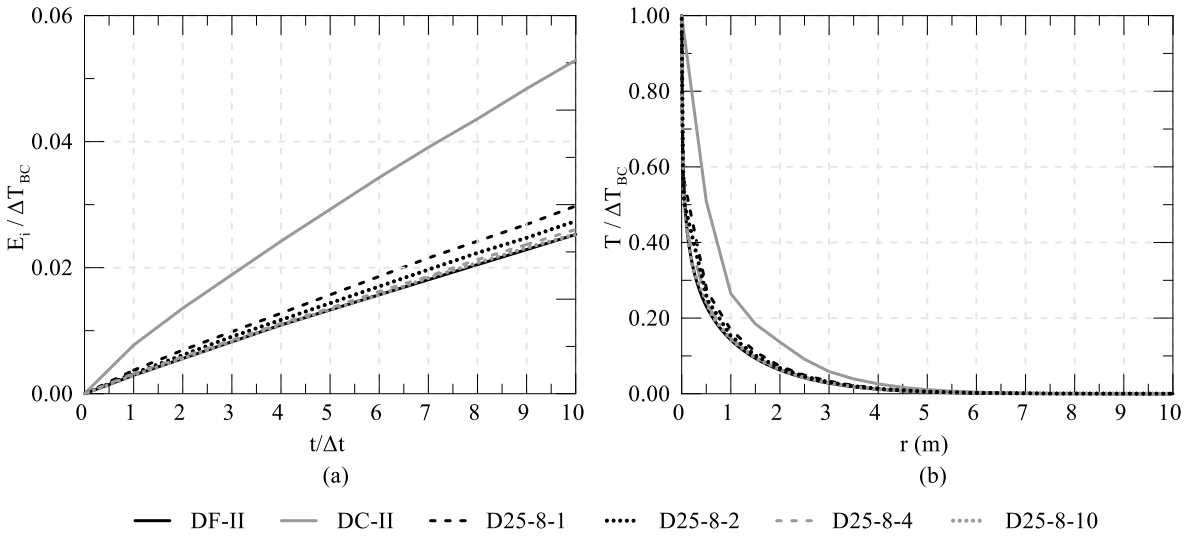

Figure D-6: Effect of size of refined area with 8-noded elements of size 0.025 m (a) variation of energy per unit volume and (b) distribution of the temperature along line 1-2 at $t/\Delta t = 10$

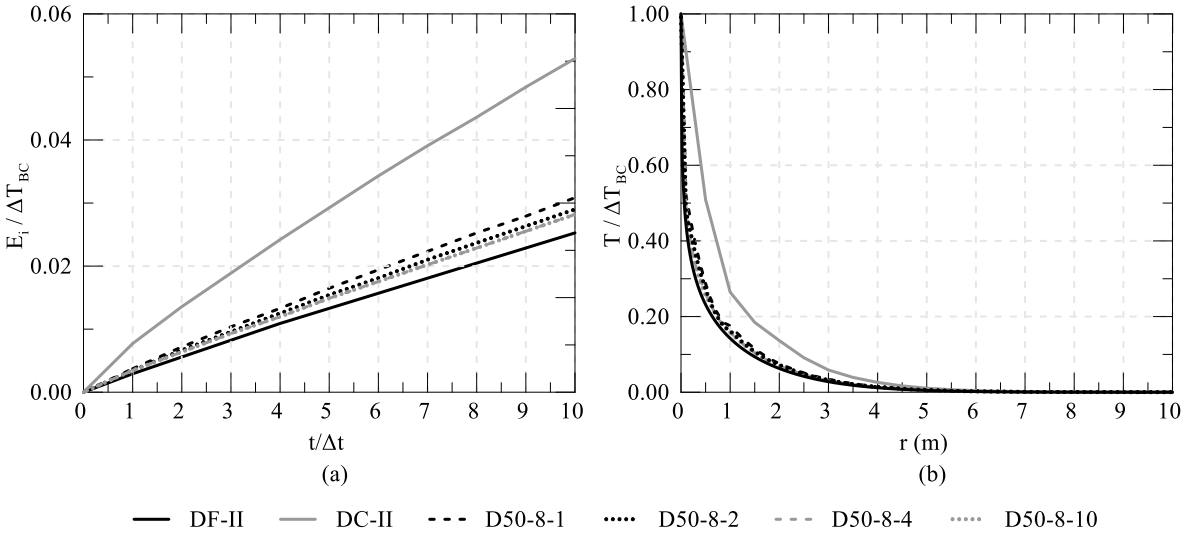

Figure D-7:Effect of size of refined area with 8-noded elements of size 0.05 m (a) variation of energy per unit volume and (b) distribution of the temperature along line 1-2 at $t/\Delta t = 10$

Appendix E

E.1 Alternative Petrov-Galerkin formulation for one-dimensional quadratic elements

The original weighting functions for the Petrov-Galerkin (PG) formulation for one-dimensional steady state advection-diffusion problems for 3-noded quadratic elements (see Figure E-1) implemented in ICFEP (see Cui et al. (2018c) and Gawecka (2017) for details) were adopted from Heinrich & Zienkiewicz (1977) and are expressed through the following equations:

$$W_{q,i}(s) = N_i(s) - \beta_{PG1} g(s) \qquad (i = 1,2) \tag{E-1}$$

$$W_{q,3}(s) = N_3(s) - 4\beta_{PG2} g(s) \tag{E-2}$$

where N_i (i=1,2,3) are the shape functions associated to the nodes in the isoparametric element depicted in Figure E-1 (see Potts & Zdravković (1999) for their equations), β_{PG1} and β_{PG2} are the PG weighting factors and the function $g(s)$ is given by:

$$g(s) = \frac{5}{8} s(s+1)(s-1) \qquad (-1 \leq s \leq 1) \tag{E-3}$$

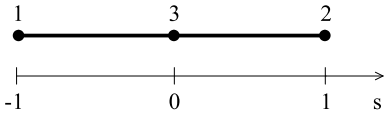

Figure E-1: 3-noded beam element in the natural coordinate system

The optimal values of the PG weighting factors β_{PG1} and β_{PG2} vary with Péclet number and are approximately equal to 1 for $Pe > 100$ (see Cui et al. (2018c) and Gawecka (2017)). Figure E-2 shows the nodal shape and weighting functions with $\beta_{PG1} = \beta_{PG2} = 1$.

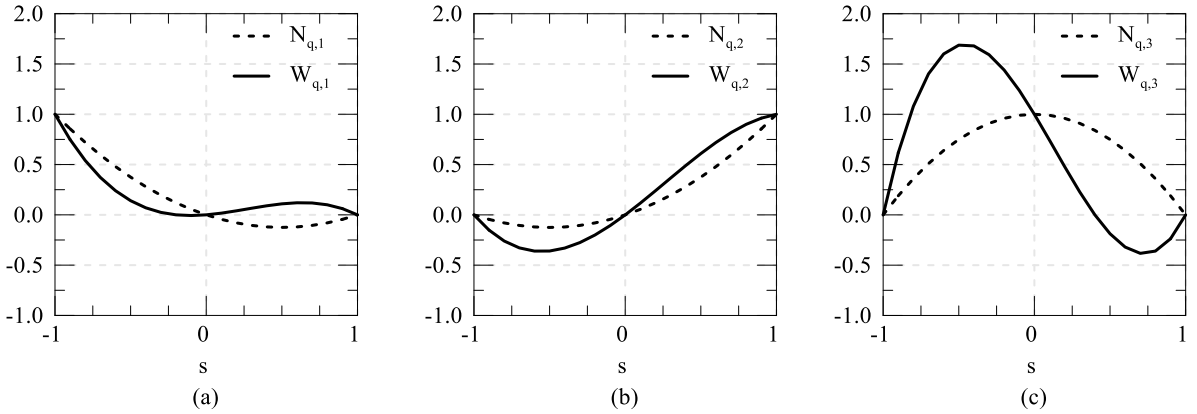

Figure E-2: Shape and weighting functions proposed by Heinrich & Zienkiewicz (1977) for quadratic elements with $\beta_{PG1} = \beta_{PG2} = 1$ at (a) node 1, (b) node 2 and (c) node 3

It should be noted that the sum of the weighting functions associated to the three nodes is not 1.0 for every value of coordinate s along the isoparametric element. Indeed, the sum is only 1.0 at s coordinates of -1, 0 and 1, while assuming positive values for $s < 0$ and negative values for $s > 0$. This was shown not to affect the numerical stability, since the results reported in Gawecka (2017) obtained with this formulation do not lead to oscillations with high Péclet numbers for different boundary conditions (i.e. prescribed temperature and thermo-hydraulic boundary condition). However, this results in erroneous solutions when a nodal heat flux boundary condition is applied. Indeed, the imbalance of the weighting functions leads to an excess or a lack of energy within the system, which is therefore not consistent with the applied boundary condition. This is dependent on the application point of the boundary condition, i.e. whether it is applied at a corner node ($i = 1,2$) or at a mid-side node, where in the former case an excess in energy of 50% is obtained, while for the latter 25% less energy than the one applied by the boundary condition is generated. This is particularly important when modelling approach 2 described in Chapter 4 is employed in conjunction with quadratic elements. Indeed, this problem does not arise with linear elements, since the PG formulation is expressed such that the sum of the weighting functions is equal to 1.0 at every point along the isoparametric element (see Cui et al. (2018c) for details).

Thus, it is clear that a new formulation for the PG weighting functions for quadratic elements should be adopted. In the following, two possible formulations are proposed, where the first is a modification of the above weighting functions established by Heinrich & Zienkiewicz (1977), which will be termed Q1, and the second derives from those proposed by Cui et al. (2018c) for 2D quadratic elements, which will be referred to as Q2.

In order for the sum of the weighting functions proposed by Heinrich & Zienkiewicz (1977) to be equal to 1.0 and thus ensure an energy balance, the weighting function for node 3 (i.e. the mid-side node

expressed in Equation (E-2)) is modified as follows, while the weighting functions for the other two nodes (see Equation (E-1)) as well as the function $g(s)$ remain unchanged:

$$W_{q,3}(s) = N_3(s) - 2\beta_{PG2}g(s) \tag{E-4}$$

Figure E-3 shows the nodal shape and weighting functions with $\beta_{PG1} = \beta_{PG2} = 1$. The introduced modification where the function $g(s)$ is multiplied by 2 instead of 4 reduces the amount of upwinding associated to the mid-side node.

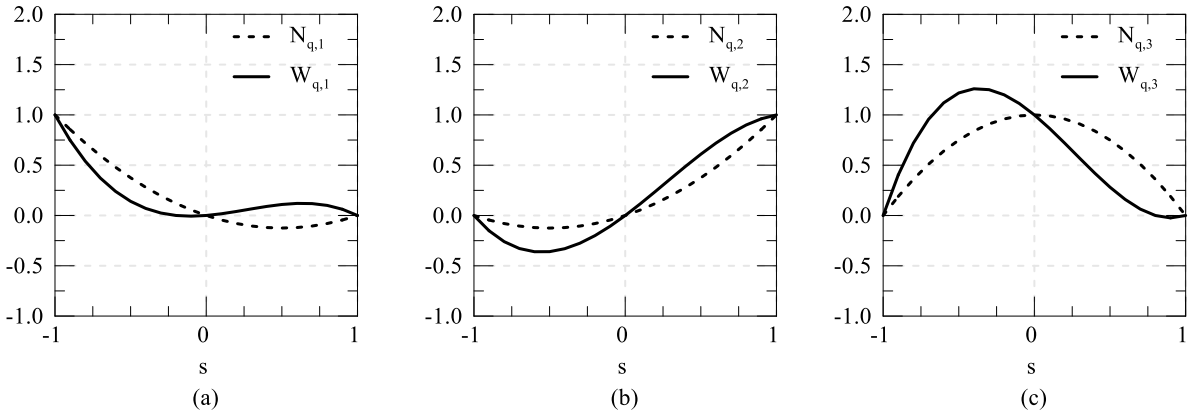

Figure E-3: Formulation Q1 - Shape and weighting functions for quadratic elements with $\beta_{PG1} = \beta_{PG2} = 1$ at (a) node 1, (b) node 2 and (c) node 3

The second considered solution was to reduce the PG weighting functions proposed by Cui et al. (2018c) for 2D quadratic elements to a 1D formulation. Thus, the weighting functions take the following form:

$$W_{q,1}(s) = N_1(s) + \alpha_{PG}f(s) - 2\beta_{PG2}g(s) \tag{E-5}$$

$$W_{q,2}(s) = N_2(s) - \alpha_{PG}f(s) - 2\beta_{PG2}g(s) \tag{E-6}$$

$$W_{q,3}(s) = N_3(s) + 4\beta_{PG2}g(s) \tag{E-7}$$

where α_{PG} is a weighting factor and the function $f(s)$ is given by:

$$f(s) = -\frac{3}{4}(1+s)(1-s) \qquad (-1 \leq s \leq 1) \tag{E-8}$$

Similar to β_{PG2} and β_{PG2}, the optimal value of α_{PG} varies with Péclet number, reaching an asymptote of 1 for $Pe > 100$. Figure E-4 shows the nodal shape and weighting functions with $\alpha_{PG} = \beta_{PG2} = 1$.

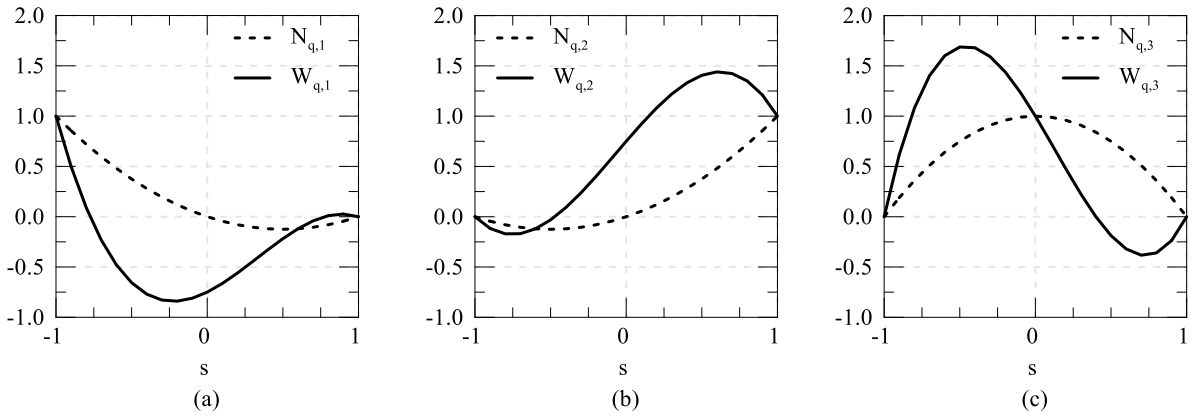

Figure E-4: Formulation Q2 - Shape and weighting functions for quadratic elements with $\alpha_{PG} = \beta_{PG2} = 1$ at (a) node 1, (b) node 2 and (c) node 3

E.2 Performance of the new formulations

E.2.1 One-dimensional problems

In order to assess the performance of the proposed new PG formulations, simple one-dimensional problems are analysed first. These consist of a 1D bar element modelled in a plane-strain analysis, 15.0 m in length, with water (C_v=4180 kJ/m^{3}K, λ = 2.0 W/mK) flowing at a constant velocity from left to right and an initial temperature of 0°C (see Figure E-5). Flows with Péclet numbers Pe of 10, 100 and 10000 were assessed by varying the fluid velocity and element size (or equivalently, the number of elements n – see Figure E-5). The θ-method with θ =2/3 for both water flow and temperatures has been adopted as the time marching scheme. A further study on the value of θ for temperatures, adopting θ =1.0, was carried out. Four cases were analysed: (1) fixed temperature of 10°C on the left hand boundary and fixed temperature of 0°C on the right hand boundary; (2) fixed temperature of 10°C on the left hand boundary and thermo-hydraulic boundary condition on the right hand boundary; (3) nodal heat flux boundary condition applied in the middle of the bar at a corner node shared by two elements and with the temperature degrees of freedom at the extremities being tied; (4) nodal heat flux boundary condition applied in the middle of the bar at a mid-side node with the temperature degrees of freedom at the extremities being tied. Note that the first two cases have similar boundary conditions to those used in the validation exercise in Cui et al. (2018c). Moreover, in cases (3) and (4), the value of the heat flux boundary condition does not affect the conclusions of the study.

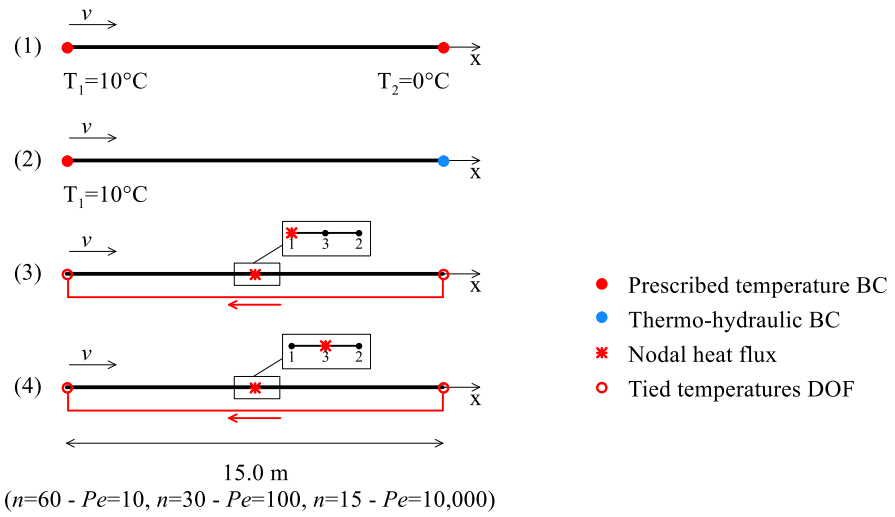

Figure E-5: One-dimensional problems for assessment of PG formulation

1D problems with θ =2/3

Figure E-6 shows the results for case (1) for both a transient stage and at steady state. It is shown that the new formulations do not affect the transient stage, while they perform slightly worse than the original one proposed by Heinrich & Zienkiewicz (1977), with Q1 (i.e. the modified Heinrich & Zienkiewicz (1977) formulation) presenting oscillations at steady state which increase with Péclet number. However, these are much smaller than those obtained when no PG is adopted (see Gawecka (2017)). Moreover, the formulation Q2, i.e. the one derived from the 2D formulation proposed by Cui et al. (2018c), presents some inaccuracies towards the end of the bar at steady state, where the temperature is reducing stepwise instead of smoothly, and this phenomenon increases with increasing Péclet number, which in this case was achieved by using larger elements.

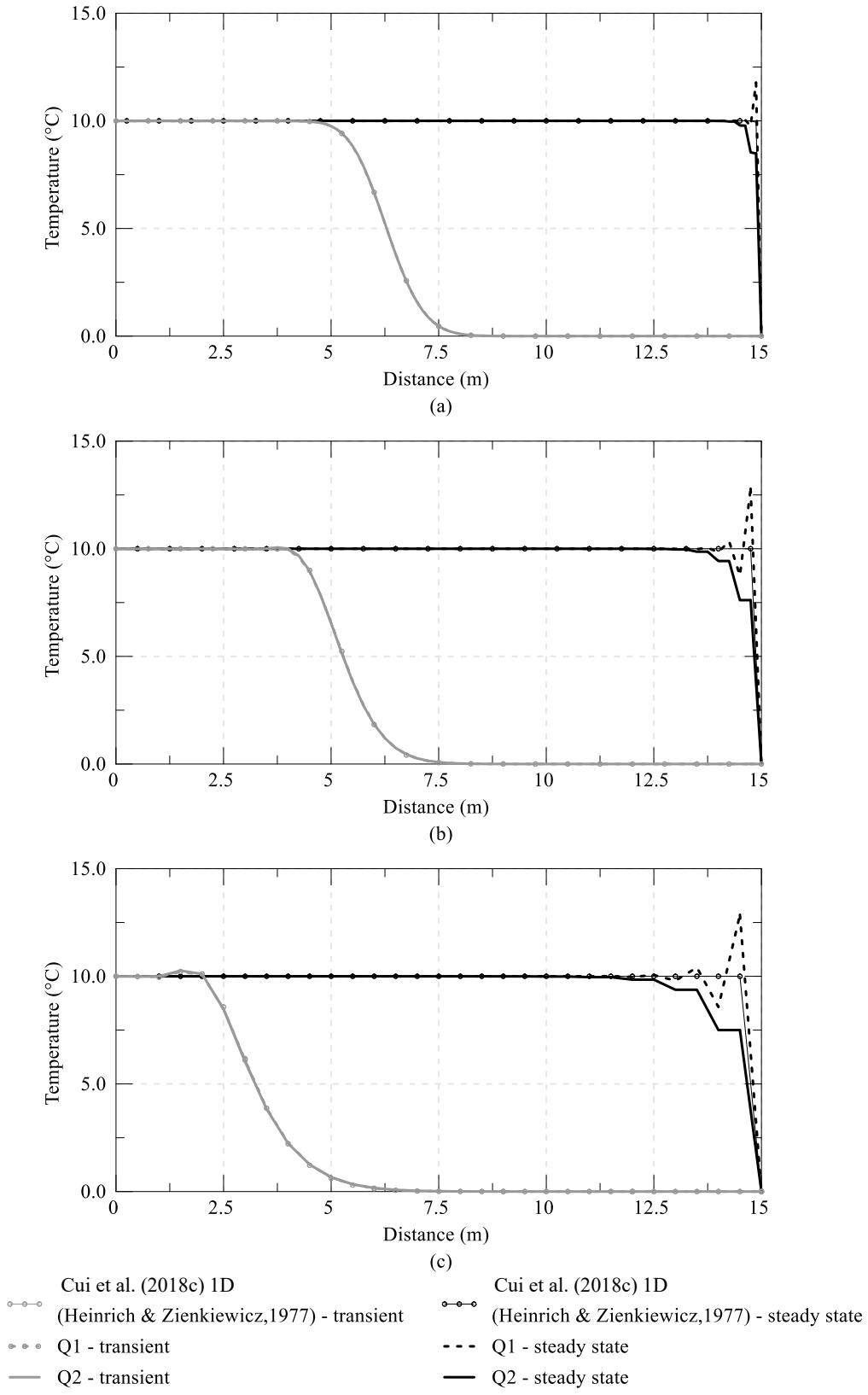

Figure E-6: Temperature distribution along bar for case (1) (a) Pe=10, (b) Pe=100 and (c) Pe=10,000

Figure E-7 shows the results for case (2) for both a transient stage and at steady state. Both new formulations cope well with the applied boundary conditions, presenting a more stable solution at steady state when compared to the one obtained using the formulation proposed by Heinrich & Zienkiewicz (1977), which shows some oscillations close to the point of application of the thermo-hydraulic boundary condition after thermal break-through and at steady state for large Pe. Formulation Q1 presents some oscillations during the transient stage, although these are smaller than those observed employing the original formulation of Heinrich & Zienkiewicz (1977), while no oscillations are recorded at steady state. When the weighting functions according to formulation Q2 are adopted, no oscillations are obtained during the transient or steady state stages.

Figure E-8 and Figure E-9 show the results for case (3) and (4), respectively. It can be noted that a large discrepancy in the temperature distributions is obtained between the analyses performed with the PG weighting functions according to Heinrich & Zienkiewicz (1977) and the two proposed herein. Indeed, as previously mentioned, when the heat flux is applied to a corner node (case (3) shown in Figure E-8), the former leads to 50% more energy within the system when compared to the applied boundary condition, whereas when it is applied to a mid-side node (case (4) shown in Figure E-9), 25% less energy is computed. This is clearly a numerical issue which leads to unrealistic results.

Conversely, both formulations Q1 and Q2, when the energy within the system is calculated according to the computed temperature change (equal to $C_v \cdot \Delta T \cdot V/\Delta t$ and expressed in kW), the value of the boundary condition is obtained. This is because, for these formulations, the sum of the weighting functions is equal to 1 everywhere along the isoparametric element and thus it results in a balanced solution from an energy perspective. It is not clear why this aspect was not considered by Heinrich & Zienkiewicz (1977) and no justification for this proposed formulation was found.

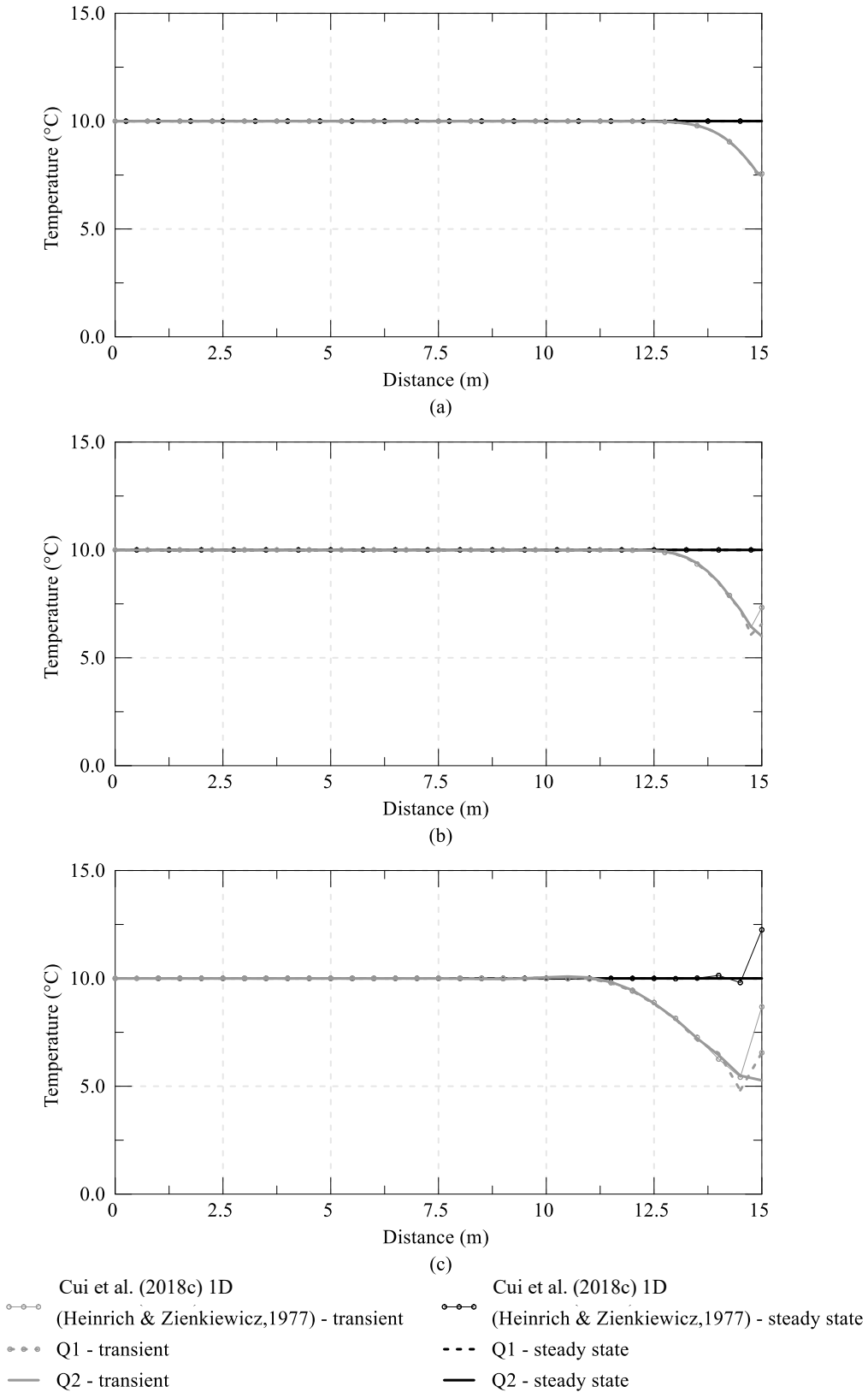

Figure E-7: Temperature distribution along bar for case (2) (a) Pe=10, (b) Pe=100 and (c) Pe=10,000

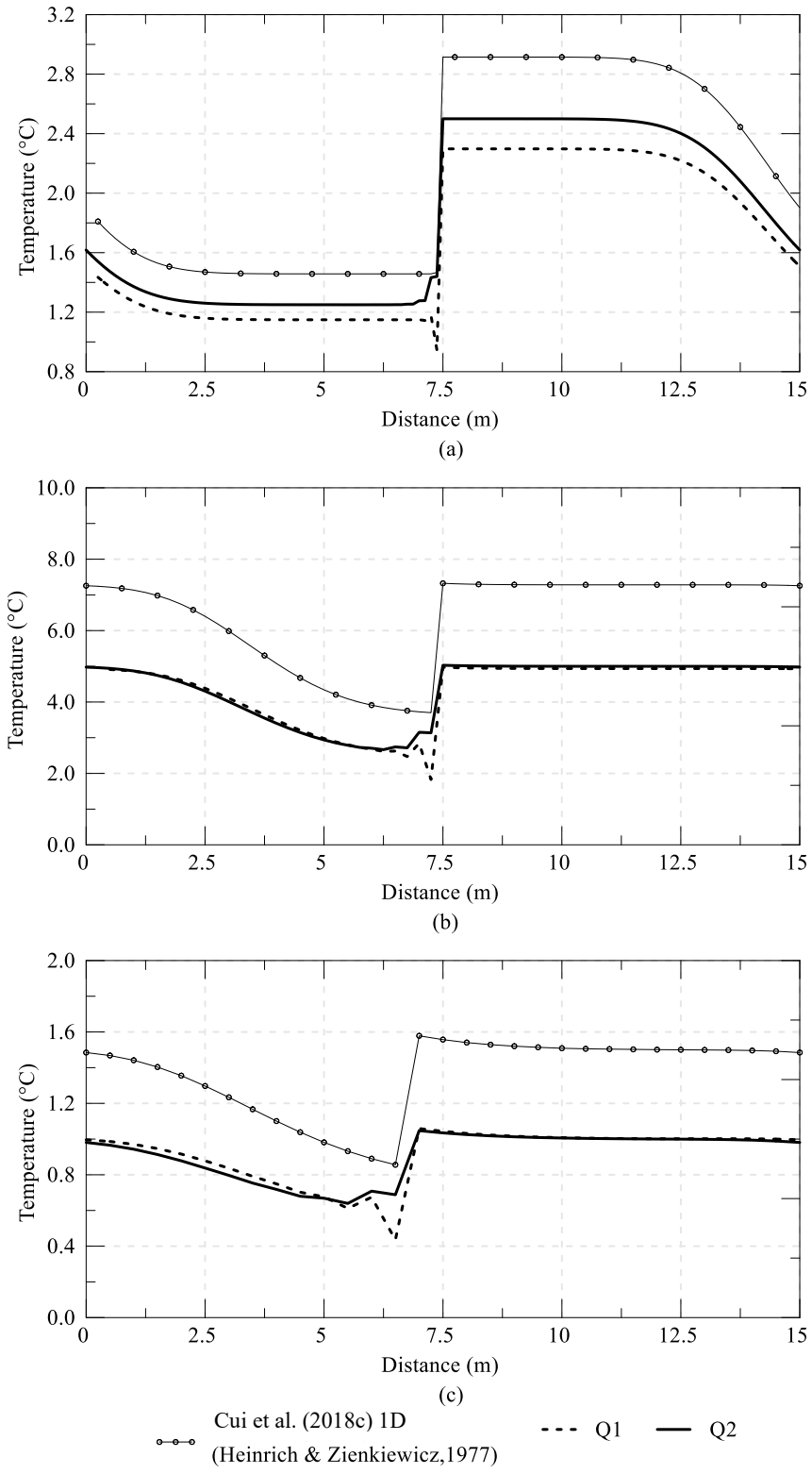

Figure E-8: Temperature distribution along bar for case (3) (a) Pe=10, (b) Pe=100 and (c) Pe=10,000

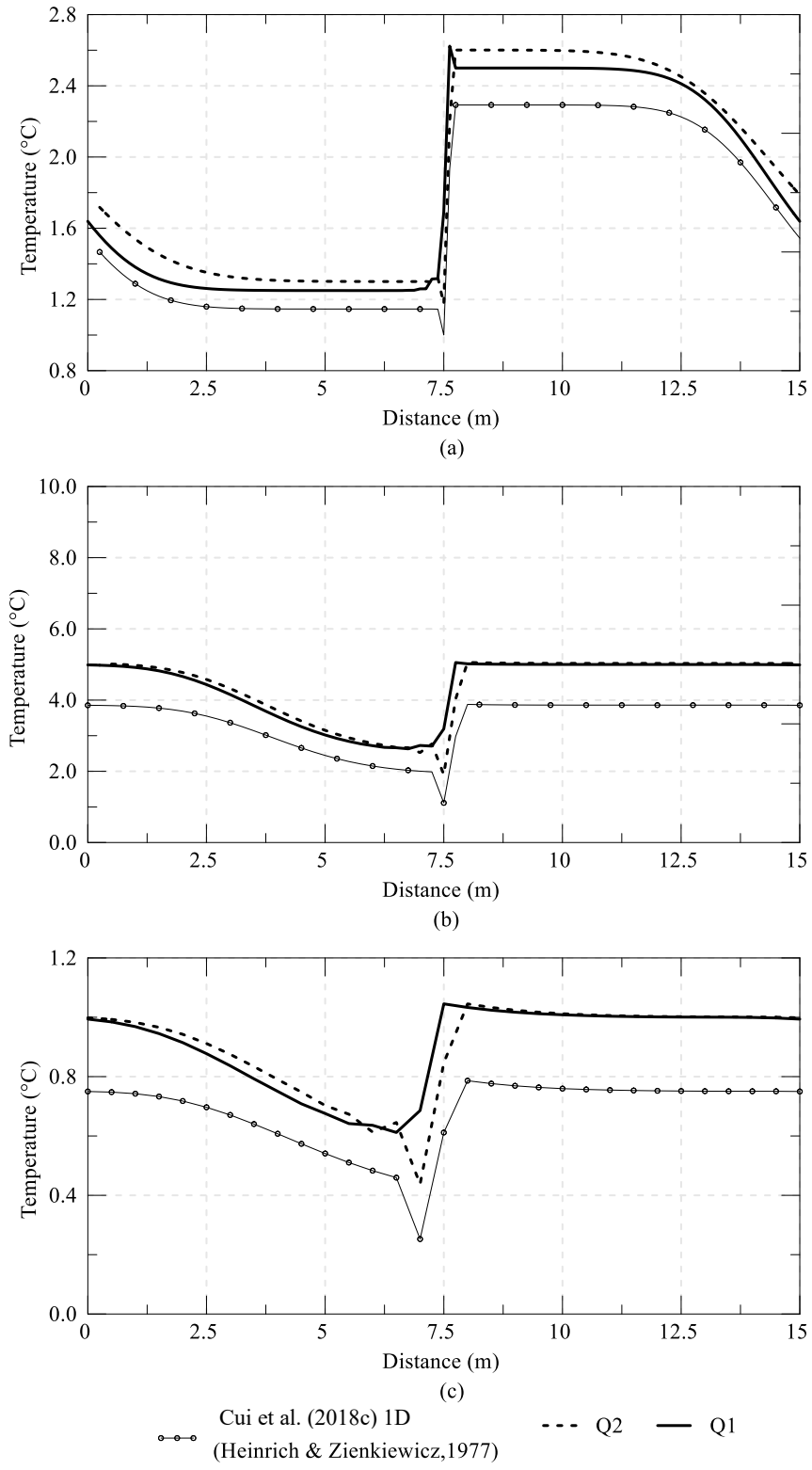

Figure E-9: Temperature distribution along bar for case (4) (a) Pe=10, (b) Pe=100 and (c) Pe=10,000

Effect of θ

Figure E-10 shows the temperature distributions for case (2) employing θ=1.0. Large oscillations are observed with high Péclet numbers for the original weighting functions (Heinrich & Zienkiewicz, 1977), both during the transient stage and at steady state. At steady state, for Pe=10000, the analysis adopting the original formulation yields results of up to 10^5°C and is therefore considered highly unstable. For Q1, oscillations are observed during the transient stage, which increase with Péclet number, while a stable solution is obtained at steady state. Conversely, small oscillations are computed employing Q2, both during the transient stage and at steady state.

Figure E-11 and Figure E-12 show the comparison between the transient stages for cases (1) and (2) employing different values of θ. It can be observed that the value of θ affects the transient stage, with the heat front moving at a faster pace for θ=2/3. Furthermore, for this case, the drop in temperature is more abrupt than when θ=1.0 is adopted. This is unlikely however to affect any boundary value problems. Note that similar conclusions were drawn for cases (3) and (4).

Final observations

There are still clearly issues for all formulations when simulating case (1), with some oscillations observed for Q1, and stepwise changing temperatures for Q2. The extent of these may, however, be easily reduced by decreasing the element size in a critical area. It is regarded that Q2 produces more stable results and it is also more consistent with the general PG formulation implemented in ICFEP. Thus, the formulation Q1 is discarded and not employed for further verification.

It should also be noted that if a heat flux boundary condition is applied along an element instead of at a node, the original Heinrich & Zienkiewicz (1977) leads to the right energy within the system, since the error in the sum of the weighting functions cancels out when the boundary condition is applied to all three nodes of the element.

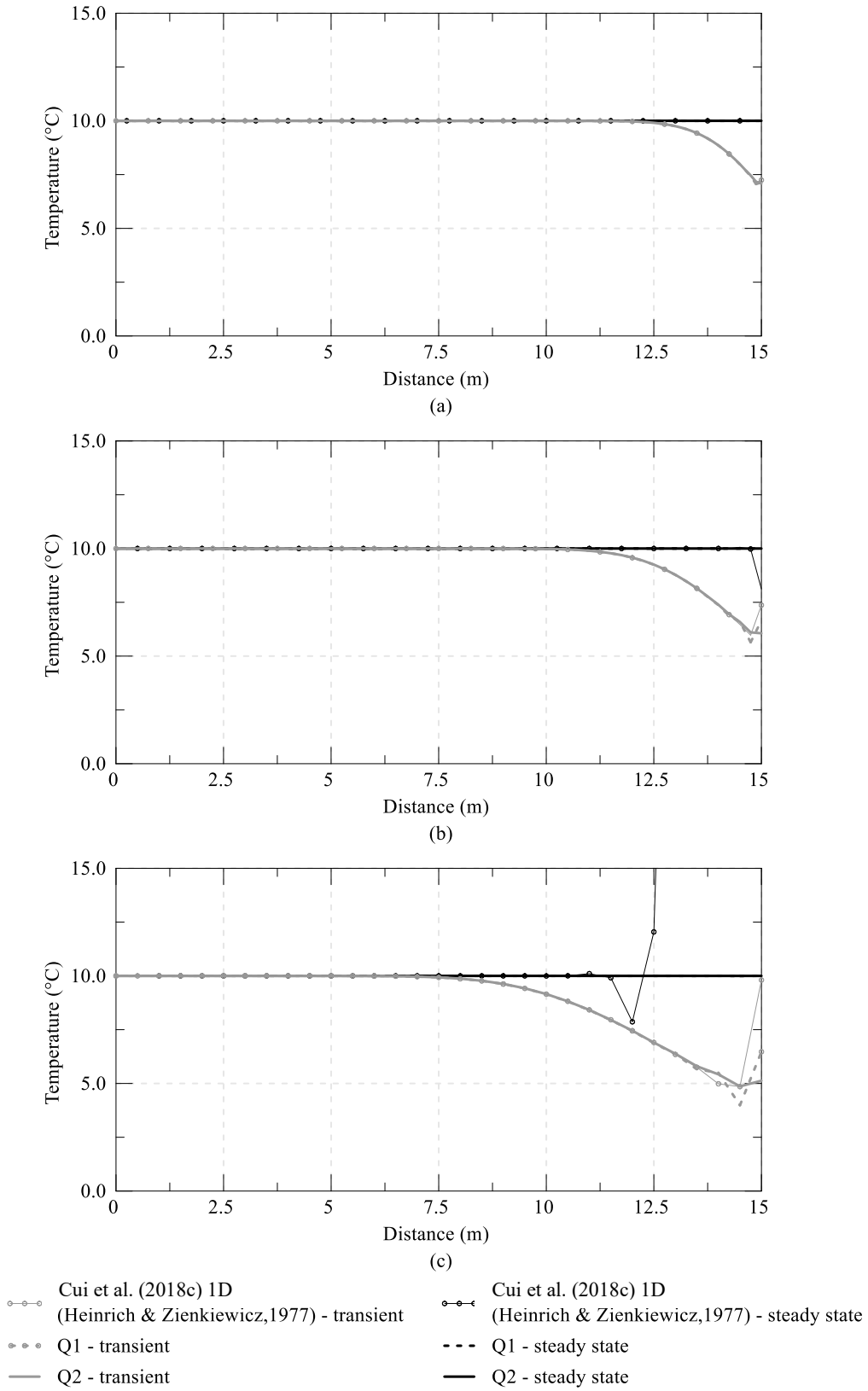

Figure E-10: Temperature distribution along bar for case (2) with $\theta = 1.0$ (a) Pe=10, (b) Pe=100 and (c) Pe=10,000

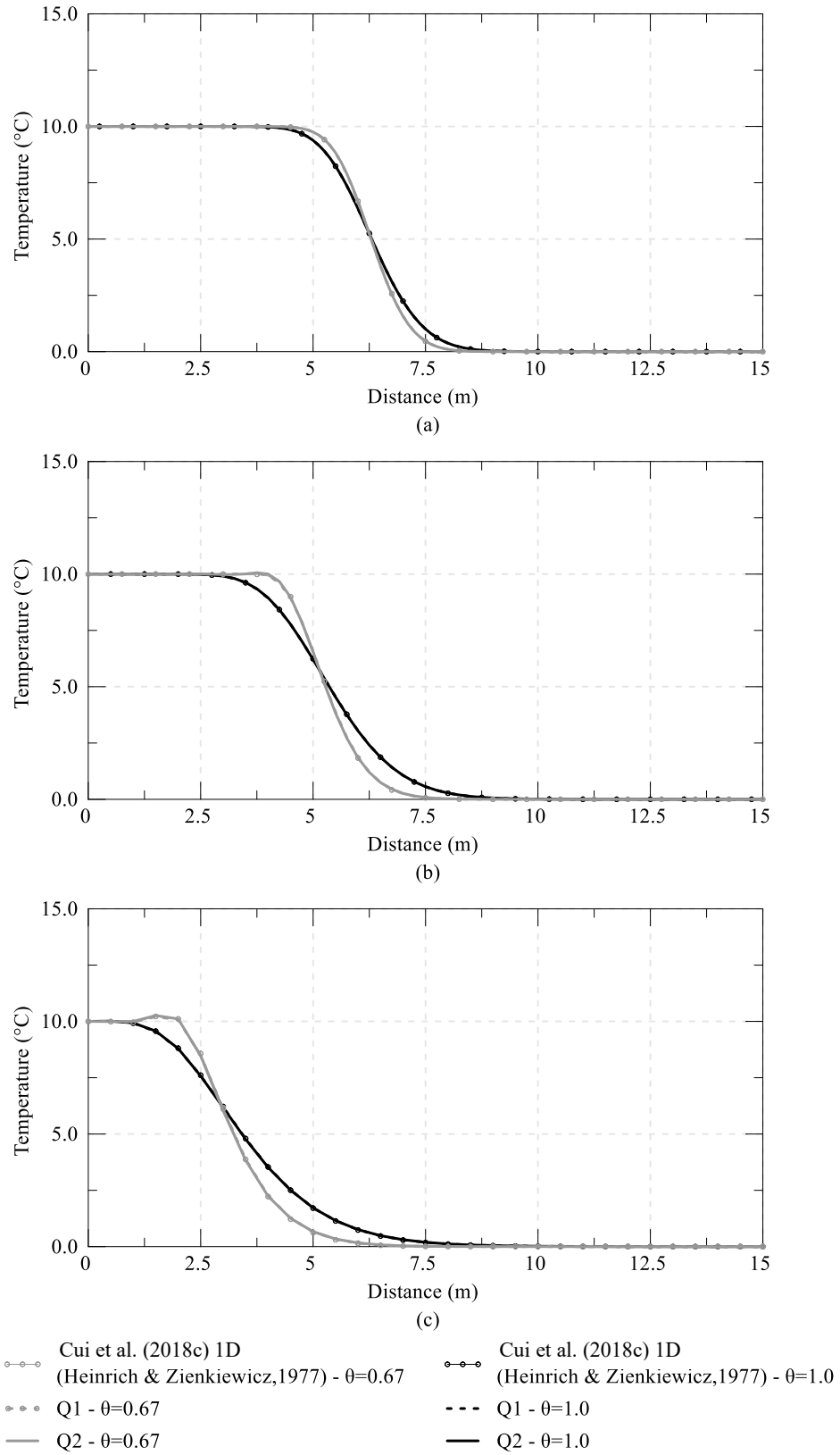

Figure E-11: Comparison of temperature distribution along bar for case (1) with different values of θ during a transient stage (a) Pe=10, (b) Pe=100 and (c) Pe=10,000

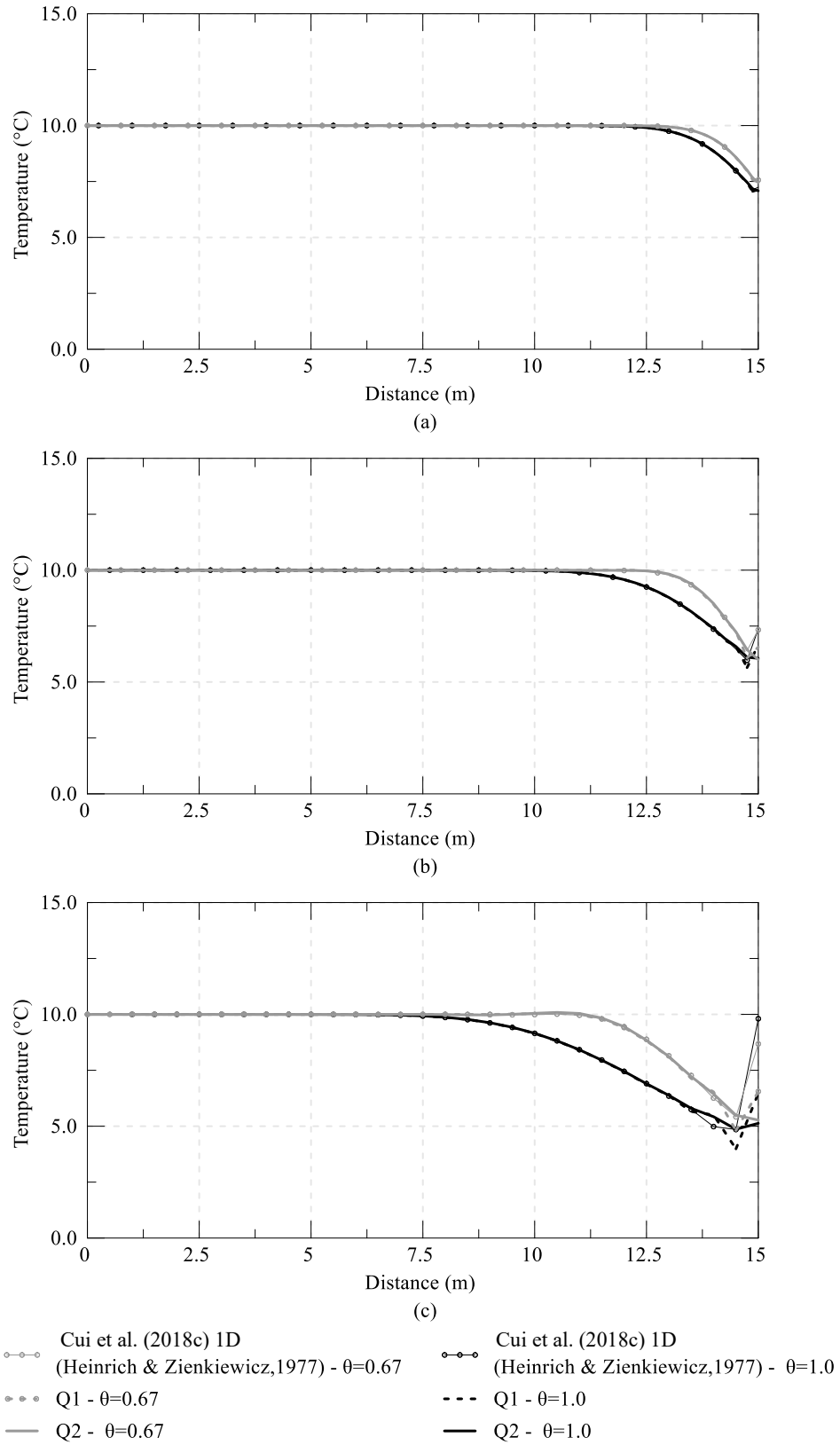

Figure E-12: Comparison of temperature distribution along bar for case (2) with different values of θ during a transient stage (a) Pe=10, (b) Pe=100 and (c) Pe=10,000

E.2.2 Assessment of a thermo-active wall problem

The impact of the new PG weighting functions obtained from the 2D formulation proposed by Cui et al. (2018c) (Q2) was assessed for the thermo-active wall problem described in Chapter 5 (reference case), which was modelled in 2D plane strain with one-dimensional elements simulating the heat exchanger pipes. While the analyses presented in Chapter 5 were performed with linear elements, the following results are obtained using 8-noded quadrilateral solid elements for concrete and soil and 3-noded one-dimensional elements for the heat exchanger pipes. All other boundary conditions and input parameters remained unchanged and θ=1.0 was used. The impact of the new PG weighting functions is assessed for a wall-air interface simulated as insulated (NF) or maintained at a constant temperature (CT).

Compared to the original formulation implemented in ICFEP (i.e. that proposed by Heinrich & Zienkiewicz (1977)), adopting the new weighting functions outlined for Q2, results in a slightly lower heat flux, as a consequence of higher temperatures within the pipes. Indeed, as shown in Figure E-13 (a), with the new formulation, a heat flux which is 1.0 W/m^2 and 0.6 W/m^2 lower than that obtain with the original weighting function, respectively for the CT and NF analyses, is obtained. This is a result of different outlet temperature, which, with the new formulation, is 0.02°C and 0.01°C, respectively for CT and NF, higher than when the weighting functions of Heinrich & Zienkiewicz (1977) are adopted (see Figure E-13 (b)). The discrepancy between the two solutions occurs when a large temperature change is encountered, as can be observed around the top of the base slab in the CT case, as it is there where the two solutions start to slightly diverge. This can also be noted in the simulation of the 1D problems shown above, where the new weighting functions displayed a stepwise decreasing temperature instead of a smooth transition. However, the differences are clearly very limited and can be considered negligible in the context of a boundary value problem. Indeed, similar changes in temperature are observed when comparing linear to quadratic elements or when a refined mesh is compared to a coarser one. It can therefore be stated that the new weighting functions, although displaying some issues when temperature changes occur, still produce a stable solution, perform better with a thermo-hydraulic boundary condition and guarantee an energy balance within the system.

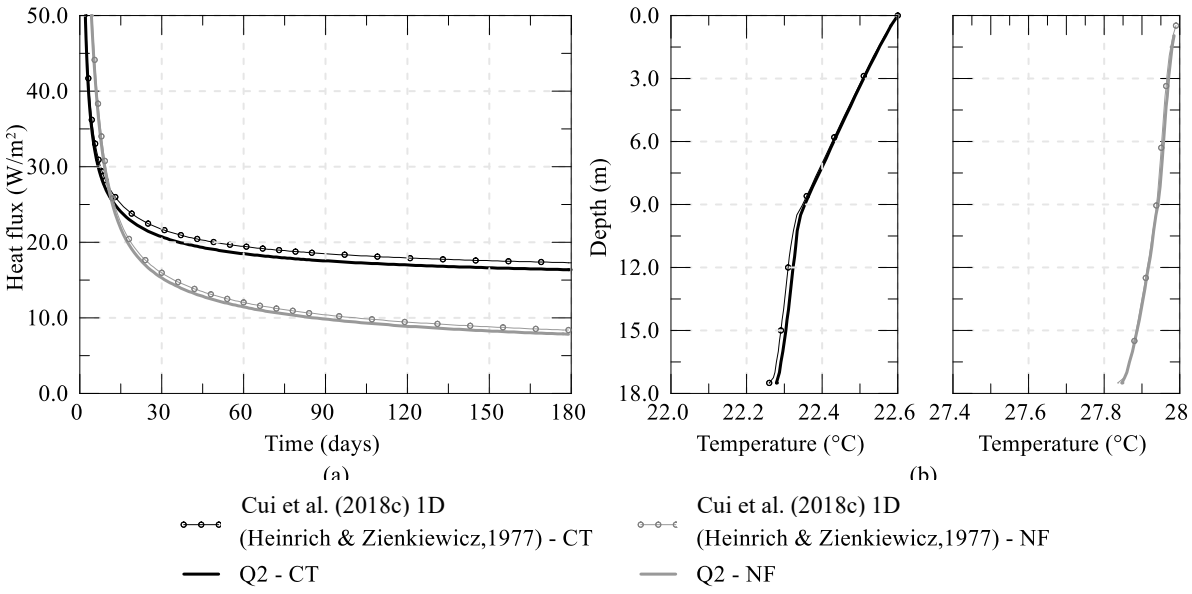

Figure E-13: Thermo-active wall analysis (a) heat flux with time and (b)temperature distribution within heat exchanger pipes after 6 months

Appendix F

F.1 Long-term effect of TEM in 3D and 2D analyses

The introduction of the thermally enhanced material (TEM) was demonstrated to be necessary to capture the heat transfer occurring between pipes simulated with one-dimensional elements and the surrounding material in the short term by successfully reproducing field tests carried out on different geometries and initial conditions, namely by Gawecka et al. (2020) for borehole heat exchangers and piles and herein for walls. However, Gawecka et al. (2020) have shown that, when analysing a single pipe, the effect of the TEM decreases with time and the results obtained with and without this approach tend to converge in the long term. Hence, the influence of the TEM on the long-term performance of the thermo-active wall problem described in Chapter 4 and Chapter 5, respectively for 3D and 2D analyses, is assessed.

F.1.1 Long-term effect of TEM in 3D analyses

For the 3D analyses, the problem described in Chapter 4 was analysed including a TEM of thermal conductivity, λ_{TEM}, of 3.5 W/mK around the heat exchanger pipe. Its effect is analysed in terms of heat flux, changes in soil temperatures and transferred energy, for both Modelling Approach 1 (MA1) and 2 (MA2).

Heat flux

The results shown in Figure F-1 for MA1 demonstrate that the effect of TEM reduces considerably with time and is less relevant for insulated walls. In fact, for such case, the presence of the TEM is negligible after 30 days of operation, where the difference in heat flux is less than 1.0 W/m^2. It then reduces to 0.2 W/m^2 (3%) after 6 months, which corresponds to a difference in outlet temperature of 0.01°C, with the temperatures within the pipes depicted in Figure F-2. For a wall exposed to an environment at constant temperature, a larger effect of the TEM is registered, with a difference in heat injection rate of 2.6 W/m^2 (which corresponds to a temperature difference within the pipes, ΔT_p, of 0.1°C) being computed after 30 days, reducing to 2.0 W/m^2 (12%) at the end of the simulation (i.e the outlet temperature increases by 0.08°C). For the wall with a convective heat transfer coefficient, h, of 2.5 W/m^{2}K, a difference of

1.7 W/m^2 is computed after 30 days, reducing to 1.0 W/m^2 (8%) at the end of the simulation period, which corresponds to a difference in outlet temperature of 0.04°C.

For MA2, the effect of the TEM is constant throughout the simulation period, as shown in Figure F-3 and leads to a larger heat flux, since the heat flux boundary condition required to reach ΔT_{in}=15°C is larger with the presence of the TEM, namely equal to 0.502 kW, 0.258 kW and 0.393 kW, for CT, NF and CH respectively, i.e. 12%, 6% and 9% larger than without TEM. The maximum difference is obtained for the CT case and is equal to 2.0 W/m^2. The effect of the TEM on the development of the inlet and outlet temperatures with time for MA2 is depicted in Figure F-4. Lower temperatures are computed for the analyses with the TEM, given the higher heat transfer rate, and a slightly larger ΔT_p is obtained due to the larger value of the heat flux boundary condition applied.

It can be seen from Figure F-5 and Figure F-6, which display the variation of the heat flux ratio q_e with time respectively for MA1 and MA2, that the increase of heat flux computed by the analyses including the TEM for the CT and CH cases is related to the increased heat transfer taking place at the wall-air interface. Indeed, a slightly larger proportion of the heat flux takes place within the exposed section of the wall with the presence of the TEM since heat transfer is enhanced. This is confirmed when observing Figure F-2 which plots the changes in temperatures within the pipes recorded for MA1 after 6 months of operation, where a larger temperature drop is observed in the pipes along the exposed part of the wall, while it appears that the temperature difference within the embedded part of the wall is not affected by the TEM.

It should be noted that, for the same geometry, the effect of TEM decreases slightly with increasing number of pipes within a wall panel, with difference between analyses with and without TEM reducing to 2%, 6% and 8% for NF, CH and CT, respectively.

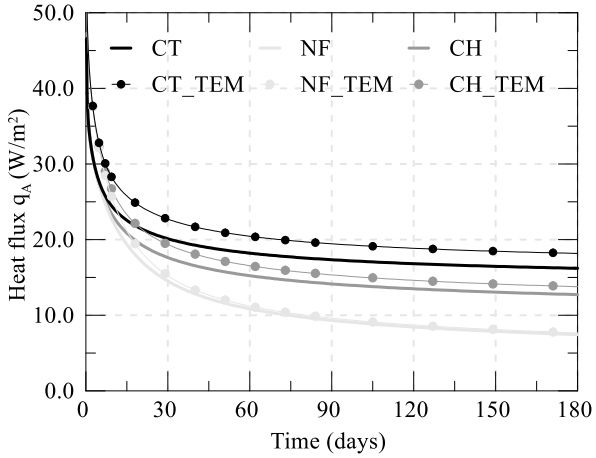

Figure F-1: Effect of TEM on heat flux – modelling approach 1

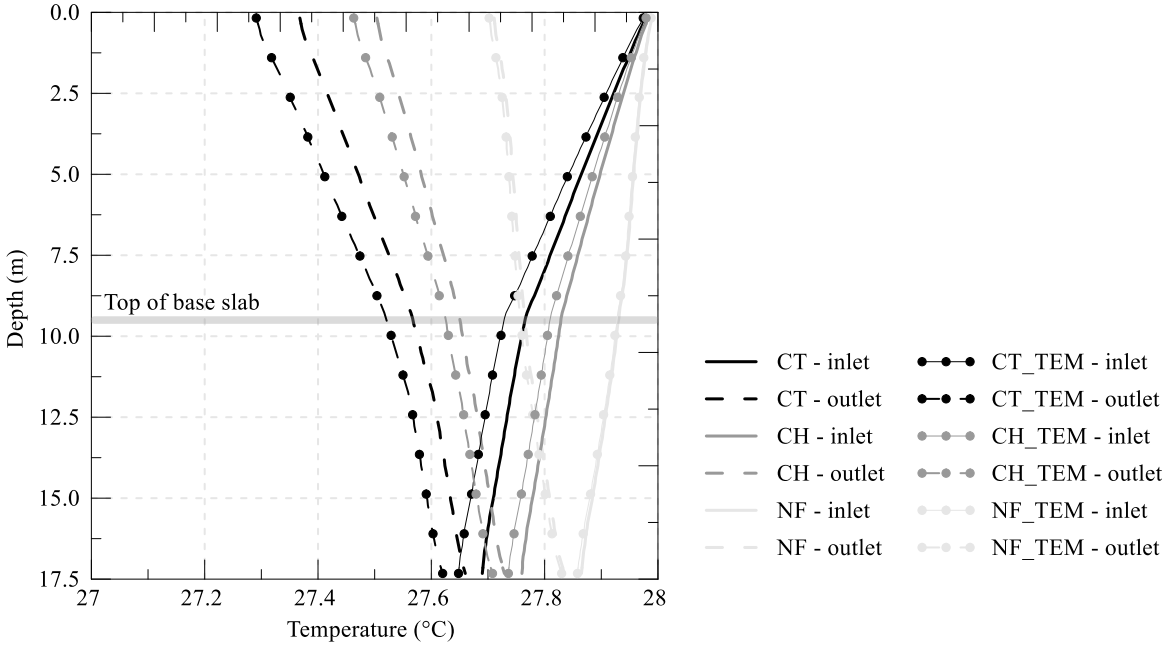

Figure F-2: Effect of TEM on temperatures in pipes – modelling approach 1

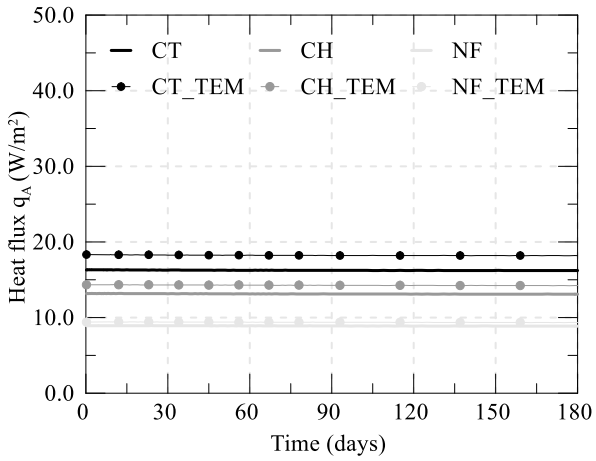

Figure F-3: Effect of TEM on heat flux– modelling approach 2

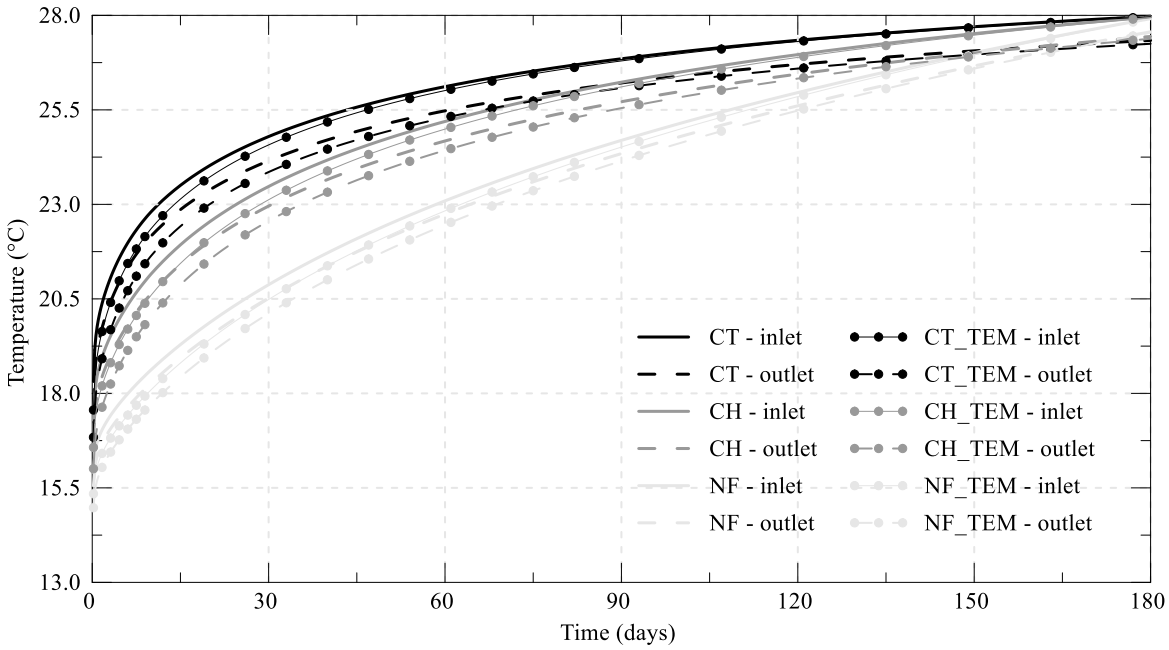

Figure F-4: Effect of TEM on inlet and outlet temperatures – modelling approach 2

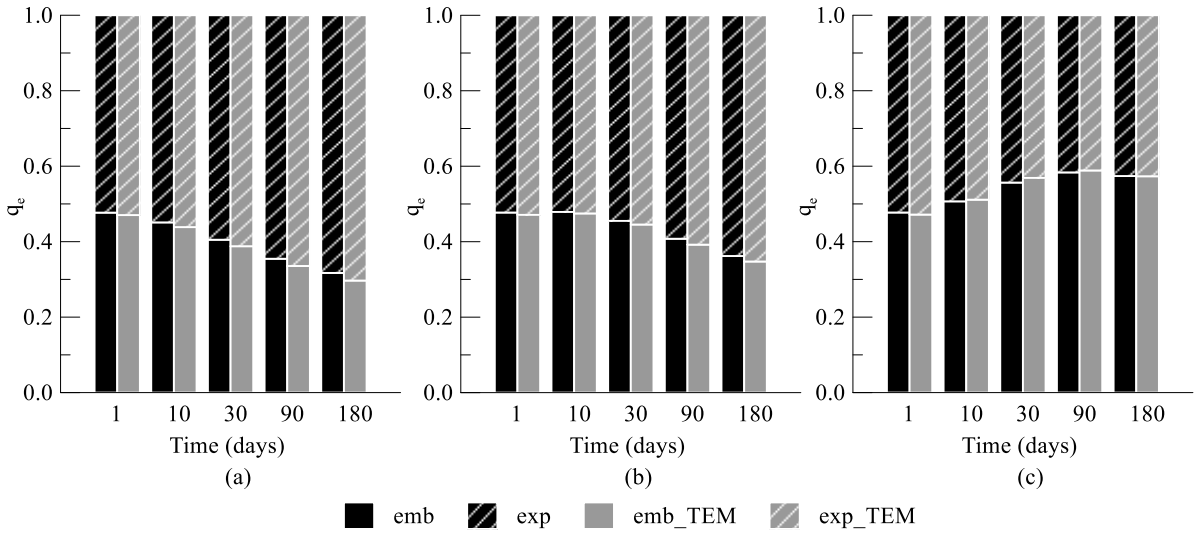

Figure F-5: Effect of TEM on heat flux ratio q_e – modelling approach 1 (a) CT, (b) CH and (c) NF

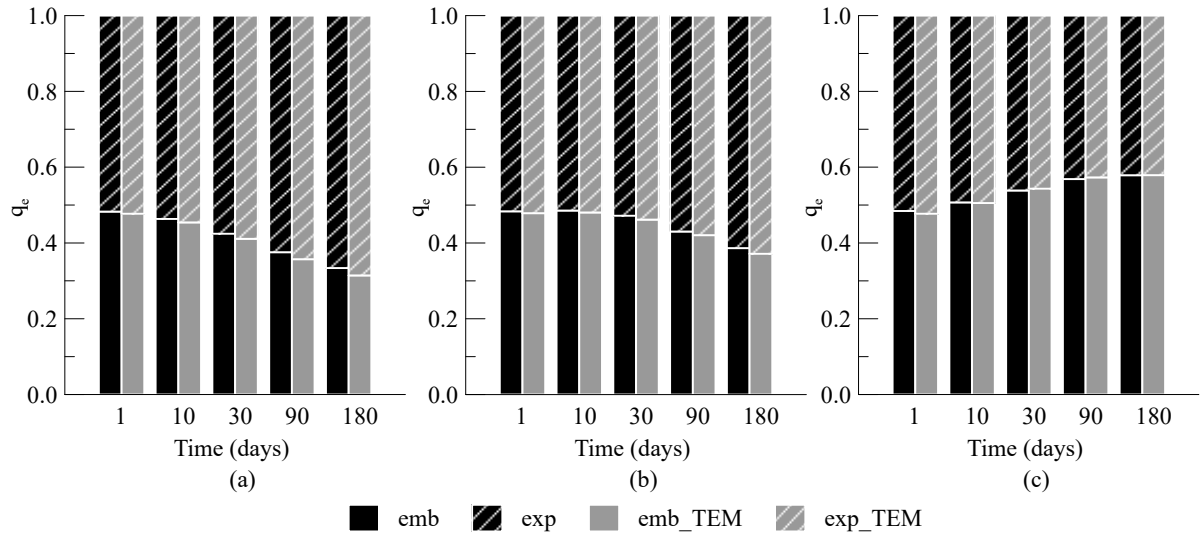

Figure F-6: Effect of TEM on heat flux ratio q_e – modelling approach 2 (a) CT, (b) CH and (c) NF

Energy

As a consequence of the increased heat flux, a larger energy output is calculated. Figure F-7 (a) and Figure F-8 (a) show the total energy per metre width calculated for all analyses, while Figure F-7 (b) Figure F-8 (b) display the environmental heat exchange, for MA1 and MA2, respectively. At the end of the simulation period, the total energy computed with MA1 for the analyses with inclusion of the TEM is 55 kWh/m, 120 kWh/m and 190 kWh/m larger than the one computed without TEM, for the NF, CH and CT analyses, respectively. This corresponds to a difference of 6%, 10% and 13% and this is attributed to the larger effect of the TEM in the short term. Similar differences are computed for MA2. For the CT and CH case, given the larger heat transfer rate, a larger environmental heat exchange takes place for the analyses with TEM.

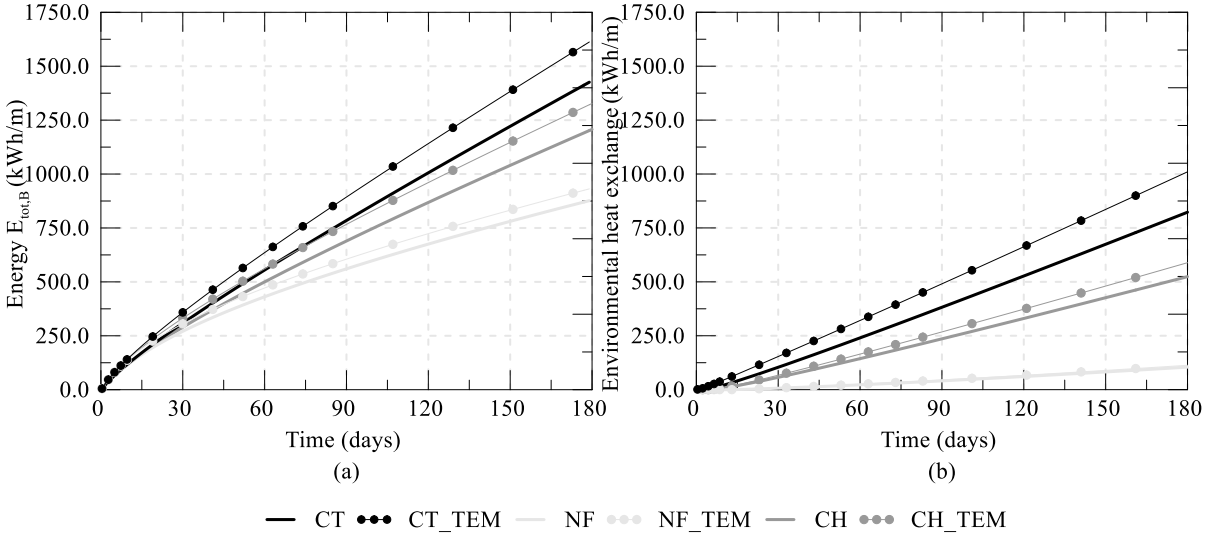

Figure F-7: Effect of TEM on transferred energy and environmental heat exchange – modelling approach 1

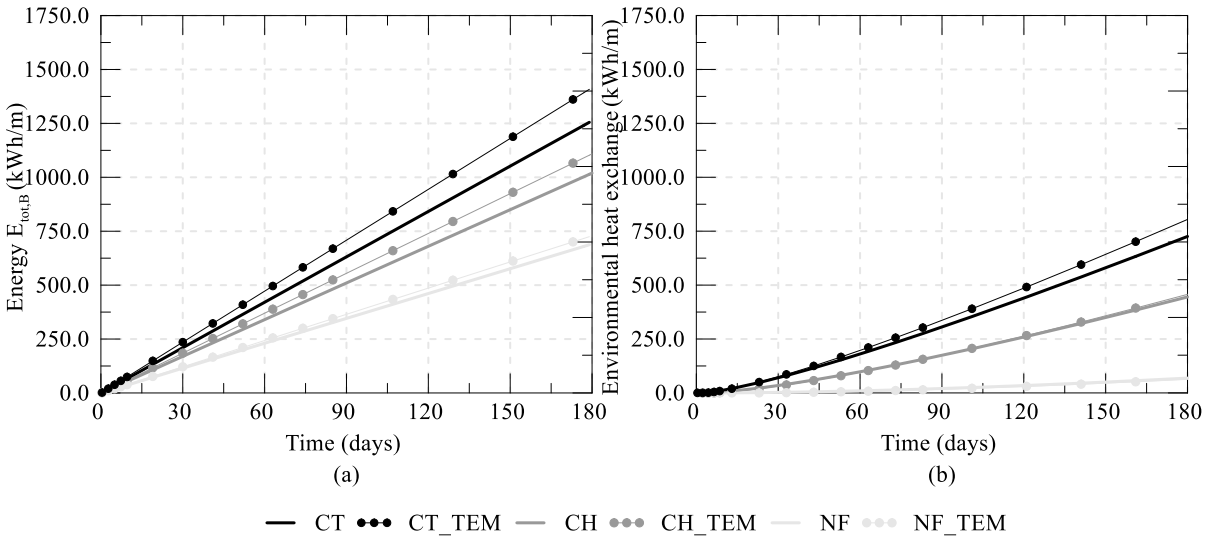

Figure F-8: Effect of TEM on transferred energy and environmental heat exchange – modelling approach 2

Soil temperatures

Figure F-9 and Figure F-10 show the changes in temperature for all the analyses with and without TEM, for MA1 and MA2, respectively. Since the TEM leads to a higher heat transfer rate, higher temperatures are recorded. Its effect is particularly pronounced at the soil-wall interface, where a maximum difference of 1.2°C for all cases is registered after approximately 10 days of operation. The difference in ground temperature, for MA1, reduces with time, and, at the end of the simulation, the difference between the analyses with and without TEM reduces to 0.9°C, 0.75°C and 0.6°C for the CT, CH and NF cases, respectively. For MA2, it increases slightly with time and reaches values which are very similar to those computed for MA1. Smaller differences are computed at larger distances of the wall: at 5.0 m from the wall, for MA1, the maximum difference is recorded in the CT case and is equal to 0.3°C, which corresponds to an increase of 11%. For the NF case, this reduces to 0.25°C, i.e. 8%. Even smaller differences are observed for the changes in temperature for MA2, which reach a maximum of 0.15°C, i.e. 6% more in comparison to the analyses without TEM.

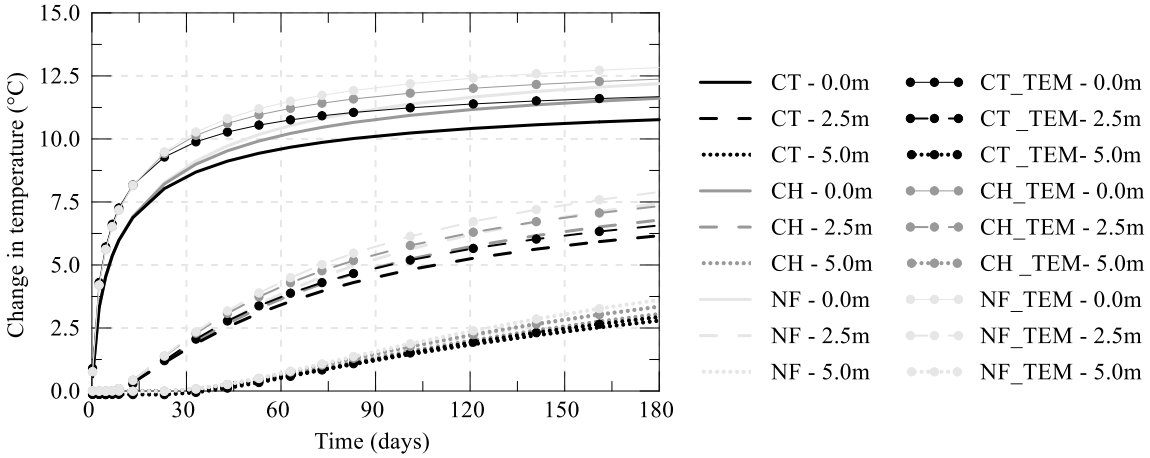

Figure F-9: Effect of TEM on soil temperatures – modelling approach 1

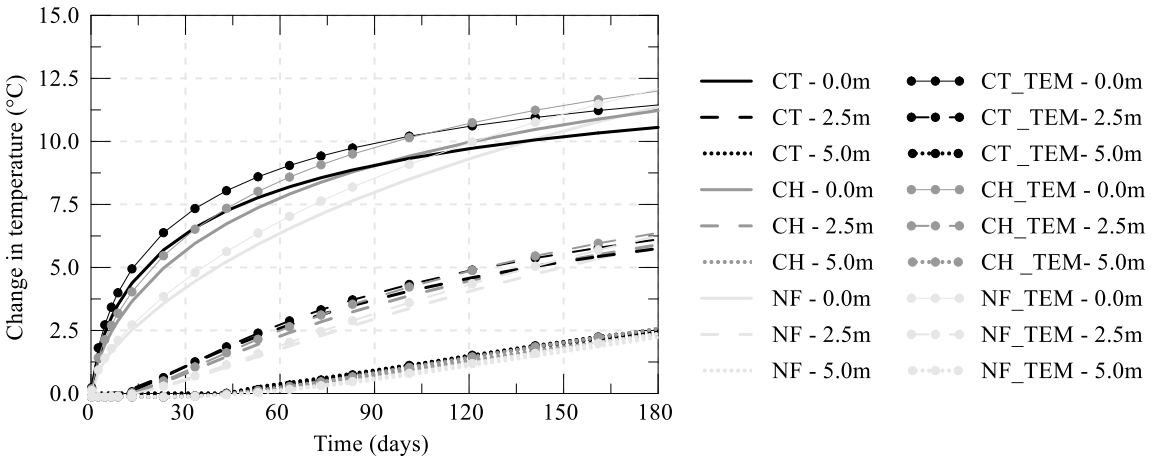

Figure F-10: Effect of TEM on soil temperatures – modelling approach 2

F.1.2 Long-term effect of TEM in 2D analyses

The effect of the TEM for the same geometry and pipe configuration has been analysed in 2D employing modelling approach 1, with the results for 2 and 4 pipes shown respectively in Figure F-11 (a) and (b). The addition of the TEM has no effect in a two-dimensional analysis, because of the different heat transfer mechanism in comparison to a 3D problem. Indeed, in 2D, the heat transfer is planar and the TEM is represented as a continuous wall in the out of plane direction. Given the limited thickness of the TEM (equal to the inner pipe diameter), its presence has a negligible impact on the results.

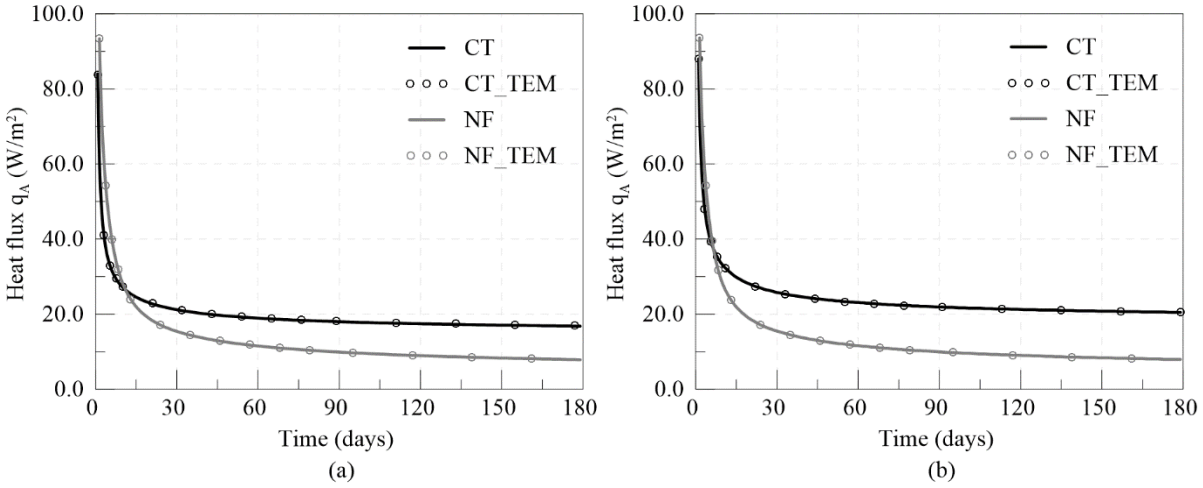

Figure F-11: Effect of TEM in 2D– modelling approach 1 – (a) 2 pipes and (b) 4 pipes

F.2 2D approximations for long-term heat flux for reference geometry employing modelling approach 1

Section 5.2 outlines approximations to enable the modelling of the thermal performance in 2D plane-strain analyses with the inclusion of one-dimensional elements for the simulation of heat exchanger pipes. Here, the results summarised in Chapter 5 are presented in more detail for each analysis and approximation.

The cases analysed in Section 5.2 are summarised in Table 5-1. Firstly, the 2D approximations for evaluating the long-term heat flux are evaluated. These are computed by adopting the approximation for the equivalent energy input (according to which the area of the pipe is modified in 2D adopting equation (5-6)) and, for walls maintained at a constant temperature (CT), the inlet temperature in 2D is modified adopting the correction factor X according to Equations (5-7) and (5-8). Subsequently, the results obtained adopting the approximations for the transferred energy are shown, where the inlet temperature for both NF (insulated walls) and CT analyses is reduced employing the correction factor Y calculated through Equation (5-10). The correction factor Y for the approximation based on the transferred energy depends on the considered operation period, with the constants for its calculation varying as outlined in Table 5-5.

Table F-1: Analyses for validation of 2D approximations (analyses Chapter 5)

Analysis	L_{exp} (m)	B (m)	n_p (-)	λ_c (W/mK)	$\overline{\lambda_s}$ (W/mK)	$\Delta T_{in,3D}$ (°C)
Ref	9.5	1.5	2	1.6	1.62	15°C
I	9.5	1.5	2	1.6	1.62	20°C
II	4.8	1.5	2	1.6	1.62	15°C
III	15.0	1.5	2	1.6	1.62	15°C
IV	9.5	1.5	4	1.6	1.62	15°C
V	15.0	1.5	4	1.6	1.62	15°C
VI	9.5	0.75	4	1.6	1.62	15°C
VII	9.5	1.5	2	2.4	1.62	15°C
VIII	9.5	1.5	2	1.2	1.62	15°C
IX	9.5	1.5	2	1.6	3.23	15°C
X	9.5	1.5	2	1.6	0.81	15°C
XI	9.5	1.5	4	1.6	3.23	15°C
XII	9.5	1.5	4	1.6	0.81	15°C

F.2.1 Approximation for the long-term heat flux

The comparison of the heat flux with time computed in 3D and corresponding 2D analyses, together with the relative and absolute errors are displayed in Figure F-12, Figure F-13 and Figure F-14. The inlet temperatures employed in the CT case are reported in Table 5-4.

Similar to the reference case, all 2D analyses display a larger heat flux in the short term due to the effects of plane-strain conditions, which lead to a faster heat transfer. However, the differences stabilise generally after 30 days of operation and remain approximately constant until the end of the simulation period. Due to the different approximations adopted for the two boundary conditions along the exposed face (i.e. for NF only a correction in the water flow rate is applied, whereas for CT the inlet temperature is modified), slightly different trends in the comparison between 3D and 2D results are observed.

For the NF case, the 2D analyses predict in almost every situation a higher heat flux in the long term with respect to the 3D analyses. The largest difference is obtained analysis IX (i.e. reference geometry with twice the soil thermal conductivity), where the 2D analysis predicts a long-term heat flux which is 16% higher than that obtained in 3D. However, this corresponds to a difference of 1.7 W/m^2, while the temperature change at the pipes, ΔT_p, is only 0.18°C higher than in 3D. Generally, the difference in the heat flux calculated for the 3D and 2D analyses drops monotonically until a constant value is reached. Exceptions to this trend are observed for analyses III and V (largest depth of excavation), IV and VI (smaller spacing between pipes) and X and XII (half the thermal conductivity of the soil). For these analyses, the 2D predicts a lower heat flux than in 3D in the medium term (between 5 and 30 days), with differences up to -13%, while, in the long term, a higher heat flux is encountered. For such cases, the increased heat transfer rate in 2D leads to unfavourable conditions, since the wall heats up quicker than in 3D and thus leads to a smaller ΔT_p in the medium term. Indeed, a larger depth of excavation, smaller spacing between pipes and a lower thermal conductivity of the soil contribute to the wall to warm up quicker than in other analyses:

- with a larger L_{exp}, a larger insulated surface is simulated;
- decreasing the spacing between the pipes is simulated in 2D by injecting more water per metre length of wall;
- decreasing the soil thermal conductivity leads to a slower heat transfer to the soil, meaning that the heat takes more time to be transferred from the wall to the soil.

These effects are encountered only in the medium term, because the 3D analysis will eventually be subjected to the same conditions, only after a longer period of time, where the results eventually converge.

Furthermore, the smallest differences in the long-term heat flux are obtained by the analyses simulating a smaller spacing between the pipes, i.e. analyses IV, V, VI, XI and XII, because the 3D simulates

conditions closer to those modelled in a 2D plane-strain analysis. Largest discrepancies are obtained when a high thermal conductivity of the soil is simulated, as it further enhances the heat transfer in 2D and thus leads to larger differences between 3D and 2D.

For the CT case, the difference between the heat flux computed in 3D and 2D monotonically reduces for all the analyses, reaching a stable value which varies between $\pm$7% of the values computed in 3D. Given the additional correction on the inlet temperature, determined empirically by matching the 3D results, a slightly better approximation is obtained for these analyses and no clear pattern is observed regarding the discrepancy between 3D and 2D.

While the relative errors, mainly for the NF analyses, in some cases exceed 10%, the absolute errors for both boundary conditions are generally limited to $\pm$1.0 W/m^2, with only few cases above this value, though never exceeding $\pm$1.8 W/m^2. Thus, the relative errors may not be appropriate to evaluate the performance of the approximations, since the calculated heat flux is a rather small number, especially for the NF case. Furthermore, as pointed out in previous sections of this thesis, there are numerous aspects that may lead to similar differences in temperature, e.g. the adopted mesh discretisation, the employed type of temperature shape function (i.e. linear or quadratic), the Petrov-Galerkin formulation (see Appendix E), etc. Hence, taking into account these uncertainties within the Finite Element analyses, the computed differences between 2D and 3D analyses are considered acceptable.

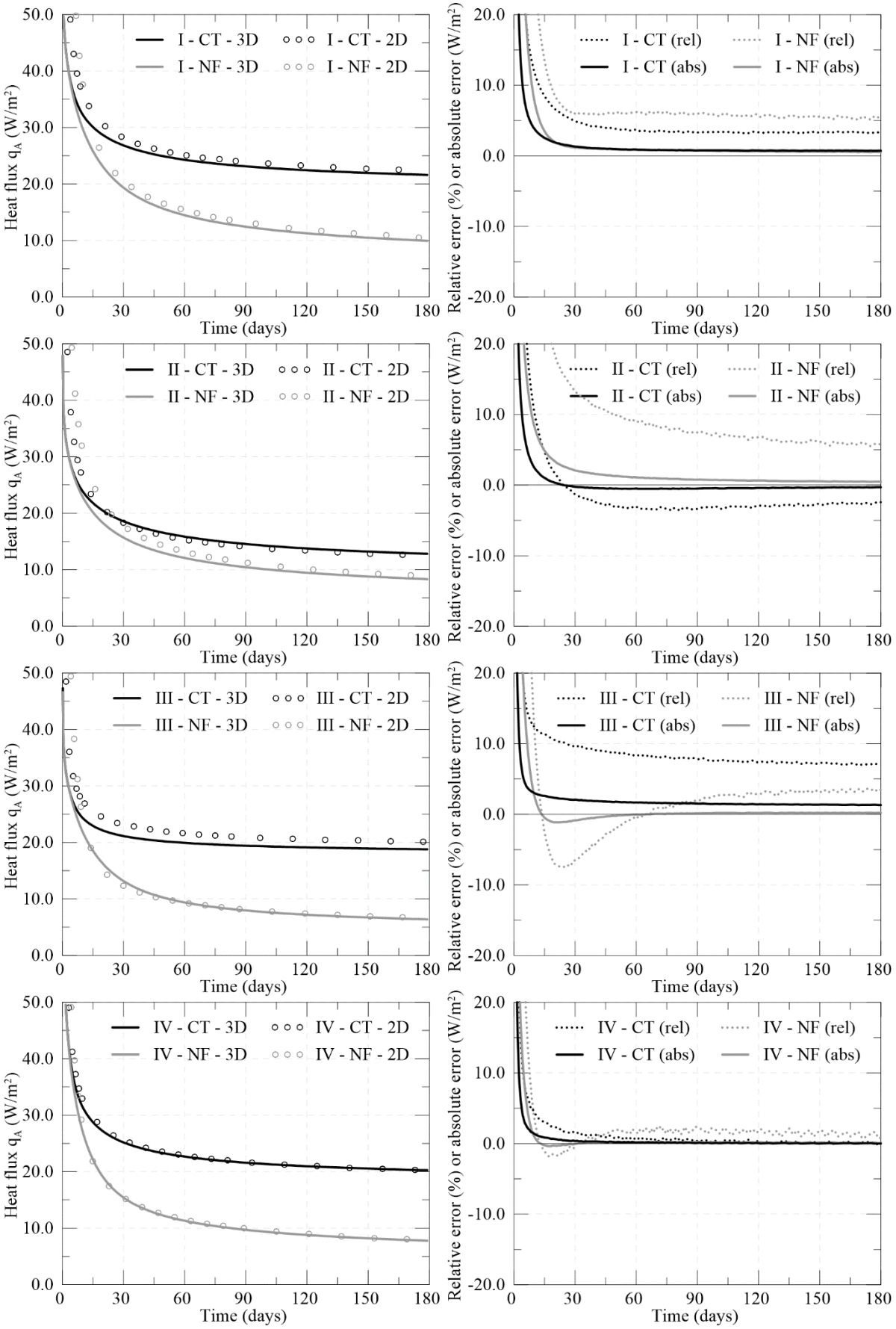

Figure F-12: Comparison of long-term heat flux between 3D and 2D – analyses I to IV

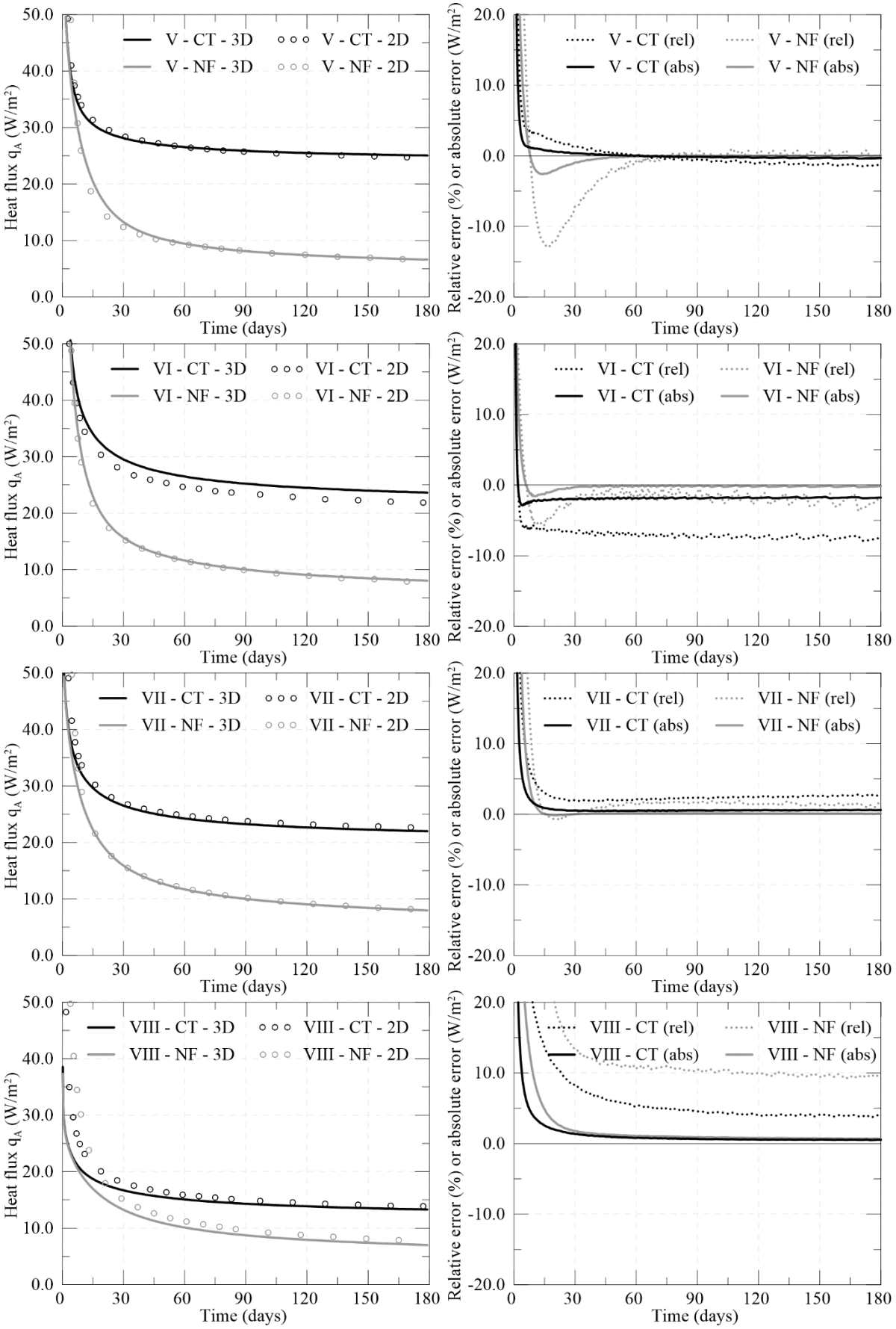

Figure F-13: Comparison of long-term heat flux between 3D and 2D – analyses V to VIII

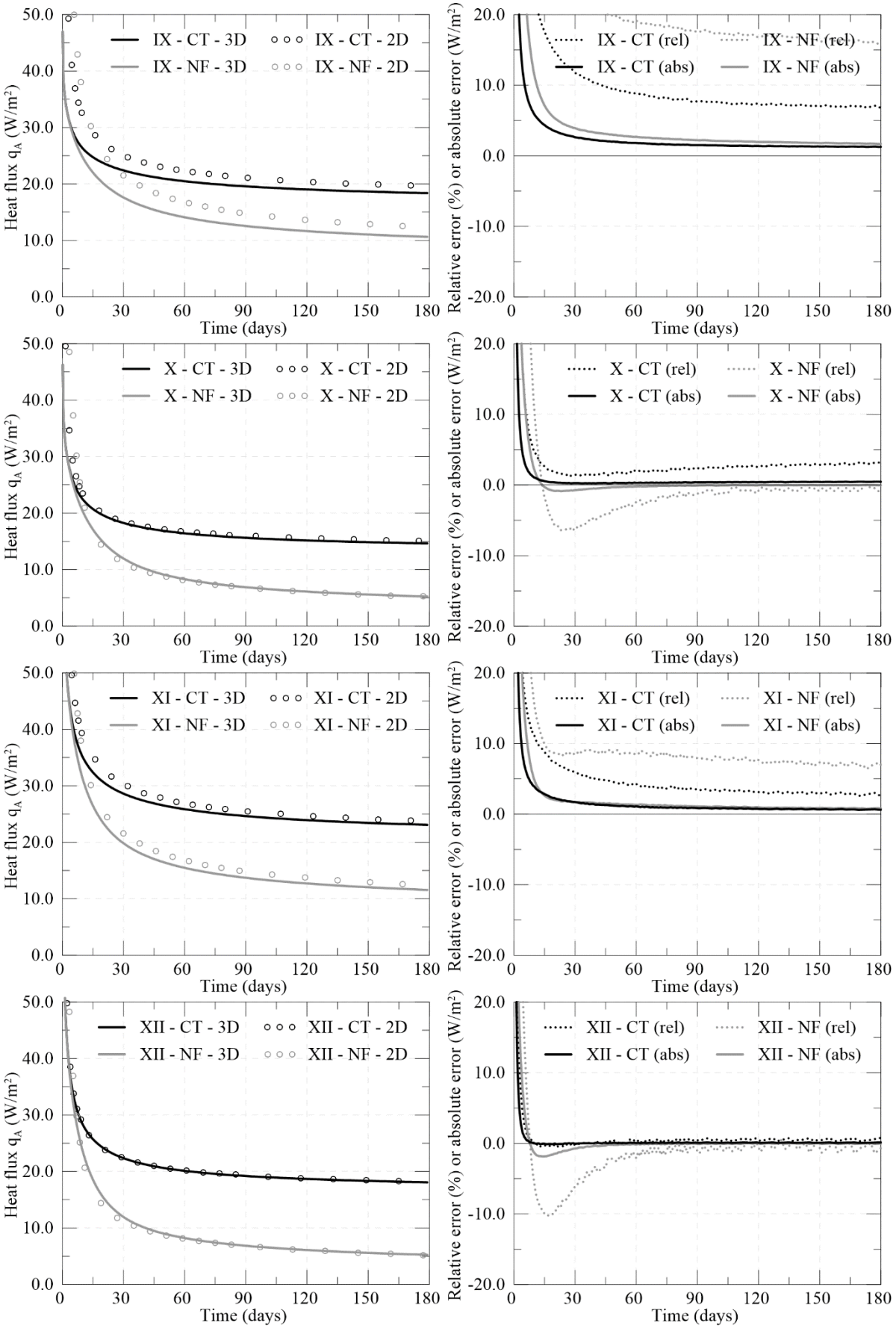

Figure F-14: Comparison of long-term heat flux between 3D and 2D – analyses IX to XII

F.2.2 Approximation for transferred energy

The development of the energy transferred during a 6 months operation period in 3D and 2D analyses is displayed in Figure F-18, Figure F-19 and Figure F-20; Figure F-21, Figure F-22 and Figure F-23 show the results for 3 months of operation and Figure F-24, Figure F-25 and Figure F-26 plot the energy for 1 month of operation. The calculated correction factors *Y* and inlet temperature are outlined in Table F-2, Table F-3 and Table F-4 for 6 months, 3 months and 1 month, respectively.

Similar to the approximation required to evaluate the long-term heat flux for a CT boundary condition along the exposed face, the correction factor *Y* aims at reducing the 2D effects (i.e. a larger heat transfer rate in 2D in the short term) by reducing the inlet temperature. The transferred energy is calculated as the integral of the heat flux with time normalised by the width of the panel (see Equation (4-2)). From the computed heat flux previously shown, it is thus unsurprising that the transferred energy in a 2D plane-strain analysis is larger than in 3D in the short term. Hence, different corrections are required to capture the transferred energy at shorter operation periods, for which lower inlet temperatures are simulated to take into account the increased heat transfer in 2D in the short term. Indeed, it can be observed that, when comparing the results obtained for the same analysis for the energy transferred after 6, 3 and 1 month, the differences between the 3D and 2D analyses in the short term reduce.

The results show a good match for all the operation periods and type of analysis, with differences within ±10% of the values evaluated in 3D, as shown in Figure F-15, Figure F-16 and Figure F-17.

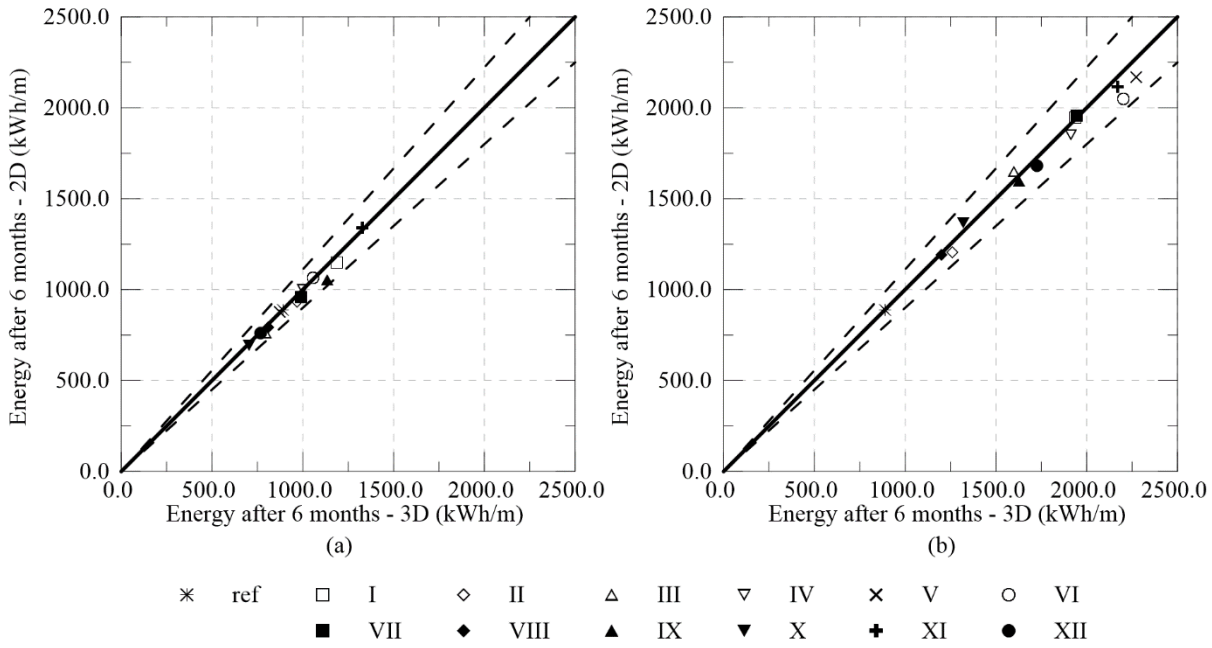

Figure F-15: Comparison of energy transferred after 6 months between 3D and 2D (a) NF and (b) CT

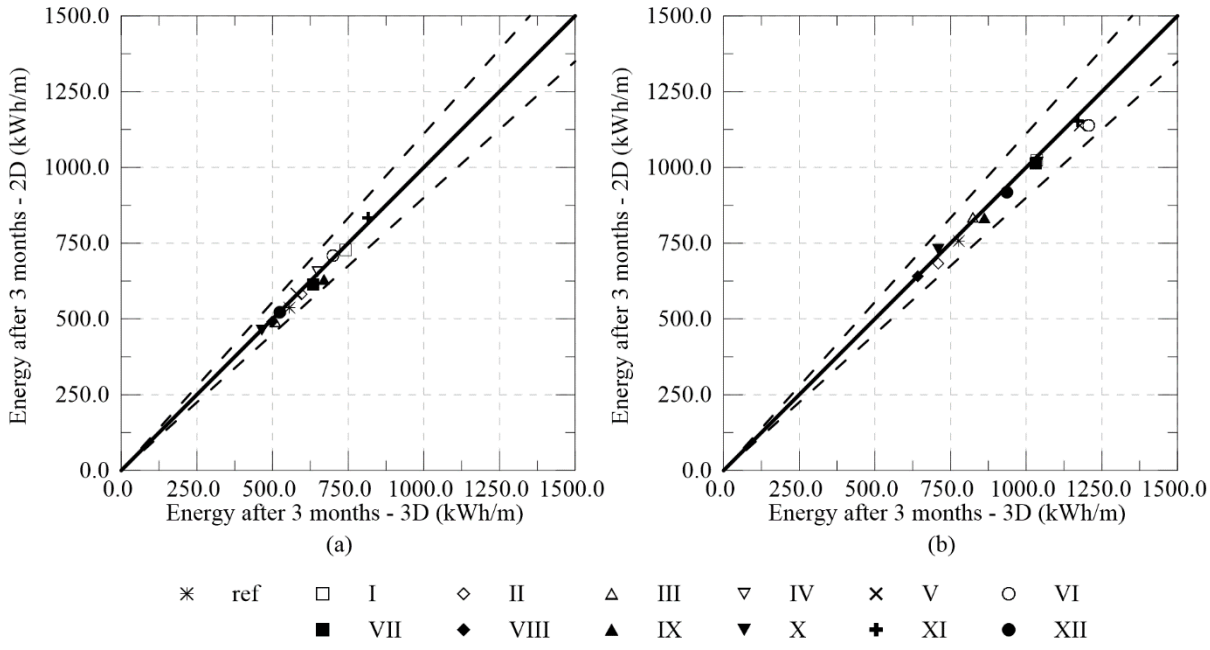

Figure F-16: Comparison of energy transferred after 3 months between 3D and 2D (a) NF and (b) CT

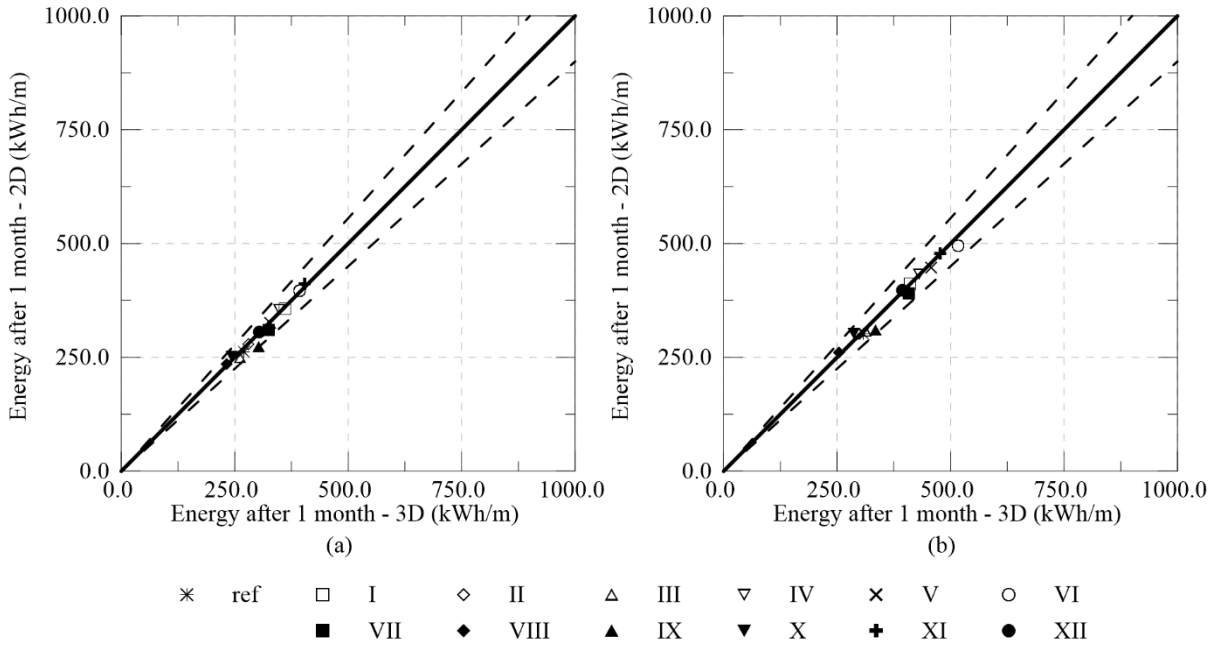

Figure F-17: Comparison of energy transferred after 1 month between 3D and 2D (a) NF and (b) CT

Table F-2: Correction factor and inlet temperature in 2D for approximation of transferred energy after 6 months

Analysis	L_{exp}/L	B/n_p	λ_c	$\overline{\lambda_s}$	Y_{NF}	Y_{CT}	$T_{in,2D,E,NF}$	$T_{in,2D,E,CT}$
	(-)	(-)	(W/mK)	(W/mK)	(-)	(-)	(°C)	(°C)
I	0.53	0.75	1.6	1.62	0.80	0.60	29.0	25.0
II	0.27	0.75	1.6	1.62	0.77	0.63	24.5	22.4
III	0.83	0.75	1.6	1.62	0.83	0.54	25.4	21.1
IV	0.53	0.375	1.6	1.62	0.91	0.75	26.7	24.2
V	0.83	0.375	1.6	1.62	0.92	0.71	26.8	23.6
VI	0.53	0.1875	1.6	1.62	0.96	0.84	27.4	25.6
VII	0.53	0.75	2.4	1.62	0.85	0.62	25.8	22.4
VIII	0.53	0.75	1.2	1.62	0.75	0.58	24.3	21.7
IX	0.53	0.75	1.6	3.23	0.70	0.56	23.5	21.4
X	0.53	0.75	1.6	0.81	0.87	0.64	26.0	22.5
XI	0.53	0.375	1.6	3.23	0.86	0.72	26.0	23.8
XII	0.53	0.375	1.6	0.81	0.94	0.77	27.1	24.5

Table F-3: Correction factor and inlet temperature in 2D for approximation of transferred energy after 3 months

Analysis	L_{exp}/L	B/n_p	λ_c	$\overline{\lambda_s}$	Y_{NF}	Y_{CT}	$T_{in,2D,E,NF}$	$T_{in,2D,E,CT}$
	(-)	(-)	(W/mK)	(W/mK)	(-)	(-)	(°C)	(°C)
I	0.53	0.75	1.6	1.62	0.75	0.57	28.0	24.4
II	0.27	0.75	1.6	1.62	0.71	0.59	23.7	21.8
III	0.83	0.75	1.6	1.62	0.78	0.52	24.7	20.8
IV	0.53	0.375	1.6	1.62	0.88	0.73	26.2	23.9
V	0.83	0.375	1.6	1.62	0.89	0.70	26.4	23.5
VI	0.53	0.1875	1.6	1.62	0.94	0.83	27.1	25.4
VI	0.53	0.75	2.4	1.62	0.82	0.59	25.3	21.9
VIII	0.53	0.75	1.2	1.62	0.69	0.56	23.3	21.3
IX	0.53	0.75	1.6	3.23	0.66	0.53	22.9	20.9
X	0.53	0.75	1.6	0.81	0.82	0.61	25.3	22.2
XI	0.53	0.375	1.6	3.23	0.83	0.70	25.5	23.5
XII	0.53	0.375	1.6	0.81	0.91	0.75	26.7	24.3

Table F-4: Correction factor and inlet temperature in 2D for approximation of transferred energy after 3 months

Analysis	L_{exp}/L (-)	B/n_p (-)	λ_c (W/mK)	$\overline{\lambda_s}$ (W/mK)	Y_{NF} (-)	Y_{CT} (-)	$T_{in,2D,E,NF}$ (°C)	$T_{in,2D,E,CT}$ (°C)
I	0.53	0.75	1.6	1.62	0.64	0.52	25.7	23.4
II	0.27	0.75	1.6	1.62	0.59	0.53	21.9	21.0
III	0.83	0.75	1.6	1.62	0.66	0.47	23.0	20.1
IV	0.53	0.375	1.6	1.62	0.80	0.68	25.0	23.2
V	0.83	0.375	1.6	1.62	0.82	0.65	25.2	22.8
VI	0.53	0.1875	1.6	1.62	0.89	0.79	26.4	24.9
VI	0.53	0.75	2.4	1.62	0.71	0.55	23.6	21.2
VIII	0.53	0.75	1.2	1.62	0.57	0.49	21.6	20.4
IX	0.53	0.75	1.6	3.23	0.53	0.45	20.9	19.8
X	0.53	0.75	1.6	0.81	0.72	0.58	23.8	21.7
XI	0.53	0.375	1.6	3.23	0.74	0.64	24.1	22.6
XII	0.53	0.375	1.6	0.81	0.85	0.72	25.7	23.8

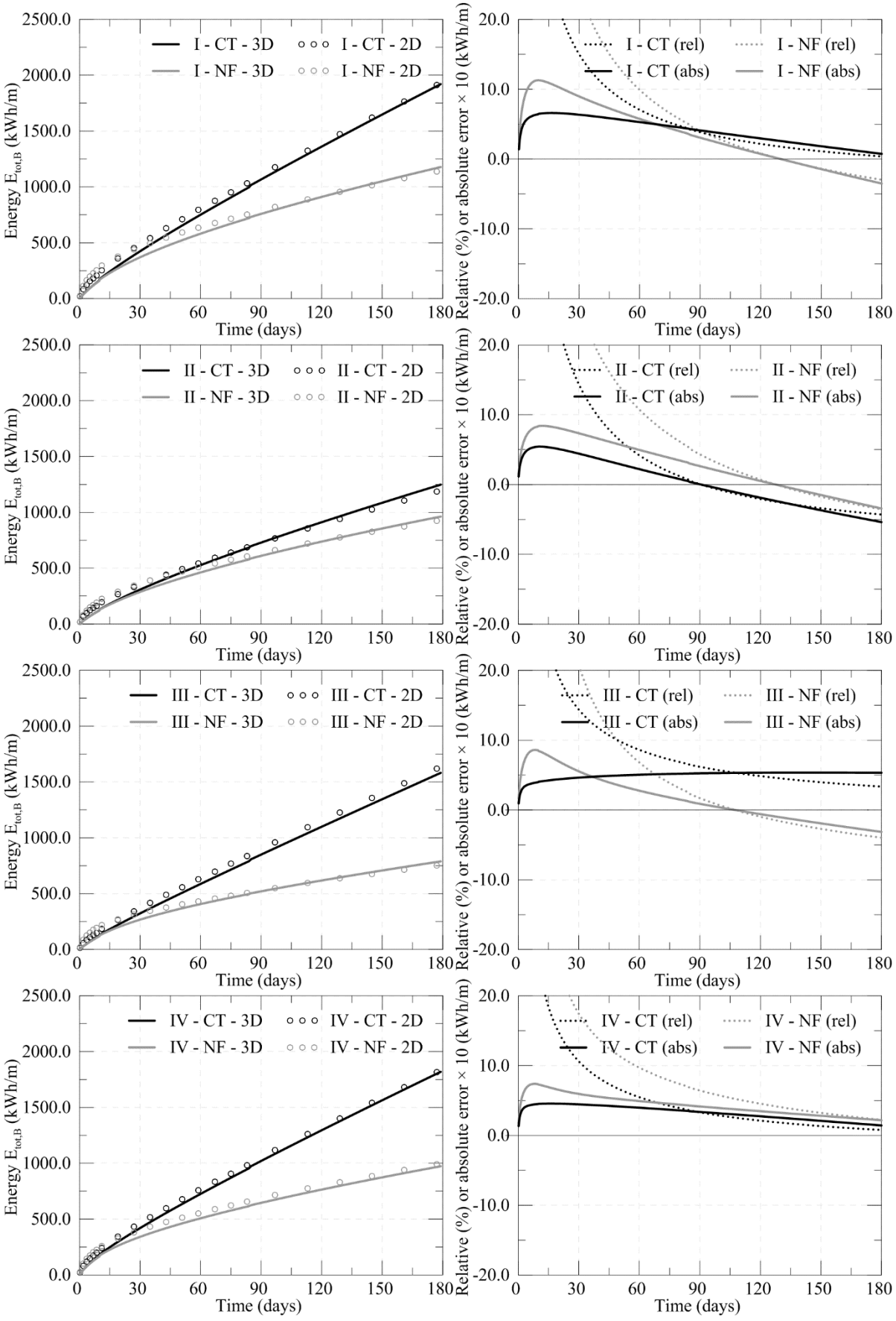

Figure F-18: Comparison of transferred energy during 6 months between 3D and 2D – analyses I to IV

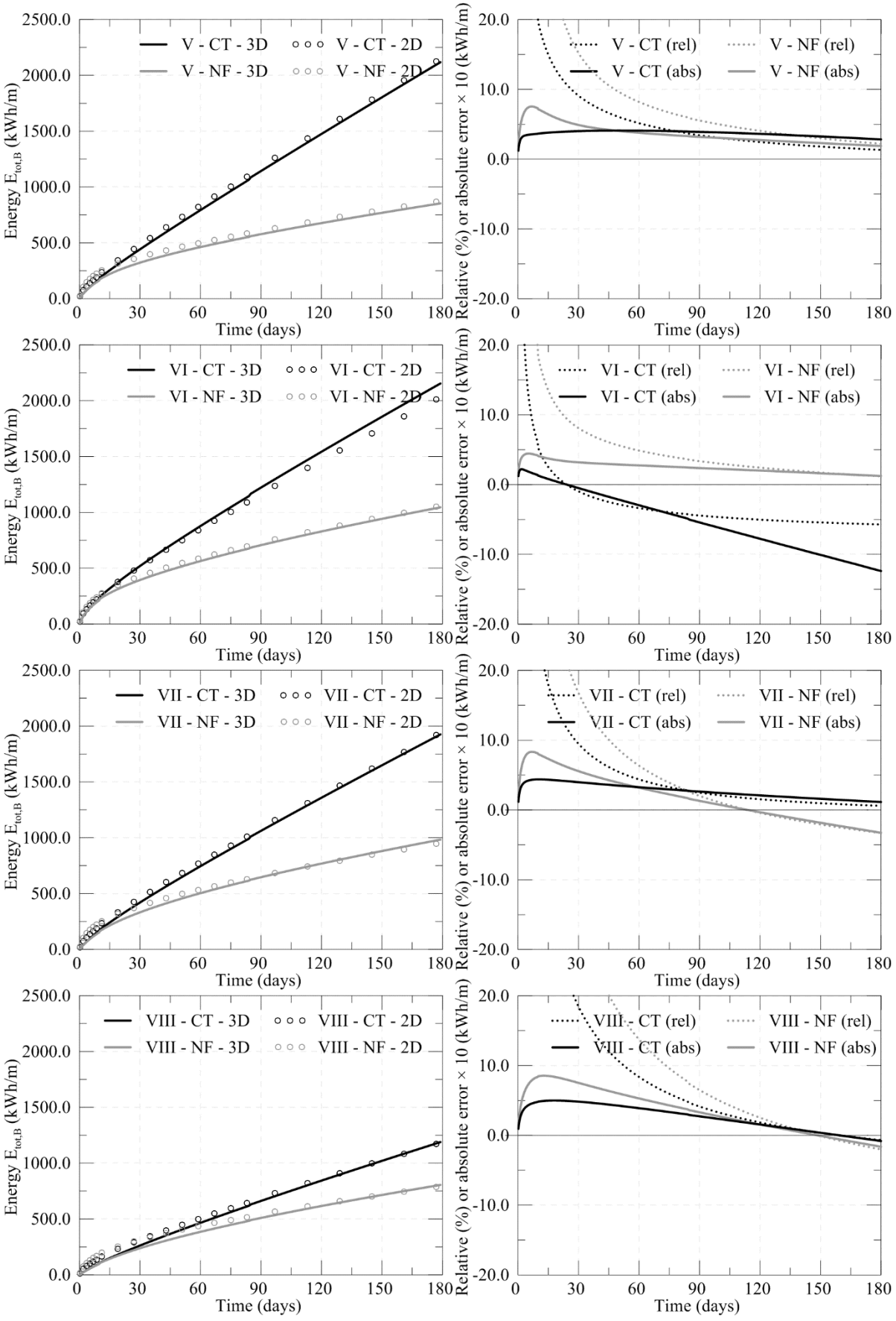

Figure F-19: Comparison of transferred energy during 6 months between 3D and 2D – analyses V to VIII

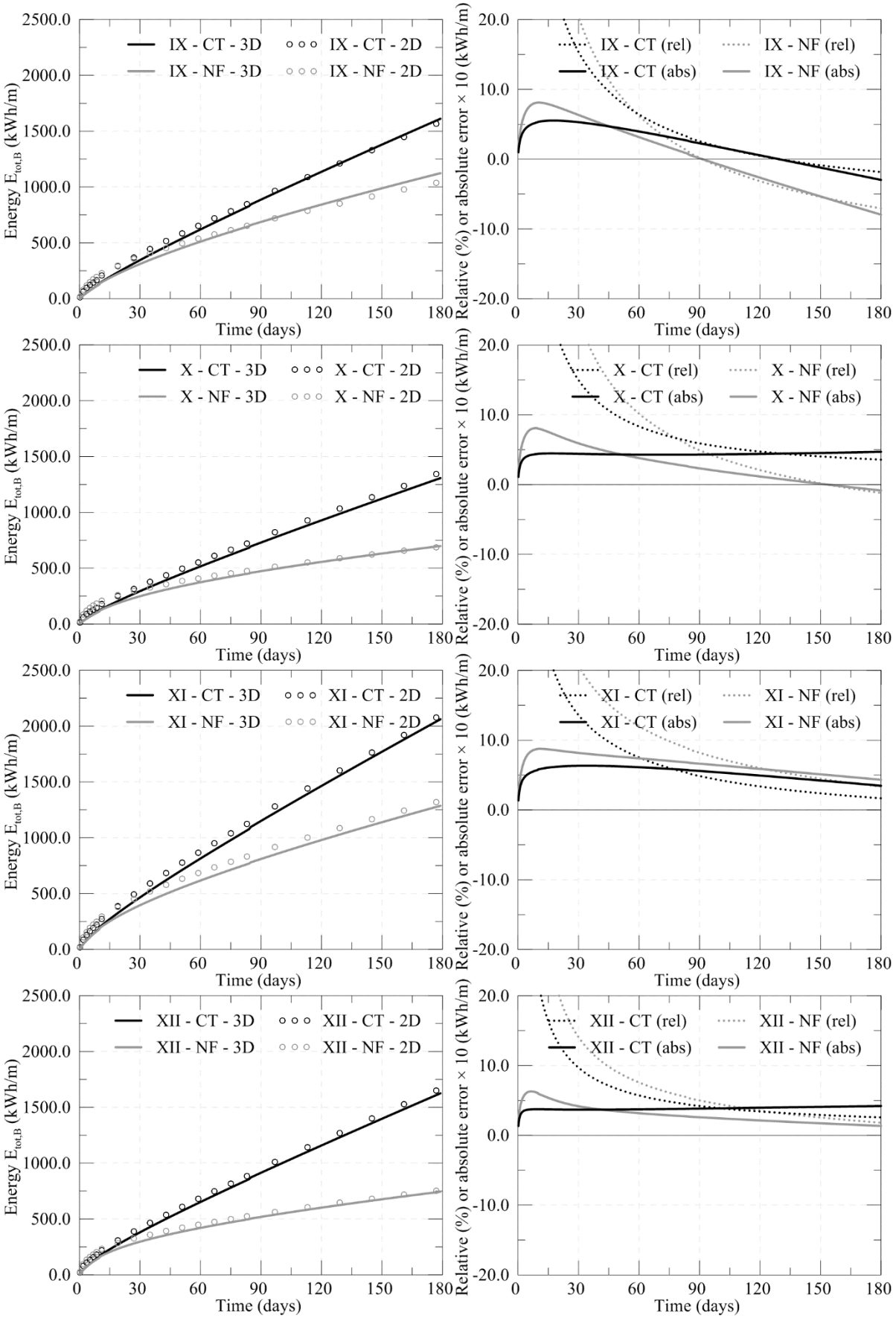

Figure F-20: Comparison of transferred energy during 6 months between 3D and 2D – analyses IX to XII

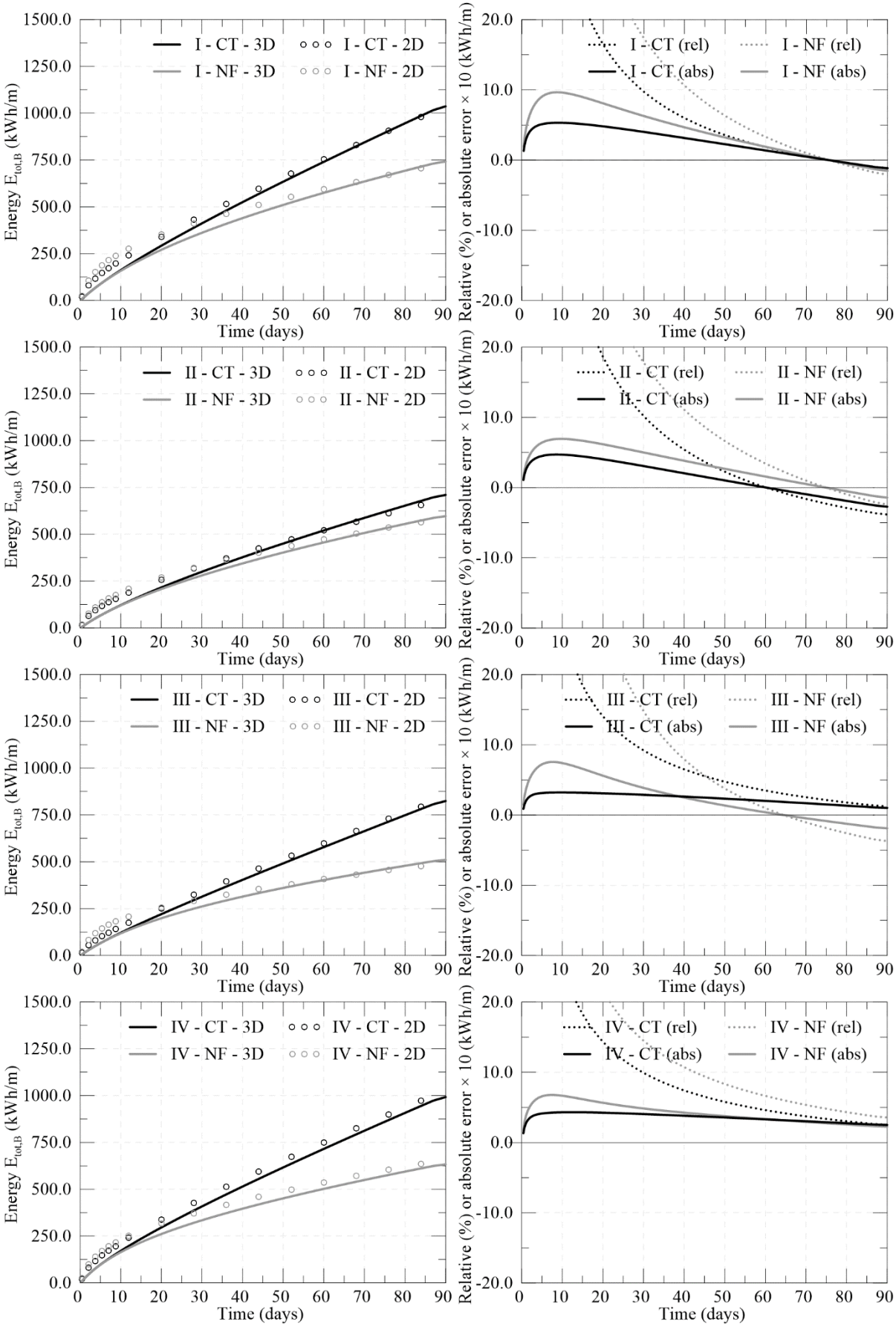

Figure F-21: Comparison of transferred energy during 3 months between 3D and 2D – analyses I to IV

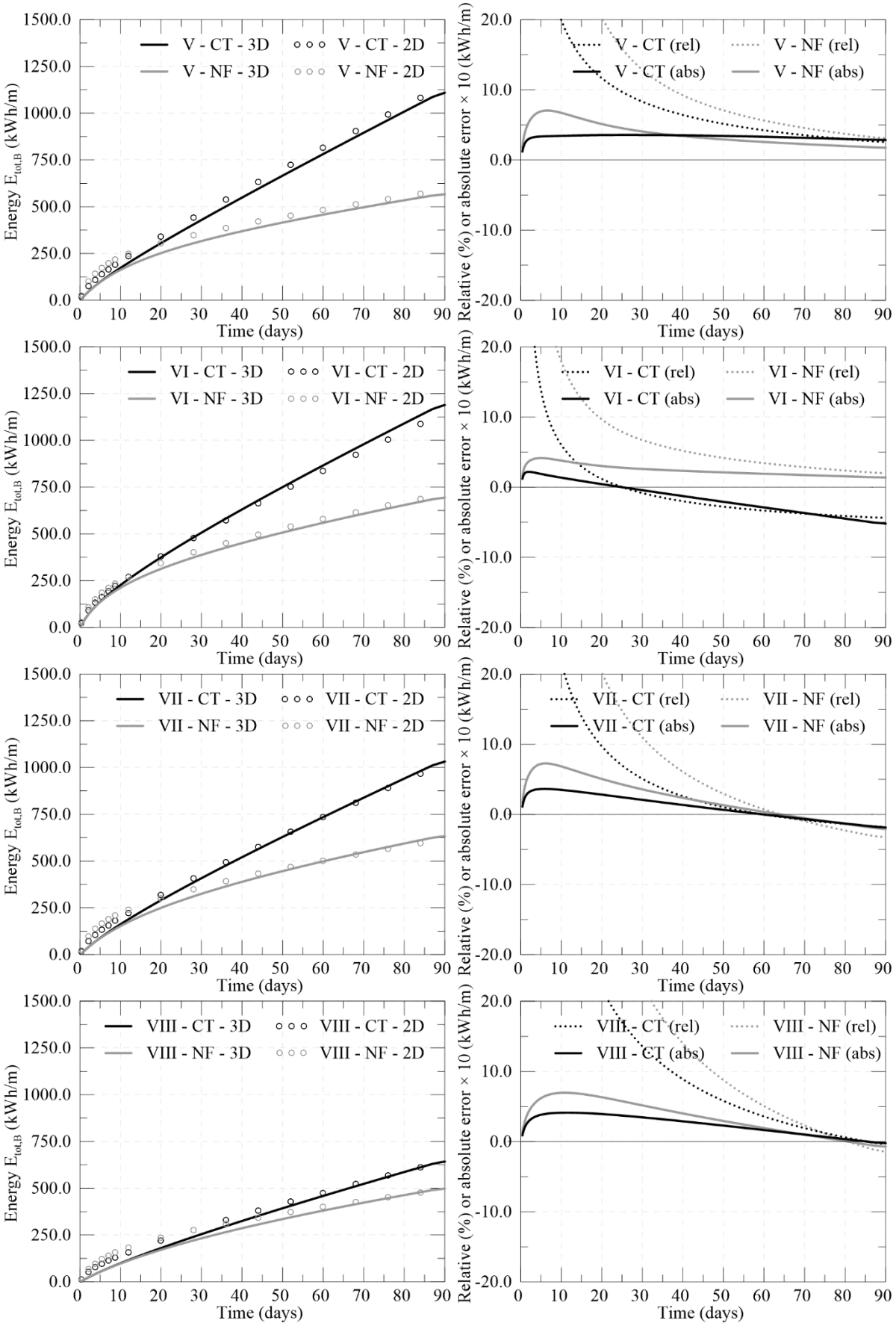

Figure F-22: Comparison of transferred energy during 3 months between 3D and 2D – analyses V to VIII

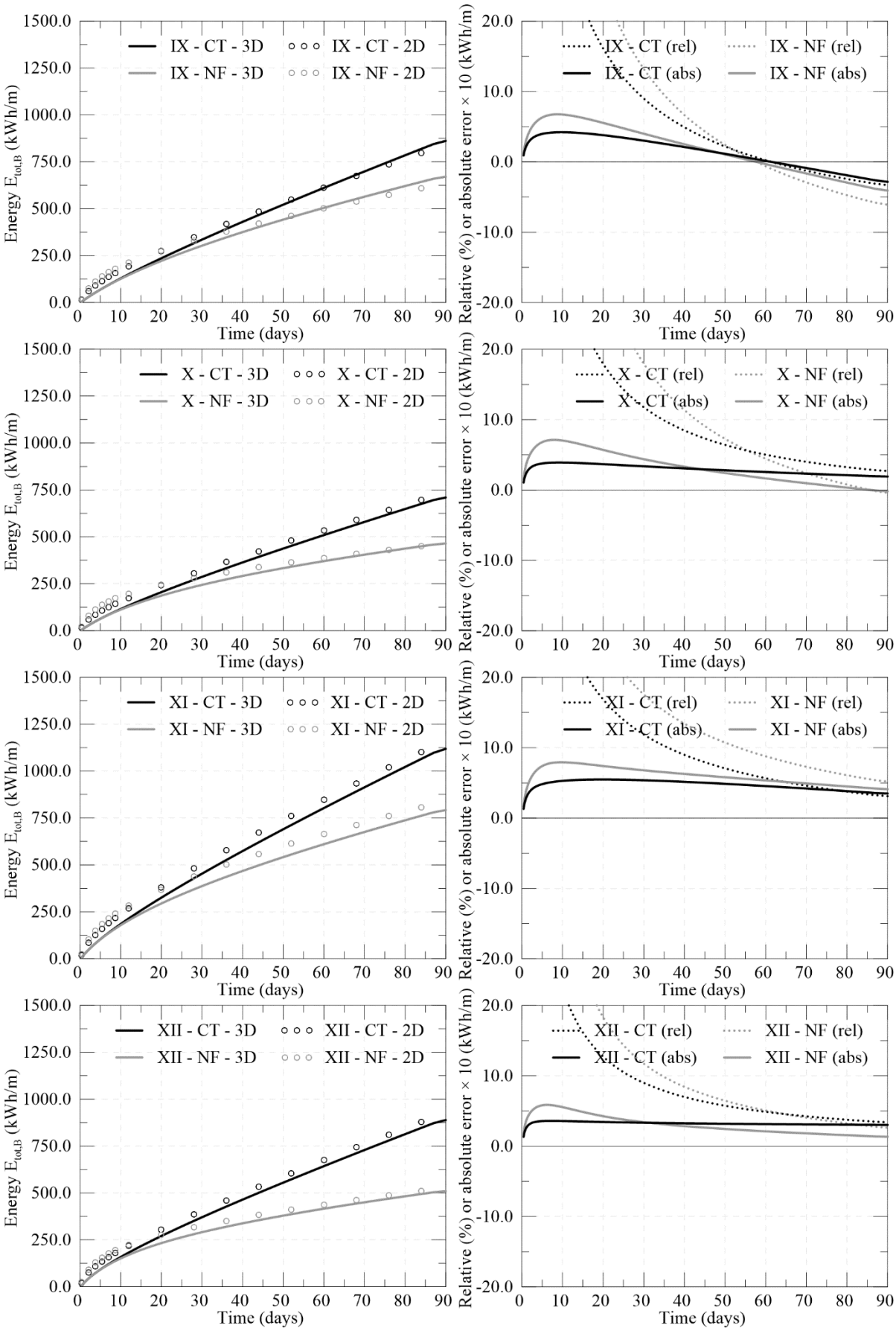

Figure F-23: Comparison of transferred energy during 3 months between 3D and 2D – analyses IX to XII

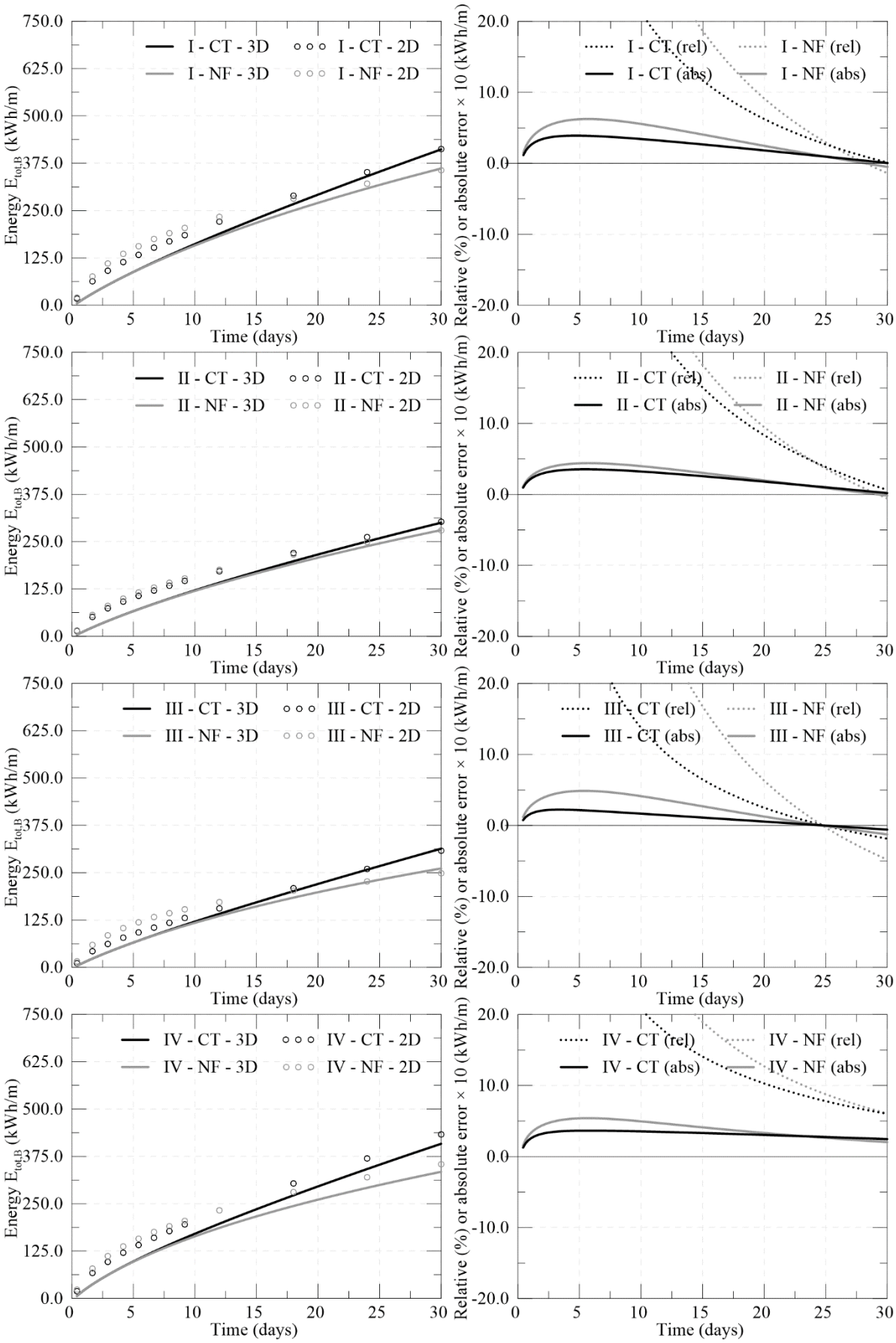

Figure F-24: Comparison of transferred energy during 1 month between 3D and 2D – analyses IX to XII

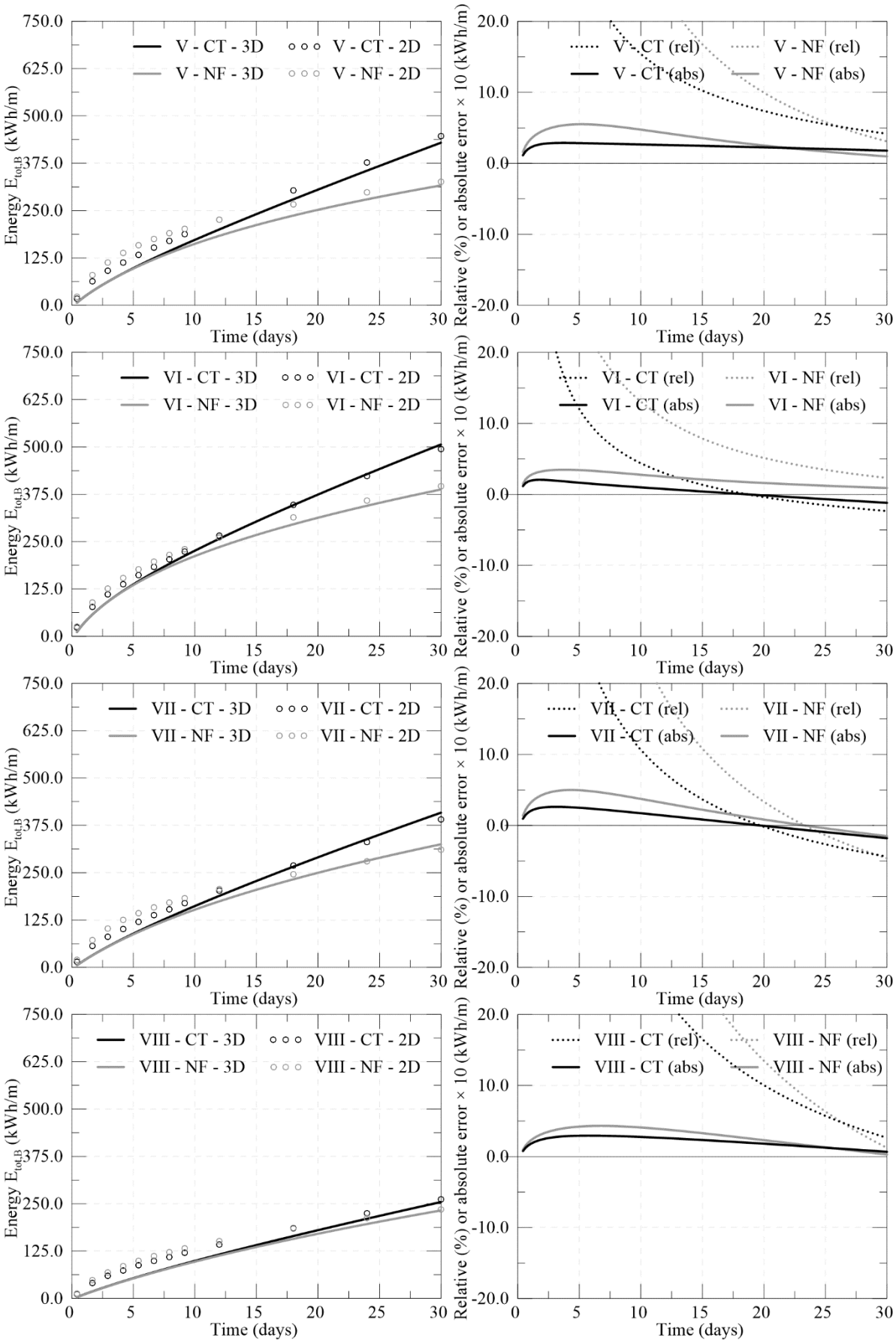

Figure F-25: Comparison of transferred energy during 1 month between 3D and 2D – analyses IX to XII

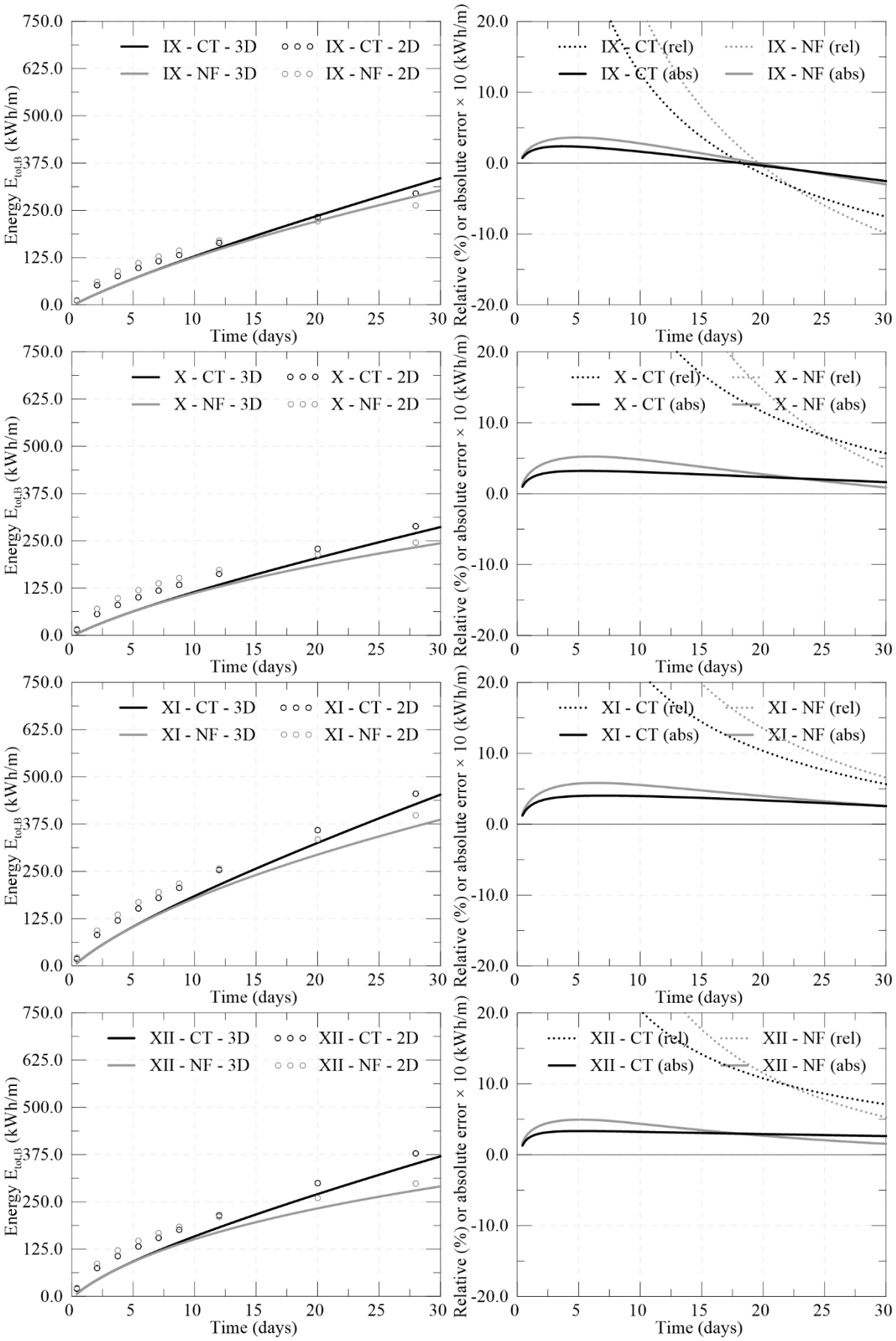

Figure F-26: Comparison of transferred energy during 1 month between 3D and 2D – analyses IX to XII

Appendix G

Assessment of the proposed method in 2D for one year of operation

The following analyses are based on the 3D problem reported in Section 6.2.1.2, which simulated 6 months of heating (heat injection). The subsequent cooling period (heat extraction) was modelled by applying a constant temperature at the inlet node of the 3D analysis, $T_{in,3D}$, of -2.0°C (i.e. ΔT_{3D}=-15.0°C). The 2D analyses correspond to the first year of operation of scenario (1) presented in Section 6.5.

The results obtained for the analyses with NF and CT boundary conditions along the exposed face are compared to those evaluated by 2D plane-strain analyses modelled using the proposed method. Figure G-1 shows the temperatures applied as a boundary condition in the 2D plane-strain analyses over a period of one year.

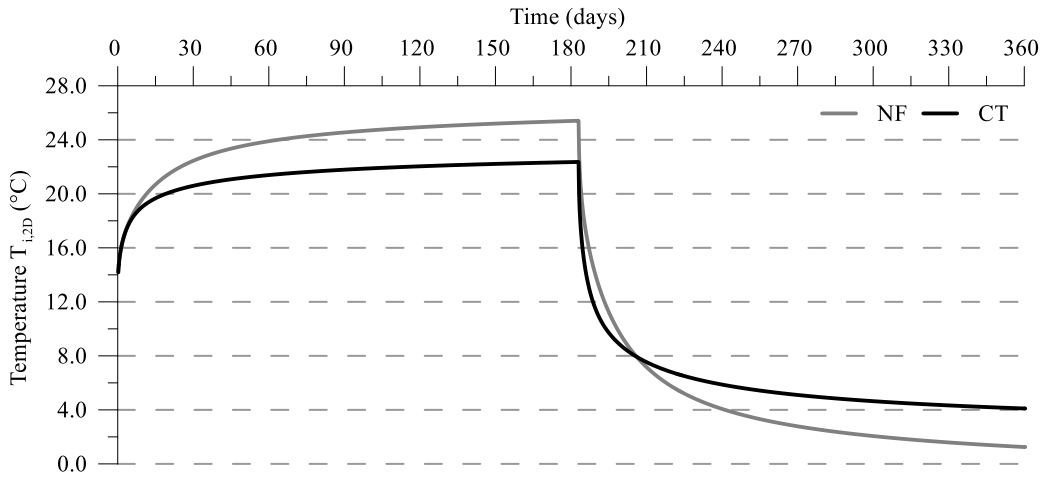

Figure G-1: Temperature values for boundary condition in 2D plane-strain THM analysis with NF and CT boundary condition

Once the cooling phase commences, the temperatures within the wall and soil decrease. The changes in temperature depicted in Figure G-2 demonstrate that the 2D analysis is able to capture the changes well both during heating and subsequent cooling with a larger discrepancy at the soil-wall interface, as previously observed. Similarly, the heat flux computed in 3D and 2D match very well, as can be seen from Figure G-3.

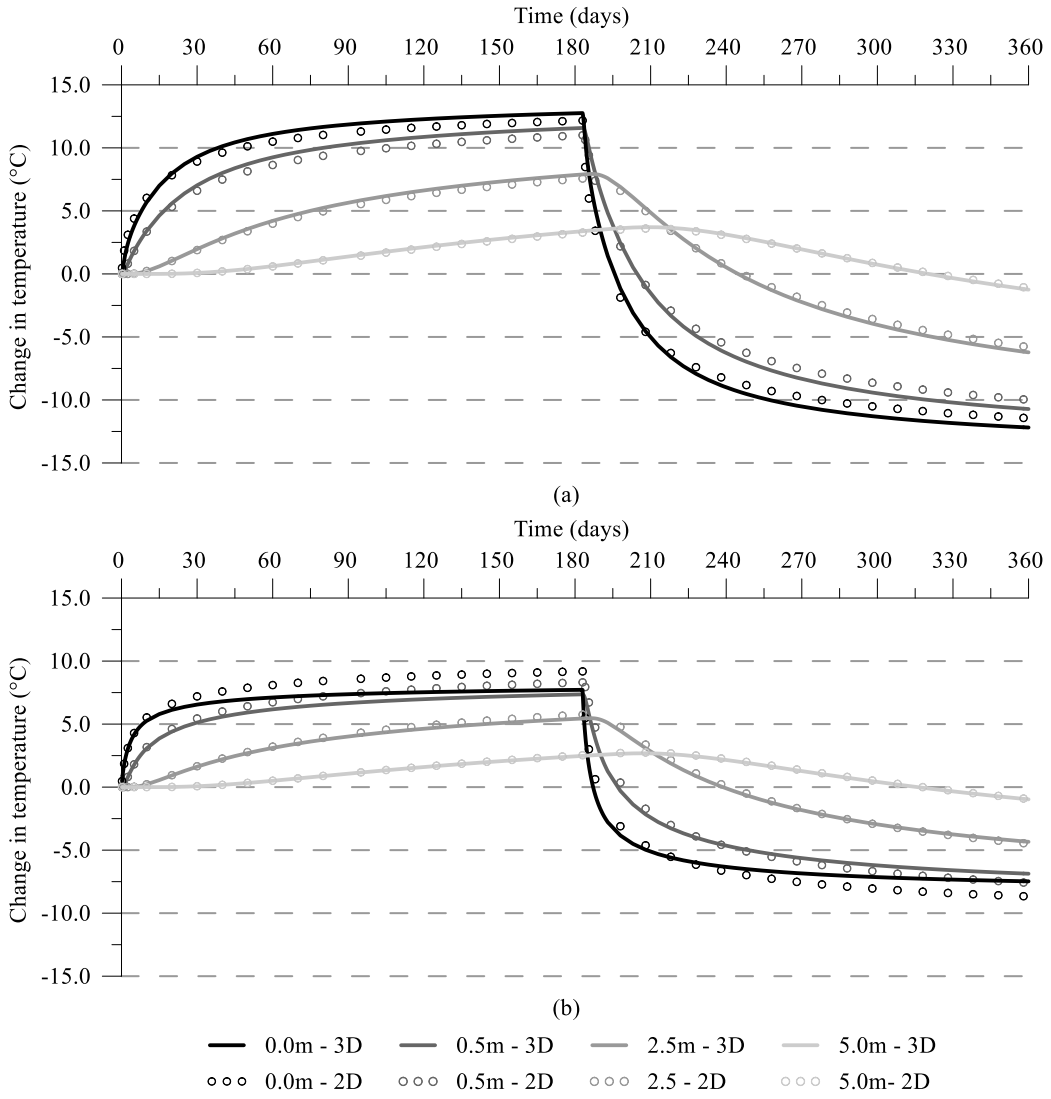

Figure G-2: Comparison between 3D and 2D analyses – Change in temperature at mid-depth of wall at different distances within the retained side (a) NF and (b) CT

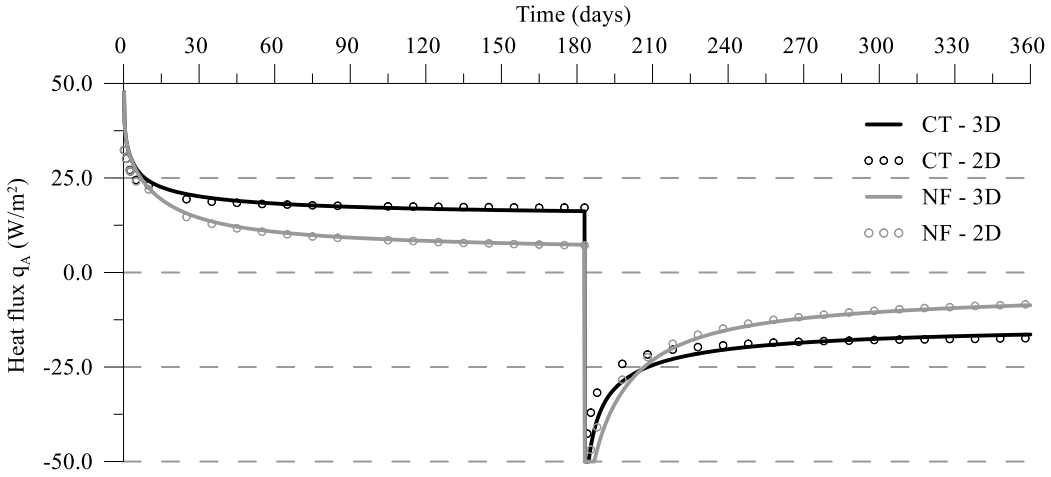

Figure G-3: Comparison between 3D and 2D analyses – Heat flux with time

Figure G-4 and Figure G-5 show the changes in axial forces, which demonstrate the small differences between the values computed in 3D and 2D. A slightly larger discrepancy is recorded for the CT case, which underestimates the tensile and compressive axial forces at the end of the heating and cooling phases respectively by 9.0 kN/m and 15 kN/m.

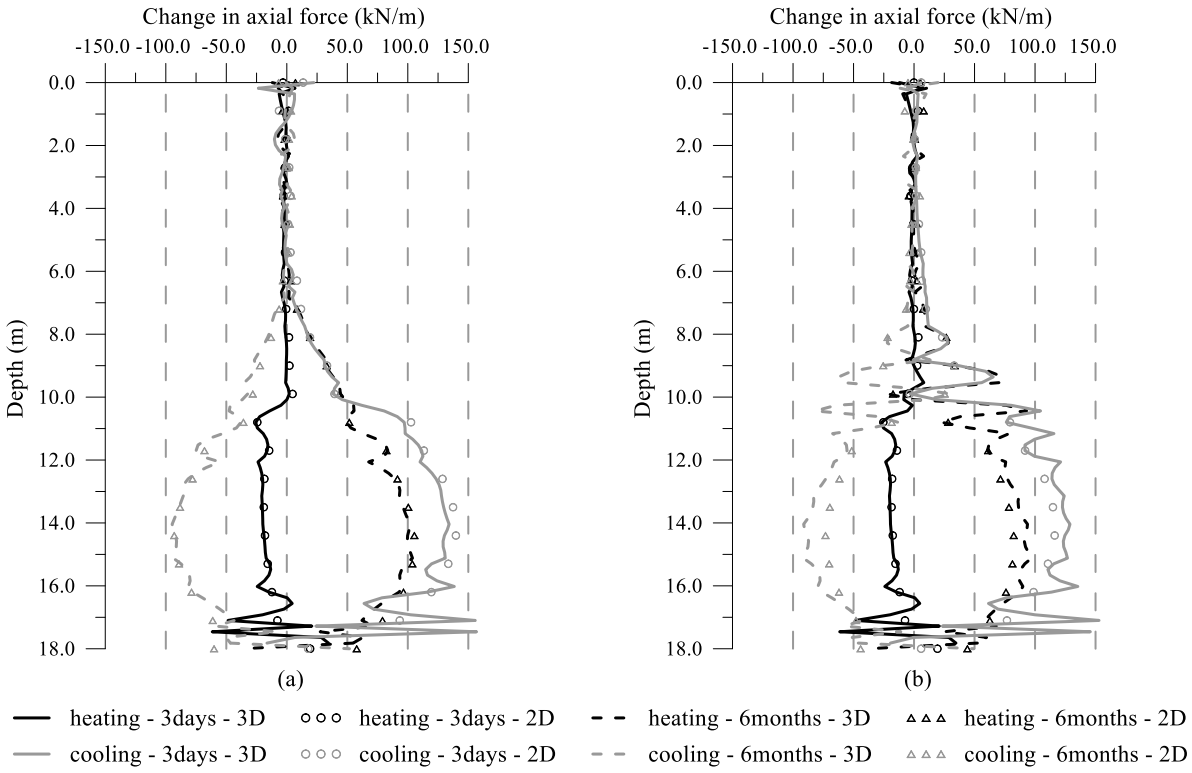

Figure G-4: Comparison between 3D and 2D analyses – Change in axial force with depth for different time instants (a) NF and (b) CT

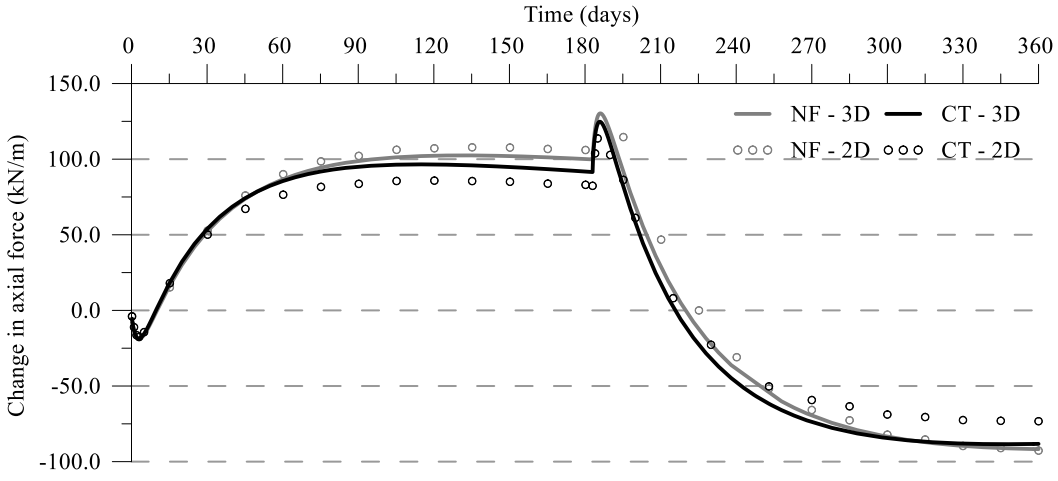

Figure G-5: Comparison between 3D and 2D analyses – Change in axial force with time at depth of 14.0m

The changes in bending moment with depth and time are shown respectively in Figure G-6 and Figure G-7. The 2D analyses are able to capture the changes in bending moment with good accuracy, with a slight overestimation in the peak changes in bending moment for the CT case (36.5 kNm/m (22%) at the end of the heating phase and 28.4 kNm/m (17%) at the end of the cooling phase).

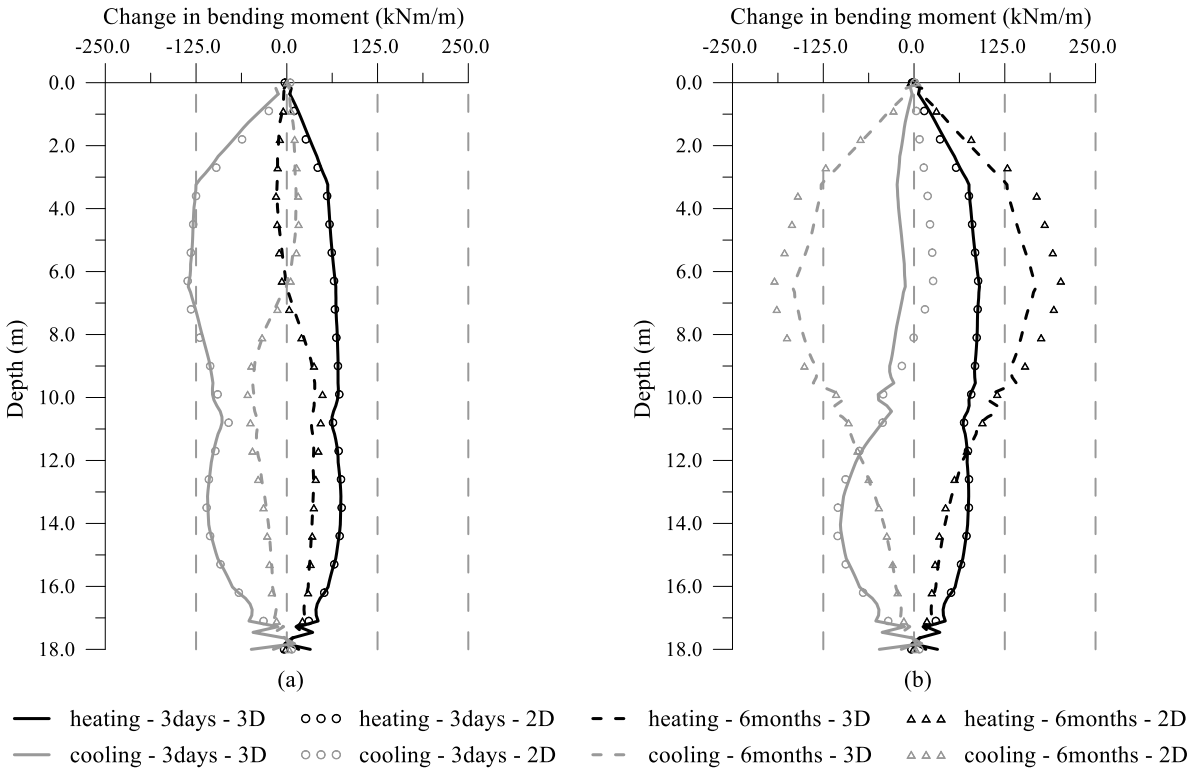

Figure G-6: Comparison between 3D and 2D analyses – Bending moment with depth for different time instants (a) NF and (b) CT

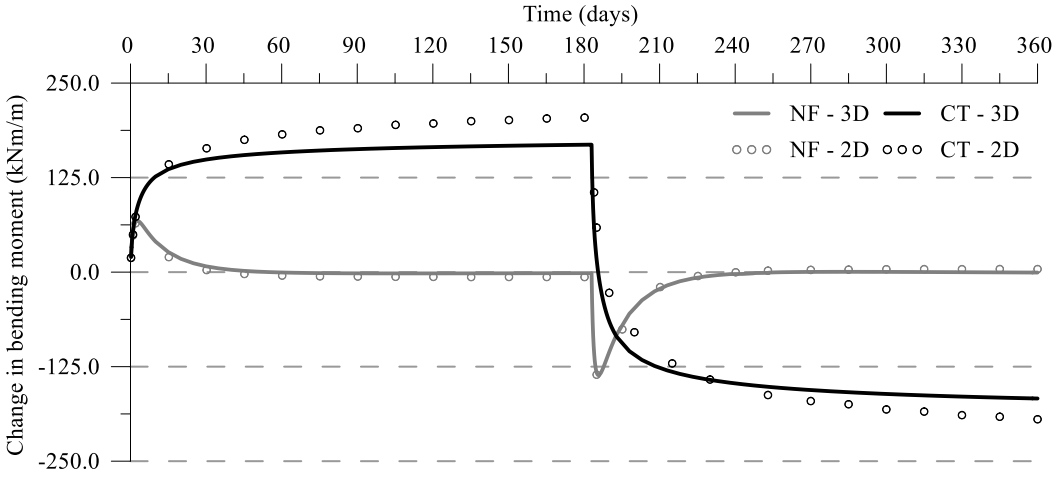

Figure G-7: Comparison between 3D and 2D analyses – Bending moment with time at depth of 6.5m

The comparison of the development of vertical movement of the top of the wall with time computed in 3D and 2D is plotted in Figure G-8. The results obtained in 2D compare very well with the 3D results, where the maximum difference is computed for the NF case at the end of the heating phase. This is equal to 0.33 mm, corresponding to a difference of 8%.

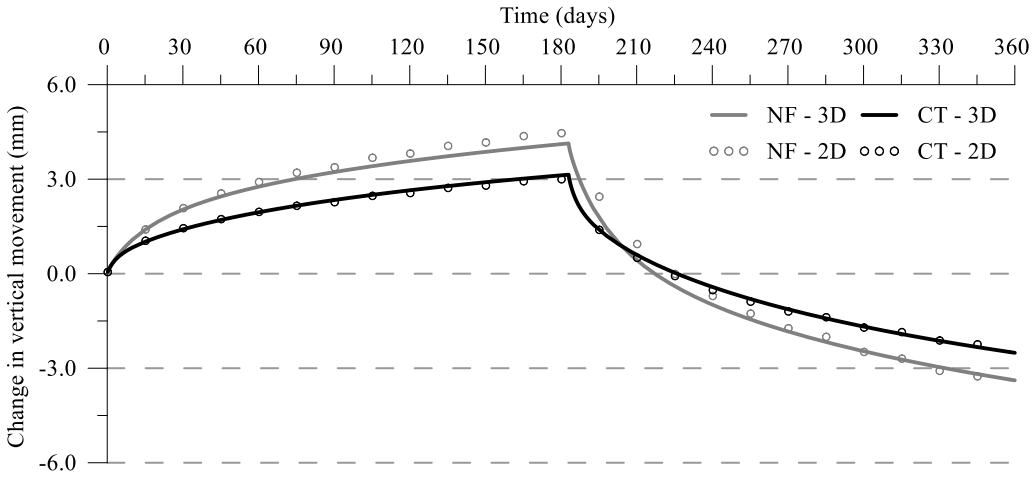

Figure G-8: Comparison between 3D and 2D analyses – Vertical displacement of top of the wall with time